Chem
QD 1
J867
copy 2

THE JOURNAL OF CHEMICAL PHYSICS

VOLUME 23 NUMBER 7

JULY 1955

Published by the
AMERICAN INSTITUTE OF PHYSICS
Incorporated
LANCASTER, PA., AND NEW YORK, N. Y.

THE JOURNAL OF CHEMICAL PHYSICS

BOARD OF EDITORS

CLYDE A. HUTCHISON, JR., *Editor*

Associate Editors

Term ending December 31, 1955	*Term ending December 31, 1956*	*Term ending December 31, 1957*
RICHARD M. BADGER	BRYCE L. CRAWFORD, JR.	JAMES R. ARNOLD
DAVID M. DENNISON	H. S. GUTOWSKY	JACOB BIGELEISEN
JOHN G. KIRKWOOD	WILLIAM N. LIPSCOMB	WALTER GORDY
G. B. KISTIAKOWSKY	ELLIOTT W. MONTROLL	ALVIN H. NIELSEN
A. W. LAWSON	GEORGE SCATCHARD	EARLE K. PLYLER
S. S. PENNER	J. W. STOUT	WAVE H. SHAFFER
ROBERT L. SCOTT	GREGORY H. WANNIER	T. F. YOUNG

THE JOURNAL OF CHEMICAL PHYSICS is published monthly by the American Institute of Physics. Its purpose is to bridge a gap between journals of physics and journals of chemistry. The artificial boundary between physics and chemistry has now been in actual fact completely eliminated, and a large and active group is engaged in research which is as much the one as the other. It is to this group that the Journal is rendering its principal service and makes its greatest appeal, both as a prompt and efficient medium for publication of research and as a convenient and carefully edited assemblage of pertinent information.

Information for Contributors

Send manuscripts to Clyde A. Hutchison, Jr., Editor, *The Journal of Chemical Physics*, Institute for Nuclear Studies, University of Chicago, Chicago 37, Illinois. Unless otherwise stated submission of a manuscript is a representation that it has been neither copyrighted, published, nor submitted for publication elsewhere. Textual material (abstract, body of the paper, tabular material, references, and figure captions) must be in English, typewritten (except mathematical expressions) double spaced with wide margins on a durable, white paper, preferably letter size. The original copy, not the carbon, should be submitted. For general style, spellings, abbreviations, and form, consult recent issues of this journal. The authors' institutions are requested to pay a publication charge of $25.00 per page which, if honored, entitles them to 100 free reprints. Instructions will be sent with galley proofs.

An abstract must accompany each article. It should be adequate as an index and as a summary.

All but the simplest mathematical expressions should be carefully printed in by hand. Be sure to distinguish between capital and small letters. Indicate clearly superscripts and subscripts by inverted carets and carets, respectively. Avoid complicated superscripts and subscripts. Avoid repetition of a complicated expression by representing it by a symbol. Identify in the margin Greek letters and unusual symbols. Use fractional exponents instead of root signs. Use the solidus (/) for fractions wherever its use will save vertical space.

References should appear as footnotes, numbered consecutively. Literature citations of technical journals should be in the form indicated in the Style Manual of the American Institute of Physics and Chemical Abstracts (Chem. Abstracts 45, I-CCLV (1951)).

Tables may be typewritten on sheets separate from the running text. Each table must have a caption which will make the data in the table intelligible without reference to the text. Avoid complicated column headings.

Wherever possible figures should be planned for the width of a column (3 in.). A convenient reduction ratio is about 2:1 or 3:1. Lettering should be large enough on the original that when reduced it shall not be less than about $\frac{1}{16}$ in. (~1.5 mm). Line drawings must be in *india ink* on white paper or tracing cloth. Coordinate paper is not desirable but if used must be blue lined and the coordinate lines which are to show must be inked over. Pictures of apparatus, etc., should be glossy prints and should have maximum black and white contrast. Identify each original drawing or photograph on the back with the author's name and the figure number. Figures should be numbered consecutively. Captions should be typed on a separate sheet of paper.

A limited number of alterations in proof are unavoidable, but the cost of making extensive alterations after the article has been set in type will be charged to the author.

Proof and all correspondence concerning papers in the process of publication should be addressed to the Publication Manager, American Institute of Physics, 57 East 55 Street, New York 22, New York.

Subscription Price

	U. S. and Canada	Elsewhere
To members of the American Institute of Physics and Affiliated Societies	$12.00	$13.00
To all others	15.00	17.00

Back Number Prices

Yearly rate when complete year is available: $18.00.
Single copies: $1.75 each.

Subscriptions, renewals, and orders for single copies should be addressed to the American Institute of Physics, 57 East 55 Street, New York 22, New York.

Changes of address should be sent to the American Institute of Physics.

The Journal of Chemical Physics is published monthly at Prince and Lemon Streets, Lancaster, Pennsylvania.

Entered as second-class matter December 30, 1932, at the Post Office at Lancaster, Pa., under the Act of August 24, 1912. Acceptance for mailing at special rate of postage, provided for in paragraph (d-2), section 34.40, P. L. & R. of 1948, authorized February 3, 1933.

Gift Prof. Halford

THE JOURNAL
OF
CHEMICAL PHYSICS

VOLUME 23, NUMBER 7 JULY, 1955

Quantum-Mechanical Properties of a One-Dimensional System Composed of Hard Spheres*†

ROBERT J. RUBIN
Applied Physics Laboratory, The Johns Hopkins University, Silver Spring, Maryland
(Received October 18, 1954)

The stationary state wave function for a one-dimensional system of hard sphere particles in a box is known to be a determinantal combination of single particle wave functions. The time-dependent wave function corresponding to a certain class of initially prepared states is shown to be a determinantal combination of single particle time-dependent wave functions. The motion of the center of gravity of such a system of particles is especially simple.

I. INTRODUCTION

MOST of the interest in one-dimensional systems of interacting particles derives from the fact that explicit analytic results can be obtained which describe the behavior of the systems. For this reason the classical statistical mechanics of a one-dimensional system of interacting particles has been treated exhaustively.[1–12]

The purpose of this paper is to discuss the quantum-mechanical behavior of a one-dimensional system of hard spheres. It will become apparent that the quantum-mechanical treatment of a system of N hard-sphere particles is simpler than the classical treatment in many respects. As an example, the classical statistical dynamical behavior of a system of N hard-sphere particles involves a combinatorial calculation which is implicit in the determinantal wave function of the quantum-mechanical system treated in Sec. III.

II. STATIONARY STATE EIGENFUNCTIONS AND EIGENVALUES FOR N HARD-SPHERE PARTICLES IN A BOX OF LENGTH a[4,13–15]

The Schrödinger equation for N hard-sphere particles of mass m and diameter b in a one-dimensional box of length $a>Nb$ is identical with the Schrödinger equation for a single particle of mass m in a special region Ω_N of an N-dimensional cube. The boundaries of the region can be defined as follows. Consider the configuration space Ω_N for the N particles if the origin of coordinates is placed at the left end of the box and if the particles are numbered in such a way that the first particle is nearest the origin, the second is next nearest, etc. If x_i is the coordinate of the center of the ith particle, then Ω_N is defined by the conditions:

$$\begin{cases} b/2\leqslant x_1\leqslant x_2-b, \\ x_1+b\leqslant x_2\leqslant x_3-b, \\ \cdots \\ x_{N-1}+b\leqslant x_N\leqslant a-b/2. \end{cases} \tag{1}$$

The boundary conditions for the wave function are that the wave function is zero on the boundary of Ω_N. If we define a new set of variables y_i such that $x_i=y_i$

* A portion of this work was reported at the April 1954 meeting of the American Physical Society; Robert J. Rubin, Phys. Rev. **95**, 643(a) (1945).

† The work reported in this paper was supported by the Bureau of Ordnance, Department of the Navy, under Contract NOrd-7386.

[1] K. F. Herzfeld and M. Goeppert-Mayer, J. Chem. Phys. **2**, 38 (1934).
[2] L. Tonks, Phys. Rev. **50**, 955 (1936).
[3] J. Frenkel, *Kinetic Theory of Liquids* (Oxford University Press, London, 1940).
[4] T. Nagamiya, Proc. Phys. Math. Soc. Japan **22**, 705 (1940).
[5] H. Takahasi, Proc. Phys. Math. Soc. Japan **24**, 60 (1942).
[6] C. W. Ufford and E. P. Wigner, Phys. Rev. **61**, 524 (1942).
[7] G. S. Rushbrooke and H. D. Ursell, Proc. Cambridge Phil. Soc. **44**, 263 (1948).
[8] F. Gürsey, Proc. Cambridge Phil. Soc. **46**, 182 (1950).
[9] L. Van Hove, Physica **16**, 137 (1950).
[10] R. Kikuchi, J. Chem. Phys. **19**, 1230 (1951).
[11] Salzburg, Zwanzig, and Kirkwood, J. Chem. Phys. **21**, 1098 (1953).
[12] Harris, Sells, and Guth, J. Chem. Phys. **21**, 1617 (1953).
[13] R. J. Rubin, Phys. Rev. **95**, 643(a) (1954).
[14] The eigenvalues for such a system were first given by A. Bijl, Physica **4**, 329 (1937). Except for a factor of $\frac{1}{4}$, Bijl's eigenvalues are identical with those obtained by Nagamiya.
[15] The quantum-mechanical system has also been discussed by R. J. Harrison who informed me about Bijl's paper as well as his own abstract. R. J. Harrison, Am. J. Phys. **20**, 399(A) (1952).

$+(i-\frac{1}{2})b$, the set of inequalities in Eq. (1) defining Ω_N can be written in the simpler form

$$0\leqslant y_1\leqslant y_2\leqslant\cdots\leqslant y_N\leqslant a-Nb. \tag{1'}$$

The normalized wave function for a particular stationary state in Ω_N is[4]

$$\Psi_{\mathbf{K}}(\mathbf{x})=D_N\left[\left(\frac{2}{a-Nb}\right)^{\frac{1}{2}}\sin\frac{K_i\pi y_j}{a-Nb}\right], \tag{2}$$

$$=D_N[\psi_i(y_j)],$$

where $D_N(\ )$ is an $N\times N$ determinant whose elements are single particle-in-box wave functions and are defined by a set of N different quantum numbers K_i and the N coordinates y_j, where the vector $\mathbf{K}$ has components K_i such that $K_i<K_j$ for $i<j$ and where $\mathbf{x}$ is the vector whose components are x_i. The energy of the state $\Psi_{\mathbf{K}}(\mathbf{x})$ is[4]

$$E_{\mathbf{K}}=\hbar^2/8m(a-Nb)^2\sum_{i=1}^{N}K_i^2. \tag{3}$$

The density of particles at x or probability per unit length, $\rho(x)$, of finding any particle at x is given by the expression

$$\rho(x)=\langle\Psi_{\mathbf{K}}^*(\mathbf{x})\sum_{r=1}^{N}\delta(x_r-x)\Psi_{\mathbf{K}}(\mathbf{x})\rangle. \tag{4}$$

III. DYNAMIC BEHAVIOR OF A SYSTEM OF N PARTICLES

With explicit expressions for the wave functions of a system of N interacting particles, one can prepare initial "nonequilibrium" states and investigate their evolution in time. For example, one can study the nonequilibrium system whose classical analog is a one-dimensional gas expanding into a vacuum or the more general case of the expansion of a high-density gas into a low-density gas at a different temperature. The properties of the one-dimensional system of particles can be described as follows. Consider the one-dimensional box of length a divided into two parts of length c and $a-c$ with m and n particles, respectively, in the two portions of the box. Let the initial state of the $m+n=N$ particles be

$$\Psi^{(0)}(\mathbf{x})=D_m\left[\left(\frac{2}{c-mb}\right)^{\frac{1}{2}}\sin\frac{K_i^{(0)}\pi y_j}{c-mb}\right]$$

$$\times D_n\left[\left(\frac{2}{a-c-nb}\right)^{\frac{1}{2}}\sin\frac{K_i^{(0)}\pi(y_j-c+mb)}{a-c-nb}\right], \tag{5}$$

$$=D_m[\phi_i^{(0)}(y_j)]D_n[\phi_i^{(0)}(y_j)],$$

with $x_i=y_i+(i-\frac{1}{2})b$ and $0\leqslant y_1\leqslant y_2\leqslant\cdots\leqslant y_m\leqslant c-mb\leqslant y_{m+1}\leqslant\cdots\leqslant y_N\leqslant a-Nb$ where the first m particles are in a stationary state in c prescribed by the quantum numbers $K_i^{(0)}$, $i=1,\cdots,m$, and the other n particles are in a stationary state in $a-c$ prescribed by the quantum numbers $K_i^{(0)}$, $i=m+1,\cdots,N$, and where $\phi_i^{(0)}$, $i=1,\cdots,m$ and $\phi_i^{(0)}$, $i=m+1,\cdots,N$ defined in Eq. (5), are single particle-in-box wave functions.

The initial state of the system $\Psi^{(0)}(\mathbf{x})$ can be expanded in terms of the set of wave functions $\Psi_{\mathbf{K}}(\mathbf{x})$ of Eq. (2) as follows:

$$\Psi(\mathbf{x},t)=\sum_{\mathbf{K}}a_{\mathbf{K}}\Psi_{\mathbf{K}}(\mathbf{x})\exp(iE_{\mathbf{K}}t/\hbar), \tag{6}$$

where

$$\Psi(\mathbf{x},0)=\Psi^{(0)}(\mathbf{x}),$$

and

$$a_{\mathbf{K}}=\int_{0\leqslant y_1\leqslant\cdots\leqslant y_m\leqslant c-mb}^{(m)}\cdots\int dy_1\cdots dy_m$$

$$\times\int_{c-mb\leqslant y_{m+1}\leqslant\cdots\leqslant a-Nb}^{(n)}\cdots\int dy_{m+1}\cdots dy_N\Psi^{(0)}(\mathbf{x})\Psi_{\mathbf{K}}(\mathbf{x}). \tag{7}$$

The coefficients $a_{\mathbf{K}}$ in Eq. (7) and the multiple sum in Eq. (6) can be evaluated with the aid of the following lemmas.

Lemma 1: If $f(\mathbf{x})$ is a symmetric function of N variables x_i, $i=1,\cdots,N$, then

$$\int_{0\leqslant x_1\leqslant\cdots\leqslant x_N\leqslant a}^{(N)}\cdots\int f(\mathbf{x})d\mathbf{x}=\frac{1}{N!}\int_0^a{}^{(N)}\cdots\int_0^a f(\mathbf{x})d\mathbf{x}. \tag{8}$$

The proof of lemma 1 is self-evident, A permutation of the inequality $0\leqslant x_1\leqslant\cdots\leqslant x_N\leqslant a$ does not change the value of the integral on the left-hand side of Eq. (8) since $f(\mathbf{x})$ is symmetric. There are $N!$ permutations of the x_i's. The sum of the left-hand side for all such permutations is equal to the integral of $f(\mathbf{x})$ over the whole N-dimensional cube, since the whole group of permutations fills the cube.

Lemma 2: If $D_N[\psi_i(x_j)]$ and $D_N[\phi_i(x_j)]$ are two $N\times N$ determinants formed from the sets of N functions $\{\psi_i(x)\}$ and $\{\phi_i(x)\}$ and N variables x_i, then

$$\frac{1}{N!}\int_a^b{}^{(N)}\cdots\int_a^b D_N[\psi_i(x_j)]D_N[\phi_i(x_j)]d\mathbf{x}$$

$$=D_N\left[\int_a^b\psi_i(x)\phi_j(x)dx\right].$$

Lemma 2 has been proved by Landsberg.[16]

Lemma 3: If $D_N[\psi_i(x_j)]$ is an $N\times N$ determinant formed from the set of N functions $\{\psi_i(x)\}$ and N variables x_i, and if $D_m[\phi_i(x_j)]$ is an $m\times n$ determinant ($m<N$)

[16] G. Landsberg, Math. Ann. **69**, 231 (1910).

formed from the set of m functions $\{\phi_i(x)\}$ *and the first m of the N variables* x_i,

$$\frac{1}{m!}\int_a^{b(m)}\cdots\int_a^b dx_1\cdots dx_m D_N[\psi_i(x_j)]D_m[\phi_i(x_j)]$$

$$=\begin{vmatrix}\int_a^b \phi_1(x)\psi_1(x)dx\cdots\int_a^b \phi_1(x)\psi_N(x)dx\\ \vdots\qquad\qquad\vdots\\ \int_a^b \phi_m(x)\psi_1(x)dx\cdots\int_a^b \phi_m(x)\psi_N(x)dx\\ \psi_1(x_{m+1})\quad\cdots\quad\psi_N(x_{m+1})\\ \vdots\qquad\qquad\vdots\\ \psi_1(x_N)\quad\cdots\quad\psi_N(x_N)\end{vmatrix}.$$

Lemma 3 is a generalization of lemma 2 and can be proved in an identical manner.

The coefficients a_K can now be evaluated by using lemmas 1 and 3 in Eq. (7). Since the product integrand $\Psi^{(0)}(\mathbf{x})\Psi_K(\mathbf{x})$ is symmetric in the permutation of the set of variables y_i, $i=1,\cdots,m$ and in the permutation of the set of variables y_i, $i=m+1,\cdots,N$, a_K can be written using lemma 1 twice as

$$a_K=\frac{1}{m!n!}\int_0^{c-mb}{}^{(m)}\cdots\int_0^{c-mb}dy_1\cdots dy_m$$

$$\times\int_{c-mb}^{a-Nb}{}^{(n)}\cdots\int_{c-mb}^{a-Nb}dy_{m+1}\cdots dy_N\Psi^{(0)}(\mathbf{x})\Psi_K(\mathbf{x}). \quad (9)$$

Using lemma 3 twice Eq. (9) becomes

$$a=\begin{vmatrix}\int_0^{c-mb}\phi_1{}^{(0)}(y)\psi_{K_1}(y)dy\cdots\int_0^{c-mb}\phi_1{}^{(0)}(y)\psi_{K_N}(y)dy\\ \vdots\qquad\qquad\vdots\\ \int_0^{c-mb}\phi^{m(0)}(y)\psi_{K_1}(y)dy\cdots\int_0^{c-mb}\phi^{m(0)}(y)\psi_{K_N}(y)dy\\ \int_{c-mb}^{a-Nb}\phi_{m+1}{}^{(0)}(y)\psi_{K_1}(y)dy\cdots\int_{c-mb}^{a-Nb}\phi_{m+1}{}^{(0)}(y)\psi_{K_N}(y)dy\\ \vdots\qquad\qquad\vdots\\ \int_{c-mb}^{a-Nb}\phi_N{}^{(0)}(y)\psi_{K_1}(y)dy\cdots\int_{c-mb}^{a-Nb}\phi_N{}^{(0)}(y)\psi_{K_N}(y)dy\end{vmatrix} \quad (10)$$

$$=D_N[a_{iK_j}],$$

where a_{iK_j} is the Fourier coefficient of $\psi_{K_j}(y)$ in the expansion of $\phi_i{}^{(0)}(y)$. The multiple sum in Eq. (6) can now be rewritten as follows:

$$\Psi(\mathbf{x},t)=\sum_{K_1<K_2<\cdots<K_N}D_N[a_{iK_j}]$$

$$\times D_N[\psi_{K_i}(y_j)\exp(i\alpha K_i{}^2t)], \quad (11)$$

where $\alpha=2\pi h/8m(a-Nb)^2$. The summand in Eq. (11) is a symmetric function in the K_j's so the restriction on the summation indices can be removed using the analog of lemma 1 for multiple sums.[17] Equation (11) becomes

$$\Psi(\mathbf{x},t)=\frac{1}{N!}\sum_{K_1=1}^{\infty}\cdots\sum_{K_N=1}^{\infty}D_N[a_{iK_j}]$$

$$\times D_N[\psi_{K_i}(y_j)\exp(i\alpha K_i{}^2t)]. \quad (12)$$

[17] The terms introduced which have $K_i=K_j$ are identically zero.

Finally, Eq. (12) can be transformed using the analog of lemma 2 for multiple sums so that

$$\Psi(\mathbf{x},t)=D_N[\sum_{K=1}^{\infty}a_{iK}\psi_K(y_j)\exp(i\alpha K^2t)],$$

$$=D_N[\psi_i(y_j,t)], \quad (13)$$

where $0\leqslant y_1\leqslant\cdots\leqslant y_N\leqslant a-Nb$ and $x_i=y_i+(i-\frac{1}{2})b$ and where $\psi_i(y_j,t)$ is the single particle time-dependent wave function for the jth particle initially in the state $\phi_i{}^{(0)}$. Thus the time-dependent wave function for the N-particle system is a determinantal combination of single particle wave functions with the restriction $0\leqslant y_1\leqslant\cdots\leqslant y_N\leqslant a-Nb$ on the coordinates.

The density $\rho(x,t)$ cannot be simply obtained for particles of finite size. However, if $b=0$, lemma 1 can

be used to obtain the result that

$$\rho(x,t)=\langle\Psi^*(\mathbf{x},t)\sum_{r=1}^{N}\delta(x_i-x)\Psi(\mathbf{x},t)\rangle, \tag{14}$$

$$=\frac{1}{N!}\int_0^{a^{(N)}}\cdots\int_0^{a}dx_1\cdots dx_N\Psi^*(\mathbf{x},t)\times\sum_{r=1}^{N}\delta(x_i-x)\Psi(\mathbf{x},t). \tag{15}$$

If in the product

$$\Psi^*(\mathbf{x},t)\sum_{r=1}^{N}\delta(x_i-x)\Psi(\mathbf{x},t),$$

the determinants are expanded by the rth column, we obtain after integrating with respect to x_r

$$\rho(x,t)=\frac{1}{N!}\sum_{r=1}^{N}\sum_{i=1}^{N}\sum_{j=1}^{N}\psi_i^*(x,t)\psi_j(x,t)\times\int_0^{a^{(N-1)}}\cdots\int_0^{a'}A_{ir}^*A_{jr}dx_1\cdots dx_N, \tag{16}$$

where the prime following the integration symbol indicates that the integration over x_r has been performed and A_{ir} is the co-factor of $\psi_i(x_r,t)$ in $D_N[\psi_i(x_j,t)]$. Using lemma 2, we find that

$$\int_0^{a^{(N-1)}}\cdots\int_0^{a'}A_{ir}^*A_{jr}dx_1\cdots dx_N=(N-1)!\delta_{ij},$$

since

$$\int_0^{a}\psi_i^*(x,t)\psi_j(x,t)dx=\sum_{K=1}^{\infty}a_{iK}a_{jK} \tag{17}$$

$$=\delta_{ij}.$$

The sum in Eq. (17) can be zero when $i\neq j$ for one of two reasons. Either the function $\psi_i(x,0)$, whose Fourier coefficients are a_{iK} is orthogonal to the function $\psi_j(x,0)$ because $\psi_i(x,0)$ and $\psi_j(x,0)$ are orthogonal on the same interval $[0,c]$ or $[c,a]$ or because $\psi_i(x,0)$ and $\psi_j(x,0)$ are defined such that $\psi_i(x)=0$ for $x\leqslant c$ and $\psi_j(x,0)=0$ for $x\geqslant c$. Thus the density $\rho(x,t)$ can be written

$$\rho(x,t)=\sum_{i=1}^{N}|\psi_i(x,t)|^2.$$

The system of interacting point particles behaves as if there were no interaction. This result is not surprising since the classical motion in a collision between two identical point particles is indistinguishable from the motion of the same two particles in the absence of interaction. If the particles have a nonzero diameter, the same situation no longer obtains and the calculation becomes more involved.[18]

The complication arises in the present case from the fact that the function

$$D_N[\psi_i^*(y_j,t)]\sum_{r=1}^{N}\delta[y_r+(r-\tfrac{1}{2})b-x]D_N[\psi_i(y_j,t)]$$

is not symmetric in the y_j's. However, if instead of calculating the density, one calculates the position of the center of gravity, $\langle x\rangle$, of the distribution of particles, a simple result can again be obtained. The expression for the position of the center of gravity is

$$\langle x\rangle=\frac{1}{N}\langle D_N[\psi_i^*(y_j,t)]\sum_{r=1}^{N}x_rD_N[\psi_i(y_j,t)]\rangle,$$

$$=\frac{1}{N}\langle D_N[\psi_i^*(y_j,t)]\sum_{r=1}^{N}y_rD_N[\psi_i(y_j,t)]\rangle+Nb/2. \tag{18}$$

The average in Eq. (18) can be treated in a manner identical with the treatment of Eq. (14). The final result is

$$\langle x(t)\rangle=\frac{1}{N}\sum_{i=1}^{N}\int_0^{a-Nb}\psi_i^*(y,t)y\psi_i(y,t)dy+Nb/2. \tag{19}$$

Thus the center of gravity of the system of interacting particles of diameter b apart from an additive constant is expressible in terms of the moments of the single particle-in-box probability distribution functions.

The expectation value of the momentum,

$$\langle\Psi_K^*(\mathbf{x},t)\sum_{r=1}^{N}\frac{\hbar}{i}\frac{\partial}{\partial x_r}\Psi_K(\mathbf{x},t)\rangle,$$

for the system being considered can be obtained in the same manner in which the position of the center of gravity was obtained. The result is

$$\langle\Psi_K^*(\mathbf{x},t)\sum_{r=1}^{N}\frac{\hbar}{i}\frac{\partial}{\partial x_r}\Psi_K(\mathbf{x},t)\rangle$$

$$=\sum_{i=1}^{N}\int_0^{a-Nb}\psi_i^*(y,t)\frac{\hbar}{i}\frac{\partial}{\partial y}\psi_i(y,t)dy,$$

$$=\frac{2}{a-Nb}\sum_{J+K=\text{odd}}a_{iJ}a_{iK}\frac{2\hbar JK}{J^2-K^2}\sin at(K^2-J^2). \tag{20}$$

The mean value of a property of the system of hard spheres has again been obtained in terms of a sum of mean values of single particle-in-box wave functions.

[18] G. E. Uhlenbeck and L. Gropper, Phys. Rev. **41**, 79 (1932).

Self-Diffusion in α White Phosphorus*

NORMAN H. NACHTRIEB AND GEORGE S. HANDLER
Institute for the Study of Metals, University of Chicago, Chicago, Illinois
(Received October 5, 1954)

The coefficient of self-diffusion in α white phosphorus from 0° to the melting point is given by the equation

$$D=1.07\times10^{-3}\exp[-9400/RT]+2\times10^{46}\exp[-80\,600/RT]\text{cm}^2\,\text{sec}^{-1}.$$

Only the first term is important for temperatures below 30°, where the vacancy mechanism is believed to operate. The activation energy in this range is in excellent agreement with the value predicted from the latent heat of fusion. A second mechanism begins to become important above 30°, with an activation energy of 80 600 calories and an exceedingly large entropy. This process is interpreted as a comparatively large scale disorder which arises on multiple vacancies. The entropy and energy are consistent with the view that liquid microphase regions containing, on the average, about 130 molecules and 10 distributed vacancies are the principal centers of diffusion near the melting point.

ALTHOUGH diffusion has been studied in many pure metals and alloy systems and in a considerable number of ionic crystals, comparatively little little attention has been devoted to molecular crystals. The only recorded investigations of molecular crystals are those of Cuddeback and Drickamer,[1] who measured the rate of self-diffusion in orthorhombic sulfur, and of Cremer,[2] who studied the rate of self-diffusion in solid hydrogen. A rapid rise in the rate of self-diffusion in sulfur which began about 30° below the transition to monoclinic sulfur was interpreted by Drickamer and Cuddeback as the effect of diffusion anisotropy; the diffusion direction was perpendicular to the ⟨111⟩ family of planes, with the consequence that the departure of the diffusion rate from a simple exponential function of temperature was thought to be due to a linear combination of different diffusion processes occurring simultaneously along two or three crystal axes. Cremer assumed that the *ortho*-parahydrogen conversion is bimolecular in the solid state, and that its rate becomes diffusion-limited when the concentration of parahydrogen molecules reaches a low value. The diffusion coefficients calculated were of the order of 10^{-20} cm^2 sec^{-1} near the melting point, and the activation energy was quite uncertain because of the experimental scatter and the necessarily narrow temperature range.

In view of the simple correlation which has been found to exist between the activation energy for self-diffusion in cubic metals and their latent heats of fusion,[3] it is of considerable importance to determine whether a similar relation obtains in crystals in which the cohesive energy is qualitatively different in origin. Molecular crystals, in which the cohesive energy is principally van der Waals in origin, *ionic crystals*, in which the binding is mainly the result of Coulomb forces, and *valence crystals*, wherein quantum-mechanical exchange energy plays the major role, are all possibilities for an experimental test of the range of validity of the relation

$$\Delta H_{\text{Act}}=CL, \tag{1}$$

where ΔH_{Act} is the activation energy for self-diffusion, L is the latent heat of fusion, and C is a constant, having the value 16.5 for face-centered and body-centered cubic metals. An interpretation of Eq. (1) has been given by the authors,[4] in which it is assumed that volume diffusion in crystals occurs as a result of the creation and movement of microphase regions which have the energy content of liquid. The microphase regions are postulated to arise at lattice vacancies by the spontaneous inward relaxation of the neighboring and next-neighboring atoms. Support for such a modified vacancy mechanism of diffusion is afforded by sodium metal, for which the pressure-dependence of the activation volume for self-diffusion parallels the pressure dependence of the volume change on melting. The self-diffusion coefficient is uniquely determined by pressure and temperature *or by the reduced temperature* T_m/T *alone:*

$$D=f(T,P)=\phi(T_m/T). \tag{2}$$

The effective number of atoms which participate in vacancy relaxation is given approximately by

$$g=\Delta V_{\text{Act}}/\Delta V_m, \tag{3}$$

where ΔV_m is the molar volume change on fusion and ΔV_{Act}, the activation volume for diffusion, is defined by

$$\Delta V_{\text{Act}}=-RT\left(\frac{\partial \ln D/\gamma a^2\nu}{\partial p}\right)_T$$

and is of the order of 14. The substance of this point of view is that diffusion, in cubic metals at least, may be more correctly discussed as a small scale cooperative

* This research was supported in part by contract with the U. S. Air Force, the sponsoring agency being the Aeronautical Research Laboratory of the Wright Air Development Center, Air Research and Development Command.

[1] R. B. Cuddeback and H. G. Drickamer, J. Chem. Phys. **19**, 790 (1951).

[2] E. Cremer, Z. physik. Chem. **B39**, 445 (1938).

[3] Nachtrieb, Catalano, Weil, and Lawson, J. Chem. Phys. **20**, 1189 (1952).

[4] N. H. Nachtrieb and G. S. Handler, Acta Metallurgica **2**, 797 (1954).

phenomenon having some similarity to fusion, rather than the elementary act of an atom moving into the site of an adjacent vacancy with essentially no participation by other atoms in the vicinity. In two essential respects the simple vacancy theory and the relaxation theory agree: (1) both are equilibrium defect theories, and (2) the concentration of defect (simple vacancy or energetically liquid region) is the same for both for a given pressure and temperature. They differ in two major respects: (1) the experimental activation energies are usually less than half the latent heat of sublimation required by the simple vacancy mechanism as a minimum, and (2) the experimental activation volume is of the order of half the molar volume required by the simple vacancy theory. In each of the latter instances the relaxed vacancy model provides an explanation which is consistent with experiment.

The only self-diffusion measurements reported for valence crystals are those of Letaw, Slifkin, and Portnoy[5] on germanium. The experimental activation energy is 73 500 cal/g atom, in disagreement with the value of 122 000 predicted by (1) with $C=16.5$. There is, however, no reason to suppose that the number of atoms involved in relaxation about a vacancy in a diamond type lattice should be the same as it is for body-centered or face-centered cubic metals. The latter have 12 nearest neighbors and the former have 8 nearest and 6 nearly equidistant next-nearest neighbors, while the diamond lattice has only 4 nearest and 12 comparatively remote next-nearest neighbors surrounding a given atom. α white phosphorus was selected for the present study primarily because it is a molecular crystal having cubic symmetry, presenting, therefore, no obvious problems of diffusion anisotropy. The unit cell was reported by Natta and Passerini[6] to have an edge length of 7.17 A and to contain 4 molecules. Recent work by Corbridge and Lowe[7] indicates that the lattice parameter is 18.51±0.03 A, however, in good agreement with the unpublished results of Frevel[8] who found $a_0=18.66\pm0.10$ A. According to Corbridge and Lowe the unit cell contains 56 molecules, whose positions have not yet been assigned. The space group is one of the following: *I432*, *I 43m*, *Im 3m*, and is therefore body-centered in any case. The nearest atom distance is assumed to be 2.21 A, in accordance with the prevailing evidence that white phosphorus consists of P_4 molecules in the form of regular tetrahedra in the liquid state and even in the vapor state up to very high temperatures. Corbridge and Lowe were unable to arrange 56 molecules in the unit cell in model experiments without appreciable overlap, however, and suggested that "an explanation of the structure may be found in some peculiar effect of the thermal motion on the packing arrangements." A high degree of thermal motion at −30°C was inferred from the rapid decrease in intensity of the Laue spots for $\rho \gtrsim 1.0$. This may be a key to the curious anomaly in the diffusion rate discussed in Sec. D.

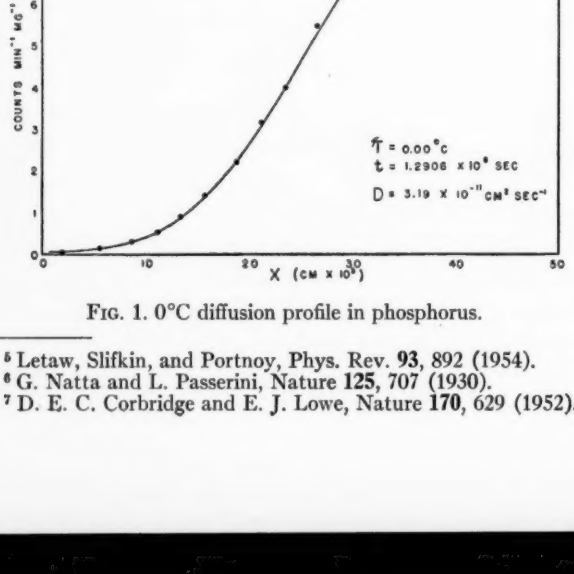

FIG. 1. 0°C diffusion profile in phosphorus.

A. Preparation of Phosphorus

The radioactive tracer used for the diffusion experiments was P^{32}, a 1.712-Mev β emitter with a 14.30-day half-life. It was prepared by neutron irradiation of red P^{31} in the thermal pile at the Oak Ridge National Laboratory. The red phosphorous, sealed in evacuated quartz capsules, underwent some conversion to white phosphorus during the 14-day irradiation periods. The capsules were crushed under water and the red phosphorus was recovered by sedimentation, followed by washing with alcohol and ether. On one occasion the material ignited when insufficient water was provided to exclude the inrush of air. White phosphorus was produced by vacuum distillation at 500°C under red light. Some reconversion to red phosphorus usually occurred during the distillation, but a water-white product could always be obtained from the colored distillate by filtration of the liquid under distilled water. For this purpose fritted glass disks of medium porosity were sealed into syringe-operated pipets. There appeared to be little, if any, solubility of the red form in liquid white phosphorus as judged by the absence of color in the filtered material. White phosphorus so obtained showed the usual pronounced tendency to supercool, but had a sharp melting point under water of 44.14°C (NBS thermometer No. L5874). Ordinary white phosphorus was prepared in the same manner by distillation *in vacuo*. It remained water white for months under protection of water with only occasional exposure to daylight. The radioactive phosphorus, on the other hand, became yellow in a matter of a day or so, the color development progressing visibly each day and necessitating filtration prior to use. When the

[5] Letaw, Slifkin, and Portnoy, Phys. Rev. **93**, 892 (1954).
[6] G. Natta and L. Passerini, Nature **125**, 707 (1930).
[7] D. E. C. Corbridge and E. J. Lowe, Nature **170**, 629 (1952).
[8] L. K. Frevel, Dow Chemical Company, Midland, Michigan (private communication).

specific activity had fallen to a comparatively low value, the rate of yellowing appeared to be correspondingly reduced.

B. Diffusion Experiments

The general method of preparing diffusion couples was similar to that used in the study of self-diffusion in sodium,[9] with the following differences. Liquid phosphorus was pipeted under protection of water into hardened stainless steel dies to provide cylinders 0.2500 in. diam. and 0.2500 in. long. Freezing of the undercooled phosphorus usually occurred at about 30°C and invariably produced an internal cavity. An excess of phosphorus was used, so that the solid could be compressed to fill the dies completely and provide a flashing which could be trimmed off immediately prior to assembly of the dies. The ordinary and radioactive phosphorus cylinders were aged near the melting point for about twenty-four hours to permit grain growth. The average grain size of the polycrystalline phosphorus was about 0.1 mm. Welding of the cylinders was accomplished by application of a pressure of 8000 psi for two minutes on the assembled dies. The composite cylinder was then extruded from the dies and transferred to a thermostat for the diffusion experiment. All of the foregoing operations were performed under freshly boiled distilled water, and during the diffusion anneal the phosphorus cylinder was contained in a capped glass vial under distilled water. The oil thermostat was of conventional design, with provision for constant circulation of cold water through copper coils and heating by means of knife-blade type immersion heaters. Temperatures were controlled to within ±0.05°C from 0° to 44°C.

The phosphorus cylinders were sectioned under distilled water at 0°C with a simple microtome, immediately following each diffusion anneal. In no case did the shrinkage cavities occur in the region of importance in the cylinders. Serial sections, approximately 0.002 in. thick in the vicinity of the boundary, were transferred to glass vials containing about 1 cm³ of water and were oxidized to phosphoric acid by the addition of excess bromine in carbon tetrachloride (10 percent solution by volume). The resulting two-phase liquid was evaporated in glass planchets under an infrared lamp, and the phosphoric acid was neutralized by the drop-wise addition of 1*M* NaOH to the color change point of thymolphthalein. Uniform deposits of Na_2HPO_4, suitable for beta counting, were obtained by spin-drying. The activity due to P^{32} was determined with a methane flow counter operated as a proportional counter at 4000 v. At least 10^4 counts above background were accumulated for each section, and the combined error due to statistical errors in counting and to variations in deposit uniformity was less than 2 percent.

[9] Nachtrieb, Catalano, and Weil, J. Chem. Phys. **20**, 1185 (1952).

TABLE I. Diffusion in white phosphorus.

T(°C)	D(cm² sec⁻¹)
0.00	3.19×10^{-11}
10.00	6.07×10^{-11}
18.70	1.07×10^{-10}
25.00	1.40×10^{-10}
30.00	1.75×10^{-10}
39.40	3.94×10^{-10}
41.30	4.58×10^{-10}
41.88	5.91×10^{-10}
42.82	8.01×10^{-10}
43.86	$>8\times10^{-10}$

Corrections for radioactive decay during the counting of a complete series of sections were necessitated by the short half-life of P^{32}.

The phosphorus content of each section was determined spectrophotometrically by means of the colored complex which orthophosphate develops in perchloric acid solution with ammonium molybdate and ammonium vanadate.[10] The mean error in the chemical determination of phosphorus was within 2 percent, and entered into the calculation of both the specific activity and the thickness of each section. Diffusion anneals varied from 24 hours to one month, depending upon the temperature; in all cases, the diffusion time was known to within 0.5 percent, and usually to within 0.1 percent.

Diffusion coefficients were calculated in the usual manner after the construction of the diffusion profile, a typical one of which is shown in Fig. 1.

C. Experimental Results

The results of ten diffusion experiments at temperatures ranging from 0°C to 43.86°C are recorded in Table I. Figure 2 shows a plot of log$D$ *vs* $1/T$, with the surprising fact that the data deviate from a straight line for temperatures above 30°C. The heat of activation for self-diffusion in the range of temperature from 0°C to 30°C (hereafter designated as range I) is calculated from the relation

$$\Delta H_I=\left[-R\frac{d\log D}{d(1/T)}\right]_P \tag{4}$$

to be 9400 cal/mole with a probable error of 225 cal/mole. The data for range I are fitted by the least squares equation

$$D_I=1.07\times10^{-3}\exp[-9400/RT]. \tag{5}$$

The data for the temperature range, 30°C to the melting point (range II) may be regarded as the linear combination of two simultaneous rate processes:

$$D_{\text{obs.}}=D_I^0\exp[-\Delta H_I/RT]+D_{II}^0\exp[-\Delta H_{II}/RT] \tag{6}$$

[10] H. H. Willard and E. J. Center, Ind. Eng. Chem., Anal. Ed. **13**, 81 (1941).

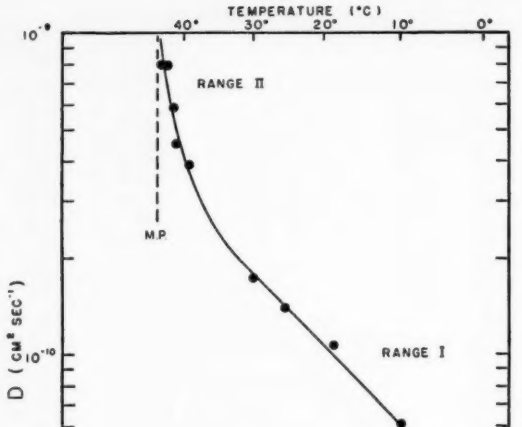

FIG. 2. Plot of log D *versus* $1/T$.

with $D_{II}^0=2\times10^{46}$ cm² sec^{-1} and $\Delta H_{II}=80\,600$ cal/mole. D_{II}^0 and ΔH_{II} are not known with high accuracy, of course, but the treatment of range II as a linear combination of simultaneous competing diffusion mechanisms is an acceptable, if not unique, representation of the data.

D. Interpretation of Results

Several interpretations of the results presented above are conceivable. In the first place, it must be recalled that all measurements were made on polycrystalline phosphorus, and the possibility may not easily be dismissed that surface or grain boundary diffusion may be involved. Diffusion profiles of both range I and range II are linear when $C/2C_0$ is plotted on arithmetic probability paper *versus* X, as Fig. 3 indicates. This is a criterion which is sometimes used to distinguish volume diffusion from grain boundary diffusion. It seems likely, however, that neither this "test" of the data nor Fisher's grain boundary analysis[11] really serves to distinguish diffusion along the boundaries between equi-axed grains from intragranular volume diffusion. Fisher's method is applicable only to diffusion along twin boundaries.

In the absence of diffusion data for single crystals, we have two alternatives: range I may be due primarily to grain boundary diffusion, with volume diffusion becoming important in range II. On the other hand, if range I is normal volume diffusion, range II must be some additional bulk diffusion mechanism which becomes important at higher temperatures. There are several objections to the first suggestion. For one, an activation energy for volume diffusion of the order of 80 kcal is difficult to reconcile with so soft and low melting a substance as phosphorus. A simple vacancy mechanism would be excluded, since the latent heat of vaporization is only 14.04 kcal[12] and places an upper limit on the energy of vacancy formation. D_0 for range I is comparatively small (1.07×10^{-3} cm² sec^{-1}) by the standards of careful work on self-diffusion in isotropic metals, in which D_0 usually lies between 0.1 and 10. It is comparable with D_0 values found for grain boundary or liquid diffusion. Zener's D_0 theory,[13] applied without modification, would lead to a negative entropy of activation and would imply some "short-circuiting path" such as grain boundary diffusion. It is doubtful that Zener's theory is applicable to molecular crystals, however. Drickamer and Cuddeback[1] report $D_{\perp c}^0=8.32\times10^{-12}$ cm² sec^{-1} for single crystals of orthorhombic sulfur, where no question of grain boundary diffusion enters.

If we pursue the second alternative and regard range I as normal volume diffusion, we note that the experimental activation energy ($\Delta H_I=9400$ cal/mole) is in excellent agreement with the value predicted by Eq. (1) (9920 cal/mole) with the latent heat of fusion[14] equal to 601 cal/mole. We conclude that diffusion in range I is the random walk of relaxed vacancies. We note also that the single bond energy of phosphorus[15] is 44 kcal and conclude that P_4 molecules and their vacancies are the diffusing species, not smaller fragments.

We may now explore several possible explanations of range II under the assumption that it is volume diffusion. Any explanation must be consistent with the very large activation energy (80.6 kcal) and the enormous pre-exponential factor (2×10^{46}). The latter, even if correct only within many orders of magnitude, has no explanation in any current theory of D_0. In this connection, it is worth noting that Cuddeback and Drickamer found $D^0_{\parallel c}=1.78\times10^{36}$ cm² sec^{-1} for orthorhombic sulfur, and Seith reported[16] $D_{\perp c}^0=2.4\times10^{46}$ cm² sec^{-1} for bismuth. Clearly it is inexplicable in terms of atom jump distances of the order of Angstrom units and characteristic lattice frequencies in the vicinity of 10^{13} sec^{-1}, since the product $a^2\nu$ is of the order of 10^{-3}. If so large a D_0 is a physically meaningful number it must necessarily be because the remaining factor in it ($e^{\Delta S/R}$) is of the order of 10^{49}, and the entropy itself is in the neighborhood of 250 eu (eu = entropy unit). A mechanism with so large a molar entropy must

[11] J. C. Fisher, J. Appl. Phys. **22**, 74 (1951).

[12] F. S. Dainton and H. M. Kimberley, Trans. Faraday Soc. **46**, 912 (1950).

[13] C. Zener, J. Appl. Phys. **22**, 372 (1950).

[14] F. Young and J. Hildebrand, J. Am. Chem. Soc. **64**, 839 (1942).

[15] Y. Syrkin and M. Dyatkina, *Structure of Molecules* (Interscience Publishers, Inc., New York, 1950) p. 235.

[16] W. Seith, Z. Elektrochem. **39**, 558 (1933).

involve many times Avogadro's number of molecules. We may immediately rule out such simple possibilities as the direct interchange of a pair of molecules or the jumps of interstitial molecules, because the entropy of activation would be too small for either of these processes. The possibility that diffusion in range II is preceded by the dissociation of P_4 molecules into P_2 fragments or P atoms is also readily discounted, since the enthalpy and entropy of these species are quite well known from spectroscopic and calorimetric studies.[17] Less than 10^{-47} atom fraction of P atoms would be present at room temperature, and, although the fraction of P_2 molecules is very much larger (10^{-16}), the entropy of formation is far too small (37 eu) in comparison with the requirements of our D_0.

We are left with the conclusion that some fairly large scale cooperative phenomenon must be operative in range II. Let us postulate that the process involves the formation of disordered or premelted regions in the lattice on a scale which is an order of magnitude larger than the lattice relaxation[4] which occurs around single vacancies. The cause of the assumed premelting does not appear to be impurities in the sense of foreign atoms. The major impurity was 0.006 percent arsenic, which would theoretically depress the freezing point only 0.006°C if uniformly distributed but completely insoluble in the solid phosphorus; as noted, the material melted at 44.13°C with no perceptible range. The disordering effect of arsenic atoms on the phosphorus lattice might be quite long range on the scale of lattice dimensions if liquid solutions of arsenic in phosphorus showed large negative deviations from Raoult's law. This would be highly unexpected, and no effects of this kind are found in solid sodium[18] of comparable purity; in that substance the heat of activation for diffusion in the solid is constant to within 0.08°C of the melting point.

Frenkel[19] has developed a general theory of heterophase fluctuations which includes premelting as a special case. It is premelting in Frenkel's sense that is assumed to be responsible for range II. The disordered regions differ from simple relaxations in that a larger number of atoms or molecules is involved, with a correspondingly larger number of distributed lattice vacancies. Following a suggestion of Mott,[20] let us assume that the free energy of formation of a mole of n-molecular disordered or premelted clusters is given by

$$\Delta F_m = nL(1-T/T_m), \tag{7}$$

where L is the latent heat of fusion. On this supposition,

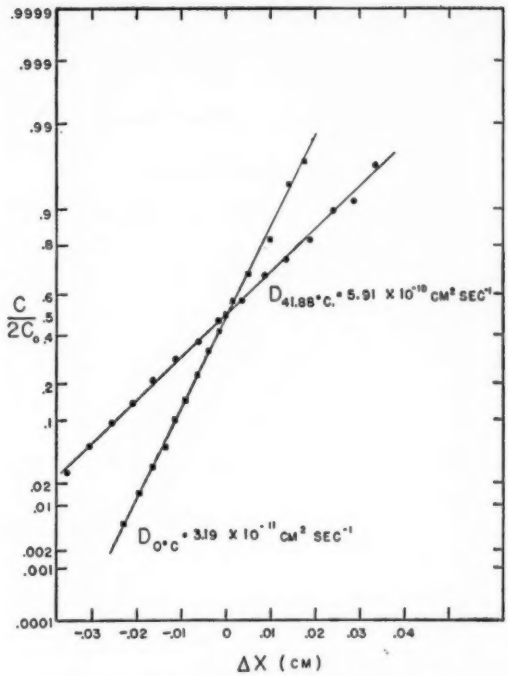

FIG. 3. Diffusion profiles on probability plot.

the diffusion coefficient in range II should be given by

$$D_{II} = K \exp^{-}\left(\frac{nL(T_m-T)}{RTT_m}\right) \tag{8}$$

and a plot of log D_{II} *versus* $(T_m-T)/T$ should be linear. Figure 4 shows such a plot, which is a severe test of the data. The points scatter considerably from a straight line but lie within the experimental uncertainty. The mean number $\bar{n}$ of molecules per cluster, averaged over the temperature range T to T_m, is calculated from the slope of Fig. 4 to be 126. This compares quite well with cluster sizes (150 molecules) estimated by Frenkel[21] for typical simple substances near their melting points.

We now assume that these comparatively large clusters are free to move about in the solid and to accomplish net atom movements thereby. The nature of their movement must now be considered. Any particular atom or molecule in a moving cluster is the property of the cluster for a very short period of time. The cluster passes through the crystal lattice like a wave packet and the atoms or molecules in its path undergo net displacements which amount only to an interatomic distance, on the average. On the other hand, the vacancy volume of the cluster moves over large distances and remains a part of the cluster until the latter disappears at a surface or a grain boundary. In support of this view, we note that the specific heats of simple solids and liquids differ only slightly at the melting point and infer that the same major vibrational

[17] D. M. Yost and H. Russell, *Systematic Inorganic Chemistry* (Prentice-Hall, Inc., New York, 1944) p. 168.
[18] R. E. Meyer and N. H. Nachtrieb (to be published).
[19] J. Frenkel, *Kinetic Theory of Liquids* (Oxford University Press, New York, 1946).
[20] N. F. Mott, *L'Etat Solide*, Solvay Conference (Stoops, Brussels, 1952) p. 518.
[21] Reference 19, p. 390.

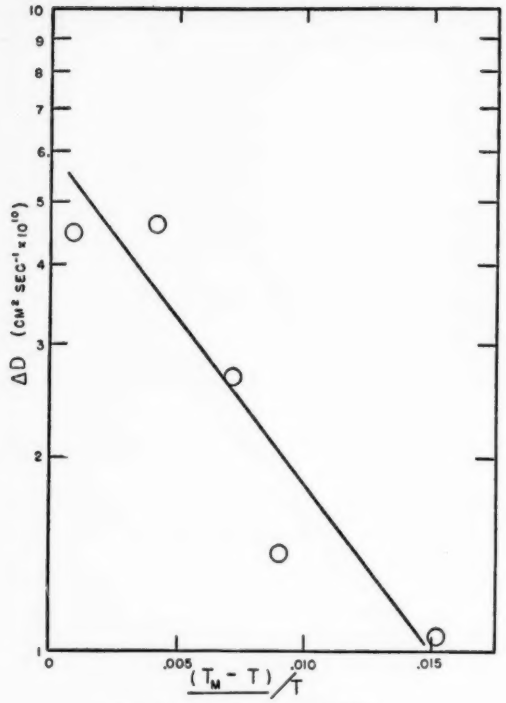

FIG. 4. Log ΔD *versus* $\Delta T/T$.

modes dominate the thermal spectra of both states. Fluctuations in the phonom spectrum, which are responsible for the random walk movement of clusters, would appear to be quite similar in both states. The consequence is that a cluster moves with about the same mean velocity in the solid as it does in the liquid. The same remarks apply to a simple relaxed vacancy, and we may say that a moving vacancy "doesn't know" whether it is in a crystalline environment or in a liquid. So to speak, a vacancy is always in a "liquid" environment.

If this be so, we may relate the rates of diffusion in the solid and liquid states: the ratio of the rates is then simply the concentration of liquid in the solid. We define the liquid at its melting point as the standard state and identify K in Eq. (8) with $f_L a^2 \nu \exp-[\Delta F_L/RT]$, where f_L is the mole fraction of liquid in solid at the melting point, i.e., the "solubility" of liquid in solid at $T=T_m$; a is the interatomic distance in the liquid; ν is the characteristic frequency in the liquid; and ΔF_L is the activation free energy for self-diffusion in the liquid. Equation (8) becomes

$$D_{II}=a^2\nu \exp[-\Delta F_L/RT] \cdot f_L \exp[-(\bar{n}L(T_m-T)/RTT_m]. \quad (9)$$

The product of the first three terms is simply the diffusion coefficient for the liquid. The remainder is simply the concentration of liquid in the solid, or the probability that a given atom is in a liquid microphase at temperature T. The last term may be separated into two terms: $\exp[\bar{n}L/RT_m]$ and $\exp[-\bar{n}L/RT]$. $\bar{n}L/T_m$ is the average entropy of formation and $\bar{n}L$ the mean enthalpy of formation of the liquid microphase in the temperature range T to T_m. Subtitution of $\bar{n}=126$ into these terms gives for ΔS: 239 eu, and for ΔH: 75 700 cal/mole. Here it should be noted that this ΔH does not include the enthalpy of activation for liquid diffusion, which is included in ΔH_{II} as it appears in Eq. (6). Equation (9) and the last term of Eq. (6) are equivalent, of course, with f_L as an adjustable parameter. f_L has a value of about 10^{-3} and is in good agreement with estimates[4] of the fraction of liquid in solid sodium at its melting point. It seems reasonable that a law of corresponding states may exist for all simple solids, in which the liquid fraction in the solid at the melting point is approximately constant and equal to *ca* 10^{-3}. This is equivalent to a limiting density of lattice vacancies at the melting point for simple substances.

The presence of a microscopic heterophase should be revealed in various bulk properties of the solid if the concentration is sufficiently large. Thus, the coefficient of thermal expansion, refractive index, specific heat, and compressibility should, in principle, show some anomaly beginning about 30°C and continuing to the melting point. This assumes that "normal" behavior of these properties is recognizable. We might assume, for example, that the coefficient of thermal expansion would be independent of temperature in the absence of multiple vacancy clusters, and attribute observed deviations to the latter. The thermal expansion of phosphorus *does* show[22] a small temperature dependence, amounting to 0.010 cm^3 $mole^{-1}$, integrated from 25° to the melting point. If we made the reasonable assumption that there is about 50 percent volume relaxation in the formation of 10-vacancy complexes, the formation volume would be approximately 350 cm^3 $mole^{-1}$. For $f_L=10^{-3}$ at T_m, corresponding to one cluster in 10^5 molecules, a mole of phosphorus need expand only 3.5×10^{-3} cm^3 $\cdots$, well within the observed value.

The energy required to form 10^{-5} moles of multivacancy complexes would be only 0.8 calories. Even the best calorimetric data are not sufficiently precise[23] to indicate so small an increase in the heat content of phosphorus over a 10° temperature interval up to the melting point.

It appears that diffusion is an exceedingly sensitive tool for the study of the solid-liquid phase change, and that other physical properties must be measured with high precision to reveal the pretransition phenomena which make solid state diffusion possible. It is interesting to speculate upon whether the anomalous diffusion here described is an isolated case, or whether it is an exaggerated instance of a very general phenomenon. Simple cubic metals appear to possess but one diffusion mechanism up to the melting point. Drickamer,[24]

[22] N. H. Nachtrieb. (to be published).
[23] G. T. Maple, Ph.D. dissertation, Massachusetts Institute of Technology, Cambridge (1952).
[24] R. Eckart and H. G. Drickamer, J. Chem. Phys. **20**, 13 (1952).

however, has found evidence for pretransitional effects in solid indium (tetragonal) which appear to be very like range II in phosphorus, except that the temperature interval is only about 0.5°C. The diffusion anisotropy in bismuth[16] with its very large entropy and enthalpy perpendicular to the C-axis suggests a cooperative mechanism. The anomalous rise in ionic conductivity in silver bromide[25] beginning over 100° below the melting point may be associated with heterophase fluctuations. In this substance there is a very pronounced rise in the heat capacity, which is noticeable over 150° below the melting point.[26] Conceivably, the kind of diffusion anomaly which appears in phosphorus and which may be present in certain other substances is possible only in solids which can tolerate multiple vacancies *below the melting point.*

[25] S. W. Kurnick, J. Chem. Phys. **20**, 218 (1952).

ACKNOWLEDGMENTS

It is a pleasure to acknowledge the many helpful discussions the authors have had with Professor A. W. Lawson and with Dr. G. Wasserburg.

[26] R. W. Christy and A. W. Lawson, J. Chem. Phys. **19**, 517 (1951).

THE JOURNAL OF CHEMICAL PHYSICS VOLUME 23, NUMBER 7 JULY, 1955

Effect of Pressure on Self-Diffusion in White Phosphorus*

NORMAN H. NACHTRIEB AND A. W. LAWSON
Institute for the Study of Metals, The University of Chicago, Chicago, Illinois

(Received October 5, 1954)

Pressure decreases the rate of self-diffusion in α white phosphorus. At 30°C the activation volume is 30 cm³, a value which indicates that considerable lattice relaxation takes place about vacancies. At 41.30°C the activation volume is about an order of magnitude larger, a behavior consistent with a view that lattice disordering on a comparatively large scale begins well below the melting point.

INTRODUCTION

ISOTHERMAL rate studies with pressure as the variable can provide valuable information relative to the activation volume for the process involved. This is readily apparent if the rate constant is expressed as an exponential function of the activation free energy. For diffusion, for example, we may write

$$D=\gamma a^2\nu \exp[-\Delta F/RT]. \quad (1)$$

The activation volume is defined by the variation in the free energy with pressure at constant temperature:

$$\Delta V_{\text{act}}=\left(\frac{\partial \Delta F}{\partial P}\right)_T=-RT\left(\frac{\partial \log(D/\gamma a^2\nu)}{\partial P}\right)_T. \quad (2)$$

It is convenient to regard the activation volume to be composed of two terms when the mechanism of diffusion requires a lattice imperfection, *viz.*, interstitial atoms or lattice vacancies. Thus,

$$\Delta V_{\text{act}}=\Delta V_{\text{form}}+\Delta V_{\text{mob}}, \quad (3)$$

where ΔV_{form} is the volume change resulting from the creation of a mole of defects, and ΔV_{mob} is the further volume change attending the simultaneous movement of a mole of defects. It is important to note that a mole of defects *may* involve very much more than Avogadro's number of molecules. ΔV_{mob} is always positive, but ΔV_{form} may be either positive or negative, depending upon whether vacancies or interstitial atoms are required by the mechanism. ΔV_{form} has the value zero for mechanisms like direct interchange, which require no lattice imperfection of any kind. If there were no lattice relaxation about a newly created vacancy, ΔV_{form} would be equal to the gram atomic volume. An inward movement of the atoms surrounding a vacancy would decrease ΔV_{form} to a value intermediate between zero and the gram atomic volume. Conversely, an outward movement of atoms neighboring a lattice vacancy would require ΔV_{form} to exceed the gram atomic volume. The determination of ΔV_{act} is therefore capable of shedding considerable light upon the nature of the lattice imperfection.

In the case of sodium metal,[1] ΔV_{act} is 12.4 cm³ at atmospheric pressure—approximately one-half the gram atomic volume. The conclusion that neighboring atoms move inward upon a newly formed vacancy is unambiguous. The mean interatomic distance in the small volume element around a vacancy must therefore be somewhat larger than in the perfect lattice. The heat content of a mole of such n-atomic volume elements is equal to $\bar{n}L$, where L is the latent heat of fusion and $\bar{n}$ is approximately 12 for cubic metals. Activation volumes are not known for other solids, but it appears that silver,

* This research was supported in part by contract with the United States Air Force, the sponsoring agency being the Aeronautical Research Laboratory of the Wright Air Development Center, Air Research and Development Command, and by contract with the Office of Naval Research.

[1] Nachtrieb, Weil, Catalano, and Lawson, J. Chem. Phys. **20**, 1189 (1952).

gold, copper, α iron, and cobalt may have activation volumes about half as large as their molar volumes from the fact that they all conform to the simple relation

$$\Delta H_{\text{act}} = 16.5L. \tag{4}$$

EXPERIMENTAL

Atmospheric pressure studies[2] of self-diffusion in white phosphorus indicate that for temperatures below 30°C the activation energy is quite accurately given by Eq. (4). For temperatures above 30°C, a second diffusion mechanism enters, which appears to be lattice disordering or premelting with an average cluster size of about 130 molecules. To test these conclusions we have carried out two series of isothermal diffusion runs at various pressures for the purpose of obtaining activation volume for the two processes.

The experimental procedures have been described.[1,2] Temperature control of the thermostatted high-pressure bomb which contained the diffusion couples was within ±0.05°C. Pressure was controlled to within ±10 kg cm^{-2}. The data for isotherms at 30.00°C and 41.30°C are summarized in Table I. Figure 1 shows plots of log D *versus* pressure for the two temperatures. The activation volume calculated from the slope of the 30° isotherm by means of Eq. (2) is 30.0 cm^3. The data are not sufficiently accurate to permit a very good calculation of the anomalous activation volume at 41.30°C. However, a rough value of 210 cm^3 at 1 atmosphere is obtained. The calculation involves extrapolation of the 30° diffusion coefficients to 41.30° and their subtraction from the observed diffusion coefficients at the latter temperature. The limiting slope of the logarithm of the *difference* plot *versus* pressure gives the activation volume for the anomalous process of range II. The value is not very accurate for several reasons, the most important of which is that small errors in the measured values become relatively large when differences are taken. Moreover, only the atmospheric pressure value of $D_{30°}$ can be accurately extrapolated to 41.30°, because ΔH is not known as a function of pressure.

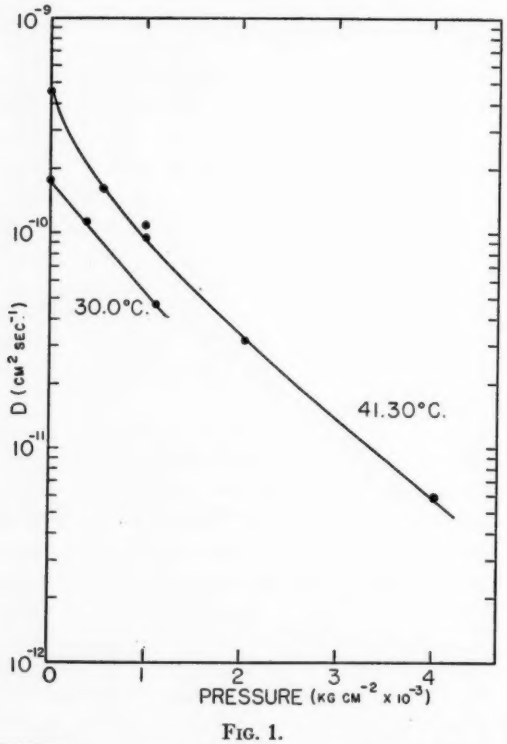

FIG. 1.

INTERPRETATION OF RESULTS

The significance of the activation volume at 30° is quite evident. Since the molar volume of white phosphorus is 68.2 cm^3, vacancy relaxation takes place with an inward displacement of the neighboring molecules. Over half of the initial vacancy volume escapes the crystal, and the remainder is probably locally distributed among the nearest dozen or so surrounding molecules. Below 30° the relaxation of single vacancies in white phosphorus is essentially the same process as it is in cubic metals.

Although the accuracy with which the activation volume is known is poor at higher temperatures, some qualitative conclusions may be drawn. An activation volume significantly larger than the molar volume must mean one of two things. If single vacancies only are involved, it could mean that they enlarge after creation by the *outward* movement of the neighboring molecules.

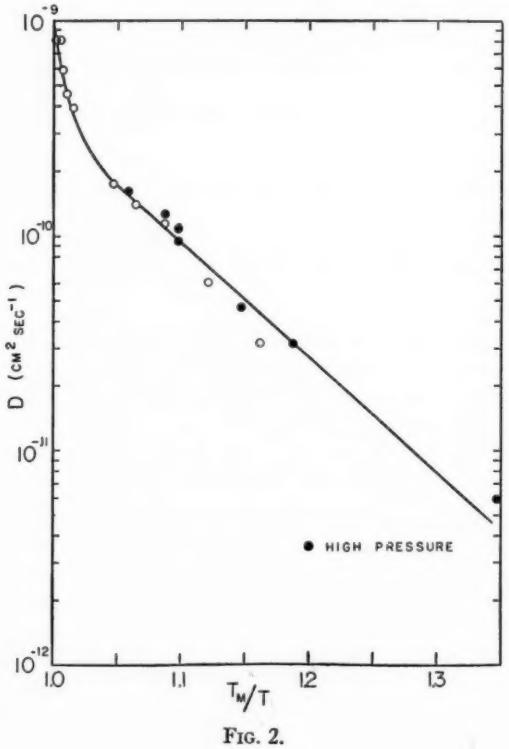

FIG. 2.

[2] N. H. Nachtrieb and G. S. Handler, J. Chem. Phys. **23**, 1187 (1955), preceding paper.

The enormous entropy of activation[2] would find no explanation if this were the case, however. Alternatively, the large activation volume could arise if extensive lattice disordering or premelting occurs as a thermally activated process. We may estimate the activation volume in several ways, accepting $\bar{n}=126$ as the average number of molecules per cluster, and with the relative volume change on fusion equal to 3.5 percent. The activation volume, given by the product of the molar volume times the volume change on melting times the number of molecules per cluster, is 300 cm³. Essentially the same value is obtained if the volume is taken to be proportional to the heat content. In this case, the activation volume is approximately given by the product of the low-temperature activation volume (30 cm³) by the ratio of the enthalpies of activation. The agreement between the expected activation volume and the value estimated from our measurements is well within the limits of our experimental uncertainty.

TABLE I. Diffusion coefficients in white phosphorus at various pressures.

P (kg cm^{-2})	T (°K)	D (cm^2 sec^{-1})
1	303.16	1.75×10^{-10}
437	303.30	1.13×10^{-10}
1088	303.30	4.65×10^{-11}
1	314.46	4.58×10^{-10}
541	314.42	1.61×10^{-10}
994	314.42	9.47×10^{-11}
994	314.42	1.09×10^{-10}
2032	314.42	3.18×10^{-11}
4012	314.42	5.93×10^{-12}

Figure 2 represents all of the data on self-diffusion in white phosphorus on a reduced temperature plot. A single straight line represents diffusion for all temperatures below 30°C at atmospheric pressure, and for all temperatures up to 41.30° at higher pressures. High pressures have the effect of raising the melting point, so that range I (relaxed vacancy diffusion) includes all (P,T) conditions for which $T_m/T\geqslant 1.05$.

THE JOURNAL OF CHEMICAL PHYSICS VOLUME 23, NUMBER 7 JULY, 1955

Methyl Alcohol. I. Microwave Spectrum*

PUTCHA VENKATESWARLU,† HOWARD D. EDWARDS,‡ AND WALTER GORDY
Department of Physics, Duke University, Durham, North Carolina
(Received September 7, 1954)

The $J=0\rightarrow1$, $K=0\rightarrow0$ rotational lines of methyl alcohol have been observed and identified with the Stark effect for $C^{12}H_3O^{16}H$, $C^{13}H_3O^{16}H$, $C^{12}H_3O^{16}D$, $C^{13}H_3O^{16}D$, $C^{12}D_3O^{16}H$, and $C^{12}D_3O^{16}D$. These lines are obtained not only for the molecules in the ground state but also for those in the first two torsional excited states, $n=1$ and $n=2$. All these lines except those of the $C^{12}D_3O^{16}D$ were observed to be doublets, the doublet separation being different for different molecules. Some further experimental data on $C^{12}D_3O^{16}H$, $C^{12}H_3O^{16}D$, and $C^{13}H_3O^{16}H$ are included in this paper.

INTRODUCTION

AN investigation of the microwave spectrum of methyl alcohol in the region of 6 mm was begun in this laboratory a few years back. Numerous lines of various isotopic species were found and measured, but they could not be identified with certainty because at that time a Stark spectrometer which would operate at 6 mm wavelength with the necessary sensitivity to identify the lines was not available. For this reason the results were not submitted for publication although the line frequencies were listed in a progress report,[1] with tentative assignment of the 0→1 lines based on a reasonable structural determination. The 0→1 transition for six different isotopic species have now been ascertained from their Stark components. The earlier tentative assignments proved to be incorrect. In addition, one of the earlier samples was incorrectly identified by the Company[2] which supplied it, so that a large number of lines of CD_3OH in the region of 30 to 45 kMc were incorrectly assigned to CD_3OD.

Hughes, Good, and Coles[3] measured the microwave spectra of $C^{12}H_3O^{16}H$, $C^{13}H_3O^{16}H$, and $C^{12}H_3O^{18}H$ below 40 000 Mc using a Stark cell. They identified the J and ΔJ values for most of the lines they measured, but did not observe the lines corresponding to the $J=0\rightarrow1$ transitions because these lines lie above the region they studied.

* This research was supported by the U. S. Air Force through the Office of Scientific Research of the Air Research and Development Command.
† Now at the Department of Physics, Muslim University, Aligarh, India.
‡ Now at the Air Force Cambridge Research Center.
[1] Edwards, Gilliam, and Gordy, Quarterly Progress Report, November, 1949. Also H. D. Edwards, Ph.D. thesis, Duke University, 1950.
[2] A chemical company, by some error which is not known to us, supplied to this laboratory a sample of CD_3OH which was specified as CD_3OD but which had only faint traces of this form.
[3] Hughes, Good, and Coles, Phys. Rev. 84, 418 (1951).

TABLE I. Observed frequencies of the rotational transitions $J=0\rightarrow1$, $K=0\rightarrow0$ of methyl alcohol in the ground state.

Molecule	Frequency ν in Mc/sec	$\Delta\nu$ in Mc/sec	Average frequency in Mc/sec
$C^{12}H_3O^{16}H$	48 377.09 48 372.60	4.49	48 374.8
$C^{13}H_3O^{16}H$	47 209.63 47 205.20	4.43	47 207.4
$C^{12}H_3O^{16}D$	45 359.43 45 344.30	15.13	45 351.9
$C^{13}H_3O^{16}D$	44 241.43 44 228.26	12.17	44 234.4
$C^{12}D_3O^{16}H$	39 069.25 39 066.21	3.04	39 067.7
$C^{12}D_3O^{16}D$	36 799.01	...	36 799.0

EXPERIMENTAL METHOD

The spectra were observed with a Stark-effect modulation spectrograph. A 100-kc pulse square wave modulation was employed. The energies above 38 000 Mc were obtained from a 1N26 multiplier driven by a K-band klystron. The absorption cell was made of a $2\frac{1}{2}$ foot long K-band wave guide, the inner surface of which was gold plated. The center electrode was supported with Teflon in the manner described by McAfee, Hughes, and Wilson.[4] Different Stark voltages ranging from 12 to 1000 volts were used. Type 1N53 crystals were used as detectors. The energy signal was taken from the crystal through a preamplifier to a phase-sensitive lock-in amplifier[5] which was coupled to a phase shift amplifier. The lock-in detector and the amplifiers were all tuned to the 100-kc fundamental frequency of the square wave generator. From the output of the lock-in amplifier the absorption signal was taken to a cathode-ray oscillograph for the display of the lines on the oscillograph. The signal was also taken to an Esterline-Angus recorder for recording the lines. With this system the Stark components point downward, and the zero field line points upward. All the lines observed in the present experiments were recorded in this way as it is necessary to study their pattern to identify their rotational transitions. Except for the weak lines all the lines were also displayed on the cathode-ray oscillograph.

Measurements of the lines were made at pressures of about 10^{-3} mm at dry-ice temperatures. The frequencies of the lines were measured[5] with frequency markers produced by multiplying to the microwave region a 5-Mc signal from a crystal-controlled oscillator. The 5-Mc signal was monitored by comparison with the standard 5-Mc frequency broadcast signal of the station WWV. The errors involved in the frequency measurements of the lines are not expected to be more than 0.5 Mc.

The sample $C^{13}H_3O^{16}H$ was the same as that used by Edwards[1] *et al.* The samples $C^{12}H_3O^{16}D$ and $C^{13}H_3O^{16}D$ were made in this Laboratory by Dr. Albert Jache. Both of these samples contained some impurities which were more volatile than methyl alcohol, and they were purified by the process of fractional distillation. The present work has been done with two samples of $C^{12}D_3O^{16}H$. One was obtained from the Tracerlab.[6] The other was the sample that was mistaken, as mentioned earlier, to be $C^{12}D_3O^{16}D$. The actual samples of $C^{12}D_3O^{16}D$ were made in this Laboratory by Dr. Jache from the two previously mentioned samples of $C^{12}D_3O^{16}H$. A mixture of small quantities of $C^{12}D_3O^{16}H$ and D_2O was heated for about five days in a sealed bulb at about 200°C to obtain $C^{12}D_3O^{16}D$. The samples of $C^{12}D_3O^{16}D$ obtained in this way contained few traces of $C^{12}D_3O^{16}H$, but this did not create any difficulty because the $C^{12}D_3O^{16}D$ lines that were measured were not overlapped by the $C^{12}D_3O^{16}H$ lines.

TABLE II. Observed frequencies of the rotational transitions $J=0\rightarrow1$, $K=0\rightarrow0$ of methyl alcohol in the excited states of torsional oscillation $n=1$ and $n=2$.

Molecule	Quantum number of the torsional oscillation	Frequency ν in Mc/sec	$\Delta\nu$ in Mc/sec	Average frequency in Mc/sec
$C^{12}H_3O^{16}H$	$n=1$	48 257.49 48 247.89	9.60	48 252.7
	$n=2$	48 192.12 48 178.0±1.0	14	48 185.0
$C^{13}H_3O^{16}H$	$n=1$	47 094.11 47 083.82	10.29	47 089.0
	$n=2$	47 030.16 47 019.5±1.0	10.7	47 024.8
$C^{12}H_3O^{16}D$	$n=1$	45 265.78 45 259.44	6.34	45 262.6
	$n=2$	45 193.36 45 189.46	3.90	45 191.4
$C^{13}H_3O^{16}D$	$n=1$	44 151.09 44 144.06	7.03	44 147.6
	$n=2$	44 079.30 44 076.55	2.75	44 077.9
$C^{12}D_3O^{16}H$	$n=1$	38 982.88 38 972.05	10.83	38 977.5
	$n=2$	38 928.89 38 923.97	4.92	38 926.4
$C^{12}D_3O^{16}D$	$n=1$	36 730.94	...	36 730.9
	$n=2$	36 673.93	...	36 673.9

$J=0\rightarrow1$ ROTATIONAL LINES

One of the fundamental vibrations of methyl alcohol is to be associated with the torsional motion of the

[4] McAfee, Hughes, and Wilson, Rev. Sci. Instr. **20**, 821 (1949).
[5] Gordy, Smith, and Trambarulo, *Microwave Spectroscopy* (John Wiley and Sons, Inc., New York, 1953).
[6] Tracerlab, Inc., 130 High Street, Boston 10, Massachusetts.

hydroxyl group with respect to the methyl group. Because of this torsional motion which is also called the hindered rotation, there will be a set of energy levels whose positions for high potential barrier are given by $h\nu_t(n+\frac{1}{2})$, where ν_t is the torsional frequency of the molecule and n is the quantum number of the torsional oscillation. Each of these levels with $n=0, 1, 2, \cdots$ etc is split into three sublevels identified by the quantum number $\tau=1$, 2, or 3. This splitting is caused by the potential with three identical minima which the hydrogen of the hydroxyl group encounters during its rotation about the symmetry axis of the methyl group. The splitting is a periodic function of K, the quantum number of the component of the angular momentum along the symmetry axis of the methyl group. Thus the energy levels of the methyl alcohol molecule which is an asymmetric hindered rotator will be represented by the quantum numbers n, τ, K, and the total angular momentum quantum number J. There are, of course, the quantum numbers of the other 11 different vibrations of the molecule which are of no importance for the present purpose.

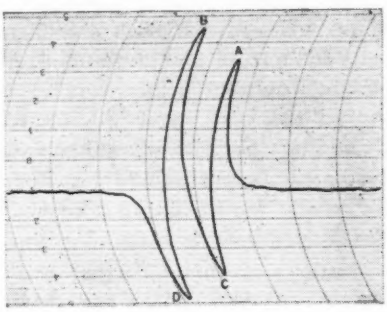

FIG. 1. The $J=0\rightarrow1$, $K=0\rightarrow0$, $n=0\rightarrow0$ lines of $C^{12}D_3O^{16}H$. The lines marked C and D are the Stark components of the lines A (39 066.2 Mc/sec) and B (39 069.3 Mc/sec).

The first lines of the normal rotational lines, namely $J=0\rightarrow1$, $K=0\rightarrow0$, $\tau=1\rightarrow1$, $\tau=2\rightarrow2$ or $\tau=3\rightarrow3$ have been measured for six different isotopic species of methyl alcohol. When K is equal to 0, the levels with $\tau=2$, and $\tau=3$ are degenerate. Therefore, for our present transitions we expect to get doublets instead of triple lines. Such doublets have been observed for $C^{12}H_3O^{16}H$, $C^{13}H_3O^{16}H$, $C^{12}H_3O^{16}D$, $C^{13}H_3O^{16}D$, and $C^{12}D_3O^{16}H$, the doublet separation being considerably different in the different molecules. The frequencies of the rotational lines including the respective doublet separations are given in Table I. The doublet could not be resolved for the zero field line of $C^{12}D_3O^{16}D$, but the Stark component resolves into two lines at Stark voltages higher than 300 volts.

The rotational lines $J=0\rightarrow1$, $K=0\rightarrow0$ were observed not only for the ground state $n=0$, but also for the excited states $n=1$ and $n=2$. The frequencies of the rotational lines for the different isotopic species in the two excited states are given in Table II.

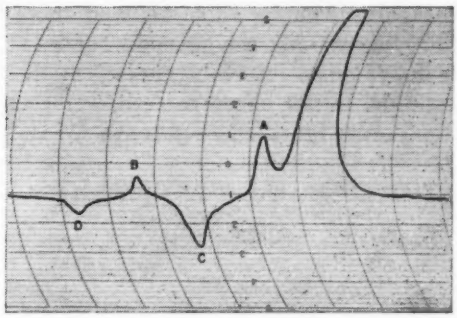

FIG. 2. The $J=0\rightarrow1$, $K=0\rightarrow0$, $n=1\rightarrow1$ lines of $C^{12}D_3O^{16}H$ at 38 972.1 and 38 982.9 Mc/sec marked A and B, respectively.

The rotational lines and their Stark components of the molecule $C^{12}D_3O^{16}H$ for the ground state $n=0$ are shown in Fig. 1, and those for the excited states $n=1$ and $n=2$ are shown in Figs. 2 and 3, respectively. For the molecule in the ground state $n=0$ or excited state $n=2$, the high-frequency line in the rotational doublet is more intense than the low-frequency lines. This shows that the low-frequency line probably corresponds to the transition $J=0\rightarrow1$, $K=0\rightarrow0$, and $\tau=1\rightarrow1$, whereas the high-frequency line corresponds to the degenerate transitions $\tau=2\rightarrow2$ and $\tau=3\rightarrow3$ with $J=0\rightarrow1$ and $K=0\rightarrow0$. For the molecule in the excited state $n=1$, the high-frequency line is weaker than the low-frequency line and therefore corresponds to $\tau=1$, whereas the other corresponds to the degenerate levels $\tau=2$ and $\tau=3$.

For the molecules $C^{12}H_3O^{16}H$, $C^{13}H_3O^{16}H$, $C^{12}H_3O^{16}D$, and $C^{13}H_3O^{16}D$ the two components of the rotational doublets in the ground state are of about the same intensity; but in the excited states, $n=1$ and $n=2$, the relative intensity of the components in all these molecules is similar to that for $C^{12}D_3O^{16}H$—that is, the low-frequency component is more intense for the excited state $n=1$, whereas the high-frequency component is more intense for the excited state $n=2$.

SPECTRUM OF CD_3OH IN THE REGION 43 502 – 1700 Mc

The frequencies of the spectral lines of $C^{12}D_3O^{16}H$ in the region 43 502–35 700 Mc excluding those caused

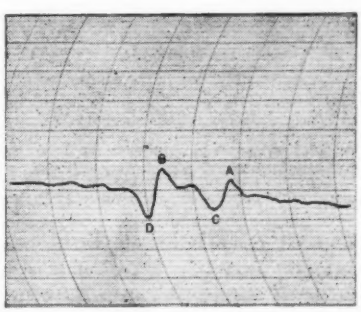

FIG. 3. The $J=0\rightarrow1$, $K=0\rightarrow0$, $n=2\rightarrow2$ lines of $C^{12}D_3O^{16}H$ at 38 924.0 and 38 928.9 Mc/sec marked A and B, respectively.

by $J=0\rightarrow1$ are given in Table III and those in the region 28 800–17 900 Mc are given in Table IV. These lines can be classified into four kinds: (1) those that show first-order Stark effect pattern, (2) those that show second-order Stark effect pattern, (3) those that show a pattern that is a mixture of the first- and second-order Stark effects, and (4) those that form doublets the components of which have second-order Stark effect pattern where the Stark coefficient of the high-frequency component has a negative sign whereas that of the low-frequency component has a positive sign. The magnitude of the Stark coefficient of the high-frequency component is in general larger than that of the low-frequency component. All the lines that come under the fourth kind are given in Table IV.

TABLE III. The spectrum of CD_3OH in the region 43 502–35 740 Mc.

Frequency Mc/sec	Intensity	Order of Stark effect	Number of Stark components	Lower J	$\pm\Delta J$
43 501.5	S	2	6	5	1
43 453.7[a]	S	mixture of 1st and 2nd orders	2 on hf side and 3 on lf side	2	1
43 325.0	S	mixture	not resolved		
42 292.1	M	1	partially resolved	>5	1
42 163.8	W	1	not resolved		1
41 684.6	M	1	partially resolved		0
40 649.5[b]	M	mixture of 1st and 2nd orders	2 on lf side and 3 on hf side	2	1
40 229.8	S	1	not resolved		0
38 967.6[c]	S	1	not resolved		
38 132.8[d]	M	2	1 (?)		
38 052.6	M	1	9 (?)		1
37 900.0	S	1	partially resolved		0
37 462.6[e]	M	mixture			
37 322.8[f]	S	2			
37 229.8[g]	S	mixture of 1st and 2nd orders	2 on lf side and 3 on hf side	2	1
36 663.0[h]	S	1	8 (?)		
36 483.9	M				
36 422.9[h]	M	1	13 (?)		1
36 332.7	M	1	not resolved		0
35 810.8 35 805.7	M M		not resolved		
35 748.2	S	1	4	4	1

[a] The Stark shifts can be represented by a formula $\Delta\nu=aME-(b+cM^2)E^2$ where E is electric field strength, M is the quantum number of the component of the angular momentum in the direction of the electric field, and a, b, and c are constants; a is greater than both b and c. The third component on the low-frequency side which shows up at voltages higher than 100 v corresponds to $M=0$ while the other two correspond to $M=1$ and $M=2$.

[b] The Stark shifts can be represented by a formula of the type $\Delta\nu=aME+(b+cM^2)E^2$ where a is greater than both b and c.

[c] The line 38 961.6 Mc is present also in CD_3OD.

[d] The Stark component of this line is not resolved but broadens at very high voltages. This component does not move much with increase in voltage.

[e] The Stark pattern is a mixture of first and second orders. Probably this has four Stark components on each side, but those on the high-frequency side move faster. Those on the low-frequency side are more intense.

[f] Up to 400 volts, this line appears to have one Stark component which does not move much with the voltage. For higher voltages the Stark component broadens and gets mixed up with the Stark components of the line at 37 229.8 Mc with the result that the J-value could not be determined.

[g] The behavior of the Stark shifts is similar to that of the lines at 40 649.5 Mc. At high voltages all the Stark components can be seen to be doublets.

[h] The first four Stark components on each side nearer to the zero field are strong and distinct, and the others are not distinct.

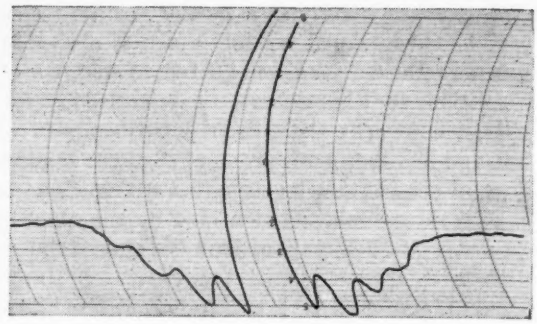

FIG. 4. The line at 35 748.2 Mc/sec of $C^{12}D_3O^{16}H$ with four first-order Stark components at about 50 volts.

Some of the lines given in Table III are well resolved, and their J and ΔJ values could be well ascertained. Because some of the lines are only partially resolved, only a limit of the J-value could be set. Finally there are a number of lines which could not be resolved, and nothing was learned about them except the order of the Stark pattern. These lines which could not be resolved are apparently those with high J-values.

Figure 4 shows a line at 35 748.2 Mc with its four first-order Stark components. Assuming the predicted Stark effect patterns given by Hughes *et al.*, one can ascertain the J and ΔJ values for the transition. Figure 5 shows a line at 43 501.5 Mc which has six second-order Stark components, the intensity distribution of which suggests that the J-value of the lower-rotational level is 5 and $\Delta J=\pm1$. The details of the Stark patterns that have been observed for different lines are included in Table III.

Figure 6 shows one of the doublets listed in Table IV. The high-frequency component at 18 395.6 Mc shows ten Stark components whereas the Stark components of the other are not resolved. Because of the large number of the Stark components involved, it was not possible to determine precisely the number of the

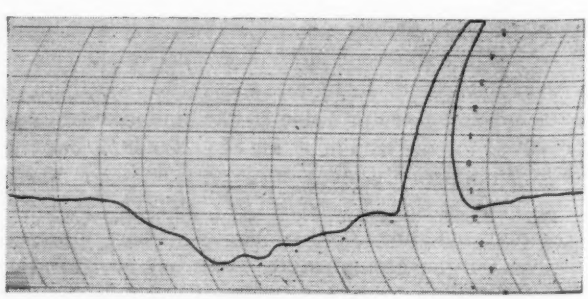

FIG. 5. The line at 43 501.5 Mc/sec of $C^{12}D_3O^{16}H$ showing six second-order Stark components at 700 volts.

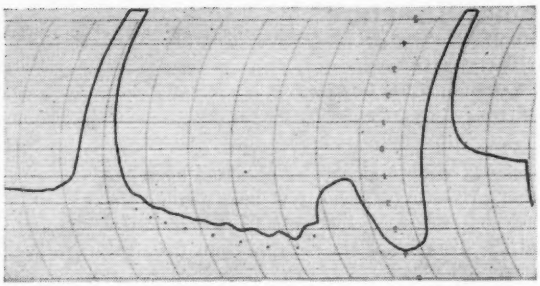

FIG. 6. The doublet (18 395.6 and 18 227.3 Mc/sec) of CD_3OH. The high-frequency component, which is on the left shows 10 Stark components. Voltage applied is 60 volts.

Stark components and the J-values for the different doublets observed.

According to Burkhard and Dennison[7] one-third of the energy levels of methyl alcohol are split into doublets and this splitting is the exact analog of the splitting of the levels of a rigid symmetric rotor when an asymmetry is introduced. The other two-thirds of the levels do not split into doublets but are doubly degenerate. The levels that are doublets which are called K-type doublets are: $K=1$, $\tau=3$; $K=2$, $\tau=2$; $K=3$, $\tau=1$; $K=4$, $\tau=3$; etc. The transitions between different K-type doublets with $\Delta J=\pm 1$ give rise to the doublet lines listed in Table IV. The levels that are doubly degenerate are: $K=1$, $\tau=2$; $K=1$, $\tau=1$; $K=2$, $\tau=1$; $K=2$, $\tau=3$; etc. The transitions between different degenerate levels give rise to first-order Stark effect lines included in Table III.

OTHER SPECTRAL LINES IDENTIFIED

During the search for the $J=0\rightarrow 1$, $K=0\rightarrow 0$ lines of the different isotopic species the Stark patterns of a large number of lines have been studied, but only a few of the lines could be definitely identified. Figure 7 shows the line at 44 068.8 Mc of $C^{12}H_3O^{16}D$, which has a second-order Stark pattern. The lower J-value for this transition is 5 and $\Delta J=\pm 1$. In the case of $C^{13}H_3O^{16}H$ a line at 48 530.0 Mc is found to have seven first-order Stark components. The lower J-value for this line is 7 and ΔJ is equal to ± 1.

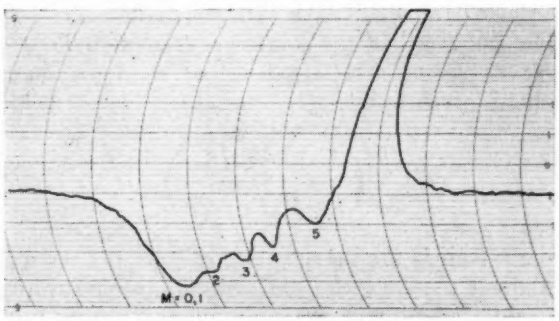

FIG. 7. The line at 44 068.8 Mc/sec of $C^{12}H_3O^{16}D$ showing second-order Stark components at 600 volts.

[7] D. G. Burkhard and D. M. Dennison, Phys. Rev. **84**, 408 (1951).

TABLE IV. Frequencies of the doublets in the spectrum of CD_3OH in the region 28 512–17 918 Mc.

Observed frequency Mc/sec	Intensity
28 511.7 28 311.9	*M*
28 032.7 27 982.7	*M*
26 715.3 26 344.7	*M*
25 133.2 24 691.9	*S*
23 750.0 23 313.9	*M*
22 550.3 22 174.1	*M*
21 519.5 21 236.4	*M*
20 642.5 20 469.8	*S*
19 905.8 19 844.8	*M*
19 294.5 18 923.7	*S*
18 796.2 18 588.6	*S*
18 395.6 18 227.3	*S*
18 097.0	*M*
18 081.2 17 918.9	*S* *M*
17 839.1 17 775.1	*M* *S*

ACKNOWLEDGMENTS

The authors wish to express their thanks to Robert Gibbons and O. R. Gilliam, who helped in the experimental part of the work on $C^{12}H_3O^{16}H$, and to Albert Jache for preparing some of the samples of the isotopic species of methyl alcohol.

Methyl Alcohol. II. Molecular Structure*

PUTCHA VENKATESWARLU† AND WALTER GORDY
Department of Physics, Duke University, Durham, North Carolina

(Received September 7, 1954)

From the moments of inertia of six different isotopic species of methyl alcohol as obtained from the $J=0\rightarrow1$ rotational lines a complete structural determination of methyl alcohol has been made. The structural parameters so obtained are the following: $d_{OH}=0.956\pm0.015$ A, $d_{CO}=1.427\pm0.007$ A, $d_{CH}=1.096\pm0.010$ A, $\angle HCH=109°2'\pm45'$, $\angle COH=108°52'\pm2°$, and the distance of the oxygen atom from the symmetry axis of the CH_3 group $=0.083\pm0.005$ A.

IN the previous paper, Part I, the measurements and identifications of microwave lines of different isotopic species of methyl alcohol are given. In the present paper certain of these lines will be analyzed and used to obtain the structure of the methyl-alcohol molecule.

Methyl alcohol has twelve fundamental vibrations of which one corresponds to the torsional motion of the hydroxyl group with respect to the methyl group. The torsional motion is called the hindered rotation. As the hydrogen of the hydroxyl group (Fig. 1) rotates in a circle whose axis is the symmetry axis of the CH_3 group, it will encounter a potential with three identical minima. If the potential barriers between the minima are high enough, the hydrogen will oscillate with the torsional frequency. If the barriers are sufficiently low, the motion will approximate a free rotation of the OH group relative to the CH_3 group.

The general theory of hindered rotation was given earlier by Nielsen[1] and that for the particular case of methyl alcohol by Koehler and Dennison.[2] Later, Burkhard and Dennison[3] improved the theory of hindered rotation of methyl alcohol and compared their predicted spectrum with the observed spectrum obtained by Hughes, Good, and Coles.[4] Recently Ivash and Dennison[5] extended the theory of Burkhard and Dennison to include the second-order Stark effect as well as a detailed discussion of K-type doubling. By using the theory of Burkhard and Dennison and the experimental results of Hughes *et al.*,[4] they evaluated the moments of inertia of normal methanol. They evaluated also the products of inertia D for the molecules $C^{12}H_3O^{16}H$, $C^{13}H_3O^{16}H$, and $C^{12}H_3O^{18}H$. By using the values of moments of inertia and the product of inertia of normal methanol together with the value of the product of inertia of $C^{13}H_3O^{16}H$, they calculated the molecular parameters of methyl alcohol assuming the C−H bond distance. These molecular parameters, as will be seen in the following, give only approximately the observed values for the $J=0\rightarrow1$ lines of the various isotopic species of methyl alcohol studied in the present experiments, except those of $C^{12}H_3O^{16}H$ for which the agreement is very close. The structure of methyl alcohol can be calculated unambiguously from the $J=0\rightarrow1$ transitions for different isotopic species of methyl alcohol. By successive approximations, the six molecular parameters have been thus obtained.

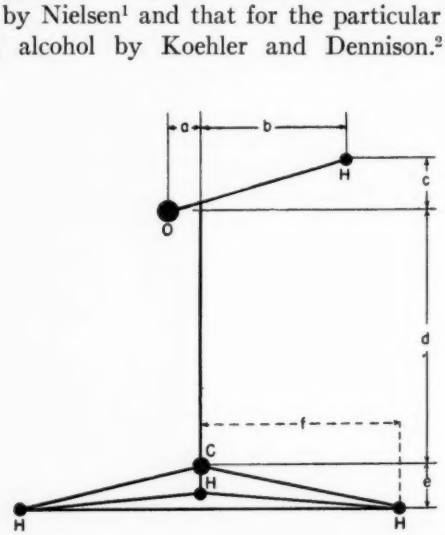

FIG. 1. Structural diagram for methyl alcohol. Except for f, the designations are the same as those used by Ivash and Dennison (reference 5).

The frequency of the rotational transition $J=0\rightarrow1$, $K=0\rightarrow0$, $n\rightarrow n$, $\tau=1\rightarrow1$, $2\rightarrow2$, or $3\rightarrow3$ for methyl alcohol is given by[5]

$$\nu=\frac{h}{8\pi^2}\left(\frac{1}{I_C}+\frac{I_{A1}}{I_BI_{A1}-D^2}\right)+\epsilon, \qquad (1)$$

where I_C and I_B are the moments of inertia of the molecule about those axes of the molecule passing through the center of mass of the molecule and perpendicular to the symmetry axis of the methyl group, I_{A1} is equal to (I_C-I_B), and D is the product of inertia of the molecule in the COH plane. The molecular diagram is given in Fig. 1. If I_A is the moment of inertia of the molecule as a whole and I_{A2} is the moment of inertia of the methyl

* This research was supported by the U. S. Air Force through the Office of Scientific Research of the Air Research and Development Command.

† Now at the Department of Physics, Muslim University, Aligarh, India.

[1] H. H. Nielsen, Phys. Rev. **40**, 445 (1932).

[2] J. S. Koehler and D. M. Dennison, Phys. Rev. **57**, 1006 (1940).

[3] D. G. Burkhard and D. M. Dennison, Phys. Rev. **84**, 408 (1951).

[4] Hughes, Good, and Coles, Phys. Rev. **84**, 418 (1951).

[5] E. V. Ivash and D. M. Dennison, J. Chem. Phys. **21**, 1804 (1953).

TABLE I. Frequencies of the rotational transitions $J=0\rightarrow1$, $K=0\rightarrow0$ calculated using the molecular parameters obtained by Ivash and Dennison.[a]

Molecule	Frequency in Mc/sec calculated using parameters obtained by Ivash and Dennison	Frequency in Mc/sec observed
$C^{12}H_3O^{16}H$	48 373	48 375
$C^{13}H_3O^{16}H$	47 184	47 207
$C^{12}H_3O^{16}D$	45 553	45 352
$C^{13}H_3O^{16}D$	44 406	44 235
$C^{12}D_3O^{16}H$	39 123	39 068
$C^{12}D_3O^{16}D$	36 984	36 799

[a] See reference 5.

group about its symmetry axis ($I_A=I_{A1}+I_{A2}$), ϵ will have two values, one for the line with $\tau=1\rightarrow1$ and the other for the degenerate lines $\tau=2\rightarrow2$ and $\tau=3\rightarrow3$. The quantity ϵ gets its main contribution from the off-diagonal matrix elements $H_{JK+1\tau'n'}{}^{JK\tau n}$ (see reference 3, page 412). The effect of D^2 in the main term on the right-hand side of the above equation is to increase the frequency of the rotational line. The effect of ϵ which is proportional to D^2 is caused mainly by the perturbation of the level $J=1$, $K=1$ on the level $J=1$, $K=0$. Both the levels $J=1$, $K=1$, $\tau=2$, and $J=1$, $K=1$, $\tau=3$ are above the degenerate level $J=1$, $K=0$, $\tau=2$ and 3. The level $J=1$, $K=1$, $\tau=1$ is above the level $J=1$, $K=0$, $\tau=1$. The perturbation effect brings down the levels $J=1$, $K=0$, $\tau=1$, 2, or 3. In other words, the effect of ϵ is to decrease the frequency of the line. Therefore, the effects of D^2 and ϵ are opposed and tend to cancel. For example, in $C^{12}H_3O^{16}H$ the effect of the off-diagonal term on the transition $J=0\rightarrow1$, $K=0\rightarrow0$, $\tau=1\rightarrow1$, $n=0\rightarrow0$ is about -6.5 Mc,[6] whereas the effect of D^2 in the main term is $+6.7$ Mc. For the molecules $C^{12}H_3O^{16}D$, $C^{13}H_3O^{16}D$, and $C^{12}D_3O^{16}D$ which have large D-values, the effects of D^2 in the main term and of ϵ will be very large but will be of opposite sign and will probably be of the same order of magnitude. Thus, as a good approximation one can neglect both D^2 and ϵ. Then Eq. (1) becomes

$$\nu=\frac{h}{8\pi^2}\left(\frac{1}{I_C}+\frac{1}{I_B}\right), \tag{2}$$

which is the equation of an asymmetric rigid rotator. Because of the opposite effects of ϵ and D^2, it is more correct to neglect both of them than to neglect only ϵ.

Table I shows the observed values for the frequencies of the rotational lines $J=0\rightarrow1$, $K=0\rightarrow0$ for the various isotopic species and the calculated values using Eq. (2) and the molecular parameters obtained by Ivash and Dennison. One can see that the over-all agreement is not very good and that the molecular parameters must be changed. If one takes D^2 into consideration while neglecting ϵ, the agreement becomes worse. From a comparison of the observed and calculated frequencies one can see that the CO distance is to be reduced, the CH and OH distances are to be increased, and the angles HCH and HOC are to be changed accordingly.

The molecular parameters that give the best fit to the experimental data are obtained by successive approximations and are given in Table II. The relative values of $\angle$HCH and d_{CH} depend upon the moment of inertia I_{A2}, and the relative values of $\angle$COH and d_{OH} depend upon the moment of inertia I_{A1}. These relative values have been so adjusted that they give about the same values for I_{A1} and I_{A2} for $C^{12}H_3O^{16}H$ as those obtained by Ivash and Dennison from the analysis of the normal methanol spectrum obtained by Hughes *et al.* The product of inertia D depends to a large extent on the distance of the oxygen atom from the symmetry axis of the methyl group. This distance has been adjusted to give about the same value of D for $C^{12}H_3O^{16}H$ as that estimated by Dennison and his collaborators from the spectra of Hughes *et al.*[4]

The moments of inertia and the products of inertia for the various isotopic species of methyl alcohol calculated from these molecular parameters are given in Table III, in which the frequencies of the rotational lines calculated using Eq. (2) as well as the corresponding observed values are included. The six molecular parameters give us calculated values in agreement with nine different observed quantities (six rotational frequencies and three products of inertia). The values of the molecular parameters and the moments of inertia I_{A1} and I_{A2} can be further checked by the measurement of the lines corresponding to the transition $J=0\rightarrow1$, $K=0\rightarrow1$.

The accuracy of the molecular parameters can probably be improved by taking both D^2 and ϵ into consideration. However, it is expected that the changes required in the molecular parameters will not be more than the errors involved from the effect of the zero-point vibrational energies. Because the zero-point vibrational energies are different for different isotopic species, the assumption that the observed molecular parameters will be unaffected by isotopic substitution is not strictly correct. The probable maximum values of the errors involved in the molecular parameters because

TABLE II. Molecular structure of methyl alcohol.

Interatomic distances used for calculation of the moments of inertia (present work)	The molecular structure: Present work	The molecular structure: Ivash and Dennison[a]
$a=0.08277$ A[b]	$d_{OH}=0.956\pm0.015$ A	0.937 A
$b=0.80218$ A	$d_{CO}=1.427\pm0.007$ A	1.434 A
$c=0.36114$ A	$d_{CH}=1.096\pm0.010$ A	1.093 (assumed)
$d=1.4247$ A	$\angle HCH=109°2'\pm45'$	109°30′
$e=0.37321$ A	$\angle COH=108°52'\pm2°$	105°56′
$f=1.03061$ A		

[a] See reference 5.
[b] Distance of the oxygen atom from the symmetry axis of the CH_3 group ($a=0.083\pm0.005$ A).

[6] Calculated by M. Mizushima and E. V. Ivash (private communication).

TABLE III. The moments of inertia, the products of inertia, and the frequencies of the transition $J=0\rightarrow1$, $K=0\rightarrow0$ of methyl alcohol calculated from the molecular dimensions given in Table II.

Molecule	I_c g cm$^2\times10^{-40}$	I_B g cm$^2\times10^{-40}$	$I_{A1}=I_C-I_B$ g cm$^2\times10^{-40}$	IA_2	ν_{calc} Mc/sec	ν_{obs} Mc/sec	D_{calc} g cm$^2\times10^{-40}$	D_{obs} g cm$^2\times10^{-40}$
$C^{12}H_3O^{16}H$	35.3159	34.0710	1.2449	5.3313	48377	48375	-0.107_6	-0.107
$C^{13}H_3O^{16}H$	36.1826	34.9376	1.2450	5.3313	47197	47207	-0.126_7	-0.126
$C^{12}H_3O^{18}H$	36.8302	35.5714	1.2588	5.3313	46362		-0.252	-0.250
$C^{12}H_3O^{16}D$	38.1975	35.8680	2.3295	5.3313	45351	45352	1.288	
$C^{13}H_3O^{16}D$	39.1428	36.8131	2.3297	5.3313	44221	44235	1.299	
$C^{12}D_3O^{16}H$	43.5783	42.3321	1.2462	10.6545	39068	39068	-0.189	
$C^{12}D_3O^{16}D$	46.8041	44.4744	2.3297	10.6545	36787	36799	1.335	

of this assumption are given in Table II. It should be emphasized that these probable errors are only estimated from a knowledge of the internal consistency of structural evaluations of this and of other molecules for which more isotopic species are measured than there are parameters to be evaluated. There is no simple way to calculate the error limits caused by zero-point vibrations in a molecule which has several degrees of vibrational freedom as has methyl alcohol.

The most surprising feature of the methyl-alcohol structure is the large value obtained for angle COH. As mentioned by Ivash and Dennison, one might expect this angle to be similar in value to the angle of the water molecule, which is 104°31′. The value obtained for the COH angle in the present work, 108°52′, is about 4.5° larger than the H_2O angle. The deviation obtained by Ivash and Dennison, while only one-third as much, is in the same direction. Actually, if the bonds to oxygen were electrically the same in the two molecules, one might expect the water angle to be the larger because of the mutual repulsion of the two protons. Nevertheless, the observed difference follows the same trend as that observed in other molecules. The H_2S angle, for example, is 8° smaller than that of SCl_2; the PH_3 angle is smaller by some 8° than that of PF_3 or PCl_3; the AsH_3 and SbH_3 angles are smaller by several degrees than those of the corresponding trihalides. Symmetrically placed hydrogens evidently form bonds of somewhat different type from those of the heavier elements. Probably the nonlocalized molecular orbital model[7] is best suited to describe the structure of the symmetrical hydrides, whereas the directed valence bond treatment applies more specifically to the bonding to the heavier elements. One might also account for the larger COH angle in methyl alcohol over that of H_2O by postulation of double bond character in the CO bond. Such double-bond character would be similar to that predicted in the C−C bond of methyl acetylene which is supposedly made possible by hyperconjugation.[8] The large COH angle which we find is in harmony with the COC angle, 111°±3°, observed in dimethyl ether.[9]

The C−CH_3 group is structurally the same as that in methane and other organic molecules so far measured. In fact, it appears that the CH_3 configuration can be treated as an invariant property to the accuracy required for most purposes.

[7] A simplified description of the water molecule will be found in C. A. Coulson's *Valence* (Oxford University Press, New York, 1952), p. 160.

[8] Mulliken, Rieke, and Brown, J. Am. Chem. Soc. **63**, 41 (1941).

[9] V. Schomaker. See P. W. Allen and L. E. Sutton, Crystallographica **3**, 53 (1950).

Mercury Photosensitized Decomposition of Nitrous Oxide*

R. J. CVETANOVIĆ
Division of Applied Chemistry, National Research Council, Ottawa, Canada
(Received October 11, 1954)

The reaction of nitrous oxide with $Hg(^3P_1)$ atoms at 23°C has been investigated. The evidence obtained indicates that the sole primary process is a splitting of the nitrous oxide molecule into a nitrogen molecule and an oxygen atom. The possible secondary reactions are discussed.

INTRODUCTION

DECOMPOSITION of nitrous oxide, induced in various ways, has been extensively studied. Direct photochemical decomposition in the far ultraviolet region has been investigated by Macdonald,[1] and later by Noyes and his collaborators.[2,3] Macdonald's suggestion that an electronically excited molecule is formed and remains sufficiently long lived to participate in subsequent reactions, has been refuted by Noyes[2] on the grounds of absorption characteristics of nitrous oxide. The accessible electronic levels of nitrous oxide[4] are repulsive and the possible primary processes are

$$N_2O+h\nu\rightarrow N_2(^1\Sigma)+O(^3P, {}^1D, \text{or } {}^1S) \quad (1)$$

or

$$N_2O+h\nu\rightarrow NO(^2\Pi)+N(^4S). \quad (2)$$

Since oxygen is a product, reaction (1) constitutes at least a part of the primary process. Large amounts of nitric oxide formed were at first[2] thought as possibly resulting from the reaction

$$N_2O+O\rightarrow 2NO \quad (3)$$

in which case the sole primary process would be reaction (1). It was found,[3] however, that oxygen atoms produced by photolysis of nitrogen dioxide reacted too slowly with N_2O and reaction (3) could not successfully compete with

$$O+\text{wall}\rightarrow\tfrac{1}{2}O_2. \quad (4)$$

It was, consequently, concluded that the primary process (1) must be accompanied by (2), followed by

$$N+N_2O\rightarrow NO+N_2 \quad (5)$$

and

$$N+\text{wall}\rightarrow\tfrac{1}{2}N_2. \quad (6)$$

The primary process in the mercury sensitized decomposition of nitrous oxide is also subject to uncertainty. Working with very small concentrations of nitrous oxide, Manning and Noyes[5] studied the process by following pressure changes. When allowed to proceed to completion, the total net reaction could be represented by

$$N_2O+Hg\rightarrow HgO+N_2 \quad (7)$$

so that there is no pressure change. There was, however, a pressure increase in the early stages of the reaction and it was assumed that nitric oxide was formed as an intermediate and eventually reacted with the excited mercury atoms to give mercuric oxide and nitrogen. An intermediate formation of oxygen was considered unacceptable in view of the rapidity of the reaction between oxygen and the excited mercury atoms. The pressure measurements were interpreted on the basis of the foregoing assumptions and the quantitative treatment of the data gave for the quenching cross section of nitrous oxide an exceptionally high value of about 100 A².

Two primary processes were considered possible

$$Hg(^3P_1)+N_2O\rightarrow NO(^2\Pi)+N(^4S)+Hg(^1S_0) \quad (8)$$

and

$$Hg(^3P_1)+N_2O\rightarrow N_2(^1\Sigma)+O(^3P, \text{or } {}^1D)+Hg(^1S_0) \quad (9)$$

but, as stated by Noyes,[2] it proved impossible to present conclusive evidence in favor of either primary step, although the initial production of a nitrogen molecule and of an oxygen atom afforded a somewhat better explanation of the experimental facts.

In an investigation of photo-oxidation of hydrocarbons,[6] mercury sensitized reaction with nitrous oxide was found to offer some distinct advantages. Interpretation of the results, however, necessitated a more reliable information as to the nature of the primary step. It was also found necessary to explain the observation that under similar conditions the nitrogen production greatly increased on addition of small quantities of a hydrocarbon to nitrous oxide, a fact incompatible with the relationships otherwise established. Furthermore, evidence was obtained[7] for a quenching cross section of nitrous oxide considerably smaller than the above value of 100 A². For these reasons some aspects of the mercury sensitized decomposition of nitrous oxide have been reinvestigated with the particular object of eliminating the uncertainty regarding the

* Contribution No. 3633 from the National Research Council, Ottawa, Canada.
[1] J. Y. Macdonald, J. Chem. Soc. **1928**, 1.
[2] W. A. Noyes, Jr., J. Chem. Phys. **5**, 807 (1937).
[3] Henriques, Duncan, and Noyes, J. Chem. Phys. **6**, 518 (1938).
[4] Zelikoff, Watanabe, and Inn, J. Chem. Phys. **21**, 1643 (1953).
[5] W. M. Manning and W. A. Noyes, Jr., J. Am. Chem. Soc. **54**, 3907 (1932).
[6] R. J. Cvetanović (to be published).
[7] R. J. Cvetanović, the following paper, J. Chem. Phys. **23**, 1208 (1955).

primary step. The evidence obtained indicates that reaction (9) is, within an analytical uncertainty of 2 to 3 percent, sole primary process. Some information has also been obtained on the secondary reactions involved and tentative mechanisms suggested.

EXPERIMENTAL

The reaction was studied in a cylindrical quartz reaction vessel (5 cm in diameter, 10 cm long), which could be isolated from the adjoining mercury saturator and the rest of the apparatus by means of stopcocks. No liquid mercury was introduced into the reaction vessel. The mercury saturator consisted of a small amount of mercury placed in a U-tube preceded by an all-glass circulating pump supported on Teflon bearings. The pump, the saturator, and the reaction vessel formed a closed circuit through which the reactants were circulated for some time either only before the reaction (static runs) or also during the reaction (circulating runs). In static runs the circulation was discontinued before the irradiation of the reactants and the reaction vessel isolated so that, apart from the initially introduced mercury vapor, no further supply was available. The reaction vessel and the mercury saturator were kept at room temperature (23±1°C).

The mercury resonance radiation was supplied from a low-pressure mercury arc, operated at a constant current of 100 mA through the lamp circuit. The light beam was roughly collimated by a highly polished aluminum cylinder. The amount of light transmitted through the cell was measured by means of a phototube connected to an amplifying circuit. A Corning 7-54 filter was placed in front of the phototube, so that essentially only λ2537 line was measured. It was found that the resonance line emitted from the arc was incompletely absorbed in the reaction vessel even in the presence of mercury vapor at a pressure corresponding to room temperature and high pressures of a quenching gas. The absorption was strongly decreased on reduction of mercury vapor concentration to that corresponding to 0°C. In the case of nitrous oxide a spontaneous depletion of mercury vapor during irradiation was observed. With a hydrocarbon (for example *n*-butane) added to nitrous oxide, or with the hydrocarbon alone, no spontaneous depletion of mercury vapor concentration occurred and the dependence of absorption on mercury concentration was verified by intentionally introducing lower concentrations of mercury vapor into the reaction vessel.

Nitrous oxide was obtained from an Ohio Chemical Canada Ltd. cylinder and was further purified by repeated bulb to bulb distillation *in vacuo*. Qualitative tests for higher nitrogen oxides were negative. Phillips reagent grade ethane and *n*-butane, and Ohio Chemical Canada Ltd. ethylene were used after repeated bulb to bulb distillation *in vacuo*.

The products were fractionated and analyzed in the conventional type of analysis system, incorporating a Le Roy still,[8] a Töpler pump, and a constant volume burette. In the decomposition of nitrous oxide alone, the gases which were noncondensable in liquid nitrogen consisted of nitrogen and oxygen only.† Oxygen was removed at around 240°C by copper oxide which had been largely reduced by carbon monoxide and hydrogen combustion in previous work. Quantitative removal of oxygen was checked by mass-spectrometer analysis on a number of random samples. From mixtures of nitrous oxide and hydrocarbons the noncondensable gases contained nitrogen, methane, carbon monoxide, and hydrogen, but no oxygen. Carbon monoxide and hydrogen were removed at 240°C on copper oxide, and the remaining gas was analyzed by mass spectrometer for nitrogen and methane. Some specific analytical methods for other products are referred to in the next section.

RESULTS

The reaction was studied by analyzing the products and by following the changes in the amount of transmitted light during the process. Pressure of nitrous oxide was varied from about 10 to 600 mm and in most cases reactions were allowed to proceed only to very small conversions.

The major and almost exclusive products of the reaction were nitrogen and oxygen, in a ratio very close to the stoichiometric ratio of 2:1. In all cases, however, there was a slight deficiency of oxygen, indicating formation of small amounts of other products. Beside the oxide of mercury, which has been established as a product previously and reflected itself in the present work in a gradual decrease in transparency of the reaction vessel, it was found that after irradiation the bulk of the unreacted nitrous oxide contained a substance or substances which liberated iodine from a potassium iodide solution. The presence of higher nitrogen oxides was shown by applying Griess's test[9] after absorption in water. A saturated solution of benzidine in ethanol was used to test for an eventual

TABLE I. Analyses for nitrite ion and for liberated iodine.

Run	p_{N_2O} mm	Irradiation min	Products (μmoles) N_2	O_2	nitrite	iodine	$\frac{1}{2}N_2-O_2$
167	101	80	6.61	3.04	0.02	not det'd	0.26
168	300	80	8.37	4.04	0.10	not det'd	0.14
169	151	70	13.0	5.99	0.11	not det'd	0.51
159	203	180	15.1	7.20	not det'd	1.4	0.35
160	202	300	49.5	23.4	not det'd	2.5	1.35
161	202	240	26.2	13.2	not det'd	3.1	0.80

[8] D. J. Le Roy, Can. J. Research, **B28**, 492 (1950).

† Mass spectrometer analysis showed only the presence of nitrogen and oxygen with possibly not more than a few tenth of a percent of nitric oxide. In view of the findings of Manning and Noyes (reference 5) any NO would be expected to remain condensed with the large excess of N_2O present.

[9] F. P. Treadwell and W. T. Hall, *Analytical Chemistry. Vol. 1. Qualitative Analysis.* (John Wiley and Sons, Inc., New York, 1949), Ninth English Edition, p. 247.

presence of ozone, but the result was inconclusive because of interference by the nitrogen oxides. Several quantitative analyses for nitrite ion and for liberated iodine, kindly made by Mr. D. S. Russell and Dr. M. Vamos, indicate that these substances are formed, at best, in very small amounts. Nitrite was determined colorimetrically[10] and iodine by titration with 0.01N sodium thiosulfate. The results of these analyses are shown in Table I.

In view of the presence of nitrogen oxides the figures in Table I for iodine determination should be regarded only as an upper limit.

The maximum possible amounts of various substances which come into consideration can be evaluated from the stiochiometry and the observed oxygen deficiency.

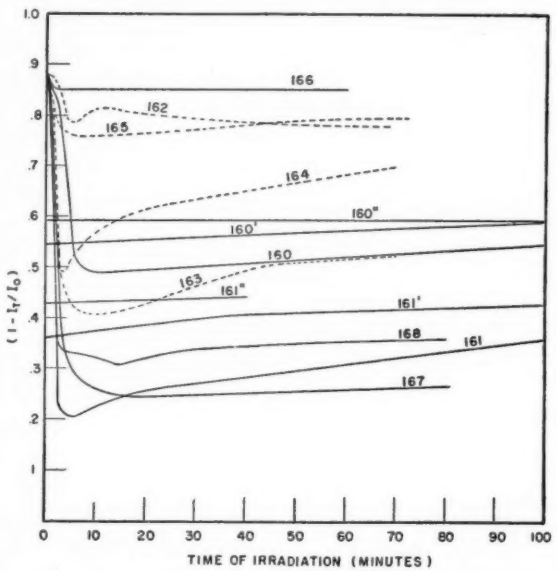

FIG. 1. Light absorption measurements. Static runs are shown in full lines, circulating runs in broken lines. Smoothed out curves through the mean values are plotted and sporadic fluctuations appearing in some circulating runs (but not in static runs) are not shown. Continuations of runs 160 and 161 after the first 100 min of irradiation are plotted as 160′, 160″, and 161′, 161″, respectively.

If $\alpha=\frac{1}{2}N_2-O_2$, and if each one of the following compounds were the only product besides nitrogen and oxygen, its amount would be in the case of HgO, 2α; O_3, $\frac{2}{3}\alpha$; NO_2, $4/3\alpha$; NO, 4α; N_2O_3, α; N_2O_5, $\frac{1}{2}\alpha$. The results for a number of representative experiments are given in Table II. It is evident that oxygen deficiency is small and is on the average only about 3 percent of the nitrogen produced.

The observed rates of nitrogen production (Table II, column 5) show great and seemingly quite unsystematic variations and are in all cases smaller than in the run 166 where ethane was added to nitrous oxide. Some variation is caused by the decreasing transparency of the reaction vessel. This, however, was found to reduce the light input at the most by 10 to 20 percent in the course of a run and was somewhat comparable in the runs reported in Table II, for which the initial transparency was kept constant by flaming the front window of the reaction vessel before each experiment. The reason for the variation in reaction rates is the spontaneous decrease in mercury vapor concentration and the consequent decrease in light absorption. From the plots in Figs. 1 and 2 the mean apparent fractions of light absorbed (not corrected for decreasing transparency of the vessel) have been computed and are given in column 9 of Table II. The parallelism with the rates of nitrogen production, given in Column 8 of Table II in arbitrary units, indicates that the rates are proportional to the amount of light absorbed. In the run 166, where 35 mm of ethane were added to 100 mm of nitrous oxide, there was no decrease in the transparency of the vessel‡ and the observed rate is somewhat larger.

In Table III a comparison is made between the rates of nitrogen production and decomposition of nitrous oxide. Even with the small initial pressures of nitrous oxide used the possible analytical error is appreciable. Within the limits of this error, the two rates were found to be identical. One experiment was conducted with 10 mm of nitrous oxide alone and several with 8 mm of ethylene added. In addition, three similar experiments were carried out with very small amounts of

TABLE II. Rates of mercury sensitized decomposition of nitrous oxide.

Run	Temp °C	p_{N_2O} mm (at 25°)	Irradiation min	Rates R_{N_2} (molec/sec $\times 10^{-18}$)	Rates R_{O_2} (molec/sec $\times 10^{-18}$)	Rates $\frac{100\alpha}{R_{N_2}}$ (molec/sec $\times 10^{-18}$)	Relative R_{N_2}	I_a apparent
Static runs								
160	23.5	202	300	1.66	0.78	2.8	0.57	0.56
161	23.5	202	240	1.10	0.51	3.4	0.38	0.36
167	23.6	101	80	0.83	0.38	3.9	0.29	0.28
168	24.2	300	80	1.05	0.51	1.6	0.36	0.36
Circulating runs								
162	22.7	558	70	2.25	1.04	3.8	0.78	0.79
163	22.5	104	70	1.42	0.61	7.0	0.49	0.49
164	22.9	196	70	1.71	0.81	2.7	0.59	0.63
165	23.1	387	70	2.16	1.04	1.9	0.75	0.78
165a[a]	22.5	103	70	1.56	0.73	3.3	0.54	0.62
Combined circulating and static runs								
169	24.1	151	70	1.87	0.86	4.0	0.65	0.72
170	24.3	101	70	0.92	0.44	2.7	0.32	0.34
Nitrous oxide +35.6 mm of ethane								
166	23.3	101	60	2.89	···	···	1.00	0.85

[a] For the run 165a condensables from run 165 were retained (at dry ice temperature) while oxygen and nitrogen were pumped off at −196°C and the N_2O pressure lowered from 387 to 103 mm.

[10] F. D. Snell and C. T. Snell, *Colorimetric Methods of Analysis* (D. Van Nostrand Company, Inc., New York, 1949), Third Edition. Vol. II, p. 803.

‡ The apparent slight initial decrease in the measured light absorption, as shown for this run in Fig. 1, is also exhibited by single hydrocarbons and, even when the reaction vessel contains no gases nor mercury vapor, it is slowly reversible on interruption of irradiation and is probably due to a change in the vessel transparency caused by desorption.

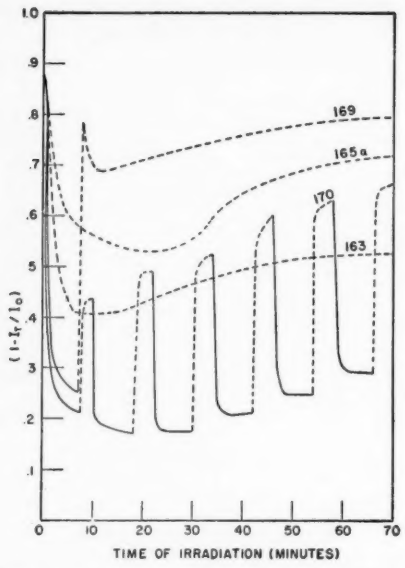

FIG. 2. Light absorption measurements. Static runs are shown in full lines, circulating runs in broken lines. Smoothed out curves through the mean values are plotted and sporadic fluctuations appearing in some circulating runs (but not in static runs) are not shown.

nitrous oxide and *n*-butane and the conversion extended to more than 50 percent in order to increase the analytical accuracy. These experiments showed that, within an analytical uncertainty of about 2 to 3 percent, the rate of nitrogen production is identical with the rate of nitrous oxide consumption.

DISCUSSION

Primary Step

Production of nitrogen and oxygen in nearly stoichiometric ratio in the decomposition of nitrous oxide requires reaction (9) to be by far the predominant and possibly the exclusive primary step. On the basis of the small oxygen deficiency it can be concluded that reaction (9) must participate in the primary process at least to the extent of about 90 percent. In the experiments in which a hydrocarbon was added to nitrous oxide any primary splitting into N atoms and NO would make $R_{N_2O} > R_{N_2}$. The observed equality of the rates of nitrogen production and decomposition of nitrous oxide, as well as the suppression of formation of higher nitrogen oxides on addition of ethane to nitrous oxide, indicate then that, within the experimental uncertainty of 2 to 3 percent, splitting into a nitrogen molecule and an oxygen atom is the sole primary process. Since certain small amounts of higher nitrogen oxides are formed, it would seem that reaction (3), or possibly an analogous reaction via ozone, does occur to some extent. Although reaction (3) is known[3] to require an activation energy of 9 to 14 kcal, it is possible that it may be somewhat enhanced by oxygen atoms carrying the excess energy after the primary splitting of the molecule.

The primary occurrence of reaction (9) requires the quantum yield of nitrogen formation to be unity. Determinations of this quantity have been made by decomposing mixtures of nitrous oxide and ethane, nitrous oxide and *n*-butane, and nitrous oxide and ethylene, and extrapolating to zero content of the hydrocarbon.[7] A value close to 0.78 was obtained for the quantum yield of nitrogen formation. The value is based on hydrogen production by mercury sensitized decomposition of *n*-butane at a pressure of 200 mm for which Bywater and Steacie[11] find a quantum yield of 0.50 at room temperature assuming complete absorption of resonance radiation. In the original actinometric determinations made by these authors a mercury arc of similar make as in the present work was used. Inasmuch as the character of the emitted light was similar, an apparent quantum yield value lower than unity would be expected due to incomplete absorption of radiation energy, although this could not explain the whole discrepancy. A quenching of mercury by nitrous oxide to the metastable ($^3P_0$) state with subsequent dissipation of energy in processes not resulting in production of nitrogen is the likely cause of the observed low quantum yield.[7]

Secondary Reactions

On the basis of the present experiments and the information available in literature the following secondary reactions appear possible:

$$\text{(A)}\quad \begin{cases} O+O+M \rightarrow O_2+M & (10) \\ O+\text{wall} \rightarrow \tfrac{1}{2}O_2 & (4) \end{cases}$$

$$\text{(B)}\quad \begin{cases} N_2O+O \rightarrow (N_2O_2) \rightarrow 2NO & (3) \\ N_2O+O_3 \rightarrow 2NO+O_2(\text{or } 2NO_2) & (3a) \end{cases}$$

$$\text{(C)}\quad \begin{cases} Hg+O(+M) \rightarrow HgO(+M) & (11) \\ Hg+NO_2 \rightarrow HgNO_2 \rightarrow HgO+NO & (11a) \\ Hg+O_3 \rightarrow HgO+O_2 & (11b) \end{cases}$$

$$\text{(D)}\quad \begin{cases} NO+O \rightarrow NO_2^* \rightarrow NO_2+h\nu & (12) \\ NO_2+O \rightarrow NO+O_2 & (13) \\ NO_2^*+O \rightarrow NO+O_2 & (13a) \end{cases}$$

$$\text{(E)}\quad \begin{cases} O_2+O(+M) \rightarrow O_3(+M) & (14) \\ O_3+O \rightarrow 2O_2 & (15) \end{cases}$$

Reactions (D) have been demonstrated in a very convincing manner by Spealman and Rodebush,[12] who also showed that reaction (13) was faster than (12). It is not certain whether (12) proceeds by a three-body collision; its exothermicity is much reduced through formation of an excited NO_2 molecule. Reaction (14) seems to require a third body and to occur at every 10^3 to 10^4 collisions at atmospheric pressure,

[11] S. Bywater and E. W. R. Steacie, J. Chem. Phys. **19**, 172 (1951).

[12] M. L. Spealman and W. H. Rodebush, J. Am. Chem. Soc. **57**, 1474 (1935).

while (15) is estimated to occur on every 2000th collision.[13]

Besides direct formation of molecular oxygen from oxygen atoms (A), there is, therefore, also possibility of an indirect formation, catalyzed by NO_2 (D) or by ozone (E). That this indirect formation of oxygen may be the predominant one throughout the course of the reaction except in its earliest stages is strongly suggested by the following considerations.

The light absorption measurements made cannot be used for quantitative kinetic conclusions. Apart from decreasing transparency of the reaction vessel due to formation of mercury oxide, two other difficulties were experienced: (1) passivation of the supply mercury in circulating runs, lowering to an unknown extent the rate of inflow of the vapor; (2) occasional lack of reproducibility of some features of the process under apparently identical conditions, as illustrated, for example, by runs 160 and 161, Fig. 1. However, regardless of these difficulties the light absorption curves possess certain distinct features which allow a number of conclusions to be drawn. Thus it is clear from Figs. 1 and 2 that depletion of mercury is fast while its concentration is high, but as it becomes rapidly reduced to a certain low value, further consumption stops. This is particularly evident from run 170 (Fig. 2) where circulating and static intervals were alternated over a period of time. It is, therefore, unlikely that mercury oxide is formed in the primary process,

$$(F)\begin{cases} Hg^*+N_2O \rightarrow N_2+HgO^* & (16)\\ HgO^* \rightarrow HgO & (17)\\ HgO^* \rightarrow (?)\rightarrow Hg+\tfrac{1}{2}O_2 & (18)\end{cases}$$

analogous to the sometimes suggested primary formation of HgH from saturated hydrocarbons. If reactions (F) were responsible for HgO and oxygen formation, the ratio R_{O_2}/R_{HgO} would at best remain independent of mercury concentration and the process would lead to complete self-inhibition in static runs. On the other hand, if HgO is a secondary product, as in reactions (C), R_{O_2}/R_{HgO} should be inversely proportional to mercury concentration and at a sufficiently low concentration depletion of mercury should virtually stop, as is actually observed. Furthermore, in order for this to be achieved, oxygen cannot be formed by reaction (10), except possibly in the earliest stages of the process. Since there is indication that at larger N_2O concentrations higher levels of mercury can persist, molecular oxygen seems to be formed by a catalytic process of the type of reactions (D) or (E). Supporting evidence for the formation of a catalyst is the fact that usually higher concentrations of mercury were maintained at the same N_2O pressure if the reaction were first allowed to proceed for a time and then continued after removal of nitrogen and oxygen, the condensable products being retained. This is illustrated by runs 163 and 165a in Fig. 2. The over-all reaction course is, therefore, determined by a balance of a number of relatively slow processes, so that a sensitivity to minute quantities of impurities, as seems to be observed, is understandable. In the presence of hydrocarbons, there is a rapid removal of oxygen atoms, and the aforementioned secondary processes do not occur.

[13] J. Schumacher, J. Am. Chem. Soc. **52**, 2377 (1930).

TABLE III. Comparison of rates of nitrogen formation and nitrous oxide decomposition.

Run	$(p_{N_2O})_i$ mm (at 25°)	$(p_{C_2H_4})_i$ mm (at 25°)	Irradiation min	$\frac{R_{N_2}}{-R_{N_2O}}$
17	10.7	...	90	1.08
34	10.6	8.1	60	0.98
23	10.5	8.1	90	1.00
32	10.5	7.9	180	0.99
29	10.6	8.1	250	1.01
31	10.5	8.2	310	1.00
30	10.5	8.1	400	1.04

CONCLUSION

The results of the present experiments support the view expressed previously by Noyes[2] that a primary splitting into N_2 and an O atom is the more likely of the two possible primary steps in the mercury sensitized reaction and indicate, in effect, that the splitting into a nitrogen atom and nitric oxide may occur at the most to the extent of 2 to 3 percent. The apparent contradiction with the previous experiments of Manning and Noyes[5] disappears when the formation of oxygen as a major product is taken into account. The further reactions of the initially produced oxygen atoms can be treated only in a tentative manner. There is strong indication that the recombination of oxygen atoms is catalyzed by the small amount of higher nitrogen oxides produced. As a consequence the concentration of the higher oxides of nitrogen remains quite small.

ACKNOWLEDGMENTS

The author is indebted to Dr. A. Tickner for mass spectrometer analysis and to Mr. J. K. Waterman for building the electrical and electronic circuits employed.

Relative Efficiencies of Quenching of Mercury Resonance Radiation and Their Temperature Independence. Mechanism of Mercury Photosensitized Decomposition of Saturated Hydrocarbons*

R. J. CVETANOVIĆ
Division of Applied Chemistry, National Research Council, Ottawa, Canada

(Received October 11, 1954)

Relative over-all efficiencies of quenching of mercury resonance radiation have been determined for N_2O, n-C_4H_{10}, C_2H_6, and C_2H_4 by studying the binary mixtures of each of the hydrocarbons with nitrous oxide at 23° and 120°C. For N_2O and n-C_4H_{10} the relative efficiency of quenching to the ground state as well as the fractions of quenching to the ground and to the metastable $6(^3P_0)$ state of mercury for each of the two compounds have also been determined. Temperature independence of the primary quenching processes has been demonstrated.

A proposed mechanism of quenching by saturated hydrocarbons, based on additional experimental information obtained with n-butane alone and its mixtures with nitrous oxide, interprets fully the experimental facts and in particular accounts for the repeatedly observed low quantum yields of hydrogen formation.

MERCURY photosensitized reactions are widely used as a convenient source of free radicals and atoms. Although the main features of the process are well understood,[1] certain aspects of its mechanism require further elaboration. In the present work mercury photosensitized reactions of binary mixtures of nitrous oxide with ethane, n-butane, and ethylene were studied in static and circulating experiments at room temperature and at 120°C. The reactions provide a simple method of determination of relative values of quenching cross sections and throw additional light on the mechanism of quenching processes.

TABLE I. Mixtures of nitrous oxide and n-butane.

Run	Temp °C	Pressure mm	$\frac{n-C_4H_{10}}{N_2O}$	Irradiation min	Rates (molec sec^{-1} ×10^{-15}) N_2	Rates (molec sec^{-1} ×10^{-15}) H_2	Quantum yields N_2	Quantum yields H_2
			Room temp, static runs					
72	21.5	308.6	2.01	170	1.09	0.408	0.506	0.189
74	23.9	155.9	0.556	200	1.43	0.140	0.672	0.065
75	23.9	202.7	1.00	180	1.32	0.234	0.620	0.110
76	24.3	254.8	1.51	180	1.18	0.326	0.557	0.154
78	23.2	131.5	0.292	180	1.54	0.081	0.736	0.039
83	21.7	528.6	4.08	180	0.79	0.604	0.380	0.290
128	24.5	394.1	2.95	110	1.96	1.07	0.437	0.237
137	22.8	107.9	0.05	60	3.21	0.067	0.753	0.016
			Room temp, circulating runs					
124	23.1	203.9	1.00	110	2.83	0.530	0.611	0.114
127	23.6	431.2	3.31	110	1.90	1.24	0.419	0.275
129	23.5	309.9	2.04	110	2.25	0.896	0.503	0.201
130	23.8	304.3	0.483	110	3.08	0.289	0.696	0.065
138	22.3	338.1	2.34	105	2.01	0.893	0.482	0.214
			123°C, static runs					
180	123.2	201.1	1.00	60	2.35	0.430	0.637	0.117
181	124.4	393.0	3.00	60	1.69	0.962	0.459	0.261
182	123.6	153.6	0.504	60	2.53	0.225	0.687	0.061
183	123.0	294.9	1.98	60	1.96	0.712	0.533	0.193

EXPERIMENTAL

The main features of the experimental arrangement and the employed reagents have been described previously.[2] For the present work the reaction vessel was contained in an aluminum block furnace, maintained at a temperature constant to within about 1°C.

The products which were noncondensable in liquid nitrogen consisted of nitrogen, hydrogen, carbon monoxide, and small amounts of methane. They were combusted in a copper oxide furnace at around 240°C to remove carbon monoxide and hydrogen. The remainder, consisting of nitrogen and methane, was analyzed by a mass spectrometer. Carbon monoxide was determined by measuring the amount of carbon dioxide formed, (recovered from dry ice-acetone). Hydrogen was determined by difference.

The quantum yields of reaction products were determined relative to the production of hydrogen by mercury sensitized decomposition of 200 mm of n-butane at 23° and 120°, taking for ϕ_{H_2} the values of 0.50 and 0.63, respectively, as found by Bywater and Steacie.[3] For the convenience of uniform graphical presentation all the quantum yield values given in the graphs (but not in the tables) have been corrected by assuming a value of 0.78 for the quantum yield of nitrogen production on extrapolation to zero content of the hydrocarbons in their respective mixtures with 100 mm of N_2O. The experimentally found values for this quantity were 0.78 ± 0.01 at room temperature and 0.80 ± 0.01 at 120°. The slight difference at the two temperatures is well within the possible experimental errors and the mean value found at room temperature is likely to be more accurate.

Over a period of time there was a slight decrease in the light absorption, amounting to less than one percent per run. Frequent determinations of yield of hydrogen

* Contribution No. 3634 from the National Research Council, Ottawa, Canada.

[1] E. W. R. Steacie, Trans. Roy. Soc. (Canada), **62** (III), 1 (1948).

[2] R. J. Cvetanović, preceding paper, J. Chem. Phys. **23**, 1203 (1955).

[3] S. Bywater and E. W. R. Steacie, J. Chem. Phys. **19**, 319 (1951).

TABLE II. Mixtures of nitrous oxide and ethane.

Run	Temp °C	Pressure mm	$\frac{C_2H_6}{N_2O}$	Irradiation min	Rates (molec sec^{-1} ×10^{-15}) N_2	H_2	Quantum yields N_2	H_2
			Room temperature					
142	23.3	346.8	3.47	60	3.04	0.10	0.730	0.025
144	23.0	203.6	1.01	60	3.10	0.11	0.750	0.027
145	24.0	668.3	5.83	60	2.94	0.10	0.721	0.025
146	23.9	307.8	2.07	60	3.08	0.12	0.750	0.028
147	24.9	516.9	9.68	60	2.88	0.11	0.705	0.027
148	23.2	426.8	3.19	60	2.98	0.08	0.734	0.020
			118°C					
173	117.8	226.2	0.995	60	2.93	0.12	0.767	0.031
174	118.7	533.1	4.42	60	2.78	0.12	0.735	0.033
175	117.9	422.6	7.39	60	2.73	0.15	0.728	0.041
176	117.9	299.2	1.99	60	2.80	0.12	0.753	0.033
177	116.7	152.0	0.505	60	2.82	0.12	0.765	0.033

from 200 mm of *n*-butane were made and the amounts of light absorbed in individual runs ascertained by interpolation.

RESULTS AND DISCUSSION

I. Relative Quenching Efficiencies

It is evident from the experimental results presented in Tables I–III and the plots in Figs. 1 and 2 that, for a wide range of experimental conditions, yields of nitrogen are quite well defined by the expression

$$\frac{1}{\phi_{N_2}}=\alpha\left(1+\beta\frac{(RH)}{(N_2O)}\right) \qquad (1)$$

independent of the time of irradiation,† light intensity, temperature, circulation, or pressure. The values of β are 0.009, 0.255, and 2.10 for C_2H_6—N_2O, n-C_4H_{10}—N_2O, and C_2H_4—N_2O mixtures, respectively, and the value of α is, as was indicated in the foregoing, close to 1.3.

TABLE III. Mixtures of nitrous oxide and ethylene.

Run	Temp °C	Pressure mm	$\frac{C_2H_4}{N_2O}$	Irradiation min	Rates (molec sec^{-1} ×10^{-15}) N_2	H_2	Quantum yields N_2	H_2
			Room temperature					
50	27.3	116.8	0.140	200	1.46	0.215	0.605	0.089
51	29.3	135.8	0.366	200	1.10	0.217	0.445	0.088
52	23.0	177.3	0.743	200	0.777	0.178	0.306	0.070
53	23.3	128.8	0.291	200	1.22	0.227	0.487	0.090
54	25.1	200.5	0.987	200	0.632	0.150	0.255	0.060
55	24.5	110.2	0.067	200	1.67	0.198	0.683	0.081
57	23.6	254.9	0.258	200	1.24	0.144	0.514	0.060
58	24.1	108.8	0.943	200	0.624	0.260	0.262	0.109
60	25.0	153.1	0.515	200	0.889	0.185	0.378	0.079
			123°C					
189	122.4	114.8	0.147	90	2.16	0.325	0.617	0.092
185	122.9	125.2	0.243	90	1.96	0.383	0.542	0.106
187	124.0	139.6	0.398	105	1.56	0.376	0.436	0.106
184	123.2	150.0	0.510	90	1.44	0.400	0.392	0.109
188	122.6	176.4	0.768	90	1.10	0.321	0.312	0.091
186	123.2	198.7	1.00	90	0.945	0.310	0.263	0.086

† Time independence of the rate of nitrogen formation has been verified in the case of N_2O—C_2H_4 mixtures. The results will be reported elsewhere.

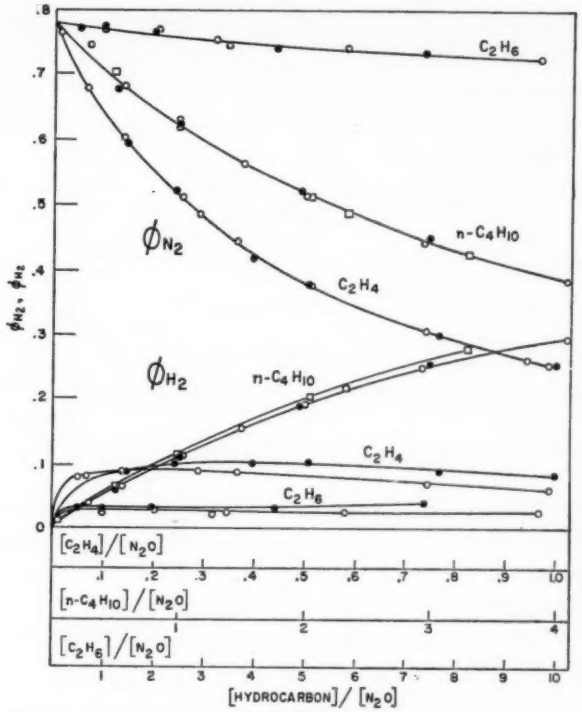

FIG. 1. Quantum yields of nitrogen and hydrogen production for different hydrocarbon to nitrous oxide ratios. The abscissa scales are different for the three hydrocarbons, as indicated. The symbols represent: ○, static runs at ~23°C; □, circulating runs at ~23°C; and ●, static runs at ~120°C.

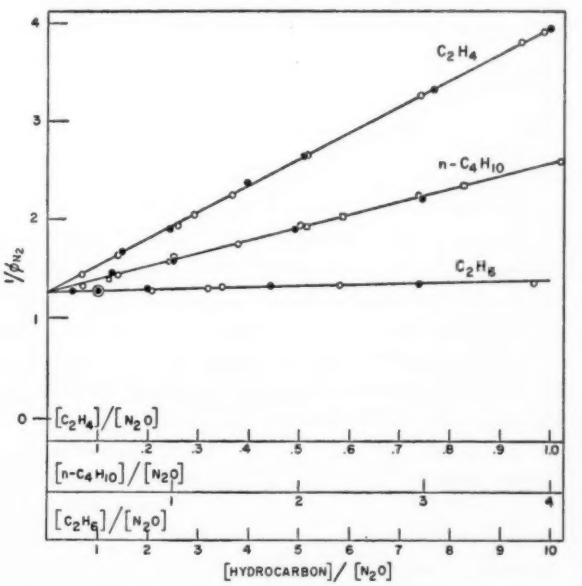

FIG. 2. Plots of $1/\phi_{N_2}$ against the hydrocarbon to nitrous oxide ratio. The abscissa scales are different for the three hydrocarbons, as indicated. The symbols represent: ○, static runs at ~23°C; □, circulating runs at ~23°C; and ●, static runs at ~120°C.

The primary products of mercury sensitized decomposition of nitrous oxide are[2] a nitrogen molecule and an oxygen atom, so that for a mixture of nitrous oxide and a hydrocarbon (RH) the following primary processes can occur:

(a) $Hg+h\nu \rightarrow Hg^*$,

(b) $Hg^* \rightarrow Hg+h\nu$,

(1) $Hg^*+N_2O \rightarrow Hg+N_2+O$,

(1′) $Hg^*+N_2O \rightarrow Hg'+N_2O$,

(2) $Hg^*+RH \rightarrow Hg+\text{products}$,

(2′) $Hg^*+RH \rightarrow Hg'+RH$.

Hg refers to Hg6($^1S_0$), Hg* to Hg6($^3P_1$), and Hg′ to Hg6($^3P_0$). At the high pressures of nitrous oxide and the other quenching gas used in the present work, no drifts in the amount of radiation imprisonment can be expected and reaction (b) can be neglected. The further fate of the metastable Hg6($^3P_0$) atoms, however, is important. The possible processes are:

(d) $Hg'+\text{wall} \rightarrow Hg$,

(e) $Hg'+M \rightarrow Hg^*+M$,

(f_1) $Hg'+N_2O \rightarrow Hg+N_2+O$,

(f_2) $Hg'+RH \rightarrow Hg+R+H$,

(g_1) $Hg'+N_2O$, (g_2) $Hg'+RH$ $\rightarrow$ deactivation of Hg′, followed by dissipation of energy.

Reaction (d) can be neglected at the pressures employed. Reaction (e) occurs readily with nitrogen and some other inert gases, but, as shown experimentally by Klumb and Pringsheim[4] a direct reaction of Hg′ with extremely small amounts of a reactive substance, such as hydrogen, can successfully compete with it, so that it can be ruled out in the present experiments. Reactions of the type (f) have been postulated before, as well as reactions (g)[3,5] which, for the moment, need not be specified in detail. A steady state treatment of reactions (a), (1), (1′), (2), (2′), (f_1), (f_2), (g_1), and (g_2), gives

$$\frac{1}{R_{N_2}}=\frac{k_1+k_1'}{k_1 Ia}\left(1+\frac{k_2+k_2'}{k_1+k_1'}\frac{(RH)}{(N_2O)}\right)\frac{1}{1+\left[\frac{k_1'}{k_1}+\frac{k_2}{k_1}\frac{(RH)}{(N_2O)}\right]\Big/\left[\frac{k_{f_1}+k_{g_1}}{k_{f_1}}+\frac{k_{f_2}+k_{g_2}}{k_{f_1}}\frac{(RH)}{(N_2O)}\right]}. \tag{2}$$

In order to reduce this expression to the experimentally observed Eq. (1) it is sufficient (a) that $k_{g_1}=0$ and $k_{f_2}/k_{f_1}=k_2/k_1$, or (b) that $k_{f_1}=0$. The respective expressions for the two possibilities are

$$\frac{1}{\phi_{N_2}}=1+\frac{k_2}{k_1}\frac{(RH)}{(N_2O)} \tag{2a}$$

and

$$\frac{1}{\phi_{N_2}}=\frac{k_1+k_1'}{k_1}\left[1+\frac{k_2+k_2'}{k_1+k_1'}\frac{(RH)}{(N_2O)}\right]. \tag{2b}$$

The first of the two alternatives is formally equivalent to the case when no quenching to the metastable state occurs. It requires the primary quantum efficiencies to be unity and, although attractively simple, it is difficult to reconcile with all the experimental observations even if an unlikely large uncertainty is assumed for actinometric determinations. For this reason it is necessary to adopt the second alternative and neglect reaction (f_1). (A comparison of yields of nitrogen and hydrogen in the N_2O—n-C_4H_{10} mixtures, discussed in the following, shows that reaction (f_2) is also unimportant.) Equation (1) assumes, therefore, the form of the Eq. (2b) and the observed experimental values for β, the slope to intercept ratios of the plots in Fig. 2, are identified with the relative over-all quenching efficiencies. The relative effective quenching cross sections are then calculated from the relationship

$$\frac{\sigma_1^2}{\sigma_2^2}=\frac{\beta_1}{\beta_2}\left(\frac{1+M_{Hg}/M_2}{1+M_{Hg}/M_1}\right)^{\frac{1}{2}}. \tag{3}$$

It is evident from the plots in Fig. 2 that the quenching cross sections are temperature independent in the investigated temperature range.

The relative quenching cross sections obtained for N_2O, n-C_4H_{10}, C_2H_6, and C_2H_4, as well as preliminary values for some oxygen containing compounds obtained in the same manner, can be compared with the quenching cross sections found in the literature, determined mainly by physical quenching measurements under vastly different experimental conditions. Assuming, arbitrarily, the quenching cross section of n-butane to be 3.6 A^2, the relative values shown in Table IV are obtained.

In view of the considerable differences in the values of quenching cross sections, obtained by different authors with the use of physical measurements, the parallelism between the two sets of values is, in general, good. The quenching cross section of ethylene oxide is much smaller than that of the isomeric acetaldehyde, and is comparable to that of a saturated hydrocarbon.

[4] H. Klumb and P. Pringsheim, Z. Physik **52**, 610 (1929).
[5] H. E. Gunning and E. W. R. Steacie. J. Chem. Phys. **14**, 544 (1946).

There is, however, an extremely large disagreement in the case of nitrous oxide. The unusually large value of 100 A^2 was obtained from pressure measurements in the course of mercury sensitized decomposition of nitrous oxide. Since it has now been shown[2] that oxygen and not the postulated nitric oxide is a major product in this process, the value of 100 A^2 may be much reduced on reinterpretation of the data.

As a further test of the correctness of the aforementioned interpretations, experiments were carried out with ternary mixtures of N_2O, C_2H_4, and n-C_4H_{10} of varying composition. For such mixtures

$$\frac{1}{\phi_{N_2}}=\frac{k_1+k_1'}{k_1}\left[1+\frac{k_2+k_2'}{k_1+k_1'}\frac{(n-C_4H_{10})}{(N_2O)}+\frac{k_3+k_3'}{k_1+k_1'}\frac{(C_2H_4)}{(N_2O)}\right], \quad (4)$$

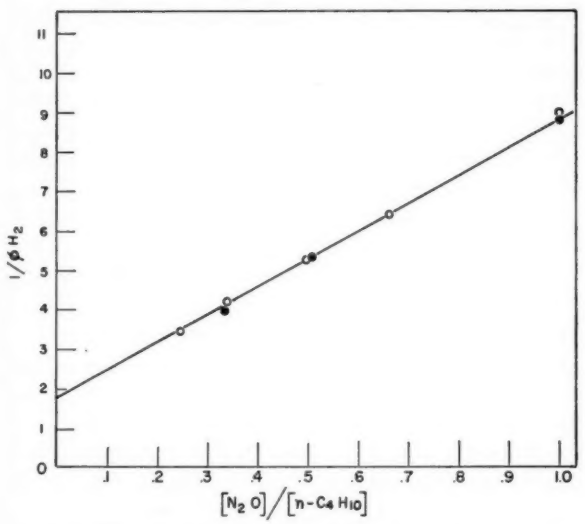

FIG. 3. Plots of $1/\phi_{H_2}$ against the nitrous oxide to n-butane. The symbols represent: ○, static runs at 23°C and ●, static runs at 123°C.

where the subscripts 1, 2, and 3 refer to N_2O, n-C_4H_{10}, and C_2H_4, respectively. The results are summarized in Table V. The observed quantum yields of nitrogen are in good agreement with the values calculated from Eq. (4) using the relative quenching efficiencies obtained with the respective binary mixtures.

The value of $k_1/(k_1+k_1')$, i.e., the fraction of quenching of nitrous oxide to the ground state of mercury, obtained from the reciprocal values of the intercepts of $1/\phi_{N_2}$ plots for the three hydrocarbons used in these studies, is 0.78±0.01 and 0.80±0.01 at 23° and 120°, based on the quantum yield values for hydrogen formation in mercury sensitized decomposition of n-butane.[3] The relative fractions of the quenching to the ground and to the metastable state of mercury appear, therefore, to be also temperature independent. That a temperature independence of these fractions is exhibited as well by n-butane is shown in the following section.

TABLE IV. Quenching cross sections.

Compound	Quenching cross sections (A^2) Present determinations	Literature data
n-Butane	3.6[a]	3.0,[b] 4.06[c]
Ethane	0.10	0.11,[b] 0.415[c]
Ethylene	22	26[d]
Nitrous oxide	12.6	100[e]
Ethylene oxide	2.7	...
Acetaldehyde	29	...
Acetone	37[f]	32[d]

[a] The value assumed as reference standard.
[b] B. deB. Darwent, J. Chem. Phys. 18, 1932 (1950).
[c] W. A. Noyes, Jr., and P. A. Leighton. *The Photochemistry of Gases* (Reinhold Publishing Corporation, New York, 1941) p. 221.
[d] deB. Darwent, Phibbs, and Hurtubise, J. Chem. Phys. 22, 859 (1954).
[e] W. M. Manning and W. A. Noyes, Jr., J. Am. Chem. Soc. 54, 3907 (1932).
[f] A slight curvature in the $1/\phi_{N_2}$ plot for acetone makes this value somewhat uncertain.

II. Mechanism of Quenching of Hg6($^3P_1$) Atoms by Saturated Hydrocarbons

In the investigated N_2O—C_2H_6 mixtures the very small amounts of hydrogen produced are subject to a large analytical error and may also be seriously affected by secondary processes. For this reason the following discussion is restricted mainly to N_2O—n-C_4H_{10} mixtures.

In Fig. 3, $1/\phi_{H_2}$ has been plotted against the N_2O to n-C_4H_{10} ratio for those static experiments with N_2O—n-C_4H_{10} mixtures at room temperature and at 123°C in which reasonably large amounts of hydrogen were produced. A good straight line can be drawn through the points in agreement with the following theoretical expression, analogous to Eq. (2b),

$$\frac{1}{\phi_{H_2}}=\frac{k_2+k_2'}{k_2}\left[1+\frac{k_1+k_1'}{k_2+k_2'}\frac{(N_2O)}{(n-C_4H_{10})}\right] \quad (5)$$

and using for $(k_1+k_1')/(k_2+k_2')$ the reciprocal of the value for $(k_2+k_2')/(k_1+k_1')$ obtained from the $1/\phi_{N_2}$ plot (subscripts 1 and 2 refer to N_2O and n-C_4H_{10}, respectively). The intercept gives for $k_2/(k_2+k_2')$ a value of 0.57. The relatively low fraction of quenching to the ground state may be compared with a similar

TABLE V. Mixtures of nitrous oxide, ethylene, and n-butane.

Run	Temp °C	N_2O mm	C_2H_4 mm	$n-C_4H_{10}$ mm	Irradiation min	R_{N_2} (molec sec^{-1} $\times10^{-16}$)	ϕ_{N_2} observed	ϕ_{N_2} calc from Eq. (4)
61	24.3	100.9	24.9	24.7	200	1.16	0.50	0.49
62	23.4	201.3	40.1	98.6	200	1.14	0.51	0.51
63	24.9	151.9	49.0	146.9	200	0.900	0.40	0.41
64	26.2	100.8	7.54	203.9	170	1.05	0.47	0.47
66	24.9	100.6	7.55	202.5	160	1.03	0.47	0.47
68	24.5	100.7	7.64	201.6	170	1.01	0.48	0.47
70	23.2	101.7	7.85	104.3	160	1.19	0.55	0.55

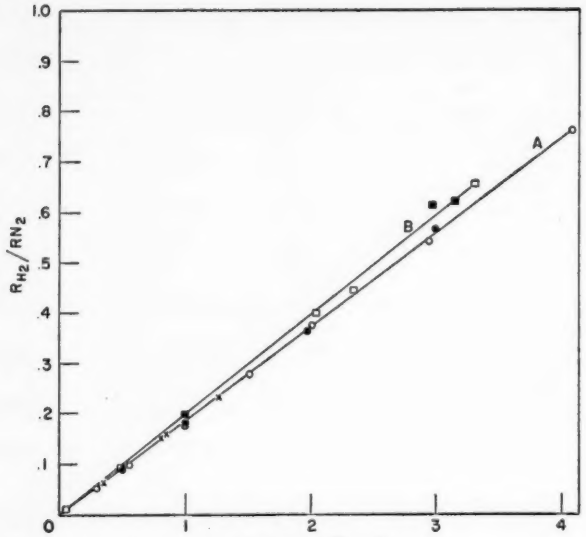

FIG. 4. Plots of R_{H_2}/R_{N_2} against the *n*-butane to nitrous oxide ratio. A——static runs; B——circulating runs. The symbols represent: ○, static runs at 23°C; ●, static runs at 123°C; □, circulating runs at 23°; and × and ■ static and circulating runs, respectively, at 23° with lowered mercury vapor concentration.

conclusion arrived at by Thomas and Gwinn[6] for quenching by hydrogen.

Since $k_1/(k_1+k_1')=0.78$, $k_2/(k_2+k_2')=0.57$, and $(k_2+k_2')/(k_1+k_1')=0.255$, it is seen that $k_2/k_1=0.18$. The outlined conceptions of competing reactions leading to the formation of N_2 and H_2, respectively, require that

$$\frac{R_{H_2}}{R_{N_2}}=\frac{k_2}{k_1}\frac{(n\text{-}C_4H_{10})}{(N_2O)} \tag{6}$$

provided all hydrogen is produced from hydrogen atoms formed in reaction (2) by abstraction of an additional hydrogen atom. The values of R_{H_2}/R_{N_2} are plotted in Fig. 4A, against $(n\text{-}C_4H_{10})/(N_2O)$ for static experiments at room temperature and at 123° for a wide variation of experimental conditions. The points lie on a straight line through the origin, as required by Eq. (6), with the slope equal to the above value of k_2/k_1. For the investigated range no temperature dependence of the relative constant k_2/k_1 is found.

The yields of nitrogen and hydrogen in mixtures of nitrous oxide and *n*-butane in static runs, therefore, lend themselves to a quantitative and mutually consistent interpretation. It is, however, also necessary to explain the following observations: (1) there is a decrease in the quantum yields with decreasing mercury concentration both in N_2O—n-C_4H_{10} mixtures and with n-C_4H_{10} alone; (2) hydrogen production is somewhat increased in circulating runs, while the yield of nitrogen remains unaffected; (3) the observation of Bywater and Steacie[3] that with increasing temperature there is a gradual increase in the quantum yield of hydrogen in the mercury sensitized decomposition of n-C_4H_{10} alone, even in the low-temperature region where no secondary formation of hydrogen by radical decomposition takes place.

The experiments performed with lowered mercury concentration are summarized in Table VI. Considering for the moment only the static runs, it is evident that with a decrease in mercury concentration R_{N_2} and R_{H_2} are reduced by a common factor since the ratios R_{H_2}/R_{N_2} show no deviation from the plot in Fig. 4A. The decrease appears, therefore, as equivalent to a lowering in light absorption. A similar effect is observed with *n*-butane alone, as shown in Table VII and Fig. 5 (curves A and C), and has also been reported by Darwent[7] for ethylene alone, Fig. 5, (curves D and E). In view of the proposed complex interpretation of the latter effect[7] experiments were carried out with 50 mm of ethylene and the mercury vapor concentration reduced to the value corresponding to 0°C. It was found that the decrease in ϕ_{H_2} was accompanied by a pronounced decrease in the amount of light absorbed as measured by a phototube placed immediately behind the back window of the reaction cell. Both the decrease in the amount of light absorption and in the yield of hydrogen were approximately comparable with those observed with *n*-butane under similar conditions. The effects with the two hydrocarbons appear, therefore, to be due to decreased absorption of the incident light coupled, possibly, with a somewhat decreased imprisonment of radiation. In other respects they do not seem to exhibit any new features necessitating further discussion. A similar conclusion was arrived at by Callear and Robb[8] who found no variation in the

TABLE VI. Mixtures of nitrous oxide and *n*-butane. Experiments with lowered mercury vapor concentration.[a]

Run	Temp	Pressure	$\frac{n\text{-}C_4H_{10}}{N_2O}$	Relative[b] ϕ_{N_2}	Irradiation min	$\frac{R_{H_2}}{R_{N_2}}$
			Static runs			
115	24.6	182.6	0.817	0.65	100	0.153
117	24.9	151.1	0.504	0.86	155	0.096
118	24.7	452.0	3.58	0.72	120	0.647
119	24.4	151.6	0.504	0.83	121	0.090
120	24.6	186.4	0.841	0.75	110	0.158
121	24.3	226.4	1.26	0.71	110	0.231
			Circulating runs			
122	22.9	153.2	0.495	0.70	110	0.090
123	24.7	416.1	3.15	0.61	110	0.622
125	22.3	204.8	1.00	0.63	110	0.199
126	23.0	398.1	2.96	0.60	110	0.615

[a] In runs 123, 125, and 126 $p_{Hg}\approx 1.8\times10^{-4}$ mm; in the other runs $1.8\times10^{-4}<p_{Hg}<18\times10^{-4}$ mm.

[b] ϕ_{N_2} expressed as a fraction of the quantum yield of nitrogen for the same ratio of the reactants when mercury vapor concentration corresponds to room temperature.

[6] L. B. Thomas and W. D. Gwinn, J. Am. Chem. Soc. **70**, 2643 (1948).

[7] B. deB. Darwent, J. Chem. Phys. **20**, 1673 (1952).

[8] A. B. Callear and J. C. Robb, Discussions Faraday Soc. **17**, 21 (1954).

quantum yield of hydrogen from ethylene alone with varying mercury vapor concentration when the incident beam from a water cooled mercury resonance lamp was well collimated. The decrease in the yields of hydrogen at low pressures of the hydrocarbons, as shown in Fig. 5, may also be caused by a decrease in the amount of light energy transferred to the hydrocarbons and, in the case of *n*-butane, by diffusion of H atoms to the reaction vessel walls. These effects are not observed in the mixtures with large amounts of N_2O employed in the present study.

In circulating runs with *n*-butane alone and *n*-butane nitrous oxide mixtures there was a distinct increase in the quantum yield of hydrogen while the yield of nitrogen remained unaffected. This is particularly evident from plots in Figs. 1, 4, and 5. Under those conditions more hydrogen is produced than could be expected on the basis of reaction (2) alone. The additional source of hydrogen is to be sought in the refinement of the reactions (g). In order to explain all the experimental observations, one is led to the following scheme of reactions as a replacement for the reactions (g) for the case of saturated hydrocarbons alone or their mixtures with nitrous oxide:

$$(4) \qquad Hg' + RH \rightarrow HgH + R,$$

$$(5) \qquad R + HgH \rightarrow Hg + RH^*,$$

$$(5a) \qquad RH^* + M \rightarrow RH + M,$$

$$(5b) \qquad RH^* \rightarrow R_1 + R_2,$$

$$(6) \qquad HgH \rightarrow Hg + H.$$

The dissipation of the excitation energy of the metastable atoms will readily occur in static runs at room temperature through reactions (4) and (5),

TABLE VII. Mercury sensitized decomposition of *n*-butane.

Run	Temp °C	Pressure mm (25°)	Irradiation min	R_{H_2} (molec sec^{-1} $\times 10^{-16}$)	ϕ_{H_2}
Mercury saturator at room temp, static runs					
79	23.7	152.3	180	0.997	0.478
80	21.6	253.5	180	1.06	0.510
81	22.5	396.0	180	1.11	0.532
82	22.0	611.7	180	1.16	0.558
84	22.2	53.5	180	0.789	0.379
85	21.1	40.3	180	0.722	0.346
86	23.3	81.9	180	0.861	0.413
109	22.2	52.0	55	1.92	0.376
112	24.6	200.6	55	2.48	0.500
Mercury saturator at room temp, circulating runs					
133	23.4	201.3	60	2.38	0.542
134	22.7	122.8	55	2.22	0.505
135	22.9	53.6	55	1.88	0.427
141	24.2	354.7	60	2.43	0.582
Mercury saturator at 0°C, static runs					
110	23.1	52.4	55	1.43	0.283
111	23.4	201.2	55	1.69	0.337
113	25.1	317.8	55	1.71	0.347
114	25.3	100.1	55	1.48	0.299

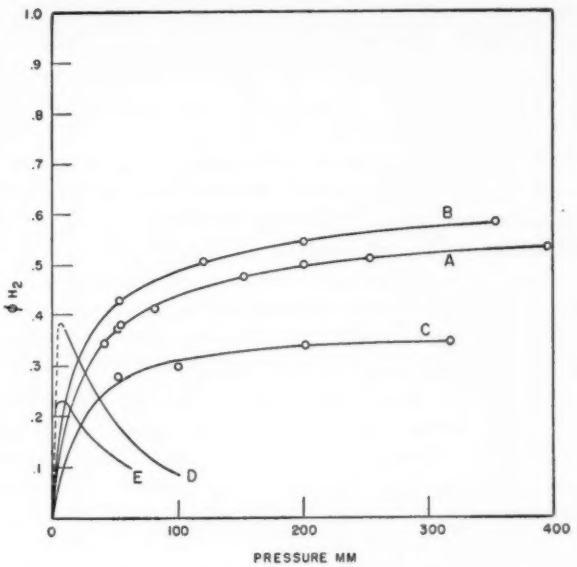

FIG. 5. Quantum yield of hydrogen production from n-C_4H_{10} alone at room temperature as a function of pressure. A——static runs and B——circulating runs with mercury vapor concentration corresponding to ~23°C; C—— static runs with mercury vapor concentration corresponding to 0°C. Curves D and E are based on Darwent's (reference 7) data for ethylene with mercury vapor concentration corresponding to 20° and 0°C, respectively.

since the local radical concentration in mercury sensitized reactions is relatively high. This explains the repeatedly observed low quantum yields in the mercury sensitized decomposition of hydrocarbons. In agreement with it the limiting value of ϕ_{H_2} at high pressures of *n*-butane alone in static runs at room temperature coincides with the value to be expected from reaction (2) followed by hydrogen abstraction from the hydrocarbon. Under those conditions reaction (6) is unimportant. Analogous conditions prevail in static runs of the *n*-butane—N_2O mixtures, both at room temperature and at 120°C, since in this case the concentration of free atoms and radicals, some of which are quite long lived, is largely enhanced. In circulating runs, on the other hand, reaction (6) (which as written symbolizes any mode of decomposition of HgH) is somewhat favored at the expense of reaction (5), since the local concentrations of R and HgH are much reduced, and an increased yield of hydrogen results. In a similar manner the observation of Bywater and Steacie[3] that in the case of *n*-butane alone ϕ_{H_2} gradually increases with temperature is explained by a gradual increase in the importance of reaction (6). For sufficiently high temperatures the experimental ϕ_{H_2} values would be expected to extrapolate approximately to unity, as has been actually observed by Bywater and Steacie[9] for a number of hydrocarbons.

The suggested reactions (4), (5), and (6) are logical possibilities in view of the extensive work performed in

[9] S. Bywater and E. W. R. Steacie, private communication.

the past in the field of quenching phenomena.[10,11] In conjunction with the other reactions suggested they explain all the reported experimental observations, and in particular the remarkable lack of temperature dependence in the N_2O—n-C_4H_{10} mixtures. That HgH molecules are capable of sufficiently long existence in vapor phase in the presence of other gases to participate in collisional processes before decomposing, is clearly indicated by the experiments of Gaviola and Wood.[10]

The proposed scheme is not of general applicability and other modes of dissipation of energy, such as "physical quenching,"[5] may be important for some types of compounds. It can, however, be extended to hydrogen, in which case it reconciles the low primary efficiency found by Thomas and Gwinn[6] with the findings of Callear and Robb.[12] The latter authors measured the heat balance of the process when small amounts of ethylene were added to hydrogen and found a primary efficiency of close to unity. Inasmuch as ethylene is capable of intercepting reaction (5) (where now R=H), a primary efficiency of unity should be observed.

Reaction (5) is strongly exothermic and may be assumed to require little energy of activation. The exothermicity is not sufficient to result in a C—H bond split in the produced hydrocarbon molecule, but may lead to a C—C bond rupture [reaction (5b)] or to a dissipation of the liberated energy by collisions [reaction (5a)]. In this respect it may be equivalent to the "atomic cracking" reactions suggested by Darwent and Steacie[13] to explain methane formation in the mercury sensitized decomposition of ethane.

The quantum yields of hydrogen in the case of ethylene–nitrous oxide mixtures exhibit the expected decline with the total pressure compatible with the postulated[14] initial formation of an excited ethylene molecule. Since some hydrogen is also formed by the action of oxygen atoms on ethylene, a detailed quantitative treatment is deferred until more experimental data are obtained.

In the work of Taylor and Zwiebel[15] on mercury sensitized reaction of nitrous oxide and hydrogen the water formed in the reaction was continuously removed by absorption with P_2O_5. The rate of diffusion of water vapor to the drier was relatively slow and some assumptions had to be made in order to correlate the observed pressure changes and the rate of the water forming reactions. In view of this and the widely different general experimental approach it is felt that an attempt to derive the relative over-all quenching efficiency for this system by extending the present treatment to the data of these authors would not be justifiable.

The values of all the obtained relative over-all quenching constants $(k+k')/(k_1+k_1')$ as well as of k_2/k_1 are independent of the actinometric determinations used as the basis for quantum yield determinations in the present work. On the other hand, the values of $k_1/(k_1+k_1')$ and $k_2/(k_2+k_2')$, for N_2O and n-butane, respectively, depend on the knowledge of the actual amount of light absorbed (Ia). In view of the difficulties inherent in the actinometric determinations, too much weight cannot be placed on the absolute value of the intercepts of the plots in Fig. 2. They may possibly be subject to an uncertainty of 10 to 20 percent. If the ratio of the value of Ia experimentally found to the actual value is a factor f different from unity, the constants $k_1/(k_1+k_1')$ and $k_2/(k_2+k_2')$ have to be multiplied by f. Since $k_1/(k_1+k_1')$ cannot be larger than unity, the upper limit for $k_2/(k_2+k_2')$ is 0.72. Regardless of the accuracy of the light absorption determinations, therefore, it is evident that a considerable part of the primary quenching of the Hg6($^3P_1$) atoms by n-butane is to the metastable Hg6($^3P_0$) state.

ACKNOWLEDGMENTS

The author is indebted to Dr. F. P. Lossing and Miss Frances Gauthier for the mass spectrometer analysis.

[10] A. C. G. Mitchell and M. W. Zemansky, *Resonance Radiation and Excited Atoms* (Cambridge University Press, Cambridge, 1934), pp. 76–79.

[11] B. deB. Darwent and F. G. Hurtubise, J. Chem. Phys. **20**, 1684 (1952).

[12] A. B. Callear and J. C. Robb, private communication (to be published).

[13] B. deB. Darwent and E. W. R. Steacie, J. Chem. Phys. **16**, 381 (1948).

[14] D. J. LeRoy and E. W. R. Steacie, J. Chem. Phys. **9**, 829 (1941).

[15] H. A. Taylor and N. Zwiebel, J. Chem. Phys. **14**, 539 (1946).

Determination of the Atomic Weight of Silicon by Physical Measurements on Quartz*†

CLIFFORD FRONDEL AND C. S. HURLBUT, JR.
Harvard University, Cambridge, Massachusetts

(Received July 23, 1954)

The value 28.095±0.005 for the atomic weight of silicon has been obtained through precision measurements of the density and unit-cell volume of an unusually pure crystal of natural quartz, SiO_2. The value is based on the Avogadro number, 6.02338, and wavelength conversion factor, 1.002030, of Birge (1945). The following experimental data were obtained: density in g/cc in vacuum at 25°, 2.64847±0.0001; unit-cell dimensions in *kX* at 25° and corrected for refraction, a_0 4.90360, c_0 5.39417, both ±0.0001; indices of refraction for λ589.29 mμ at 18°, *nO* 1.544258, *nE* 1.553380, both ±0.00001; inversion temperature 573.3° on both heating and cooling cycles. Direct analysis gave (weight percent): Li_2O 0.0005, Na_2O 0.0004, K_2O 0.0002, Al_2O_3 0.0008, TiO_2 0.0001, MnO_2 0.00002, Fe_2O_3 0.0000. The major systematic errors in this method stem from compositional variation in the quartz, of the nature of a coupled substitution of Al for Si with interstitial (Li,Na), and probably lead to a high value for the atomic weight. For purposes of comparison, data are also given for smoky quartz, rose quartz, and a synthetic quartz containing much Al and Li in solid solution.

INTRODUCTION

MODERN determinations by chemical methods of the atomic weight of silicon range from 28.06 to 28.38, with the most recent values[1] ranging between 28.089 and 28.11. Recently, Straumanis and Aka[2] have determined the atomic weight by the physical method. Their value, 28.083±0.013, agrees, within the limits of precision stated, with the chemical atomic weight 28.09 recommended by the International Committee of Atomic Weights in 1951.[1] The measurements of Straumanis and Aka involved precision measurement of the unit-cell volume and density of synthetic crystals of silicon containing about 0.03 weight percent of C. It is not known if the C is present in solid solution or as enclosed particles of graphite or SiC. The accuracy, rather than the precision, of their density determinations may be questioned in lack of evidence identifying the observed variation in density with particular characters of the crystals, or that the particular experimental values selected by them are liminal for the substance and not merely liminal for the particular preparation at hand.

The low-temperature polymorph of SiO_2, quartz, appears to be better suited to the determination by the physical method of the atomic weight of silicon than elemental silicon. The transparency of the substance permits careful inspection for cracks and inclusions of foreign matter, and material of relatively high chemical purity can be obtained in bulk either from natural crystals or by hydrothermal synthesis. There is further an extensive background of precision measurements on the density, unit-cell dimensions, and other properties relevant to the problem.

DESCRIPTION OF MATERIAL USED

The main study was made on a colorless, transparent crystal of natural quartz from Hot Springs, Arkansas, designated hereafter as C105, of the type known in trade as of "optical quality." The sphere and prism cut from this flawless crystal, described beyond, were examined both in polarized light and after etching with HF to ensure the absence of twinning. The material also was found free from inclusions, cracks, and other physical imperfections visible under moderate magnification. Since it is well established that the properties of quartz show a very small but significant variation, due to variation in the chemical composition of the substance, a chemical analysis and certain physical measurements sensitive to composition were made on the crystal to characterize it more fully.

CHEMICAL COMPOSITION

Table I cites an analysis of quartz C105 in comparison with analyses made at the same time on selected samples of smoky, amethystine, and rose quartz. The determinations were made on acid-washed samples of large size. The alkali determinations were made by the flame photometer by R. B. Ellestad of the U. S. Geological Survey. The Ti and Mn determinations were made colorimetrically and the Fe and Al determinations by the thioglycolic acid and aluminon methods, by J. A. Maxwell of the Rock Analysis Laboratory, University of Minnesota. Amethyst and rose quartz are shown by the present analyses and by earlier work to be characterized by the presence of relatively large amounts of

TABLE I. Chemical analyses of quartz samples.

	Li_2O	Na_2O	K_2O	Al_2O_3	Fe_2O_3	MnO_2	TiO_2
Colorless, C105	0.0005	0.0004	0.0002	0.0008	0.0000	0.00002	0.0001
Smoky, S101	0.0004	0.0000	0.0000	0.0008	0.0005	0.00002	0.0002
Rose, R102	0.0038	0.0011	0.0001	0.0001	0.0003	0.00005	0.0015
Rose	0.0038	0.0104	0.0010	0.0004	0.0006	0.00004	0.0011
Amethyst	...	...	...	0.0004	0.0216	0.00000	0.0004

* Contribution from the Department of Mineralogy and Petrography, Harvard University, No. 352.

†The data here presented are part of an investigation of the properties of quartz made under contract with the Frequency Control Branch, U. S. Army Signal Corps, Fort Monmouth, New Jersey.

[1] E. Wichers, J. Am. Chem. Soc. **74**, 2447 (1952); Chem. Eng. News **29**, 4077, (1951); J. Am. Chem. Soc. **76**, 2033 (1954).

[2] M. Straumanis and E. Z. Aka, J. Appl. Phys. **23**, 330 (1952).

TABLE II. Indices of refraction of colorless C105 and smoky S101 quartz for Na light ($\lambda = 589.29$) at 18°C. The probable error is ±0.00001.

Material	*nO*	*nE*
Colorless C105	1.544258	1.553380
Smoky S101	1.544214	1.553369
"Most probable value" of Sosman[a]	1.544246	1.553355

[a] See reference 3.

Fe and Ti, respectively. The interpretation of the analyses of quartz in general, particularly with regard to the content of alkalies, is complicated by the common occurrence in quartz of minute cavities containing entrapped solution.

INDICES OF REFRACTION

The indices of refraction of quartz are known from numerous, highly precise measurements[3] to vary significantly. Unfortunately, the values for ideally pure quartz are not known, the extent of variation is not established and none of the earlier measurements were made on analyzed samples. The present data, cited in Table II, were obtained on a 60° prism by the method of minimum deviation, using a Fuess single-circle optical goniometer reading directly by filar micrometer to 10 seconds of arc and capable of interpolation to about 2 sec. The measurements were made at known temperature in a constant-temperature room, and are here given as reduced to 18° by the coefficients of Micheli.[4] The prism was sawed under x-ray control so that the *c*-axis was parallel to the prism edge within 5 minutes of arc. The two faces were polished to a flatness of $\frac{1}{4}$ wavelength for Na light. The indices obtained on quartz C105 are virtually identical with the values at the same wavelength and temperature derived by Sosman[3] as representing the most probable value for a randomly selected, natural colorless quartz crystal of optical grade (Table II). Since the value of Sosman is essentially an average, the indices cannot refer to ideally pure quartz. A specimen of very deep colored smoky quartz, S101 (analysis given in Table I) was found to have indices of refraction slightly lower than the colorless sample C105. After the prism of this material was decolorized by heating at 350° the indices increased.

INVERSION TEMPERATURE

The temperature of the enantiotropic inversion between low and high quartz has been shown by Keith and Tuttle[5] to vary significantly, chiefly as a function of the substitution of Al for Si. The inversion temperature decreases and the inversion becomes sluggish as the content of Al increases, but the quantitative relation is not known. An examination by Keith of sample C105 gave the inversion temperature as 573.3° on both the heating and cooling cycles. The inversion temperature for pure quartz appears from the data of Keith and Tuttle to be in the range 573.3° to 573.6° on heating and 573.3° to 574.0° on cooling. Sample C105 is one of a few out of about 250 samples examined that falls in this range, and thus from this evidence appears to be relatively pure.

EXPERIMENTAL METHOD

Density

The size, clarity, and physical perfection of some quartz crystals permits the use of bulk single-crystal methods for the determination of density. The method here employed is a modification of that of various early workers[6] who determined the volume and weight independently of large shaped objects of quartz. Some of these density measurements have a precision of the order of 0.000002, and they doubtless include the best determinations yet made on any crystalline substance. In the present work, a sphere approximately 2.77 cm in diameter was ground and polished from crystal C105 by the Jones Optical Company, Cambridge, Massachusetts. The departure from sphericity was stated by them to be random and less than 0.00002 cm. The volume of the sphere was then determined at known temperature by micrometer measurements of the diameter made independently in the laboratories of the Ames Instrument Company, Waltham, Massachusetts, the Watertown Arsenal, Watertown, Massachusetts, and the Pratt and Whitney Company, Hartford, Connecticut. The diameter was measured at many different points on the surface of the sphere and the values averaged; no systematic departure from sphericity was observed. The measured volume was corrected to vacuum at 25° from the temperatures of measurement. The weight of the sphere (~29.6 g) was then obtained directly by double-weighing, using a balance sensitive to 0.01 mg. The weight was corrected to vacuum, and the density computed in g/cm³ at 25°. An independent determination of the density was made at the National Bureau of Standards by the method of hydrostatic weighing. The several sets of data are tabulated in Table III. The measurements obtained by Ames Instrument Company were rejected because of a question as to the actual temperature of the sphere during measurement. The average of the various micrometer values and of the hydrostatic value is 2.64847, and this is taken as the density, at 25°, of the sample. The experimental and systematic errors are difficult to assess, but the precision of the value given probably is about ±0.0001.

A parallel set of measurements was made on a

[3] See summary in R. B. Sosman, *The Properties of Silica* (Chemical Catalog Company, New York, 1927).
[4] Cited in Sosman, reference 3.
[5] M. L. Keith and O. F. Tuttle, Am. J. Sci., Bowen Volume, 203 (1952).
[6] See summary in Sosman, reference 3.

polished sphere of flawless smoky quartz (analysis given in Table I). These data, also given in Table III, afford a value for the density of 2.64849±0.0001, virtually identical with that of the colorless material. Tests by the very sensitive but qualitative heavy-liquid method mentioned beyond showed that the colorless and smoky material had virtually the same density, the smoky material being very slightly more dense. A much greater difference was shown by a sample of rose quartz (analysis R102 in Table I), the density of which, determined by the sphere method, was less than those of the colorless and smoky material by about 0.0004. These observations confirm the precision at least of the density measurements.

The precision measurements of the density of colorless quartz of optical grade reported in the literature indicate that there is a variation between different samples of probably as much as 0.0005. As in the case of the indices of refraction, however, the quantitative relation between density and composition is not known, and the liminal value for ideally pure quartz is not known. Sosman[3] gives the most probable value for the density of a randomly selected, natural colorless quartz crystal of optical grade as 2.6506±0.0001 at 0° and atmospheric pressure (2.6483±0.0001 at 25°). The reality of the variation of the density of quartz can be easily shown by placing a dozen or so small flawless fragments of colorless quartz from different sources in a tube filled with a liquid such as a mixture of methylene bromide and bromoform that has been carefully adjusted in density to a value so that all of the fragments just barely float. If the liquid is now very slowly and uniformly warmed, to decrease its density, the fragments will sink unequally.

Unit-Cell Dimensions

The unit-cell dimensions of quartz C105 were measured by the x-ray powder diffraction method using a precision symmetrical back-reflection camera.[7] A number of separate films were made from trim pieces of the sphere C105 used in the density determinations. Each film was measured three times, and each measurement of each film, comprising the d-spacings of the 16 highest order α_1 and α_2 reflections, was extrapolated to $\theta=90°$ using the function of Nelson and Riley.[8] The separate measurements for all films were than averaged to give the final cell dimensions: $a_0=4.90360$, $c_0=5.39417$ in kX at 25°. The maximum variation in both a_0 and c_0 present in the extrapolated values of all film measurements was 0.00022 kX, and the average deviation was 0.00005 kX. The precision of the averaged measurements is estimated at about 1 part in 50 000.

[7] The design and use of this camera has been described by C. Frondel, Am. Mineralogist (to be published).

[8] J. B. Nelson and D. P. Riley, Proc. Phys. Soc. (London) **57**, 160 (1945).

TABLE III. Density of colorless and smoky quartz (reduced to 25° from temperature of measurement).

	Colorless, C105	Smoky, S101
Watertown Arsenal	2.64841	2.64847
Pratt and Whitney (1 lb press.)	2.64832	2.64835
Pratt and Whitney (2.5 lb press.)	2.64855	2.64864
Average	2.64843	2.64849
Bureau of Standards (hydrostatic method)	2.64851	2.64849
Average	2.64847	2.64849

The cell dimensions were reduced to 25° from the thermostated temperature (31.1°C) using the coefficients of thermal expansion of Jay,[9] and a refraction correction was applied. The Siegbahn wavelengths used in the calculations were CuK_{α_1} 1.537395, CuK_{α_2} 1.541232 kX. A check determination by the writers on another back-reflection camera of lower precision gave $a_0=4.9037$, $c_0=5.3941$ (both ±0.0002) in kX reduced to 25° from 31.1°. An independent check[10] on a precision 16-cm central-mount camera made at 25°, using diamond ($a_0=3.55969$ kX at 25°) for film calibration, gave the closely agreeing dimensions $a_0=4.90363$, $c_0=5.39421$ kX. A number of other precision determinations of the unit cell dimensions of colorless quartz have been reported[11] but without information as to the content of trace elements or the density of the samples. The values range from about $a_0=4.9037$, $c_0=5.3941$ to $a_0=4.9031$, $c_0=5.3936$ (in kX at 25°).

The cell dimensions of the smoky quartz of analysis S101, Table I, were found to be slightly less than those of colorless quartz C105, as were the indices of refraction before decolorization, although the density and composition of the two samples is virtually identical (Tables I and III). Hammond[12] also has found that the cell dimensions of smoky quartz are lower than those of colorless material. It is not known what change if any takes place in the density and unit cell dimensions on decolorization. The elastic constants of this particular sample of smoky quartz were found by Frondel[13] to alter appreciably on decolorization. Smoky quartz does not seem to be suitable material for atomic weight measurements.

[9] A. H. Jay, Proc. Roy. Soc. (London) **142A**, 237 (1933).

[10] B. Skinner, "Thermal Expansion of Selected Isometric Minerals as Determined by X-Ray Measurements," Harvard University, thesis, 1954. The a_0 value for diamond cited is the average of 12 precision determinations reported in the literature and has a standard deviation of ±0.00009 kX.

[11] See in particular H. D. Keith, Proc. Phys. Soc. (London) **63B**, 208 (1950); A. J. Bradley and A. H. Jay, Proc. Phys. Soc. (London) **45**, 507 (1933); A. J. C. Wilson and H. Lipson, Proc. Phys. Soc. (London) **53**, 245 (1941); M. L. Keith and O. F. Tuttle, reference 5.

[12] D. L. Hammond, Squier Laboratory, Fort Monmouth, New Jersey, private communication, 1953. Also in contract DA-36-039-SC-66, Rept. January, 1953.

[13] C. Frondel, Phys. Rev. **69**, 543 (1946).

Experimental Results and Discussion

Using the values for the density (2.64847±0.0001 at 25°) and the unit cell dimensions (a_0 4.90360, c_0 5.39417, both ±0.0001, in kX units, at 25°) of the analyzed colorless quartz C105, the atomic weight of Si can be derived from the relation

$$\text{mole wt. } SiO_2 = VNd/Z,$$

where V is the volume at known temperature of the unit cell ($=a_0^2 c_0 \sin 60°$). The cell dimensions are here converted from the Siegbahn scale to the grating scale by the factor 1.00203 of Birge (1945).[14] N equals 6.02338, the value of the Avogadro number of Birge (1945), d is density in g/cc at the same temperature, and Z is 3, the number of formula units of SiO_2 in the unit cell.

From the molecular weight of SiO_2 thus determined, the atomic weight of Si on the basis of O=16 (chemical scale) is 28.095±0.005. The limits of this value are given as half the difference between the maximum and minimum values afforded by the individual limits of variation stated for the experimental data. As noted, the cell dimensions contain a correction for refraction. There is some question of the propriety of this correction for diffraction from powders; omitting it, the value for the atomic weight is lowered by approximately 0.001.

The value 28.095±0.005 here obtained overlaps the value 28.083±0.013 obtained by Straumanis and Aka.[2] The value of these authors is based on a different Avogadro number,[15] corresponding to 6.02385 on the grating scale. Using the value of Birge (1945) here employed, their data affords the atomic weight 28.080 ±0.013. The two values then overlap between 28.090 and 28.093.

The principal systematic errors in the measurements appear to be due to variation in the composition of the quartz, from which stems the variations in properties. The compositional differences are chiefly a serial substitution of Al^3 for Si^4 in the (SiO_4) tetrahedra with a concomitant substitution of alkali ions, mostly the small ions Li and Na, in interstitial positions in the amount needed for valence compensation. In the relatively open structures of the high-temperature polymorphs of SiO_2, tridymite and cristobalite, extensive solid solution series are known to form by this mechanism. The substitution of Mn^4, Ti^4, or Ti^3 for Si also may be important, especially in rose quartz, and the coupled substitution of (OH) for O may be an added mechanism of valence compensation. While the extent of these substitutions in ordinary quartz and the quantitative relation to the properties is not known, their qualitative effects on the unit-cell dimensions and the density can be predicted. The unit-cell dimensions should increase as the content of Al, Ti, or Mn^4 increases, because these ions are larger than Si. The (Li, Na) ions act to increase the cell dimensions little if at all, since they occupy available interstices of approximately their own dimension in the structure. Thus, a sample of synthetic quartz prepared for us by G. C. Kennedy at 890° from a hydrothermal solution saturated in Al and Li was found to have the cell dimensions a_0=4.9045 kX, c_0=5.3950, both about 0.009 kX higher than sample C105. The temperature of high-low inversion of this sample was found by Dr. Keith to be very low, about 556° on heating and 565° on cooling, and the transition was extremely sluggish. A chemical analysis could not be obtained of this material due to intimate admixture with $LiAlSiO_4$, and precision optical and density measurements were precluded by the fine particle size of the material.

The substitution Al+(Li,Na)=Si, because of the increase in molecular weight, would increase the density if there were not an accompanying change in the cell volume. Actually the cell volume increases, thus tending to reduce the density, due to the substitution of Al. The net change probably is a small increase in density, especially if Na is the dominant alkali, but sufficient information is lacking to permit the question to be settled with certainty. A sample of synthetic quartz, grown from a solution lacking Al but containing Na, was found on direct comparison with C105 by the heavy-liquid method to have the same density.

The systematic error stemming from compositional variation in the natural-quartz sample employed thus tends toward high values for the cell volume, and probably also for the density, leading to a relatively high value for the atomic weight. The error in the cell volume probably is the most important of the systematic errors. Systematic error of other origin doubtless also is present in the measurements, principally in the temperature controls and in the anvil-pressure of the micrometers employed. A temperature error of 0.5°C, however, in the same direction in all of the controlled measurements changes the value for the atomic weight within the stated limits of precision. It may be noted that a measurable variation has been found in the O^{18} : O^{16} isotope ratio in different samples of quartz,[5] and that there are variations in the isotopic constitution of Si in different minerals.[16]

ACKNOWLEDGMENTS

The authors wish to express their appreciation to Miss Mary E. Morse, Mr. Peter Piston, and Mr. George Robinson for aid in the measurement and computation

[14] R. T. Birge, Am. J. Phys. **13**, 67 (1945).
[15] Compare M. Straumanis, Z. Physik **126**, 49, 64 (1949); Acta Cryst. **2**, 82 (1949).
[16] J. H. Reynolds and J. Verhoogen, Geochim. et Cosmochim. Acta **3**, 224 (1953); K. Rankama, *Isotope Geology* (London, 1954).

of the x-ray diffraction photographs, and to Mr. Henry Wenden for assistance in making the optical measurements. Dr. George Kennedy of the University of California and Dr. M. L. Keith of the Geophysical Laboratory, Washington, aided certain aspects of the work. Thanks also are expressed to officials of the Ames Instrument Company, the Pratt and Whitney Company, the Watertown Arsenal, and the National Bureau of Standards for their interest and aid in measurement of the quartz spheres.

THE JOURNAL OF CHEMICAL PHYSICS VOLUME 23, NUMBER 7 JULY, 1955

Effects of Anharmonicity of Vibration on the Diffraction of Electrons by Free Molecules

L. S. Bartell
Department of Chemistry, Iowa State College, Ames, Iowa
(Received July 22, 1954)

The increased experimental precision now attainable in electron diffraction by free molecules has necessitated a re-examination of the methods of interpretation of diffraction data to allow for the effects of nonrigidity of molecules. It is shown that conventional procedures of analysis of data lead to ambiguous results which are likely to differ from the true equilibrium internuclear distances by the order of 0.01 A. More exact expressions are presented for the intensity of electrons diffracted by vibrating molecules and for the corresponding experimental radial distribution curves in terms of the parameters characterizing the potential fields of the molecules. The case of diatomic molecules is treated in detail, including the effect of temperature, assuming a Morse potential energy function. Some aspects of polyatomic molecules are discussed.

RECENT improvements in the experimental technique of electron diffraction by gases have made it possible to obtain diffraction data of considerably greater precision than that available when the methods currently used for analyzing data were developed. Certain approximations employed in the conventional interpretational procedures introduce appreciably greater uncertainties into the determination of molecular structure than does the experimental error in the best data now attainable. The interpretational errors due to the neglect of non-nuclear scattering and to the failure of the Born approximation have been discussed elsewhere.[1,2] Other sources of error arise from failure to allow satisfactorily for the internal motion of the molecule being studied, and must be carefully considered if the full benefit is to be derived from the improved experimental techniques and if significant comparisons are to be made with spectroscopic results.

It is now customary to compensate for the gross effects of intramolecular motion by assuming that the motions of the nuclei from equilibrium positions are symmetrical functions of the displacement coordinates. While this treatment is a great improvement over the older one based on rigid molecules, it yields results which are in error by several parts per thousand or more. The purpose of this paper is to estimate the magnitude of the effects of molecular motion on internuclear distances and to propose a refined method for interpreting diffraction data.

[1] Bartell, Brockway, and Schwendeman (to be published).
[2] V. Schomaker and R. Glauber, Phys. Rev. **89**, 667 (1953); L. Bartell and L. Brockway, Nature **171**, 978 (1953).

DIATOMIC MOLECULES

The following calculations are based on the Morse potential energy function

$$V(r)=D\{e^{-2ax}-2e^{-ax}\}, \tag{1}$$

where $x=r-r_e$. While this function is rarely a good approximation over a large range of r, it is certainly superior to a Hooke's-law potential and, in the case of diatomic molecules, is probably completely satisfactory for the characterization of electron diffraction data which depend only on the lowest vibrational levels. It will be convenient to specify the results of the calculations in terms of the parameters a and α, where $\alpha=4\pi^2\mu\nu_0/h$. The probability functions, $P(r)$, which express the distribution in nuclear separation for the Morse anharmonic oscillator, are expansions computed from the eigenfunctions obtained by Morse.[3]

Lowest Energy Level

For the lowest vibrational and rotational level, $P_0(r)$ is given by

$$P_0(r)=(\alpha/\pi)^{\frac{1}{2}}\{1+ax+a^2x^2/2 +(a^3+2a\alpha)x^3/6+\cdots\}\exp(-\alpha x^2).$$

The terms in the expansion beyond the first may be regarded as correction terms added to the harmonic oscillator distribution $(\alpha/\pi)^{\frac{1}{2}}\exp(-\alpha x^2)$. It is sufficient in the investigation of effects of anharmonicity to use

$$P_0(r)=(\alpha/\pi)^{\frac{1}{2}}\{1+ax+a\alpha x^3/3\}\exp(-\alpha x^2). \tag{2}$$

[3] P. M. Morse, Phys. Rev. **34**, 57 (1929).

It is important to distinguish at the outset between alternative internuclear distance parameters, any one of which, taken with the parameters a and α could serve to characterize $P_0(r)$:

(i) The position of the minimum of $V(r)$ is r_e.

(ii) The position, $r_m(n)$, of the maximum of the function $P_0(r)/r^n$ is

$$r_m(n)=r_e+a/2\alpha-n/2\alpha r_e. \tag{3}$$

(iii) The center of gravity, $r_g(n)$, of the function $P_0(r)/r^n$ is

$$r_g(n)=r_e+3a/4\alpha-n/2\alpha r_e. \tag{4}$$

(iv) The average value $\langle(r^n)\rangle_{Av}^{1/n}$ is given by

$$\langle(r^n)\rangle_{Av}^{1/n}=r_e+3a/4\alpha+(n-1)/4\alpha r_e. \tag{5}$$

Previously these parameters were taken to be essentially equivalent by workers in the field of electron diffraction. The above approximations, correct to terms in α^{-1}, are correct to better than $10^{-4}A$ for representative values of n, a, α, and r_e.

The internuclear distance determined (as in spectroscopy) from the average moment of inertia of a diatomic molecule is $\langle(r^{-2})\rangle_{Av}^{-\frac{1}{2}}$. No such simple generality can be given for the distances as determined by electron diffraction, for there are two different ways by which electron diffraction data are analyzed, namely, the intensity correlation method and the radial distribution method. Neither of these has heretofore been specified sufficiently to remove the ambiguity resulting from anharmonicity of vibration.

Both methods make use of the electron diffraction intensity function $M(s)$, the ratio of the molecular intensity to the atomic intensity, where $s=(4\pi\sin\frac{1}{2}\theta)/\lambda$. In the remainder of this paper it will be assumed that the experimental $M(s)$ function has been corrected as described elsewhere[1] to eliminate the effect of nonnuclear scattering. The theoretical relationship between $M(s)$ and $P(r)$ is then given by[4]

$$M(s)=c\int_0^\infty P(r)\ (\sin sr)/sr dr, \tag{6}$$

where c is a constant related to the scattering power of the atoms.

Introduction of the asymmetric $P_0(r)$ into Eq. (6) gives, if s is small compared to $2\alpha r_e$,

$$M(s)=c\exp(-s^2/4\alpha)[\sin s\{r_e+\rho(s)\}]/sr_e \tag{7}$$

where

$$\rho(s)=a/2\alpha-1/2\alpha r_e+a\eta(s)/4\alpha.$$

The function $\eta(s)$ has the following properties:

$$\eta(s)\sim 1-s^2/6\alpha, \qquad s<(6\alpha)^{\frac{1}{2}}$$
$$\eta(s)\to 0, \qquad s>(6\alpha)^{\frac{1}{2}}.$$

[4] P. Debye, J. Chem. Phys. **9**, 55 (1941).

For s less than $(6\alpha)^{\frac{1}{2}}$, the function approaches zero somewhat more rapidly than $\exp(-s^2/6\alpha)$. The behavior in the vicinity of $(6\alpha)^{\frac{1}{2}}$ was not studied. The expression for a harmonically vibrating molecule results if a is put equal to zero. It is apparent that the interatomic distance as deduced by the conventional correlation method is not r_e, but rather is somewhere between $r_g(1)$ and $r_m(1)$ of Eqs. (3) and (4). The exact value depends upon the value of s at which the correlation is made.

A Fourier analysis can be performed upon an experimentally determined $M(s)$ to obtain a measure of $P(r)/r$. It is customary to evaluate the radial distribution function $f(r)$ instead of $P(r)/r$, due to the lack of diffraction data to $s=\infty$, where

$$f(r)=\int_0^{s(\max)} sM(s)\exp(-bs^2)\sin sr ds. \tag{8}$$

If $s(\max)$ or b is sufficiently large, $f(r)$ is insensitive to $s(\max)$ and is related to $P(r)$ as follows:

$$f(r)=c(\pi/16b)^{\frac{1}{2}}\int_{-\infty}^{\infty}\rho^{-1}P(\rho)\exp\{-(r-\rho)^2/4b\}d\rho.$$

Thus $f(r)$ can be expressed in terms of the molecular parameters r_e, a, and α, giving

$$f(r)=\frac{c}{2r_e}\left(\frac{\alpha\pi}{\gamma}\right)^{\frac{1}{2}}\left\{1+\frac{(a-r_e^{-1})x}{\gamma}-\frac{a(\gamma-1)x}{2\gamma^2}-\frac{a\alpha x^3}{3\gamma^3}\right\}\exp\left(-\frac{\alpha x^2}{\gamma}\right), \tag{9}$$

where $\gamma=4b\alpha+1$. The unimportant quadratic term has been omitted from the expansion. It is to be noted that, while the center of gravity of $f(r)$ is the same as the center of gravity of $P(r)/r$, the position of the maximum depends upon the value of b chosen and is generally at greater r than either r_e or $r_m(1)$.

Effect of Temperature

The centrifugal stretching δr_{rot}, experienced by a diatomic molecule with a rotational energy of kT is

$$\delta r_{\text{rot}}=2kT/r_e k_e, \tag{10}$$

where k_e is the force constant of the bond. The thermal distribution of internuclear separations is represented sufficiently well at room temperature for most diatomic molecules by an expression

$$P_{\text{ave}}(r)\simeq(1-\beta)P_0(r)+\beta P_1(r) \tag{11}$$

in which $P_0(r)$ and $P_1(r)$ are the distributions based on a Morse potential for the lowest- and first-excited vibrational states, respectively, and $\beta=\{1+\exp(h\nu_0/kT)\}^{-1}$. The center of gravity of $P_{\text{ave}}(r)$ shifts toward a larger

internuclear separation by an amount $\{3a\beta/2\alpha+\delta r_{\text{rot}}\}$ as the temperature increases.[5] The position of the maximum of $P_{\text{ave}}(r)$, on the other hand, tends to a *smaller* separation by an amount $\{a\beta/\alpha-\delta r_{\text{rot}}\}$.

The expression for the temperature dependent intensity function is found to be very nearly

$$M(s)=c\exp\{-(1+2\beta)s^2/4\alpha\}\times[\sin s\{r_e+\rho(s,T)\}]/sr_e, \quad (12)$$

where

$$\rho(s,T)=(1-2\beta)a/2\alpha-(1+2\beta)/2\alpha r_e+\{\eta(s)+10\beta\zeta(s)\}a/4\alpha+\delta r_{\text{rot}}$$

in which $\eta(s)$ is defined under Eq. (7), δr_{rot} is given by Eq. (10), and $\zeta(s)$ is a function approximated by

$$\zeta(s)\simeq\exp(-0.4s^2/\alpha).$$

In the intensity correlation method a value for r_e could be chosen directly from a comparison of the experimental intensity function, $M(s)$, with theoretical functions properly corrected for asymmetry. This method would be unprofitably laborious because present methods[6] of computing theoretical intensity curves are not readily adaptable to inclusion of frequency modulation of the sinusoidal functions. Present methods can, nevertheless, be used without modification if it is recognized that the s/s_0 values as conventionally obtained should not be constant. If the "theoretical curve" is calculated, as usual, according to

$$M(s)=c\exp(-l^2s^2/2)[\sin sr_{ij}]/sr_{ij}, \quad (13)$$

then a comparison of Eq. (12) with Eq. (13) shows that

$$r_e=sr_{ij}/s_0-\rho(s,T).$$

The upper two-thirds or so of the temperature dependent radial distribution peak is found to be well represented by

$$f(r)=\frac{c}{2r_e}\left(\frac{\alpha\pi}{\gamma}\right)^{\frac{1}{2}}\left\{1+\frac{(a^2+4\alpha\beta)y^2}{2\gamma^2}+\frac{a\alpha(1+11\beta)y^3}{3\gamma^3}\right\}\exp\left(-\frac{\alpha y^2}{\gamma}\right), \quad (14)$$

where $y=r-r_{RD}$. The position, r_{RD}, of the maximum of $f(r)$ is related to r_e according to

$$r_{RD}=r_e+\delta r_{\text{rot}}+\delta r_{\text{vibr}}$$

with

$$\delta r_{\text{vibr}}=\frac{a}{2\alpha}\left[\left(\frac{3\gamma-1}{2\gamma^2}\right)(\gamma-5\beta)+3\beta\right]-\frac{(1+2\beta)}{2\alpha r_e}.$$

[5] For this particular quantity the complete expression averaged over all vibrational levels can be evaluated, giving

$$\{3a\beta/2\alpha(1-2\beta)+\delta r_{\text{rot}}\}.$$

[6] J. Karle and I. L. Karle, J. Chem. Phys. **19**, 961 (1950). Anharmonicity corrections would, perhaps, double the computational labor.

A careful fitting of a very accurate experimental $M(s)$ or $f(r)$ curve with the corresponding theoretical curve would be expected to yield values of all three parameters, r_e, α, and a, which characterize the potential field. In practice it is found that α, which is a measure of the amplitude of vibration, can be found by measuring the breadth of the radial distribution peak, and that if a is known, r_e can be found as previously shown. The influence on the diffraction data of a, the asymmetry parameter, however, is too subtle to permit the derivation of accurate values of a at the present state of development of diffraction technique. Values of a suitable for use in interpretation of diffraction data are available from spectroscopic sources or can be calculated from values of α and D obtained from diffraction and thermal measurements. Since a is approximately 2.0 A^{-1} for a wide variety of single bonds and slightly higher for double and triple bonds, it can usually be estimated reasonably well for these small corrections if experimental values are lacking.

It is interesting to note that perfectly precise electron diffraction data would give a measure of $P(r)$ from which in principle, $V(r)$, and thus the dissociation energy, could be calculated. If the Morse curve were a good representation of $V(r)$ over a large range of r, (it is generally not), then it would follow that

$$D=(\alpha h/2\pi a)^2/2\mu.$$

The best electron diffraction data obtained to date at the University of Michigan have yielded reasonable values of α and rough estimates of a and, accordingly, of D, but it is not seriously anticipated that this severely limited method will ever be important in measuring D.

It is helpful to examine the order of magnitude of the various correction terms encountered in the reduction of data to the equilibrium internuclear distance, r_e. The molecule Cl_2 serves as a fairly typical example with $a\sim2.0$ A^{-1}, $\alpha\sim290$ A^{-2}, $r\sim2.0$ A, and $\beta\sim0.06$ at 300°K.[7] The correction terms for Cl_2 are

$$\begin{aligned}\delta r_{\text{rot}} &= 0.001 \text{ A},\\ \delta r_{\text{vibr}} &= 0.002 \text{ A for small } b\\ &= 0.005 \text{ A for large } b,\\ \rho(s,T) &= 0.006 \text{ A at small } s\\ &= 0.003 \text{ A at large } s.\end{aligned}$$

It should be pointed out that the corrections for polyatomic molecules may be much larger than the corresponding corrections for diatomic molecules, and even larger than the uncertainties not infrequently assigned to the distances recorded in the literature.

POLYATOMIC MOLECULES

It is probably not feasible to reduce analysis of diffraction data to equilibrium internuclear distances

[7] Values computed from data in G. Herzberg, *Molecular Spectra and Molecular Structure* (D. Van Nostrand Company, Inc., New York, 1950), second edition.

in the case of any but the simplest molecules. Nevertheless, any parameters for which accuracy of a few thousandths of an Angstrom unit or better is claimed should be free of the arbitrariness associated with the selection of b in the radial distribution method or the range of s studied in the correlation method, and the interpretation should be explicitly specified. Perhaps the most realistic values to report would be the $r_g(1)$ or $r_m(1)$. The interpretation of data in terms of bond angles is also, of course, complicated by asymmetry. Careful computation as well as precise data would be necessary to keep angular uncertainties less than a few tenths of a degree.

A rigorous treatment of asymmetry of the $P_{ij}(r)$ would require tedious calculations for each molecular structural type. An approximate treatment is presented below which should give reasonable magnitudes for some of the corrections with little computational labor.

Bonded Atoms

Asymmetry of vibration may be more serious in the case of polyatomic molecules than for diatomic molecules because each mode of vibration may contribute to the over-all amplitude of vibration with respect to a given pair of atoms. For a diatomic molecule at low temperature the root-mean-square vibrational displacement from equilibrium, $l=\langle(x^2)\rangle_{Av}^{\frac{1}{2}}$, is given by

$$l=(1/2\alpha)^{\frac{1}{2}}.$$

It can be seen that the aforementioned corrections for effects of asymmetry are proportional to l^2, a result which is also in accord with calculations of the center of gravity based on classical mechanics. It is reasonable, then, to expect the corresponding corrections at low temperatures for bond distances of atoms which are bonded to just one other atom in polyatomic molecules to be about the same as those for diatomic molecules if, for the parameter α in the latter case, the quantity $1/2l^2$ is substituted. The corrections are probably reliable only with reference to the center of gravity. The value of the amplitude, l, to be used for correcting diffraction results can be found from the diffraction data itself according to the customary procedure provided the value is corrected for the failure of the Born approximation.[2] The value for a can be estimated from force constant data and dissociation energies, as before, and should remain essentially the same for a given type of bond in any molecule.

Nonbonded Atoms

Anharmonicity corrections for nonbonded atoms are much more difficult to treat because of the complexity of the asymmetry of the distribution function. The effect of asymmetry should be more important than for bonded atoms because of the greater amplitude of vibration, and accordingly the sinusoidal intensity curves for molecules such as methyl halides, in which the predominant molecular scattering is from nonbonded atoms, should show a perceptible frequency modulation due to anharmonicity. This has been observed.[1,8] Anharmonicity effects are probably the explanation of some of the "anomalous" systematic deviations from constancy of s/s_0 values found occasionally in the past even by the use of the visual method of interpretation.

CONCLUSION

A systematic investigation of the effect of molecular motion upon the interpretation of electron diffraction data has been initiated in order to permit exploitation of improved experimental techniques. Particular attention is called to the need for careful specification of the parameter reported for "internuclear distance" and procedures are outlined for the interconversion of related parameters.

It is gratifying that the application of the above principles has led to electron diffraction results which are in agreement with the best results of microwave spectroscopy to within about 0.002 A in the half-dozen cases studied to date[8] for which comparisons could be made.

[8] L. S. Bartell and L. O. Brockway (to be published); C. G. Thornton and L. O. Brockway (to be published).

Microwave Spectrum of Propiolic Aldehyde*

JOHN A. HOWE AND J. H. GOLDSTEIN
Chemistry Department, Emory University, Emory University, Georgia
(Received October 4, 1954)

The microwave spectrum of propiolic aldehyde has been studied in the 18–37 Kmc region. Analysis of the ground state spectrum provides the following rotational constants: $b=4826.31\pm0.03$ Mc, $c=4499.75\pm0.03$ Mc, and $\delta=0.00594\pm0.0030$ Mc, consistent with a planar model. Strong vibrational satellites were observed and fitted, and approximate values of the two lowest vibrational frequencies were found from intensity ratios to be roughly 150 cm^{-1} and 230 cm^{-1}. The dipole moment of the ground vibrational state is $2.46\pm0.04D$, as determined from quantitative Stark effect studies.

INTRODUCTION

PROPIOLIC aldehyde, HC≡C−CHO, is structurally the simplest of the conjugated carbonyl compounds. Its chemical properties are those typical of conjugated aldehydes, but it is of special interest because it contains the acetylene group. The scarcity of reported work on the structural and spectroscopic properties of propiolic aldehyde suggested an investigation of its microwave spectrum. The results reported here will subsequently be correlated with data obtained for other carbonyl compounds now under study in this laboratory.

Assuming a planar structure and adopting typical values for the structural parameters, the following tentative rotational constants were calculated: $a=74\,930$ Mc, $b=4850$ Mc, and $c=4560$ Mc. The dipole moment was judged to be in excess of $2D$, and roughly parallel to the a-axis. With these results it was predicted that the $J=1\rightarrow2$ and $J=2\rightarrow3$ groups of transitions would occur at about 19 000 Mc and 28 000 Mc, respectively.

The aldehyde was prepared from commerical propiolic alcohol by oxidation with chromic acid in acidic aqueous medium under reduced pressure.[1] Since the compound decomposes rapidly at room temperature, purification was effected by bulb-to-bulb distillation under reduced pressure through a series of four traps cooled with dry ice-acetone mixture. The purified aldehyde was stored indefinitely at dry ice temperatures without noticeable decomposition.

All observations and measurements were made with a square wave-modulated spectrograph employing visual presentation. Frequency measurements were made with a frequency standard monitored against signals from station WWV. Other experimental details are given below.

TABLE I. Microwave spectrum of propiolic aldehyde.

Transition	State	Obs frequency	Calc frequency
1. $1_{11}\rightarrow2_{12}$	Gnd.	18 325.76 Mc	18 325.56 Mc
2. $1_{01}\rightarrow2_{02}$		18 650.68	18 650.54
3. $1_{10}\rightarrow2_{11}$		18 978.79	18 978.68
4. $2_{12}\rightarrow3_{13}$		27 487.44	27 487.44
5. $2_{02}\rightarrow3_{03}$		27 972.36	27 972.35
6. $2_{21}\rightarrow3_{22}$		...	27 978.19
7. $2_{20}\rightarrow3_{21}$		...	27 984.03
8. $2_{11}\rightarrow3_{12}$		28 467.11	28 467.11
9. $3_{12}\rightarrow4_{13}$		37 954.95	37 954.44
10. $2_{12}\rightarrow3_{13}$	$v_{11}=1$	27 570.57	27 570.55
11. $2_{02}\rightarrow3_{03}$		28 044.06	28 044.14
12. $2_{11}\rightarrow3_{12}$		28 527.18	28 527.16
13. $3_{13}\rightarrow4_{13}$		37 034.77	38 034.57
14. $2_{12}\rightarrow3_{13}$	$v_{12}=1$	27 578.10	27 578.13
15. $2_{02}\rightarrow3_{03}$		27 077.49	28 077.50
16. $2_{11}\rightarrow3_{12}$		28 587.40	28 587.41
17. $3_{12}\rightarrow4_{13}$		38 114.42	38 114.72

GROUND-STATE SPECTRUM AND ASSIGNMENTS

The spectrum of propiolic aldehyde was found and correlated with initial predictions without difficulty. Identification of the lines was made certain by qualitative observation of the Stark effect and by estimations of relative intensities within each group. The results are given in Table I.

The symbols v_{11} and v_{12} in Table I are the quantum numbers describing the two lowest frequency vibrational modes of propiolic aldehyde. The rotational spectra of the excited vibrational states is discussed separately below.

In the ground vibrational state the estimated uncertainties in the frequency measurements are about 0.17 Mc for the $J=1\rightarrow2$ group and 0.10 Mc for the remaining lines. The corresponding value for the excited states is about 0.15 Mc. All frequency values represent the average of several measurements, with the mean deviation taken as the uncertainty.

The rotational constants, b, c, and δ, were calculated from the most reliably measured transitions, the $J=2\rightarrow3$ group. These results are given in Table II.

TABLE II. Rotational constants of propiolic aldehyde.

State	b	c	δ
Gnd.	4826.31±0.03 Mc	4499.75±0.03 Mc	0.00594±0.0003
$v_{11}=1$	4848.84±0.04	4512.41±0.04	0.00617±0.0005
$v_{12}=1$	4834.39±0.04	4515.52±0.04	0.00583±0.0005

* This work was sponsored by the Office of Ordnance Research, U. S. Army.

[1] F. Wille and L. Saffer, Ann. **568**, 34 (1950).

TABLE III. Stark effect for propiolic aldehyde.

Transition	Component	$\Delta\nu/E^2$ (obs)	$\Delta\nu/E^2$ (calc)
$2_{02}\rightarrow 3_{03}$	2	0.662	0.666
	0	0.367	0.367
$1_{01}\rightarrow 2_{02}$	1	1.747	1.735

The predicted spectrum, shown in the last column of Table I, was calculated with the constants of Table II and is seen to be in acceptable agreement with the observed values. Lines 6 and 7 of Table I were observed but were not measured because of Stark effect difficulties in this crowded region of the spectrum. The fact that none of the observed transitions depend very strongly on δ is reflected in the relatively greater uncertainty listed for this parameter. Centrifugal distortion corrections cannot be reliably estimated from our data, and although they are expected to be small, their omission adds to the uncertainty in δ. On the other hand, the constants b and c have been quite reliably determined with the data available. The net effect of all this is that the derived constants are consistent with a planar model, and reproduce the spectrum quite well, but do not yield very good values for a or I_a.

SPECTRUM OF EXCITED VIBRATIONAL STATES

A pair of strong satellites was observed on the high-frequency side of each of the originally predicted transitions. Because of their location and since their Stark effect was so similar to that of the ground-state lines, they were assigned to analogous transitions in the first excited states of the two lowest vibrational modes. The intensity behavior of these satellites, on cooling the wave guide with dry ice, verified this assignment. The observed and calculated frequencies of these transitions are given in Table I and the rotational constants of the excited states are listed in Table II.

In order to estimate the vibrational frequencies it was necessary to measure the intensities of the satellite lines relative to that of the parent line. This was done by measuring line heights on a calibrated oscilloscope screen at power levels judged to be low enough to avoid saturation. The wave guide was terminated and tuned as well as possible in order to minimize effects arising from standing waves. The observed relative intensities for the three $2_{11}\rightarrow 3_{12}$ lines were 1:0.53:0.34 at 23.5°C, and 1:0.30:0.17 at −76°C. Relative intensities in the other groups showed a similar trend but were not as reproducible. By averaging the ratios measured at the two temperatures, we obtain 150 ± 15 cm^{-1} and 230 ± 10 cm^{-1}, respectively, for the frequencies of the two lowest vibrational modes of propiolic aldehyde. Despite good agreement at the two temperatures, the accurate measurement of microwave intensities presents such difficulties that these frequencies must be considered as only approximate values.

At somewhat higher frequencies than each of the above satellites there occurs still another pair of satellites. Their appearance, intensity, and location suggest that they may arise from the second excited states of the two lowest vibrational modes. These transitions have not been studied in detail.

TABLE IV. Dipole moment of propiolic aldehyde.

μ_a	$2.39\pm 0.04D$
μ_b	0.60 ± 0.10
μ	2.46 ± 0.04

GROUND-STATE STARK EFFECT AND DIPOLE MOMENT

The wave guide used for Stark effect measurements was calibrated against the $J=1\rightarrow 2$ line of OCS.[2] Twelve calibration measurements were treated by least squares, providing a wave guide constant with a probable error, assuming random errors, of less than 1 percent.

Stark effect displacements for propiolic aldehyde were measured for the three lobes shown in Table III. In each case the effect was quadratic and the values of $\Delta\nu/E^2$ were obtained graphically. Equations for the three ratios were obtained, as functions of μ_a and μ_b, by the method of Golden and Wilson.[3] The best values of μ_a and μ_b were determined graphically and are given, together with the resultant μ, in Table IV. The comparison between observed and calculated Stark effects is shown in Table III. It should be remarked that the relatively large uncertainty in μ_b scarcely affects the values of the resultant.

DISCUSSION

With the two rotational constants obtained from the microwave spectrum only a limited structural discussion is possible. It can be shown, however, that the results are consistent with a planar model based on parameters that have been accurately determined for numerous other molecules containing similar structural units.[4] Writing the molecular formula $H_1C_1C_2C_3H_2O$, the interatomic distances so chosen are: $H_1C_1=1.06$, $C_1C_2=1.204$, $C_2C_3=1.46$, $C_3H_2=1.08$, and $C_3O=1.21$, all in A. The angles used are: $C_2C_3H_2=120°$ and $C_2C_3O=123°$. The principal moments calculated from this structure are 7.74, 104.49, and 112.22 amu-A^2, which are to be compared with 7.60, 104.71, and 112.31 amu-A^2, calculated from the spectrum assuming planarity. In view of this agreement, and since the choice of structural parameters is not arbitrary, the true structure is not expected to differ greatly from that assumed above.

Since the Stark effect calculations only provide

[2] R. G. Shulman and C. H. Townes, Phys. Rev. **77**, 500 (1950).
[3] S. Golden and E. B. Wilson, Jr., J. Chem. Phys. **16**, 669 (1948).
[4] See, for example, Gordy, Smith, and Trambarulo, *Microwave Spectroscopy* (John Wiley and Sons, Inc., New York, 1953), p. 371.

absolute values of the electric moment components, there are four possible orientations for the resultant vector, corresponding to $\pm\mu_a$ and $\pm\mu_b$. For propiolic aldehyde the most plausible choice should place the vector as near as possible to the primary moment of the carbonyl bond. This criterion places the moment at $14\pm3°$ with respect to the positive a-axis. From the assumed structure the carbonyl bond is found to lie at 43° which places the dipole moment 25–30° from the carbonyl bond, toward the aldehyde hydrogen. Even allowing for uncertainties in μ_b and the assumed structure, it seems clear that the moment has undergone an appreciable shift away from the carbonyl bond. The value of the resultant, $2.46D$, is lower than the vapor phase moments of propionaldehyde, $2.73D$,[5] and acrolein, $3.04D$.[6] The large value of the moment in acrolein relative to saturated aldehydes has been attributed to the resonating polar structure $(+)CH_2-CH=CHO(-)$, produced by conjugation.[6] The low value obtained for propiolic aldehyde suggests that, among other factors, conjugation is decreased and/or oppositely charged structures are involved.

The two lowest vibrational frequencies of propiolic aldehyde may be ascribed to skeletal bending modes, one of which is out-of-plane. No Raman data seem to be available for propiolic aldehyde, but for the somewhat similar molecule, vinylacetylene, Raman frequencies of 219 cm^{-1} and 309 cm^{-1} have been assigned to these modes.[7,8] Our frequencies are about 75 cm^{-1} lower than these, but, in view of their approximate nature, these differences are not to be stressed. In both cases the rather low frequencies are to be expected in light of the weak force constant associated with bending around an sp-hybridized carbon atom.

ACKNOWLEDGMENTS

We wish to thank Dr. R. H. Rohrer, Dr. J. W. Simmons, and Mr. J. Fine for their assistance in various phases of this investigation.

[5] E. C. Hurdis and C. P. Smyth, J. Am. Chem. Soc. **65**, 89 (1943).
[6] N. B. Hannay and C. P. Smyth, J. Am. Chem. Soc. **68**, 1357 (1946).
[7] Stamm, Halverson, and Whalen, J. Chem. Phys. **17**, 104 (1949).
[8] N. Sheppard, J. Chem. Phys. **17**, 74 (1949).

THE JOURNAL OF CHEMICAL PHYSICS VOLUME 23, NUMBER 7 JULY, 1955

Entropy, Heat Capacity, and Heats of Transition of 1,2,3-Trimethylbenzene*

R. Dean Taylor,† B. H. Johnson,‡ and John E. Kilpatrick
Department of Chemistry, The Rice Institute, Houston, Texas
(Received October 22, 1954)

The heat capacity and the heats and temperatures of transition of 1,2,3-trimethyl benzene have been determined experimentally. The entropy of the ideal gas at 25°C and one atmos has been found to be 91.98 ± 0.15 cal/deg mole.

APPARATUS

THIS investigation was carried out in two different calorimeters: Series A in calorimeter A during 1950–1951 and series B in calorimeter B during 1952–1953. Both calorimeters were of the Giauque-Eucken isothermal type in that a massive copper block enclosed the sample container.

Calorimeter A was modeled after a design due to Ruehrwein and Huffman.[1] The copper block was suspended from a metal refrigerant tank and a heavy copper radiation shield attached to this tank surrounded the block. Attached to a second tank, located above the first tank, was another radiation shield which enclosed the first tank and shield. This assembly was suspended from the lid of a large metal Dewar. The connecting space between the radiation shields, around the refrigerant tanks and inside the block could be evacuated. This apparatus had the advantage that it could be opened easily without cutting any vacuum lines or unsoldering any joints but it did not prove to be very efficient for calorimetry. Even when both refrigerant tanks were cooled to below the nitrogen triple point it was difficult to cool the block and sample far below the nitrogen normal boiling point.

Although reasonably complete thermal data on the sample was obtained in calorimeter A over the range 74°K–301°K, it was apparent that it was impracticable to use this apparatus at very low temperature. For this reason the investigation was continued in a second calorimeter which incorporated numerous improvements, both from the standpoint of convenience and of accuracy.

Calorimeter B was built along more conventional

* The material in this paper has been taken in part from the doctoral theses of R. D. Taylor (1954) and B. H. Johnson (1951), Department of Chemistry, The Rice Institute.
† Present address: Los Alamos Scientific Laboratory, Los Alamos, New Mexico.
‡ Present address: Humble Oil and Refining Corporation, Baytown, Texas.
[1] R. A. Ruehrwein and H. M. Huffman, J. Am. Chem. Soc. **65**, 1620 (1943).

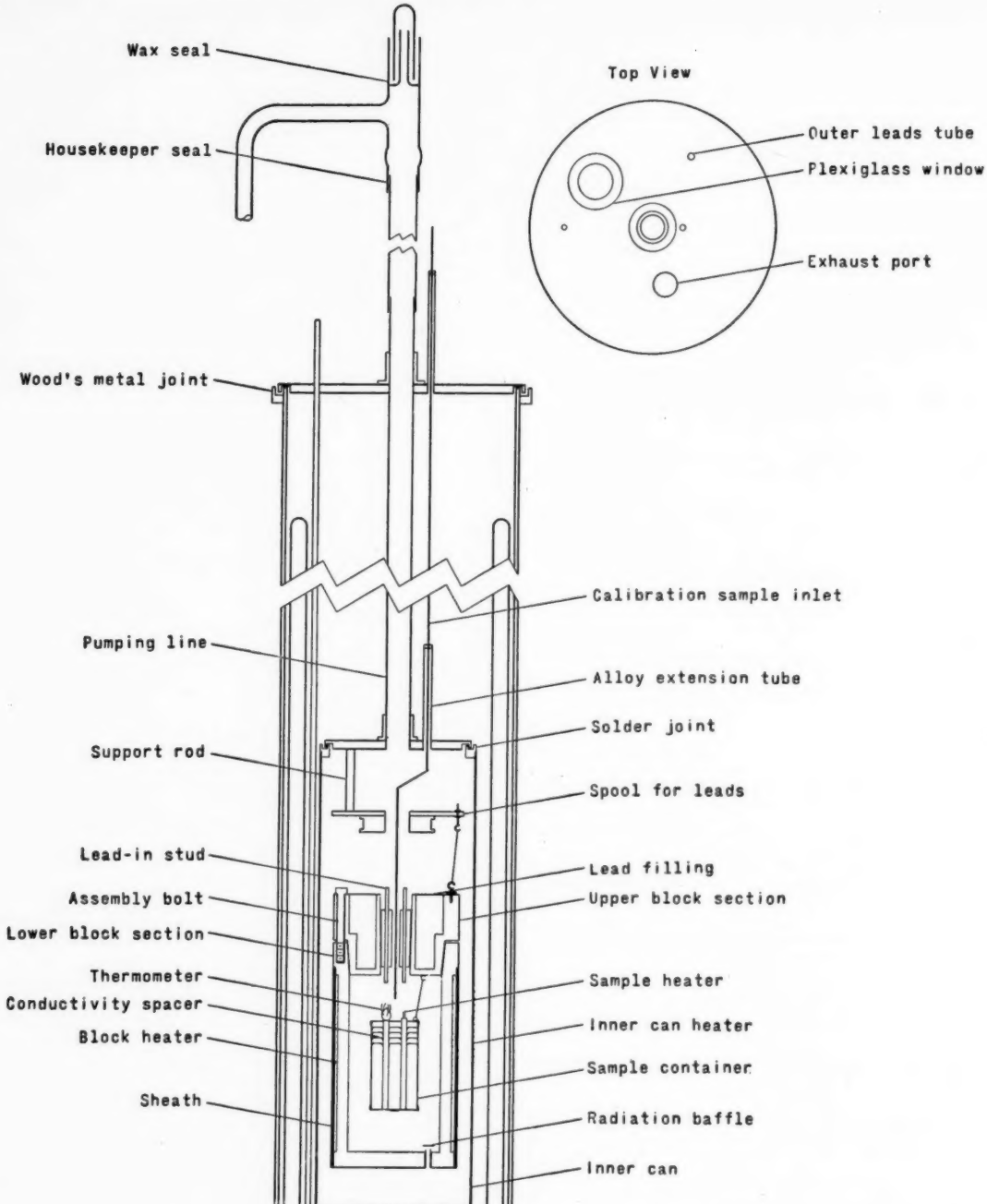

FIG. 1. Cross section of calorimeter *B*.

lines. The general design is shown in Fig. 1. The block was suspended in a metal vacuum chamber which in turn was located near the bottom of a tall glass Dewar. The level of the refrigerating liquid in this Dewar could be observed through a plastic window in the top of the apparatus. The heater winding on the block was isolated from the insulating vacuum space by a copper case. The leads were brought into the vacuum space

TABLE I. Molal heat capacity of 1,2,3-trimethylbenzene in cal/deg mole.

Series A		Series A		Series B		Series B	
T°K	C_p	T°K	C_p	T°K	C_p	T°K	C_p
114.06	22.18	244.16	41.79	heat F-B1		234.00	40.54
121.74	23.28	heat F-A2		260.34	48.72	236.82	41.05
129.46	24.56	258.69	48.32	250.96	48.06	239.56	41.58
137.68	25.46	265.51	48.78	256.30	48.47	242.28	42.08
146.27	26.70	272.73	49.38			heat F-B3	
154.34	27.89	280.45	49.96	69.57	14.97	256.34	48.51
163.22	29.25	288.66	50.62			temp F-B2	
169.96	30.31	301.03	51.70	70.86	15.21	222.56	49.39
177.72	31.54	temp F-A1		80.24	16.95	224.64	49.99
185.95	33.06	74.72	15.94	88.67	18.43	226.76	51.55
194.49	34.83	78.77	16.61	96.43	19.65	228.95	54.38
203.03	37.33	83.46	17.51	103.80	20.77	heat I-B1	
211.99	40.56	88.88	18.41	115.52	22.54	209.96	39.90
heat II-A1		93.93	19.22	125.67	24.03	215.88	43.97
222.28	49.40	99.85	20.09	134.64	25.32		
heat I-A1		107.21	21.22	143.49	26.56	212.14	40.81
temp II-A1		113.88	22.21	152.87	27.88	216.22	43.52
221.06	49.25	120.44	23.14	162.61	29.31		
		128.30	24.29	171.94	30.76	215.52	42.70
220.87	49.29	135.79	25.31	181.14	32.34	217.73	49.85
223.84	49.51	heat II-A4		190.10	34.09	temp II-B1	
226.67	51.49	heat I-A4		198.75	36.16	heat II-B3	
		241.36	41.54	206.80	38.67	heat I-B2	
213.79	41.51			214.02	41.96	heat II-B4	
216.38	43.05	Series B		heat II-B2		heat I-B3	
heat II-A2		249.98	47.94	221.92	49.39	252.83	48.15
220.76	49.03	254.89	48.32	225.19	50.41	258.81	48.62
224.57	50.13	261.24	48.84	228.71	54.19	265.34	49.13
heat I-A2		207.30	49.30			273.21	49.75
231.73	39.78			234.80	40.26	280.39	50.32
237.84	40.90	241.87	41.51	239.53	41.02		
244.29	41.69	temp I-B1		temp I-B3		255.18	48.27
		242.96	42.41	235.46	40.27	261.78	48.85
238.65	41.05	temp F-B1				267.85	49.32
243.15	41.70	252.25	48.11	236.19	40.75	281.04	50.36
heat F-A1		heat II-B1					
255.57	48.07			233.50	40.35	18.94	2.862
261.19	48.51	222.73	49.61	240.06	41.12	21.39	3.565
heat II-A3		226.56	51.48	243.40	41.38	26.53	5.058
221.51	49.22	228.31	52.80			31.83	6.504
224.63	50.12	229.69	55.67	189.39	33.93	36.01	7.629
227.80	52.90	temp I-B2		199.10	36.25	39.57	8.532
heat I-A3		124.12	23.80	207.40	38.88	43.83	9.523
235.18	40.43	132.00	24.94	heat F-B2		48.07	10.535
242.31	41.47			256.61	48.52	52.28	11.46
		131.26	24.83			56.95	12.44
237.73	40.94			233.75	40.46	62.30	13.56
242.36	41.72	235.76	40.47	237.05	41.14		
				240.40	41.71	288.66	50.91
				243.56	42.31	298.28	51.93
				246.20	42.91		

through a miniature metal-to-glass seal. The interior of this space was filled with helium. This arrangement eliminated the trouble we had experienced previously with gas evolved from the heater winding.

The same platinum resistance thermometer was used in both series A and B. The resistance element consisted of 0.0028-in. diameter platinum wire wound in the form of a double helix and was supported on a mica cross. The shell was made of platinum tubing 0.265-in. o.d., 0.005-in. wall thickness and about 2.5 in. long. The four leads were brought out through a soft glass seal. This thermometer has been calibrated several times over a period of years and is quite satisfactorily stable. Its resistance at the ice point is about 93 ohms. The reference points used to determine the constants of the Callender-Van Dusen equation were the benzoic acid melting point (using a calibrated Bureau of Standards cell), the water triple point, the nitrous oxide triple point, and the oxygen boiling point. We have found the benzoic acid and nitrous oxide points to be satisfactory substitutes for the sulfur and water boiling points and to be much more convenient for our purposes. Our

thermometer and a Bureau of Standards calibrated Leeds and Northrup calorimetric thermometer were compared at numerous temperatures, down to and including the hydrogen triple point, in order to establish a temperature scale below the oxygen boiling point and to check our scale above this temperature.

The resistance of the thermometer could be determined to better than 0.0003 ohm, relative to a nominal 100 ohm standard. Above 90°K the precision and estimated accuracy of temperature determinations are 0.001° and 0.002°, respectively. These limits increase at lower temperatures until at 20°K, they are 0.004° and 0.01°. Temperature differences, of course, could be determined more accurately.

All temperatures determined in this work are given on the absolute scale. Below 90°K they are on the thermodynamic scale to the accuracy to which it is known; above 90°K the temperature given is 273.160°K plus the International Scale centigrade temperature.

In series A the platinum resistance thermometer was used both to measure temperature and as the heater for introducing energy into the sample. In series B a separate manganin heater was used. This nearly constant resistance heater makes it possible to measure energy inputs much more accurately than is the case with a platinum heater.

The sample containers used in both series were made of copper and had approximately 70 ml volume. The container used in series A had an axial well for the resistance thermometer. Thermal contact was made with Apiezon *N* grease. Thin copper disks making a tight friction fit with the walls of the well and the cylindrical walls of the container were provided in order to increase the rate of approach to thermal equilibrium. The sample container used in series B had two wells and the copper disks were soldered in place. In addition container *B* had a copper surface thermometer. This winding was covered with aluminum foil. The radiation correction in heats of transition could be made by a considerably more reliable method in series B than was possible in series A.

The electrical measurements of this investigation were all made with a White double potentiometer. In series A the second pulses from station WWV at the Bureau of Standards were used to provide a time scale and automatically to start and stop the flow of heating

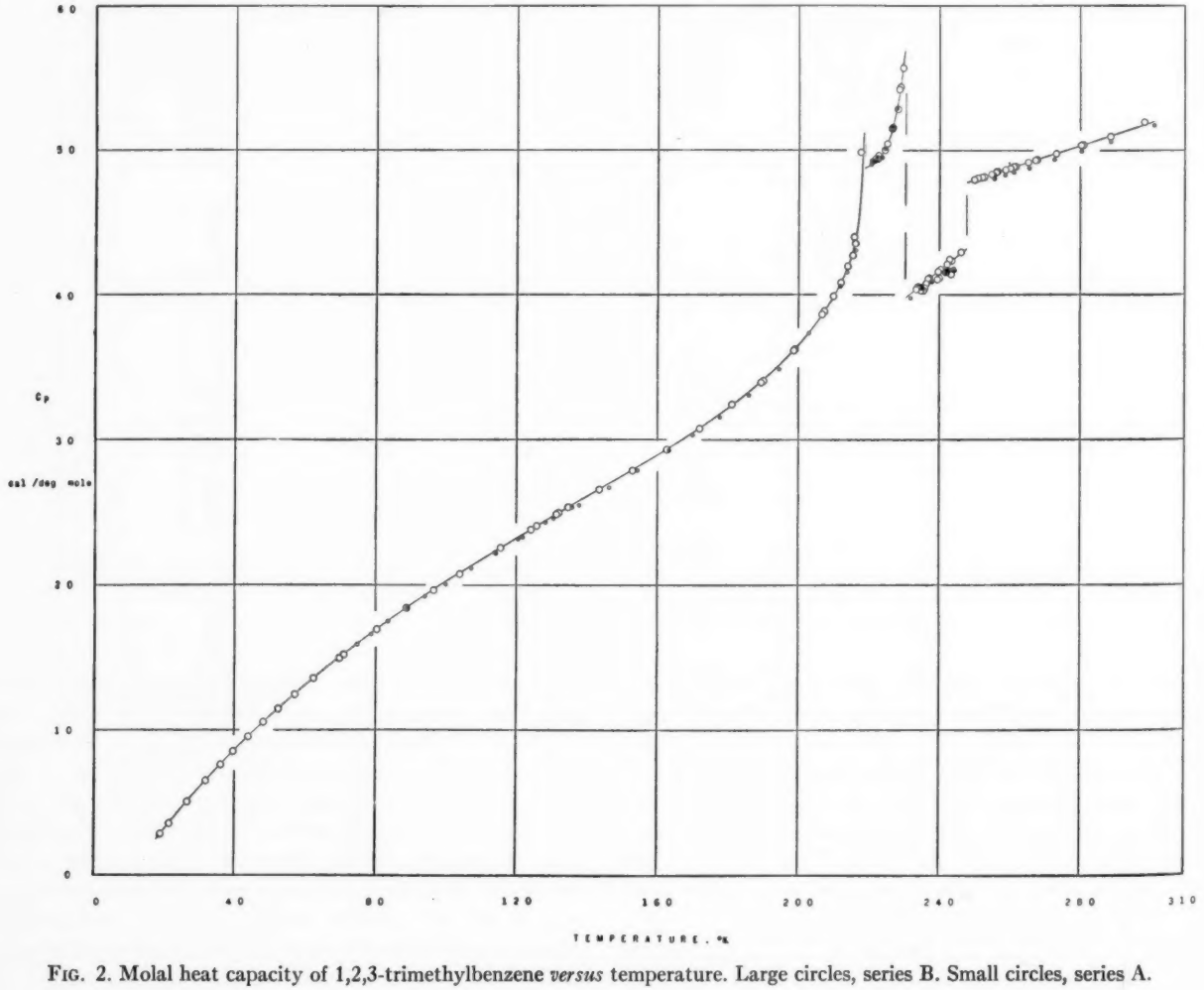

FIG. 2. Molal heat capacity of 1,2,3-trimethylbenzene *versus* temperature. Large circles, series B. Small circles, series A.

energy. In series B much clearer second pulses were generated by a precision pendulum clock which in turn was monitored by the WWV signals. The optical and electric system used in this timing system will be described elsewhere. The timing measurements had an error of well less than 0.001 second.

The unit of energy for this research is the defined calorie (1 calorie=4.18401 absolute joules).

Sample

This sample of API Research hydrocarbon has been made available by the American Petroleum Institute through the API Research Project 44 at the Carnegie Institute of Technology. The sample was purified by the API Research Project 6 from material supplied by the API Research Project 45 at Ohio State University, Columbus, Ohio. Description of the purification and purity of this sample is given in the following reference: Streiff, Murphy, Sedlak, Willingham, and Rossini, J. Research Natl. Bur. Standards **37**, 331 (1946). It had been found to contain 0.010±0.009 mole percent impurity. In series A a sample of 0.36968 mole was used; in series B, 0.35763 mole. The molecular weight was taken to be 120.186.

TABLE II. Molal heat capacity at rounded temperatures.

Temp. °K	C_p cal/deg mole	Temp. °K	C_p cal/deg mole
20	3.16	170	30.45
25	4.63	175	31.27
30	6.04	180	32.13
35	7.36	185	33.06
40	8.62	190	34.07
45	9.82	195	35.20
50	10.96	200	36.51
55	12.04	205	38.06
60	13.09	210	39.91
65	14.09	215	42.70
70	15.05	220	48.96
75	15.99	225	50.45
80	16.91	230	56.47
85	17.79		
90	18.63	235	40.71
95	19.43	240	41.65
100	20.20	245	42.59
105	20.96		
110	21.73	250	47.98
115	22.46	255	48.35
120	23.20	260	48.73
125	23.93	265	49.11
130	24.65	270	49.49
135	25.37	275	49.88
140	26.07	280	50.28
145	26.76	285	50.66
150	27.47	290	51.06
155	28.18	295	51.47
160	28.92	300	51.89
165	29.67		

RESULTS

Heat Capacities

One fusion and two solid-solid transitions have been observed for 1,2,3-trimethylbenzene. For the purpose of discussing the phases and transitions the following names, in the order of decreasing temperature, have been adapted: liquid, fusion, solid I, transition I, solid II, transition II, and solid III. In order to establish the chronology of the measurements, corresponding abbreviations have been inserted at appropriate places in the table of heat capacities. For example, "Temp. I-B3" refers to the third determination of the temperature of transition I in series B.

The heat capacity data for all phases are listed in Table I in the chronological order of their determinations. In this table a space indicates a break in the series of measurements.

An analysis of the errors involved indicates that above 270°K the heat capacities should have a precision of better than 0.3 percent. At extremely low temperature the precision should be better than one percent and the probable error less than three percent. In the intermediate region a precision of better than 0.03 percent and a probable accuracy of better than 0.1 percent should be realized.

TABLE III. The temperature of the triple point.

% in high temp. phase	Temperature °K
Temp. F-A1	
18	247.773
40	247.792
70	247.799
extrapolated	(247.808)
Temp. F-B1	
13	247.710
28	247.760
48	247.780
72	247.790
extrapolated	(247.808)
Temp. F-B2	
18	247.732
33	247.766
51	247.781
76	247.791
extrapolated	(247.809)

Best value: 247.809±0.002°K

TABLE IV. The temperature of transition I.

% in high temp. phase	Temperature °K
Temp. I-B1	
10–12	230.19
30–40	230.26
45–55	230.25
55–65	230.27
65–75	230.30
Temp. I-B2	
20–30	230.23
35–45	230.26
60–70	230.35
75–85	230.36
Temp. I-B3	
65–75	230.25
85–95	230.29

Best value, 50%: 230.27±0.06°K

TABLE V. The temperature of transition II.

% in high temp. phase	Temperature °K
Temp. II-A1	
30	218.673
60	218.700
92	218.776
(50)	(218.690)
Temp. II-B1	
21	218.681
46	218.698
69	218.717
92	218.793
(50)	(218.699)

Best value, 50%: 218.70±0.03°K

As may be seen from the plot of the heat capacity data in Fig. 2, the scatter in the 210°K to 250°K region exceeds that predicted. This scatter, which is more pronounced on solid I than on the other phases, is apparr ently a characteristic of the compound; no such scatter in this region appears in the empty calorimeter runs no- in other samples.

One plausible cause of this apparent irreproducibility of the solid heat capacities is that conversion from one solid phase to another appears to be slow. This argument is supported by the fact that heat capacities of solid I obtained by just freezing the liquid were much smoother than the heat capacities of solid I obtained by heating solid II.

A premelting correction has been applied to the solid I heat capacities. This correction is derived from the thermodynamic equation for the depression of the freezing point by a liquid-soluble, solid-insoluble impurity and accounts for any prefusion heat which has occurred in the heat capacity interval. The corrected heat capacities "for the pure sample" probably should lie on a smooth, nearly straight curve; and in practice, that impurity which best accomplishes this aim is used. The impurity calculated from premelting in series A is 0.011 mole percent; in series B, 0.013 mole percent.

The molal heat capacity at rounded temperatures is given in Table II.

Temperatures of Fusion and Transitions

The data obtained in three series of observations of the temperature of the triple point are given in Table III. The temperature of the triple point of the pure substance was found to be 247.809±0.002°K. The impurity of the sample was found to be 0.011±0.002 mole percent in series A and 0.022±0.002 mole percent in series B. The disagreement of this later value with the value determined from premelting probably indicates the presence of some solid soluble impurity.

TABLE VI. The heat of fusion at 247.809°K.

Run	Temp. interval, °K	Heat input,[a] cal	$\int C_p dT$ [a] cal	Pretrans. cal	ΔH cal/mole
F-A1	246.92–254.05	892.79	175.51	5.81	1956.0
F-A2	245.93–251.98	866.65	146.70	2.74	1954.9
F-B1	239.86–254.26	1036.53	337.37	0.71	1957.0
F-B2	241.38–254.66	1011.09	313.16	0.88	1954.0
F-B3	243.40–253.91	933.28	235.87	1.29	1953.7

Best value: 1955.1±2.0 cal/mole

[a] Sample plus sample container.

TABLE VII. The heat of transition I at 230.27°K.

Run	Temp. interval, °K	Heat input,[a] cal	$\int C_p dT$ [a] cal	ΔH cal/mole
I-A1	224.32–233.95	355.66	237.54	319.52
I-A2	226.49–233.71	294.47	175.86	320.85
I-A3	229.35–233.51	213.67	96.34	317.38
I-A4	229.80–231.71	189.17	70.82	320.14
I-B1	226.75–240.58	432.78	319.64	316.38
I-B2	224.45–243.76	565.31	449.69	323.32
I-B3	227.15–236.98	342.95	229.25	317.92

Best value: 319.3±3.0 cal/mole

[a] Sample plus sample container.

The temperature of transition I was very difficult to determine. Conversion in either direction between phases I and II appears to be slow. In fact, at normal rates of heating or cooling, the heat content of the system was always changed to such an extent before the conversion process began to proceed at an appreciable rate that the system ended up completely through the transition. The addition or subtraction of enough energy to correspond to partial conversion, followed by an adiabatic waiting period of several days never appeared to initiate the transition. Partial conversion was finally achieved by the technique of very rapidly introducing a suitable amount of energy. Apparently the sample was considerably superheated in the neighborhood of the heater and conversion was initiated.

The apparent equilibrium temperatures showed a spread of 0.2° over the range 10 percent–90 percent converted. These temperatures are symmetrically distributed about the point 50 percent converted, 230.27°K. The extremely slow rate of approach to equilibrium confuses the issue and the data are consistent with either of two hypotheses: (1) a narrow region (about 0.2° wide) of very high heat capacity in the shape, not of a lambda point, but of an error function, (2) an isothermal

TABLE VIII. The heat of transition II at 218.70°K.

Run	Temp. interval, °K	Heat input,[a] cal	$\int C_p dT$ [a] cal	ΔH cal/mole
II-A1	213.80–223.53	293.87	235.39	158.19
II-A2	217.65–219.60	106.99	48.44	158.38
II-A3	218.53–219.99	95.25	36.42	159.16
II-A4	218.20–220.21	110.06	50.22	161.87
II-B1	216.69–219.95	135.47	78.77	158.55
II-B2	217.56–220.24	122.06	66.09	156.49
II-B3	215.00–223.81	268.01	212.97	153.89
II-B4	212.64–227.23	407.81	352.03	155.98

Best value: 157.4±3.0 cal/mole

[a] Sample plus sample container.

TABLE IX. Comparison with other investigators of the heats and temperatures of fusion and transition.

Reference	ΔH cal/mole	Temp. °K	Impurity, mole %
	Fusion		
Mair[a]		247.69	0.05
Rossini[b]	2000 ±50	247.7	
Hirschler[c]	2000	247.76[f]	0.6
Glasgow[d]		247.788[f]	0.2
Streiff[e]		247.785[f]	0.018
This research	1955.1±2.0	247.809[g]	0.02
	Transition I		
Rossini[b]	360 ±40	227.2	
Hirschler[c]	200 ±70	230.26	
This research	319.3± 3.0	230.27	
	Transition II		
Rossini[b]	280 ±40	215.2	
Hirschler[c]	120 ±60	218.16	
This research	157.4± 3.0	218.70	

[a] B. J. Mair and S. T. Schicktanz, J. Research Natl. Bur. Standards **11**, 665 (1933).
[b] F. D. Rossini, J. Research Natl. Bur. Standards **11**, 553 (1933).
[c] A. E. Hirschler and W. B. M. Faulconer, J. Am. Chem. Soc. **68**, 210 (1946).
[d] Glasgow, Streiff, and Rossini, J. Research Natl. Bur. Standards **35**, 355 (1945).
[e] Streiff, Murphy, Sedlak, Willingham, and Rossini, J. Research Natl. Bur. Standards **37**, 331 (1946).
[f] In air, one atmos.
[g] Under about 58 cm pressure of helium, zero impurity.

transition at 230.27°K. The data for this transition have been calculated on the basis of the later hypothesis. The temperature data for this transition are shown in Table IV. The uncertainty in the heat content of the system is due to the very long waiting periods necessary for an even approximate approach to equilibrium.

The data for the temperature of transition II are given in Table V. No tendency for this transition to superheat was observed. The final result reported (218.70°K) is for the temperature at 50 percent conversion as determined by graphical interpolation.

Heats of Fusion and Transition

The data for the heat of fusion are shown in Table VI. The several determinations show an unusually large scatter. The principal source of this error is probably the uncertainty in the heat capacity curve just below the fusion. The mean of the results of the five determinations of the heat of fusion is 1955.1±2.0 cal/mole.

The data for the heats of transitions I and II are given in Tables VII and VIII. The heat of transition I was found to be 319.3±3.0 cal/mole; for transition II, 157.4±3.0 cal/mole. The scatter in values for transition I is certainly related to the behavior of the heat capacity of phase I. We have no explanation of the similar scatter for transition II.

Experimental heat capacities of 1,2,3-trimethylbenzene have not previously been reported. Several investigators have reported data on the several transitions. A comparison of the results of this investigation with the data from the literature is given in Table IX.

TABLE X. Molal entropy in the ideal gaseous state at 25°C.

	cal/deg mole
0°–20°, Debye (0=120°, six deg freedom)	1.260
20°–218.70°, $\int C_p d \ln T$	38.925
Trans. II, 157.4/218.70	0.720
218.70°–230.27°, $\int C_p d \ln T$	2.628
Trans. I, 319.3/230.27	1.387
230.27°–247.81°, $\int C_p d \ln T$	3.043
Fusion, 1955.1/247.81	7.890
247.81°–298.16°, $\int C_p d \ln T$	9.190
$S_{298.16}$ (liquid)	64.04±0.1
Vaporization, 11 725/298.16	39.325
Gas imperfection	0.001
Compression, $R \ln(1.49/760)$	−12.389
$S°_{298.16}$ (ideal gas)	91.98±0.15

The earlier temperature data was obtained from heating and/or cooling curves; the heat data by comparison with standard substances in the same apparatus.

Entropy

A summary of the entropy calculations is given in Table X. A Debye function with six degrees of freedom, $\theta=120$°K, was found to represent the heat capacity fairly well up to 30°K. This function was used to compute the entropy up to 20°K. The heat of vaporization at 25°C has been determined by Osborne and Ginnings[2] to be 11 725 cal/mole with a probable error of 0.1 percent. The vapor pressure has been determined by a number of investigators,[3–7] but unfortunately, mostly in the temperature region either above or below 25°C. The value of the vapor pressure at 25°C used in the entropy calculation, 1.49 mm, was found from the best straight line through all of the experimental data on an Antoine type plot and happens to coincide with the value given by Forziatti, Norris, and Rossini's equation.

The entropy of the ideal gas has been calculated by an approximate statistical method by Taylor *et al.*[8] Considering the nature of the approximations involved and the very severe interaction between the three methyl groups, it is not surprising that this calculated value (93.50 cal/deg mole) differs by 1.5 cal/deg mole from the experimental value from this research (91.98 ±0.15 cal/deg mole).

[2] N. S. Osborne and D. C. Ginnings, J. Research Natl. Bur Standards **39**, 453 (1947).
[3] L. I. Smith and L. J. Spillane, J. Am. Chem. Soc. **62**, 2642 (1940).
[4] Rossini, Pitzer, Taylor, Ebert, Kilpatrick, Beckett, Williams, and Werner, "Selected Values of Properties of Hydrocarbons," NBS Circ. 461, U. S. Govt. Printing Office, Washington (1947).
[5] E. R. Hopke and G. W. Sears, J. Am. Chem. Soc. **70**, 3801 (1948).
[6] Forziatti, Norris, and Rossini, J. Research Natl. Bur. Standards **43**, 562 (1949).
[7] Rossini, Mair, and Streiff, *Hydrocarbons from Petroleum* (Reinhold Publishing Corporation, New York, 1953).
[8] Taylor, Wagman, Williams, Pitzer, and Rossini, J. Research Natl. Bur. Standards **37**, 95 (1946).

Entropy, Heat Capacity, and Heats of Transition of 1,3,5-Trimethylbenzene*

R. Dean Taylor† and John E. Kilpatrick
Department of Chemistry, The Rice Institute, Houston, Texas
(Received November 1, 1954)

The heat capacity and the heats and temperatures of fusion of 1,3,5-trimethylbenzene have been determined experimentally. This substance exhibits three melting points: at 228.424°K, at 223.346°K, and at 221.462°K. The only solid phase having reproducible heat capacities was found to be the one having the highest melting point. The entropy of the ideal gas at 25°C and one atmos pressure has been found to be 92.09±0.15 cal/deg mole.

APPARATUS

THIS investigation was carried out in our calorimeter, *B*, which is described in the preceding article.[1] Some minor changes were made in the sample container which necessitated a redetermination of the heat capacities of the empty apparatus. A check on some of the fixed points of the thermometer verified the earlier calibrations.

SAMPLE

This sample of API Research hydrocarbon has been made available by the American Petroleum Institute through the API Research Project 44 at the Carnegie Institute of Technology. The sample was purified by the API Research Project 6 from material supplied by the API Research Project 45 at Ohio State University, Columbus, Ohio. Description of the purification and purity of the sample is given in reference 2. It had been found to contain 0.04±0.02 mole percent impurity. A sample of 0.28836 mole was used. The molecular weight was taken to be 120.186.

RESULTS

Phases

Three different melting points have been observed for 1,3,5-trimethylbenzene. This has led to some confusion in the literature. For the purpose of discussing the various phases the following system of naming has been adopted: "fusion I" refers to the melting point of "solid I" near 228.4°K; "fusion II" refers to the melting point of metastable "solid II" near 223.3°K; and "fusion III" to the melting point of metastable "solid III" near 221.5°K. This nomenclature differs from that used for 1,2,3-trimethylbenzene,[1] which has only one melting point and several stable solid phases.

Streiff *et al.*,[2,3] were the first to report all three melting points. Mair and Schicktanz[4] found it necessary to plunge a rod which had been cooled in liquid air into the cold liquid in order to get solid I. It was a bit surprising to find that all three solid phases could be obtained in the isolated sample container of the calorimeter.

Numerous heating and cooling curves were run on this compound in the hope of defining its phase behavior and determining what paths could best be used in measuring the entropy. These curves were obtained by recording the difference between the potential drop across the platinum resistance thermometer (from about 1 mv to 85 mv) and an adjustable bucking potential from a portable precision potentiometer with a Speedomax recording potentiometer (10-mv range).

The liquid supercooled easily (as much as 10° below fusion III) and invariably froze into solid III. The cooling curve for solid III showed a flat at about 83°K. The succeeding heating curve showed a moderately sharp inflection at about 94°K (indicating a narrow region of high heat capacity); upon cooling this resulting phase down, the cooling curve again indicated a flat near 83°K. The next heating curve through the 94° region, however, showed a much less pronounced hold. Repetition of this heating-cooling cycle gave more curves of the latter form. The flat at 83°K and both varities of flats near 94°K apparently do not correspond to isothermal transitions. On the other hand, freshly frozen solid III or old solid III that had been cycled one or more times, when cooled to only about 87°K, showed no inflection near 94°K on the subsequent heating curve.

All of the solids resulting from the above treatment usually underwent an irreversible evolution of heat in the neighborhood of 221°K and then melted at 228.4°K. Melting at 221.5°K could be accomplished by heating solid III which had been cooled only a few degrees below its freezing point. Solid II was obtained by heating solid III which had been cooled to about 170°K. This procedure did not always yield solid II; oftimes solid I resulted. A cooling curve followed by a heating curve for this process (solid III converting to solid II) was smooth with no holds or inflections below the fusion region. The cooling curve of solid II was smooth;

* This paper is based on a thesis (R. D. Taylor) submitted to the faculty of The Rice Institute in partial fulfilment of the requirements of the degree of Doctor of Philosophy.

† Present address: Los Alamos Scientific Laboratory, Los Alamos, New Mexico.

[1] Taylor, Johnson, and Kilpatrick, J. Chem. Phys. **23**, 1225 (1955).

[2] Streiff, Murphy, Sedlak, Willingham, and Rossini, J. Research Natl. Bur. Standards **37**, 331 (1946).

[3] Streiff *et al.*,"Selected values of physical properties of hydrocarbons," API Research Project 44 (August, 1945), Table 5.

[4] B. J. Mair and S. T. Schicktanz, J. Research Natl. Bur. Standards **11**, 665 (1933).

however, like solid III, solid II often converted to solid I at about 221°K with the evolution of heat. This spontaneous evolution of heat almost eliminates these two paths for entropy purposes. Furthermore, the heat capacity of either solid II or solid III was found to be irreproducible regardless of the thermal history of the sample.

Heat Capacity

Heat capacities were determined over the usual range for the liquid and solid I. Before each set of measurements on solid I was made, the sample was held for several hours in fusion I in order to assure complete conversion from either of the two metastable solid phases. These data are shown in Table I and in Fig. 1. There is a small hump in the heat capacity curve near 60°K which was found to be quite reproducible. The entropy contribution of this hump is about 0.08 cal/deg mole. The premelting heat capacity (which has been subtracted in the data shown in Table I) indicated about 0.050 mole percent impurity. The molal heat capacity at rounded temperatures is given in Table II.

TABLE I. Molal heat capacity of the stable phases of 1,3,5-trimethylbenzene.

Temp. °K	C_p cal/deg mole	Temp. °K	C_p cal/deg mole
64.11	15.67	219.52	34.28
70.47	16.66	223.14	34.66
76.95	17.65	226.02	35.46
83.82	18.70		
90.70	19.65	Temp. of Fusion I	
97.20	20.43		
104.11	21.26	65.26	15.83
113.38	22.34		
124.06	23.59	99.69	20.72
134.64	24.80		
145.22	25.95	220.96	34.22
155.88	27.14	224.32	34.26
61.95	15.41	Heat of Fusion Ib	
69.82	16.57		
79.74	18.08	259.85	46.64
90.88	19.67	266.53	47.19
101.68	20.95	272.84	47.71
112.63	22.26	279.02	48.28
124.44	23.63	285.29	48.86
135.81	24.93	290.88	49.38
147.17	26.16	297.71	50.03
159.53	27.53	304.50	50.41
172.47	28.93		
185.01	30.34	227.33	44.19
196.95	31.70		
208.20	32.98	17.15	2.686
218.98	34.14	19.27	3.509
		21.42	4.305
Heat of Fusion Ia		23.71	5.174
		26.22	6.097
		29.09	7.123
230.02	44.35	32.30	8.262
233.37	44.56	35.78	9.345
236.97	44.83	40.53	10.581
238.90	44.95	46.58	12.170
243.14	45.23	52.47	13.556
		58.40	14.907
224.11	43.99	65.01	15.80
231.53	44.46	73.30	17.10
239.03	44.97	83.03	18.59
246.63	45.55	92.35	19.85
254.82	46.21		
263.23	46.93	Heat of Fusion Ic	
272.38	47.75		
281.13	48.51	Heat of Fusion Id	
179.81	23.76	60.29	15.20
191.32	31.06		
202.26	32.36	61.22	15.27
210.76	33.34		
215.74	33.84	Heat of Fusion Ie	

Temperatures of Fusions

The temperature of fusion was determined for each of the three solid phases. The data are given in Table III. The extrapolated temperatures for the "pure sample" for fusions I, II, and III, respectively, are 228.424±0.004°K, 223.346±0.004°K, and 221.462 ±0.004°K. The impurity, as calculated from the sharpness of fusion I, is 0.059±0.005 mole percent which is in good agreement with the somewhat rougher figures: 0.05 from premelting and 0.04±0.02 as stated by the suppliers of the sample. From fusion II, the impurity was found to be 0.023±0.003; and from fusion III, 0.032±0.004.

Heats of Fusion

The five determinations of the heat of fusion I are summarized in Table IV. In all cases the sample was held in fusion I before cooling down. The best value was taken to be the mean of the five determinations and is 2274.1±3.0 cal/mole. The heats of fusions II and III were also determined. Since reproducible heat capacities

TABLE II. Molal heat capacity at rounded temperatures of the stable phases of 1,3,5-trimethylbenzene.

Temp. °K	C_p cal/deg mole	Temp. °K	C_p cal/deg mole
20	3.77	165	28.12
25	5.67	170	28.67
30	7.48	175	29.22
35	9.09	180	29.78
40	10.49	185	30.34
45	11.77	190	30.90
50	12.97	195	31.48
55	14.19	200	32.05
60	15.16	205	32.62
65	15.80	210	33.18
70	16.59	215	33.75
75	17.37	220	34.31
80	18.18	225	34.86
85	18.87		
90	19.55	230	44.36
95	20.17	235	44.68
100	20.76	240	45.04
105	21.36	245	45.42
110	21.95	250	45.82
115	22.54	255	46.23
120	23.12	260	46.66
125	23.70	265	47.08
130	24.28	270	47.51
135	24.84	275	47.95
140	25.39	280	48.39
145	25.92	285	48.84
150	26.48	290	49.29
155	27.04	295	49.74
160	27.58	300	50.20

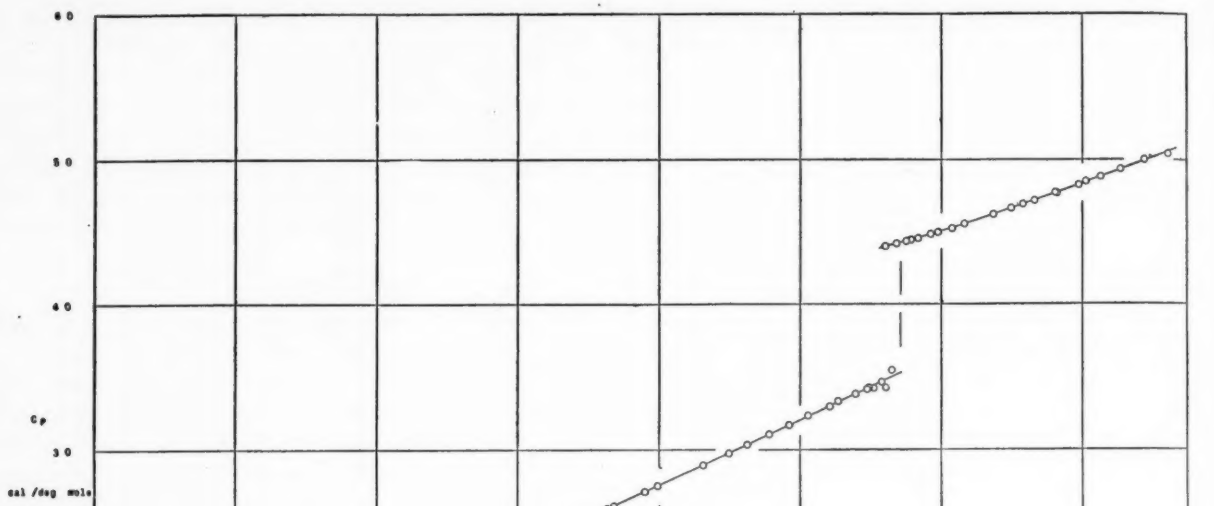

FIG. 1. Molal heat capacity of 1,3,5-trimethylbenzene *versus* temperature.

were not obtained on these solid phases, the (nearly equal) heat capacities of solid I were assumed for the calculation. The heat of fusion II was found to be 1932±10 cal/mole from a single determination and for fusion III, 1892±8 cal/mole from two determinations.

The temperatures and heats of the fusions are compared with the results of other investigators in Table V.

TABLE III. Equilibrium temperatures of the three fusions of 1,3,5-trimethylbenzene.

Percent melted	Temperature °K
Fusion I	
33	228.342
43	228.362
59	228.379
84	228.392
Extrapolated value, pure sample	(228.424)
Fusion II	
25	223.300
38	223.315
57	223.326
88	223.332
Extrapolated value, pure sample	(223.346)
Fusion III	
23	221.392
38	221.418
53	221.431
82	221.443
Extrapolated value, pure sample	(221.462)

Entropy

A Debye function of eight degrees of freedom, (θ=126.7°K), was found to best represent the lowest

TABLE IV. Molal heats of fusion I at 228.424°K of 1,3,5-trimethylbenzene.

No.	Temp. interval °K	Heat input[a] cal	$\int C_p dT$ [a] cal	Pretrans. cal/sample	ΔH cal/mole
Ia	224.17–236.11	881.34	228.01	3.45	2277.6
Ib	217.67–237.34	1018.39	363.95	1.33	2274.1
Ic	219.61–236.72	972.18	318.46	1.63	2272.7
Id	222.04–233.65	868.17	215.07	2.28	2272.8
Ie	218.31–236.24	984.68	330.63	1.42	2273.1
Best value					2274.1±3.0

[a] Sample plus sample container.

TABLE V. Comparison with other investigators of the heats and temperatures of fusion.

Reference	ΔH cal/mole	Temp. °K	Impurity mole %
	Fusion I		
Mair[c]		228.40	
Rossini[d]	2280 ±60	228.36	
Hirschler[e]		228.43 ±0.15[a]	0.3
Glasgow[f]		228.422	0.04
Streiff[g]		228.440±0.010[a]	0.05
This research	2274.1± 3.0	228.424±0.004[b]	0.059
	Fusion II		
Hirschler[e]		223.34 ±0.15[a]	
Streiff[g]		223.370±0.020[a]	
Rossini[h]	1980	223.37[a]	
This research	1932 ±10	223.346±0.004[b]	
	Fusion III		
Mair[c]		221.44	
Rossini[d]	1910 ±50	221.46	
Hirschler[e]		221.35 ±0.15[a]	
Streiff[g]		221.480±0.020[a]	
This research	1892 ± 8	221.462±0.004[b]	

[a] In air, zero impurity.
[b] Under about 58 cm pressure of helium, zero impurity.
[c] See reference 4.
[d] F. D. Rossini, J. Research Natl. Bur. Standards **11**, 553 (1933).
[e] A. E. Hirschler and W. B. M. Faulconer, J. Am. Chem. Soc. **68**, 210 (1946).
[f] Glasgow, Murphy, Willingham, and Rossini, J. Research Natl. Bur. Standards **37**, 141 (1946).
[g] Streiff, Murphy, Sedlak, Willingham, and Rossini, J. Research Natl. Bur. Standards **37**, 331 (1946).
[h] See reference 6.

six heat capacities. A six degree of freedom function might seem more plausible; however, the eight degree function gave a better representation. In any event, the effect on the entropy is small.

The entropy of the liquid at 298.16°K was found to be 65.38±0.10 cal/deg mole. The calculation is summarized in Table VI. The standard entropy of the ideal gas at 298.16°K, 1 atmos was calculated to be 92.09 ±0.15 cal/deg mole. Osborne and Ginnings'[5] value of the heat of vaporization at 25°C, 11 346 cal/mole, was used. The vapor pressure at 25°C was calculated to be 2.52 mm by the system used in reference 1 from the data of a number of investigators.[6–11]

[5] N. S. Osborne and D. C. Ginnings, J. Research Natl. Bur. Standards **39**, 453 (1947).

TABLE VI. Molal entropy at 25°C of 1,3,5-trimethylbenzene.

	cal/deg mole
0–20°K, Debye (θ=126.7°, eight deg of freedom)	1.467
20–228.424°K, $\int C_p d \ln T$	41.470
Fusion I, 2274.1/228.424	9.956
228.424–298.16°K, $\int C_p d \ln T$	12.486
$S_{298.16°K}$ (liquid)	65.38±0.1
Vaporization, 11 346/298.16	38.053
Gas imperfection (Berthelot)	0.002
Compression, $R \ln(2.52/760)$	−11.345
$S°_{298.16°K}$ (ideal gas)	92.09±0.15

The entropy of the ideal gas has been calculated by Pitzer and Scott[12] and by Taylor *et al.*[13] to be 92.17 and 92.15 cal/deg mole, respectively. These calculated values are in excellent agreement with the experimental value from this research. In both calculations the thermodynamic effect of the three restricted methyl rotations was estimated from the effects found in *m*-xylene and toluene. Since in the case of 1,3,5-trimethylbenzene the methyl coupling is quite closely related to that found in *m*-xylene, it is not too surprising that the agreement is much better than that found in the case of 1,2,3-trimethylbenzene[1]: calc, 93.50; experimental, 91.98. In this case the methyl coupling is particularly tight and has no precise counterpart in the xylenes.

[6] F. D. Rossini *et al.*, "Selected values of properties of hydrocarbons," AP1RP44 Natl. Bur. Standards Circular 461, U. S. Government Printing Office, Washington, D. C., (1947).
[7] E. R. Hopke and G. W. Sears, J. Am. Chem. Soc. **70**, 3801 (1948).
[8] Forziati, Norris, and Rossini, J. Research Natl. Bur. Standards **43**, 562 (1949).
[9] Rossini, Mair, and Streiff, *Hydrocarbons from Petroleum* (Reinhold Publishing Corporation, New York, 1953).
[10] G. Egloff, *Physical Constants of Hydrocarbons* (Reinhold Publishing Corporation, New York, 1946), Vol. III.
[11] J. M. Stuckey and J. H. Saylor, J. Am. Chem. Soc. **62**, 2922 (1940).
[12] K. S. Pitzer and D. W. Scott, J. Am. Chem. Soc. **65**, 803 (1943).
[13] Taylor, Wagman, Williams, Pitzer, and Rossini, J. Research Natl. Bur. Standards **37**, 95 (1946).

Contribution to the Theory of Fast Reaction Rates

R. DE VOGELAERE* AND M. BOUDART
The James Forrestal Research Center, Princeton University, Princeton, New Jersey
(Received August 28, 1953)

Classical calculations of the motion of a mass point on a potential surface are carried out. The surface corresponds to a reaction of the type $AB+A=A+BA$ and is characterized by a single saddle-point. With reference to the mathematically similar problem of the allowed cone of cosmic radiation, a novel feature of fast chemical kinetics is described: the possibility of a substantial decrease of the transmission coefficient above a certain critical energy of the system. This result does not depend on the analytical expression of the surface chosen in the present work. The generality and some consequences of this phenomenon are discussed.

THE theoretical foundations of the transition state method have been examined critically by Wigner.[1] If the reaction is adiabatic and quantum effects do not affect its rate, a single potential energy surface must be constructed at the start. For a reaction of the type $AB+C\rightarrow A+BC$, we consider at first only collisions where the atoms A, B, and C are collinear. Then, to each pair of value of r_{AB} and r_{BC}, the distance between A and B on the one hand and B and C on the other hand, there corresponds a definite value of E the energy of the system (see Fig. 1). Although no surface of this kind has ever been calculated with reasonable accuracy, the generality of the theory rests on the realization that, in many cases, the surface will present a valley of reactants and a valley of products separated by a mountain ridge, the lowest point of which is the saddle-point. If the latter has a height E_s which is *much greater than thermal energies*, statistical mechanics may be used to calculate the rate because an equilibrium supply of activated complexes is maintained. These complexes are fictitious molecules the configuration of which is determined by the saddle-point and its immediate neighborhood. If all paths starting in the reactant valley and reaching the ridge of the barrier cross the latter only once, as follows naturally from the assumptions made heretofore, the transition state method gives the correct rate even without any detailed knowledge of the shape of the surface.

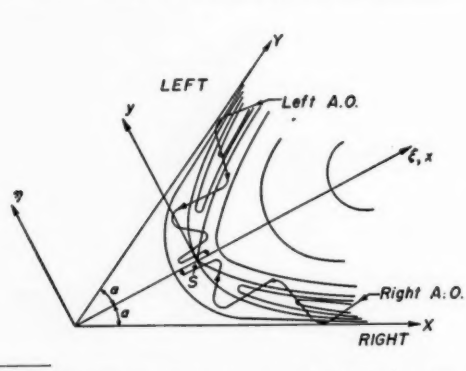

FIG. 1.

If, on the other hand, E_s becomes comparable in magnitude with RT, that is at very high temperatures or for certain types of radical reactions at moderate temperatures, many paths coming from the initial valley will cross the ridge very far from the saddle-point, and they do not have necessarily a highest point. Thus the concept of an activated complex loses its usefulness, expecially when there are reasons to believe that a given path may not lead to reaction even if it has crossed the ridge once. This can be seen intuitively by means of a slightly more complex surface. This is shown in Fig. 2, where a given path may oscillate in the intermediate basin B in such a fashion that its final direction remains uncertain. For such a case, Wigner[1] argues that the transmission coefficient γ, defined as the ratio of the number of crossings through the first ridge RR' which lead to reaction to the total number of crossings, ought to decrease with increasing temperature. Indeed, the probability for a given system of finding its way back to its starting point through RR' increases with the energy of this system.

Consequently, a calculation of γ becomes necessary whenever RT becomes comparable with E_s. Such a calculation has never been performed so that it is impossible to predict if and when the transition state method will fail owing to a small value of γ. Wigner[1] has indicated how this problem should be attacked mathematically: the computation of γ is similar to that of the allowed cone of cosmic radiation.[2-5] We have applied the methods used in the latter problem to the solution of the former. Although we have not yet reached the end of this work, the results obtained thus far have definite physical meaning. Publication at this stage thus seems justified.

EQUATIONS OF THE PROBLEM

It is expected that actual numerical values of γ are very sensitive to the detailed profile of the potential energy surface adopted for the calculation. However, just as in the transition state method, general results presumably depend only on the nature of the surface.

* Laval University, Department of Mathematics, Quebec, Canada. Present address: Department of Mathematics, University of Notre Dame, Notre Dame, Indiana.

[1] E. Wigner, Trans. Faraday Soc. **34**, 29 (1938).

[2] G. Lemaitre and M. S. Vallarta, Phys. Rev. **43**, 87 (1933).

[3] Lemaitre, Vallarta, and Bouckaert, Phys. Rev. **47**, 434 (1935).

[4] T. Yong-Li, Ann. soc. sci. Bruxelles **59**, 285 (1939).

[5] R. De Vogelaere, Ann. soc. sci. Bruxelles **64**, 83 (1950).

For reasons of convenience, we decided to construct an acceptable surface for the symmetrical atom-molecule exchange reaction $AB+A=A+BA$. The equation of this surface reads:

$$V=D\{[1-\exp[-a''(\xi-\xi_0)]\cosh a'\eta]^2 + k\exp[-a''(\xi-\xi_0)]\}. \quad (1)$$

The coordinate system (ξ,η) is such that the ξ axis is defined by the plane of the symmetry of the surface, the η axis being perpendicular to the former through the origin (Fig. 1). Symbols in Eq. (1) have the following meaning: $a'=a\cos\alpha$, $a''=a\sin\alpha$, $a''\xi_0=\ln 2+ar_0$. The parameters of the Morse function for the AB molecule are D, a, and r_0, thus

$$V=D\{1-\exp[-a(r-r_0)]\}^2. \quad (2)$$

In first approximation, kD is equal to the saddle-point energy E_s. Thus k is a small quantity ($k\simeq 0.06D$). The angle 2α of the asymptotic directions of the two valleys, is related to the masses m_1 and m_2 of A and B by the expression[6]

$$\cos 2\alpha=m_1/(m_1+m_2).$$

The surface defined by Eq. (1) has two interesting features. A cut perpendicular to an asymptote sufficiently far from the origin gives a Morse curve as seen in Eq. (2), where r is the distance to the asymptote. A cut along the ridge (the ξ axis) gives

$$V=D\{1-\exp[-a''(\xi-\xi_0)]\}^2 + Dk\exp[-a''(\xi-\xi_0)]. \quad (3)$$

It can be seen that Eq. (3) also resembles a Morse curve slightly modified by the second term the role of which is to obtain the desired height of the saddle-point. Also, Eq. (1) contains enough parameters which all have a physical meaning.

The Lagrangian L of the problem is

$$L=T-V=(\tfrac{1}{2})m(\dot\xi^2+\dot\eta^2)-V,$$

where m is the mass of the representative point the classical motion of which one has to study. It is recalled that[6]

$$m=\frac{m_1(m_1+m_2)}{2m_1+m_2}.$$

It is convenient to put

$$m=1, \quad D=1, \quad 1/a'=1.$$

These relations define the natural units of mass, energy, and length, respectively.

With a change of variables $x=\xi-\xi_0$, $y=\eta$, the Lagrangian becomes

$$L=1/2(\dot x^2+\dot y^2)-(1-e^{-bx}\cosh y)^2-ke^{-bx}, \quad (4)$$

[6] J. O. Hirschfelder, thesis, Princeton, 1935.

FIG. 2.

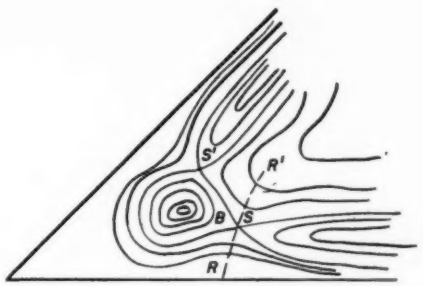

where $b=tg\alpha$. The equations of motion are thus

$$\ddot x=\frac{\partial L}{\partial x}=-2b(1-e^{-bx}\cosh y)e^{-bx}\cosh y+kbe^{-bx},$$
$$\ddot y=\frac{\partial L}{\partial y}=2(1-e^{-bx}\cosh y)e^{-bx}\sinh y, \quad (5)$$

and the energy integral corresponding to Eq. (4) is

$$\dot x^2+\dot y^2=-2(1-e^{-bx}\cosh y)^2-2ke^{-bx}+2V_0\equiv 2U.$$

Thus, the natural unit of time is

$$(1/a')\cdot(m/2D)^{\frac{1}{2}}=(m/a)(2/m_1D)^{\frac{1}{2}}.$$

We shall use the symbols E and V for the energy in ordinary and natural units, respectively. The position of the saddle-point in the new system of coordinates is given by

by $U=0$, $\partial U/\partial x=0$, $\partial U/\partial y=0$. Hence,

$$y_s=0, \quad x_s=-(1/b)\ln[1-(k/2)]. \quad (6)$$

Since k is small compared to unity, $x_s\cong 0$. The corresponding saddle-point energy is

$$E_s/D=V_s=k[1-(k/4)] \quad (7)$$

in agreement with the statement made previously that $E_s\cong kD$.

As will be explained later, a study of the neighborhood of some important trajectories (which we will call orbits) is necessary. The variational equations of motion to the first order will then be required. If x, y as well as $x+\xi$, $y+\eta$ (where ξ and η are small quantities that must not be confused with the symbols used above for the axes) are solutions of Eqs. (5), we get, after substitution and neglecting all terms of order larger than unity,

$$\frac{d\dot\xi}{dt}=-\frac{\partial^2V}{\partial x^2}\xi-\frac{\partial^2V}{\partial x\partial y}\eta,$$
$$\frac{d\dot\eta}{dt}=-\frac{\partial^2V}{\partial x\partial y}\xi-\frac{\partial^2V}{\partial y^2}\eta \quad (8)$$

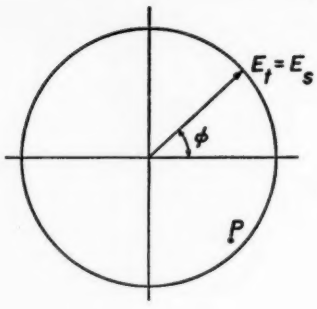

FIG. 3.

with

$$a_0 \equiv -\frac{\partial^2 V}{\partial x^2} = -kb^2 e^{-bx} + 2b^2 \cosh y e^{-bx} - 4b^2 e^{-2bx} \cosh^2 y,$$

$$b_0 \equiv -\frac{\partial^2 V}{\partial y^2} = 2e^{-bx} \cosh y - 2e^{-2bx} \cosh 2y, \qquad (9)$$

$$c_0 \equiv -\frac{\partial^2 V}{\partial x \partial y} = -2be^{-bx} \sinh y + 2be^{-2bx} \sinh 2y.$$

An exposé of the methods used together with the results obtained from the equations of this paragraph, will now be presented. All mathematical developments have been assembled in the Appendix in order to bring out more clearly the underlying physical ideas in the exposé itself.

METHODS AND RESULTS

Definition of the Transmission Coefficient

Since we consider only collisions in which all three atoms are collinear, the energy of rotation can be left out of consideration. Let us examine all the orbits starting from a section of the valley of the reactants sufficiently far away from the saddle-point region so that intermolecular forces are effectively zero. If we consider all the orbits with a given total energy E, there will be a twofold infinity of them differing by their phase $0 \leq \varphi < 2\pi$ and the value of their translational energy $0 < E_t \leq E$ corresponding to the relative motion of the system. The phase is that of the harmonic vibrational motion in the remote section under consideration. Although the notion of phase is purely classical, it will be appreciated that we are concerned only with high-energy levels. Wigner and Hirschfelder[7] have shown that classical and quantum-mechanical transmission coefficients rapidly converge, so that the purely classical approach ought to yield meaningful results.

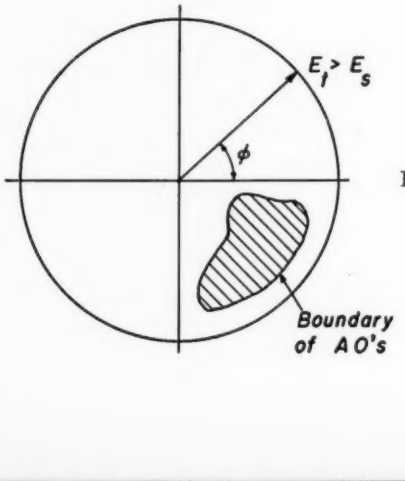

FIG. 4.

Among all the orbits of a given E, some will pass over the barrier and lead to reaction and some will not. The ratio of the number of the former to the total number of them, integrated over all possible values of φ and E_t, we call reaction yield κ_E. The concept of κ_E is more general than that of γ, the transmission coefficient of the transition state method. It is possible, in principle, to calculate the reaction rate from κ_E if the distribution in energy of the reactants is known. This distribution may be arbitrary and need not be an equilibrium one.

Role of Orbits Asymptotic to the Principal Orbits

The method of calculating κ_E will now be outlined. It rests upon the determination of certain types of orbits which will be defined at first. Periodic orbits (PO) are such that the system comes back to its initial conditions after a time T called period. On our surface, PO's on the ridge are revealed by mere inspection but there are other ones. There exist two kinds of PO's: stable (SPO) or unstable (UPO). For a given PO, this can be decided by examination of its neighborhood by means of the first-order variational equations. If a PO is slightly perturbed either it will stay in its vicinity during a long period of time, not necessarily infinite (SPO), or it will pull away from it indefinitely (UPO). Every UPO can be further characterized by its number of crossings n per period of the unperturbed PO, n being even $(\text{UPO})_e$ or odd $(\text{UPO})_0$. For a given (UPO), there can be found asymptotic orbits (AO) that come nearer to the (UPO) indefinitely. The role of the AO's is essential. Indeed, the calculation of κ_E consists in

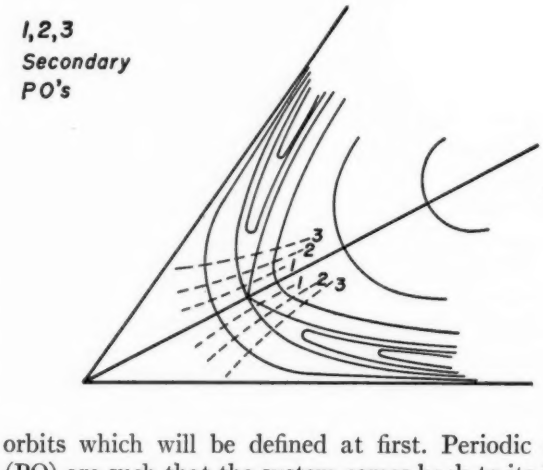

FIG. 5.

[7] J. O. Hirschfelder and E. Wigner, J. Chem. Phys. 7, 616 (1939).

determining these AO's because they form the limit between two families of orbits: those which cross the (UPO) in question and those which return to their initial valley. The situation can be clarified further as follows.

As shown in Appendix 1, when $E=E_s$, there exists only one AO to the $(UPO)_{n=0}$, the latter reducing itself to a single point, the saddle-point. This result can be illustrated by means of a polar diagram (E,φ) as seen in Fig. 3. The AO is represented by a single point corresponding to a translational energy E_t only slightly smaller than $E=E_s$, since a representative point leaving the saddle-point with zero kinetic energy would reach the bottom of the valley with only a slight amount of vibrational motion. When E is larger than E_s but smaller than a critical energy E^* which will be discussed presently, there is now an infinity of AO's that define a closed contour in the polar diagram (Fig. 4): all orbits corresponding to points inside the contour of AO's lead to reaction, all orbits outside come back to their initial valley. Thus, κ_E is proportional to the area bounded by the AO curve and the latter ought to be computed for a complete calculation of reaction rate.[8]

Secondary Orbits and Related Effects

This program has not been carried out so far but an interesting effect has been discovered, that constitutes the main contribution of this work. In the situation just described, for each value of the total energy E there is only one $(UPO)_e$ and a single infinity of AO's corresponding to it. If other UPO's were to appear, they ought to be taken into account. Such new UPO's do appear indeed, as shown in Appendixes 2 and 3, when E exceeds a critical energy E^*. Then the PO's on the ridge become stable but two new families of PO's are discovered: the calculation (Appendix 4 and 5) shows that they are unstable with $n=0$. Consequently, they play the role of secondary PO's by opposition to the $(UPO)_{n=0}$'s on the ridge which we call principal. The PO's on the ridge become unstable again with n odd when the energy is further increased and becomes larger than a certain value of $E=E^*$. But this latter circumstance does not change essentially the following discussion which exposes the consequences of the appearance of secondary PO's.

A number of secondary PO's is represented schematically in Fig. 5, for increasing values of the energy. If we consider what happens at a given energy, two secondaries must be examined, one RS (on the right, towards the valley of reactants) and one LS (on the left, towards the valley of products). The AO's to the RS (Fig. 6) define the limit between orbits which penetrate into the region enclosed by the two secondaries and orbits that return to infinity in the valley of

[8] In Fig. 4, to a certain extent, the circle $E_t=E$ corresponds to Störmer's cone in the cosmic ray problem (see reference 2) and our contour determined by the AO's to the principal PO's corresponds to the principal cone of the same problem.

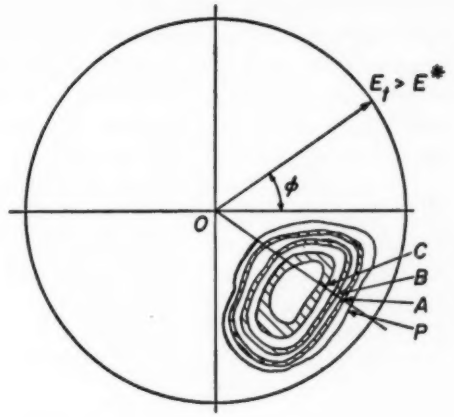

FIG. 6.

reactants. The region on the surface between the two secondaries, we call pseudobasin, by analogy to the case of Fig. 2 where the presence of a true basin leads to complications of a similar nature.

Let us now analyze what happens inside the contour of Fig. 6 determined by these AO's. Let us examine first the left secondary and the orbits which travel toward the valley of products: the orbits which cross the secondary and those which do not, are separated by the right AO's—LS. The latter, however, do not necessarily penetrate into the valley of reactants. If they do, they give way to curves inside the contour already defined on the polar diagram of Fig. 6. There again, the right AO's—LS which cross the RS and those which do not cross the latter are separated by a left AO—RS. We then have an orbit asymptotic to both the LS and the RS: it is a heteroclinic orbit, according to the terminology of Poincaré[9] (see Fig. 7). It is easy to prove the existence of two heteroclinic orbits for $E^*<E<E^*$. An orbit starting on the ridge but perpendicular to it, at an equipotential line E, will remain in the neighborhood of the ridge because the PO on the ridge is stable. Another orbit starting on the ridge, perpendicular to it but in the vicinity of the saddle-point will enter one of the valleys and cross, say, the RS. Between these two orbits, there exists a left AO—RS that also starts on the ridge perpendicular to it. Because of the latter circumstances and of the symmetry

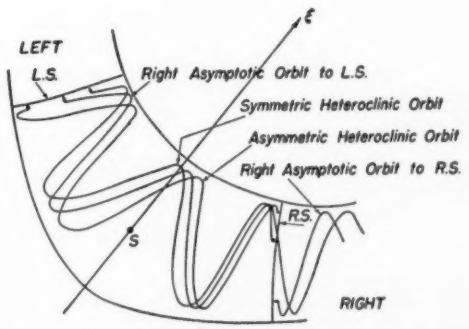

FIG. 7.

[9] H. Poincaré, *Nouvelles Methodes de la Mecanique Celeste* (Gauthier-Villars, Paris 1899), Vol. I.

of the surface, this orbit is thus at the same time a right AO−LS. It is also a simple matter to find two nonsymmetric heteroclinic orbits. It can be stated without proof that an enumerable infinity of other heteroclinic orbits that oscillate a number of times in the pseudobasin can also be found.

The situation created by the secondary and heteroclinic orbits is analogous to that analyzed by Tchang Yung-Li and one of us[5] in the cosmic ray problem near the equator. As has been demonstrated in that case, the heteroclinic orbits determine a fine structure inside the principal cone. This fine structure is due to alternate zones of crossing and noncrossing relative to the secondary orbits.[10]

In the reaction rate problem, the effect of secondary orbits may be explained as follows. Consider at first only two symmetric and two nonsymmetric heteroclinic orbits, which do not oscillate in the pseudobasin. Suppose we leave the valley of reactants in the neighborhood of a right AO−RS. If the translational energy is increased, the orbit under examination will follow the right AO−RS very closely. If E_t is still increased, the RS will be crossed and the orbit will now follow a left AO−RS. The number of oscillations N of the orbit between the moment it crosses the RS and the moment it crosses, say, the x-axis, will be the larger, the closer the orbit was to the right AO−RS in the valley. For this orbit to be at the same time a right AO−LS, it must be very close to a heteroclinic orbit. The latter condition may be fulfilled in more than one way. With four heteroclinic orbits, as supposed above, it may be fulfilled in four different ways for each value of N. Thus, when we move up along OP, a succession of points will be met, corresponding to all possible ways of fulfilling the condition just described. These points, A, B, C, etc., . . . define various regions in the polar diagram with alternative reaction or nonreaction. A fine structure of the area defining κ_E now replaces the continuum of Fig. 4, and there is an accumulation of strips adjacent to the limit of the principal cone. This effect determines the "first-order cone." To sum up, the RS acts upon the right AO−LS in the valley of the reactants so as to produce a sort of diffraction effect.

The real situation is more complex owing to the enumerable infinity of heteroclinic orbits that cause further splitting of the first-order cone. Other PO's complicate the picture even more, but it seems that the secondary cone, as pictured previously, will be the most important one, especially for small values of N.

The meaning of this fine structure is clear in connection with the cosmic ray problem. There, for small geomagnetic latitudes, the area of fine structure constitutes a *small percentage* of the total possible area.[5] In our problem, the calculations show that this fine structure is quite complex, so that an exact calculation of κ_E has not been performed as yet and will be quite laborious. It can be stated, however, that the appearance of the pseudobasin may lead to a substantial decrease of κ_E. This effect confirms the intuitive reasoning of Wigner for the case of a true basin. No statement can be made at present concerning the order of magnitude of κ_E, and its dependence on energy and the detailed shape of the surface.[11]

CONCLUSIONS AND DISCUSSION

The main effect reported here is the appearance of a pseudobasin and the fall in reaction yield at a critical energy value E^*. We have found (Appendix 4) that the ratio E^*/E_s increases with the angle α but is practically ndependent of k. With an error less than 4 percent:

$$E^*=\frac{2(m_1+m_2)}{2m_1+m_2}E_s,$$

when $0<m_1\leq m_2$ and $0<E_s\leq(12/100)D$. The pseudobasin becomes quite large at moderately large values of E. Thus the average distance of the boundaries of the pseudobasin from the ridge is, in natural units:

$$0.5 \quad \text{at} \quad E=1.5E_s$$

and

$$1.0 \quad \text{at} \quad E=2E_s$$

(Appendix 5).

The situation for larger values of E(4 or 5 times E_s) has not been explored and nothing can be said about the transmission coefficient for these very high values of the energy.

Although the value of E^* is not very high, it is too high for normal slow kinetics. It is known empirically that the transmission coefficient is not very different from unity in all cases of adiabatic reactions that have been analyzed by means of the transition state method. Exceptions to this rule and agreement with the present theory must be sought among flame reactions or reactions involving hot atoms. It seems of interest to discuss briefly a case where a decrease of transmission coefficient at high values of the energy seems to have been observed.

Schwarz *et al.*[12] have recently photolyzed HI ($\lambda=2537$ A) at various temperatures with or without foreign gases (H_2 and He) acting as moderators. This term must be understood as follows. Upon absorption of a light quantum, the HI molecule dissociates and the products possess translational energy in excess of the thermal amount. Thus hot hydrogen atoms H* are produced with an excess energy up to 42 kcal. The

[10] Let us note some differences between the cosmic ray and the chemical reaction problems. In the cosmic ray situation, the fine structure appears between the principal cone and the Stormer cone and the role of both RS and LS is played by a single PO. The orbits asymptotic to the latter in both directions are then called homoclinic (reference 9). In spite of the differences, the general lines of reasoning are the same in both cases.

[11] The order of magnitude of κ_E for the potential surface chosen, will be determined by a quantity analogous to the χ of the cosmic-ray problem (see reference 5).

[12] Schwarz, Williams, and Hamill, J. Am. Chem. Soc. **74**, 6007 (1952).

photolysis is accompanied by the reactions:

$$H^*+HI=H_2+I, \tag{10}$$

$$H^*+I_2=HI+I. \tag{11}$$

Analysis of halogen content of the photolyzed iodide after a given length of time permits us to calculate the ratio $R=k_2/k_1$ of the rate constants of Eqs. (11) and (10). The role of the moderators is to bring back H atoms to thermal energies. Thus extrapolated values of R for large values of the moderator pressure should yield the thermal value of R, say R_∞. The data give $R_\infty=10^{-2}\exp(4500/RT)$. Without moderator on the other hand $R_0=4.2$ at all temperatures. This corresponds to the reactions in Eqs. (10) and (11) with hot H atoms.

Now, one may expect the activation energy of Eq. (11) to be very low ($E_2\cong 0$) whereas $E_1\cong 4$ kcal for Eq. (10) in accordance with Hirschfelder's rule. The value 10^{-2} for the ratio of pre-exponential factors is the normal one on the basis of absolute rate theory, on the assumption that both transmission coefficients are unity. But this value also should be the value of R_0, that is for the hot hydrogen atoms. This not being the case, Williams, *et al.*, conclude that the pre-exponential factors are energy dependent.

In view of our theoretical results, it appears worth while to speculate about this anomalous energy dependence. At low energies, the transmission coefficients of both Eq. (10) and Eq. (11) are very near to unity as shown by the good agreement between calculated and observed R_∞. Since however $E_2\cong 0$, it seems that the transmission coefficient of Eq. (11) is not significantly energy dependent since such a dependence would show up even at low energies. This would mean then that the transmission coefficient of Eq. (10) decreases from a value near to unity at low energies to a value of about 10^{-2} for hot atoms. Such a decrease might perhaps be explained by our theory, if further calculations along the lines of this work are pursued with the aim of obtaining numerical values of κ_E. Such calculations are being planned.

APPENDIXES

The methods and results contained in the appendixes are of great generality and could be easily applied to analogous situations.

The following notation will be useful:

$$N=e^{-bx},\quad S=\sinh y,\quad C=\cosh y,$$
$$S_2=\sinh 2y,\quad C_2=\cosh 2y.$$

Appendix 1. Asymptotic Orbits

A first-order approximation of the asymptotic orbit at the saddle-point is given first. A better approximation is then computed, the results being given for different values of E_s/D and m_1/m_2. Use will be made of these computations in subsequent work.

With the new notation, at the saddle-point, one has, according to Eqs. (6) and (7),

$$C=1,\quad S=0,\quad N=\rho=1-k/2=(1-V_s)^{\frac{1}{2}}.$$

In the vicinity of the saddle-point, the solution is given by Eq. (8) with the particular values of Eq. (9),

$$a_0=b^2\rho(2-4\rho-k)$$
$$b_0=2\rho-2\rho^2,$$
$$c_0=0.$$

Thus:

$$\xi=A'\sin(\omega t+B')$$
$$\eta=A_1e^{\Omega t}+B_1e^{-\Omega t} \tag{12}$$

with

$$\omega=(-a_0)^{\frac{1}{2}}=\sqrt{2}\cdot b\rho$$
$$\Omega=(b_0)^{\frac{1}{2}}=(k\rho)^{\frac{1}{2}}. \tag{13}$$

The relations Eq. (12) characterize a saddle-point if $k>0$ and a stable point if $k<0$. In the latter case, the surface would have a basin where both valleys meet but no saddle-points.

The frequency in the direction of the x-axis is, in natural units,

$$\nu=(\sqrt{2}/2\pi)\cdot b\rho$$

and, in ordinary units,

$$\nu=\frac{a}{2\pi}\left[\frac{(2m_1+m_2)m_2}{(m_1+m_2)^2m_1}\cdot(D-E_s)\right]^{\frac{1}{2}}.$$

Later on, we shall need:

$$\Omega T=\Omega/\nu=\frac{\pi}{b}\left(\frac{2k}{\rho}\right)^{\frac{1}{2}}. \tag{14}$$

The AO to the saddle-point is given by Eq. (12) where $A'=0$, $B_1=0$: it approaches the saddle-point indefinitely when $t\to-\infty$. We may put $A_1=1$, since changing A_1 corresponds only to a change of the origin of time. The expression $\xi=0$, $\eta=e^{\Omega t}$ is valid only very near to the saddle-point; at a larger distance, it is necessary to study the variational equations to higher orders.

TABLE I

$k\times10$	10Ω	α	$B\times10$	$-C\times10$	$-D\times10$	E	$F\times10$	$-G\times10$
0.3000	1.7190	30°	4.1630	7.1824	4.4922	1.19342		
		35°	4.3797	5.4308	4.0727	0.74942		
		40°	4.5318	4.2013	3.6473	0.48295		
		45°	4.6411	3.3178	3.2584	0.31898		
0.6000	2.4125	30°	3.5338	6.1591	2.5911	0.74455	2.1539	9.1955
		35°	3.8691	4.8457	2.6329	0.51862	2.1105	5.8920
		40°	4.1212	3.8584	2.5873	0.36345	1.9862	3.7920
		45°	4.3119	3.1114	2.4910	0.25675	1.8202	2.4524
1.2000	2.7713	30°	3.1944	5.6078	1.8898	0.57158		
		35°	3.5761	4.5104	2.0319	0.41878		
		40°	3.8745	3.6525	2.0958	0.30642		
		45°	4.1071	2.9836	2.1029	0.22451		
2.4000	4.5957	30°	1.6379	3.0783	0.2307	0.12294		
		35°	2.0441	2.7568	0.3341	0.11224		
		40°	2.4332	2.4487	0.4515	0.10079		
		45°	2.7941	2.1630	0.5775	0.08910		

The generalized expressions for the variations are

$$\xi=\frac{1}{b}(Be^{2\Omega t}+De^{4\Omega t}+Fe^{6\Omega t}+\cdots)$$

$$\eta=e^{\Omega t}+Ce^{3\Omega t}+Ee^{5\Omega t}+Ge^{7\Omega t}+\cdots,$$

where B, C, D, E, F, and G are obtained by recurrent relations and given in Table I for different values of the saddle-point energy (k) and different ratios of the masses (α). The asymptotic solution through the saddle-point is deduced immediately:

$$x=(1/b)\ln\rho+\xi,$$
$$y=\eta.$$

Appendix 2. Periodic Orbits on the Ridge

If, in Eq. (5) we put $y=0$, the second one is verified while the first and third are equivalent:

$$\dot{x}^2=4\rho N-2N^2-2(1-V_0).$$

If x is expressed as a function of N,

$$\dot{x}^2=\dot{N}^2/b^2N^2.$$

The solution is given by elementary functions

$$(1-V_0)N^{-1}=\rho-[(V_0-V_s)^{\frac{1}{2}}\cdot\cos\omega t]$$

with $\omega=[2(1-V_0)]^{\frac{1}{2}}\cdot b$. For each value of $V_0\geq V_s$, there exists a periodic orbit which reduces itself to the equilibrium solution for $V_0=V_s$.

Appendix 3. Vicinity of the Periodic Orbits on the Ridge

For these periodic orbits, the variational equations in Eq. (8) become simply:

$$\frac{d\dot{\xi}}{dt}=\frac{\partial^2U}{\partial x^2}\xi;\quad \frac{d\dot{\eta}}{dt}=\frac{\partial^2U}{\partial y^2}\eta;\quad \dot{x}\dot{\xi}=\ddot{x}\xi.$$

The first equation is now equivalent to the last one, the solution of which is

$$\xi=C\dot{x}.$$

This is a trivial solution giving the original orbit with a small change in the origin of time. To solve the second one, it is necessary to express $\partial^2U/\partial y^2$ in terms of t. The solution is

$$\eta=Ae^{\Omega t}\varphi(t)+Be^{-\Omega t}\varphi(-t), \tag{15}$$

where φ is a periodic function with a period equal to that of the PO and Ω is the so-called characteristic exponent.[5]

TABLE II

V_0/V_s	1	1.1	1.2	V^*/V_s	1.375	V^+/V_s	2	5
$\cosh\Omega T$	3.463	2.768	2.117	1.000	0.961	−1.000	−4.109	−47.93

For the numerical computation, the method exposed at length in reference 5 has been followed. It is easier to use the real quantity $\cosh\Omega T$ for the discussion, T being the period of the periodic orbit. The results are condensed in Table II, for $k=0.060$ and $b=\pi/6$.

For $V_0/V_s=1$, the result follows from Eq. (14).

(1) When $\cosh\Omega T>1$, the periodic orbits are unstable and of even order. This happens when $V_s<V_0<V^*$: the orbits are of zero order and are called the principal periodic orbits.

(2) When $-1<\cosh\Omega T<-1$, the periodic orbits are stable. This happens when $V^*<V_0<V^+$.

(3) When $\cosh\Omega T<-1$, the periodic orbits are unstable and of odd order. This happens when $V_0>V^+$: the order of these orbits is one.

Qualitatively, analogous results would be obtained for other values of k and b: $\cosh\Omega T$ being >1 for $V_0=V_s$ and <0 but very large in absolute value for V_0/V_s large. This generalization can be safely inferred from our calculations although a rigorous proof is still lacking.

Appendix 4. Secondary Orbits Infinitely Close to the Periodic Orbits Near the Ridge

With respect to the transmission coefficient, the value of V^* is essential while that of V^+ is unimportant. As has been shown, V^* is defined by $\cosh\Omega T=1$. At the same time, one solution (Eq. 15) of the variational equations becomes a periodic function representing a periodic orbit infinitely close to the ridge, called a secondary orbit. The latter can be found by an iteration process.[5] A Fourier series expansion must be written at first:

$$-\frac{1}{\omega^2}\frac{\partial^2U}{\partial y^2}=-\frac{2N(1-N)}{\omega^2}=B_0+2\sum_1^\infty B_m\cos m\omega t;$$

but

$$N=\frac{V}{p^2-2p\cos\omega t+1}=\frac{V}{(p-z)(p-z^{-1})},$$

with $z=e^{i\omega t}$, and

$$\frac{V}{2p}=\frac{1-V_0}{(V_0-V_c)^{\frac{1}{2}}},\quad \frac{V}{1+p^2}=\frac{1-V_0}{(1-v_c)^{\frac{1}{2}}}. \tag{16}$$

Then

$$B_m=\frac{1}{\pi}\cdot\int_0^{2\pi}\frac{N(N-1)}{\omega^2}e^{im\omega t}d\omega t,$$

or

$$B_m=\frac{-i}{\pi}\oint\frac{N(N-1)}{\omega^2}z^{m-1}dz,$$

the integration being carried out on a circle of unit radius in the complex plane.

If we take p from Eq. (16), since $p<1$, there is

TABLE III.

	$\alpha=\pi/6$ or $b=0.5774$			
k	0.0000	0.0300	0.0600	0.1200
p	0.0000	0.05164	0.07543	0.11390
V_s	0.00000	0.02978	0.05910	0.11640
V^*	0.00000	0.04008	0.08028	0.16109
V^*/V_s	1.3333	1.3458	1.3583	1.3839
C_0	1.0000	1.0000	1.0000	1.0000
C_1		0.2990	0.4220	0.5952
C_2		0.0193	0.0396	0.0839
C_3		0.0011	0.0034	0.0108
C_4		0.0001	0.0003	0.0013
C_5				0.0002
	$\alpha=\pi/4$ or $b=1.000$			
k	0.0000	0.0300	0.0600	0.1200
p	0.0000	0.08853	0.12808	0.19016
V_s	0.00000	0.02978	0.05910	0.11640
V^*	0.00000	0.05973	0.11886	0.23544
V^*/V_s	2.0000	2.0057	2.0112	2.0227
C_0	1.0000	1.0000	1.0000	1.0000
C_1		0.1754	0.2513	0.3657
C_2		0.0117	0.0242	0.0525
C_3		0.0009	0.0026	0.0085
C_4		0.0001	0.0003	0.0015
C_5				0.0003

only one pole inside the circle and

$$B_m=\text{residue at } p \text{ of}\left[\frac{2N(N-1)}{\omega^2}z^{m-1}\right]$$

for the part with a simple pole:

$$B_{m,1}=-\frac{2V}{\omega^2}\left(\frac{-z^m}{zp-1}\right)_{z=p}=-\frac{2V}{\omega^2}\frac{p^m}{1-p^2}.$$

For the other part with a double pole at p:

$$B_{m,2}=\left[\frac{D}{Dz}\frac{2V^2z^{m+1}}{\omega^2(zp-1)^2}\right]_{z=p}=\frac{2V^2}{\omega^2}\left[\frac{(m+1)p^m}{(1-p^2)^2}+\frac{2p^{m+2}}{(1-p^2)^3}\right].$$

Substituting V from Eq. (16) in $B_{m,1}$ and V^2 in $B_{m,2}$ as given also by Eq. (16),

$$\frac{V^2}{(1-p^2)^2}=1-V_0=\frac{\omega^2}{2b^2}$$

we find,

$$B_m=B_{m,1}+B_{m,2}=\frac{1}{b^2}\left(m-\frac{k}{2-k}\cdot\frac{1+p^2}{1-p^2}\right)p^m. \quad (17)$$

But we have also:

$$\frac{V_0}{V_s}=1+\left(\frac{2p}{1+p^2}\right)^2\cdot\frac{1}{[1-(k/2)]^{-2}-1}. \quad (18)$$

The solution can be found from a first approximation of both η and p. This was done first for $k=0.06$, $b=tg\times(\pi/6)$ with the solution for $V_0=1.3750\ V_s$: $\eta=1+0.432\cos\omega t+0.042\cos2\omega t+0.004\cos3\omega t$. Later on, the results (Table III) have shown that it is possible to start from a solution corresponding to very small values of k.

Now, k and p^2 are of the same order when (V_0/V_s) varies little with k and the limit value is different from unity as $k\to0$. Then a first approximation is obtained by solving the Mathieu equation:

$$\frac{d\dot\eta}{dt}+\left(-\frac{k}{2b^2}+\frac{2p}{b^2}\cos\omega t\right)\eta=0.$$

We find

$$4\left(-\frac{k}{2b^2}\right)\cong-32\left(\frac{p}{2b^2}\right)^2.$$

Thus,

$$\frac{V_0}{V_s}\cong1+\frac{4p^2}{k}\cong1+b^2$$

and

$$\eta=1+\frac{2p}{b^2}\cos\omega t+\frac{p^2}{2b^4}\cos2\omega t.$$

It turns out that the approximation is quite good for V^*/V_s but less satisfactory for the other quantities. Indeed, the exact computation shows that with an error less than 4 percent:

$$V^*\simeq V_s\sec^2\alpha$$

when

$$\pi/6\leq\alpha\leq\pi/4$$

and

$$0<k\leq0.12.$$

Table III gives the results for two values of the angle as well as of V^* and shows the solutions representing the secondary periodic orbit for this value of V_0:

$$\eta=C_0+C_1\cos\omega t+C_2\cos2\omega t.$$

Appendix 5. Other Secondary Periodic Orbits

The existence of PO's for V close to V^* has been established: they oscillate in the valley in the immediate vicinity of the PO on the ridge. The investigation of the vicinity of the ridge by means of the variational

TABLE IV.

	$V_0=\frac{3}{2}V_s$	$V_0=2V_s$
x_0	0.31695	0.88414
x_1	−0.20889	−0.18747
x_2	−0.01310	−0.01571
x_3	−0.00127	−0.00190
x_4	−0.00016	−0.00026
x_5	−0.00002	−0.00004
y_0	0.50228	0.98077
y_1	0.16408	0.24313
y_2	0.01628	0.02476
y_3	0.00182	0.00313
y_4	0.00021	0.00044
y_5	0.00003	0.00007
ω	1.01369	1.26241
$\cosh\Omega T$	1.3263	1.1439

equations is not a powerful method if one wants to calculate other orbits for different values of V. This can be done by trial and error, the step by step integration being carried out following a method due to one of us. We have done it for $k=0.06$, $\alpha=30°$, for $V_0=(3/2)V_s$ and $V_0=2V_s$. Seven orbits were computed in each case before the PO was obtained. Final results are condensed in Table IV with the following notations:

$$x=x_0+x_1\cos\omega t+x_2\cos 2\omega t+\cdots,$$
$$y=y_0+y_1\cos\omega t+y_2\cos 2\omega+\cdots.$$

Finally, the first-order variational equations were solved. The values of $\cosh\Omega T$ indicate that the second-ary orbits are unstable of even order and the solutions show that $n=0$.

ACKNOWLEDGMENTS

One of us (R. de V.) wishes to thank the Department of Chemistry at Princeton University for a grant of research funds which made part of this work possible. Our thanks are also due Dean Hugh S. Taylor for encouragement and advice .

The present work was supported in part by the United States Air Force under Contract Bo. AF 33(038)-23976, monitored by the office of Scientific Research.

THE JOURNAL OF CHEMICAL PHYSICS VOLUME 23, NUMBER 7 JULY, 1955

Proton Magnetic Resonance Studies of Chloroform in Solution: Evidence for Hydrogen Bonding*

CHARLES M. HUGGINS AND GEORGE C. PIMENTEL, *Department of Chemistry and Chemical Engineering, University of California, Berkeley, California*

AND

JAMES N. SHOOLERY, *Varian Associates, Inc., Palo Alto, California*

(Received October 8, 1954)

The concentration and temperature dependences of proton magnetic resonance measurements on chloroform in acetone and triethylamine solutions are presented. The behavior is similar to hydrogen bonding systems and it is concluded that there is a specific interaction involving the chloroform proton and the solvent molecule. In each system the data are consistent with the assumption of a one-to-one complex. Equilibrium constants and heats of formation are calculated.

INTRODUCTION

THE nature of the interaction between chloroform and basic solvents has been discussed recently in connection with infrared studies of the C−D stretch of deuterochloroform.[1] The band corresponding to this motion does not show a frequency shift varying systematically with the solvent base strength, but the integrated band intensity is quite sensitive to this solvent property. The unexpected spectral behavior casts enough doubt on the nature of the chloroform-solvent interaction to make it desirable to obtain other clarifying data. In particular, it is interesting to attempt to corroborate the postulate that the interaction predominantly involves the chloroform hydrogen in a specific interaction which can be properly called a "hydrogen bond."

The usefulness of high-resolution nuclear magnetic resonance (hereafter called NMR) measurements in studies of hydrogen bonding systems has been recognized by a number of workers.[2,3] The usefulness is based upon the relatively large change in the diamagnetic shielding of the proton upon the formation of a hydrogen bond. This change has been interpreted to be associated with a significant decrease in the effective electron density near the proton.[4,5] The behavior of the proton resonance of the chloroform hydrogen is, then, a property which can be compared to the behavior of proton resonances in other well-recognized hydrogen bonding systems.

NMR measurements were carried out on two systems: chloroform-acetone and chloroform-triethylamine solutions. These two solvents permit an interesting contrast since infrared studies show that the C−D stretch of deuterochloroform behaves quite differently in these two solvents.[1]

EXPERIMENTAL

Materials

Acetone.—Commercial solvent-grade acetone was distilled twice from anhydrous $CaCl_2$ in a thirty-plate,

* The results of this work were presented at the Symposium on Spectroscopy and Molecular Structure, The Ohio State University, Columbus, Ohio, in June, 1954.

[1] C. M. Huggins and G. C. Pimentel, J. Chem. Phys. **23**, 896 (1955).

[2] U. Liddel and N. F. Ramsey, J. Chem. Phys. **19**, 1608 (1951).

[3] H. S. Gutowsky and A. Saika, J. Chem. Phys. **21**, 1688 (1953).

[4] R. A. Ogg, Jr., J. Chem. Phys. **22**, 560 (1954).

[5] J. N. Shoolery and B. J. Alder (to be published).

bubble-cap column and a center fraction boiling at 56.0±0.1°C was chosen.

Chloroform.—Merck reagent-grade chloroform was repurified by the technique of Fieser[6] and a center fraction boiling at 61.4±0.1°C was chosen from the same multi-plate column.

Triethylamine.—Eastman Kodak White Label triethylamine was refluxed and redistilled from KOH in the same multi-plate column, and a center fraction boiling at 89.5±0.5°C was chosen.

The infrared spectrum of each liquid was examined for evidence of impurities with particular attention to the spectral regions characteristic of O−H and C=O functional groups.

Apparatus

The apparatus used was a Varian Associates V-4300 High Resolution NMR spectrometer and associated 12-in. electromagnet system. The magnetic field employed was approximately 7050 gauss, corresponding to a precession frequency for the protons of 30 megacycles. Samples were examined in 5-mm o.d. Pryex tubes containing approximately 0.5 ml of solution.

Measuring Technique

The convenient side-band technique for measuring the frequency separation of NMR signals, described by Arnold and Packard,[7] was adopted, using for an internal reference the well-identified signal from the methyl groups of acetone or the methyl groups of triethylamine. An audio-frequency signal from a calibrated Hewlett Packard 200 C audio oscillator was used to modulate the magnetic field impressed upon the sample. The resultant side bands differ from the Larmor precessional frequency by multiples of the modulating frequency. This audio-frequency is adjusted until the first side band of the methyl proton resonance occurs at precisely the magnetic field at which the chloroform proton displays resonance absorption. In the concentrated chloroform solutions, the side band of the chloroform resonance was superimposed on the methyl peak. A sensitive criterion for superposition is the absence of a beat frequency in the transient decay following these very sharp resonances, which permits measurements to be reproduced to within a fraction of a cycle.

In this type of measurement, it is assumed that the effect of change of the solvent environment with concentration around the methyl group produces no NMR perturbation other than that which can be attributed to bulk diamagnetic shielding. Since it is expected that such a bulk diamagnetic shielding will alter the chloroform proton magnetic resonance by exactly the same amount, the side-band technique as used here automatically removes this bulk environmental effect.

[6] L. F. Fieser, *Experiments in Organic Chemistry* (D. C. Heath and Company, Boston, 1941), pp. 365–366.

[7] J. T. Arnold and M. E. Packard, J. Chem. Phys. **19**, 1608 (1951).

It might, however, be argued that forming a hydrogen bond to the carbonyl group in acetone would shift the resonance of the methyl peaks slightly. This would not affect the results in concentrated acetone solutions, but in the concentrated chloroform solutions a small shift might be expected. In order to determine the magnitude of this effect, a small amount of cyclohexane was added to the chloroform-acetone solutions described immediately above, and from relative measurements the methyl peak in the acetone was found to shift only about 3 cycles to lower magnetic fields. It is assumed that the cyclohexane NMR signals are not concentration dependent. Shifts of the chloroform resonance relative to the methyl peak of the acetone were then corrected for this effect. Solutions of triethylamine in chloroform were also examined over a range of concentrations to determine whether the shift varies between the CH_2 and CH_3 groups in the amine. A four-cycle variation was found. Since the CH_2 group is adjacent to the hydrogen bonding site in the triethylamine molecule, most of the shift should be associated with this resonance and the CH_3 resonance should be much less dependent on concentration. It was therefore not considered necessary to correct the chloroform shifts measured relative to this reference.

Low-temperature measurements were conducted by suspending the sample tube in a miniature Dewar filled with a carbon tetrachloride or perchloroethylene slush. The temperature was assumed to be the freezing point of the partially frozen bath liquid. When carbon tetrachloride was used (all measurements on chloroform-acetone) the temperature was measured with a copper-constantan thermocouple immediately after each measurement and in each case the temperature was found to be within one degree of the freezing point of carbon tetrachloride.

RESULTS

For each solution, only one absorption was observed which could be attributed to the chloroform proton.

TABLE I. NMR frequencies of chloroform solutions.

Chloroform-acetone (28°C)			Chloroform-triethylamine (28°C)	
$\frac{C}{C+B}$	ν' observed	Correction	$\frac{C}{C+B}$	ν' observed
0.037	176.9	+0.2	0.066	219.8
0.093	176.1	+0.4	0.149	218.0
0.187	175.6	+0.8	0.219	217.0
0.303	172.5	+1.4	0.260	216.0
0.381	171.2	+1.7	0.412	212.0
0.480	168.5	+2.1	0.551	206.8
0.580	165.7	+2.5	0.637	201.7
0.681	161.5	+3.0	0.715	197.2
0.788	159.1	+3.4	0.814	194.3
0.915	155.4	+3.9	0.875	191.3
0.980	153.3	+4.3	0.946	186.7
			0.978	186.0

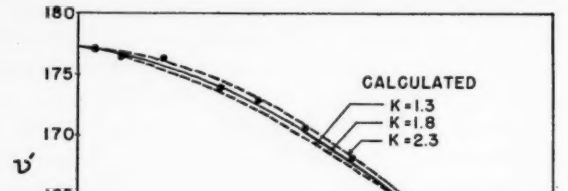

FIG. 1. Corrected proton magnetic resonance frequencies of chloroform *vs* apparent mole fraction in acetone solution.

For each solvent, this absorption was found at a lower magnetic field (measured in equivalent frequency units by the side-band audio generator) than the solvent methyl proton resonance, and this separation increased smoothly as the chloroform concentration was decreased. The measured frequencies and solution compositions are shown in Table I. Each frequency listed is the average of at least three measurements and the probable error is estimated at ± 0.5 cycle. At room temperature, the maximum change in the separation (obtained by extrapolation to zero concentration of chloroform) in chloroform-acetone solution is 20.4 cycles and in chloroform-triethylamine is 34.0 cycles. The presence of a single resonance peak and the concentration dependence are in accord with the behavior expected from a system in which protons are present in two molecular species in rapid equilibrium.[3] It is concluded that the qualitative behavior of the proton magnetic resonance of chloroform in either acetone or triethylamine supports the supposition that there is a strong interaction similar to a hydrogen bond involving the chloroform proton and a solvent molecule.

To investigate the quantitative significance of the concentration dependence, a simple one-to-one complex was assumed to exist between chloroform and the solvent base. For example,

$$CCl_3H+N(C_2H_5)_3=CCl_3H\cdot N(C_2H_5)_3.$$

The equilibrium constant is defined in mole fraction units:

$$K=\frac{(X)(C+B-X)}{(C-X)(B-X)}, \tag{1}$$

X = moles complex formed,

C = moles chloroform originally present,

B = moles base originally present.

To relate the NMR measurements to the equilibrium, it is assumed that the free and complexed chloroform each have characteristic precessional frequencies (respectively, ν_c and ν_x) and that the observed resonance frequency (ν') is the weighted arithmetic mean,

$$\nu'=\frac{X}{C}\nu_x+\frac{C-X}{C}\nu_c. \tag{2}$$

The weighting factors, X/C and $(C-X)/C$, give the fractions of the chloroform molecules in the complexed and free states, respectively. This type of expression has been discussed theoretically by Gutowsky[3] and has been utilized by others. It carries the inherent assumption that the lifetimes of each configuration exceed the time of one Larmor precession (about 3×10^{-8} second for the 7050 gauss field used here) but are short compared to the reciprocal of the frequency separation. There are four unknown quantities in (1) and (2): X, ν_x, ν_c, and K. The two equations can be used to eliminate one of the quantities, say X. Another of these, ν_c, can be obtained by extrapolation of the measured ν' to pure chloroform. In pure chloroform, $B\rightarrow 0$ and $X\rightarrow 0$, hence $(\nu')_{B=0}=\nu_c$. In the limit of infinite dilution, $C\rightarrow 0$ and $X\rightarrow 0$; however, from (1) the ratio of complexed to free chloroform approaches the equilibrium constant, $X/(C-X)\rightarrow K$. Substitution of this limiting condition into Eq. (2) indicates the limiting value of ν' in pure base:

$$(\nu')_{C=0}=\frac{1}{(1+K)}[K\nu_x+\nu_c].$$

It is convenient to solve this expression for ν_x, substituting $\nu_c=(\nu')_{B=0}$:

$$\nu_x=(\nu')_{C=0}+\frac{1}{K}[(\nu')_{C=0}-(\nu')_{B=0}]. \tag{3}$$

Thus the two experimental data $(\nu')_{C=0}$ and $(\nu')_{B=0}$, obtained by extrapolation, and an assumed value of the equilibrium constant, K, determine ν_x. With K and ν_x the remainder of the curve of ν' *vs* the apparent mole fraction of chloroform in the solution, $C/(C+B)$, can be calculated. Figure 1 shows the experimental points for the chloroform-acetone system together with the curves

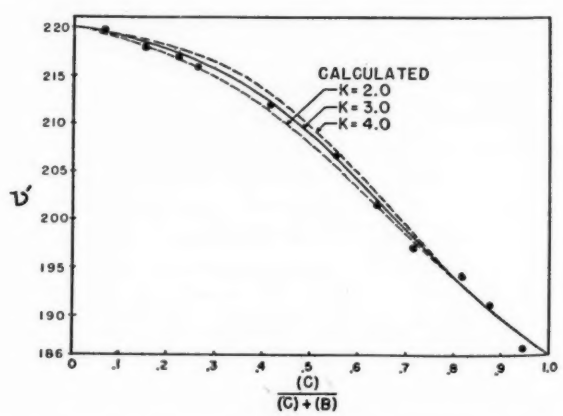

FIG. 2. Observed proton magnetic resonance frequencies of chloroform *vs* apparent mole fraction in triethylamine solution.

calculated with assumed values of $K=1.3$, 1.8, and 2.3; given the two data, $(\nu')_{B=0}=157.0$ and $(\nu')_{C=0}=177.4$. Figure 2 shows the same information for the chloroform-triethylamine system with assumed values of $K=2.0$, 3.0, and 4.0; given the two data, $(\nu')_{B=0}=186.0$ and $(\nu')_{C=0}=220.0$. It is clear that the parameter K can be selected to give a reasonable fit of the experimental data, but the data are not sufficient to determine K by closer than about 30 percent.

The smaller number of low-temperature measurements which could be obtained, due to more stringent experimental conditions, provide only an order of magnitude determination of the heat of formation of the bond in the assumed one-to-one complex. Since these data are not sufficiently numerous to determine the extreme values of ν', the optimum value of K was calculated by assuming ν_e and ν_x are temperature independent properties of chloroform and the complex, i.e., that the electronic distributions in these molecules are constant throughout this temperature range. Some justification of this assumption was provided by the apparent constancy of the measured frequency at even lower temperatures in the chloroform solutions containing over 0.9 mole fraction of chloroform. For chloroform-acetone solutions at -23°C, the data are best fitted with $K=4.0$. For chloroform-triethylamine solutions at -22.4°C, the data are best fitted with $K=12$. The values of the equilibrium constants and the heats of formation of the complexes are presented in Table II.

DISCUSSION

With the results presented in Table II, some comparisons with other data are possible. The heat of formation for the chloroform-acetone complex was calculated by Moelwyn-Hughes[8] to be -4.1 kcal. The heat of formation presented here, -2.5 kcal, must be assigned an uncertainty of at least a factor of two because of the uncertainty in determining the slope from data at only two temperatures. The values of K for the same system can be compared with those obtained by Schulze,[9] and Beckman and Faust.[10] Figure 3 presents the data of these authors together with an extrapolation based upon the linearity of the log K *vs* $1/T$ plot of their data. The equilibrium constants obtained in the present research are also included and the agreement is adequate.

TABLE II. Equilibrium constants and heats of formation of chloroform hydrogen bonds.

	Chloroform-acetone	Chloroform-triethylamine
K(28°C)	1.8±0.6	3.0±1.0
K(−23°C)	4.0±2.0	12.0±4.0
ΔH	−2500 cal	−4000 cal

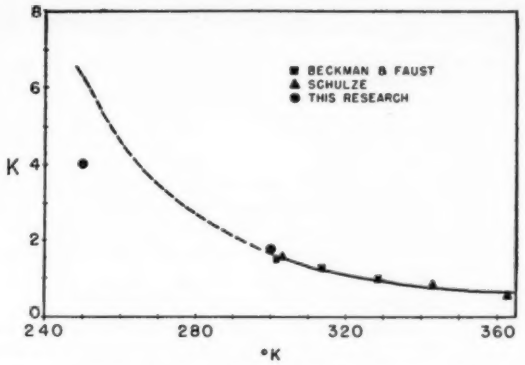

FIG. 3. Equilibrium constants for chloroform-acetone association *vs* temperature. [The data of Beckman and Faust (see reference 10) and Schulze (see reference 9) were extrapolated with a linear log K *vs* $1/T$ curve.]

It is concluded that the proton magnetic resonance measurements indicate a specific interaction involving the proton of chloroform. Furthermore, the direction of change of the diamagnetic shielding is consistent with the results of similar studies of other hydrogen bonding systems.[2] The assumption of one-to-one complexes leads to predictions of the proton magnetic resonance frequencies which can be brought into agreement with the data by the proper selection of the equilibrium constants. In the chloroform-acetone system, the equilibrium constant at room temperature is quite close to an experimental value based upon vapor pressure data. In deuterochloroform-triethylamine solutions,[1] the observations of two distinct infrared absorptions which can be ascribed to the C−D stretching vibrations of the hydrogen bonded and nonhydrogen bonded molecular species present entirely separate substantiation of the existence of two distinguishable species in these solutions. The additional evidence obtained in this research corroborates the existence of molecular interaction of the hydrogen bonding type.

[8] E. A. Moelwyn-Hughes and A. Sherman, J. Chem. Soc. **1936**, 101.

[9] A. Schulze, Z. physik. Chem. **93**, 370 (1919).

[10] E. Beckman and O. Faust, Z. physik. Chem. **89**, 247 (1914).

Infrared and Raman Spectra of Nitrogen Trifluoride*

E. L. PACE AND LOUIS PIERCE
Morely Chemical Laboratory, Western Reserve University, Cleveland, Ohio

(Received October 22, 1954)

The infrared spectrum of gaseous nitrogen trifluoride has been investigated with prism instruments in the range from 400 cm^{-1} to 3000 cm^{-1}. The Raman spectrum of liquid nitrogen trifluoride has been investigated in the range from 400 cm^{-1} to 2000 cm^{-1}. The fundamental frequency assignment made from the infrared data is $\nu_1(A_1)=1031$ cm^{-1}, $\nu_2(A_1)=642$ cm^{-1}, $\nu_3(E)=907$ cm^{-1}, and $\nu_4(E)=497$ cm^{-1}. The corresponding Raman shifts in the liquid are $\nu_1(A_1)=1050$ cm^{-1}, $\nu_2(A_1)=667$ cm^{-1}, $\nu_3(E)=905$ cm^{-1}, and $\nu_4(E)=515$ cm^{-1}.

Differences from the results of previous investigators appear either in the assignment of the fundamental frequencies or in the interpretation of the overtone and combination bands in the infrared spectrum. The present results are considered more reliable because of (1) the added weight of an investigation of the Raman spectrum and (2) the use of a sample of known high purity.

INTRODUCTION

THE present work is concerned with the infrared and Raman spectra of nitrogen trifluoride. Two previous investigations of the infrared spectrum have been reported, but these are in disagreement as to the assignment of the fundamental frequencies. Bailey, Hale, and Thompson[1] assigned three of the fundamental frequencies on the basis of their infrared measurements and estimated the value of the fourth. Wilson and Polo[2] were able to make the complete assignment of the fundamentals from a thorough investigation of the infrared spectrum. Because of the use of a carbon electrode in its preparation, the sample used by the latter investigators appeared to contain appreciable amounts of interfering impurities, particularly carbon tetrafluoride. No previous work on the Raman spectrum is reported in the literature. It was the purpose of this research to obtain a more certain assignment of the fundamental frequencies by reexamining the infrared spectrum using a highly purified sample of nitrogen trifluoride, and also by adding to the considerations, the results of the Raman spectrum carried out with a liquid sample.

EXPERIMENTAL

The method of preparation and purification of the gaseous nitrogen trifluoride has been described in a previous paper.[3] Measurements on the triple point temperature of the sample indicated that the amount of liquid soluble-solid insoluble impurity was of the order of 0.001 mole percent. The order of the impurity was confirmed by mass spectrometric analysis.[4] This spectrum pointed to the essentially complete absence of carbon tetrafluoride and to the presence of a small amount of an impurity which we have interpreted as being silicon tetrafluoride.

The infrared spectrum of nitrogen trifluoride in the range from 750 cm^{-1} to 3000 cm^{-1} was measured with a 10-cm gas cell and a Perkin-Elmer 12C spectrometer equipped with NaCl optics. The range from 400 cm^{-1} to 750 cm^{-1} was measured with an 85-cm gas cell in a prism spectrometer equipped with Perkin-Elmer KBr optics.

The Raman spectrum of liquid nitrogen trifluoride was taken with a photoelectric recording spectrometer of the grating type. We are indebted to the B. F. Goodrich Research Laboratory and particularly to Mr. J. Shipman for the help and cooperation we received in making the Raman measurements. The sample tube which contained the sample was fused to the bottom of the inner cylinder of a Dewar flask. By keeping the Dewar flask filled with liquid nitrogen, it was possible to condense the sample and maintain it as a liquid during the measurement.

Sodium nitrite solution was circulated in an outer jacket surrounding the Dewar cell. A 1300-watt helical mercury lamp was used as a source of radiation. With the preceding arrangement, it was possible to observe the Raman shifts even though the background was relatively high.

Table I lists the observed infrared and Raman frequencies together with the band assignments for this work. For the purpose of comparison, Table I also includes the observations and interpretations of the infrared spectrum by Wilson and Polo[2] and Bailey *et al.*[1] The observed infrared spectrum, plotted on a linear frequency scale, is shown in Fig. 1.

DISCUSSION

Electron diffraction[5] and microwave measurements[6] with nitrogen trifluoride have shown it to have C_{3v}

* This work has been supported by a research grant from the National Science Foundation (Grant G–585).

[1] Bailey, Hale, and Thompson, J. Chem. Phys. **5**, 274 (1937).
[2] M. Kent Wilson and S. R. Polo, J. Chem. Phys. **20**, 1716 (1952).
[3] Louis Pierce and E. L. Pace, J. Chem. Phys. **22**, 1271 (1954).
[4] Louis Pierce, Ph.D. thesis, Western Reserve University (1954).
[5] V. Schomaker and C. S. Lu, J. Am. Chem. Soc. **72**, 1182 (1950).
[6] J. Sheridan and W. Gordy, Phys. Rev. **79**, 513 (1950).

TABLE I. Observed frequencies and band assignments for nitrogen trifluoride.

Present Work (cm^{-1})			Wilson and Polo[a] (cm^{-1})		Bailey, Hale, and Thompson[b] (cm^{-1})	
Raman	Infrared	Assignment	Infrared	Assignment	Infrared	Assignment
515	497	$\nu_4(E)$	493	$\nu_4(E)$	(420)[c]	ν_4
667	642	$\nu_2(A_1)$	647	$\nu_2(A_1)$	505	ν_2
905	907	$\nu_3(E)$	905	$\nu_3(E)$	908	ν_1
	985	$2\nu_4(A_1+E)$	985	$2\nu_4(A_1+E)$	1004	ν_3
1050	1031	$\nu_1(A_1)$	1032	$\nu_1(A_1)$		
	1135	$\nu_4+\nu_2(E)$	1136	$\nu_4+\nu_2(E)$		
	1283	$2\nu_2(A_1)$	...	...		
	1525	$\nu_4+\nu_1(E)$	1523	$\nu_4+\nu_1(E)$		
	1545	$\nu_2+\nu_3(E)$	...	...		
	1809	$2\nu_3(A_1+E)$	1809	$2\nu_3(A_1+E)$		
	1929	$\nu_3+\nu_1(E)$	1929	$\nu_3+\nu_1(E)$		
		...	2180	$2\nu_2+\nu_3(E)$		
	2681	$3\nu_3(A_1+A_2+E)$	2680	$3\nu_3(A_1+A_2+E)$		

[a] See reference 2.
[b] See reference 1.
[c] Estimated.

symmetry. For a molecule with this symmetry, all four fundamentals are allowed both in the infrared and in the Raman spectrum. Only four Raman bands were observed. Their frequency values were 515, 667, 905 and 1050 cm^{-1}. Since combination and overtone bands are generally very weak in Raman spectra, the four frequencies were assigned to fundamental vibrations of the molecule. Corresponding bands appeared in the infrared spectrum at the slightly different values of 497, 642, 907, and 1031 cm^{-1}. Except for small differences in the frequency values, the assignments are in agreement with those of Wilson and Polo.[2] Since no polarization data were obtained on the Raman lines, no information is provided concerning the assignment of symmetric and degenerate modes beyond that already presented by the preceding investigators.

The overtone and combination bands observed in this work agree with those of Wilson and Polo[2] except

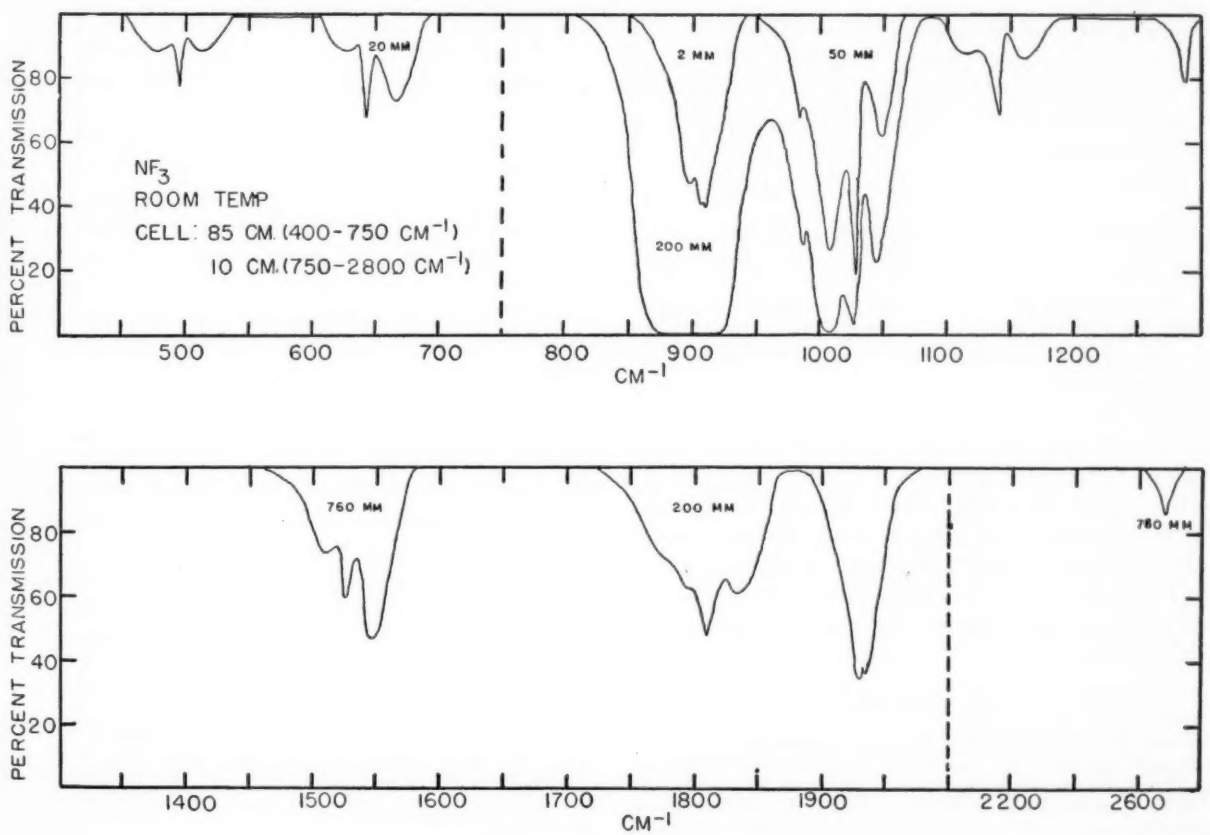

FIG. 1. Infrared spectrum for nitrogen trifluoride.

for three bands at 1283, 1545, and 2180 cm^{-1}. In their work, the nature of the band at 1283 cm^{-1} appears to have been obscured by the strong absorption of carbon tetrafluoride which was present in appreciable quantities in their sample. Also, the band at about 1545 cm^{-1} was observed but it was not associated with nitrogen trifluoride. On the basis of having used a sample in our work which did not contain carbon tetrafluoride or any appreciable quantity of other impurities, we believe the bands at 1283 cm^{-1} and 1545 cm^{-1} to be due to nitrogen trifluoride, and that at 2180 cm^{-1} to an impurity. The band at 1283 cm^{-1} can be reasonably interpreted as $2\nu_2(A_1)$ and that at 1545 cm^{-1} as $\nu_2+\nu_3(E)$.

THE JOURNAL OF CHEMICAL PHYSICS VOLUME 23, NUMBER 7 JULY, 1955

Critical Isotherm and the Equation of State of Liquid-Vapor Systems*

B. WIDOM† AND O. K. RICE
Department of Chemistry, University of North Carolina, Chapel Hill, North Carolina
(Received September 30, 1954)

Pressure-volume-temperature data on xenon, carbon dioxide, and hydrogen are analyzed. Special attention is paid to the regions fairly close to, but not in the immediate neighborhood of, the critical point. It is shown that in each case the critical isotherm is of the fourth degree, one degree higher than that of the coexistence curve, as is required by the theorem of Rice. However, the relation between the critical isotherm and the coexistence curve is determined by the almost constant value of $\partial^2P/\partial T\partial\rho$ in the PVT region considered, and this is different from its value at the critical point. The critical isobar is also considered and it is shown that it is of the fourth degree near the critical point, but of lower degree further away. A general equation of state is deduced for the PVT region under discussion, and the implications of this equation of state with respect to the coexistence curve and the critical isotherm are considered.

I. INTRODUCTION

IT is generally recognized that the coexistence curve for liquid-vapor equilibrium is of the third degree,[1] that is, that the equation of the coexistence curve in the temperature-density plane, in the neighborhood of the critical point, is

$$|\rho-\rho_c|=a^{-\frac{1}{3}}|T-T_c|^{\frac{1}{3}}. \tag{1}$$

A term in $T-T_c$ has been omitted from the right-hand side of Eq. (1), this term being negligible compared to the one retained, in the temperature region in which we are interested. It is the term in $T-T_c$ which gives an inclination to the rectilinear diameter, and thus a slight asymmetry to the coexistence curve. Also being ignored in Eq. (1) is the possibility that the coexistence curve has a short flat section in the immediate neighborhood of the critical point.

Rice[2] has recently shown that the critical isotherm must be of degree one greater in $\rho-\rho_c$, than the degree of the coexistence curve. More specifically, accepting Eq. (1), it follows from Rice's theorem that the equation of the critical isotherm, in the neighborhood of the critical point, is

$$|P-P_c|=a(\partial^2P/\partial T\partial\rho)_c|\rho-\rho_c|^4, \tag{2}$$

the subscript c implying evaluation at the critical point.

It is only very close to the critical point that Rice was able to approximate the experimentally determined critical isotherms of xenon and carbon dioxide, with Eq. (2). At a short distance from the critical point, the experimental isotherms rose, on the liquid side, and fell, on the vapor side, more steeply than could be accounted for by the coefficient $a(\partial^2P/\partial T\partial\rho)_c$. This was associated with a lack of constancy of the derivative $\partial^2P/\partial T\partial\rho$.

We shall show in this paper that another region exists, where $|\rho-\rho_c|$ is somewhat greater, in which the experimental data follow another equation of the same form as Eq. (2). In this region the coefficient exceeds the quantity $a(\partial^2P/\partial T\partial\rho)_c$, previously estimated by Rice,[2] by a factor of 2.5 in the case of xenon and 6 in the case of carbon dioxide. The correct value of the coefficient is more nearly equal to a multiplied by the approximately constant value of $\partial^2P/\partial T\partial\rho$ which is characteristic of the region slightly removed from the critical point, and the principal aim of this paper is to analyze the situation existing in this somewhat more distant region of the critical isotherm.

II. THE CRITICAL ISOTHERM OF XENON

Habgood and Schneider[3] have determined the critical isotherm of xenon, and tabulated P as a function of ρ.

* Work supported by the Office of Naval Research.
† Present address: Department of Chemistry, Cornell University, Ithaca, New York.
[1] E. A. Guggenheim, *Thermodynamics, An Advanced Treatment for Chemists and Physicists* (North-Holland Publishing Company, Amsterdam, 1950), second edition, p. 141.
[2] O. K. Rice, J. Chem. Phys. **23**, 164 (1955).
[3] H. W. Habgood and W. G. Schneider, Can. J. Chem. **32**, 98 (1954).

Accepting the value $P_c=57.636$ atmos as reported by these authors, and the value $\rho_c=1.105$ g/cm³, as found by Weinberger and Schneider,[4] one can use Habgood and Schneider's tabulated data to find $|P-P_c|$ as a function of $|\rho-\rho_c|$ along the critical isotherm. This function is plotted logarithmically in Fig. 1.

As the critical point is approached, $|P-P_c|$ and $|\rho-\rho_c|$ eventually become of the same order of magnitude as the uncertainties in P_c and ρ_c, respectively. Such points would have scattered meaninglessly to the lower left of the logarithmic figure, and are therefore not included. The point (P_m,ρ_m) which comes closest to the critical point among those points which are included in Fig. 1, is such that

$$|P_m-P_c|=0.00014P_c \quad \text{and} \quad |\rho_m-\rho_c|=0.11\rho_c.$$

Figure 1 is a reasonably good straight line of slope 4.2. If the degree of the critical isotherm is integral, this is strong evidence for the integer in question being 4. On the assumption that it is exactly 4, a recalculation of the points of Fig. 1 leads to

$$|1-P/P_c|=1.18|1-\rho/\rho_c|^4$$

as the equation of the critical isotherm in the region covered by the figure. The uncertainty in the coefficient 1.18 is 8 percent (mean deviation).

There is only the slightest suggestion that the liquid and vapor points do not lie on the same line. It is probably not significant.

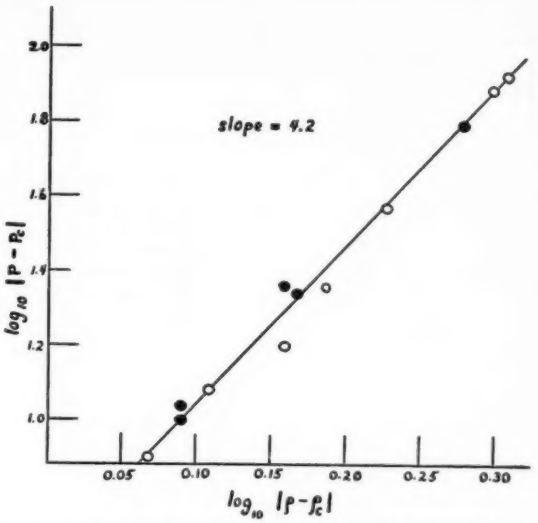

FIG. 1. Critical isotherm of xenon. P in units of 10^{-3} atmos, ρ in units of 10^{-1} g/cm³. Filled circles are vapor side, open circles are liquid side.

III. THE CRITICAL ISOTHERM OF CARBON DIOXIDE

Michels, Blaisse, and Michels[5] reported measurements of several isotherms above and below the critical isotherm of carbon dioxide. From their data, we constructed isochores in the P, T plane and observed them to be linear for densities between 169.5 and 285.7 Amagat units. Two points on each linear isochore fixed its equation, and its intersection with the line $T=T_c$ was then readily calculated. This intersection gave directly a point (P,ρ) on the critical isotherm, and one such point was obtained for each of eight isochores, two on the liquid side and six on the vapor side.

With the values[5] $P_c=72.85$ atmos and $\rho_c=236.7$ Amagat units, it was then possible to plot $|P-P_c|$ as a function of $|\rho-\rho_c|$. The logarithmic plot is shown in Fig. 2.

As with xenon, one cannot in this manner obtain significant points very close to the critical point. The closest point, (P_m,ρ_m), is such that

$$|P_m-P_c|=0.00041P_c \quad \text{and} \quad |\rho_m-\rho_c|=0.14\rho_c.$$

Figure 2 is seen to be a fairly good straight line of slope 4.0, again verifying that the critical isotherm is of the fourth degree. Its equation in this case is

$$|1-P/P_c|=1.16|1-\rho/\rho_c|^4,$$

the uncertainty in the coefficient 1.16 being 10 percent.

The suggestion that the liquid and vapor points do not lie on the same line is slightly more marked than in the case of xenon, but no attempt was made to draw separate lines for them. In Sec. VI where the quantity $\partial^2P/\partial T\partial\rho$ is discussed, it will again appear that the liquid and vapor sides might differ in the case of carbon dioxide, though they do not appear to do so in the case of xenon.

IV. THE CRITICAL ISOBAR OF CARBON DIOXIDE

If, in the P, T plane, one finds the intersections of the isochores with the line $P=P_c$ instead of with the

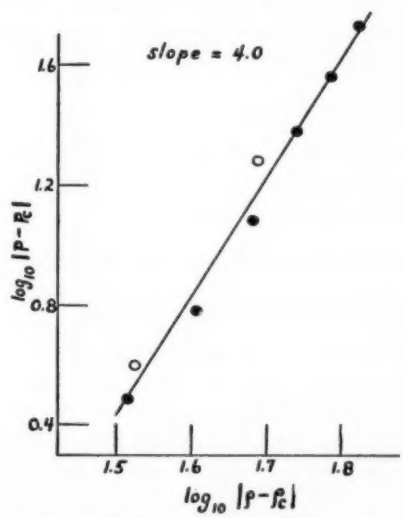

FIG. 2. Critical isotherm of carbon dioxide. P in units of 10^{-2} atmos, ρ in Amagat density units. Filled circles are vapor side, open circles liquid side.

[4] M. A. Weinberger and W. G. Schneider, Can. J. Chem. **30**, 422 (1952).

[5] Michels, Blaisse, and Michels, Proc. Roy. Soc. (London) **A160**, 358 (1937).

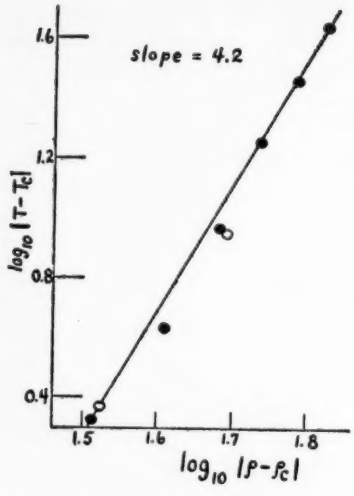

FIG. 3. Critical isobar of carbon dioxide. T in units of 10^{-2} °K, ρ in Amagat density units. Filled circles are vapor side, open circles liquid side.

line $T=T_c$, one obtains points on the critical isobar instead of the critical isotherm. With the value[5] $T_c=304.20$°K, a logarithmic plot was made of $|T-T_c|$ as a function of $|\rho-\rho_c|$ for this isobar. The result is shown in Fig. 3.

The temperature closest to the critical, T_m, is such that

$$|T_m-T_c|=0.000069T_c$$

and ρ_m is the same as in Fig. 2.

Figure 3 is a straight line of slope 4.2. Assuming an exponent of exactly 4, the equation of the critical isobar in this region is

$$|1-T/T_c|=0.191|1-\rho/\rho_c|^4$$

with an uncertainty of 9 percent in the coefficient.

V. THE CRITICAL ISOTHERM AND CRITICAL ISOBAR OF HYDROGEN

Johnston, Keller, and Friedman[6] made compressibility measurements on liquid hydrogen. From their data they derived isochores which were linear, and which they represented by

$$P=A(\rho)+B(\rho)T. \tag{3}$$

They tabulated $A(\rho)$ and $B(\rho)$, and pointed out that $B(\rho)$ was itself linear in ρ.

Equation (3) can be rewritten

$$P-P_c=A(\rho)+T_cB(\rho)-P_c+B(\rho)(T-T_c). \tag{4}$$

Thus, the critical isotherm is given by

$$|P-P_c|=|A(\rho)+T_cB(\rho)-P_c| \tag{5}$$

and the critical isobar by

$$|T-T_c|=|B(\rho)^{-1}[A(\rho)+T_cB(\rho)-P_c]| \tag{6}$$

and $|P-P_c|$ and $|T-T_c|$, as given by Eqs. (5) and (6), are plotted logarithmically as functions of $|\rho-\rho_c|$ in Figs. 4 and 5. In making these plots, Johnston, Keller, and Friedman's tables of $A(\rho)$ and $B(\rho)$ were used, as were the Ohio State values $P_c=12.797$ atmos and $T_c=33.24$°K, quoted by Kobe and Lynn.[7] Also used was the Leiden value $\rho_c=0.01539$ mole/cm^3, quoted by Kobe and Lynn.[7]

On the critical isotherm, the point (P_m,ρ_m) of Fig. 4 which comes closest to the critical point, is such that

$$|P_m-P_c|=0.41P_c \quad \text{and} \quad |\rho_m-\rho_c|=0.67\rho_c.$$

On the critical isobar, Fig. 5, T_m is such that

$$|T_m-T_c|=0.039T_c.$$

Thus, these data do not extend nearly so close to the critical point as do the xenon and carbon dioxide data. Also, as distinguished from the latter two cases, these data provide points only on the liquid side of the critical isotherm and isobar, and none on the vapor side.

Figure 4 is a straight line of slope 4.2. Assuming an exponent of exactly 4, the equation of the critical isotherm in this region is

$$|1-P/P_c|=2.55|1-\rho/\rho_c|^4$$

with an uncertainty of 5 percent in the coefficient.

Figure 5 is a straight line of slope 3.1, so that in this region the critical isobar is cubic, not quartic. The reason for this is that $B(\rho)$ is a linear function[6] of $\rho-\rho_c$, and in the region covered by Figs. 4 and 5 the term in $\rho-\rho_c$ is by far the larger part of $B(\rho)$. Thus, the degree of (6) is one less than that of (5). In the case of carbon dioxide, the region covered was so close to the critical point, that the analog of $B(\rho)$ was dominated by its constant term, which was never less than about four times as large as the term in $\rho-\rho_c$; so that the critical isobar was of the same degree as the critical isotherm.

VI. DISCUSSION

The pressure can be expanded about the critical point in a Taylor series in $\rho-\rho_c$ and $T-T_c$. Since the critical isotherm is of the fourth degree in $\rho-\rho_c$, this

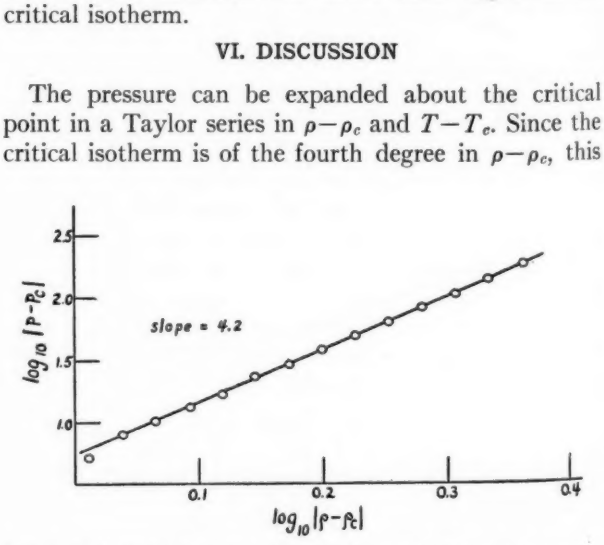

FIG. 4. Critical isotherm of hydrogen, liquid side. P in atmos, ρ in units of 10^{-2} mole/cm^3.

[6] Johnston, Keller, and Friedman, J. Am. Chem. Soc. **76**, 1482 (1954).

[7] K. A. Kobe and R. E. Lynn, Jr., Chem. Revs. **52**, 117 (1953).

expansion takes the form

$$P-P_c=\alpha(T-T_c)+\beta(\rho-\rho_c)(T-T_c)\pm\gamma(\rho-\rho_c)^4, \quad (7)$$

neglecting terms of higher order. α, β, γ are positive constants. The $\pm$ signs must be included, the top sign to be used when $\rho>\rho_c$ and the bottom sign when $\rho<\rho_c$. The change from one sign to the other is necessary in order that $P-P_c$ be a monotonically increasing function of $\rho-\rho_c$ along the critical isotherm, and it implies a discontinuity[2] in $\partial^4P/\partial\rho^4$ at $\rho=\rho_c$. Such a discontinuity can be avoided only with a critical isotherm of odd degree, as in van der Waals' classical theory.

From Eq. (7), the equation of the critical isochore is

$$P-P_c=\alpha(T-T_c). \quad (8)$$

Now, in the neighborhood of the critical point the vapor pressure is a linear function of the temperature, as can be seen, for example, by plotting the vapor-pressure data for xenon[3] or carbon dioxide,[5] or by glancing at the vapor pressure curves of hydrogen,[8] deuterium,[9] or nitrogen.[10]

It is also known that the vapor pressure curve extends itself into the critical isochore without a change of slope.[11] Thus Eq. (8) is not only the equation of the critical isochore, but it is also the equation of the vapor pressure line in the neighborhood of the critical point.

The coexistence curve is obtained by finding the intersections of the isochores, as given by the equation of state (7), with the vapor pressure line, as given by Eq. (8). The equation determining the coexistence curve is then

$$0=\beta(\rho-\rho_c)(T-T_c)\pm\gamma(\rho-\rho_c)^4,$$

or, discarding the irrelevant root $\rho=\rho_c$, which just says that the critical isochore is collinear with the vapor pressure line, one obtains for the coexistence curve

$$|T-T_c|=\gamma\beta^{-1}|\rho-\rho_c|^3 \quad (9)$$

which has the form of Eq. (1).

The critical isotherm, obtained from Eq. (7), is

$$|P-P_c|=\gamma|\rho-\rho_c|^4 \quad (10)$$

and the critical isobar is

$$|T-T_c|=\gamma|\rho-\rho_c|^4|\alpha+\beta(\rho-\rho_c)|^{-1}. \quad (11)$$

The quantity $\gamma\beta^{-1}$ in Eq. (9) was called a in Eq. (1). From Eq. (7),

$$\partial^2P/\partial T\partial\rho=\beta. \quad (12)$$

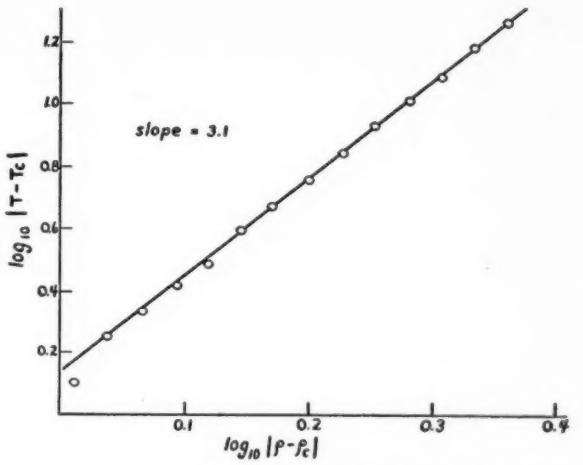

FIG. 5. Critical isobar of hydrogen, liquid side. T in °K, ρ in units of 10^{-2} mole/cm^3.

Thus

$$\gamma=a\partial^2P/\partial T\partial\rho. \quad (13)$$

Since Eq. (7) represents the first few terms of a Taylor expansion about the critical point, the constant β in Eq. (12) might be expected to be equal to $(\partial^2P/\partial T\partial\rho)_c$, and the constant γ to $a(\partial^2P/\partial T\partial\rho)_c$, as in Eq. (2). With these constants inserted, Eq. (7) could be expected to apply in the immediate neighborhood of the critical point, provided a Taylor expansion is, indeed, possible. However, it holds only over a narrow range of the variables; higher terms would be necessary to make it valid in a larger region.

Nevertheless, as noted in the Introduction, the relations which are derived from Eq. (7) also appear to hold true as far as their form is concerned, over a range of variables in another region not quite so close to the critical point. It is only necessary, in this region, to insert a different value of β or $\partial^2P/\partial T\partial\rho$; the constant a appears to have the same value as in the immediate neighborhood of the critical point, that is, the ratio of $|T_c-T|$ to $|\rho-\rho_c|^3$ appears to be virtually unchanged in passing from the immediate neighborhood of the critical point (neglecting any small flat portion) into the more distant region that interests us in this paper. The constant α is also practically unchanged from the critical point through the region we are interested in.

These results suggest that we should treat Eq. (7) as a sort of pseudo-Taylor series expansion about the critical point, when the value of $\partial^2P/\partial T\partial\rho$ which is characteristic of the region slightly removed from the critical point, is inserted. This value is almost constant, and the deviations from constancy occur in a region so close to the critical point that one can overlook them when considering the critical region "in the large." Thus the derivation of Eq. (9) from Eq. (7) must be considered to be an approximate derivation, but the result agrees with the experimental data. It must be stated that even the critical region "in the large" is a

[8] White, Friedman, and Johnston, J. Am. Chem. Soc. **72**, 3927 (1950).

[9] Friedman, White, and Johnston, J. Am. Chem. Soc. **73**, 1310 (1951).

[10] A. S. Friedman and D. White, J. Am. Chem. Soc. **72**, 3931 (1950).

[11] Professor W. H. Keesom of Leiden has kindly communicated to us a simple thermodynamic proof of this fact.

FIG. 6. $(\partial P/\partial T)_\rho$ for carbon dioxide.

rather limited region. Actually the data which we have examined in the cases of carbon dioxide and xenon do not extend much beyond a region in which $|T-T_c|<1°$, that is, a region which is close to the top of the coexistence curve. In the case of hydrogen the data extend much farther, and, as we shall see, there are certain characteristic differences in the parameters.

We shall now consider the actual numerical value of γ. Rewriting Eq. (10) the critical isotherm is given by

$$|1-P/P_c|=\gamma\rho_c^4P_c^{-1}|1-\rho/\rho_c|^4. \tag{14}$$

The value of $\gamma\rho_c^4P_c^{-1}$ in this equation was found to be 1.18 for xenon (Sec. II) and 1.16 for carbon dioxide (Sec. III). It will be interesting to see how much these results differ from what would be obtained if $(\partial^2P/\partial T\partial\rho)_c$ were inserted in Eq. (13), as would be justified if $\partial^2P/\partial T\partial\rho$ were constant throughout. Using the experimentally determined values of a and $(\partial^2P/\partial T\partial\rho)_c$ (see reference 2) we find

$$a(\partial^2P/\partial T\partial\rho)_c\rho_c^4P_c^{-1}=\begin{cases}0.46 & \text{Xe}\\ 0.21 & \text{CO}_2\end{cases}. \tag{15}$$

It is seen that a considerable discrepancy in γ would result from using the value of $\partial^2P/\partial T\partial\rho$ at the critical point.

It is desirable to trace the variation in $\partial^2P/\partial T\partial\rho$ as one leaves the critical point. To this end we plotted the tabulated isochores of xenon[3] in addition to the isochores of carbon dioxide, and measured their slopes. It is well known that the isochores are nearly straight lines; however, they have a slight curvature just in the neighborhood of T_c, which is related, through the equation

$$T(\partial^2P/\partial T^2)_V=(\partial C_v/\partial V)_T$$

to the specific heat anomaly in the critical region. In the case of carbon dioxide this curvature was not even visible in our plot, in the density range of Fig. 2 and the temperature range of $|T-T_c|\leq 1°$. In the case of xenon the curvature was evident, and the slopes were measured at $T-T_c\sim 1°$. We have plotted $(\partial P/\partial T)_\rho$ as a function of ρ in Figs. 6 and 7; we call this derivative $B(\rho)$, as in Eq. (4). It will be observed that $\partial^2P/\partial T\partial\rho$ approaches constancy, at least on the vapor side and probably on the liquid side also. There is a region near $\rho=\rho_c$ in which $\partial^2P/\partial T\partial\rho$ has a smaller value.

This means that Eq. (7) must actually be used in two separate regions, one on the liquid side and one on the vapor side, but that it cannot be used in the same way near the critical density, even 1° above the critical temperature. It would be possible to have different constants on the liquid and vapor sides, and in fact Fig. 6 suggests that this may be the case for carbon dioxide. Using the limiting slopes on the vapor side and the experimental values of a, we now obtain from Eq. (13)

$$\gamma\rho_c^4P_c^{-1}=\begin{cases}1.60, & \text{Xe}\\ 1.25, & \text{CO}_2\end{cases}. \tag{16}$$

These numbers are again to be compared with 1.18 and 1.16, respectively.

It is seen that the numbers in Eq. (16) are somewhat large, and this is probably due to the fact that the isochores do have a curvature in the region of T_c, and this must be important in determining the coexistence curve by Eq. (9), and thus in fixing the relation between γ, β, and a. The reasons for the differences between carbon dioxide and xenon are not, however, entirely clear.

Rice[2] has already made an analysis of the behavior of $\partial^2P/\partial T\partial\rho$ at the critical temperature, and by implication along the coexistence curve, as long as T_c-T is sufficiently small. On the supposition that, at a temperature, say T', somewhat above the critical temperature, $\partial^2P/\partial T\partial\rho$ was independent of ρ, and considering the behavior[3] of $\partial^3P/\partial T^2\partial\rho$ (see Sec. 3 and Fig. 2 of reference 2) he concluded that $\partial^2P/\partial T\partial\rho$ at T_c would increase as $|\rho-\rho_c|$ increased and would eventually become greater than $\partial^2P/\partial T\partial\rho$ at T'. This conclusion is undoubtedly correct, and the increase at T_c with $|\rho-\rho_c|$ would be made more marked by the fact, now noted, that even at T' an increase occurs. However, we now observe, from Eq. (16), that the effective value of $\partial^2P/\partial T\partial\rho$ for use in Eq. (9) is less than $\partial^2P/\partial T\partial\rho$ at T' (if T' may be taken as $T_c+1°$). This presumably occurs because, as soon as $|\rho-\rho_c|$ becomes great enough so that along the coexistence curve T_c-T has a value noticeably different from zero, most of the curvature in the isochores occurs at a temperature *below* T_c, and the relation is such that $d(\partial P/\partial T)_\rho/d\rho$ (where the total derivative indicates differentiation along the coexistence curve) is less than $\partial^2P/\partial T\partial\rho$ at T_c. We are actually interested in neither $\partial^2P/\partial T\partial\rho$ at T_c nor in $d(\partial P/\partial T)_\rho/d\rho$, but in something in between, and the relations involved are sufficiently complicated so that it is not easy to see beforehand just what should be expected.

Equation (15) shows that the dimensionless quantity $\gamma\rho_c^4P_c^{-1}$ is different for carbon dioxide and for xenon, at the critical point. As pointed out previously,[2] this indicates a failure of these substances to obey, between themselves, a law of corresponding states at the critical point. However, the numbers 1.18 and 1.16, found for this coefficient in roughly comparable regions further from the critical point, seem to indicate that in these regions a law of corresponding states begins to hold. It is reasonable to suppose that this is true despite Eq. (16).

In the case of hydrogen the value of $\gamma\rho_c^4P_c^{-1}$ found in Sec. V was 2.55, much larger than was found for carbon dixoide and for xenon. It is to be noted that the hydrogen data were taken farther from the critical point than those for xenon and for carbon dioxide, and this may have something to do with the larger value.

Equations (7), (10), and (11) are correct in form for hydrogen also, if one inserts the appropriate parameters. Equation (7) has the same form as Eq. (4), since $A(\rho)+T_cB(\rho)-P_c$ was found to be proportional to $(\rho-\rho_c)^4$, and $B(\rho)$ is linear[6] in $\rho-\rho_c$. In the region studied by Johnston, Keller, and Friedman, $B(\rho)$ is represented by[6]

$$B(\rho)=-7.11+437\rho \quad (B \text{ in atm/deg}, \quad \rho \text{ in mol/cm}^3)$$

or

$$B(\rho)=-0.55+437(\rho-\rho_c).$$

But the constant term in $B(\rho)$ should be equal to α, the slope of the vapor pressure line at the critical point, which is positive. Thus, in form, but not numerically, Eq. (7) is consistent with the hydrogen data, though these were taken quite far from the critical point.

From Eq. (11), the critical isobar, sufficiently close to the critical point, should be given by

$$|1-T/T_c|=(\gamma\rho_c^4/\alpha T_c)\,|1-\rho/\rho_c|^4. \qquad (17)$$

The coefficients in Eqs. (14) and (17) were found, for carbon dioxide, in Secs. III and IV, and are 1.16 and 0.191, respectively. Thus

$$\alpha=1.16P_c/0.191T_c$$
$$=1.45 \text{ atmos/deg.}$$

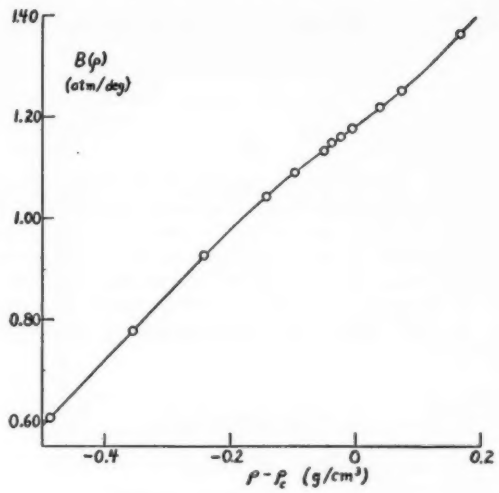

FIG. 7. $(\partial P/\partial T)_\rho$ for xenon.

But from the slope of the vapor pressure line[5] near the critical point,

$$\alpha=1.67 \text{ atmos/deg.}$$

The discrepancy is within the limits of uncertainty in the ratio 1.16/0.191. Thus the ratio itself is approximately correct, though neither the numerator nor the denominator in the ratio is correct at the critical point, and, indeed, as we have seen, our application of Eq. (7), upon which Eqs. (14) and (17) are based, breaks down near the critical isochore. The correctness of the ratio is possible, because in forming the ratio, the quantity γ, which is related to $\partial^2P/\partial T\partial\rho$ by Eq. (13), cancels from numerator and denominator. The significance of this result is not too clear, but it presumably means, (as would be supposed already from the constancy of α, previously noted) that the responsibility for the fact that Eq. (7) cannot be used near the critical point with the same constants which make it applicable in the more distant region lies with the last two terms on the right-hand side of Eq. (7) rather than with the first one.

We are indebted to Professor Joseph E. Mayer for reading the manuscript and making a number of helpful suggestions.

Molecular Orbitals for the Hydrogen Molecule Ground State*

RICHARD F. WALLIS
Applied Physics Laboratory, The Johns Hopkins University, Silver Spring, Maryland
(Received October 20, 1954)

The ground-state energy of the hydrogen molecule has been calculated using a wave function constructed from LCAO molecular orbitals. The effective nuclear charge in the MO for one electron is taken to be different from that for the MO for the second electron. The best value of the dissociation energy is found to be 3.565 ev for values of the effective nuclear charge equal to 1.5 and 0.9. A physical interpretation of these values of the effective nuclear charge is given. Calculations have also been made using a wave function having a variable ratio of homopolar terms to ionic terms and having two effective nuclear charges. The best value of the dissociation energy for this case is found to be 4.08 ev.

I. INTRODUCTION

IN a previous paper[1] the energy of the ground electronic state of the hydrogen molecule was investigated using one-electron two-center wave functions (diatomic orbitals, DO's) as molecular orbitals (MO's). It was found that if the DO of each electron is assigned the same effective nuclear charge Z, the best value of the dissociation energy is 3.485 ev for $Z=0.7825$. Furthermore, it was found that the dissociation energy is improved if the effective nuclear charge for the DO of one electron is taken to be different from that for the DO of the second electron. This point has recently been emphasized by Mulliken.[2] If the values of Z for the two orbitals are taken to be 1.0 and 0.5 as suggested by Hylleraas,[3] the dissociation energy is found to be 3.68 ev. Physically, these values of Z correspond to one electron moving in the field of the bare protons and to the other electron moving in the field of two protons each shielded by one-half unit of electronic charge.

Coulson[4] and Weinbaum[5] have studied the ground state of H_2 using molecular orbitals taken as linear combinations of atomic orbitals (LCAO). Aside from a normalization factor their molecular orbital ψ is the sum of two $1s$ hydrogenic atomic orbitals of effective nuclear charge Z; namely,

$$\psi=e^{-Zr_a}+e^{-Zr_b}. \tag{1}$$

In Eq. (1), r_a and r_b are the distances of the electron from nuclei a and b, respectively, measured in units of the Bohr radius, $a_0=0.5292$ A. Coulson and Weinbaum assigned both electrons to MO's having the same value of Z. The best value of the dissociation energy was found to be 3.47 ev at $Z=1.193$.

It is the purpose of the present paper to extend the results of Coulson and of Weinbaum for the ground state of H_2 by assigning one electron to an MO of the form given by Eq. (1) with effective nuclear charge Z_A and assigning the second electron to a similar MO with a different nuclear charge Z_B.

II. ENERGY CALCULATIONS

The Hamiltonian for the hydrogen molecule was taken to have the form

$$\mathbf{H}=-\tfrac{1}{2}\nabla_1^2-\tfrac{1}{2}\nabla_2^2+\frac{1}{r_{12}}+\frac{1}{r_{ab}}-\frac{1}{r_{a1}}-\frac{1}{r_{b1}}-\frac{1}{r_{a2}}-\frac{1}{r_{b2}}, \tag{2}$$

where the subscripts 1 and 2 designate the two electrons and the subscripts a and b designate the two nuclei. Energy is measured in units of $e^2/a_0=27.20$ ev and length in units of $a_0=0.5292$ A. The approximation considered in this paper to the orbital part of the electronic wave function Ψ for the ground state of H_2 may be written as

$$\Psi=\psi_A(1)\psi_B(2)+\psi_A(2)\psi_B(1) \tag{3}$$

where

$$\psi_A=e^{-Z_Ar_a}+e^{-Z_Ar_b}, \tag{3a}$$

$$\psi_B=e^{-Z_Br_a}+e^{-Z_Br_b}, \tag{3b}$$

and the numbers 1 and 2 designate the electrons. The energy E of the ground state is given by

$$E=W/N, \tag{4}$$

where

$$W=\int\Psi\mathbf{H}\Psi dv_1dv_2, \tag{4a}$$

$$N=\int\Psi\Psi dv_1dv_2, \tag{4b}$$

and dv_1, dv_2 are the volume elements of electrons 1 and 2, respectively.

The integrals which occur in Eqs. (4a) and (4b) for the most part can be evaluated by methods familiar to workers in molecular quantum mechanics. The only integrals which will be discussed here are the exchange

* Part of the work reported in this paper was done while the author was at the Institute for Fluid Dynamics and Applied Mathematics, University of Maryland, College Park, Maryland. The author acknowledges the recent support of the Bureau of Ordnance, Department of the Navy under Contract NOrd-7386.

[1] R. F. Wallis and H. M. Hulburt, J. Chem. Phys. **22**, 774 (1954).

[2] R. S. Mulliken, Proc. Natl. Acad. Sci. U. S. **38**, 160 (1952).

[3] E. A. Hylleraas, Z. Physik **71**, 739 (1931).

[4] C. A. Coulson, Trans. Faraday Soc. **33**, 1479 (1937).

[5] S. Weinbaum, quoted in L. Pauling and E. B. Wilson, Jr., *Introduction to Quantum Mechanics* (McGraw-Hill Book Company, Inc., New York, 1935), p. 347.

integrals

$$\int (1/r_{12}) \exp(-Z_A r_{a1} - Z_B r_{b1} - Z_A r_{a2} - Z_B r_{b2}) dv_1 dv_2$$

and

$$\int (1/r_{12}) \exp(-Z_A r_{a1} - Z_B r_{b1} - Z_A r_{b2} - Z_B r_{a2}) dv_1 dv_2.$$

These integrals have been discussed by Rüdenberg.[6] They were evaluated by using the Neumann expansion for $1/r_{12}$ in elliptic coordinates and integrating term by term. The resulting series do not terminate, but the convergence is sufficiently rapid so that only a few terms need be used.

The results of the ground-state energy calculations based on the wave function given by Eq. (3) are given in Table I.

TABLE I. Ground-state dissociation energy of H_2 as a function of effective nuclear charges Z_A, Z_B.

Z_A	Z_B	Dissociation energy ev
1.4	0.8	3.344
1.3	0.9	3.351
1.4	0.9	3.543
1.5	0.9	3.565
1.4	1.0	3.551
1.5	1.0	3.475
1.6	0.8	3.382
1.6	0.9	3.407
	Experimental value	4.72

III. DISCUSSION

It may be seen from Table I that the best value of the dissociation energy, 3.565 ev for $Z_A=1.5$ and $Z_B=0.9$, is somewhat superior to the value 3.47 ev obtained by Coulson and by Weinbaum for the case $Z_A=Z_B$, but differs from the experimental value, 4.72 ev, by more than 1 ev. This behavior is similar to that found when DO's are used as molecular orbitals. The average of the aforementioned values of Z_A and Z_B is 1.2 which is very nearly the same as the best value of the effective nuclear charge found by Coulson and by Weinbaum.

If the interelectronic repulsion term $1/r_{12}$ is omitted from the Hamiltonian, the best value of the energy occurs when Z_A and Z_B each take on the value appropriate to the best LCAO approximation to the ground-state wave function for one electron moving in the field of two nuclei each having one unit of charge, i.e., for the hydrogen molecular ion, H_2^+. Finkelstein and Horowitz[7] have calculated the electronic energy of the ground state of the hydrogen molecular ion using a wave function of the form given by Eq. (3a). For the internuclear distance $r_{ab}=1.4$ au the energy is a minimum at a value of the effective nuclear charge of 1.4.

The effect of the interelectronic repulsion is to increase Z_A by 0.1 from 1.4 to 1.5 and to decrease Z_B by 0.5 from 1.4 to 0.9. The value of Z_A may be considered to arise from a negative screening of each nucleus by 0.1 unit by the electron in the MO with effective nuclear charge Z_B. Similarly the value of Z_B may be considered to correspond to an ordinary screening of each nucleus by 0.5 unit by the electron in the MO with effective nuclear charge Z_A. A similar behavior is found in the helium atom[8] for which the best values of the effective nuclear charges for the two orbitals are 2.15 and 1.19, respectively, when the effect of the interelectronic repulsion is included. When the interelectronic repulsion is neglected the effective nuclear charges each take the value 2.00.

IV. ACKNOWLEDGMENTS

The author wishes to thank Dr. R. C. Herman for his encouragement and helpful suggestions and Dr. R. J. Rubin for reading the manuscript. He also wishes to thank Miss Esther Puschett and Miss Jacquelyn Siler for carrying out the numerical calculations and Miss Shirley Thomas for assistance in the preparation of the manuscript.

V. APPENDIX

Additional calculations of the ground-state dissociation energy of H_2 have been made using the wave function[9]

$$\Psi = 1S_a^A(1)1S_b^B(2) + 1S_b^A(1)1S_a^B(2) + 1S_a^B(1)1S_b^A(2) + 1S_b^B(1)1S_a^A(2) + \lambda[1S_a^A(1)1S_a^B(2) + 1S_b^A(1)1S_b^B(2) + 1S_a^B(1)1S_a^A(2) + 1S_b^B(1)1S_b^A(2)],$$

where, for example, $1s_a^A(1)$ is equal to $\exp(-Z_A r_{a1})$. For $\lambda=1$ this wave function reduces to that considered

TABLE II. Ground-state dissociation energy, D, of H_2 as a function of effective nuclear charges Z_A, Z_B, and of the parameter λ.

Z_A	Z_B	Generalized Wang D(ev)	Generalized Weinbaum D(ev)	λ
1.4	0.8	3.687	3.771	0.1835
1.3	0.9	3.707	3.807	0.1906
1.4	0.9	3.865	4.017	0.2227
1.5	0.9	3.843	4.057	0.2515
1.4	1.0	3.837	4.080	0.2584
1.5	1.0	3.684	4.013	0.2850
1.6	0.8	3.653	3.834	0.2429
1.6	0.9	3.619	3.911	0.2791

[6] K. Rüdenberg, J. Chem. Phys. **19**, 1459 (1951).
[7] B. N. Finkelstein and G. E. Horowitz, Z. Physik **48**, 118 (1928).
[8] E. A. Hylleraas, Z. Physik **54**, 347 (1929); C. Eckart, Phys. Rev. **36**, 878 (1930).
[9] The author is indebted to Dr. Charles W. Scherr for suggesting the introduction of the parameter λ in the present calculation.

in the main body of the paper while for $\lambda=0$ it constitutes a generalization to two effective nuclear charges of the Wang wave function[10] for which the best value of the dissociation energy is 3.76 ev when $Z=1.166$. When the parameter λ is varied to minimize the energy, the calculation constitutes a generalization of that due to Weinbaum[11] who obtained a dissociation energy of 4.00 ev when $Z=1.193$ and $\lambda=0.256$. The results of the present calculations are given in Table II. It may be seen that both the Wang and the Weinbaum calculations are improved by about 0.1 ev by the use of two effective nuclear charges.

[10] S. C. Wang, Phys. Rev. **31**, 579 (1928).

[11] S. Weinbaum, J. Chem. Phys. **1**, 593 (1933).

THE JOURNAL OF CHEMICAL PHYSICS VOLUME 23, NUMBER 7 JULY, 1955

Infrared Spectra of Gaseous and Solid Hydrazoic Acid and Deutero-Hydrazoic Acid: The Thermodynamic Properties of HN_3

DAVID A. DOWS* AND GEORGE C. PIMENTEL
Department of Chemistry and Chemical Engineering, University of California, Berkeley, California

(Received October 11, 1954)

Infrared studies of HN_3 and DN_3 in the gas and solid phases and of HN_3 in CCl_4 solutions are presented. The two low-frequency skeletal bending modes are identified, permitting calculation of the thermodynamic properties of hydrazoic acid. Hydrogen bonding of HN_3 and DN_3 in the solid state is indicated by frequency shifts of the NH and ND stretching motions (216 and 151 cm^{-1}, respectively). No evidence of hydrogen bonding was observed in solutions of HN_3 in CCl_4 at concentrations up to 0.3 M. An irreversible phase transition is observed on warming solid hydrazoic acid above about 120°K.

THE infrared spectrum of gaseous hydrazoic acid has been given by Davies[1] and by Eyster and Gillette.[2] These authors are in general agreement except on the spectral features observed in the region below 800 cm^{-1}. There is question as to the spectral locations of the two fundamental vibrations expected below 800 cm^{-1}, the skeletal bending motions. In the studies reported here, the structure observed in the region 600–750 cm^{-1} is well enough resolved to aid in the selection of these fundamentals.

An infrared study of the hydrogen bonding of HN_3 and DN_3 in solution has been made by Buswell, McMillan, Rodebush, and Wall.[3] No evidence of hydrogen bonding between two HN_3 molecules was detected although it was concluded that there is a strong interaction between HN_3 and ether or water. The spectrum of solid hydrazoic acid is interesting in comparison with these results.

The structure of hydrazoic acid is known from the analysis by Eyster[4] of the spectrum of the second overtone of the N—H stretching frequency and it is confirmed by the microwave study of Amble and Dailey.[5] The three nitrogen atoms of HN_3 are colinear and the hydrogen atom is attached at one end with an angle of 112° between the NH bond and the N_3 skeleton. Thus the molecule has symmetry C_s with five type A' vibrations (in-plane) and one type A'' vibration (out-of-plane). All vibrations are both infrared- and Raman-active. If the molecule is treated as a symmetric top (which it closely approaches) the A'' fundamental is expected to be a pure perpendicular band, while the A' fundamentals are expected to be hybrids consisting of superimposed parallel and perpendicular bands. The parallel components should have the appearance of a parallel band of a linear molecule, the Q-branch being quite weak. With the structure given by Amble and Dailey and assuming the moments of inertia do not change as a function of vibrational state, the separations of the P- and R-branch maxima are calculated to be 26 cm^{-1} for both HN_3 and DN_3, while the Q-branches of the perpendicular bands should be 36 and 22 cm^{-1} apart for HN_3 and DN_3, respectively.

EXPERIMENTAL

Hydrazoic acid was prepared by adding a large excess of stearic acid to sodium azide and heating to about 90°C under vacuum, allowing the HN_3 to distill out of the reaction mixture as it formed. Explosion shielding was provided. The pressure of hydrazoic acid was maintained below 50 mm during the preparation and the gas came in contact with glass, mercury, and Apiezon N stopcock grease. The infrared spectrum of the gas showed no evidence of impurities or decomposition over a storage period exceeding one month at room temperature.

Deutero-hydrazoic acid was prepared in the same manner using monodeutero-stearic acid. This material was prepared from sodium stearate, dried first at 130°C

* Present address: Department of Chemistry, Cornell University, Ithaca, New York.

[1] M. M. Davies, Trans. Faraday Soc. **35**, 1184 (1939).

[2] E. H. Eyster and R. H. Gillette, J. Chem. Phys. **8**, 369 (1940).

[3] Buswell, McMillan, Rodebush, and Wall, J. Am. Chem. Soc. **61**, 2809 (1939).

[4] E. H. Eyster, J. Chem. Phys. **8**, 135 (1940).

[5] E. Amble and B. P. Dailey, J. Chem. Phys. **18**, 1422 (1950).

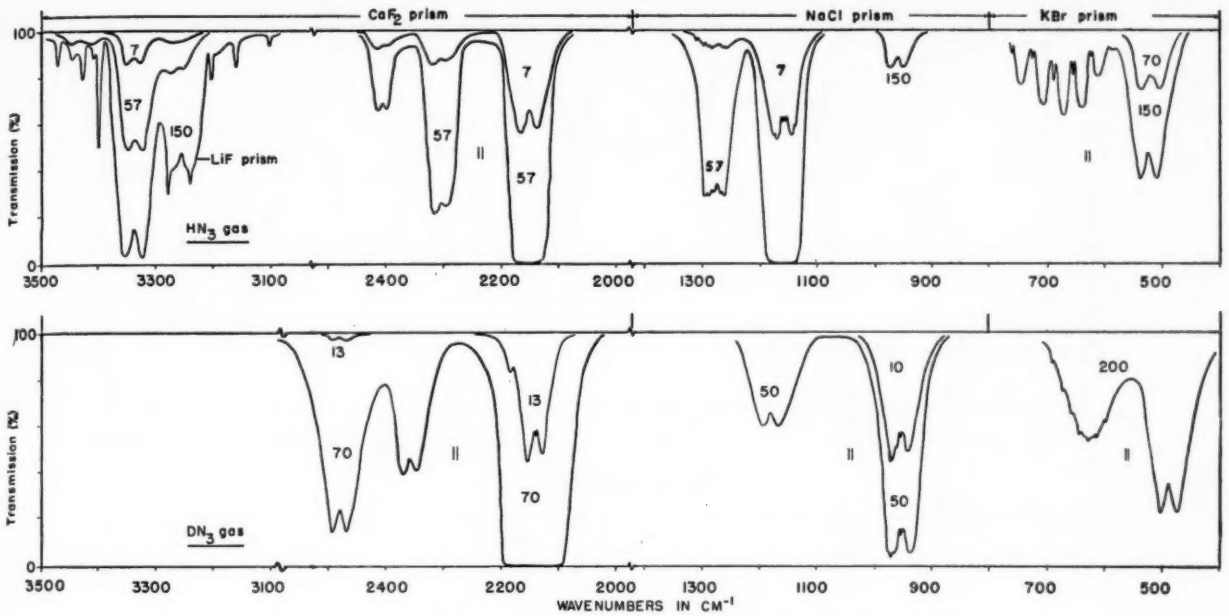

FIG. 1. Infrared spectra of HN_3 gas and DN_3 gas (pressure given in mm of Hg).

for 24 hours and then at room temperature in a vacuum desiccator over P_2O_5 for 48 hours. In a dry box, P_2O_5 was added to 99.5 percent D_2O, the dried sodium stearate was added to this solution of deuterated phosphoric acid, and the mixture was warmed until the deuterated stearic acid melted. The mixture was cooled, filtered, and the deuterated stearic acid was placed in in a vacuum desiccator over P_2O_5. The sample probably contained some unreacted sodium stearate.

The DN_3 prepared from the deuterated acid contained about 15 percent HN_3, presumably because the P_2O_5 was not completely dry, and about 10 percent D_2O. The gases were condensed at 77°K and warmed to −20°C to transfer the DN_3 to another bulb; this procedure was repeated until the infrared spectrum gave no more evidence of D_2O. The HN_3 interfered in the spectral studies because of the overlap of the absorption of HN_3 at 1150 cm^{-1} with the weaker absorption of DN_3 near 1180 cm^{-1}.

The spectra were obtained with a Perkin-Elmer Model 21 spectrophotometer (NaCl and CaF_2 prisms) and a Perkin-Elmer Model 12-C spectrometer (LiF and KBr prisms). The spectral slit widths are shown on the spectra. Frequency accuracy ranges from about 3 cm^{-1} at 500 cm^{-1} to about 5 cm^{-1} at 3300 cm^{-1}. For the gas spectra, 10-cm cells with KBr windows were used. In obtaining the solid spectra, gas was sprayed onto a salt window cooled to about 80°K with liquid nitrogen. The low-temperature cell is similar to that described by Wagner and Hornig[6] with a glass spray-on tube added to facilitate transfer of the sample onto the cold salt window. The temperature was measured during every spectral study using a copper-constantan thermocouple embedded in the salt window. Both NaCl and AgCl windows were used, with no differences in the spectra.

[6] E. L. Wagner and D. F. Hornig, J. Chem. Phys. **18**, 296 (1950).

SPECTRA

The spectra of gaseous HN_3 and DN_3 are shown in Fig. 1. The structure of the HN_3 band at 2150 cm^{-1} observed with the lithium fluoride prism agreed closely with that given by Davies.[1] The spectrum of DN_3 was examined in this same region, using both LiF and CaF_2 prisms, and no resolution differences were observed.

Above 900 cm^{-1} the spectrum of HN_3 is in agreement with that given by previous investigators except that a weak doublet was observed at 950 cm^{-1} (with a spacing appropriate to the calculated $P-R$ spacing of HN_3) and no absorption was detected at 1381 cm^{-1}, a band listed by Eyster and Gillette[2] but not by Davies.[1]

The absorptions near 522 cm^{-1} for HN_3 and 498 cm^{-1} for DN_3 have the doublet appearance appropriate to parallel bands; hence these features are assigned to the in-plane bending motion, ν_5. Assignment of the HN_3 band at 522 cm^{-1} to a difference frequency, as is done by Eyster and Gillette,[2] is implausible since the corresponding sum frequency is not observed.

Figure 2 shows the structure near 700 cm^{-1} under optimum spectral conditions using a NaCl prism. For both HN_3 and DN_3 the structure is indicative of a perpendicular band and hence is assigned to the A'' vibration, the out-of-plane bending, ν_6. The choice of the band centers, at 672 cm^{-1} for HN_3 and 638 cm^{-1} for DN_3, is discussed later.

When HN_3 was condensed on a salt window cooled to 80°K, a solid material, phase I, was obtained having

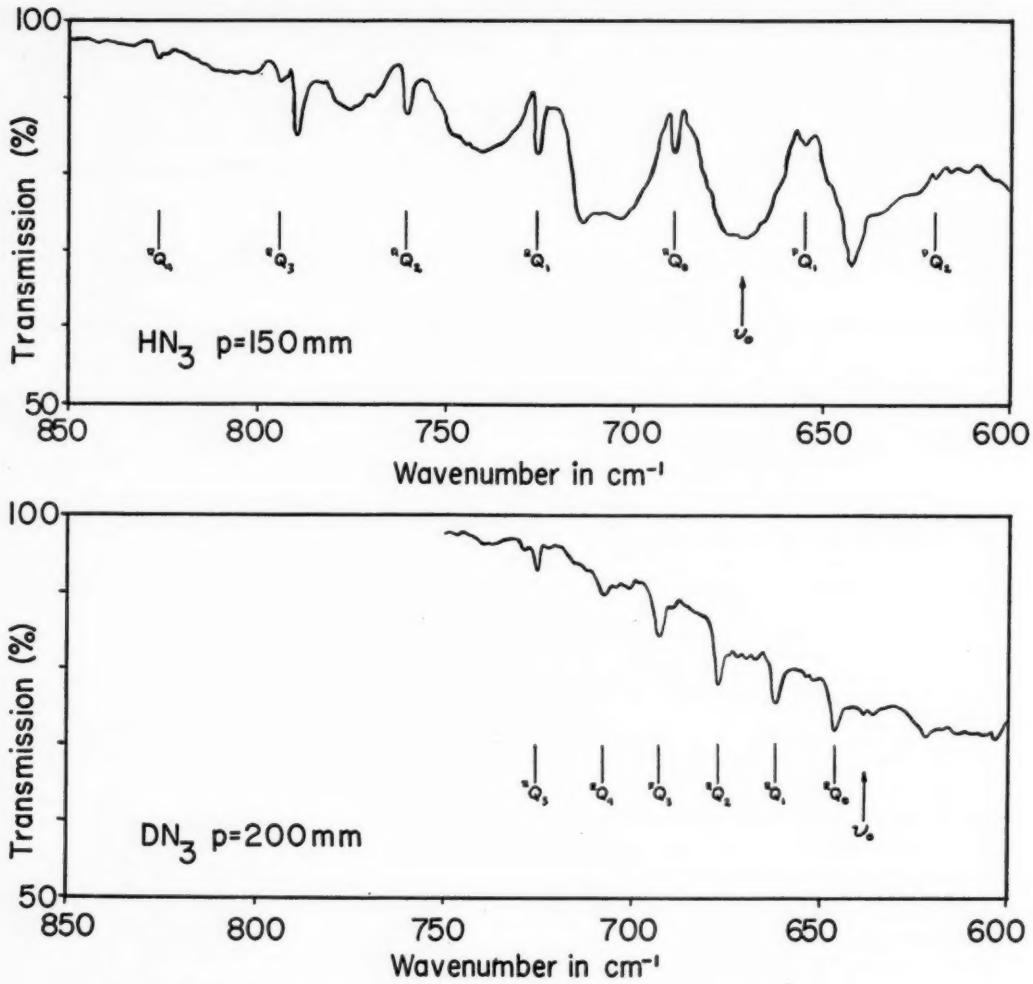

FIG. 2. Infrared spectra near 700 cm^{-1} of HN_3 gas and DN_3 gas: Q-branch assignments.

the spectrum shown by a dotted line in Fig. 3(a). When the solid was allowed to warm slowly, an abrupt transition occurred at about 120°K to give a solid, phase II, having the spectrum shown by a solid line in Fig. 3a. No further changes in the spectrum of phase II occurred on cooling the solid slowly to 80°K or on warming to about 170°K where HN_3 began distilling off the window.

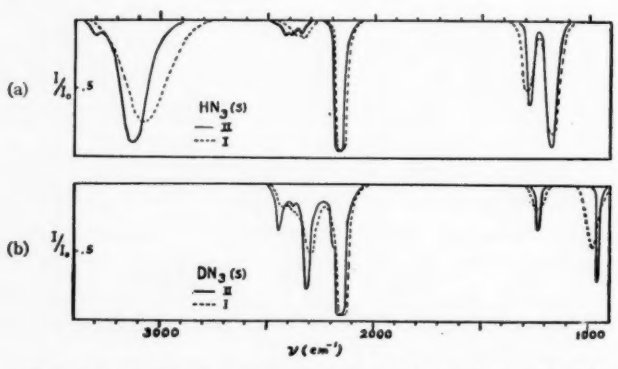

FIG. 3(a). Infrared spectra of phases I and II of solid HN_3 (80°K). 3(b). Infrared spectra of phases I and II of solid DN_3 (80°K).

The spectrum of solid DN_3 was obtained using a sample containing about 25 percent HN_3. The solid exhibited a transition from a low-temperature phase I [dotted line, Fig. 3(b)] to another phase II [solid line, Fig. 3(b)] as did HN_3, but the transition temperature was not measured. The large amount of HN_3 prevented accurate determination of the shape of the absorptions of DN_3 near 2160 and 1230 cm^{-1}.

The frequencies observed in the spectra of HN_3 and DN_3 in the gas state and in the solid phase II are listed in Table I with proposed assignments. The frequencies observed for the solids in phase I are given in Table II. Table III lists those sharp features observed near 700 cm^{-1} in the spectra of gaseous HN_3 and DN_3 which are interpreted to be associated with Q-branches of the sub-bands of a perpendicular band. The average spacings observed are 34.5 and 16.0 cm^{-1} for HN_3 and DN_3, respectively.

DISCUSSION

Spectra of the Gas Phases

In attempting to interpret the detailed structure of the absorptions near 700 cm^{-1}, it is possible to account for the qualitative difference in appearance of the HN_3 and DN_3 spectra. The calculated separations of the *P*- and *R*-branch maxima, 26 cm^{-1}, indicates that the *P*- and *R*-branches of neighboring sub-bands will overlap and reinforce each other for HN_3 where the average *Q*-branch spacing is 34.5 cm^{-1}. The *P*- and *R*-branch maxima will be separated by about 26 cm^{-1} for DN_3 also, but the observed *Q*-branch spacing, 16.0 cm^{-1}, is too small to permit the reinforcement observed for HN_3.

The spacings between Q-branches permit calculation of values of I_a' if hydrazoic is assumed to be a symmetrical top, if Coriolis interaction is neglected, and if the large moment of inertia of the hypothetical symmetrical top is assumed to be the arithmetic mean of the largest moments of inertia of hydrazoic acid, $I_b'=\frac{1}{2}(I_b+I_c)$ (the prime denotes the upper vibrational state). This calculation gives 1.6 and $3.7\cdot10^{-40}$ g cm^2 for I_a' of HN_3 and DN_3, respectively. From the known structure of HN_3, the values of I_a are calculated to be 1.54 and $2.51\cdot10^{-40}$ g cm^2 for HN_3 and DN_3, respectively. The discrepancy between I_a and I_a' seems too large to attribute wholly to a change in the moment of inertia of DN_3 (but not HN_3) in its excited vibrational state.

TABLE I. Infrared spectra of HN_3 and DN_3: gas phase and solid phase II.

$HN_3(g)$	$HN_3(sII)$	$DN_3(g)$	$DN_3(sII)$	Assignment
3336 m	3120 vs	2480 m	2329 s	ν_1
3250 w	3305 w			$\nu_2+\nu_4$
		2358 m	2442 m	$2\nu_3$
	2435 w		2380 w	$\nu_2+\nu_7$
2402 m	2402 w	2170 w	2202 w	$\nu_3+\nu_4$
2304 s	2298 w			$2\nu_4$
2140 vs	2169 vs	2141 vs	2165 vs	ν_2
1274 m	1280 m	1183 m	1229 m	ν_3
1150 vs	1182 vs	955 s	958 s	ν_4
950 vw				$\nu_2-\nu_4$
672 w		638 w		ν_6
522 w		498 w		ν_5
	(266) (?)		(215) (?)	ν_7

The band center of a perpendicular band is expected to lie between the two most intense *Q*-branches. The rather obvious maximum in absorption of the band of DN_3 indicates the band center is at 622, 638, or 654 cm^{-1}. These figures were obtained by extrapolation of the resolved *Q*-branch frequencies (see Table II) to the maximum in absorption as observed with the KBr prism. The spectrum of HN_3 has no clear maximum of absorption but three possible band center positions halfway between *Q*-branches are 637, 672, and 708 cm^{-1}. The Teller-Redlich product rule applied to the A'' class indicates that the ratio $\nu_6(HN_3)/\nu_6(DN_3)$ is 1.06. Among the possible band centers mentioned above, the pair 672 cm^{-1} (HN_3) and 638 cm^{-1} (DN_3) are in the ratio of 1.05. This ratio is quite reasonable if anharmonicity is considered. The next best selection, the pair 637 cm^{-1} (HN_3) and 622 cm^{-1} (DN_3), are in the ratio 1.02 and seem less likely. Still, in calculating thermodynamic properties of HN_3, it seems wise to attach an uncertainty of 35 cm^{-1} to the assignment of $\nu_6=672$ cm^{-1}.

TABLE II. Infrared spectra of HN_3 and DN_3: solid phase I.

$HN_3(sI)$	$DN_3(sI)$	Assignment
3090	2308	ν_1
	2412	$2\nu_3$
2379		
	2380	$\nu_2+\nu_7$
2349		$2\nu_4$
2162	2155	ν_2
1299	1230	ν_3
1180	977	ν_4

Three lines, located at 643.0, 714.5, and 790.0 cm^{-1}, are observed in the spectrum of HN_3 but do not have obvious assignments.

The proposed assignments in Table II present some interesting points. The HN_3 band at 950 cm^{-1}, not observed by earlier workers, has been tentatively assigned as the difference frequency, $\nu_2-\nu_4$. This assignment is strengthened by the appearance of the corresponding sum, $\nu_2+\nu_4$, at 3250 cm^{-1}, but the discrepancy between the calculated and observed difference frequency is larger than expected for a difference frequency.

The combination $2\nu_4$ is observed in the spectra of gaseous and solid HN_3 while $2\nu_3$ is observed in the spectra of DN_3. Furthermore, the relative intensities of ν_3 and ν_4 differ in the spectra of gaseous HN_3 and DN_3 and in the transition from gas to solid, ν_4 shifts more than ν_3 for HN_3 while the reverse is true for DN_3. All of these observations show a change of character of these two vibrations upon deuterium substitution, the vibration ν_3 taking on more of the character of the

TABLE III. *Q*-branch frequencies near 700 cm^{-1}: HN_3 and DN_3.

Branch	$HN_3(g)$	$\Delta\nu$	$DN_3(g)$	$\Delta\nu$
RQ_5	(?) 864.0		726.0	
		37.5		17.5
RQ_4	826.5		708.5	
		32.5		15.0
RQ_3	794.0		693.5	
		33.5		16.0
RQ_2	760.5		677.5	
		35.0		15.0
RQ_1	725.5		662.5	
		36.5		16.5
RQ_0	689.0		646.0	
		34.5		
PQ_1	654.5			
		34.5		
PQ_2	620.0			

hydrogen bending motion. The combination $\nu_3+\nu_4$ is not affected by this change and is observed in the spectra of both HN_3 and DN_3.

Thermodynamic Properties of HN_3

The rather definite assignment of the low-frequency vibrations, ν_5 and ν_6, provides a basis for the calculation of the thermodynamic properties of hydrazoic acid in the perfect gas state. Table IV gives the values of C_p^0, $(H^0-H_0^0)/T$, $(F^0-F_0^0/T)$, and S^0 at various temperatures. These calculations are based on the molecular parameters given by Amble and Dailey[5] with the product of the moments of inertia equal to $6963\cdot10^{-120}$ g^3 cm^6. The uncertainty of these values is probably determined by the uncertainty of ±35 cm^{-1} in the assignment of ν_6.

Hydrogen Bonding

The principal differences between the spectra of gaseous and solid hydrazoic acid are of the type observed when hydrogen bonding occurs. The bands associated with NH and ND stretching motions shift to lower frequencies and are intensified relative to other bands. The bands assigned as the fundamentals ν_2, ν_3, and ν_4 all shift to higher frequencies. For ν_3 and ν_4, which involve hydrogen bending motion, the upward shift also indicates hydrogen bonding.

This evidence for hydrogen bonding in the solids of both HN_3 and DN_3 contrasts with the results of Buswell *et al.*,[3] concerning hydrogen bonding of hydrazoic acid in solution. To clarify the situation, a portion of their studies of HN_3 in CCl_4 was repeated. Solutions with HN_3 concentrations 0.32, 0.093, and 0.027 M were studied in the spectral region 3500–2000 cm^{-1}. The 0.32 M solution was prepared by condensing together known amounts of HN_3 and CCl_4 in vacuum and warming to room temperature. The other solutions were prepared by dilution of the 0.32 M solution.

TABLE IV. Thermodynamic properties of hydrazoic acid, cal/deg mole.

T °K	C_p^0	$(H^0-H_0^0)/T$	$-(F^0-H_0^0)/T$	S^0
273.16	10.095	8.577	47.606	56.179
298.16	10.443	8.721	48.366	57.083
100	8.023	7.959	39.428	47.384
200	9.072	8.212	44.997	53.204
300	10.464	8.730	48.417	57.139
400	11.740	9.326	51.008	60.330
500	12.805	9.922	53.153	63.071
600	13.709	10.482	55.014	65.493
700	14.462	10.997	56.667	67.660
800	15.102	11.472	58.164	69.631
900	15.651	11.907	59.540	71.443
1000	16.122	12.305	60.817	73.117
1100	16.529	12.670	62.007	74.673
1200	16.879	13.008	63.120	76.124
1300	17.189	13.312	64.174	77.482
1400	17.454	13.602	65.173	78.771
1500	17.681	13.868	66.123	79.987

Bands were observed in the spectra of the solutions at frequencies 3320, 3250, 2394, 2298, and 2140 cm^{-1}, in close agreement with the gas phase frequencies. Within experimental uncertainty, the optical density of each of these bands varied directly with the concentration of HN_3. The intensity of the NH stretching band relative to other bands was approximately the same as in the gas phase. The spectral studies of CCl_4 solutions of HN_3 corroborate the conclusion of Buswell *et al.* that HN_3 does not form hydrogen bonded polymers in solution.

Examination of the shifts of the NH and ND stretching frequencies in the solid state (216 and 151 cm^{-1}) reveals normal behavior of deuterium relative to hydrogen. The band attributed by Buswell *et al.*[3] to the hydrogen bonded ND stretching motion (observed in this investigation at 2202 cm^{-1} in the solid phase) is also present in the spectrum of gaseous DN_3 (at 2170 cm^{-1}) and can be assigned as a combination, $\nu_3+\nu_4$. Thus no evidence was found which corroborates the abnormal hydrogen bonding properties of DN_3 proposed by Buswell *et al.*[3]

The shift of the NH stretching frequency with hydrogen bonding may be compared to the corresponding shift for δ-valerolactam, for which Tsuboi[7] reported a shift of 210 cm^{-1} and a hydrogen bonding energy of 5.1 kcal per bond in CCl_4 solution. It is likely that the similar frequency shifts of HN_3 and δ-valerolactam are indicative of similar hydrogen bond energies. Hence the absence of polymerization of HN_3 in solution is probably associated with entropy terms opposing formation of open dimers or polymers from an extended molecule like HN_3. Cyclic dimers probably do not form because of unfavorable bonding angles.

More detailed study of the spectra of solid HN_3 and DN_3 reveals no evidence of splitting of bands, even in the hydrogen stretching regions where the intermolecular interactions are strong because of hydrogen bonding. Two of the possible explanations of the absence of splitting of the NH or ND stretching motions are that the unit cell contains only one molecule or that there are several molecules per unit cell and the factor group selection rules provide only one infrared-active hydrogen stretching mode.

All the combinations observed in the gas phase spectra are also observed in the solid spectra. In addition solid HN_3 and DN_3 each show a band for which there is no counterpart in the gas phase spectrum, either 2402 or 2435 cm^{-1} for HN_3 (one of these is associated with the combination, $\nu_3+\nu_4$) and 2380 cm^{-1} for DN_3. It is possible that these new bands may be due to combinations between ν_2 and lattice torsional motions of hydrazoic acid about the axis of smallest moment of inertia. These torsional motions, called ν_7, are tentatively assigned at 266 or 233 cm^{-1} for HN_3 and 215 cm^{-1} for DN_3.

[7] M. Tsuboi, Bull. Chem. Soc. Japan **22**, 215 (1949).

The spectra of the solid phases I and II differ in several ways. For both HN_3 and DN_3, several bands are distinctly sharper in phase II and the frequencies of ν_1, ν_3, and ν_4 suggest stronger hydrogen bonding in phase I than in phase II. The band assigned to $\nu_2+\nu_7$ is present in the spectrum of $DN_3(sI)$ but was not observed in the spectrum of $HN_3(sI)$.

Mador and Williams[8] have recently mentioned a transition in solid hydrazoic acid occurring at 148°K. The low-temperature phase is a clear colorless glass and the transition produces a polycrystalline material. No obvious change of this sort was noted in the present work and the light scattering by the solid was small and about the same for both phases I and II. In view of the discrepancy between the observed transition temperatures (148°K[8] and about 120°K), it does not seem likely that the glassy low-temperature phase observed by Mador and Williams is identical to phase I.

The observation that phase I cannot be obtained by cooling phase II below the transition point could be due to supercooling of phase II, and phase I may be a stable crystal modification. On the other hand, the broadness of the bands suggests a certain amount of disorder in phase I, and this phase may have a glassy structure (as indicated by Mador and Williams[8]) or it may be an unstable disordered crystalline arrangement (due to fast growth) which becomes ordered on warming. A transition from a glass to a crystal usually can be identified by a marked increase in scattering, which was not observed. Hence the last proposal, an unstable, partially disordered crystal, seems to be the most likely explanation of solid phase I. It is interesting to notice that similar transitions have been reported by Malherbe and Bernstein[9] and by Nightingale and Wagner.[10] Ammonium azide also shows a transition with the temperature behavior described in the foregoing.[11]

[8] I. L. Mador and M. C. Williams, J. Chem. Phys. **22**, 1627 (1954).

[9] F. E. Malherbe and H. J. Bernstein, J. Chem. Phys. **19**, 1607 (1951).

[10] R. E. Nightingale and E. L. Wagner, J. Chem. Phys. **22**, 203 (1954).

[11] Dows, Whittle, and Pimentel (to be published).

THE JOURNAL OF CHEMICAL PHYSICS VOLUME 23, NUMBER 7 JULY, 1955

Ion Pair Yields in the X-Ray Decomposition of Hydrogen Bromide in Rare Gas Atmospheres*

EDWARD G. ZUBLER,† WILLIAM H. HAMILL, AND RUSSELL R. WILLIAMS, JR.
Department of Chemistry, University of Notre Dame, Notre Dame, Indiana

(Received September 23, 1954)

The rate of x-ray induced decomposition of hydrogen bromide has been measured both in the pure gas and in rare gas atmospheres. The rate of ion pair formation under identical irradiation has been determined from the saturation ionization currents in rare gases and ion pair yields for decomposition of hydrogen bromide have been computed. Average yields were A-HBr, 4.7; Kr-HBr, 4.0; Xe-HBr, 4.7; HBr, 4.6; HBr-Xe, 5.2; where the first substance named is the major component. A mechanism for decomposition by ion formation accounts for a yield of 4.0. Values above this are attributed to dissociative excitation without ionization.

INTRODUCTION

THE ion pair yield, M/N, for decomposition and synthesis of hydrogen bromide by alpha-particle bombardment has been computed previously[1,2] from estimates of the ionization produced by a known amount of radon added to the systems. Based on the measurements of Lind and Livingston,[2] a theory and mechanism for these reactions were developed by Eyring, Hirschfelder, and Taylor.[3] For decomposition of pure hydrogen bromide, that mechanism contains the following steps:

$$HBr \rightsquigarrow HBr^+ + e \quad (1)$$

$$e + HBr \rightarrow H + Br^- \quad (2)$$

$$Br^- + HBr^+ \rightarrow H + 2Br \quad (3)$$

$$H + HBr \rightarrow H_2 + Br \quad (4)$$

$$2Br + M \rightarrow Br_2 + M \quad (5)$$

which can account for an ion pair yield of 4.0. If dissociative excitation of hydrogen bromide occurs, the number of molecules decomposed per ion pair formed may be greater than 4.0 by 2.0 molecules per dissociation.

In this work we have estimated the number of ion pairs by saturation ionization current measurements. This is difficult or impossible in mixtures containing hydrogen bromide, and therefore, we have had to base

* From the Ph.D. dissertation of E. G. Zubler. Presented at the 125th American Chemical Society meeting, Kansas City, Missouri, March 23–April 1, 1954.

† Present address: General Electric Company, Nela Park, Cleveland, Ohio.

[1] R. Gillerot, Bull. soc. chim. Belges **39**, 509 (1930).

[2] S. Lind and R. Livingston, J. Am. Chem. Soc. **58**, 612 (1936).

[3] Eyring, Hirschfelder, and Taylor, J. Chem. Phys. **4**, 570 (1936).

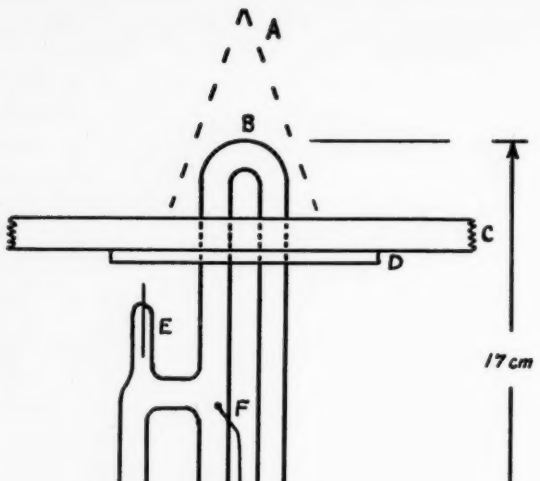

FIG. 1. Radiation cell. *A*. cone of x-rays, *B*. thin glass, *C*. supporting shelf, *D*. lead mask, *E*. cathode lead, *F*. anode lead, *G*. capillary, *H*. spectrophotometer cell, J. manifold connection.

our yield computations on ion current measurements made in the absence of hydrogen bromide. These electrical measurements were followed by measurement of chemical reaction under identical irradiation conditions. When the proportion of hydrogen bromide is small there is little uncertainty in the rate of ion formation since that is largely due to the rare gas and in these systems we anticipate that charge will be efficiently transferred to the hydrogen bromide:

$$A^+ + HBr \rightarrow A + HBr^+. \quad (6)$$

The ionization potentials for the rare gases used are A=15.76 v, Kr=14.00 v, Xe=12.13 v,[4] and the ionization potential of hydrogen bromide is 12.04 v,[5] which is probably experimentally indistinguishable from that of xenon. In addition to the question of charge transfer we must also take into account the efficacy of excitation transfer in dissociation of hydrogen bromide:

$$A^* + HBr \rightarrow HBr^* + A$$
$$\text{or} \rightarrow H + Br + A. \quad (7)$$

[4] G. Herzberg, *Atomic Spectra and Atomic Structure* (Dover Publications, New York, 1944).
[5] W. C. Price, Proc. Roy. Soc. (London) **A167**, 216 (1938).

When the irradiated gas is pure, or nearly pure hydrogen bromide, reactions (6) and (7) have little importance, but in these cases we must rely on estimates of the relative ionization efficiency of hydrogen bromide, since current measurements were not made.

EXPERIMENTAL

Reagents

Gases used were obtained from the Matheson Company, and their stated purities (with major impurities) were as follows: HBr, 99.5 percent (N_2); CH_4, 99.0 percent (C_2H_6, N_2, CO_2); C_2H_6, 95 percent (C_2H_4, C_3H_8, C_3H_6, CH_4); C_3H_8, 99 percent (C_2H_6, i-C_4H_{10}). Hydrogen bromide was distilled in vacuum; hydrocarbons were passed through helix filled traps at −78°C; argon, 99.6 percent, was passed over copper at 700° and then through a trap at −78°; and krypton and xenon of research grade were used as received.

Apparatus

The source of radiation was a Machlett AEG–50–T x-ray tube with a beryllium window operated at 47.5 kv. When operated at 50 kv this tube gives a continuous x-ray spectrum from 0.25 to 4.4 A with a maximum at 1.7 A. Maximum plate current for this tube is 50 ma, but in this work it never exceeded 17 ma.

The irradiation cell, shown in cross section in Fig. 1, was in the form of two concentric Pyrex cylinders with spherical ends forming an annular reaction space. The walls were chemically silvered for ionization measurements, and two tungsten electrodes carried the current through the walls. The outer wall was blown very thin at the hemispherical end, to cut down x-ray absorption. A similar cell, filled with a mixture of argon and methane was sealed and used to monitor the x-ray intensity at frequent intervals. No drift in the x-ray tube output was observed.

The rf high-voltage supply of a Berkeley G-M scaler circuit was used to supply the collecting voltage for ionization measurements. A calibrated 50 μamp meter with shielded leads connected between one side of the chamber and ground measured the ionization current.

Procedure

The chamber was joined at *J*, Fig. 1, to a vacuum line, flamed gently, and evacuated to $<10^{-5}$ mm. Rare gas (A, Kr, or Xe) and quencher gas (CH_4, C_2H_6, or C_3H_8) were measured in to predetermined pressures. The cell was sealed off, mounted in a reproducible position with respect to the x-ray tube, and irradiated at a fixed voltage and plate current. The ionization current was measured at 200-volt intervals up to 2400 volts ion collecting voltage. All such measurements were made in a single reaction cell.

Measurements of chemical decomposition were made in the same cell after removing the silver electrodes

with nitric acid. The cell was thoroughly rinsed, dried, and evacuated with gentle heating as before. A little hydrogen bromide was admitted for 10 minutes and discarded before introducing the reaction mixture.

A typical mixture for irradiation consisted of hydrogen bromide at 14 mm and rare gas at 500 mm. Irradiation was performed under the same conditions as in the case of the current measurements, except that no ion collecting potential was applied.

The amount of bromine produced in a typical exposure was so small that it was necessary to greatly increase its concentration to permit spectrophotometric analysis. This was accomplished by condensing the mixture in the small cell *H* (made of square tubing) at −196° (as shown in Fig. 1), retaining the bromine by warming to −120°, while cooling the other side arm to −196°. This operation was repeated several times with argon mixtures because of its high vapor pressure at −196°. The analytical cell was sealed off at *G*, (see Fig. 1) and the bromine determined by transmission measurements at 4070 A in a Beckman DU spectrophotometer.

RESULTS

Under the present experimental conditions it was not possible to obtain satisfactory saturation currents with pure rare gas, i.e., current-voltage curves yielded plateaus with small positive slopes. By analogy with G-M counter techniques small admixtures of hydrocarbons were tried and found helpful. With the addition of such a quencher, saturation ionization currents varied less than one percent over a range of 1000 volts and, for argon, were approximately ten percent less than the values obtained without a quencher. All subsequent current measurements were made with *ca* 100 mm of hydrocarbon added to the rare gas. Under these conditions the saturation ionization currents were quite linear in both rare gas pressure (see Figs. 2 and 3) and in x-ray plate current. The intercepts are evidently to

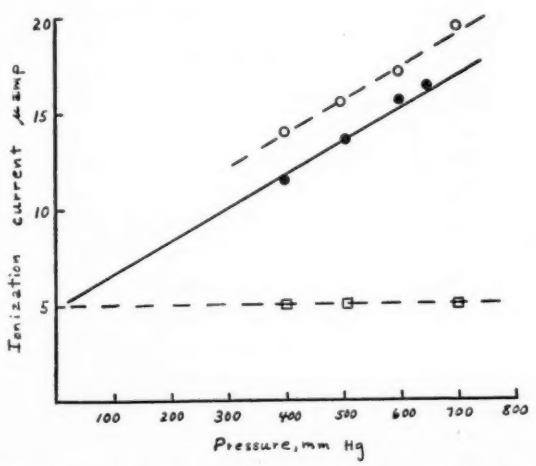

FIG. 2. Saturation ionization current in argon ○, methane □, argon plus methane quencher ●. (In the latter case the partial pressure of argon is plotted.)

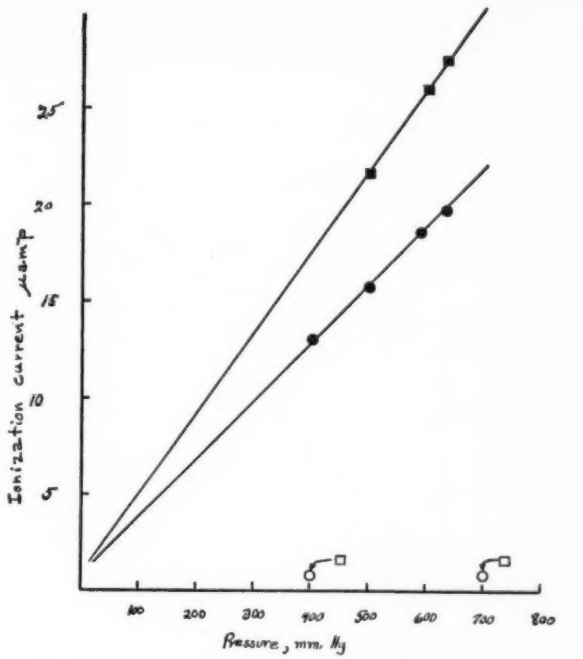

FIG. 3. Saturation ionization current in ethane ○, propane □, krypton with ethane quencher ●, xenon with propane quencher ■. (In the latter two cases the partial pressure of the rare gas is plotted.)

be attributed to soft electrons from the wall of the ionization chamber, since they do not change with various pressures of hydrocarbon gas alone. Because of the necessary removal of the silver on the walls between the electrical and chemical runs, values of *N* were based on the slopes of the curves in Figs. 2 and 3, which presumes that the wall effect is associated with the silver coating.

The effect of adding hydrocarbons to the rare gas is presumably to destroy metastable states which can lead to ionization[6] by processes such as

$$A^*+A \rightarrow A_2^++e, \tag{8}$$

and, by charge transfer, to prevent secondary electron emission upon neutralization of A^+ at the wall. Values of *M* from chemical runs might be high if the added hydrogen bromide does not prevent such processes, since each A_2^+ should lead to decomposition of four hydrogen bromide molecules, while each A^* would lead at most to decomposition of two molecules.

It was not possible to measure saturation ionization currents in the ranges of voltage and pressure employed for gas mixtures containing even as little as two mole percent hydrogen bromide, and therefore, the contribution of hydrogen bromide to the ion pair formation must be estimated. The uncertainty involved in this estimate is serious only in the case of mixtures containing large proportions of hydrogen bromide.

In all chemical runs the conditions were identical,

[6] J. A. Hornbeck and J. P. Molnar, Phys. Rev. 84, 621 (1951).

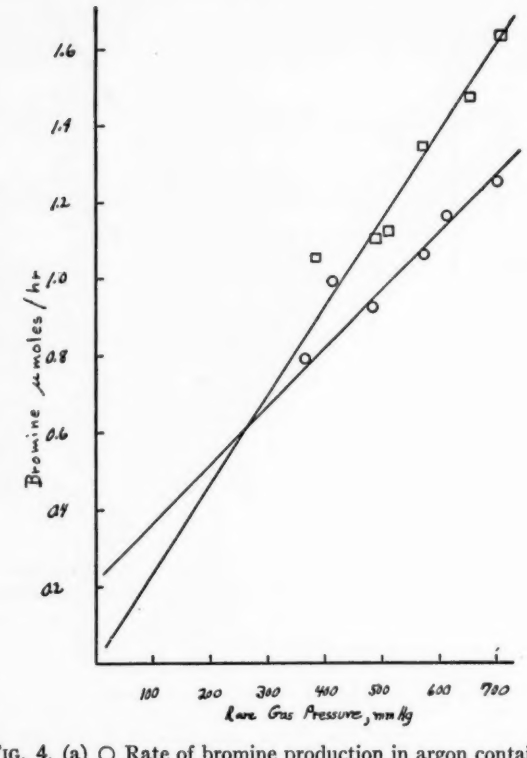

FIG. 4. (a) ○ Rate of bromine production in argon containing 14.2 mm hydrogen bromide. X-ray plate current = 17 ma. (b) □ in krypton containing 14.2 mm hydrogen bromide x-ray plate current = 2.7 ma.

unless otherwise specified, with the corresponding electrical runs except for the omission of the hydrocarbon quencher and the addition of 14 mm of hydrogen bromide. Larger amounts of the latter did not further increase the decomposition yield. The results of these experiments are summarized in Figs. 4 and 5. Figure 6 shows the results of experiments on the x-ray decomposition of pure hydrogen bromide and hydrogen bromide containing 10–20 mm of xenon. Since the abscissas refer to partial pressures of the major components, intercepts include both the limiting effect of the minor component at constant partial pressure and also possible wall effects analogous to that observed in the electrical runs. To avoid uncertainty, values of M are based on the slopes in Figs. 4, 5, and 6. Reproducibility was never as good for these experiments as for current measurements, and even after every imaginable precaution one still found occasional erratic results. The worst of these (one in A-HBr, one in Kr-HBr, and two in HBr) were ignored in computing slopes. In Fig. 5, the slope used is indicated by the straight line. Deviation of points at higher pressure is susceptible to the following simple explanation.

DISCUSSION

In the case of Xe-HBr mixtures, as shown by Fig. 5, the rate of decomposition of hydrogen bromide is proportional to the pressure of rare gas (and therefore, to the rate of energy absorption) only up to 385 mm. At higher pressures of rare gas, little further increase in decomposition rate is observed. We attribute this phenomenon to a high ion density, resulting in recapture of electrons by Xe^+ in competition with reaction 2. This explanation is substantiated by experiments with increased x-ray plate current, for instance one at 300 mm. Xe with a doubled plate current, which show that the yield is determined by the product: gas pressure times relative plate current (RPC), rather than by the gas pressure alone. Figure 5 also indicates that increased hydrogen bromide pressure in the anomalous region of pressure of rare gas also increases the yield. Therefore, we ignore the high-pressure region in computing the rate of hydrogen bromide decomposition and use the limiting slope indicated in the figure.

Since no significant ionization current measurements have been made on gas mixtures containing hydrogen bromide, it is necessary to estimate the contribution of added hydrogen bromide to the ion pair formation observed with the rare gas alone. While we may expect hydrogen bromide to absorb very nearly the same energy as an equal pressure of krypton, the efficiency of ion pair production will be different. Platzman[7] estimates that W_{HBr}^{β} is *ca* 26.5 ev/ion pair in comparison with $W_{Kr}^{\beta} = 24.1$ ev/ion pair. He also estimates, with considerable uncertainty, that the number of excited molecules is about equal to the number of ions in hydrogen bromide.

In mixtures containing only a small proportion of hydrogen bromide, it suffices to attribute to the hydrogen bromide itself an ion pair formation rate equal to that of krypton at the same partial pressure. This has been done in computing the ion pair yields of items 1, 2, and 3 in Table I. On the other hand, when hydrogen

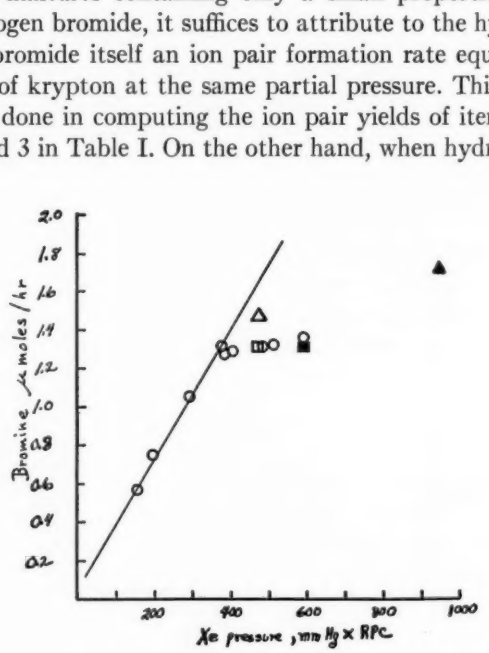

FIG. 5. ○ Rate of bromine production in xenon containing hydrogen bromide at 14.2 mm, x-ray plate current = 2.7 ma, except as noted. □ hydrogen bromide 21 mm, △ hydrogen bromide 42 mm, ■ plate current 5.4 ma. RPC = 2, ▲ plate current 8.1 ma RPC = 4.

[7] R. Platzman (private communication).

TABLE I. Ion pair yields in decomposition of HBr.

Item	HBr (mm Hg)	Rare gas (mm Hg)	M/N
1	14.2	A, 370–700	4.7
2	14.2	Kr, 385–700	4.0
3	14.2	Xe, 175–385	4.7
4	290–635	none	4.6
5	280–565	Xe, 10–20	5.2

bromide is the major component, as in items 4 and 5 of Table I, the correction indicated above must be applied in estimating the ion pair formation rate in hydrogen bromide from the measured rate in krypton.

All of the observed values of M/N are equal to or greater than 4.0, the value expected from the ion formation mechanism given in reactions 1–5. Eyring, Hirschfelder, and Taylor[3] also considered the possibility of formation of an ion such as H_2Br^+, but if this were formed and neutralized by Br^-, the ion pair yield would be 6.0, a value higher than any observed in this work. It seems more reasonable to adopt the mechanism giving an ion pair yield of 4.0 and to attribute the entire difference between this and the observed values to decomposition *via* excited molecules. Each such dissociation would lead to decomposition of one more hydrogen bromide molecule through reaction 4, and thus the ratio of excited (dissociating state) to ionized molecules of hydrogen bromide will be given by $N_x/N_+ = [(M/N)_{obs} - 4.0]/2$.

In pure hydrogen bromide, and in hydrogen bromide with a little added xenon (items 4 and 5), the values of M_x/N_+ are 0.3 and 0.6, respectively. If Platzman's estimate[7] that the number of excited molecules and ions are about equal in hydrogen bromide is used, these numbers indicate that 30 and 60 percent, respectively, of the excited molecules decompose. Considering the uncertainty of the estimates of the ionization-excitation properties of hydrogen bromide, these numbers seem to be of a reasonable magnitude, but an explanation of the difference between them, which is greater than the uncertainty in the experimental values, does not readily occur.

In considering the yields obtained in rare gases with small additions of hydrogen bromide, we assume that charge is completely transferred to hydrogen bromide, since the ionization potential of the latter is less than that of any of the three rare gases. Again we attribute the ion pair yields in excess of 4.0 to dissociation by excitation, with an added factor in this case for the

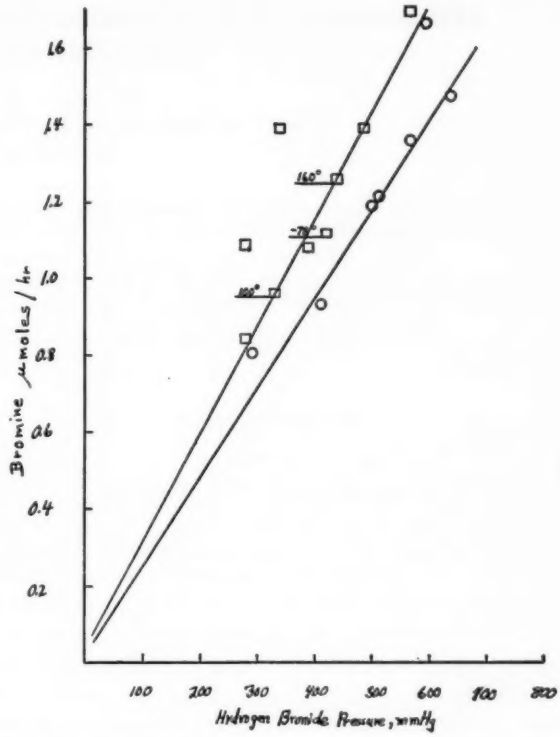

FIG. 6. (a) ○ Rate of bromine production in pure hydrogen bromide, (b) □ in hydrogen bromide containing 10–20 mm. Xenon, x-ray plate current = 2.7 ma.

efficiency of reaction 7. Information about the yield of excited atoms is fairly reliable in the rare gases and according to Platzman[7] the ratio N_x/N_+ is about 0.4 for all rare gases. Our ion pair yields in the A-HBr and Xe-HBr indicate that the efficiency of reaction 7 is about unity, but much smaller than unity for Kr-HBr.

It appears unlikely that the omission of quencher in the chemical runs has increased N by processes such as reaction 8, since this would indicate that the computed values in Table I are greater than the true ion pair yields. In the case of Kr-HBr the computed value is already as small as can be explained.

ACKNOWLEDGMENTS

This work was supported in part by the U. S. Atomic Energy Commission through Contract At(11–1)–38 and by U. S. Navy equipment loan contract Nonr-06900. We are indebted to Dr. Robert Platzman of Purdue University for his most helpful comments.

Measurement of the Chapman-Jouguet Pressure and Reaction Zone Length in a Detonating High Explosive

RUSSELL E. DUFF AND EDWIN HOUSTON
University of California, Los Alamos Scientific Laboratory, Los Alamos, New Mexico
(Received September 13, 1954)

The Chapman-Jouguet pressure and the reaction zone length in detonating Composition B containing 63 percent RDX at a density of 1.67 g/cc have been measured by determining the initial free surface velocity imparted to aluminum plates as a function of plate thickness. The *C-J* pressure is 0.272 megabar and the reaction zone length is 0.13 mm. The experimental free surface velocity-plate thickness curve provides powerful confirmation for the pressure profile in a detonating explosive predicted by the hydrodynamic theory of detonation proposed by Zeldovich, von Neumann, and Doring.

INTRODUCTION

IN 1945 Goranson[1] suggested that the reaction zone of a detonating solid explosive could be investigated by determining the initial free surface velocity imparted to thin metal plates as a function of plate thickness. In particular he showed that reaction zone length and Chapman-Jouguet pressure could be estimated in this way. Unfortunately, the original results obtained by Goranson are available only in a classified report from this laboratory. This paper describes similar but improved theoretical and experimental results obtained during and since 1950.

THEORY OF THE EXPERIMENT

The generally accepted picture of the structure of a steady-state, plane detonation wave was proposed independently by Zeldovich,[2] von Neumann,[3] and Döring.[4] The wave is assumed to consist of a nonreactive shock followed by a steady-state reaction zone which is terminated at the Chapman-Jouguet surface where the local flow velocity plus sound speed equals the detonation velocity. It can be shown that this condition is fulfilled at the point of tangency in the p-v plane of a straight line from the initial state to the final Hugoniot curve calculated for a fixed composition of the product gases.[5] Figure 1 shows a representation of the detonation process in the p-v plane. Reference to the laws of conservation of mass and momentum shows immediately that if viscosity and heat conduction are neglected, the succession of state points assumed by the reacting explosive is represented by the straight line from p_1v_1 to the *C-J* point. The rate at which an element of explosive passes from p_1v_1 to the *C-J* state depends on the kinetics of the reactions involved and cannot be determined from hydrodynamic considerations. It follows, therefore, that the pressure-distance profile of a detonation wave consists most probably of a monotone but otherwise unspecified decrease in pressure from p_1 to $p_{C\text{-}J}$ in an unspecified distance. Two profiles often considered are shown qualitatively in Fig. 2. They correspond to a reaction rate determined by grain burning and to a rate determined by a first or second order adiabatic reaction of the Arrhenius type. The unsteady flow behind the Chapman-Jouguet plane has been investigated by Taylor.[6] This flow may be simply described as a rarefaction wave ending either in cavitation or in a steady-state region required to match

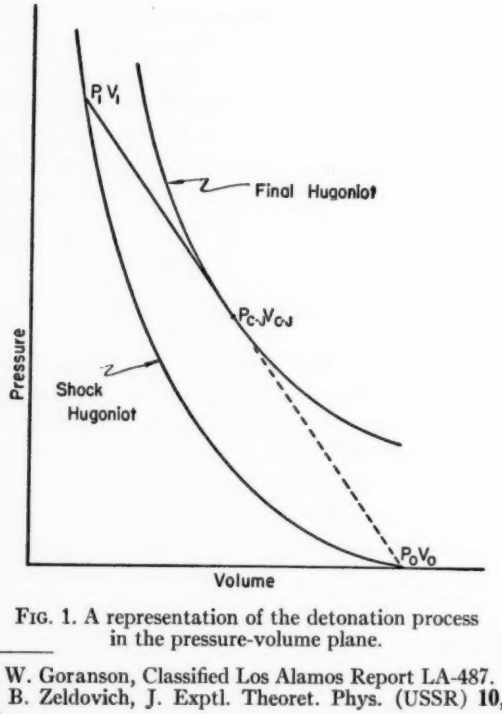

FIG. 1. A representation of the detonation process in the pressure-volume plane.

[1] R. W. Goranson, Classified Los Alamos Report LA-487.
[2] Y. B. Zeldovich, J. Exptl. Theoret. Phys. (USSR) **10**, 542 (1940).
[3] J. von Neumann, O.S.R.D. Report No. 549, (1942).
[4] W. Döring, Ann. Physik **43**, 421 (1943).
[5] More specifically, the *C-J* point is the tangent point on a Hugoniot curve for the product gases whose composition is assumed fixed at the equilibrium values appropriate for the tangent point. The relation of this statement of the Chapman-Jouguet condition to the usual statement, namely, that the *C-J* point is the tangent point on a Hugoniot every point of which is in chemical equilibrium, is not clear at the moment because of uncertainties in the equation of state of the detonation products. The former statement can be derived from a recent theoretical investigation of the structure of a steady-state plane detonation wave by Kirkwood and Wood, J. Chem. Phys. **22**, 1920 (1954). It should be mentioned that this statement of the *C-J* condition has been shown to apply to all detonations which are not pathological in the von Neumann sense. Finally, no pathological detonation has yet been observed.
[6] G. I. Taylor, Proc. Roy. Soc. (London) **A200**, 235 (1950).

boundary conditions at the back boundary of the explosive products.

When a plane detonation wave is incident normally on a metal plate, a shock wave is transmitted into the metal which is followed by a rarefaction wave corresponding to the pressure drop in the reaction zone of the explosive. The foot of this rarefaction wave will travel with a velocity equal to the sum of the local flow velocity and sound speed. It will overtake the shock in the metal after the shock has been attenuated by the rest of the rarefaction wave. The strength of the shock wave will decrease relatively quickly as this interaction proceeds because of the small thickness of the reaction zone. As a result, the velocity imparted to a thin metal plate, which depends directly on the strength of the shock in the plate, should change with plate thickness qualitatively as shown in Fig. 3.

It has been shown that to a very good approximation the shock particle velocity of a metal in the high

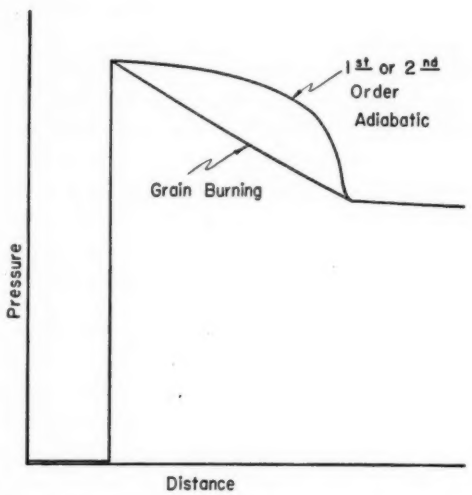

FIG. 2. Two representative pressure profiles for the reaction zone of solid explosives.

explosive pressure range is one-half of the free surface velocity.[7] This fact makes it possible to determine the Chapman-Jouguet pressure in the explosive from the free surface velocity of a metal plate corresponding to the end of the interaction caused by the reaction zone. This velocity is v in Fig. 3. An immediate consequence of the laws of conservation of mass and momentum is that the pressure behind a shock wave moving into a medium at rest is

$$p=\rho_0 uD, \tag{1}$$

where ρ_0 is the density of the unshocked material, u is the shock particle velocity, and D is the shock velocity. In all of the experiments discussed in the next section the metal used was aluminum or dural. For these materials Walsh[7] has determined experimentally a relation between shock velocity and free surface velocity

[7] J. M. Walsh and R. H. Christian, Phys. Rev. **97**, 1544 (1955).

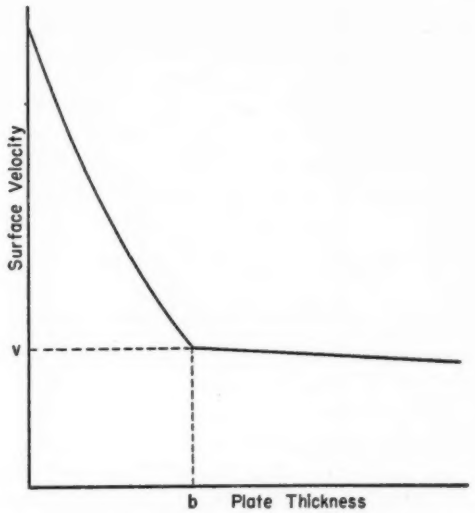

FIG. 3. Free surface velocity of a metal plate as a function of plate thickness showing the high velocity produced in thin plates by the von Neumann spike in the explosive.

in an investigation of the equation of state of the metals. The pressure in the metal can therefore be determined from the measured metal density, the free surface velocity, and this relation.

By applying the usual boundary conditions of equality of pressure and continuity of flow velocity at the interface between explosive and metal, the following expression can be developed relating incident pressure in the explosive to transmitted pressure in the metal:

$$\frac{p_m}{p_x}=\frac{\rho_2 D_2}{\rho_1 D_1}\left(\frac{\rho_1 D_1+\rho_3 D_3}{\rho_2 D_2+\rho_3 D_3}\right). \tag{2}$$

The subscripts 1, 2, and 3 refer to the properties of the undetonated explosive, the metal, and the explosive products, respectively. The pressure in the explosive, p_x, corresponding to the Chapman-Jouguet state can now be calculated if $\rho_3 D_3$ is known. An error analysis of this relation shows that

$$\frac{\delta p_x}{p_x}=\frac{(\rho_1 D_1-\rho_2 D_2)\rho_3 D_3}{(\rho_1 D_1+\rho_3 D_3)(\rho_2 D_2+\rho_3 D_3)}\frac{\delta(\rho_3 D_3)}{\rho_3 D_3}.$$

If the acoustic approximation is made that $\rho_1 D_1=\rho_3 D_3$ and values appropriate for Composition B (nominally 60 percent RDX−40 percent TNT) are inserted, then

$$\frac{\delta p_x}{p_x}=-0.1\frac{\delta(\rho_3 D_3)}{\rho_3 D_3}.$$

Thus it is clear that the Chapman-Jouguet pressure is quite insensitive to the value of $\rho_3 D_3$ assumed. Furthermore, the acoustic approximation is correct insofar as the velocity of the reflected shock can be assumed equal to the velocity of a rarefaction wave in the product

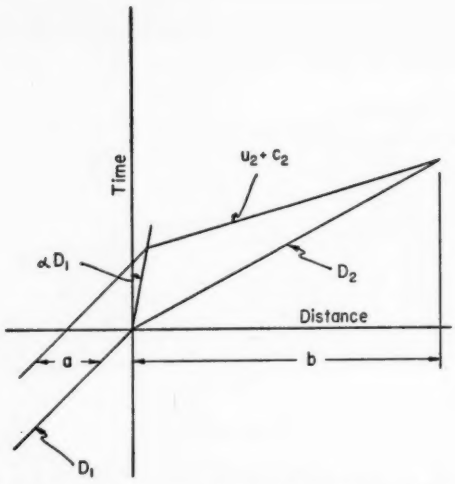

FIG. 4. Distance-time representation of the interactions between the von Neumann spike in the explosive and the metal plate.

gases. Therefore, to a good approximation

$$p_m/p_x=2\rho_2D_2/(\rho_1D_1+\rho_2D_2). \quad (3)$$

An estimate of the reaction zone length can be made from a determination of the distance required for the end of the rarefaction corresponding to the Chapman-Jouguet plane to overtake the shock wave in the metal. This distance is b in Fig. 3. If it is assumed that the metal is a perfect impedance match to the explosive so that no wave is reflected back into the explosive, an $x-t$ representation of the interaction will be as shown in Fig. 4. The interface is initially assumed to be at $x=0$. A detonation wave comes in from the left with a velocity D_1. The reaction zone length is a. The velocity of the interface through the reaction zone is αD_1, the shock velocity in the metal is D_2, and the velocity of the foot of the rarefaction wave is u_2+c_2. D_2 and α will vary as the interaction proceeds. The values used in the formula below and those indicated in Fig. 4 are the appropriate average values. As long as the flow behind the shock can be considered isentropic (a good approximation), u_2+c_2 depends only on pressure and is the value corresponding to the C-J state transmitted into the metal. Simple analytical geometry leads to the following relation between the reaction zone length in the explosive and the interaction distance in the metal:

$$a=b[D_1(u_2+c_2-D_2)(1-\alpha)][D_2(u_2+c_2-\alpha D_1)]^{-1}. \quad (4)$$

The appropriate average value of D_2 can be determined from the free surface velocity-plate thickness relation since at every value of thickness this relation gives the corresponding shock velocity by using the equation of state. It can easily be seen that the appropriate average to be used in the above equation is the inverse average; i.e.,

$$D_2=\left(\frac{1}{b}\int_0^b \frac{dx}{D(x)}\right)^{-1}. \quad (5)$$

Likewise α should be determined from a similar inverse average of the interface velocity.

It is possible to calculate in detail the free surface velocity as a function of plate thickness by using the procedure outlined by Courant and Friedrichs[8] under the assumption mentioned above; namely, that the flow behind the shock can be considered isentropic. In particular, if the reaction zone rarefaction and the Taylor wave are both assumed to be centered rarefaction waves, and if a ratio of explosive charge length and reaction zone length is assumed, the ratio of slopes of the free surface velocity-thickness curve for the two waves at the point corresponding to the end of the reaction zone can be calculated. This ratio is about 25 if the charge length is 200 times the reaction zone length and if the spike pressure is 1.5 times the Chapman-Jouguet pressure. In practical cases the ratio of charge length to reaction zone length is much greater than 200 so the change of slope would be even larger than indicated above. This calculation justifies the sharp change in slope of the free surface velocity-plate thickness curve shown in Fig. 3.

It should be remembered that it was assumed in this calculation that the reaction zone rarefaction could be approximated by a centered rarefaction wave. However, most reaction rate expressions show that equilibrium is approached asymptotically in time. If such expressions are appropriate for solid explosives, and there is no experimental evidence that they are, the ratio of slopes could conceivably approach unity. However, the long reaction tail predicted by these kinetic expressions corresponds to a very small percentage of the total detonation reaction, and a rapid rate of change of slope would be expected not at a plate thickness corresponding to the C-J state but at a thinner one, corresponding to essentially complete reaction.

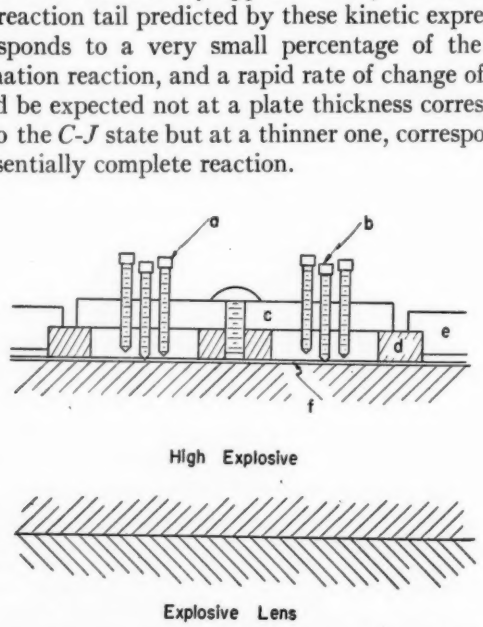

FIG. 5. Cross section of an experiment to determine the free surface velocity of a very thin plate or foil. (a) 0–80 pointed steel screws used as surface velocity pins. (b) Center ground contact pin also used to hold foil against the high explosive. (c) Texalite pin mounting plate. (d) Aluminum backing plate $3\frac{1}{4}$ in. o.d., $\frac{1}{4}$ in. thick. (e) Blast shield 8 in. o.d., $\frac{3}{8}$ in. thick. (f) Aluminum foil.

[8] R. Courant and K. O. Friedrichs, *Supersonic Flow and Shock Waves* (Interscience Publishers, Inc., New York, 1948), p. 164.

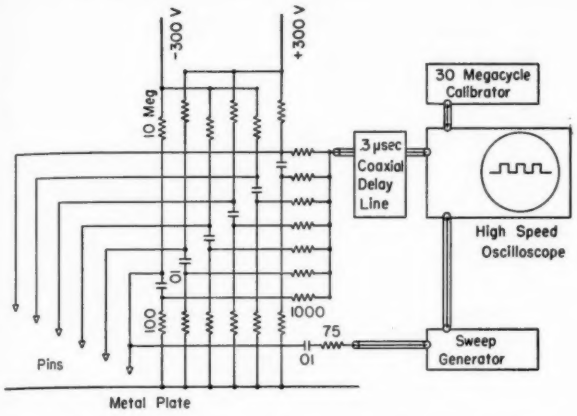

FIG. 6. Electronic circuitry used to measure free surface velocity. The component values are the same for all circuits. Resistance values are ohms and capacitor values μfd unless otherwise indicated.

EXPERIMENTAL TECHNIQUE

Free surface velocity was measured by recording the time of arrival of the metal surface at a series of metal contactors or pins. The technique used is identical with that described by Minshall.[9] In these experiments two or in some cases four velocity measurements were made in each experiment by using either two or four groups of pins each consisting of six pins set in a $\frac{1}{4}$-in. diameter circle. The spacing between pins measured perpendicular to the free surface was 0.003 in. for the thin plates 0.030 in. thick and under, and 0.006 in. for all thicker plates. A cross section through a thin foil experiment is shown in Fig. 5.

The electronic circuitry used is indicated in Fig. 6. As each pin is shorted to the moving plate, a condenser is discharged through the network producing a signal on the oscilloscope. Successive pins have alternate polarities so that an ideal record would resemble the square wave indicated in the figure. A time base is provided by a trace from an accurately calibrated 30-megacycle crystal oscillator displaced slightly from the velocity record.

The high-speed recording oscilloscopes used in these experiments were similar to the system described by the Radiation Laboratory.[10] A sweep speed of 10 in./μsec was used and twenty thousand volts post acceleration was required in order to obtain single traces intense enough to photograph clearly at this high writing speed.

A photograph of a setup ready to be used is shown in Fig. 7. The pulse-forming networks are sealed in the plastic blocks located near each pin group.

Precautions were necessary to eliminate two possible sources of error. The shock wave in air preceding the free surface was strong enough to discharge the pin circuits before the arrival of the surface. This difficulty was eliminated by maintaining a methane atmosphere around the pins. If velocity measurements were made on a machined and polished surface, the first several pins were often discharged prematurely by what appeared to be a fine spray of metal jetted out from the surface. This spray was eliminated by using unworked surfaces whenever possible and covering the surface with a very thin, almost invisible coating of light oil.

EXPERIMENTAL RESULTS

Experimental Data

Thirty-three separate experiments were performed in which eighty-seven measurements of free surface velocity were made. In the first twelve of the experiments the metal used was dural and the remainder pure aluminum was used. Walsh[7] has shown that the particle velocity-shock velocity relationship is identical within experimental error for both metals. The explosive was Composition B which was cast into large blocks and then machined into pieces $5\frac{1}{2}$ in.$\times 5\frac{1}{2}$ in.$\times 3$ in. The composition and density of the explosive varied by roughly 2 percent RDX and 0.01 g/cc from charge to charge and within a given charge. These charges were prepared in 1950 and are not of as high a quality as those prepared currently.

All of the experimental results were corrected to the following standard conditions: metal density$=2.71$ g/cc; explosive density 1.67 g/cc; explosive composition 63 percent RDX; and detonation velocity 7.868 mm/μsec. The following error expression was used in this correction:

$$\delta u_2/u_2 = -0.861\delta\rho_1 - 0.0023\delta \text{ percent RDX} + 0.192\delta\rho_2.$$

In most cases the corrections made velocity changes of less than 1 percent. A random error of $1\frac{1}{2}$ percent is

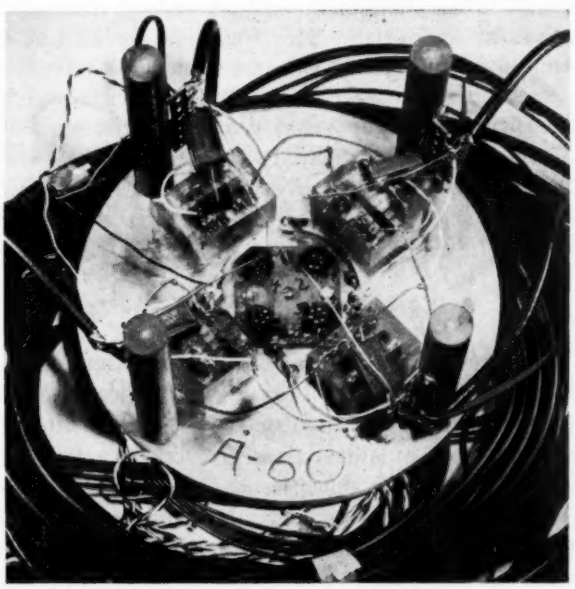

FIG. 7. A photograph of an experiment ready to be fired.

[9] F. S. Minshall, J. Appl. Phys. **26**, 463 (1955).
[10] M.I.T. Radiation Laboratory Report No. 1001 (1946).

caused by the composition and density fluctuations within a given charge. The average values of the velocities measured are presented in Table I. These data are also presented in Fig. 8.

Two subjects deserve comment before conclusions are drawn from this data. First, the standard deviations reported in Table I are unfortunately large. However, this large standard deviation arises mainly from a systematic source. As discussed above, velocities are determined from measurements of position and time of the metal free surface by means of pins set in a circle. If the metal surface is not perfectly plane and if it does not move perfectly parallel to its initial position, a systematic error in the arrival time of the surface at each pin will be introduced which may be reflected into the surface velocity as determined by least squares techniques. It can be shown that the velocity calculated is related to the true velocity as follows:

$$V = V_{\text{calc}}\left(1+\frac{R\alpha}{d}\epsilon\sin\theta\right),$$

where R is the radius of the pin circle, d is the incremental pin spacing, α is the angle of tilt of the surface, ϵ is a constant $=0.11$ for the pin geometry used in these experiments, and θ is an angle which describes the orientation of the pin circle with respect to the tilted wave. A wave tilt of as much as 0.03 radian was observed for some of the charges used. Therefore, this cause alone could produce a velocity error of 15 percent in plates 0.030 in. thick or thinner and $7\frac{1}{2}$ percent for thicker plates. For this reason many measurements were made, especially on the thinner plates, so as to obtain a reliable value for the average velocity.

Second, it is desirable to place all of the pins close enough to the free surface so that the velocity measurement can be completed before a second disturbance arrives at the surface. This was done for all but the thinnest foil. One might expect a weak shock wave to be the second disturbance to arrive at the surface giving it a small increase in velocity at about the middle of the velocity measurement. Examination of the records does not indicate a noticeable increase in velocity. However, the velocity associated with the 0.0085 in. foil may be slightly high.

Explosive Pressure

Two pressures in the explosive can be estimated from the surface velocity plot of Fig. 8. A least squares straight line has been fitted to the experimental measurements at thicknesses greater than 0.030 in. Each of the average velocities was given a weight equal to the number of measurements included. A smooth curve was drawn through the remaining four measurements on thin plates. The Chapman-Jouguet pressure can be determined from the free surface velocity

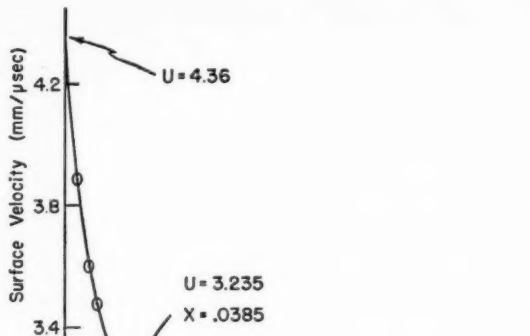

FIG. 8. Measured free surface velocity as a function of plate thickness.

indicated by the intersection of these two lines, 3.235 mm/μsec.

In the metal[11]

$$p_m=\rho_2 u_2 D_2$$

$$=2.71\times\frac{3.235}{2}\times 7.55=0.3309 \text{ megabar.}$$

In the explosive

$$p_{C\text{-}J}=\frac{p_m(\rho_1 D_1+\rho_2 D_2)}{\rho_2 D_2}=0.272 \text{ megabar.}$$

Thus the Chapman-Jouguet pressure in Composition B explosive containing 63 percent RDX at a density of 1.67 g/cc is 0.272 megabar. This number is thought to be correct to within 2 percent.

The extrapolation of the free surface velocity to zero plate thickness in what is thought to be a reasonable manner gives a limiting velocity of 4.36 mm/μsec. From this number and the extrapolation of the equation of state data for aluminum made by Fickett, a peak pressure in the explosive of 0.385 megabar is estimated for the von Neumann spike. It is interesting to note that the spike pressure appears to be only 1.42 the Chapman-Jouguet pressure. It should be emphasized that the extrapolation to zero thickness is only what appears to be a reasonable one. There is no theoretical justification for the assumed form of the curve because the form

[11] The equation of state data of Walsh, see reference 7, has been analyzed by Fickett (unpublished communication). An analytic form of the equation of state was derived which agreed with Walsh's data at low pressures and with Fermi-Thomas-Dirac calculations at high pressures. The following fit of shock velocity as a function of free surface velocity is appropriate for the pressure range of interest in these experiments:

$$D=4.8375+1.1235u-0.1095u^2+0.0066u^3.$$

depends on the details of the chemical kinetics of the detonation reaction about which essentially nothing is known.

Reaction Zone Length

The reaction zone length was calculated from Eq. (4) using a value of D_2 determined from the experimental results as required by Eq. (5). α was determined from the two values of interface velocity which could be estimated from the experimental data, namely, the initial and final values. The assumption was made that the interface velocity changed with distance in the same way the shock velocity did. A value of u_2+c_2 was obtained from the equation of state calculation for aluminum made by Fickett. The actual numbers used are as follows: $D_1=7.868$, $D_2=7.771$, $u_2+c_2=9.065$ mm/μsec, and $\alpha=0.232$; giving $a/b=0.139$. b was estimated to be 0.0385 in. Therefore, $a=0.005$ in. or 0.13 mm. This estimate of reaction zone length of slightly greater than one-tenth of a millimeter is probably accurate to within 20 percent except for the possible errors discussed below.

Two assumptions have been made in the estimation of reaction zone length. First the shock wave reflected from the metal back into the explosive has been ignored. This assumption is questionable because the changes in temperature and pressure caused by the wave may decisively influence the kinetics in the as yet unreacted explosive into which it moves. Therefore, the value of reaction zone length determined is probably best described as a lower limit value.

The effect of this reflected shock wave on the detonation kinetics and reaction zone length could be investigated by varying the metal used in experiments of this type. In particular, the effect could be maximized by using a heavy material like brass which has a large acoustic impedance and minimized by using magnesium which is almost a perfect impedance match for Composition B.

The second assumption concerns the shape of the reaction zone. The experimental results have been represented by a profile similar to that of a rarefaction wave in an inert material. However, as discussed above, there could be a slow reaction tail which would cause true reaction zone length to be somewhat longer than that indicated.

TABLE I. Measured free surface velocity as a function of plate thickness.

Plate thickness (in.)	Average velocity (mm/μsec)	Standard deviation of the mean (mm/μsec)	Number of measurements
0.0085	3.89	0.34	12
0.016	3.60	0.26	15
0.021	3.48	0.25	11
0.030	3.32	0.10	11
0.048	3.20	0.20	10
0.057	3.22	0.02	2
0.098	3.25	0.09	8
0.150	3.04	0.06	4
0.198	3.11	0.07	6
0.248	3.01	0.09	4
0.300	3.02	0.04	4

CONCLUSIONS

A conclusion can be drawn from the data presented above which is fundamental to the understanding of the detonation phenomenon. Namely, the experimental results provide powerful confirmation for the hydrodynamic theory of the detonation process proposed by Zeldovich, von Neumann, and Döring. In fact, this is thought to be the first experimental evidence published which directly verifies this theory which has, however, attained almost universal acceptance because of its hydrodynamic completeness.

The Chapman-Jouguet pressure in Composition B explosive containing 63 percent RDX at a density of 1.67 g/cc was measured to be 0.272 megabar. The reaction zone length for the same explosive is 0.13 mm.

ACKNOWLEDGMENTS

The authors are indebted to many people for assistance in various phases of this work. In particular, we are happy to acknowledge the help of the following individuals: R. Holbrook, E. Gittings, R. E. Faudree, and V. Thurlow for assistance in the actual performance of the experiments; C. L. Miller for the preparation of the many explosive charges used; C. W. Mautz for the derivation of Eq. (4); and W. W. Wood for many valuable discussions of the theoretical problems involved and also for making the detailed calculation of the attenuation of a shock wave in metal by a centered simple rarefaction wave.

Conductances of Trimethylphenylammonium Chloride and Iodide in Water and in Dimethylformamide at 25°C*

PAUL G. SEARS, EUGENE D. WILHOIT, AND LYLE R. DAWSON
Department of Chemistry, University of Kentucky, Lexington, Kentucky

(Received September 7, 1954)

The conductances of trimethylphenylammonium chloride and iodide in water and in dimethylformamide have been measured at 25°C. Solute concentrations ranged from 0.6 to $30\times10^{-4}N$. Limiting equivalent conductances for the salts in both solvents have been evaluated by the Shedlovsky extrapolation method. Trimethylphenylammonium chloride and iodide are more conducting but only slightly more highly dissociated in water than in dimethylformamide. A possible explanation for the reversal of the magnitude of the conductance of the iodide and the chloride ions in very dilute solutions in these two solvents is given.

OWING to the fact that dimethylformamide has a dielectric constant of only 37.6 compared to 78.54 for water at 25°C, it would be expected that electrolytes would be dissociated to a lesser extent in dimethylformamide than in water. However, in a previous paper from this Laboratory,[1] conductance measurements have been reported indicating that many potassium and sodium salts, which are known to be completely dissociated in dilute aqueous solutions, are completely dissociated also in dimethylformamide at concentrations less than $2\times10^{-3}N$. These unexpected results seemed to warrant a comparison of the conductimetric behavior of quaternary ammonium salts in these two solvents. Trimethylphenylammonium chloride and iodide were selected for such a comparative study because their conductances had not been measured previously in either water or dimethylformamide.

EXPERIMENTAL

Dimethylformamide was fractionated at atmospheric pressure and then redistilled at 10 mm pressure. The middle fraction, which was retained, had a conductivity of 1.5×10^{-7} ohm^{-1} cm^{-1}. Distilled water from a stock supply having a conductivity of 1×10^{-6} ohm^{-1} cm^{-1} was used without further purification. Trimethylphenylammonium chloride and iodide obtained from Distillation Products Industries were recrystallized three times from suitable solvents and dried to constant weight in a vacuum oven at 60°C.

Resistances were measured with a Jones bridge assembly at a frequency of 1000 cycles per second. Frequently, resistance measurements were made also at 500 and 2000 cycles per second; however, no significant frequency dependence for resistance was found. Resistances greater than 30 000 ohms were measured in parallel with 30 000 ohms of shunted bridge resistance, and the series cell resistances were computed from the values measured in parallel.

Three flask cells with lightly platinized electrodes, similar to those designed by Daggett, Bair, and Kraus,[2] were employed in the measurements. The cell constants of 0.4204, 0.4224, and 0.4443 cm^{-1} were determined through the intercomparison of these with two Jones cells having constants of 1.0312 and 1.0606 cm^{-1} which were evaluated by the method of Jones and Bradshaw.[3] All measurements were carried out in an oil-filled thermostat at 25.00±0.01°C.

Although adsorption effects caused the resistance of the more dilute solutions to decrease slightly with time, in some cases as much as 0.3 percent even though temperature equilibrium had been established, it was found that the measured resistance was reproducible if the immersed cells were manually manipulated in a manner so as to change the solution between the electrodes immediately prior to each measurement. A mean value of the resistance based upon three or four determinations, each of which was made after changing the solution between the electrodes, was used in calculating the conductivity of each solution.

The weight dilution method was used for the preparation of the solutions in the flask cells. Friedman-LaMer weighing pipettes were employed for the transfer of the stock solutions into the cells. Necessary precautions was taken to protect the dimethylformamide solutions from appreciable atmospheric contamination. In calculating concentrations on a volume basis, it was assumed that the densities of the solutions were equal to that of the solvent. All weights were corrected to vacuum. The conductivity of a salt was obtained by subtracting the conductivity of the solvent from that of the solution.

The following data for the solvents at 25°C were used in the calculations: water—dielectric constant, 78.54[4]; viscosity, 8.902×10^{-3} poise[5,6]; density, 0.9971 g/ml dimethylformamide—dielectric constant, 36.71[7]; viscosity, 7.96×10^{-3} poise[1]; density, 0.9443 g/ml.[1] The

* Based in part upon research performed under a contract with the U. S. Army Signal Corps.

[1] D. P. Ames and P. G. Sears, J. Chem. Phys. **59**, 16 (1955).
[2] Daggett, Bair, and Kraus, J. Am. Chem. Soc. **73**, 799 (1951).
[3] G. Jones and B. C. Bradshaw, J. Am. Chem. Soc. **55**, 1780 (1933).
[4] A. A. Maryott and E. R. Smith, Natl. Bur. Standards Circular 514, August 10, 1951.
[5] J. R. Coe and T. B. Godfrey, J. Appl. Phys. **15**, 625 (1944).
[6] Swindels, Coe, and Godfrey, J. Research Natl. Bur. Standards, **48**, 1 (1952).
[7] G. R. Leader and J. F. Gormley, J. Am. Chem. Soc. **73**, 5731 (1951).

values of the fundamental constants were taken from the latest report by the Subcommittee on Fundamental Constants.[8]

RESULTS

Values of the equivalent conductance, Λ, and the concentration in gram-equivalents per liter, C, are presented in Tables I and II for the salts in water and in dimethylformamide. These results represent two independent series of conductance measurements for each salt in each solvent.

Figure 1 shows plots of Λ *versus* $\sqrt{C}$ for the systems studied. The observed and theoretical Onsager slopes of the plots for the salts in water agree within approximately one percent. Consequently, the Shedlovsky rearrangement of the Onsager equation[9] was particularly useful for calculating the limiting equivalent conductance directly from the individual Λ values. The calculated values, designated by Λ_0', have been included in Table I. The mean calculated values of Λ_0 for trimethylphenylammonium chloride and iodide in water were found to be 111.0 and 111.5 ohm^{-1} cm^2 equiv.$^{-1}$, respectively. Examination of the data in Table I reveals that for each salt the maximum deviation of Λ_0' from the mean remained within the estimated experimental error of 0.2 percent. McDowell and Kraus[10] have reported that the limiting equivalent conductance of trimethylphenylammonium bromide is 112.8 ohm^{-1} cm^2 equiv.$^{-1}$ at 25°C, from which they calculated the limiting ionic conductance of the trimethylphenylammonium ion as 34.3 ohm^{-1} cm^2 equiv.$^{-1}$. Adding their value of the limiting ionic conductance of this ion to each of the presently accepted values for the limiting ionic conductances of the chloride and iodide ions,[11] one obtains 110.8 and 111.3 ohm^{-1} cm^2 equiv.$^{-1}$ as the limiting equivalent conductances of trimethylphenylammonium chloride and iodide, respectively, in water. Our values deviate from these by less than 0.2 percent which is within the limits of the estimated experimental error.

Taking into consideration now the conductance of these quarternary ammonium salts in dimethylformamide, it should be pointed out first that the differences between the limiting experimental slope and the Onsager slope of the Λ *versus* $\sqrt{C}$ plots were found to be approximately 51 and 8 percent, respectively, for trimethylphenylammonium chloride and iodide. The more negative experimental slopes are evidence of some association of the ions of the solutes in dimethylformamide, and for this reason the conductance data were analyzed by the Shedlovsky extrapolation method.[12] Plots of $S\Lambda$ *versus* $Cf^2S^2\Lambda^2$ may be observed in Fig. 2. Limiting equivalent conductances, obtained by extrapolations by the method of least squares, were found to be 86.9 and 84.2 ohm^{-1} cm^2 equiv.$^{-1}$, respectively, for trimethylphenylammonium chloride and iodide. From the values of Λ_0 and the slopes, the respective dissociation constants were calculated to be 0.02 and 0.1; however, it should be emphasized that dissociation constants of this magnitude, which are based on conductance measurements, may be subject to appreciable error. The conductance data for the salts in water were treated also by the Shedlovsky extrapolation method. The plots of $S\Lambda$ *versus* $Cf^2S^2\Lambda^2$ for the salts in water may be observed also in Fig. 2. The Λ_0 values determined by this method were identical with the mean Λ_0' values previously discussed. Within possible experimental uncertainties, both trimethylphenyl-

TABLE I. Conductance of trimethylphenylammonium chloride and iodide in water at 25°C.

(a) Trimethylphenylammonium chloride			(b) Trimethylphenylammonium iodide		
$C\times10^4$	Λ	Λ_0'	$C\times10^4$	Λ	Λ_0'
1.288	110.1	111.1	1.080	110.7	111.6
1.298	110.0	111.0	1.596	110.4	111.5
1.391	110.0	111.0	2.241	110.2	111.5
3.016	109.4	110.8	2.694	110.2	111.6
3.370	109.3	110.9	3.121	110.0	111.5
3.624	109.3	110.9	4.108	109.8	111.5
6.509	108.8	110.9	6.078	109.5	111.6
7.047	108.7	111.0	6.581	109.4	111.6
7.627	108.6	111.0	7.295	109.3	111.6
12.16	107.9	110.9	10.37	108.7	111.4
13.24	107.8	110.9	11.24	108.6	111.5
13.60	107.7	110.8	11.60	108.6	111.6
19.65	107.1	110.9	14.87	108.2	111.5
21.00	107.0	111.0	16.34	108.1	111.5
21.39	107.0	111.0	16.44	108.0	111.5
28.77	106.4	111.1	21.11	107.6	111.6
31.71	106.2	111.0	24.40	107.2	111.5
31.83	106.1	110.9	25.00	107.2	111.5

TABLE II. Conductance of trimethylphenylammonium chloride and iodide in dimethylformamide at 25°C.

(a) Trimethylphenylammonium chloride		(b) Trimethylphenylammonium iodide	
$C\times10^4$	Λ	$C\times10^4$	Λ
0.598	85.3	0.678	82.9
0.881	85.1	0.751	82.8
0.966	84.8	1.241	82.5
1.800	84.0	1.784	82.1
2.133	83.8	2.933	81.4
3.642	82.5	3.298	81.3
3.982	82.3	5.248	80.5
5.935	80.9	5.376	80.3
5.959	80.9	7.337	79.6
9.439	79.0	7.919	79.5
9.754	78.9	10.05	78.7
13.79	77.0	10.71	78.7
16.20	76.1	13.92	77.8
19.31	74.9	16.04	77.5
21.73	74.1	18.12	76.9
23.37	73.6	21.64	76.4

[8] F. D. Rossini *et al.*, J. Am. Chem. Soc. **74**, 2699 (1952).
[9] T. Shedlovsky, J. Am. Chem. Soc. **54**, 1405 (1932).
[10] M. J. McDowell and C. A. Kraus, J. Am. Chem. Soc. **73**, 2173 (1951).
[11] H. S. Harned and B. B. Owen, *The Physical Chemistry of Electrolytic Solutions* ACS Monograph Series No. 95 (Reinhold Publishing Corporation, New York, 1943).
[12] T. Shedlovsky, J. Franklin Inst. **225**, 739 (1938).

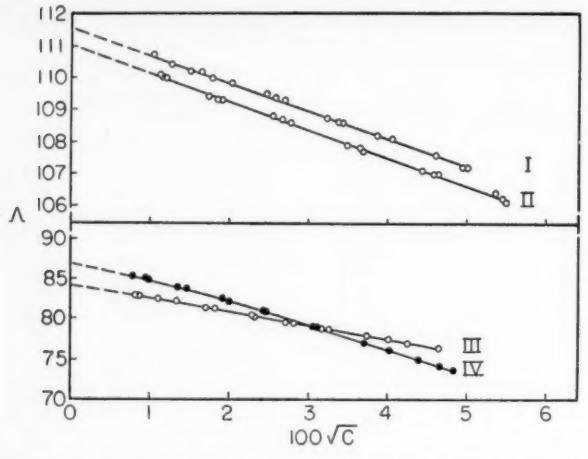

FIG. 1. Kohlrausch plots for trimethylphenylammonium salts at 25°: I-iodide in water; II-chloride in water; III-iodide in DMF; IV-chloride in DMF.

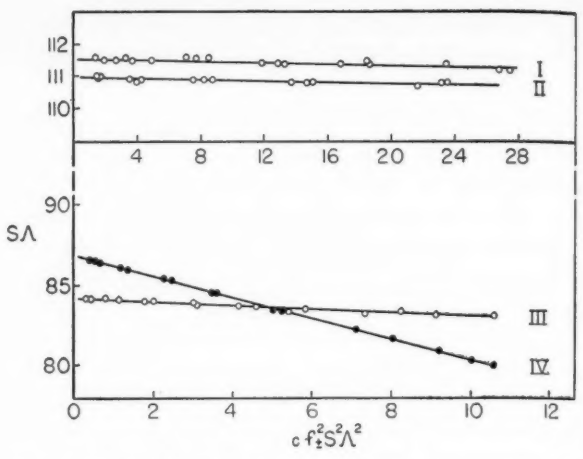

FIG. 2. Shedlovsky plots for trimethylphenylammonium salts at 25°: I-iodide in water; II-chloride in water; III-iodide in DMF; IV-chloride in DMF.

ammonium chloride and iodide in dilute aqueous solutions were found to be completely dissociated. Hence, the experimental evidence indicates that the quaternary salts studied are somewhat more highly dissociated in water than in dimethylformamide. Probably this behavior is a consequence of the higher dielectric constant of water.

Although dimethylformamide is less viscous than water, salts are less conducting in it than in water. Whether this results from larger effective sizes of the solvodynamic units in dimethylformamide or for some other reasons is unknown. As in most other organic solvents, the limiting equivalent conductance-viscosity product in dimethylformamide is equal to 0.65–0.70.

It may be observed also from Figs. 1 and 2 that at low concentrations the chloride is more conducting than the iodide in dimethylformamide, whereas it is less conducting in water. If it is assumed that in dilute solutions the cation has a constant ionic conductance irrespective of the anion, these results can be explained on the basis of the relative sizes of the anions in each of the two solvents. Because of the greater charge density of the chloride ion it would induce more ion-dipole attraction producing an ion-dipole entity which in water is larger than the solvodynamic unit having the iodide ion at the center. Similarly in dimethylformamide electrostatic solvation alone would make the chloride ion larger, and less conducting, than the iodide. Since in this solvent the conductance is in the reverse order, the comparative effects of chemical interaction between the solute and solvent must be considered. Whereas the solvation of the chloride ion in any medium probably occurs by electrostatic mechanisms only, the solvation of the iodide may occur by either electrostatic (physical) or acid-base (chemical) mechanisms, or by both. Owing to the fact that dimethylformamide is more basic than water[13,14] and that the iodide ion can function as a Lewis acid,[15] it seems probable that Lewis acid-base reactions proceed to a much greater extent in the organic solvent. The combined effects of both types of solvation of the iodide ion make it larger, hence less mobile, than the chloride ion in dimethylformamide.

[13] Pifer, Wollish, and Schmall, J. Am. Pharm. Assoc. Sci. Ed. **42**, 509 (1953).
[14] J. S. Fritz, Anal. Chem. **25**, 179 (1953).
[15] R. B. Sandin, Chem. Revs. **32**, 249 (1953).

Infrared Spectra of Liquid Anhydrous Hydrogen Fluoride, Liquid Sulfur Dioxide, and Hydrogen Fluoride-Sulfur Dioxide Solutions

ROBERT H. MAYBURY,* SHEFFIELD GORDON, AND JOSEPH J. KATZ
Chemistry Division, Argonne National Laboratory, Lemont, Illinois
(Received October 5, 1954)

The infrared spectra of anhydrous liquid hydrogen fluoride, anhydrous liquid sulfur dioxide and mixtures of the two have been measured in the region from 1μ to 25μ. A value for the extinction coefficient for the polymer peak in the region higher than previously reported has been found, reflecting the existence of a greater proportion of higher hydrogen fluoride polymers in the liquid as compared with the gas. A study of the change in the spectra of solutions of varying concentration of anhydrous liquid hydrogen fluoride in anhydrous liquid sulfur dioxide has been made and its possible relation to the structure of the polymers in liquid hydrogen fluoride examined. The possible applicability of obtaining spectra of protein dissolved in anhydrous liquid mixtures of hydrogen fluoride and sulfur dioxide has been explored and a spectrum of silk fibroin in this solvent is presented.

INTRODUCTION

HYDROGEN fluoride, in both the gaseous and liquid state, has long been known to be complex in structure; numerous physical properties indicate a very considerable degree of association for both the gas and the liquid.[1] Among other methods, infrared spectroscopy has been applied to the question of the structure of hydrogen fluoride. For the gas, distinct regions of absorption in the infrared can be recognized for the monomer and polymer forms, respectively, and the existing data in the literature for the gas, while not entirely free from anomalies, is both extensive are varied.[2,3] The situation with respect to the liquid is less satisfactory, the only previous work on the infrared absorption spectrum of liquid hydrogen fluoride being that of Safari[4] who examined the infrared spectrum in the region 0.95 to 4.25μ. We have been able to examine the infrared spectrum of anhydrous liquid hydrogen fluoride in the region from 1 to 25μ, and have also been able to make a study of hydrogen fluoride dissolved in liquid sulfur dioxide as a function of hydrogen fluoride concentration. These results bridge the gap between the pure liquid, where maximum association of the hydrogen fluoride is found, and the observation of Buswell, Maycock, and Rodebush[3] on dilute solutions of hydrogen fluoride in carbon tetrachloride where monomeric hydrogen fluoride predominates.

In the course of this work, we have made a number of incidental observations; among these are the infrared spectrum of liquid sulfur dioxide, which does not appear to have been reported earlier, and the infrared spectrum of the HF_2^- (solvated) ion in hydrogen fluoride solution.

EXPERIMENTAL

All measurements were made on a Perkin-Elmer, Model 21, double beam recording infrared spectrophotometer. Calcium fluoride optics were used in the range 10 000 cm^{-1} to 1200 cm^{-1}, sodium chloride from 4000 cm^{-1} to 700 cm^{-1}, and potassium bromide in the region 1000 cm^{-1} to 400 cm^{-1}.

The cell was constructed of nickel with silver chloride windows which were found to be very satisfactorily resistant for the substances studied here. The path length was adjustable by the use of platinum shims from 6μ to 1 mm. The path length was ascertained by two methods: (a) by counting interference fringes produced by the infrared radiation,[5] and (b) by using liquids of known absorption coefficients such as benzene. All infrared measurements were carried out at room temperature. The cell was filled by being attached to a conventional all-metal hydrogen fluoride high-vacuum line[6] and distilling hydrogen fluoride and sulfur dioxide into the cell. A detailed description of the infrared absorption cell used in this work is given elsewhere.[7]

Hydrogen fluoride was obtained from the Pennsylvania Salt Manufacturing Company. It was purified by trap-to-trap distillation and by treatment with cobaltic fluoride, CoF_3, which effectively serves to fluorinate traces of water which might be present. Sulfur dioxide was obtained from the Ohio Chemical and Surgical Equipment Company and was purified by trap-to-trap distillation. Other reagents were of standard laboratory quality.

INFRARED SPECTRUM OF LIQUID HYDROGEN FLUORIDE

The infrared absorption spectrum of liquid hydrogen fluoride from 1 to 25μ (10 000 cm^{-1} to 400 cm^{-1}) is shown in Fig. 1. Our results are in agreement with Safari[4] only in regard to the location of the maxima at

* Present address, University of Redlands, Redlands, California.

[1] J. H. Simons in *Fluorine Chemistry* (Academic Press, Inc., New York, 1950), Vol. I, pp. 225–256.

[2] R. D. Shelton and A. H. Nielsen, J. Chem. Phys. **19**, 1312–1313 (1951).

[3] Buswell, Maycock, and Rodebush, J. Chem. Phys. **8**, 362 (1940).

[4] E. Safari, Ann. phys. **9**, 203–254 (1954).

[5] D. C. Smith and E. C. Miller, J. Opt. Soc. Am. **34**, 130 (1944).

[6] Adams, Bernstein, and Katz, J. Chem. Phys. **22**, 13–21 (1954).

[7] Maybury, Katz, and Gordon, Rev. Sci. Instr. **25**, 1135 (1954)

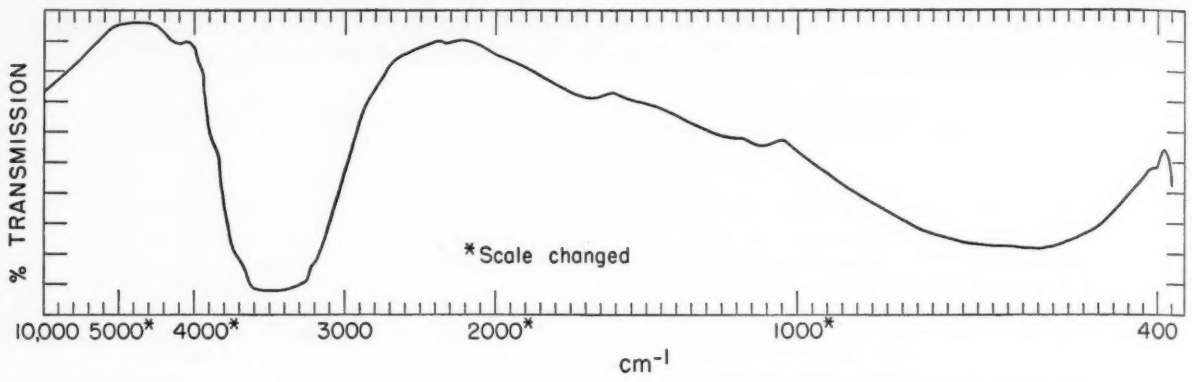

FIG. 1. Infrared spectrum of liquid hydrogen fluoride from 10 000 cm^{-1} to 400 cm^{-1}. Cell thickness 6μ. * indicates scale change.

4100 cm^{-1} and at 3450 cm^{-1}. Safari reported a value of 20 for the absorption coefficient of the polymer peak in the liquid, considerably less than the value of 50 found for the vapor; this proved difficult to explain. Since Safari used a cell width of 30μ, it is apparent that his measurement was carried out at practically complete absorption between 3000 and 3600 cm^{-1}; we also feel that there is a possibility that Safari's cells were not completely filled with liquid. We found it necessary to use a cell width of 6μ in order to observe the entire peak for which we calculate a value of 77 for the absorption coefficient; this reflects the existence of a greater proportion of higher hydrogen fluoride polymers in the liquid as compared with the gas, as would be expected. The broad absorption band between 1000 and 400 cm^{-1} compares with a similar broad region of absorption found in liquid water[8] which is attributable to absorption arising from intermolecular interactions. It is interesting to note that whereas in water this region of absorption is found only in the spectrum of the liquid, in hydrogen fluoride it is found in the spectra of both the liquid and the gas. This is in agreement with the view that both phases are associated to a similar degree only in hydrogen fluoride.

INFRARED SPECTRUM OF LIQUID SULFUR DIOXIDE

The infrared spectrum of liquid sulfur dioxide is shown in Fig. 2. The complete agreement found to exist between the fundamental vibrational frequencies as observed by infrared absorption and in Raman spectroscopy[9] is shown in Table I. The absence of any absorption in liquid sulfur dioxide between 10 000 cm^{-1} and 2450 cm^{-1} together with the recent observation that hydrogen fluoride and sulfur dioxide are miscible in all proportions[10] indicates the suitability of this solvent for dilution studies of hydrogen fluoride in which attention is centered on the peaks between 4000 and 3000 cm^{-1}. The availability of a cell which makes it very convenient to use liquid SO_2 at room temperature, the wide variety of organic compounds soluble in sulfur dioxide and its relative transparency all combine to suggest the utility of liquid sulfur dioxide as a solvent for infrared measurements.

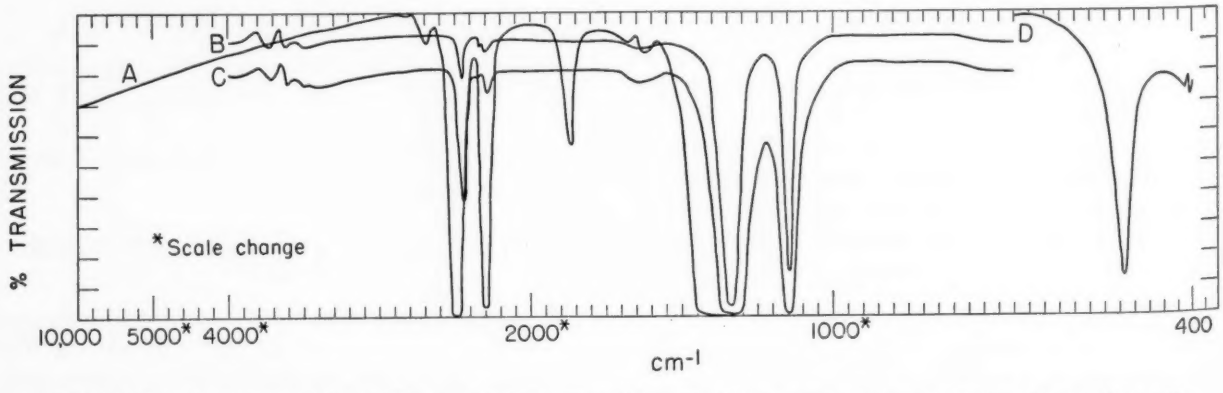

FIG. 2. Infrared spectrum of liquid SO_2 from 10 000 cm^{-1} to 400 cm^{-1}. *A*, 1 mm cell; *B*, 6μ cell; *C*, 39μ cell; *D*, 17.8μ cell.

[8] E. K. Plyler and N. Acquista, J. Opt. Soc. Am. **44**, 505 (1954).
[9] Shelton, Nielsen, and Fletcher, J. Chem. Phys. **21**, 2178–83 (1953); G. Herzberg, *Infrared and Raman Spectra of Polyatomic Molecules* (D. Van Nostrand Company, Inc., New York, 1945), pp. 285, 535.
[10] J. J. Katz, Arch. Biochem. Biophys. **51**, 302 (1954).

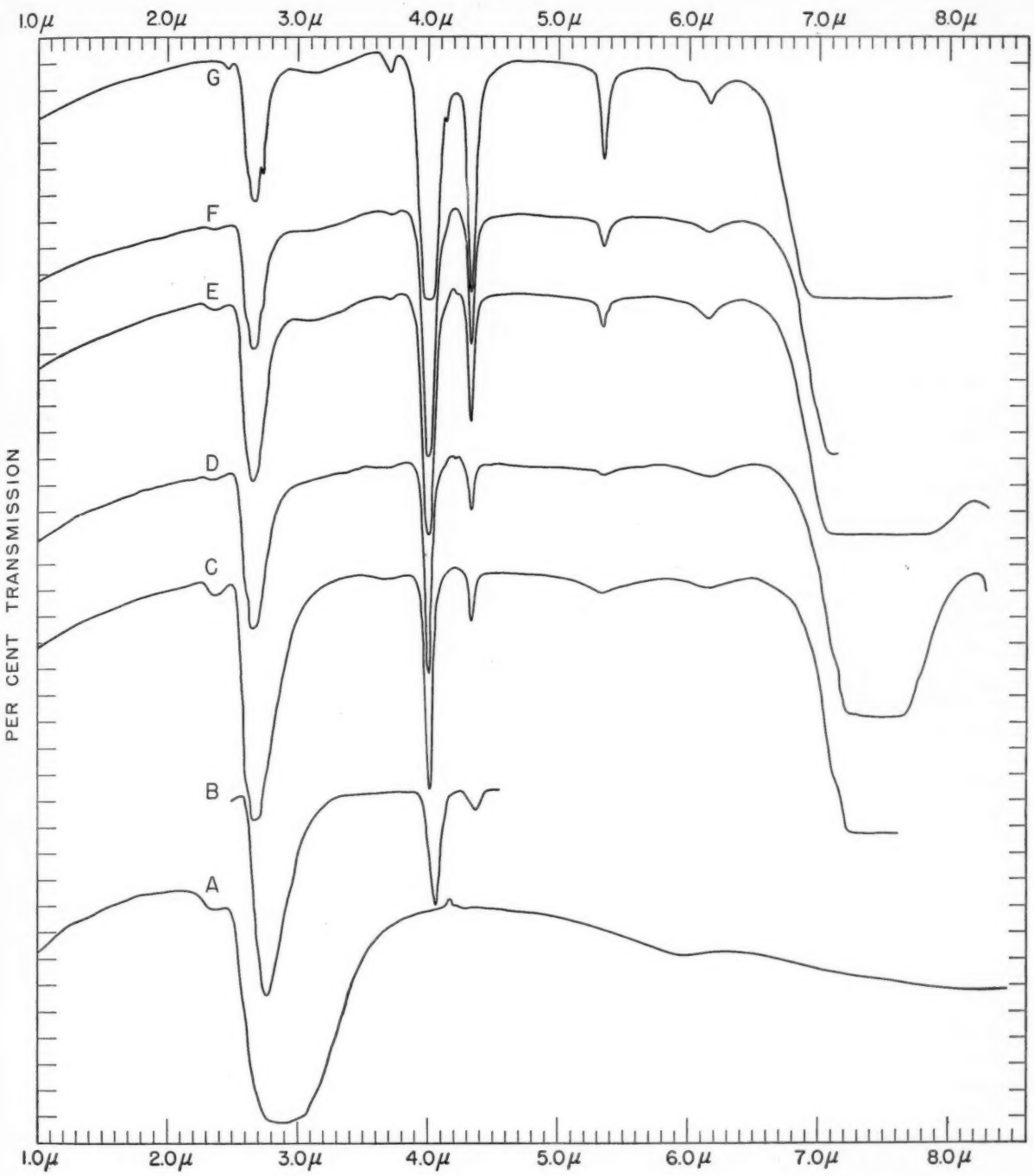

FIG. 3. Infrared spectra of SO_2—HF solutions. *A*, pure liquid HF, 6μ cell; *B*, 3.9 *f* HF, 39μ cell; *C*, 1.9 *f* HF, 73μ cell; *D*, 0.64 *f* HF, 73μ cell; *E*. 0.27 *f* HF, 255μ cell; *F*, 0.14 *f* HF, 255μ cell; *G*, 0.034 *f* HF, 1 mm cell.

HYDROGEN FLUORIDE-SULFUR DIOXIDE MIXTURES

Infrared absorption curves for a series of hydrogen fluoride solutions in liquid sulfur dioxide over the concentration range 0.034*f* to 3.9*f* HF are shown in Fig. 3. As the hydrogen fluoride concentration is decreased, the peaks at 3450 cm^{-1}, generally assumed to arise from absorption by hydrogen fluoride polymers, gradually diminish in intensity. The two peaks remaining on dilution at 4100 cm^{-1} and 3760 cm^{-1} may be identified as the *R* and *P* branches respectively of the monomer observed so clearly in the vapor by Shelton and Nielsen[2] and Safari,[4] and which Buswell, Maycock, and Rodebush[3] observed for monomer HF in carbon tetrachloride solution. It must be emphasized that this identification for the peaks observed in the liquid is quite speculative

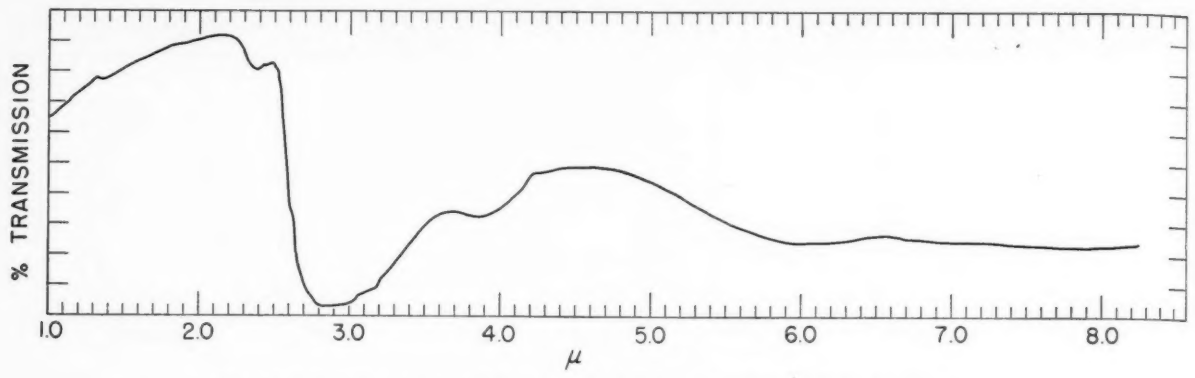

FIG. 4. Infrared spectrum of NaF dissolved in HF (2*f* NaF). Cell thickness, 17.4μ.

since the existence of rotational structure in the liquid has been questioned. In the liquid, these peaks may, in fact, arise from a lower polymer rather than the pure monomer. Molar extinction coefficients calculated on the assumption that the peak at 3760 cm^{-1} represents the entire monomer contribution to the absorption show a steady decline with increasing hydrogen fluoride concentration. An estimate of the relative amounts of monomer and polymer present at any concentration can be calculated by extrapolating the molar extinction coefficient to infinite dilution ($k_0=300$ 1 $mole^{-1}$ cm^{-1}) and using this limiting value of k to calculate an apparent degree of dissociation $\alpha=k/k_0$. These are listed in Table II.

If it is assumed that only two discrete species exist in these solutions, an equilibrium constant can be evaluated for the system:

$$(HF)_n=nHF$$

$$K_{eq}=\frac{[HF]^n}{[HF]_n}$$

$$\log K_{eq}=n\log[HF]-\log[(HF)_n]$$

where $[HF]=m\alpha$ and $[(HF)_n]=m(1-\alpha)$. It is interesting to note that only for $n=2$ is a reasonable constancy in the calculated K_{eq} achieved.† This is in contrast to the results of previous investigators on the gas; thus, Morrell, Hildebrand, and Long[11] find that their data on HF vapor densities can best be accounted for on the basis of an equilibrium between monomer and hexamer. More precise results on the HF-SO_2 system, particularly at a number of different temperatures, may clarify matters.

That the peak at 3760 cm^{-1} is not due to HF_2^- species is made very probable by an examination of Fig. 4. In this figure is shown the spectrum of sodium fluoride dissolved in hydrogen fluoride. An additional peak appears at 2500 cm^{-1} and appears to be due to absorption by HF_2^- (solvated) ion. The absence of this peak in pure hydrogen fluoride is additional confirmation of the low self-ionization of the pure liquid.

TABLE I. Infrared and Raman vibrational frequencies for sulfur dioxide.[a]

Assignment	I.R. (gas)	Raman (liquid)	This invest. (liquid)
$\nu_2(a_1)$	517.69	524.5	523
$\nu_1(a_1)$	1151.38	1144.3	1148
$\nu_3(b_1)$	1361.76	1336	1338
$\nu_2+\nu_3(B_1)$	1875.55		1866
$2\nu_1(A_1)$	2295.88		2304
$\nu_1+\nu_3(B_1)$	2499.55		2488

[a] See reference 9.

† The assumption of only two discrete species is arbitrary. If the 4100 cm^{-1} and 3760 cm^{-1} bands are not ascribable to monomer but rather to a low polymer, then the equilibrium observed exists between two or more polymers and upon dilution the lower polymer increases in concentration.

INFRARED SPECTRUM OF PROTEINS IN HYDROGEN FLUORIDE SOLUTION

In earlier work[10] it was reported that hydrogen fluoride or hydrogen fluoride-sulfur dioxide mixtures are capable of dissolving many proteins, some of which like silk fibroin are insoluble in water. In Fig. 5, the spectrum of silk fibroin dissolved in a hydrogen

TABLE II. Optical density of *F* hydrogen fluoride—sulfur dioxide solutions.

Experiment*	Hydrogen fluoride conc. *f*/1	λ_{max} μ	Optical density	k_1, 1 mole cm^{-1}	$k/k_0=\alpha$
B	3.9	2.76	1.75	115	0.38
C	1.9	2.67	2.44	176	0.59
D	0.64	2.66	0.945	202	0.67
E	0.27	2.66	1.47	213	0.71
F	0.14	2.66	0.765	214	0.71
G	0.034	2.68	0.920	270	0.90
	0			[300]†	1

* See curves on Fig. 3.
† Extrapolated from plot of k *vs* conc.

[11] Long, Hildebrand, and Morrell, J. Am. Chem. Soc. 65, 182 (1943).

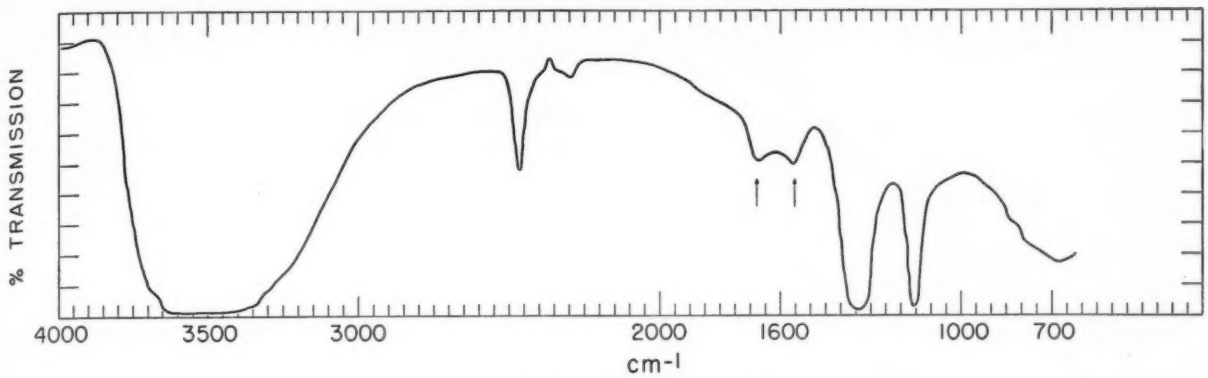

FIG. 5. Infrared spectrum of silk fibroin dissolved in a SO_2—HF mixture.

fluoride-sulfur dioxide mixture is shown and represents our first attempt in the direction of using these solvents for studying infrared spectra of proteins in solutions. The appearance of the twin peaks at 1670 and 1550 cm^{-1} presents a picture in agreement with infrared data for a large class of proteins and polypeptides in water solution[12] and in dried films.[13] Further studies with polypeptides and proteins in these solvents are planned.

[12] E. R. Blount and H. Lenormant, J. Opt. Soc. Am. **43**, 1093 (1953).
[13] Klotz, Griswold, and Gruen, J. Am. Chem. Soc. **71**, 1615 (1949).

THE JOURNAL OF CHEMICAL PHYSICS VOLUME 23, NUMBER 7 JULY, 1955

Vibrational Relaxation Times of Diatomic Molecules and Rocket Performance*†

H. C. PENNY‡ AND HENRY AROESTE
Guggenheim Jet Propulsion Center, California Institute of Technology, Pasadena, California
(Received October 11, 1954)

Computations are presented for the variation of vibrational excitation probabilities with temperature for mixtures of O_2 and N_2, and of HF and H_2. The values of six different excitation probabilities in each mixture are reported for temperatures up to 3000°K. For each of the probabilities there is a lower temperature limit given, below which the theory of Schwartz, Slawsky, and Herzfeld, which is used here, is not applicable. Using the results for H_2—HF mixtures, we present some considerations which suggest that the expansion through the de Laval nozzle for representative H_2—F_2 rocket motors may be taken as vibrational near-equilibrium flow.

I. CALCULATION OF VIBRATIONAL EXCITATION PROBABILITIES

FOR the computation on vibrational excitation probabilities we have used the method described by Schwartz, Slawsky and Herzfeld.[1] For the mixture of molecules of type a and b, we may define the probabilities $P_{0\to0}(a,a)$, $P_{0\to0}(b,b)$, $P_{0\to0}(a,b)$, $P_{0\to0}(b,a)$, $P_{0\to1}(a,b)$, $P_{0\to1}(b,a)$. In each of these cases, the molecule, the symbol of which appears first in the parenthesis, was initially in the first excited vibrational state and finally in the ground, or zero, vibrational state. The subscript designates the behavior of the vibrational quantum number of the molecule, the symbol of which appears second in the parenthesis. Each of these probabilities has been tabulated and graphed as functions of temperature for both the O_2—N_2 and the HF—H_2 gaseous mixtures.

The probability $P_{0\to1}(b,a)$ may be obtained simply from the relation

$$P_{0\to1}(b,a)=P_{0\to1}(a,b)\exp[-h(\nu_a-\nu_b)/kT]. \quad (1)$$

The others are determined independently. Summarizing the results of Schwartz *et al.* with slight modification we write for the probabilities,

$$P=CP', \quad (2)$$

$$P'=1.18[8\pi^2\mu\Delta E/\alpha^{*2}h^2]^2\sigma_1^{\frac{1}{3}}\exp(-\sigma)\textstyle\prod_i V^2(i), \quad (3)$$

$$C=0.45[(1+\sigma_1 kT/3\epsilon)^{\frac{1}{3}}+1]^{\frac{1}{3}}\exp(-\epsilon/kT), \quad (4)$$

* Supported by contract with the Office of Naval Research and the Office of Ordnance Research.
† Presented at the 126th National Meeting of the American Chemical Society, New York, New York, September, 1954.
‡ This article uses, in part, the results of a thesis submitted by H. C. Penny, Lieutenant, U. S. Navy, in partial fulfillment of requirements for the degree of Aeronautical Engineer, California Institute of Technology, June 1954.
[1] Schwartz, Slawsky, and Herzfeld, J. Chem. Phys. **20**, 1591 (1952); R. Schwartz and K. Herzfeld, J. Chem. Phys. **22**, 8768 (1954). We thank Dr. Schwartz and Professor Herzfeld for sending us a preprint of the latter paper.

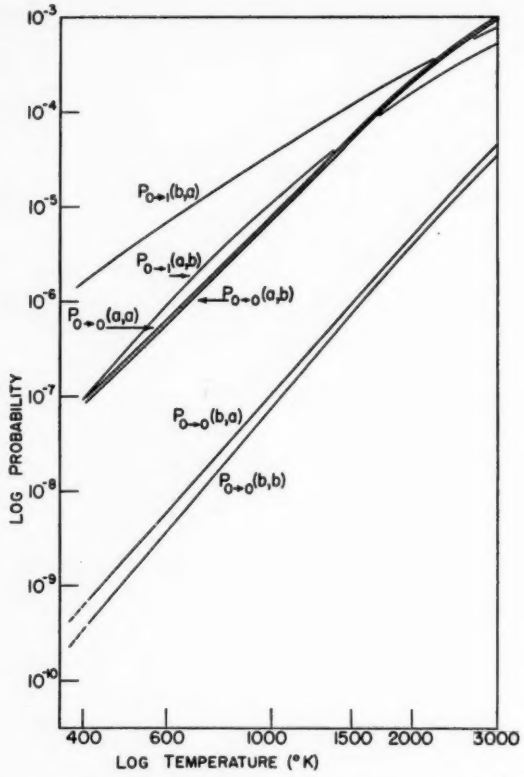

FIG. 1. Variation of probabilities with temperature ($a=O_2$, $b=N_2$). Limit temperatures, below which the theory becomes inapplicable, correspond to the junction between the solid and dotted portions of the curves.

where

$$\sigma_1=3\mu v_0^{*2}/2kT, \tag{5}$$

$$\sigma=\sigma_1\pm\Delta E/2kT, \tag{6}$$

$$v_0^*=[4\pi^2kT\Delta E/\alpha^*h\mu]^{\frac{1}{2}} \mp(\Delta E/2\mu)[4\pi^2kT\Delta E/\alpha^*h\mu]^{-\frac{1}{2}}+\cdots. \tag{7}$$

Here μ is the reduced mass of the two colliding molecules, ΔE represents the amount of energy exchanged between vibration and translation, ϵ and r_0 are the usual constants in the Lennard-Jones interaction potential, and $V(i)$ is the perturbation integral over harmonic oscillator wave functions. For α^* we use the approximate relation $\alpha^*=17.5/r_0$. In the case of HF, where no sufficient data is available, the collision diameter, r_0, was estimated by plotting r_0 as a function of the electronegativity of the halogen atoms. In this manner it is seen that the value of r_0 for HF is, approximately, 1.7 A.

TABLE I. Lower temperature limits for which the probabilities can be calculated from the theory of Schwartz and Herzfeld.

Probability	Temperature °K O_2-N_2	$HF-H_2$
$P_{0\to0}(a,a)$	326	1390
$P_{0\to0}(b,b)$	405	2700
$P_{0\to0}(a,b)$	330	2380
$P_{0\to0}(b,a)$	403	2440
$P_{0\to1}(a,b)$	231	592
$P_{0\to1}(b,a)$	231	592

The condition

$$\mu v_0^{*2}/2>\Delta E \tag{8}$$

will not hold below a certain temperature for each of the probabilities. We need inequality (8) to write the expansion,

$$v_f^*=v_0^*+\Delta E/\mu v_0^*-(\Delta E)^2/2\mu^2v_0^{*3}+\cdots. \tag{9}$$

It is not necessary that

$$\mu v_0^{*2}/2\gg\Delta E, \tag{10}$$

although the larger the inequality, the better the convergence. Schwartz and Herzfeld, in the appendix of their paper, have given a more complex method of computation which applies in the region of or below the limit temperatures. We have indicated these limit temperatures in Table I.

The above relationships have been used to compute the values of the probabilities listed in Table II which are shown graphically in Figs. 1 and 2. Using log scales for both the probabilities and the temperatures, the curves are seen to approximate straight lines except at the higher temperatures.

II. APPLICATION TO ADIABATIC EXPANSION THROUGH DE LAVAL NOZZLES

We now present brief considerations which enable us to determine whether or not the expansion through the

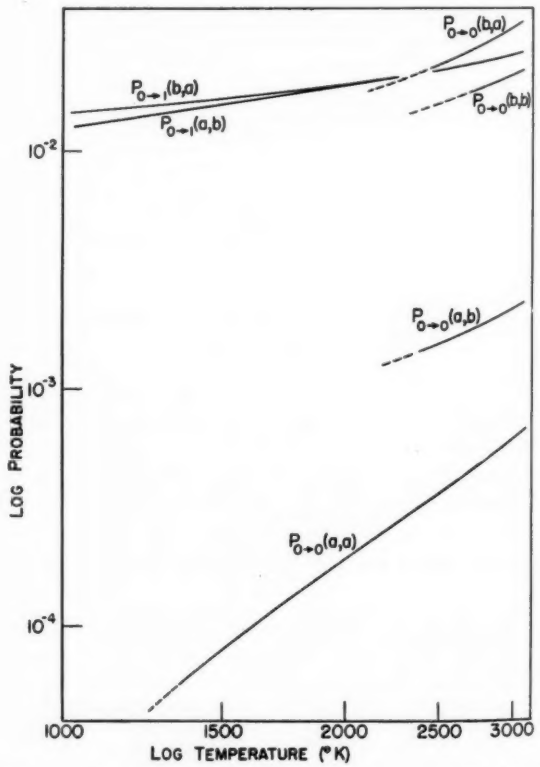

FIG. 2. Variation of probabilities with temperature ($a=HF$, $b=H_2$). Limit temperatures, below which the theory becomes inapplicable, correspond to the junction between the solid and dotted portions of the curves.

TABLE II. Variation of probabilities with temperature.

°K	$P_{0\to0}(a,a)$	$P_{0\to0}(b,b)$	$P_{0\to0}(a,b)$	$P_{0\to0}(b,a)$	$P_{0\to1}(a,b)$	$P_{0\to1}(b,a)$
			O_2-N_2			
400	8.8×10^{-8}	3.3×10^{-10}	9.0×10^{-8}	7.1×10^{-10}	9.5×10^{-8}	1.6×10^{-6}
600	6.8×10^{-7}	3.6×10^{-9}	6.1×10^{-7}	5.7×10^{-9}	1.0×10^{-6}	6.9×10^{-6}
1000	8.3×10^{-6}	7.5×10^{-8}	7.7×10^{-6}	1.1×10^{-7}	8.2×10^{-6}	3.5×10^{-5}
1500	5.5×10^{-5}	7.2×10^{-7}	5.1×10^{-5}	1.2×10^{-6}	5.6×10^{-5}	1.2×10^{-4}
2000	2.0×10^{-4}	3.9×10^{-6}	1.9×10^{-4}	4.8×10^{-6}	1.6×10^{-4}	2.8×10^{-4}
2500	5.2×10^{-4}	1.3×10^{-5}	4.9×10^{-4}	1.7×10^{-5}	3.1×10^{-4}	4.8×10^{-4}
3000	1.0×10^{-3}	3.4×10^{-5}	9.0×10^{-4}	4.5×10^{-5}	5.3×10^{-4}	7.7×10^{-4}
			$HF-H_2$			
1000	...	...	...	...	1.1×10^{-2}	1.6×10^{-2}
1500	7.9×10^{-5}	...	...	...	1.6×10^{-2}	2.1×10^{-2}
2000	1.9×10^{-4}	...	...	...	1.9×10^{-2}	2.3×10^{-2}
2500	3.6×10^{-4}	...	1.6×10^{-3}	2.3×10^{-2}	2.2×10^{-2}	2.6×10^{-2}
3000	6.1×10^{-4}	2.1×10^{-2}	2.2×10^{-3}	3.3×10^{-2}	2.5×10^{-2}	2.8×10^{-2}

de Laval nozzle for a hydrogen-fluorine rocket motor may be taken as vibrational near-equilibrium flow. The reactants are taken in such proportion that H_2 will be in excess, and the products of combustion passing through the nozzle consist essentially of a mixture of HF and H_2.

Following a procedure analogous to that of Penner in his treatment of chemical reaction in nozzle flow, we take as an estimate for the vibrational temperature lag, ΔT, present for vibrational near-equilibrium flow the relation

$$\Delta T\cong(-DT/Dt)\tau, \tag{11}$$

where τ is the vibrational relaxation time, and D/Dt is the Euler time derivative.[2] For representative nozzles in 100 psia thrust motors, it has been found that the cooling rate $(-DT/Dt)\cong(T_c-T_e)/t_r\cong3\times10^7$ °K sec^{-1}.[3] The use of very small nozzles will increase the rate of cooling, but for nozzles in larger thrust motors $(-DT/Dt)$ will be smaller than 3×10^7 °K sec^{-1}.

From Fig. 2, it can be seen that the probability, $P_{0\to1}(a,b)$, is approximately as large as some of the other probabilities and much larger than the others. The smaller probabilities contribute little to the effective relaxation time. The probabilities which are approximately as large as $P_{0\to1}(a,b)$ all contribute to the effective relaxation time. For the purpose of simplicity, however, let us assume that we may approximate the maximum value of the effective relaxation time as

$$\tau_M\cong1/X_aX_bM_{ab}P_{0\to1}(a,b). \tag{12}$$

The actual value of the effective relaxation time must of necessity be smaller than τ_M as the other probabilities, which are approximately as large as $P_{0\to1}(a,b)$, have not been considered in computing τ_M and would lower its value. If we can show, however, that vibrational near-equilibrium flow exists for the calculated upper limit τ_M, the conclusion certainly will hold for the real τ which is smaller than τ_M.

In Eq. (12) X_a and X_b are the mole fractions of HF and H_2 respectively, M_{ab} denotes the number of collisions per second between HF and H_2, and $P_{0\to1}(a,b)$ is the probability that upon a collision an HF molecule will be reduced from the first excited vibrational state to the zeroth state, while the H_2 molecule will undergo a change from the zeroth to the first state.

Since M_{ab} increases markedly with pressure it is apparent that if the conditions at the nozzle exit are such that vibrational near-equilibrium flow exists there, then it must also exist everywhere in the nozzle. The value of ΔT was therefore computed at the nozzle exit where it is a maximum.[4]

In this computation the nozzle exit pressure has been taken as one atmosphere. Also, the product X_aX_b will vary between the narrow limits of 0.25 and approximately 0.20 and will usually be about 0.23. The product of M_{ab} and $P_{0\to1}(a,b)$ will not differ appreciably from 4×10^7 sec^{-1} between 1400°K and 3000°K. Therefore, for exit temperatures between 1400°K and 3000°K we obtain $\tau_M\leq1\times10^{-7}$ sec. For $(-DT/dt)\leq3\times10^7$ °K sec^{-1}, we have $\Delta T_M\leq3$°K.

The estimate that the vibrational temperature lag cannot exceed 3°K reasonably indicates that vibrational near-equilibrium flow occurs during expansion in a de Laval nozzle for representative H_2-F_2 rocket motors.

We wish to thank Dr. S. S. Penner for helpful discussions.

[2] S. S. Penner, J. Chem. Phys. **19**, 877 (1951).
[3] D. Altman and S. S. Penner, J. Chem. Phys. **17**, 56 (1949).
[4] For a more detailed description of iterative lag calculations during nozzle flow, see S. S. Penner, "Linearization Procedures of the Study of Chemical Reactions in Flow Systems," 1953 Iowa Thermodynamic Symposium, Iowa City (1954).

Heat Capacity of NiF_2 from 12 to 300°K. Thermodynamic Functions of NiF_2. The Thermal Anomaly Associated with the Antiferromagnetic Ordering

EDWARD CATALANO* AND J. W. STOUT
Institute for the Study of Metals and Department of Chemistry, University of Chicago, Chicago, Illinois
(Received October 20, 1954)

The heat capacity of NiF_2 has been measured calorimetrically between 12 and 300°K. There is an anomaly in heat capacity rising to a maximum of 9.23 cal deg^{-1} $mole^{-1}$ at 73.22°K. The anomaly is associated with the antiferromagnetic ordering of the magnetic moments of the nickel ions. Values of heat capacity, entropy, enthalpy, and free energy are tabulated at selected temperatures. The entropy at 298.16°K is 17.59±0.04 cal deg^{-1} $mole^{-1}$. For the reaction $NiF_2+H_2=Ni+2HF$, $\Delta H_0^0=29.56\pm0.20$ kcal and $\Delta H^0=30.06\pm0.20$ kcal at 298.16°K.

THE anhydrous difluorides of manganese, iron, cobalt, nickel, and zinc form an isomorphous series of compounds in which the number of 3*d* electrons increases from five in MnF_2 to the completed shell of ten in ZnF_2. The crystal structure of these fluorides is of the rutile type, space group $D^{14}{}_{4h}$-$P4/mnm$, and the lattice parameters[1] do not change radically in going from one compound to another. Because they possess an incompletely filled 3*d* shell, MnF_2, FeF_2, CoF_2, and NiF_2 are paramagnetic and at room temperature there is an appreciable contribution to their entropy arising from the random distribution of the magnetic ions among low-lying electronic states. The mechanism of the loss of this electronic entropy at lower temperature is a cooperative one, involving interactions between neighboring magnetic ions. Measurements of the magnetic susceptibility,[2,3] magnetic anisotropy,[4] and of the structure by neutron diffraction[5] indicate that the low temperature ordered state is an antiferromagnetic[6] one with the spins aligned parallel and antiparallel to the fourfold axis of the tetragonal crystal. In NiF_2 there is evidence from the neutron diffraction pattern[5] that the spins are cocked slightly away from strict alignment along the tetragonal axis and the magnetic anisotropy results[4c] indicate that this cocking is such as to lead to a small ferromagnetic moment at temperatures below that at which long-range order begins.

An approximate molecular field theory of the ordering process in an antiferromagnetic material, equivalent to the Weiss-Heisenberg theory of ferromagnetism, has been given by Van Vleck.[7] This theory neglects the short-range order existing above the temperature of maximum heat capacity. Measurements of low temperature heat capacity are a powerful experimental tool for the investigation of the ordering process. Through the use of the third law of thermodynamics the entropy at various temperatures may be calculated directly from the heat capacity measurements, and the entropy in turn is directly related to the disorder. The observed entropy, however, arises both from the disordering of the magnetic system and from the lattice vibrations, and to focus attention on the magnetic system, it is necessary to subtract the lattice entropy. Measurements of the low-temperature heat capacity of MnF_2 have been reported[8] previously. A brief note calling attention to the thermal anomalies found in FeF_2, CoF_2, and NiF_2 has been published.[9] The present paper presents in detail the measurements on NiF_2. Results on FeF_2, CoF_2, and the isomorphous diamagnetic compound ZnF_2, which was measured to assist in the estimation of the lattice entropy in the antiferromagnetic fluorides, will be given in later papers.

APPARATUS AND CALORIMETRIC PROCEDURES

For the measurement of heat capacity a vacuum calorimeter surrounded by a massive isothermal shield was used. The construction of this shield and of the external parts of the cryostat were similar to that described by Giauque and Egan,[10] except that the seal at the top of the vacuum can was made with Rose metal solder rather than by a mechanical joint.

The calorimeter consisted of a copper cylinder, 10.8 cm long, 4.5 cm diameter, and 0.25 mm wall, closed at the top and bottom with end caps of 0.5 mm wall thickness. The filling tube, a short piece of 0.95 cm cupronickel tubing, is at the bottom when the calorimeter is in the cryostat. All joints in the calorimeter are silver-soldered except the cap on the filling tube which was soft-soldered. This cap contained a small pinhole through which air was evacuated and helium exchange gas introduced after the sample was in the calorimeter

* Eastman Kodak Company Fellow 1951–1952; Allied Chemical and Dye Corporation Fellow 1952–1953.

[1] J. W. Stout and Stanley A. Reed, J. Am. Chem. Soc. **76**, 5279 (1954). References to earlier work are given in reference 1.

[2] (a) W. J. de Haas and B. H. Schultz, Physica **6**, 481 (1939); (b) de Haas, Schultz, and Koolhaas, Physica **7**, 57 (1940).

[3] (a) H. Bizette and B. Tsai, Compt. rend. **212**, 119 (1941); (b) H. Bizette, Ann phys. [12] **1**, 295 (1946).

[4] (a) M. Griffel and J. W. Stout, J. Chem. Phys. **18**, 1455 (1950); (b) J. W. Stout and L. M. Matarrese, Revs. Modern Phys. **25**, 338 (1953); (c) L. M. Matarrese and J. W. Stout, Phys. Rev. **94**, 1792 (1954).

[5] R. A. Erickson, Phys. Rev. **90**, 779 (1953).

[6] See (a) L. Néel, Proc. Phys. Soc. (London) **A65**, 869 (1952); (b) A. B. Lidiard, Repts. Progr. in Phys. **17**, 201 (1954).

[7] J. H. Van Vleck, J. Chem. Phys. **9**, 85 (1941).

[8] J. W. Stout and H. E. Adams, J. Am. Chem. Soc. **64**, 1535 (1942).

[9] J. W. Stout and E. Catalano, Phys. Rev. **92**, 1575 (1953).

[10] W. F. Giauque and C. J. Egan, J. Chem. Phys. **5**, 45 (1937).

and the cap soldered on the filling tube. After the introduction of helium gas, the pinhole was sealed with Rose metal. The resistance thermometer-heater, sealed in its case, slipped into a dead-end copper tube open at the top, centrally located in the calorimeter and extending for about two-thirds of its length. Thermal contact between the thermometer-heater and the calorimeter was made with a solder (49 percent Bi, 18 percent Pb, 15 percent Sn, 18 percent In) melting at 58°C. This solder adhered well to the copper surfaces and was much more satisfactory than Wood's metal which we had used at first.The outside of the calorimeter was gold plated. The calorimeter had a capacity of 152 ml and, including the resistance thermometer, weighed 103 g.

The resistance thermometer-heater, made of pure platinum wire, is similar to the strain-free type described by Meyers.[11] The platinum wire, 0.07 mm diameter, was wound on a 0.28 mm diameter steel piano wire. The steel wire was then dissolved in dilute HCl and the helical platinum coil, stretched slightly so no turns touched, was wound on a mica cross. The platinum coil mounted on the mica cross was annealed in helium for 24 hours at 450°C. It was then inserted into the thermometer case, made of a 0.25 mm wall copper tube. The two ends of the thermometer wire were welded to heavy Pt leads, 19×0.64 mm, which were soldered inside the two Kovar tubes of a commercial "Stupakoff" ceramic seal which was in turn soldered in the top of the thermometer case. We adopted this procedure after unsatisfactory attempts to obtain a Pt-glass seal which did not develop cracks over a period of time. A pinhole was left in the bottom of the thermometer case for pumping and filling with helium gas. After assembly of the thermometer its resistance was measured at the triple point of water and it was annealed several times, with intervening checks of the triple point resistance, by passing currents sufficient to raise the temperature to 450°C through the wire while the case was evacuated and immersed in liquid nitrogen. Helium at one atmosphere was then introduced into the thermometer case and the pinhole sealed with solder. The thermometer was calibrated over the range 12 to 300°K against a laboratory standard Leeds and Northrup 25 ohm platinum resistance thermometer which had been calibrated by the Bureau of Standards. The weight of the thermometer and case was 13 g. The ice point resistance was 183.12 ohms and the resistance at 12°K had dropped to 0.242 ohm.

The electrical measurements of current and potential drop in the resistance thermometer-heater and of the emf of copper-constantan thermocouples used for rough control of the temperature of the shield and bath were made with an autocalibrated White double potentiometer in conjunction with a high sensitivity Leeds and Northrup galvanometer and calibrated standard cells, standard resistances, and voltage divider. The energy input was automatically started and stopped with a timer similar to that described by Johnston.[12]

The heat capacity of the empty calorimeter was measured in a separate series of experiments. The heat capacity measurements were further corrected for the changes in amount of helium gas and solder compared to the empty runs, for energy developed in the 0.013 ×2.5 cm platinum leads connecting the heater leads to the heavy copper wires in thermal contact with the shield, and for small effects associated with nonlinearity with time in the rise of temperature during energy input. A more important correction at the highest temperatures arises from finite thermal resistance within the calorimeter. When heat is entering or leaving the calorimeter, during the fore and after rating periods, a steady-state temperature gradient may be established between the thermometer and the mean temperature of the sample. If, for example, the shield temperature is intermediate between the temperature of the calorimeter before and after energy input this gradient will change sign in the fore and after periods and the temperature rise of the thermometer will not be identical with that of the mean sample. A similar correction arises to the heat exchange between calorimeter and shield during energy input since the temperature of that part of the calorimeter exchanging energy with the surroundings is not identical with the temperature it would have if thermal equilibrium were instantaneous. This correction has been treated by Giauque and Wiebe[13] for a calorimeter where the thermometer-heater is wound on the outside and it may be assumed that the temperature of the heater wire is that of the outside of the calorimeter. This is not the case in our calorimeter and we therefore determined experimentally the effect of a change of shield temperature upon the resistance of the thermometer and used these data to make the correction.

In our calorimeter the thermometer is in the center and so protected from direct heat exchange by radiation or gas conduction with the shield. Thus in the measurements on the empty calorimeter the observed rise in temperature of the thermometer is slightly greater than that of the mean (weighted according to heat capacity) temperature rise of the calorimeter and a positive correction must be made to the heat capacity. When the calorimeter is filled with sample it is possible for the correction to be either positive or negative, since, depending on the values of the thermal conductances between various parts of the calorimeter and thermometer and the distribution of heat capacity, the temperature rise of the thermometer may be greater or less than the mean temperature rise of the calorimeter. It was therefore necessary to determine experi-

[11] C. H. Meyers, J. Research Natl. Bur. Standards **9**, 807 (1932).

[12] H. L. Johnston, J. Opt. Soc. Am. **17**, 381 (1928).

[13] W. F. Giauque and R. Wiebe, J. Am. Chem. Soc. **50**, 101 (1928).

TABLE I. The heat capacity of NiF_2. 0°C=273.16°K. Molecular weight 96.69.

T_{Av} °K	Approx ΔT	$\Delta H/\Delta T$ cal deg^{-1} mole^{-1}
SERIES I		
81.52	2.91	5.959
84.63	3.29	6.058
88.35	4.09	6.229
SERIES II		
53.13	4.21	3.835
57.39	4.29	4.543
62.27	5.47	5.451
66.72	3.42	6.430
69.92	2.97	7.346
73.33	3.83	7.655
77.68	4.79	6.012
82.32	4.47	5.987
SERIES III		
88.78	3.96	6.257
93.09	4.66	6.484
98.05	5.15	6.796
103.01	4.77	7.127
108.30	5.85	7.488
114.03	5.56	7.874
119.90	6.18	8.280
126.22	6.68	8.689
132.78	6.48	9.127
139.07	6.07	9.353
145.54	6.83	9.936
152.20	6.42	10.32
156.92	6.14	10.58
163.35	6.67	10.91
169.87	6.34	11.24
176.70	7.22	11.57
183.79	6.87	11.90
190.98	7.17	12.23
198.08	6.87	12.50
205.90	6.55	12.81
213.03	7.57	13.01*
220.58	7.29	13.22*
227.40	5.84	13.51*
236.39	6.68	13.79
243.24	6.87	14.01
251.28	6.63	14.19
258.75	7.70	14.35
266.19	7.47	14.53
274.30	7.45	14.76
282.40	8.70	14.95
290.31	8.53	15.13
298.25	8.25	15.37
SERIES IV		
11.14	0.52	0.044
11.88	0.98	0.050
13.76	1.40	0.072
15.42	1.71	0.102
17.40	2.25	0.146
19.73	2.24	0.222
22.09	2.26	0.327
24.74	2.76	0.484
27.54	2.84	0.687
30.23	2.92	0.912
33.21	2.99	1.204
36.25	3.08	1.533
39.37	3.18	1.895
42.67	3.35	2.309
46.53	4.36	2.847
50.85	4.34	3.480
59.27	13.54	4.894
74.95	17.41	6.653
SERIES V		
55.69	4.70	4.244
60.27	4.46	5.063
63.73	2.54	5.749
66.27	2.47	6.315
68.72	2.39	6.951
70.79	1.73	7.658
73.05	0.68	8.986
73.84	0.70	7.041
74.51	0.64	6.460
75.16	0.66	6.246
75.88	0.78	6.120
76.94	1.35	6.048
78.29	1.38	5.979
80.10	2.26	5.944
83.25	4.04	6.004
SERIES VI		
72.636	0.249	8.72
72.852	0.147	8.95
72.998	0.126	9.07
73.128	0.096	9.18
73.232	0.096	9.22
73.339	0.100	8.75
73.450	0.106	8.07
73.568	0.107	7.57
73.686	0.115	7.22
73.810	0.118	6.99
73.934	0.120	6.86
74.060	0.121	6.75
74.192	0.123	6.63
74.320	0.124	6.56
74.448	0.125	6.52
74.581	0.126	6.44
74.707	0.127	6.39
74.837	0.128	6.35
74.967	0.129	6.30
75.097	0.130	6.26
75.228	0.130	6.24
SERIES VII		
71.530	0.182	8.02
71.711	0.182	8.07
71.897	0.180	8.18
72.087	0.179	8.33
72.243	0.100	8.48
72.352	0.100	8.53
72.460	0.100	8.59
72.568	0.099	8.69
72.683	0.099	8.76
72.787	0.098	8.90
72.891	0.097	8.98
72.994	0.097	9.07
73.100	0.096	9.18
73.201	0.096	9.23
73.302	0.098	8.99
73.407	0.105	8.20
SERIES VIII		
81.25	2.67	5.956
83.84	2.56	6.029
216.10	7.26	13.18
223.52	6.98	13.42
230.55	6.73	13.63
237.50	6.51	13.86
299.99	6.50	15.30

* Point unreliable because of bad vacuum conditions.

mentally the value of the correction for every filling of the calorimeter. In the measurements on NiF_2 the correction was positive and its maximum value amounted to 1.4 percent at 298°K. The correction is proportional to the thermal conductance between the calorimeter and shield and decreases rapidly as the temperature is lowered. Thus in the measurements on NiF_2 it was down to 0.2 percent at 200°K and rapidly became negligible at lower temperatures. After the completion of the measurements on NiF_2 it was discovered that in the filling of the thermometer case with helium some air had inadvertently been introduced. Upon refilling the case with pure helium the thermal conductance between the wire and the case increased by a factor of about three. This brought the thermometer in better contact with the outside of the calorimeter and in the measurements on FeF_2, CoF_2, and ZnF_2 to be described in later papers the correction discussed above was negative in sign and considerably smaller in magnitude than was the case for NiF_2.

PREPARATION OF SAMPLE

Hydrated nickel fluoride was prepared following the general procedure of Kurtenacker, Finger, and Hey.[14] Nickel carbonate was precipitated by adding a solution of sodium bicarbonate to one prepared by dissolving commercial "Special low cobalt" $NiSO_4 \cdot 6H_2O$ in distilled water. An excess of the nickel sulfate solution was used in order to minimize the precipitation of other metallic carbonates. The precipitated carbonate, after filtering and washing, was added to an aqueous solution of HF contained in a plastic dish. $NiF_2 \cdot 4H_2O$ crystallized from this solution and a larger yield was obtained by the addition of ethanol. The filtered $NiF_2 \cdot 4H_2O$ was dried in an oven at 120°C. The resulting product corresponded approximately to the monohydrate. The remaining water was removed by heating the material in a nickel boat contained in a nickel tube through which commercial anhydrous hydrogen fluoride was passed. The water came off at a temperature of 350–400°C. In order to insure complete dehydration and to obtain larger crystallites of NiF_2 the temperature of the furnace was increased gradually to 900°C and kept at this temperature for about an hour with HF passing over the sample. The NiF_2 so prepared was a light greenish-yellow color.

Microscopic examination showed that the sample consisted of crystallites with a range of 0.005 to 0.01 mm in diameter. The individual crystallites showed extinctions when rotated between crossed Nicols, indicating that they were single crystals of an optically anisotropic material such as NiF_2. The crystal size observed was sufficiently large so that surface effects would be negligible in the thermal properties. In a spectrochemical analysis of the NiF_2 the only metallic

[14] Kurtenacker, Finger, and Hey, Z. anorg. Chem. **211**, 83 (1933).

impurities found were, in weight percent: Cu, 0.005; Co, 0.004; Fe, 0.003; Mn, 0.001. X-ray diffraction photographs[1] showed no lines not attributable to NiF_2. The sintered NiF_2 was extremely inert to attack by chemical reagents and we did not find a satisfactory method of dissolving it so as to make an accurate analytical determination of the nickel content of the sample. It was found that if the NiF_2 was heated with ground silica the fluoride was converted to an oxide which could be dissolved in HCl, and the nickel then determined gravimetrically by a dimethylglyoxime precipitation. Four such determinations gave results ranging from 60.9 to 63.1 percent of nickel in the original sample, compared to 60.70 percent calculated from the formula NiF_2.

EXPERIMENTAL RESULTS

The observed heat capacity data are given, in chronological order, in Table I. The sample of NiF_2 weighed 123.97 g *in vacuo* (1.2822 moles). The defined calorie used is equal to 4.1840 absolute joules. The heat capacities listed in Table I are values of $\Delta H/\Delta T$ (H is the enthalpy) and are equal to the true differential heat capacity, C_p, only if the correction for curvature is negligible. Actually the correction for curvature exceeds the experimental error only in the points in the vicinity of the anomaly near 73°K. Also listed in Table I are values of the approximate temperature rise of each measurement. The temperature given for each point is the arithmetic mean of the initial and final temperatures.

Series I comprises several exploratory measurements after the initial cooling of the calorimeter to liquid nitrogen temperatures. The calorimeter was then cooled to 51°K and the data of series II taken. The calorimeter remained at about 85° for three days and then the measurements of Series III, extending to room temperature, were made.

The three points in this series, at temperatures between 210 and 230°K and marked by an asterisk in Table I, are below a smooth curve. The thermal drift during these points was abnormally large, caused probably by poor vacuum from the evaporation of condensed CO_2. Under such conditions the precision of the measurements is poor and these points should be given little weight. The region of temperature between 210 and 240°K was covered, with good vacuum conditions, by points listed under Series VIII. Two days after the completion of Series III the calorimeter was cooled to liquid hydrogen temperatures and the data of Series IV obtained. The last two points in this series are very long runs designed to obtain accurate values for the change in enthalpy through the region of anomalous heat capacity. The calorimeter then stood for one day at 83°K, was cooled to 49.8°K, and warmed overnight to 50.5°K where the measurements of Series V began. A point in this series at 72.2°K has been discarded because of uncertainty in the energy input readings.

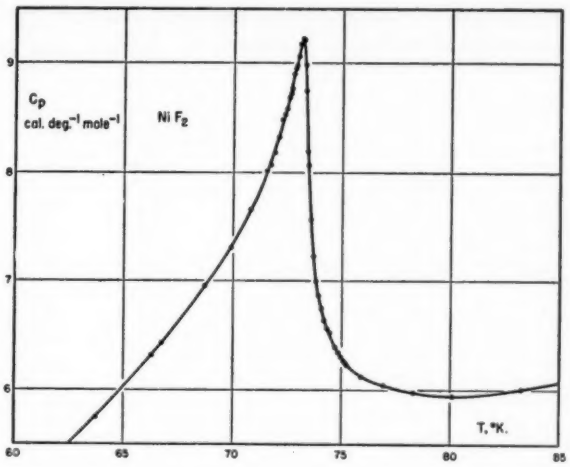

FIG. 1. Heat capacity of NiF_2 in the anomalous region.

In order to define more closely the shape of the curve in the anomalous region heat capacity measurements with a temperature rise of about one-tenth degree were taken in Series VI and VII. Because of the small temperature rise these measurements are less accurate than the usual ones. We estimate that they are reliable to about 0.5 percent. Although the error in the absolute temperature calculated from the resistance thermometer may be several hundredths of a degree, small differences in temperature are known to better than one thousandth of a degree. In Table I we have listed the mean temperature of the measurements of Series VI and VII to the nearest 0.001° in order to show the variation of heat capacity with temperature. Two days after the completion of Series V, the calorimeter, which had remained at 85°K, was cooled to 72.5°K and the measurements of Series VI were taken. Seven days later the temperature of the calorimeter had risen to 120°K. It was cooled to 71.4°K and Series VII begun. There is no evidence from any of the measurements of dependence of the observed heat capacity on the thermal history of the sample and the points from all series are consistent within the expected error. In the neighborhood of the maximum in heat capacity there was no evidence of slowness in the attainment of thermal equilibrium.

THE ANOMALY IN HEAT CAPACITY

The heat capacity data between 60 and 85°K are plotted in Fig. 1. Points in which the temperature rise was so large that the mean heat capacity, $\Delta H/\Delta T$, deviates appreciably from the heat capacity at the mean temperature have been omitted. The observed mean heat capacity of such points agrees within 0.2 percent with that obtained from integration of the smooth curve. The anomaly in heat capacity has the lambda shape characteristic of processes where cooperative ordering is taking place. The peak in heat

TABLE II. Thermodynamic properties of NiF_2.

T °K	C_p^0 cal deg^{-1} mole^{-1}	S^0 cal deg^{-1} mole^{-1}	$H^0-H_0^0$ cal mole^{-1}	$-\frac{F^0-H_0^0}{T}$ cal deg^{-1} mole^{-1}
15	0.094	0.050	0.44	0.020
20	0.232	0.093	1.21	0.033
25	0.500	0.171	2.98	0.052
30	0.891	0.295	6.42	0.081
35	1.393	0.469	12.10	0.124
40	1.969	0.692	20.47	0.180
45	2.626	0.961	31.92	0.252
50	3.354	1.275	46.87	0.338
55	4.127	1.631	65.53	0.439
60	5.013	2.027	88.34	0.555
65	6.025	2.467	115.8	0.685
70	7.36	2.958	149.0	0.829
73.22	9.23	3.320	175.2	0.927
75	6.28	3.489	187.6	0.986
80	5.943	3.878	217.8	1.155
85	6.076	4.241	247.8	1.326
90	6.316	4.595	278.7	1.498
100	6.925	5.290	344.8	1.842
110	7.598	5.982	417.4	2.187
120	8.286	6.672	496.8	2.532
130	8.949	7.362	583.0	2.877
140	9.592	8.049	675.7	3.222
150	10.19	8.731	774.7	3.567
160	10.73	9.407	879.4	3.911
170	11.25	10.073	989.3	4.254
180	11.72	10.729	1104.2	4.595
190	12.16	11.375	1223.6	4.935
200	12.57	12.009	1347.3	5.273
210	12.96	12.632	1474.9	5.609
220	13.31	13.243	1606.3	5.942
230	13.61	13.841	1740.9	6.272
240	13.90	14.427	1878.5	6.600
250	14.16	15.000	2018.8	6.924
260	14.41	15.560	2161.7	7.246
270	14.65	16.109	2307.0	7.564
280	14.89	16.646	2454.7	7.879
290	15.12	17.172	2604.7	8.190
300	15.36	17.689	2757.1	8.498
273.16	14.72	16.28	2353	7.66
298.16	15.31	17.59	2729	8.44
		±0.04	±5	±0.02

capacity is narrower and appears somewhat sharper than that observed[8] in MnF_2. The question as to whether the curve near the maximum is continuous with continuous derivative, or cusped, cannot be unambiguously answered from the data. Because of the finite temperature increment in each heat capacity measurement a cusped curve would appear smoothed out. Any further reduction in the temperature increment below the approximately 0.1° we used would decrease the precision and not assist in deciding the shape of the curve. It appears from a large scale plot of the data in the immediate neighborhood of the maximum that, taking into account the finite resolution and precision of the points, the data are better represented by a smooth curve than by a cusped one. Undoubtedly there is a large change from positive to negative slope in the heat capacity-temperature curve between 73.15 and 73.3°K. The maximum heat capacity is 9.23 cal mole^{-1} deg^{-1} at a temperature of 73.22±0.05°K.

The heat capacity anomaly is evidently connected with the ordering of the atomic magnetic moments. From an extrapolation of magnetic structure factors obtained in neutron diffraction experiments Erikson[5] concluded that the long-range order disappears at 83°K. The extrapolation was based on the assumption that the magnetization of each sublattice is that calculated from the Van Vleck theory.[7] It seems probable from the narrowness of the heat capacity anomaly that the actual sublattice magnetization near the Curie temperature is varying much more rapidly with temperature than is given by the Van Vleck theory and a reasonable extrapolation of Erickson's data to a temperature of 73.22°K may be made. Matarrese and Stout[4c] found that the temperature below which an anomalous behavior in the magnetic anisotropy of a single crystal of NiF_2 appeared was close to the 73.22°K of the maximum in heat capacity.

THERMODYNAMIC PROPERTIES OF NiF_2

Values of the heat capacity, entropy, and the enthalpy and free energy functions of NiF_2 at selected temperatures are listed in Table II. The values of C_p are differential heat capacities and in drawing the smooth curves the experimental points were corrected for curvature. It was found that the experimental values of the heat capacity at the lowest temperatures were varying much more slowly with temperature than predicted by a Debye function. Since much of this heat capacity arises from the magnetic properties of NiF_2, which are imperfectly understood theoretically, the extrapolation to 0°K was made by an arbitrary extension, on a plot of C_p/T *versus* T, of a reasonable curve to the absolute zero. The extrapolated contribution to the entropy below 11°K is only 0.03 cal deg^{-1} mole^{-1}. The accuracy of the smoothed heat capacity data is estimated as 3 percent at 15°K, 1 percent at 20°K and 0.2 percent at 40°K. In the neighborhood of the maximum the smooth curve may be in error by 0.5 percent. From 75°K to 200°K the accuracy is about 0.2 percent and, because of the increased heat leak and uncertainty in the corrections for temperature gradients in the calorimeter, rises to about 0.5 percent at 300°K. Although the accuracy of the functions S^0, $H^0-H_0^0$ and $-(F^0-H_0^0)/T$ is about 0.2 percent above 100°K the numbers in Table II are given to a higher precision than this so that they will be internally consistent.

The values of entropy and free energy in Table II do not include the contributions arising from nuclear spin randomness or isotope mixing. They do, however, include that arising from randomness in the orientation of electronic spins. The magnetic susceptibility [2,4c] and neutron diffraction[5] data show that the spin system is essentially completely ordered at 12°K and calculations to be presented in a later paper show that the anomalous heat capacity is consistent with an entropy loss of R ln3

per mole of NiF_2. The values of the thermodynamic quantities listed in Table II are therefore the correct ones to be used in calculations of chemical equilibria.

With the thermodynamic functions calculated from the low-temperature heat capacity measurement it is possible to obtain from equilibrium data more accurate values for the heats of chemical reactions involving NiF_2 than may be calculated from the temperature coefficient of the equilibrium constant. As an example we shall consider the reaction $NiF_2+H_2=Ni+2HF$. Equilibrium constants have been measured over the range 573–773°K by Jellinek and Rudat.[15] Values of the free energy and entropy functions are given for HF by Cole, Farber, and Elverum,[16] for Ni by Busey and Giauque[17] and Kelley,[18] and those for H_2 are taken from the summary of Wagman *et al.*[19] An extrapolation of the observed heat capacity data on NiF_2 was made, passing through the value 17.7 cal deg^{-1} mole^{-1} at 500°K and 19.1 at 800°K, and values of the free energy and enthalpy functions were calculated from this curve. From the x-ray examination[1] of single crystals grown from the melt it is likely that no phase changes occur in NiF_2 in this region of temperature. Although the extrapolation of the heat capacity is uncertain, this uncertainty does not introduce a large error in the free energy function. Thus if one makes the extreme assumption that the heat capacity of NiF_2 remains constant at all temperatures above 300°K the values of $-(F^0-H_0^0)/T$ are below those calculated from our extrapolated curve by 0.10 and 0.54 cal deg^{-1} mole^{-1} at 500 and 773°K, respectively. Table III summarizes the calculation of the values of ΔH_0^0. In calculating the mean value, the datum at 573°K has been given half weight. We estimate the error, arising from uncertainties in the extrapolation of the heat capacity of NiF_2 and from the scatter of the values of ΔH_0^0, to be 0.20 kcal. The values of ΔH^0 at other temperatures may be calculated from the tables of $H^0-H_0^0$. For the reaction $NiF_2+H_2=Ni+2HF$ we obtain $\Delta H_0^0=29.56\pm0.20$ kcal and $\Delta H^0=30.06\pm0.20$ kcal at $T=298.16$°K. From the temperature coefficient of the equilibrium constant Jellinek and Rudat calculated a value of $\Delta H^0=29.6$ kcal at $T=673$°K. Using our values of the extrapolated enthalpy of NiF_2 this becomes $\Delta H^0=30.7$ kcal at $T=298.16$. This value is considerably less accurate than the 30.06 ± 0.20 kcal we have calculated from the same equilibrium data by using low-temperature heat capacity data and the third law of thermodynamics, both because of the errors inherent in determining the temperature coefficient of an equilibrium constant over a limited temperature range and because the possible errors in the enthalpy function of NiF_2, arising from uncertainty in the extrapolation of the heat capacity, are about four times those in the free energy function.

TABLE III. ΔH_0^0 for reaction $NiF_2+H_2=Ni+2HF$. Equilibrium data of Jellinek and Rudat (see text).

T,°K	$\log(P^2_{HF}/P_{H_2})$	$\Delta F^0/T$ cal deg^{-1}	$\Delta(F^0-H_0^0)/T$ cal deg^{-1}	ΔH_0^0 kcal
573	−2.48	11.35	−40.06	29.46
673	−0.86	3.94	−39.91	29.51
723	−0.26	1.19	−39.82	29.65
773	0.32	−1.46	−39.73	29.58
			Mean	29.56

We thank Miss Myrtle Bachelder for the chemical analysis, Mrs. Althea Tompkins for the spectrochemical analysis, and Mr. Stanley Reed for assistance with the calculations. The preparation of the material in this paper for publication was supported in part by the Office of Naval Research (Contract N6 ori-02051).

[15] K. Jellinek and A. Rudat, Z. anorg. Chem. **175**, 281 (1928).
[16] Cole, Farber, and Elverum, J. Chem. Phys. **20**, 588 (1952).
[17] R. H. Busey and W. F. Giauque, J. Am. Chem. Soc. **74**, 3157 (1952).
[18] K. K. Kelley, *U. S. Bureau of Mines Bulletin*, No. 476, 121 (1949).
[19] Wagman, Kilpatrick, Taylor, Pitzer, and Rossini, J. Research Natl. Bur. Standards **34**, 143 (1945).

Coupling of the Out-of-Plane Bending Mode in Nitrates and Carbonates of the Aragonite Structure*

J. C. Decius†
Department of Chemistry, Oregon State College, Corvallis, Oregon
(Received October 4, 1954)

The infrared absorption of polycrystalline samples of KNO_3 and $BaCO_3$ in the form of Nujol mulls has been observed between 11.3 and 12.5 microns under conditions such that the rotational lines of the NH_3 spectrum separated by 1.5 cm^{-1} could be clearly resolved. When the N^{15} or C^{13} content is increased to the order of 50 percent, fine structure is observed which is not present e.g., in $NaNO_3$, which possesses a crystal structure similar to calcite. The fine structure is interpreted by postulating a force constant which couples the out-of-plane vibrations of nearest neighbors in the aragonite-type lattice.

Very satisfactory agreement between the calculated and observed spectra is then found; in the case of $BaCO_3$, the vibrations of CO_3 ions which occur in isotopic isolation, as pairs, triplets, and quadruplets are resolved. The significance of the coupling constant is discussed; in principle, it may be used to evaluate the dipole derivative for the mode under consideration.

INTRODUCTION

In two previous communications[1] attention has been directed to certain features of the N^{15} and C^{13} isotope effect on the infrared absorption of crystalline nitrates and in the region of 12μ which have been interpreted as arising from intermolecular coupling between nearest neighbors in the aragonite-type lattice. In the present paper a fuller account of these studies will be given, including a suitable development of the theory, which accounts very well for the observed fine structure and the qualitative intensity pattern.

The utility of isotopic dilution as a technique for the study of intermolecular coupling of vibrational modes in crystals has been previously described by Hrostowski and Pimentel[2] and by Hiebert and Hornig.[3]

When deuterium is substituted for hydrogen, the normal modes of the two isotopic species are practically completely uncoupled owing to the large percentage difference between the unperturbed frequencies. In the case of $N^{14}-N^{15}$ and $C^{12}-C^{13}$ isotope shifts, however, the much smaller difference between the unperturbed frequencies necessitates the use of a second-order perturbation treatment, especially in order to account successfully for the distribution of intensity through the absorption band.

EXPERIMENTAL PROCEDURE

The infrared absorption data were obtained with a Perkin-Elmer Model 112C instrument which employs the Walsh[4] double-pass monochromator principle. All work was done with a sodium chloride prism between 11.3 and 12.5 microns. Frequent calibrations were carried out using the NH_3 spectrum; although the frequencies of the absorption maxima are reported to 0.1 cm^{-1}, the error probably amounts to 0.5 cm^{-1} by a rough statistical test. Under optimum conditions, the P branch lines of the NH_3 10.5 micron band reported by Sheng, Barker, and Dennison,[5] at 809.68, 812.53, 814.13 were easily resolved from one another and from 815.55 and 816.48, although the latter two were not clearly separated. Accordingly, it will be assumed that 1.5 cm^{-1} is the approximate limit of resolution.

The nitrates and carbonates employed in these studies were either Analytical Reagents containing the natural abundance ratios of the isotopes, or contained enhanced amounts of N^{15} or C^{13} obtained as KNO_3 (62 percent N^{15}) or $BaCO_3$ (60 percent C^{13}) from Eastman Organic Chemicals. Because of a happy coincidence, the Eastman Kodak Company supplies both the N^{15} and C^{13} in the form of substances which crystallize in the aragonite-type lattice. Nitrates of isotopic composition intermediate between the highest available N^{15} concentration and the natural abundance ratio were prepared by gravimetric synthesis, solution in hot water, and recrystallization upon addition of excess chilled ethanol.

The Nujol emulsions were prepared, starting with a fine, uniform powder, by mulling the salt with a minimum amount of the oil, and then rubbing the emulsion between two rocksalt windows whose inner faces were left unpolished after grinding with No. 600 wet or dry paper.

EXPERIMENTAL RESULTS

The absorption curves for KNO_3 containing 50 percent and 20 percent N^{15} are exhibited in Fig. 1. At the 20 percent composition, the N^{15} region shows two absorption maxima at 807.3 and 810.4 cm^{-1}, of which the latter is more intense. The N^{14} region

* Published with the approval of the Monographs Publication Committee, Oregon State College, as Research Paper No. 271, School of Science, Department of Chemistry.

† This research was supported by a Summer Research Grant from E. I. du Pont de Nemours and Company.

[1] J. C. Decius, J. Chem. Phys. **22**, 1946 (1954); **22**, 1941 (1954).

[2] H. J. Hrostowski and G. C. Pimentel, J. Chem. Phys. **19**, 661 (1951).

[3] G. L. Hiebert and D. F. Hornig, J. Chem. Phys. **20**, 918 (1952).

[4] A. Walsh, J. Opt. Soc. Am. **42**, 94, 96 (1952).

[5] Sheng, Barker, and Dennison, Phys. Rev. **60**, 786 (1941).

consists of a single, asymmetric band with a maximum at 826.0 cm^{-1} and more absorption on the high-frequency than on the low-frequency side of the maximum.

The 50 percent sample exhibits absorption maxima at essentially the same positions in the N^{15} region as the 20 percent sample, but the lower frequency peak is now more intense, and the absorption extends to lower frequencies. In the N^{14} region, three separate maxima are resolved falling approximately at 828, 830.6, and 836.5 cm^{-1}. Perhaps the most striking feature of the 50 percent absorption curve is the decidedly greater intensity of the absorption in the N^{15} region.

Figure 2 presents the infrared absorption of a sample of $BaCO_3$ containing 60 percent C^{13}. It is somewhat similar to the 50 percent N^{15} KNO_3 curve, except that three maxima are resolved in the C^{13} region (832.7, 835.0, and a shoulder at 839–840) and four maxima are observed in the C^{12} region 860.8, 862.6, 866.7, and 874.0 cm^{-1}.

THEORY

Sign of Coupling Constant

Carbonates and nitrates which crystallize in the aragonite-type lattice are so arranged that the nearest neighbor carbonate or nitrate ions occupy positions vertically above one another, taking the plane of the ion itself as horizontal. The distance between such nearest neighbor ions is appreciably less than in the calcite-type lattice, where the nearest neighbors are coplanar.‡ In $CaCO_3$ itself, these distances are 2.86 A (aragonite) and 4.981 A (calcite).[6] Similarly, the vertical distance between nearest neighbor nitrate ions in KNO_3 is 3.225 A, whereas in $NaNO_3$, the distance between nearest, coplanar neighbors, is 5.064 A. Since as we shall see below, the phenomena under consideration are adequately explained by the introduction of a negative force constant coupling the out-of-plane vibrations of nearest neighbors in the aragonite structures, it is interesting to note that the electrostatic dipole-dipole energy for this geometry would lead to a negative constant. Such an interaction energy can be expressed in the form:

$$V'=\frac{-\mu_1\mu_2}{R^3}(2\cos\theta_1\cos\theta_2-\sin\theta_1\sin\theta_2\cos\chi), \quad (1)$$

where μ_1 and μ_2 are the magnitudes of the two dipoles, R is the distance between their centers, θ_1 and θ_2 are the angles which μ_1 and μ_2 respectively subtend from the line between the centers, and χ is the angle between the projections of the dipoles in the plane perpendicular to the line between centers. If the dipoles (which vanish at equilibrium) are assumed to be linear in the out-of-plane coordinates, δ_i, of two adjacent nitrate ions

$$\mu_i=a\delta_i, \quad (2)$$

the potential energy can be written

$$2V=F(\delta_1^2+\delta_2^2)+2F'\delta_1\delta_2, \quad (3)$$

where F is the "free molecule" force constant for the perpendicular (out-of-plane) bending mode, and F', the coupling constant, is

$$F'=-2a^2/R^3, \quad (4)$$

since in the aragonite structure, $\theta_1=\theta_2=0$, for the mode under consideration. Thus one is led to expect a negative interaction constant. We shall return to the electrostatic theory of the coupling below; the next task is the development of a suitable coupled oscillator theory for the crystal, in which a very large number of nitrate ions occur at the repeat distance, R.

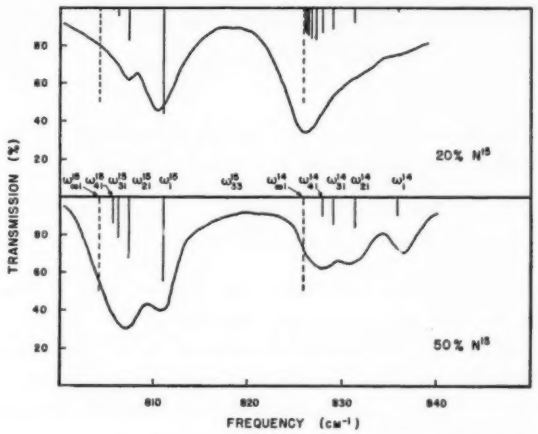

FIG. 1. Infrared absorption of KNO_3 containing 20 percent and 50 percent N^{15} as Nujol mulls. The solid vertical lines indicate theoretical frequencies and relative intensities. Dotted lines indicate frequencies for isotopically pure crystals.

Frequencies

Consider first a crystal containing only one species of isotope. The G matrix for the out-of-plane vibrations will be a constant matrix with diagonal element $3\mu_X+\mu_Y$ for the XY_3 ion. Here μ_X and μ_Y signify the reciprocals of the masses of the X and Y atoms. The potential

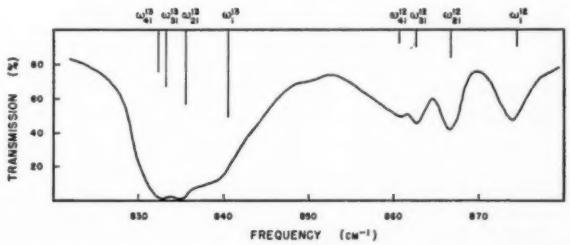

FIG. 2. Infrared absorption of $BaCO_3$ containing 60 percent C^{13} as Nujol mull. Vertical lines indicate theoretical spectrum.

‡ In the calcite lattice there exists one set of closer neighbors than the coplanar ones, but the angular factor in (1) is very small for this set.

[6] R. W. G. Wyckoff, *Crystal Structures* (Interscience Publishers, Inc., New York, 1948).

energy can be written

$$2V=F\sum_i \delta_i^2+2F'\sum_i \delta_i\delta_{i+1}. \tag{5}$$

The Born and von Karman[7] cyclic boundary conditions yield a spectrum defined by

$$\begin{aligned}\lambda(\phi)&=4\pi^2c^2[\omega(\phi)]^2\\&=(3\mu_X+\mu_Y)(F+2F'\cos\phi),\end{aligned} \tag{6}$$

where ϕ, which measures the phase shift between adjacent XY_3 ions can vary between 0 and 2π. In such a crystal, only the totally symmetric mode with respect to translation ($\phi=0$) is active in infrared absorption, so one would expect to observe only the single frequency determined by

$$\lambda(0)=(3\mu_X+\mu_Y)(F+2F').$$

The absorption of natural nitrates and carbonates should be very accurately expressed by this formula, since nearly 99 percent of the nitrogen or carbon atoms are of the same isotopic species.

In order to discuss the spectrum of isotopic mixtures, it becomes necessary to deal with a series of secular determinants of finite size (1, 2, 3, 4, ... rows and columns). Such determinants correspond to the following situations: an isolated XY_3 ion with both nearest neighbors of the other isotopic species, two XY_3 ions of one species with the nearest neighbor at each end of the other species, three of one kind terminated at each end by the other kind, etc. (see Fig. 3).
Consider the situation for *three* of the same kind. The G and F matrices have the forms:

$$\begin{array}{ccccc|ccccc}
G' & 0 & 0 & 0 & 0 & F & F' & 0 & 0 & 0\\
0 & G & 0 & 0 & 0 & F' & F & F' & 0 & 0\\
0 & 0 & G & 0 & 0 & 0 & F' & F & F' & 0\\
0 & 0 & 0 & G & 0 & 0 & 0 & F' & F & F'.\\
0 & 0 & 0 & 0 & G' & 0 & 0 & 0 & F' & F
\end{array} \tag{7}$$

(These matrices are, of course, included in much larger ones, but since the coupling constant acts only between nearest neighbors, we need only consider this part, for a perturbation calculation.) If one attempts to treat this problem by perturbation theory, treating the coupling constant F' as the perturbation, it is first found that the degeneracy of the three roots for the central rows and columns must be removed. It is therefore convenient to make a temporary distinction between the interaction constant which couples the three modes with matrix element G from the terminal ones with matrix element G'. Thus, if one assumes the potential energy is represented by

$$\begin{array}{ccccc}
F & F'' & 0 & 0 & 0\\
F'' & F & F' & 0 & 0\\
0 & F' & F & F' & 0\\
0 & 0 & F' & F & F''\\
0 & 0 & 0 & F'' & F
\end{array}, \tag{8}$$

and treats F'' as the perturbation term, the roots of the central 3×3 unperturbed determinant turn out to be $\lambda^\circ_{31}=G(F+\sqrt{2}F')$, $\lambda^\circ_{32}=GF$, and $\lambda^\circ_{33}=G(F-\sqrt{2}F')$. At the same time, the matrix which transforms the unperturbed F and G matrices to diagonal form is found to be

$$U=\begin{pmatrix} \frac{1}{2} & 2^{-\frac{1}{2}} & \frac{1}{2}\\ 2^{-\frac{1}{2}} & 0 & -2^{-\frac{1}{2}}\\ \frac{1}{2} & -2^{-\frac{1}{2}} & \frac{1}{2}\end{pmatrix}=\|U_{kk'}\|\lambda. \tag{9}$$

To find the effect of the perturbation F'' (numerically equal to F') which couples the three unperturbed modes just described to the modes of the two terminal ions of the other isotopic species, one may then make a second-order perturbation calculation which yields a correction to λ given by

$$\lambda_{3k}''=(U_{k1}^2+U_{k3}^2)GG'(F')^2/(\lambda^\circ_{3k}-G'F). \tag{10}$$

For an isolated ion, $U_{k1}^2+U_{k3}^2$ is replaced by 2; for n ions of one kind, $U_{k1}^2+U_{k3}^2$ is replaced by $U_{k1}^2+U_{kn}^2$. Note that the second-order correction, λ_{nk}'', is negative for the heavier isotope ($\lambda^\circ_{nk}<G'F$) and positive for the lighter isotope ($\lambda^\circ_{nk}>G'F$). Expressions for the unperturbed roots, the second-order correction, and the transformation matrices are summarized in Table I for $n=1$ through 4.

TABLE I. Summary of unperturbed roots, second-order corrections, and transformation matrices for out-of-plane vibrations in aragonite-type lattice.[a,b]

n	k	λ°	λ''	U
1		GF	2ρ	1
2	1	$G(F+F')$	ρ	$\begin{pmatrix}2^{-\frac{1}{2}} & 2^{-\frac{1}{2}}\\ 2^{-\frac{1}{2}} & -2^{-\frac{1}{2}}\end{pmatrix}$
	2	$G(F-F')$	ρ	
3	1	$G(F+2^{\frac{1}{2}}F')$	$\frac{1}{2}\rho$	$\begin{pmatrix}\frac{1}{2} & 2^{-\frac{1}{2}} & \frac{1}{2}\\ 2^{-\frac{1}{2}} & 0 & -2^{-\frac{1}{2}}\\ \frac{1}{2} & -2^{-\frac{1}{2}} & \frac{1}{2}\end{pmatrix}$
	2	GF	ρ	
	3	$G(F-2^{\frac{1}{2}}F')$	$\frac{1}{2}\rho$	
4	1	$G[F+(3+5^{\frac{1}{2}}/2)F']$	0.2764ρ	$\begin{pmatrix}0.3718 & 0.6015 & 0.6015 & 0.3718\\ \cdots & \cdots & \cdots & \cdots\\ \cdots & \cdots & \cdots & \cdots\\ \cdots & \cdots & \cdots & \cdots\end{pmatrix}$
	2	$G[F+(3-5^{\frac{1}{2}}/2)F']$	...	
	3	$G[F-(3-5^{\frac{1}{2}}/2)F']$	...	
	4	$G[F-(3+5^{\frac{1}{2}}/2)F']$	...	

[a] $\rho=GG'(F')^2/(\lambda^\circ_{nk}-G'F)$.
[b] Modes 42, 43, and 44 were not calculated in detail, since their contributions to the over-all intensity are small.

Intensities

In order to account for the intensity distribution through the bands under consideration it is only necessary (*i*) to calculate the relative intensities of the various modes described above, and (*ii*) to find the distribution of each isotope with respect to its occurrence isolated ($n=1$), in pairs ($n=2$), etc. In general, the intensities of vibrational absorption are proportional to $(\partial\mu/\partial Q)^2$ where μ is the dipole moment and Q the normal coordinate. If the transformation between normal coordinates and the basis coordinates (here the δ_i) is given by

$$\delta_i=\sum_k L_{ik}Q_k, \tag{11}$$

[7] M. Born and Th. von Karman, Physik. Z. 13, 297 (1912).

it is evident that

$$\left(\frac{\partial\mu}{\partial Q_k}\right)^2=\sum_i \frac{\partial\mu}{\partial\delta_i}\frac{\partial\delta_i}{\partial Q_k}\sum_i \frac{\partial\mu}{\partial\delta_j}\frac{\partial\delta_j}{\partial Q_k}$$
$$=a^2\sum_{ij} L_{ik}L_{jk}. \tag{12}$$

The transformation coefficients are supposed to be normalized to satisfy the matrix equation

$$\mathbf{L}\mathbf{L}^\dagger=\mathbf{G}, \tag{13}$$

where the dagger indicates (conjugate) transpose. Since our intensity data consist merely of percent transmission curves, we shall ignore the slight difference in intensities which should arise from

$$\sum_k L_{ik}^2=G_{ii}=3\mu_X+\mu_Y, \tag{14}$$

and

$$\sum_k L_{i'k}^2=G_{i'i'}=3\mu_{X'}+\mu_Y, \tag{15}$$

where G_{ii} and $G_{i'i'}$ refer to the two isotopes. Furthermore, since we are interested only in relative intensities, we can normalize to unity. It is important however to recognize and account for the "edge" effect, i.e., the coupling between the modes of a set of n adjacent ions of one isotopic species with the two terminal ions of the other species. Thus a given mode will involve amplitudes (as indicated in Table I) together with amplitudes of the terminal ions which according to standard preturbation theory are given by $U_{k1}G'F'/\lambda^\circ_{nk}-G'F$ and $U_{kn}G'F'/\lambda^\circ_{nk}-G'F$. Such modes are indicated in Fig. 3 for $n=1$ through 3.

Probably the most important feature of this figure is the qualitative explanation of the intensity asymmetry noted above for the 50 percent N^{15} KNO_3, spectrum. Compare, for example, $\omega_{21}{}^H$ (lowest frequency mode for two isotopically similar ions of $H=$*heavier* isotope), with $\omega_{21}{}^L$ (same mode for *lighter* isotope). For ω^H the terminal oscillators vibrate with the same phase as the central ones, but in ω^L they move with opposite phase, thereby leading to a lower intensity. This is a direct consequence of the negative sign of F', since $U_{k1}G'F'/\lambda^\circ_{nk}-G'F$ will have the same sign as U_{k1} when $F'<0$, $\lambda^\circ_{nk}<G'F$. One may also observe qualitatively that the lowest frequency mode in each set of frequencies, for n adjacent indentical neighbors, is the most intense mode in the set. Indeed, ω_{22} and ω_{32} have zero intensity and ω_{33} is very weak. One might, therefore, express matters by stating that the intensities for finite sets rapidly approach the limit for the infinite set in which all modes except the totally symmetric one, which in this case ($F'<0$) is the lowest frequency mode, have zero intensity.

Finally, in order to compare the theoretical spectrum with the experimental one, it is necessary to evaluate the distribution of isotopic molecules of a given kind in sets of one, two, three, etc. We employ essentially the distribution applied by Flory[8] to the problem of polymer length distribution. Thus, if the fraction of isotopic molecules of one kind is p, the chance that one molecule of this kind will be found in a set with exactly n members is given by

$$f_n(p)=np^{n-1}(1-p)^2. \tag{16}$$

If N is the total number of molecules of both isotopic species, pN is the total number of the given species, and it then follows that

$$g_n(p)=pNf_n(p)/n, \tag{17}$$

is the total number of sets composed of n members. The total intensity of the k-th mode of sets of n members will then be proportional to

$$I_{kn}(p)=g_n(p)(\partial\mu/\partial Q_k)^2. \tag{18}$$

It is shown in an Appendix that (18) yields a correct result for the intensity when all frequencies of one isotope are coincident due to vanishing of the coupling constant.

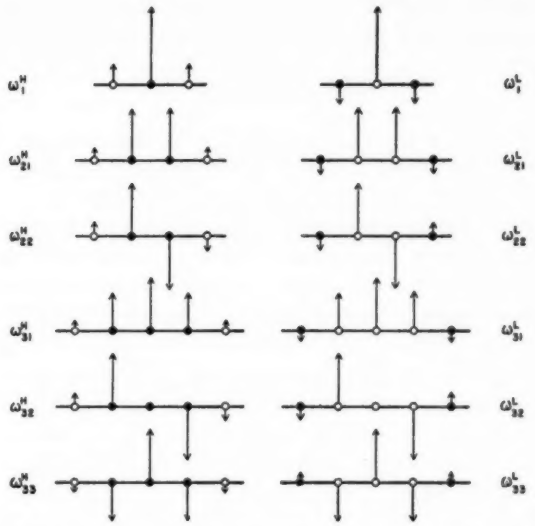

FIG. 3. Normal modes for one, two, and three molecules of one isotopic species surrounded by other species. Arrows indicate relative amplitude schematically, L is lighter isotope, and H is heavier isotope.

Comparison with Experiment

The two force constant parameters F and F' were first calculated, employing only the data from the natural material and the formulas for a pure lattice (lighter isotope, higher observed frequency) and for an isolated molecule (heavier isotope, lower observed frequency). The numerical values of the force constants thus found were, for KNO_3, $F=1.48166$ and $F'=-0.01495$; for $BaCO_3$, $F=1.43048$ and $F'=-0.02261$ (all in millidynes per angstrom).

On this basis, the "line" frequencies and strengths indicated in Fig. 1 and 2 were calculated. The close

[8] P. J. Flory, J. Am. Chem. Soc. **58**, 1877 (1936).

agreement between experiment and theory affords a conclusive proof of the assumptions in the vibrational theory.

CONCLUSION

In conclusion, it seems worthwhile to evaluate the dipole derivative, a, from the coupling constant, F', with the aid of Eq. (4). This is done in Table II.

The coupling constants for calcium and strontium carbonates are taken from reference (1). Aside from the fact that the values for a are of a reasonable order of magnitude, it is difficult to assess their reliability, since no studies of the absolute intensities of the band in question have yet been reported. We hope to carry out such an investigation in the near future. The bending mode of carbon dioxide gas has an intensity[9] which leads to a value of 0.985 debye/A when converted to similar units.

One implication of the dipole-dipole interaction theory which we have attempted to test experimentally, is that the in-plane modes, ω_3 and ω_4 for these same substances should exhibit a positive coupling constant. It has been found that the lower frequency mode (principally degenerate bending) is nearly unshifted by isotopic substitution; moreover, its intensity is relatively low, so that it is not surprising that no effects could be observed. The higher frequency mode is very intense, and might therefore be expected to give rise to large coupling effects. When the substance is studied in polycrystalline form at room temperature, however, the absorption is much too broad to permit resolution of any fine structure. Such shifts as are observed do not contradict the possibility of a positive coupling constant.

ACKNOWLEDGMENT

The author wishes to express his gratitude for a Grant in Aid from the General Research Funds of Oregon State College which made possible the purchase of the isotopically enriched substances.

[9] D. F. Eggers, Jr., and B. L. Crawford, Jr., J. Chem. Phys. **19**, 1554 (1951).

TABLE II. Dipole derivative, $a=(\partial\mu/\partial\delta)$, for out-of-plane vibration of nitrate and carbonate ions.

Substance	$F'(10^5$ dynes/cm)	$R(A)$	$a(10^{-10}$ e.s.u. $=1$ debye/$A)$
KNO_3	−0.015	3.225	1.6
$CaCO_3$	−0.027	2.860	1.8
$SrCO_3$	−0.026	3.050	1.9
$BaCO_3$	−0.023	3.275	2.1

APPENDIX

If the coupling constant vanishes, the frequencies for a given isotopic species but for different k and n become identical, and the total intensity is obtained by summing (18) over all possible values of k and n. The summation over k yields

$$\sum_k I_{kn}(p)=a^2g_n(p)\sum_k\sum_{i,j}L_{ik}L_{jk}$$

$$=a^2g_n(p)\sum_{i,j}\sum_k L_{ik}L_{kj}^{\dagger}$$

$$=a^2g_n(p)\sum_{i,j}\delta_{ij}G_{ii}$$

$$=a^2g_n(p)nG_{ii}.$$

This result follows from (12), (13), and (14). The summation over n then yields

$$\sum_n\sum_k I_{kn}=a^2G_{ii}\sum_n ng_n(p)$$

$$=a^2G_{ii}pN\sum_n f_n(p)$$

$$=a^2G_{ii}pN,$$

since $\sum f_n(p)=1$, for large N. This result exhibits the correct proportionality of the intensity to the total number of isotopic molecules of one kind, pN.

Self-Diffusion of Ions in Molten Electrolyte under the Influence of an Electric Field

LING YANG AND M. SIMNAD
Metals Research Laboratory, Carnegie Institute of Technology, Pittsburgh, Pennsylvania
(Received November 3, 1954)

By taking into account both self-diffusion and electric migration of the radioactive ions formed by the electrolytic dissolution of a radioactive metal anode, an equation has been derived for the distribution of the radioactivity as a function of the distance from the anode surface along the diffusion path. Based on this equation, the error involved in the direct determination of ionic mobility by measuring the distance of spreading of the radioactivity and neglecting the role of self-diffusion is analyzed. It is shown that for a system with a given diffusivity, the error decreases with the increase of the time of electrolysis, t, and the applied potential, E. To obtain the true ionic mobility, it is suggested that measurements should be made for a number of "t" or "E" values. The apparent ionic mobility obtained is then plotted against $1/t$ or $1/E$ and extrapolated to $1/t=0$ or $1/E=0$ to give the true value.

IN our recent measurements[1] of the mobility of Fe^{++} in fused iron silicates, a radioactive anode was used and the distance of spreading of the radioactivity due to electrolytic dissolution and subsequent migration of the Fe^{++} was measured by autoradiograph techniques. The mobility μ (in cm^2/volt sec) of Fe^{++} was calculated from this distance, d (in cm), the time of electrolysis, t (in seconds), the applied potential V (in volts), and the distance between the electrodes l (in cm) by using the equation

$$\mu=\frac{d}{t}\frac{l}{E}. \tag{1}$$

Since the movement of the radioactive Fe^{++} involves both diffusion and electric migration, the aforementioned calculation cannot be exact unless the spreading of radioactivity by diffusion is negligible compared with that by electric migration. This is, however, not necessarily true, especially when E/l is small. It therefore seems desirable to know how much error is involved in neglecting the role of diffusion and how this error can be minimized. An equation representing the distribution of radioactivity as a function of distance from the anode surface was therefore derived by taking into account both diffusion and electric migration of the radioactive metal ions. Based on this equation, the error introduced in calculating the ionic mobility by Eq. (1) is analyzed and discussed.

DERIVATION OF THE EQUATION

In order to be comparable to the conditions prevailing during electrolysis and yet without introducing too many mathematical complications, the case treated is that shown in Fig. 1, which possesses the following characteristics:

(1) Only the cation conducts the current. Every metal ion formed by anodic dissolution will take part in conducting the current. Therefore, there is no accumulation of radioactivity near the anode. This is actually the case for many molten electrolytes having large anions.

(2) The distance between the electrodes is large in comparison to the distance traveled by the radioactive metal ions during the electrolysis. The current density is uniform over the whole anode and cathode surfaces and there is no diffusion of the radioactive metal ions into the solid container of the electrolyte. The diffusion is therefore one dimensional and the system can be considered as a semi-infinite one.

(3) The size of the radioactive anode is large in comparison with the amount dissolved during the electrolysis. Also the shift of the anode-electrolyte interface caused by electrolytic dissolution of the anode is assumed to be negligible. Thus, for a given current of electrolysis, there exists a constant concentration c_0 of radioactive metal ions at the anode-electrolyte interface.

The equation of diffusion under the influence of external forces is[2]:

$$\frac{\partial c}{\partial t}=D\frac{\partial^2 c}{\partial x^2}-\frac{\partial}{\partial x}(cv), \tag{2}$$

where D is the self-diffusion coefficient of the metal ion in the molten electrolyte, c is the concentration of radioactive metal ions at time t and a distance x from the anode-electrolyte interface where $x=0$. Also v is the steady velocity of the ion$=F\mu$, F being the force acting on the ion and μ the mobility of the ion, i.e., velocity of the ion under a force of 1 dyne. For the present case, $F=ZeE/300l$, where Z=valence of the ion, e=the electronic charge (in esu), E=electric potential across the electrodes, which drives the ions through the electrolyte (in volts), l=distance between the electrodes (in cm). The initial and the boundary conditions are:

t=all values,	$x=0$	$c=c_0$
$t=0$	$x>0$	$c=0$
$t>0$	$x>0$	$c=f(x,t)$ which is the function to be determined.

[1] Results to be published.

[2] W. Jost, *Diffusion in Solids, Liquids, Gases* (Academic Press, Inc., New York, New York, 1952), p. 47.

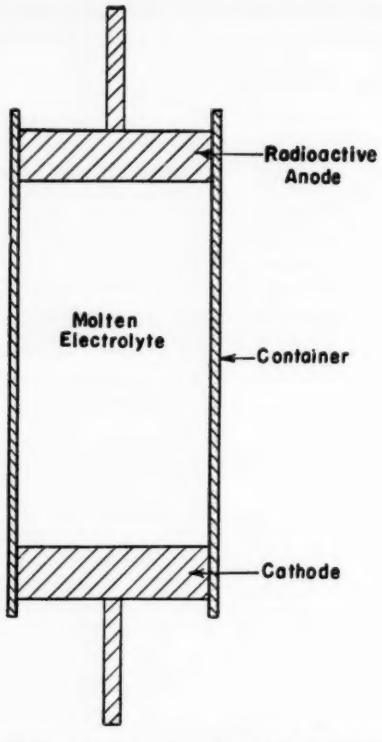

FIG. 1. Schematic arrangement of the electrolytic cell.

Since the potential gradient between the electrodes is constant, therefore v is independent of x and Eq. (2) becomes

$$\frac{\partial c}{\partial t}=D\frac{\partial^2 c}{\partial x^2}-v\frac{\partial c}{\partial x}. \tag{3}$$

Shift the c-axis by the amount c_0 and let $c_1=c-c_0$, Eq. (3) becomes

$$\frac{\partial c_1}{\partial t}=D\frac{\partial^2 c_1}{\partial x^2}-v\frac{\partial c_1}{\partial x} \tag{4}$$

and the initial and the boundary conditions are:

$$\begin{array}{lll} t=\text{all values}, & x=0 & c_1=0 \\ t=0 & x>0 & c_1=-c_0 \\ t>0 & x>0 & c_1=f_1(x,t). \end{array}$$

By a further transformation:

$$c_1=c^*\exp\left[\frac{vx}{2D}-\frac{v^2t}{4D}\right]. \tag{5}$$

Equation (4) becomes:

$$\frac{\partial c^*}{\partial t}=D\frac{\partial^2 c^*}{\partial x^2}, \tag{6}$$

which is the same form as Fick's second law and the initial and the boundary conditions become:

$$\begin{array}{lll} t=\text{all values}, & x=0 & c^*=0 \\ t=0 & x>0 & c^*=-c_0\exp\left[-\dfrac{vx}{2D}\right] \\ t>0 & x>0 & c^*=f^*(x,t). \end{array}$$

This is equivalent to a case having the initial conditions:

$$\begin{aligned} &t=0 \quad x=-\infty\to 0 \quad c^*=c_0\exp\left[\frac{vx}{2D}\right] \\ &x=0\to+\infty \quad c^*=-c_0\exp\left[-\frac{vx}{2D}\right]. \end{aligned} \tag{7}$$

The general solution of Fick's second-law equation is

$$c^*=\frac{1}{2(\pi Dt)^{\frac{1}{2}}}\int_{-\infty}^{+\infty}f(x')\exp\left[-\frac{(x-x')^2}{4Dt}\right]dx', \tag{8}$$

where $f(x')$ is the distribution of c^* with respect to x at $t=0$. Substitute (7) into (8) after changing the x in (7) to x', we obtain

$$\begin{aligned} c^*=\frac{1}{2(\pi Dt)^{\frac{1}{2}}}\Bigg[&\int_{-\infty}^{0}c_0\exp\left(\frac{vx'}{2D}\right) \\ &\times\exp\left(\frac{-(x-x')^2}{4Dt}\right)dx' \\ &+\int_{0}^{+\infty}(-c_0)\exp\left(\frac{-vx'}{2D}\right) \\ &\times\exp\left(\frac{-(x-x')^2}{4Dt}\right)dx'\Bigg]. \end{aligned} \tag{9}$$

Substitute

$$\xi_1^2=\frac{1}{4Dt}(x'-tv-x)^2,$$

$$\xi_2^2=\frac{1}{4Dt}(x'+tv-x)^2$$

and change the integration limits, (9) becomes:

$$\begin{aligned} c^*=\frac{c_0}{\sqrt{\pi}}&\exp\left(\frac{tv^2}{4D}\right) \\ &\times\Bigg[\exp\left(\frac{vx}{2D}\right)\int_{-\infty}^{[-tv-x/2(Dt)^{\frac{1}{2}}]}\exp(-\xi_1^2)d\xi_1 \\ &-\exp\left(\frac{-vx}{2D}\right)\int_{[tv-x/2(Dt)^{\frac{1}{2}}]}^{+\infty}\exp(-\xi_2^2)d\xi_2\Bigg]. \end{aligned} \tag{10}$$

Substituting (10) into (5), we obtain

$$c_1=\frac{c_0}{\sqrt{\pi}}\left[\exp\left(\frac{vx}{D}\right)\int_{-\infty}^{[-lv-x/2(Dl)^{\frac{1}{2}}]}\exp(-\xi_1^2)d\xi_1 - \int_{[lv-x/2(Dl)^{\frac{1}{2}}]}^{+\infty}\exp(-\xi_2^2)d\xi_2\right]. \quad (11)$$

Since $c_1=c-c_0$,

$$c=c_0\left\{1+\frac{1}{\sqrt{\pi}}\left[\exp\left(\frac{vx}{D}\right)\int_{-\infty}^{[-lv-x/2(Dl)^{\frac{1}{2}}]}\times\exp(-\xi_1^2)d\xi_1-\int_{[lv-x/2(Dl)^{\frac{1}{2}}]}^{+\infty}\exp(-\xi_2^2)d\xi_2\right]\right\}. \quad (12)$$

Substitute $v=F\mu=(Ze/300)(E/l)(D/kT)=KED$, where $K=(Ze/300)(1/kTl)$, k being the Boltzmann constant and T the temperature (°K) and Eq. (12) becomes:

$$c=\frac{c_0}{2}\left\{\left[1+\operatorname{erf}\left(\frac{KEDt-x}{2(Dt)^{\frac{1}{2}}}\right)\right]+\exp(KEx)\left[1-\operatorname{erf}\left(\frac{KEDt+x}{2(Dt)^{\frac{1}{2}}}\right)\right]\right\} \quad (13)$$

where "erf" is the probability integral,

$$\operatorname{erf}(x)=\frac{2}{\sqrt{\pi}}\int_0^x\exp(-\xi^2)d\xi.$$

Equation (13) represents the distribution of radioactivity along the migration path of the metal ions as a function of time, t, distance from the anode-electrolyte interface x, applied electric potential E and the diffusion coefficient D.

ERROR INTRODUCED IN CALCULATING IONIC MOBILITY BY EQUATION (1) BY NEGLECTING THE ROLE OF SELF-DIFFUSION

If c/c_0 of Eq. (13) is plotted against x for given values of t, E, K, and D, curves shown in Fig. 2 are obtained. In Fig. 2, the curves shown are for $D=10^{-5}$, 3×10^{-5}, 6×10^{-5}, and 10^{-4} cm^2/sec, respectively, assuming $E=40$ volts, $t=1000$ seconds, and $K=1$ ($K=1$ when $l=15$ cm, $Z=2$, $T=1523$°K). If the experimental conditions satisfy the assumptions made in deriving Eq. (13), the shape of these curves should also be that of the density tracings of autoradiographs obtained, since c_0 is a constant. Theoretically speaking, $c=0$ only when $x=\infty$, i.e., the distance of spreading of the radioactivity in the molten electrolyte should be infinity. However, in the actual case, the autoradiograph and its "microdensitometric" tracing would not be able to detect the radioactivity when c is below a certain value. The distance d of spreading of the radioactivity, as detected in the autoradiograph, therefore depends upon the sensitivity of the autoradiographic and the tracing techniques, as well as the specific activity of the radioactive anode. We have calculated the d-values for the aforementioned E-, t-, K-, and D-values, using Eq. (13) and assuming that the lowest detectable values of c are 0.1 c_0 and 0.001 c_0, respectively. From these d-values, the apparent values of the ionic mobility are calculated by Eq. (1), assuming that the spreading of radioactivity is all due to electric migration. The results thus obtained are compared with the true values of the ionic mobility computed from the D-values by the Nernst-Einstein relationship and the percentage errors evaluated. The data are shown in Table I.

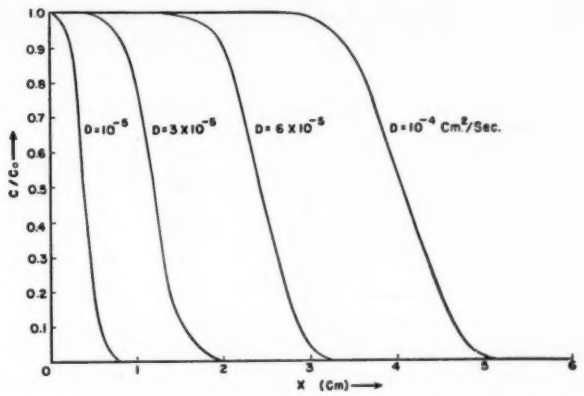

FIG. 2. Distribution of radioactivity as a function of distance from the anode-electrolyte interface, calculated from Eq. (13). $E=40$ volts, $t=1000$ seconds, $l=15$ cm, $T=1523$°K, $Z=2$.

It can be seen from Table I that for given values of E, t, l, and T, the higher the value of D (therefore the value of μ) is, the smaller is the error introduced in the ionic mobility calculated from autoradiographic results by Eq. (1), in which the role of self-diffusion in spreading the radioactivity is neglected. This is because although a higher value of D increases the role of self-diffusion in spreading the radioactivity, it increases even more the role of electric migration, since the velocity of electric migration is directly proportional to D. This is quite evident from the shape of the curves in Fig. 2. Since, in Eq. (13), D and t always occur together, they should influence the aforementioned error in the same way. In other words, for given values of E, D, l, and T, the longer the time of electrolysis is, the smaller is the error introduced by neglecting the role of self-diffusion. The same is true if a higher electric potential E is used in pushing the ions through the electrolyte, as the role of electric migration in spreading the radioactivity is directly proportional to E. It can be shown that for $D=10^{-5}$ cm^2/sec, $t=1000$ seconds, $T=1523$°K, $l=15$ cm, and a lowest detectable value of $c=0.01$ c_0, the error introduced in neglecting the role of self-diffusion is 105 percent if $E=40$ volts and that the error drops to 7 percent if E is increased to 400 volts.

Thus in actual experiments, the best way to obtain the true value of the ionic mobility is to determine the

TABLE I. Error introduced in the calculation of ionic mobility from autoradiograph tracing by Eq. (1); $E=40$ volts, $t=1000$ seconds, $l=15$ cm, $T=1523°K$, $Z=2$.

True value of D (cm^2/sec)	True value of $\mu=\frac{D}{kT}\frac{Ze}{300}$ ($cm^2/volt\ sec$)	x_1 (for $c/c_0=0.01$) calc from Eq. (13) (cm)	Apparent value of $\mu_1=\frac{x_1}{t}\frac{l}{E}$ ($cm^2/volt\ sec$)	% error $=\frac{\mu_1-\mu}{\mu}\times100$	x_2 (for $c/c_0=0.001$) calc from Eq. (13) (cm)	Apparent value of $\mu_2=\frac{x_2}{t}\frac{l}{E}$ ($cm^2/volt\ sec$)	% error $=\frac{\mu_2-\mu}{\mu}\times100$
10^{-5}	1.52×10^{-4}	0.74	3.11×10^{-4}	105%	0.85	3.19×10^{-4}	110%
3×10^{-5}	4.56×10^{-4}	1.78	6.69×10^{-4}	47%	1.97	7.40×10^{-4}	62%
6×10^{-5}	9.12×10^{-4}	3.25	1.22×10^{-3}	34%	3.50	1.31×10^{-3}	44%
10^{-4}	1.52×10^{-3}	5.05	1.90×10^{-3}	25%	5.40	2.03×10^{-3}	34%

apparent values from the autoradiographic tracings, using Eq. (1), for several different values of t or E. These values are then plotted against $1/t$ or $1/E$ and extrapolated to $1/t=0$ or $1/E=0$. The ionic mobility thus obtained should be very near to the true value. Owing to the fact that there is always some radioactive anode left after the electrolysis, the autoradiograph of the anode compartment after the electrolysis is a composite picture due to the activity of the anode left and that of the radioactive ions in the electrolyte. The shape of the tracing therefore may not be the same as that shown in Fig. 2.

Even when the restricted conditions required by mathematical derivation cannot be fully met, the rigorous derivation can serve as a useful guide in the planning and evaluation of experimental work.

ACKNOWLEDGMENT

We wish to thank Dr. G. Derge for his help and interest in this work. We also wish to thank Dr. Y. Y. Li and Dr. Andrew S. C. Ying for helpful discussions. Support of this work has been given by a research program sponsored by the U. S. Atomic Energy Commission.

THE JOURNAL OF CHEMICAL PHYSICS VOLUME 23, NUMBER 7 JULY, 1955

Evaporation of Submicroscopic Ice Crystals*

MARY FOULKS GOURLEY AND W. D. CROZIER
Research and Development Division, New Mexico Institute of Mining and Technology, Socorro, New Mexico

(Originally received October 30, 1953; Revised manuscript received October 2, 1954)

Experiments, designed to interpret certain meteorological observations, provide evidence that very small ice crystals may have evaporation rates much lower than predicted on the basis of the vapor pressure of macroscopic ice. Small ice crystals, formed by spontaneous sublimation in nuclei-free air, were suspended in a strongly desiccating atmosphere for a time far longer than should have been sufficient for their complete evaporation. Though they decreased in size below the minimum observable optically, their presence was demonstrated by their ability to nucleate visible ice particles when exposed to a supersaturated atmosphere. In representative experiments, ice-forming nuclei were observed in a 250-cm^3 chamber three hours after the admission of nucleus-free ice particles of about 1-micron radius, the chamber containing an atmosphere at $-20°C$ with water vapor pressure at about 50 percent of saturation with respect to macroscopic ice. There was some evidence, however, that the ice-forming residues diminish in effectiveness at a low time rate.

INTRODUCTION

THE temperature at which ice crystal nucleation occurs in a cloud of supercooled water droplets has been measured for many nucleating substances and found to range from about $-12°C$ to $-25°C$.[1] With the possible exception of silver iodide, no known substance could be responsible for the initiation of large numbers of ice crystals in a supercooled cloud at $-10°C$ or warmer. Yet, some meteorological phenomena, such as precipitation of snow from relatively warm clouds, suggest the presence in the atmosphere of ice-forming nuclei more effective than those observed in laboratory cold chambers. It has been proposed[2] that these nuclei may be small, highly-bonded "cells" of ice, but attempts to detect such nuclei with optical instruments have been unsuccessful. An experiment was designed to synthesize small ice crystals, subject them to controlled evaporation, and verify the existence of persistent residues by observing their nucleating properties. The experimental evidence thus obtained indicates that submicroscopic ice crystals may have very low rates of solid-to-vapor

* This work was supported by Office of Naval Research contract.

[1] E. J. Workman, Phys. Rev. 81, 659 (1951). See also V. J. Schaefer, Project Cirrus Occ. Rep. No. 20 General Electric Research Laboratory Report No. RL-308 (1950).

[2] E. J. Workman, post-deadline paper at the 307th meeting of the American Physical Society, Vancouver, B. C., June 25–28, 1951.

phase transition. It has not been demonstrated that small ice particles made persistent by this property are important in meteorological situations, but the possibility, at least, appears to exist.

APPARATUS

A special expansion chamber apparatus used for the experiment is illustrated schematically in Fig. 1. The essential features are: (a) the chamber, (b) a source of nuclei-free gas, and (c) a source of ice particles formed in the absence of foreign nuclei.

(a) The Chamber

The chamber is a heavy-walled copper vessel of cylindrical form providing a test space of about 250 cm³. A microscope and illuminating system are arranged for ultramicroscopic examination of a small region near the center. The floor of the chamber is perforated to provide for the control of vapor density by a vapor sink in the form of a layer of ice supported on a plate thermally insulated from the chamber and kept at a temperature lower than the temperature of the chamber. Temperature control is achieved by balancing the heat input from resistance wire elements with a dry ice cooling system. Thermocouples measure the temperature of the air in the chamber and the temperature of the vapor sink to ± 0.1°C. Gas pressure in the chamber is kept at a predetermined value above atmospheric during a significant portion of the experimental cycle; adiabatic expansions may be made by opening the indicated expansion valve.

(b) The Gas Supply

Ordinary commercial compressed gas from a tank (see Fig. 1) is processed to remove nuclei by saturating it with water vapor at $+20$°C in humidifier 1, then cooling to dry ice temperature as it passes through a filter. Glass wool traps and coils of aluminum tubing in the filter remove the nuclei and excess water vapor. The effectiveness of the denucleating process can be tested by running gas from the filter directly into the chamber, permitting it to become saturated with water vapor from the sink, and then cooling by adiabatic expansion. No ice or water particles appeared with a volumetric expansion ratio of 1.22, the limit imposed by the manometers used. Expansions representing volume ratios about 6 percent larger than those employed subsequently for detecting nuclei are used for routine testing of the system.

(c) The Ice Particles

Ice particles are produced in the nuclei-free gas by passing it over a surface of distilled water at room temperature, then cooling it in a glass bulb at low temperature (-42°C to -78°C). Particles in the 1-micron size range produced in this manner can be introduced into the chamber by allowing a prescribed volume of gas to flow through the system to the chamber, carrying the ice particles with it.

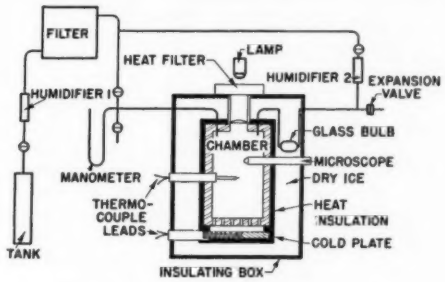

FIG. 1. Expansion chamber apparatus.

EXPERIMENTAL PROCEDURE

In the normal experimental cycle the chamber is flushed with gas from the filter and tested for the absence of nuclei. After the temperatures of the chamber and vapor sink have been adjusted to give a desired value of subsaturation in the chamber, ice particles are introduced from the cold bulb system. These are observable in the field of the microscope, where they frequently scintillate, showing that they are crystalline. In the subsaturated atmosphere of the chamber the ice particles are reduced by evaporation, becoming in less than a minute too small to be seen with the microscope (smaller than approximately 0.05-μ radius). The pressure is then raised, by the admission of a small amount of gas from the filter, to a value which will give a desired expansion ratio when the expansion valve eventually is opened to the atmosphere. The chamber is now allowed to stand for a desired interval of time. The first few minutes of this interval are required for the establishment of equilibrium, after which the submicroscopic ice particles are subjected to the predetermined subsaturation. At the end of the desired time interval, regarded for convenience as beginning when the ice particles are admitted to the chamber, the expansion valve is opened. If the momentary supersaturation thus produced is sufficiently high, the nuclei present will grow to a size visible in the microscope. For a fixed set of evaporation conditions (subsaturation, temperature, and time) there exists an expansion, with a corresponding supersaturation, which may be considered *critical* in the sense that smaller expansions can be made without observable nucleation and larger expansions will produce observable particles.

RESULTS

By means of the procedure just outlined, nuclei have been observed in the chamber for 3 hours after the introduction of the ice particles into an atmosphere (at a temperature of about -20°C) about 50 percent

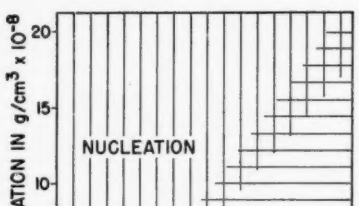

FIG. 2. Maximum excess vapor density (supersaturation) at expansion *vs* deficiency of vapor density (subsaturation) during evaporation for 75-minute evaporation periods.

saturated with respect to a macroscopic surface of ice.[3] That the observed nuclei are the products of the ice evaporation process has been confirmed by experiments in which the glass bulb was heated so that no ice particles would be formed in it. The same volume of gas from the bulb, containing the same amount of water substance in the form of vapor, was tested for nuclei in the same manner as in the experiments where ice particles from the bulb were admitted to the chamber. No nuclei were observed.

In the experimental cycle as described, the particles nucleated are so small that direct observation does not establish whether they are of ice or water. In order to answer this question, auxiliary apparatus was devised which the nuclei were led into a cloud of supercooled water droplets. There they nucleated particles that quickly grew large enough to scintillate, proving that the nuclei were ice-forming.

The ice-particle concentration in the chamber following introduction of the particles from the cold bulb system was typically of the order of 10^4 particles/cm^3. The nuclei concentration present after exposure to subsaturation was a substantial fraction of the original ice-particle concentration, if the exposure to subsaturation was of moderate length—30 min, for example. In experiments including progressively longer exposures to the subsaturation, the nuclei concentrations became progressively smaller; this undoubtedly was partly due to diffusion of nuclei to the walls of the small (250 cm^3) chamber. It is possible that a contributing factor was the eventual disappearance of nuclei as the end result of the very slow evaporation phenomenon described below.

Air, nitrogen, argon, and helium were used as carrier gases in exploratory experiments; the persistence of nuclei was found in each of these gases. In the case of helium, however, considerable difficulty was encountered in conducting ice particles into the chamber from the glass bulb system. Most of the experimentation was done with nitrogen.

[3] The values for the saturation vapor density with respect to a macroscopic surface of ice were taken from the tables of Paul J. Kiefer, Monthly Weather Rev. **69**, 329 (1941). Subsaturations and supersaturations were computed from this vapor density *vs* temperature relation.

The evaporation-nucleation studies were conducted with the evaporation process carried on usually in the temperature range -18°C to -30°C. The lower limit of temperature was set by the requirement that the temperature after expansion be not lower than -39°C in order to avoid confusion of the nucleation by submicroscopic ice crystals with other ice-forming processes thought to occur at lower temperatures. Extension of the experiments to higher temperatures was made difficult by the steepness of the vapor-pressure *vs* temperature relation[3] for the vapor sink, which requires very close temperature control for the maintenance of a given subsaturation. A few tests did demonstrate the persistence phenomenon at temperatures as high as -14°C.

It can be observed that the appearance or non-appearance of particles after a given expansion depends both upon the magnitude of the expansion and upon the evaporation conditions to which the nuclei have been subjected. Although the magnitude of the expansion governs the amount of vapor available for particle growth, no quantitative relation has been established. It is possible, however, to compute the maximum value of the supersaturation (with respect to a macroscopic ice surface) produced by a given expansion and to use this quantity as an empirical parameter. Of particular interest (in comparing the nucleating effectiveness of the residues from different evaporation processes) is the maximum supersaturation in an expansion which is just sufficient to produce observable particles. Such a supersaturation will be called an n-supersaturation. Determination of an n-supersaturation for the nuclei remaining after a given set of evaporation conditions requires a series of observations in which the experimental cycle is repeated with varying supersaturations until a value is obtained, above which observable particles appear and below which they do not appear. Such a series of observations must be made for each desired set of evaporation conditions.

Because of the statistical nature of the nucleation and growth processes, the n-supersaturation properly should be defined in probability terms. For the present purpose it is sufficient to recognize that the statistical fluctuations, together with the experimental uncertainties, produce a spread in the observed values of the n-supersaturation.

Figure 2 shows the variation in nucleating effectiveness of nuclei held for a constant time (75 minutes) at different subsaturations, while Fig. 3 shows the variation in nucleating effectiveness of nuclei subjected to a constant subsaturation (vapor density deficiency of 30×10^{-8} g/cm^3) for varying times. The regions of nucleation and non-nucleation are shown, and the zone of overlapping of the regions covers the spread in observed values of n-supersaturation. It is apparent from these observational uncertainties and the inherent limitations of the technique that only a general trend has been determined, i.e., the tendency of the n-super-

saturation to increase with increasing subsaturation and increasing time of exposure. If it is assumed, however, that the *n*-supersaturation, which is a measure of nucleating effectiveness, is inversely related to the size of the nuclei (an assumption having considerable theoretical justification), the foregoing results are consistent with the view that, although the nuclei are surprisingly persistent, they do evaporate at a very slow rate, the rate being dependent upon the subsaturation.

An important feature of the results depicted in Fig. 2 is the contrast between the rates of particle evaporation and particle growth. For example, the size loss of an evaporating ice particle that occurred during a 75-minute exposure to a vapor deficiency of 40×10^{-8} g/cm³ can be restored during a few seconds of growth where the maximum vapor excess is only 16×10^{-8} g/cm³. If diffusion of vapor were the only important mechanism for evaporation and growth, the product of the vapor density gradient and time for the two processes should be of the same order. Here one exceeds the other by a factor of approximately 5000.

DISCUSSION

Since nucleation occurs only when ice particles have been present in the chamber, the observed nuclei are thought to be the residues of a partial evaporation of the ice crystals, residues either too small or too skeletal to be detected by optical scattering but capable of serving as centers for crystal growth. That such residues should persist in a vapor regime subsaturated with respect to macroscopic ice requires some explanation.

Such a phenomenon has not been predicted from diffusion theories of evaporation. The hypothesis of Woodland and Mack[4] and the theory of Fuchs,[5] as interpreted by Bradley, Evans, and Whytlaw-Gray,[6] indicates that for particles smaller than 0.1-micron radius the rate of evaporation is proportional to the surface area, i.e., the radius decreases at a constant rate. Using the equation of Bradley *et al.*, and assuming that the equilibrium vapor pressure of the particles is the same as that of macroscopic ice, it was calculated that a 0.1-micron particle should evaporate to zero radius in a time of the order of a millisecond in an atmosphere 50 percent saturated at −20°C. It has been seen that such particles persist at least 10^8 times as long as this. The calculation involved an assumed accommodation coefficient of approximately unity, it is true, but it seems impossible that the accommodation coefficient can be low enough to account for such a discrepancy, for it would not be possible for ice crystals to grow from these nuclei fast enough to become visible in the short periods of supersaturation used in the above experiments.

[4] D. J. Woodland and E. J. Mack, Am. Chem. Soc. **55**, 3149 (1933).
[5] N. Fuchs, Physik. Z. Sowjetunion **6**, 224 (1934).
[6] Bradley, Evans, and Whytlaw-Gray, Proc. Roy. Soc. (London), **A186**, 368 (1946).

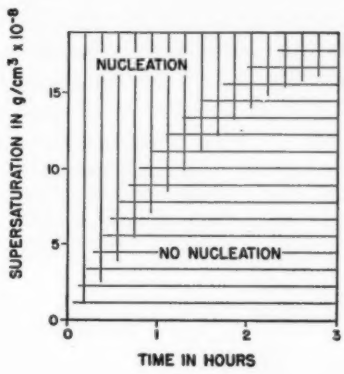

FIG. 3. Supersaturation at expansion *vs* time of evaporation for a vapor deficiency of 30×10^{-8} g/cm³ at 250°K.

It seems reasonable to think that the thermodynamic properties of microcrystals of ice may be different from those of macroscopic ice either because the surface energy of the crystal is a function of its size or because impurities, even those present in the form of gas molecules or ions, may exert a profound influence upon the behavior of ice. The limitations in the application of theories derived statistically from the assumption of large numbers of molecules to problems involving aggregates of a few hundred to a few million molecules are well known. The effects of impurities in ice are not so well known. It has been established[7] that ice is able to incorporate ions from dilute aqueous solutions selectively into its structure, and that the presence of these ions in quantities of one per million molecules[8] of H_2O will affect the electrical properties of the ice.[9] As the electrical behavior of a very small unit of ice is affected by an impurity center occupying a lattice site within the ice structure, so may the possibility arise that the seemingly anomalous thermodynamic properties too are related to structures modified by the inclusion of an impurity center. Present observations show only that such impurities as may exist in the system are incapable of nucleating ice crystals without first being associated with or included in ice crystals. However, inasmuch as ice has never been observed free from impurities, it is necessary to regard even those effects which are catalyzed by impurity centers as properties of ice. In this case it is believed that the ice crystals had a high degree of purity; but since ice has a large "capture cross section" for certain impurities and since these impurities can provide high-energy bonding, the relation of the observed phenomena to pure or impure ice on the molecular scale now considered effective must await further determinations.

[7] E. J. Workman and S. E. Reynolds, Phys. Rev. **78**, 254 (1950).
[8] It should be pointed out that the mention of one impurity center per million water molecules does not imply, nor require, the existence of such a concentration in the gas of the chamber. The very high energy associated with the incorporation of impurity centers as observed for the bulk water-ice interface during growth provides higher bonding energy through dipole-dipole interaction. It is suggested that this condition of intermolecular bonding may, in the case of microcrystalline particles, extend to large numbers of suitably oriented water molecules, thus influencing the effective vapor pressure about such particles.
[9] F. K. Truby, Phys. Rev. **92**, 543(A) (1953).

Photolysis of Hexafluoroazomethane

J. R. Dacey and D. M. Young
Department of Chemistry, Royal Military College of Canada, Kingston, Ontario, Canada
(Received November 1, 1954)

Hexafluoroazomethane is decomposed by light of 2537 A to yield nitrogen, hexafluoroethane, perfluorotetramethyl hydrazine, and perfluorohexamethyl tetrazine. The relative amounts of the various products vary with the pressure: the compounds of higher molecular weight being produced more abundantly at higher pressures. A free radical mechanism is proposed for the reaction.

INTRODUCTION

THE photolysis of azomethane has been studied by a number of investigators,[1–3] and it is generally agreed that the decomposition takes place by a free radical mechanism. The primary step is the formation of a nitrogen molecule and two methyl radicals. The methyl radicals react with one another and with the starting material so that the products of the reaction are variable amounts of simple hydrocarbons and nitrogen. Since it is known from the work of Ruff[4] that the ultraviolet adsorption spectrum of hexafluoroazomethane resembles that of azomethane, it was concluded that the fluorinated compound would probably decompose in a manner similar to azomethane. Thus it was hoped that hexafluoroazomethane would be a good source of trifluoromethyl radicals for further investigations of their reactions. The present paper describes the preliminary work on photolysis of hexafluoroazomethane.

EXPERIMENTAL

Preparation of Hexafluoroazomethane

Hexafluoroazomethane was prepared by a modification of the method used by Ruff,[4] who showed that cyanogen iodide and iodine pentafluoride would react at 125°C to give hexafluoroazomethane and a number of other products. Whereas Ruff carried out the reaction at high pressure in an iron bomb, we found it more convenient to use Pyrex apparatus at ordinary pressure. The reaction vessel consisted of a two liter flask the neck of which had been replaced by a tube 100 cm long and 5 cm in diameter. This extended neck acted as an air cooled condenser to collect the iodine formed by the reaction. The top of the condenser was connected through a standard taper to a train of two traps cooled by liquid air.

The main impurity in the iodine pentafluoride was hydrofluoric acid which was removed by shaking with dry potassium fluoride. After filtering, the pentafluoride was placed in the bottom of the flask by means of a long funnel and the flask cooled in an ice bath. An equal weight (200 g) of cyanogen iodide, recrystallized from ether, was added and the flask shaken until a slurry was formed. The flask was then heated on an oil bath until the temperature reached 85° where gaseous products were formed and collected in the cooled traps. After the reaction had subsided the temperature was raised slowly to 135° above which no further products were formed. The mixture of products was passed through a train of scrubbers containing sodium hydroxide, soda lime, and anhydrous calcium sulfate. The product was further purified by several distillations the final fractionation being made with a Podbielniak column. Hexafluoroazomethane is a pale greenish yellow liquid boiling under 760 mm at −32.2°C. A yield of 35 percent was obtained by the above procedure.

Description of the Photolysis Apparatus

The photolysis was carried out in a silica cell, 10 cm deep and 5 cm in diameter, which was illuminated with light of 2537 A wavelength. The light source was a mercury resonance lamp the output of which was collimated by a lens system. The intensity of the light was determined by actinometry using potassium ferrioxalate.[5]

The reaction cell was part of a closed circuit which contained a volume of 3600 ml when the reaction pressure was below 1 cm and 300 ml when higher pressures were used. The reacting gas was continually circulated around this circuit by means of a magnetically operated all-glass pump. A U-tube trap was included in the circuit. The closed circuit was connected through a stopcock to a vacuum manifold. Beyond the stopcock, and also connected to the manifold, was a McLeod gauge.

Procedure

In making a run the reaction space was first evacuated and then filled to the desired pressure through the stopcock. The stopcock was then closed and the circulating pump started. Traces of mercury vapor were removed from the gas by allowing it to circulate for several hours over gold or indium which had been placed in the U-tube.[6] The photolysis was then started by opening

[1] M. Burton *et al.*, J. Am. Chem. Soc. **60**, 10 (1938); J. Am. Chem. Soc. **59**, 1989 (1937); J. Chem. Phys. **7**, 1080 (1939).
[2] H. A. Taylor and A. Gordon, J. Am. Chem. Soc. **63**, 3435 (1941).
[3] H. C. Ramsperger, J. Am. Chem. Soc. **50**, 123 (1928).
[4] O. Ruff and W. Willenberg, Ber. **73B**, 724 (1940).
[5] C. A. Parker, Proc. Roy. Soc. (London) **A220**, 104 (1953).
[6] E. A. Flood and R. D. Heyding, Can. J. Chem. **32**, 591 (1954).

a shutter between the reaction vessel and the lamp. After the run was terminated, which was usually after about 10 percent of the reacting gas had decomposed, liquid air was placed around the U-tube. With all the condensable gases frozen in this trap, the pressure of the noncondensable gases was measured by opening the system to the McLeod gauge. The noncondensable gases were then removed by pumping and the trap allowed to warm, whereupon the pressure of the condensable products and the remaining starting material was measured. The products were then removed for analysis.

The products were separated with a Podbielniak column when a sufficient amount was available. A Ward still, similar to that described by LeRoy[7] was used to separate small amounts of product. Mass spectrograph analyses were obtained of the products of several runs and separately on the higher and lower boiling fractions.

RESULTS

Light Absorption of Hexafluoroazomethane

The light absorption of hexafluoroazomethane was determined between 2000 and 4500 A by means of a Beckman spectrophotometer. The results are shown in Fig. 1 which also gives the absorption of azomethane taken from Ramsperger[8] and the data of Ruff[4] for hexafluoroazomethane in solution in methyl chloride.

Products of the Reaction

The photolysis of hexafluoroazomethane yields nitrogen, hexafluoroethane, and two new compounds, perfluorotetramethyl hydrazine and perfluorohexamethyl tetrazine. The latter two compounds were identified by means of molecular weight determinations and analysis.

Perfluorohexamethyl tetrazine was found to have a molecular weight by gas density of 468 while the calculated value is 470. The total fluorine by analysis was 72.27 percent while the calculated value is 72.75 percent. It is a colorless liquid boiling at 100.4°C.

Perfluorotetramethyl hydrazine had a molecular weight of 305, calculated value 304. The fluorine analysis gave 77.58 percent, calculated value 74.97 percent. It is a colorless liquid boiling at 32°C.

Effect of Pressure on the Products of the Reaction

It was found that at pressures below 1 mm the main products of the decomposition were nitrogen and hexafluoroethane, while at higher pressures increasing amounts of the tetrazine and hydrazine were formed. In Fig. 2 the fraction of the condensible products consisting of hexafluoromethane is plotted against the logarithm of the reaction pressure. The two curves are data obtained at different light intensities. For the upper curve the intensity was 1.2×10^{17} quanta per sec entering the cell, while for the lower curve it was 6.7×10^{16} quanta per second.

The ratio of tetrazine to hydrazine in the products increased as the pressure increased. At 10 mm pressure this ratio was 1:6.6 while at 100 mm it was 1:2.6.

Quantum Yield

The quantum yield was determined at 50 cm and at 28 cm pressure. The average value was 0.25.

DISCUSSION

Mechanism of the Reaction

There is no doubt that the initial step in this photolysis is the division of the hexafluoroazomethane into

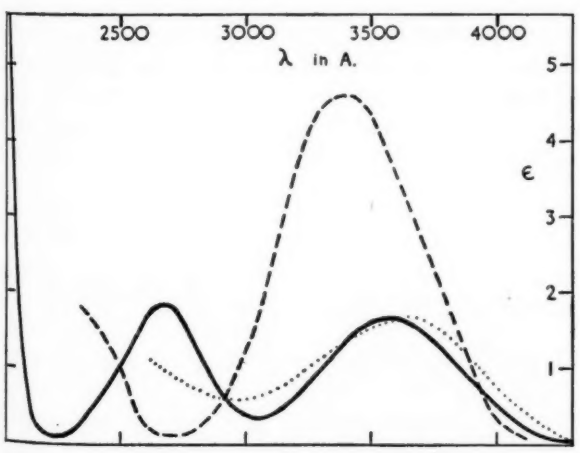

FIG. 1. ——— The absorption of hexafluoroazomethane. - - - - The absorption of azomethane from the data of Ramsperger (see reference 3). ····· The absorption of hexafluoroazomethane in methyl chloride solution from the data of Ruff (see reference 4).

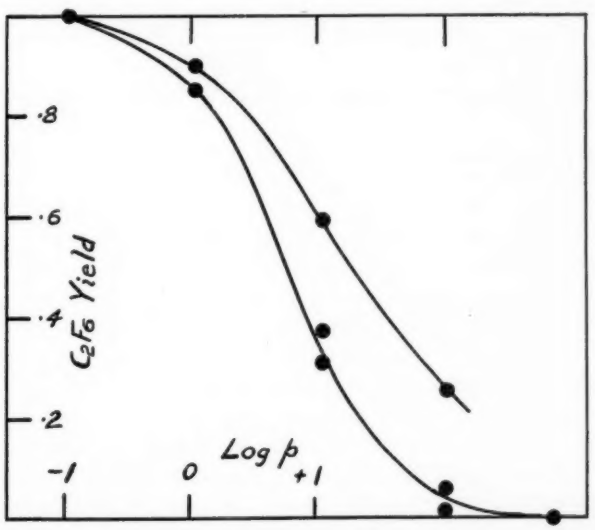

FIG. 2. The fraction of the condensable products consisting of hexafluoroethane plotted against the log$p$ in mm. For the upper curve the light intensity was 1.2×10^{17} quanta per sec and for the lower curve 6.7×10^{16} quanta per sec.

[7] D. J. LeRoy, Can. J. Research **B28**, 492 (1950).
[8] H. C. Ramsperger, J. Am. Chem. Soc. **50**, 123 (1928).

a molecule of nitrogen and two trifluoromethyl radicals.

$$CF_3-N=N-CF_3 \rightarrow N_2+2CF_3. \quad (1)$$

Whether this occurs in two stages or not is impossible to determine from these experiments and in fact would make no difference to the subsequent steps of the over-all reaction. The radicals formed by reaction (1) may react with one another to form hexafluoroethane or with the parent material to form a new free radical.

$$2CF_3\cdot + M \rightarrow C_2F_6 + M \quad (2)$$

$$CF_3\cdot + CF_3-N=N-CF_3 \rightarrow \begin{matrix} CF_3 & & CF_3 \\ & \diagdown\ \diagup & \\ & N-N & \\ & \diagup\ \diagdown & \\ CF_3 & & \end{matrix} \quad (3)$$

The hydrazo radical formed by reaction (3) may react with a trifluoromethyl radical to form perfluorotetramethyl hydrazine or two hydrazo radicals may join together to form perfluorohexamethyl tetrazine

$$\begin{matrix} CF_3 & & CF_3 \\ & \diagdown\ \diagup & \\ & N-N & \\ & \diagup\ \diagdown & \\ CF_3 & & \cdot \end{matrix} + \cdot CF_3 \rightarrow \begin{matrix} CF_3 & & CF_3 \\ & \diagdown\ \diagup & \\ & N-N & \\ & \diagup\ \diagdown & \\ CF_3 & & CF_3 \end{matrix} \quad (4)$$

$$2 \begin{matrix} CF_3 & & CF_3 \\ & \diagdown\ \diagup & \\ & N-N & \\ & \diagup\ \diagdown & \\ CF_3 & & \cdot \end{matrix} \rightarrow \begin{matrix} CF_3 & & & & CF_3 \\ & \diagdown & & \diagup & \\ & N-N-N-N & & & \\ & \diagup & & \diagdown & \\ CF_3 & & CF_3 & & CF_3 \end{matrix} \quad (5)$$

The tetrazine, however, could also be formed by the reaction of the hydrazo radical with the starting material forming a tetrazo radical which would in turn react with a trifluoromethyl radical.

$$\begin{matrix} CF_3 & & CF_3 \\ & \diagdown\ \diagup & \\ & N-N & \\ & \diagup\ \diagdown & \\ CF_3 & & \cdot \end{matrix} + CF_3-N=N-CF_3 \rightarrow$$

$$\begin{matrix} CF_3 & & & & CF_3 \\ & \diagdown & & \diagup & \\ & N-N-N-N & & & \\ & \diagup & & \diagdown & \\ CF_3 & & CF_3 & & \cdot \end{matrix} \quad (6)$$

$$\begin{matrix} CF_3 & & & & CF_3 \\ & \diagdown & & \diagup & \\ & N-N-N-N & & & \\ & \diagup & & \diagdown & \\ CF_3 & & CF_3 & & \cdot \end{matrix} + \cdot CF_3 \rightarrow$$

$$\begin{matrix} CF_3 & & & & CF_3 \\ & \diagdown & & \diagup & \\ & N-N-N-N & & & \\ & \diagup & & \diagdown & \\ CF_3 & & CF_3 & & CF_3 \end{matrix} \quad (7)$$

Since the quantum yield is considerably less than unity no chain reactions occur. Hence the $CF_3\cdot$ radical, at least at room temperature, does not break the carbon-nitrogen bond of hexafluoroazomethane, but prefers to open the nitrogen-nitrogen double bond. It is also interesting to note that the $CF_3\cdot$ radical will not, at room temperature, abstract a fluorine atom from another structure containing a CF_3 group. No carbon tetrafluoride was found among the products at any time.

At constant light intensity the rate of formation of trifluoromethyl radicals is proportional to the pressure, except at the highest pressure used where an appreciable amount of the total light is absorbed. Therefore, the ratio of the chance of a trifluoromethyl radical colliding with another trifluoromethyl radical to the chance of it colliding with a molecule of hexafluoroazomethane is independent of the pressure. Despite this the formation of hexafluoroethane is favored by low pressures. We, therefore, conclude that this process takes place mainly on the walls of the vessel. For a low pressure we may calculate the average time required for a trifluoromethyl radical to diffuse from the body of the gas to the wall. The number of collisions between such a radical and the molecules of hexafluoroazomethane during this time may also be calculated. The result of such a calculation, together with the experimental data, is that only one collision in 2×10^7 is effective in forming a hydrazo radical. If one assumes a steric factor of 0.1 this gives an activation energy for reaction (3) of 8700 cal per mole.

ACKNOWLEDGMENTS

The assistance of Professor H. Shiff of McGill University in carrying out the mass spectrograph analyses is gratefully acknowledged.

Effect of Isotopic Substitution on the Mass Spectra of Molecules. II. Oxygen and Carbon Dioxide, Experimental*

OLIVER A. SCHAEFFER AND HENRY R. OWEN
Chemistry Department, Brookhaven National Laboratory, Upton, Long Island, New York
(Received November 18, 1954)

The relative changes in the probability of bond breaking following electron impact have been studied for the molecules $O^{16}O^{16}$ and $O^{16}O^{18}$; $O^{16}C^{12}O^{16}$, $O^{16}C^{13}O^{16}$, and $O^{16}C^{12}O^{18}$. The experimental results were obtained with a 60° mass spectrometer employing a source designed to equalize the collection efficiency of the fragment ions formed. The relative changes were studied systematically as a function of the various ion source voltages. In the case of oxygen the ratio of bond breaking in $O^{16}O^{18}$ divided by that in $O^{16}O^{16}$ is 0.98. The formation of C^+ from $O^{16}C^{13}O^{16}$ is 1.022 times the formation of C^+ from $O^{16}C^{12}O^{16}$ while the formation of C^+ from $O^{16}C^{12}O^{18}$ is 0.997 times the formation of C^+ from $O^{16}C^{12}O^{16}$. The formation of CO^+ from $O^{16}C^{13}O^{16}$ is 0.974 times that from $O^{16}C^{12}O^{16}$ while the relative formation of $C^{12}O^{18+}$ from $O^{16}C^{12}O^{18}$ is 1.03 times and that of $C^{12}O^{16+}$ is 0.97 times the formation of CO^+ from $O^{16}C^{12}O^{16}$. Finally the relative formation of O^{16+} is 1.05 times and that of O^{18+} is 0.98 times the formation of O^+ from $O^{16}C^{12}O^{16}$. The values for $O^{16}C^{13}O^{16}$ are compared to previous values in the literature.

INTRODUCTION

WHEN a molecule is bombarded with electrons, a large variety of positive ions are formed representing more or less complete breakdown of the original molecule. The list of the relative amount of each ionic species formed by electron impact is usually called the pattern of the molecule. Except for analytical purposes, there has been no extensive successful use of the large amount of information available in the large number of patterns of molecules which have been observed with mass spectrometers. The reasons are perhaps twofold; on the one hand, the electronic structures of molecules are so complicated that no really successful theoretical approach to the problem has been achieved; while on the other hand the mass spectrometric data are to a great extent instrumental; that is, the patterns are dependent on the particular design and operating conditions of a given instrument.

If one narrows the subject to changes in pattern upon isotopic substitution, many of the systematic experimental errors cancel in the comparison made in the form of a ratio between the patterns of two isotopic molecules. The theoretical interpretation is also simplified as the electronic states of isotopic molecules are the same. However, in spite of this, the major difficulty in obtaining a theoretical interpretation of the changes in pattern is a scarcity of reliable experimental data. The experiments described in this article were made in an attempt to obtain interpretable data for isotopic oxygen and carbon dioxide molecules.

The mass spectra of O^{18} substituted carbon dioxide and oxygen are here reported for the first time. There are previous data in the literature on C^{13} substituted carbon dioxide[1–3] and the present data will be compared with them.

INSTRUMENTAL

The data were obtained using a 60° sector mass spectrometer with a 6 in. radius of curvature. The mass spectrum was scanned magnetically. The ion current was measured with an Applied Physics Corporation vibrating reed electrometer using Victoreen 2×10^{10} and 10^{11} ohm resistors, and recorded on a Leeds and Northrup speedomax recorder.

The ionizing beam of electrons was supplied from a tungsten filament 0.001 in. by 0.005 in. in cross section and was electronically regulated to maintain a constant trap current. The regulation was never critically tested but was certainly better than one percent. It was possible to remain on the top of a peak to within a few tenths of a percent of the peak height. The spectrometer was operated with the collector slit opened as wide as possible and at the same time with complete resolution maintained at mass 45.

The ion source was specially designed for these experiments and was used as described elsewhere[4] for the oxygen data. For the C^{13} enriched carbon dioxide data the source was modified in the successful attempt to improve pattern stability by splitting the repeller plate so that it consisted of two almost square pieces. In this way a transverse field, in addition to the usual repeller field, could be applied. For the O^{18} enriched carbon dioxide data the arrangement was further modified by spot welding small angles to the repeller plates to accentuate the transverse field, resulting in even better pattern stability and making the pattern more nearly independent of repeller voltage.

At the start of each series of scans, the transverse repeller, ion source draw out, and focus voltages were adjusted to give maximum ion beam intensity over the region to be scanned. It was found that adjustment could be made so that the ion currents for all masses from 12 to 48 were maximized for one setting of these voltages.

* Research performed under the auspices of the U. S. Atomic Energy Commission.
[1] Dibeler, Wells, and Reese, Phys. Rev. **79**, 223 (1950).
[2] F. S. Stein, Phys. Rev. **87**, 236 (1952).
[3] O. A. Schaeffer, J. Chem. Phys. **18**, 1501 (1950).
[4] O. A. Schaeffer, Rev. Sci. Instr. **25**, 660 (1954).

SAMPLE PREPARATIONS

The O^{18} enriched oxygen sample was kindly donated by A. O. Nier, University of Minnesota. This sample was used without further purification.

The O^{18} enriched carbon dioxide was obtained from A. D. Kirshenbaum of Temple University, and was purified by condensing in a liquid nitrogen bath followed by distillation from a dry ice bath.

The C^{13} enriched carbon dioxide sample was prepared from two sources by several methods. One source was Eastman Kodak C^{13} enriched barium carbonate. Carbon dioxide was prepared from this sample by two methods: (1) by heating the barium carbonate with lead chloride[5] and (2) by adding sulfuric acid to the barium carbonate. The resulting carbon dioxide was purified by distillation as was done for the O^{18} enriched carbon dioxide. The other source of C^{13} enriched carbon dioxide was a sample of C^{13} enriched carbon obtained from Isotopes Division, U. S. Atomic Energy Commission, Oak Ridge, Tennessee. This sample was combusted in a stream of oxygen to carbon dioxide. We would like to thank David Christman and Nancy Day of this laboratory for performing most of the above preparations.

There was no distinguishable difference in the results for the various C^{13} enriched carbon dioxide samples, such as might be the case if there were a small impurity in one or the other. As this was the case, most of the material used for the data obtained below was prepared by the lead chloride method and it is felt that the possibility of an error due to an impurity in the sample is negligible.

EXPERIMENTAL RESULTS

Oxygen

For the diatomic molecules nitrogen[6] and carbon monoxide,[1] the experimentally observed change in pattern was in both cases larger than the theoretically predicted change,[3] while the reverse should be the case. As the experimental results are subject to systematic errors it was thought that a careful investigation of a particular case could shed some light on the problem. In this respect, oxygen was investigated. Oxygen was chosen because a sample was available and in addition the change in pattern on substituting O^{18} for O^{16} should be, if anything, larger than the previously discussed cases because of the greater relative change in mass between O^{18} and O^{16} as compared to the change between N^{15} and N^{14} or C^{13} and C^{12}.

While the water background peak was very small, it was still about 5 percent of the M/e 18 peak so that a correction for the water of at least 20 percent accuracy had to be made in order to be sure of the O^{18+} ion yield to an accuracy of one percent. The water background correction could not be made by measuring the M/e 18 peak when no sample was being introduced and subtracting this value from the M/e 18 peak when a sample was being introduced as a major source of the water was a reaction of the oxygen with some hydrogeneous material in the mass spectrometer. A similar effect has been previously observed by Hagstrum and Tate.[7] The correction was made by reducing the electron energy to 15 volts (below the threshold for O^+), in order to monitor the water.

The O^{18} enriched sample contained 65 percent $O^{16}O^{16}$, 33 percent $O^{16}O^{18}$, 0.5 percent $O^{18}O^{18}$, 1.4 percent $O^{16}O^{17}$, and 0.07 percent $O^{17}O^{18}$ so that the corrections to the 16 and 18 peaks for ions from molecules other than $O^{16}O^{16}$ and $O^{16}O^{18}$ were almost zero. The small corrections were made, however, by assuming that the patterns were the same as for $O^{16}O^{16}$ which was determined using natural abundance oxygen.

TABLE I. Relative change in pattern for O^{18} substituted oxygen.

Nominal electron energy (volts)	$O^{16+}/\Sigma O^{16}O^{16}$	$2O^{18+}/\Sigma O^{18}O^{16}/O^{16+}/\Sigma O^{16}O^{16}$ obs.	calc.
20	0.019	0.88	0.930
25	0.045	0.98	0.948
35	0.069	0.97	0.959

TABLE II. Effect of ion gauge on pattern of carbon dioxide.[a]

Ion gauge	12/44 (percent)	13/45 / 12/44	28/44 (percent)	29/45 / 28/44
on	3.81	1.021	11.01	0.967
off	3.84	1.024	10.54	0.987

[a] Trap = 4.5 μa; A.V. = 3 kv; El. V. = 45 v; repeller = 22.5 v.

The ratios of the ion currents, $2O^{18+}/\Sigma O^{16}O^{18}/O^{16+}/\Sigma O^{16}O^{16}$ ($\Sigma O^{16}O^{18}$ being the total ions from $O^{16}O^{18}$, $\Sigma O^{16}O^{16}$ being the corresponding quantity for $O^{16}O^{16}$) were measured at several electron energies using a 7000 volt ion accelerating potential. The ratio is the relative change in pattern of the $O^{16}O^{18}$ molecule compared to the $O^{16}O^{16}$ molecule. The observed ratio is compared to a calculated value based on the pattern in Table I. The observed ratios had an average deviation of about two percent, which represents the random fluctuation of the data. The agreement between the calculated and experimental value is reasonable except for the value using 20 volt electrons; this value is especially suspect, because of the large water correction. At this voltage the O^+ peak is relatively small and the water correction amounts to 20 percent of the mass 18 ion current; while at 35 volt electrons the water correction is only five percent of the mass 18 ion current.

It should be noted that, excepting the 20 volt value, the observed ratios are closer to unity than the calcu-

[5] Zwiebel, Turkevich, and Miller, J. Am. Chem. Soc. **71**, 376 (1949).

[6] Dibeler, Mohler, and Reese, J. Chem. Phys. **18**, 156 (1950).

[7] H. B. Hagstrum and J. T. Tate, Phys. Rev. **57**, 1071 (1940).

lated ratios which is what one would expect. It is possible that the differences in Table I between calculation and experiment are real, representing the fact that the ions arise from several ionic states. However, the accuracy of the data is not good enough to draw any meaningful conclusions along these lines.

Carbon Dioxide

As the pattern of a molecule is dependent on the operating conditions, a systematic survey was made, using C^{13} labeled carbon dioxide, of the pattern and the relative change in pattern as a function of the various parameters of the mass spectrometer.

It had been observed for a previously used more open ion source that thermal decomposition products formed in the ion gauge entered the ionization region. The present ionization region is considerably more enclosed and it should have a correspondingly smaller amount of thermal decomposition products. The comparison of the pattern with the ion gauge on and with the ion gauge off in Table II shows that some thermal decomposition products still enter the ionization region. The change in pattern is most predominant in the 28/44 ratio. As seen, this ratio decreases about five percent when the ion gauge is turned off and at the same time the 29/45 ratio does not decrease proportionately as shown by the two percent rise in the 29/45/28/44 ratio. On the other hand, the 12/44 ratio is practically unchanged.

The major thermal decomposition product of carbon dioxide is most likely carbon monoxide with carbon from the filament entering into part of the reaction. As the C^{13} content of the carbon on the filament will be different from that of the carbon dioxide sample, the C^{13} content of the resulting carbon monoxide will be some intermediate value. From a qualitative viewpoint the observed changes in pattern are reasonable.

The variation in the pattern for CO_2 and the relative patterns for the two isotopic molecules $O^{16}C^{12}O^{16}$ and $O^{16}C^{13}O^{16}$ were determined for different operating conditions of the mass spectrometer. For trap currents from 2 to 10 μa, repeller voltages from 3 to 45 v, accelerating voltages from 3 to 6 kv, and electron voltages from 35 to 45 v there were no changes in the relative patterns although the individual patterns varied considerably.

The ratio of the pattern of $O^{16}C^{13}O^{16}$ to $O^{16}C^{12}O^{16}$ is compared to previous values in Table III. The results for the present research are the average of all the observations made as there were no observed systematic trends in the ratio of the patterns. The results of F. S. Stein were determined on a 60° mass spectrometer using a conventional source, while those of Dibeler, Wells, and Reese were determined on a 180° consolidated mass spectrometer. The agreement is reasonably good for the C^+ ion except for the value of Dibeler, Wells, and Reese; while the present value for CO^+ is in disagreement with both previous values. It is felt that the results of Dibeler, Wells, and Reese are possibly a few percent low because of the way they obtained the data, i.e., using electrostatic scanning. For the diatomic molecules discussed previously,[3] the values of Dibeler and co-workers were a few percent lower than calculated values. Stein used magnetic scanning and his value for C^+ is in good agreement with the present research. It is possible that the value of Stein for the CO^+ could be low because of thermal decomposition contributing to the 28 peak, in the type source he used. In previous work at this laboratory, with a source similar to the one Stein used, it was not possible to obtain a reproducible value for this quantity because of the large contribution of thermally produced CO.

TABLE III. Relative change in pattern for $O^{16}C^{12}O^{16}$ and $O^{16}C^{13}O^{16}$.

	CO^+ $\frac{29/45}{28/44}$	C^+ $\frac{13/45}{12/44}$
Stein[a]	0.948	1.022
Dibeler, Wells, and Reese[b]	0.949	0.961
Previous value[c]	[d]	1.007
Present research[e]	0.974±0.004	1.022±0.006

[a] See reference 2.
[b] See reference 1.
[c] See reference 3.
[d] Not determined because of large contribution to 28 peak of thermally produced CO.
[e] The deviations listed are the average deviations.

To obtain the data for O^{18} substituted carbon dioxide the mass spectrometer was operated using 6-volt repeller, 4.5 μa trap current, 45-volt electrons, and 6-kv ion accelerating potential. The O^{18} enriched sample has the composition 72.2 percent $O^{16}C^{12}O^{16}$, 23.7 percent $O^{16}C^{12}O^{18}$, 1.95 percent $O^{18}C^{12}O^{18}$, 0.94 percent $O^{16}C^{12}O^{17}$, 0.81 percent $O^{16}C^{13}O^{16}$, 0.28 percent $O^{16}C^{13}O^{18}$, 0.12 percent $O^{17}C^{12}O^{18}$, and less than 0.01 percent of other possible isotopic carbon dioxide molecules, as determined from an analysis of the 44–48 mass region. The sample is mainly $O^{16}C^{12}O^{16}$ and $O^{16}C^{12}O^{18}$. To obtain a pattern for $O^{16}C^{12}O^{18}$, a natural abundance sample was run immediately before and and after the O^{18} enriched one. The contributions of the $O^{16}C^{12}O^{16}$ molecule were then determined on the basis of the natural abundance pattern and subtracted from the O^{18} enriched sample peaks. The results appear in Table IV. The three sets of data were obtained over a time interval of a month. The changes in pattern are typical of the source performance.

For each set of data, three scans of natural abundance carbon dioxide were obtained, then the spectrometer was flushed with O^{18} enriched carbon dioxide and, after adjusting the sample pressure to the same value as the natural abundance run, three scans were made of the O^{18} enriched sample. This was repeated for the natural abundance material, followed by a repeat of

TABLE IV. Pattern of O^{18} enriched carbon dioxide.

Mass No.	Set I Natural abundance	Set I O^{18} enriched	Set I Pattern of O^{18} component	Set II Natural abundance	Set II O^{18} enriched	Set II Pattern of O^{18} component	Set III Natural abundance	Set III O^{18} enriched	Set III Pattern of O^{18} component
12	4.03	5.51	3.99	4.39	6.02	4.42	4.15	5.68	4.13
16	9.10	10.77	9.72	9.22	10.90	9.78	9.17	10.81	9.45
18		1.76	9.05		1.74	8.96			8.90
22	0.2			0.2			0.2		11.15
28	11.63	13.70	10.15	11.72	13.63	11.25	11.37	13.31	11.66
30			11.99		2.33	12.13		2.26	
32	0.02			0.02			0.02		
44	100.00	100.00		100.00	100.00		100.00	100.00	
45	1.18	2.49		1.18	2.49		1.18	2.45	
46	0.47	33.3		0.43	33.1		0.44	33.4	
47		0.59			0.58			0.58	
48		2.78			2.78			2.75	

the O^{18} enriched sample and finally running the natural abundance carbon dioxide again. The nine scans for the natural abundance sample were averaged and appear in Table IV along with the average of the six scans of the O^{18} enriched sample. The peaks at 22 and 32 are reported for completeness in the natural abundance samples. In each such run the natural abundance pattern was stable to better than one percent.

The background corrections were made by subtracting the residual peaks at mass numbers 16, 28, and 44 obtained before any sample had been run. The corrections were all less than one percent. For the mass number 18 correction to the O^{18} enriched data, the amount subtracted was the amount of the mass number 18 ion current when running natural abundance carbon dioxide, as some of the 18 peak was due to water formation in the spectrometer.

The pattern of the O^{18} component was obtained by subtracting the natural abundance pattern from the O^{18} enriched data and then dividing the remainder by the appropriate sum of parents as follows:

$$P_{C^{12}}=O^{16}C^{12}O^{17}+O^{16}C^{12}O^{18}+O^{17}C^{12}O^{18}+O^{18}C^{12}O^{18}$$

$$P_{O^{16}}=\tfrac{1}{2}(O^{16}C^{12}O^{17}+O^{16}C^{12}O^{18}+O^{16}C^{13}O^{18})$$

$$P_{O^{18}}=\tfrac{1}{2}(O^{16}C^{12}O^{18}+O^{17}C^{12}O^{18})+O^{18}C^{12}O^{18}$$

$$P_{C^{12}O^{16}}=\tfrac{1}{2}(O^{16}C^{12}O^{17}+O^{16}C^{12}O^{18})$$

$$P_{C^{12}O^{18}}=\tfrac{1}{2}(O^{16}C^{12}O^{18}+O^{17}C^{12}O^{18})+O^{18}C^{12}O^{18}.$$

All the peaks in the parent region correspond to a single ionic species except the 47 peak which is partly $O^{16}C^{13}O^{18}$ and partly $O^{17}C^{12}O^{18}$. This was unraveled by assuming that the $O^{16}C^{13}O^{18}/O^{16}C^{12}O^{18}$ ratio was the same as the $O^{16}C^{13}O^{16}/O^{16}C^{12}O^{16}$ ratio. Then all the parents can be readily obtained.

TABLE V. Relative change in pattern of $O^{16}C^{12}O^{18}$ to $O^{16}C^{12}O^{16}$.

Ion	Ratio $O^{16}C^{12}O^{18}$ pattern/$O^{16}C^{13}O^{16}$ pattern
C^{12+}	0.997±0.006
O^{16+}	1.05 ±0.02
O^{18+}	0.98 ±0.01
$C^{12}O^{16+}$	0.97 ±0.01
$C^{12}O^{18+}$	1.03 ±0.01

The average relative change in pattern is tabulated as a ratio of the O^{18} component to the $O^{16}C^{12}O^{16}$ pattern for each ionic fragment in Table V. The relative change is due mainly to $O^{16}C^{12}O^{18}$ since this constitutes about 90 percent of the residual. The deviations listed are the average deviations of the data and represent the precision of the results.

DISCUSSION

While the results of this research are probably more reliable than previous data, there is still room for improvement. The main difficulty in the present results is the poor long-time stability of the patterns. On a given day the pattern is usually stable to better than one percent but over a period of a week or more the pattern may change. The change is independent of any of the variables studied in these experiments. It seems to be connected with the electron beam shifting in the source, either because the surface on which it is collected becomes slightly insulating and shifts the beam position, or emits more or less secondary electrons, or because the emitting surface of the filament undergoes a change which shifts the electron density distribution in the source. As these changes do occur, especially in the 12/44 ratio, the pattern on an absolute basis should be considered only approximate; as a result, any conclusions concerning the electronic states of the ionic states leading to the fragment ions can at best be only qualitative. The ratio of the patterns for two isotopic molecules, on the other hand, shows only about a one percent fluctuation. It should be noted that there are two types of isotope effect present in the data. The two are the decrease in fragmentation of the heavier molecule as evidenced by O^{+} from $O^{16}O^{18}$ by $C^{13}O^{16+}$ from $O^{16}C^{13}O^{16}$, $C^{12}O^{16+}$, and by O^{18+} and C^{12+} from

$O^{16}C^{12}O^{18}$ (although the latter is unity to within experimental error), and the enhancement in fragmentation of the heavier molecule as evidenced by C^{13+} from $O^{16}C^{13}O^{16}$ and by O^{16+} and $C^{12}O^{18+}$ from $O^{16}C^{12}O^{18}$. These effects will be considered from a theoretical viewpoint in the accompanying paper.

ACKNOWLEDGMENTS

We would like to acknowledge the help of the electronics department of Brookhaven National Laboratory for their assistance in design construction and maintenance of a number of the electronic components used in this research.

THE JOURNAL OF CHEMICAL PHYSICS VOLUME 23, NUMBER 7 JULY, 1955

Effect of Isotopic Substitution on the Mass Spectra of Molecules. III. Carbon Dioxide, Theoretical Interpretation*

OLIVER A. SCHAEFFER

Chemistry Department, Brookhaven National Laboratory, Upton, Long Island, New York

(Received November 18, 1954)

The relative changes in pattern for O^{18} and C^{13} substituted carbon dioxide are calculated. The frequencies for the isotopic carbon dioxide molecules and the associated normal coordinates are obtained for a harmonic potential function. These are then used as the basis for the ground-state vibrational wave functions. The bond breaking probability integrals are evaluated for various values of the "critical" internuclear separation r_c, and a study is made of the change in predicted bond breaking ratios as a function of r_c. The values of r_c are chosen which give the experimental pattern for $O^{16}C^{12}O^{16}$ and then the relative changes in pattern are calculated for the other molecules and are compared with experimental values. Especially striking is the fact that the calculation faithfully reproduces the change in pattern for the case of a heavier molecule, which is more likely to fragment than a lighter one, as well as for the reverse case. It is concluded that a Franck-Condon type calculation adequately describes the electron impact process in carbon dioxide.

INTRODUCTION

THERE are essentially two theoretical approaches to the problem of the fragmentation of an ion following electron impact. One is based on a Franck-Condon type calculation[1] and the other, a statistical approach,[2] based on reaction rate theory.

The Franck-Condon mechanism assumes that the transitions are vertical ones, that is, the molecule after electron impact suddenly finds itself in the field of one less electron, with or without excitation. It then, in a time of the order of a molecular vibration, decomposes to a particular final state. The final state is dependent only on the configuration of the nuclei at the instant of impact, for a given electronic transition. In carrying out the calculation of the probabilities for the various transitions it is common to make some approximations. The various approximations are discussed in detail by Coolidge, James, and Present[3] for electronic transitions following electron impact in hydrogen. These calculations were verified by Coolidge[4] by a controlled experiment. The vertical transition mechanism outlined above is essentially the approximation of replacing the wave functions of the final state by delta functions at the classical turning points and using the correct initial state wave function. This was shown[3] to give results in good agreement with a more exact calculation which used correct wave functions for both initial and final states.

The statistical approach, on the other hand, assumes that the molecules will decompose over a time of several vibrations. The model is that the electronically excited ions resulting from electron impact make transitions in electronic state with the many (in polyatomic molecules) nearby states, in so doing redistributing energy among the vibrational modes, until decomposition ensues. The particular end products are not so much a function of the configuration of the molecule at impact as they are a function of the probability of transferring energy to a particular bond or vibrational mode when the molecule is in an excited electronic state. The statistical approach would not be expected to be applicable when the electronic states are widely separated as is true in the simpler molecules.

The difficulty, at present, with both these theoretical interpretations is that not enough information is available concerning the excited electronic states to make a meaningful calculation in any but the simplest cases. In the case of diatomic molecules it seems quite clear that the electron impact process is adequately described by the Franck-Condon mechanism. However, for reasons pointed out before,[2] this does not mean that more complicated molecules will necessarily be described in the same way.

If one narrows the subject to the changes in pattern

* Research performed under the auspices of the U. S. Atomic Energy Commission.

[1] Bleakney, Condon, and Smith, J. Chem. Phys. **41**, 197 (1937).

[2] Rosenstock, Warhaftig, and Erying, Proc. Natl. Acad. Sci. **38**, 667 (1952).

[3] Coolidge, James, and Present, J. Chem. Phys. **4**, 193 (1936).

[4] A. S. Coolidge, Phys. Rev. **65**, 236 (1944).

on isotopic substitution, the problem is greatly simplified. In particular, as the electronic states of isotopic molecules are for all practical purposes identical, it is possible to make a calculation with practically no information about the electronic states involved. In addition, many of the systematic experimental errors cancel when a comparison is made in the form of a ratio between the patterns of two isotopic molecules. A method has been presented,[5] based on a Franck-Condon mechanism for bond rupture, for calculating the relative change in pattern of a polyatomic molecule following isotopic substitution. While the method of calculation, in its present form, does not describe the electron impact process in detail, it is felt that it can serve as a basis for deciding the mechanism of the process. In the present paper, the calculation is extended to isotopic carbon dioxide molecules, O^{18} and C^{13}, substitution. The calculated changes in pattern are compared with experimental values reported in the previous paper.

NORMAL COORDINATES

In order to make the calculation, one needs the ground state vibrational wave functions. To obtain the latter one needs the normal coordinates for the different isotopic carbon dioxides.

The harmonic oscillator approximation to the wave function was used. Stevenson[6] has compared the harmonic oscillator and the anharmonic oscillator approximations for bond rupture in hydrogen and deuterium. It was found that while the individual ratios H^+/H_2^+ and D^+/D_2^+ differed by more than a factor of 2, for the harmonic oscillator compared to the anharmonic oscillator, the relative changes in pattern were the same to within less than one percent for the two approximations. As this paper is concerned only with relative changes and as the anharmonicity is much smaller in the case of carbon dioxide (because of the relatively heavy atoms involved), the harmonic oscillator approximation should be adequate.

The bending vibrational modes are perpendicular to the bonds and lead to a very small change in bond length. In addition, for bending motions the potential never becomes repulsive. These two reasons make it acceptable to neglect the bending modes with reasonable assurance that the calculation will be valid.

The bond stretching frequencies and their associated normal coordinates were calculated from the atomic masses and a set of force constants derived from the observed frequencies for $O^{16}C^{12}O^{16}$. A valence force field was chosen:

$$2V=k_1R_1^2+2k_2R_1R_2+k_1R_2^2, \tag{1}$$

where k_1 is the restoring force constant for stretching a C—O bond; k_2 is the interaction force constant between the two bonds. R_1 and R_2 represent the displacements of the two bonds, respectively, from equilibrium. The equations representing the frequencies in terms of the force constants and atomic masses are given by Herzberg.[7] The force constants calculated from these equations are $k_1=15.512\times10^5$ and $k_2=1.326\times10^5$ dynes per centimeter. The frequencies used were $\nu_1=1336.8$ and $\nu_2=2349.3$ cm^{-1}. The atomic masses used were $O^{16}=16.0000$, $C^{12}=12.00386$, and $O^{18}=18.00485$ atomic mass units with the conversion 1 atomic mass unit $=1.6599\times10^{-24}$g.

The frequencies of the $O^{16}C^{13}O^{16}$ and $O^{18}C^{12}O^{18}$ molecules were calculated from the same equations using the above numerical values. For the $O^{16}C^{12}O^{18}$ molecule the equations given do not apply because of the loss of symmetry. For $O^{16}C^{12}O^{18}$ the secular equation is:

$$\begin{vmatrix} \left(\frac{1}{2m_{18}}+\frac{1}{2m_{12}}\right)(k_1+k_2)-\lambda & \left(\frac{1}{2m_{16}}-\frac{1}{2m_{12}}\right)(k_1-k_2) \\ \left(\frac{1}{2m_{16}}-\frac{1}{2m_{12}}\right)(k_1+k_2) & \left(\frac{1}{2m_{16}}+\frac{2}{m_{12}}+\frac{1}{2m_{18}}\right)(k_1-k_2)-\lambda \end{vmatrix}=0, \tag{2}$$

where m_{18} is the mass of O^{18}, m_{16} the mass of O^{16}, and m_{12} the mass of C^{12}. The resulting quadratic equation was solved for the two frequencies of $O^{16}C^{12}O^{18}$. In Table I are listed the calculated frequencies for the different molecules. The observed values for $O^{16}C^{13}O^{16}$ are 1336.8 and 2284.5 cm^{-1} which are in good agreement with the calculated values.

For the symmetrical molecules the symmetry coordinates:

$$S_1=\frac{1}{\sqrt{2}}(R_1+R_2) \tag{3}$$

and

$$S_2=\frac{1}{\sqrt{2}}(R_1-R_2) \tag{4}$$

are also normal coordinates.

The potential and kinetic energy are given by

$$2V=(k_1+\tfrac{1}{2}k_2)S_1^2+(k_1-\tfrac{1}{2}k_2)S_2^2 \tag{5}$$

and

$$2T=m_o\dot{S}_1^2+\frac{m_om_c}{m_{co_2}}\dot{S}_2^2, \tag{6}$$

[5] O. A. Schaeffer, J. Chem. Phys. **18**, 1501 (1950).
[6] D. P. Stevenson, J. Chem. Phys. **15**, 409 (1947).
[7] G. Herzberg, *Infrared and Raman Spectra* (D. Van Nostrand Company, Inc., New York, 1945), p. 187.

where m_o=mass of the oxygen atom and m_c=mass of the carbon atom.

For $O^{16}C^{12}O^{18}$, the normal coordinates were obtained by the usual method.[8] The transformation from internal coordinates R_1 and R_2 to normal coordinates L_1 and L_2 is given by

$$L_1=5.3052R_1-0.11867R_2 \quad (7)$$

$$L_2=0.07193R_1+2.7110R_2. \quad (8)$$

L_1 is the normal coordinate for the symmetrical frequency and L_2 the normal coordinate for the antisymmetrical frequency. R_1 is the change in the $O^{16}C^{12}$ bond from equilibrium and R_2 the corresponding change in the $O^{18}C^{12}$ bond. The transformation is normalized so that the kinetic energy matrix is a unit matrix and the potential energy matrix is a diagonal matrix whose elements are the λ's.

BOND BREAKING PROBABILITIES

The ground-state normalized harmonic oscillator approximation to the vibrational wave function for the normal coordinate L_i is

$$\psi(L_i)=(\alpha_i/\pi)^{\frac{1}{4}}\exp(-\alpha_i L_i^2/2), \quad (9)$$

where

$$\alpha_i=4\pi^2\mu_i\omega_i c/h. \quad (10)$$

The other symbols have the usual meanings.[9] (For the normalized coordinates $\mu_i=1$.)

TABLE I. Calculated frequencies of isotopic carbon dioxide molecules.

	$O^{16}C^{12}O^{16}$	$O^{16}C^{12}O^{16}$	$O^{16}C^{12}O^{18}$	$O^{18}C^{12}O^{18}$
$\nu_1(cm^{-1})$	1336.8[a]	1336.8	1298.2	1260.2
$\nu_2(cm^{-1})$	2349.3[a]	2282.6	2331.9	2313.3

[a] Experimental values used to evaluate force constants.

The bond breaking probabilities were obtained by the method described before[5] by evaluating the integrals

$$P_0=\int\int_{\substack{R_1>r_c\\R_2>r_c}}\psi^2(L_1)\psi^2(L_2)dL_1dL_2, \quad (11)$$

$$P_{1a}=\int\int_{\substack{R_1>r_c\\R_2<r_c}}\psi^2(L_1)\psi^2(L_2)dL_1dL_2, \quad (12)$$

$$P_{1b}=\int\int_{\substack{R_1<r_c\\R_2>r_c}}\psi^2(L_1)\psi^2(L_2)dL_1dL_2, \quad (13)$$

[8] See, e.g., E. B. Wilson, Jr., J. Chem. Phys. **9**, 76 (1941).
[9] See, e.g., G. Herzberg, *Spectra of Diatomic Molecules*, (D. Van Nostrand Company, Inc., New York, 1950), second edition.

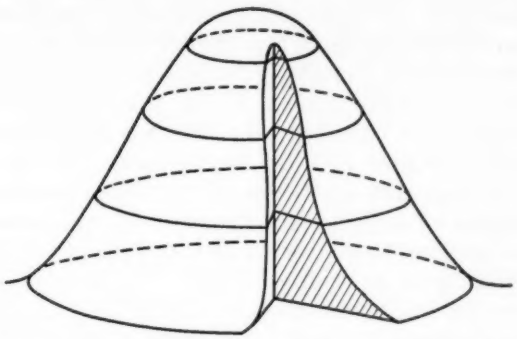

FIG. 1. $\psi^2(Q_1,Q_2)$ for carbon dioxide, the missing segment represents the volume corresponding to the breaking of both C−O bonds.

and

$$P_2=\int\int_{\substack{R_1<r_c\\R_2<r_c}}\psi^2(L_1)\psi^2(L_2)dL_1dL_2, \quad (14)$$

where P_0 is the probability of breaking no bonds, P_{1a} the probability of breaking one bond, P_{1b} the probability of breaking the other bond, and P_2 the probability of breaking both bonds; L_1 and L_2 are the normal coordinates for the two stretching vibrations; and r_c is the critical bond distance for the C−O bond.

At this point it is convenient to introduce the transformation

$$Q_i=(\alpha_i)^{\frac{1}{2}}L_i, \quad (15)$$

as then the wave function takes the symmetrical form

$$\psi^2(Q_1,Q_2)=(1/\pi)\exp[-(Q_1^2+Q_2^2)]. \quad (16)$$

The function $\psi^2(Q_1,Q_2)$ is the familiar bell-shaped error function in three dimensions. Figure 1 is a representation of the function with a segment removed. The missing segment represents the probability of breaking both bonds. The function $\psi^2(Q_1,Q_2)$ is symmetrical about the z axis for all the molecules under consideration. This would not be the case if one represented the function in terms of the L's.

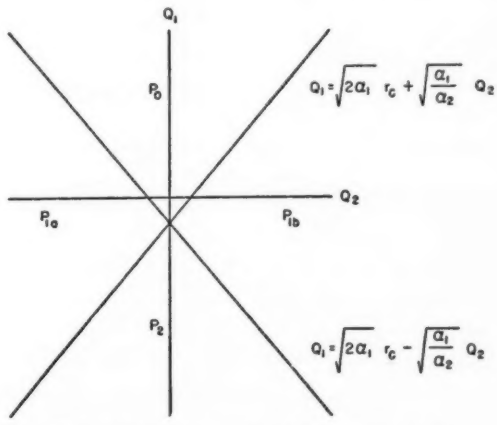

FIG. 2. Limits on probability integrals for symmetrical carbon dioxide.

The limits are most easily represented graphically. When the inequalities of Eqs. (11) to (14) are expressed in terms of the Q's, they can be represented by two planes parallel to the z axis of Fig. 1. The intersection of these planes with the base of Fig. 1 is shown in Figs. 2 and 3. Figure 2 is the symmetrical case for the symmetrical carbon dioxides. The two lines have equal slopes but of opposite sign. Here $P_{1b}=P_{1a}$, as it should. That is, there should be no difference in the probability of breaking either bond.

For the antisymmetrical case $O^{16}C^{12}O^{18}$, P_{1a} corresponds to breaking the $C^{12}-O^{18}$ bond and P_{1b} breaking the $C^{12}-O^{16}$ bond. One can see from Fig. 3 that $P_{1b}>P_{1a}$.

The problem is now completely defined except for the evaluation of r_c. The value of r_c to form C^+ will be different from that to form CO^+ or O^+ in the event that they are formed by transitions to different ionic states. As the electronic states are not known in sufficient detail to evaluate r_c, recourse must be made to mass spectral data.

In principle, the value of r_c can be determined from the pattern of one of the isotopic carbon dioxides by the use of relations (11) to (14). Instead of doing this directly, the integrals were evaluated for each molecule for each of a set of values of r_c. In this way one can evaluate how sensitive the relative change in pattern is to r_c or "equivalently" to the pattern.

The integrals were evaluated numerically by choosing a set of values for Q_1 and evaluating the integral over Q_2 for each such Q_1 from a table[10] of values. These were then multiplied by $\exp(-Q_1^2)$, summed according to Euler's rule, and normalized. To test the accuracy, the interval on Q_1 was made smaller, in effect summing over more values. The calculation for the smaller increment should be more accurate. There was no significant change in the integral, and it is felt that the results are accurate to a tenth of a percent.

The relative bond breaking probabilities R were computed by taking the ratio of the bond breaking probability P for a given molecule to the corresponding P for $O^{16}C^{12}O^{16}$. R was then plotted as a function of P for $O^{16}C^{12}O^{16}$ and appears in Figs. 4 and 5. Figure 4 is for the case of breaking both bonds and Fig. 5 is for the case of breaking one bond.

COMPARISON WITH EXPERIMENTAL RESULTS

In order to compare the calculated values with experimental results, it is necessary to evaluate r_c for each process. This was done by determining the values of r_c which would give the observed probabilities for $O^{16}C^{12}O^{16}$. For this set of values of r_c the relative bond breaking probability can be compared directly with the experimental results of the preceding article. Table II lists the calculated and observed results.

A theoretical relative yield of C^+ from $O^{16}C^{13}O^{16}$ and $O^{16}C^{12}O^{16}$ had been compared with an experimental value before.[3] In the previous treatment it was assumed that all the C^+ arose from the symmetrical mode of vibration and as this mode is the same in $O^{16}C^{12}O^{16}$ and $O^{16}C^{13}O^{16}$ the relative yield of C^+ should not change. The present calculation, which takes into account both the stretching vibrations, indicates that the relative amount of C^+ is not 1.00, and in fact C^+ is more likely to be produced from $O^{16}C^{13}O^{16}$ than from $O^{16}C^{12}O^{16}$. The present calculation shows good agreement with the experimental result.

Physically this can be understood as follows. The amplitude of the symmetrical mode is the same in both molecules while the amplitude of the unsymmetrical mode is larger for the lighter molecule. Now consider the two cases, $Q_2=0$, i.e., in the equilibrium position and $Q_2=\delta$, a small displacement from equilibrium. For $Q_2=0$ both bonds will break for $Q_1=r_c$ or less; while for $Q_2=\delta$ both bonds will break for $Q_1=r_c-\delta$ or less, i.e., for a smaller region. As a lighter molecule is more likely to have Q_1 extended it will be less likely to break both bonds. As shown in Fig. 4, this value does not change appreciably with r_c. A similar sort of effect occurs

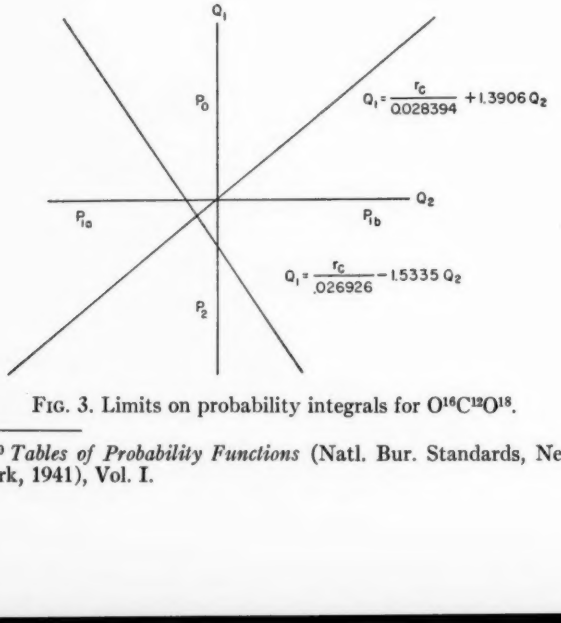

FIG. 3. Limits on probability integrals for $O^{16}C^{12}O^{18}$.

[10] *Tables of Probability Functions* (Natl. Bur. Standards, New York, 1941), Vol. I.

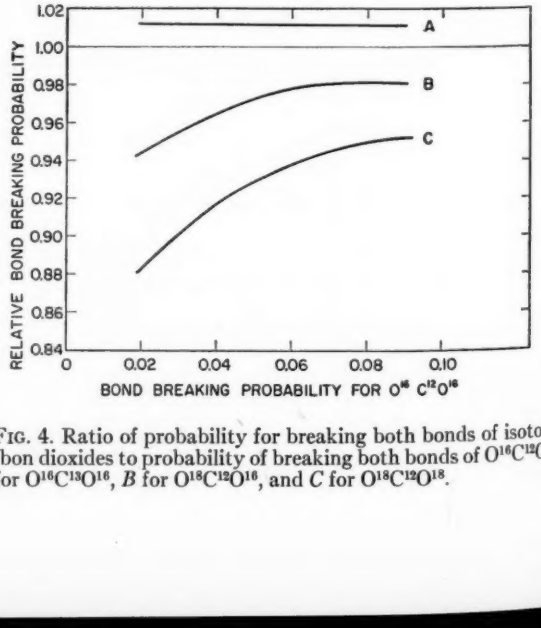

FIG. 4. Ratio of probability for breaking both bonds of isotopic carbon dioxides to probability of breaking both bonds of $O^{16}C^{12}O^{16}$: A for $O^{16}C^{13}O^{16}$, B for $O^{18}C^{12}O^{16}$, and C for $O^{18}C^{12}O^{18}$.

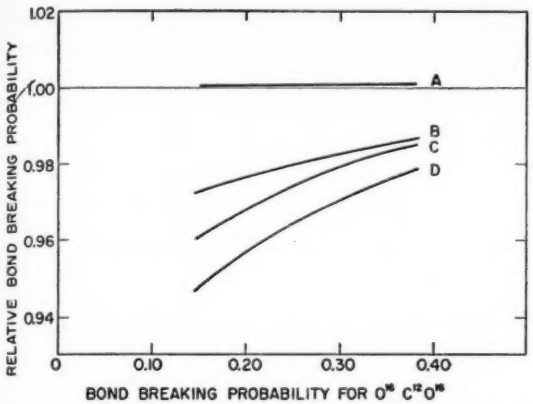

FIG. 5. Ratio of probability for breaking one bond of isotopic carbon dioxides to probability of breaking one bond of $O^{16}C^{12}O^{16}$: *A* for $C^{12}O^{16}$ bond in $O^{18}C^{12}O^{16}$, *B* for $O^{16}C^{13}O^{16}$, *C* for $C^{12}O^{18}$ bond in $O^{18}C^{12}O^{16}$, and *D* for $O^{18}C^{12}O^{18}$.

in the yield of $C^{12}O^{16+}$ from $O^{16}C^{12}O^{18}$ compared to the yield of $C^{12}O^{16}$ from $O^{16}C^{12}O^{16}$. Here, however, both modes change and in this case the change is brought about by the fact that the amplitude of the $C^{12}-O^{16}$ bond in $O^{18}C^{12}O^{16}$ is larger than the $C^{12}-O^{18}$ bond in $O^{18}C^{12}O^{16}$, and in fact slightly larger than the $C^{12}-O^{16}$ amplitude in $O^{16}C^{12}O^{16}$. So that in this case also, the fragmentation of the heavier molecule is calculated to be more probable.

TABLE II. Comparison with experimental results.

Process	Relative ion yield Calculated	Observed[a]
$O^{16}C^{13}O^{16} \rightarrow C^{13+}$	1.011	1.022±0.006
$O^{18}C^{12}O^{16} \rightarrow C^{12+}$	0.976	0.997±0.006
$O^{18}C^{12}O^{18} \rightarrow C^{12+}$	0.934	···
$O^{16}C^{13}O^{16} \rightarrow C^{13}O^{16+}$	0.972	0.974±0.004
$O^{18}C^{12}O^{16} \rightarrow C^{12}O^{16+}$	0.960	0.97 ±0.01
$O^{18}C^{12}O^{16} \rightarrow C^{12}O^{18+}$	1.001	1.03 ±0.01
$O^{18}C^{12}O^{18} \rightarrow C^{12}O^{18+}$	0.946	···
$O^{18}C^{12}O^{16} \rightarrow O^{18+}$	0.960	0.98 ±0.01
$O^{18}C^{12}O^{16} \rightarrow O^{16+}$	1.001	1.05 ±0.05

[a] The deviations listed are the average deviations.

The agreement between experimental results and calculated ones is not as sharp as might be desired, mainly because the effects are small and difficult to measure to much better than one percent accuracy. However the striking agreement between calculation and experiment as to which bonds break more easily is borne out in every case. This is perhaps the most cogent evidence for accepting the validity of the assumption involved in making the calculation and leads to the conclusion that in the case of CO_2 the electron impact process can be understood on the basis of a Franck-Condon mechanism coupled with the method of calculation outlined before.[5]

THE JOURNAL OF CHEMICAL PHYSICS VOLUME 23, NUMBER 7 JULY, 1955

Infrared Spectrum of SOF_2

J. KENNETH O'LOANE,* *Chemistry Department, University of New Hampshire, Durham, New Hampshire*

AND

M. KENT WILSON, *Mallinckrodt Chemical Laboratory, Harvard University, Cambridge, Massachusetts*

(Received October 22, 1954)

An investigation of the infrared spectrum of gaseous thionyl fluoride results in the following fundamental assignment:

$\nu_1(a')=1333\ cm^{-1}$, $\nu_2(a')=808\ cm^{-1}$, $\nu_3(a')=530\ cm^{-1}$.
$\nu_4(a')=(410)\ cm^{-1}$, $\nu_5(a'')=748\ cm^{-1}$, $\nu_6(a'')=390\ cm^{-1}$.

Thermodynamic functions for SOF_2 are calculated with the usual assumptions.

INTRODUCTION

A RECENT investigation of the infrared spectrum of SO_2F_2[1] indicated that the S−O stretching force constant in SO_2F_2 was higher than that found in SO_2. This tightening of the bond is to be expected if, indeed, the S−O bond length in SO_2F_2 is only 1.37 A as reported by Fristrom.[2] As part of an attempt to obtain further information concerning the S−O bond in related molecules, the infrared spectrum of SOF_2 has been investigated.

Since the Raman data[3] for SOF_2 include no depolarization factors and the six fundamental frequencies listed are consistent with C_s or C_{2v} symmetry, no conclusion regarding the molecular configuration is possible from the vibration spectrum. However, both the electron diffraction results[4] and the microwave

* Present address: Industrial Laboratory, Kodak Park Works, Eastman Kodak Company, Rochester 4, New York.

[1] W. D. Perkins and M. K. Wilson, J. Chem. Phys. **20**, 1791 (1952).

[2] R. M. Fristrom, J. Chem. Phys. **20**, 1 (1952).

[3] Best and Trampe, quoted by D. M. Yost, Proc. Indian Acad. Sci. **8**, 333 (1938).

[4] Stevenson and Beach quoted by Yost and Russell, *Systematic Inorganic Chemistry* (Prentice-Hall, Inc., New York, 1944), p. 306.

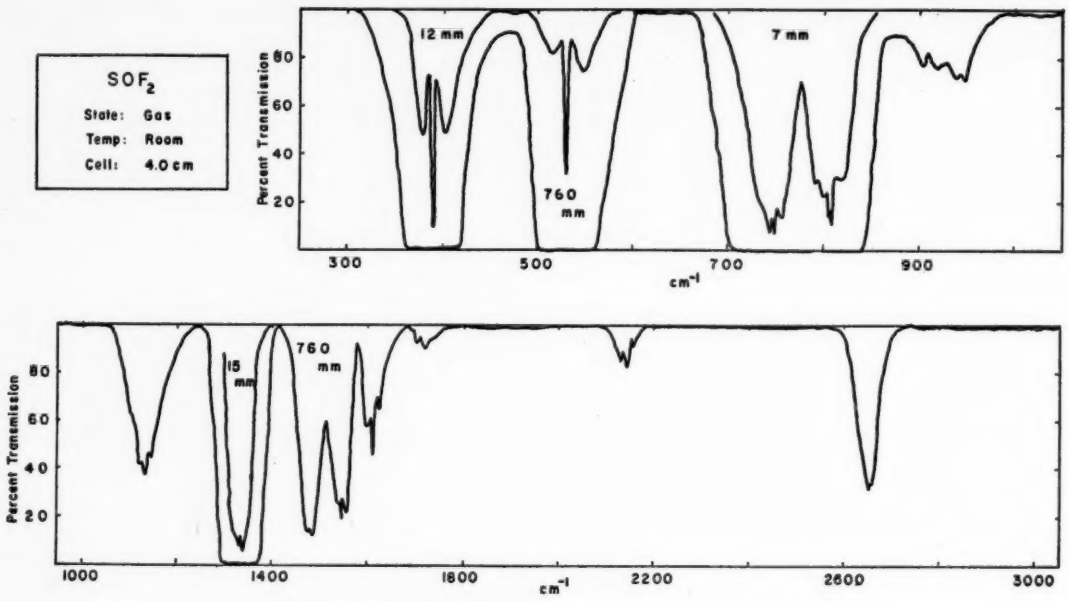

FIG. 1. Infrared absorption spectrum of gaseous SOF_2.

spectrum[5] indicate that the molecule has C_s symmetry. The microwave data yield a value of 1.412±0.001 A for the S−O distance, which is greater than the value of 1.37 A reported for SO_2F_2[2], but less than the S−O distance of 1.432 found in SO_2.[6]

EXPERIMENTAL

Thionyl fluoride was prepared by a modification of the method of Booth and Mericola.[7] Thionyl chloride (Eastman 246) was purified just before use by pumping until no SO_2 bands could be detected in the infrared spectrum and the observed vapor pressure agreed with that reported for $SOCl_2$ by Cherton.[8] This material was then distilled into a 1-l flask equipped with a freeze-out tube containing sublimed SbF_3 and $SbCl_5$. On gradually warming the reaction mixture to room temperature and allowing it to stand for several days, or by heating to 100° on a steam bath for 3–4 hr, the reaction was found to go nearly to completion. Since there is an induction period, care must be taken or a violent explosion may result on too rapid heating.

The principal impurities SOFCl, $SOCl_2$, and SiF_4 were removed by fractional distillation in a vacuum at −100° to −110°C, and by allowing the gaseous product to stand over Hg. The purification was continued until the infrared spectrum remained unchanged, the bands of SOFCl, $SOCl_2$, and SiF_4 having disappeared, and the vapor pressure agreed with that given by Booth and Mericola.[7]

The infrared spectrum of the gas was observed between 240 cm^{-1} and 5000 cm^{-1} with a Perkin-Elmer Model 12C Spectrograph modified for double-pass operation and equipped with CaF_2, NaCl, KBr, KRS-5, and CsBr prisms, and with a Baird Associates spectrophotometer equipped with NaCl optics. The gas cells had KBr windows sealed with Glyptal cement.

RESULTS AND DISCUSSION

The observed spectrum replotted on a linear frequency scale is given in Fig. 1. Although the spectrum was investigated to 5000 cm^{-1} at a pressure of 760 mm Hg in a 4.0 cm cell, no bands were observed beyond 2652 cm^{-1}. The measured frequencies and band assignments are listed in Table I.

The four totally symmetric (a') vibrations may be described broadly as an S−O stretching motion, a symmetric S−F stretch, a motion in which all angles increase simultaneously, and a motion in which the FSF angle increases while the OSF angles decrease. The two antisymmetric (a'') vibrations are an S−F stretching motion and a deformation of the SOF_2 pyramid. All six fundamentals and all combinations and overtones are both infrared and Raman active.

By comparison with the S−O stretching frequencies in SO_2,[9,10] SO_2F_2[1], $SOCl_2$,[11–13] and SO_2Cl_2,[14] the band at 1332 cm^{-1} may be assigned as $\nu_1(a')$. The somewhat atypical appearance of this band perhaps is due to the presence of $(\nu_2+\nu_3)(A')$ in the same region.

[5] R. C. Ferguson, J. Am. Chem. Soc. **76**, 850 (1954).
[6] D. Kivelson, J. Chem. Phys. **22**, 904 (1954).
[7] H. S. Booth and F. C. Mericola, J. Am. Chem. Soc. **62**, 640 (1940).
[8] R. Cherton Bull. soc. roy. sci. Liège **11**, 54 (1942).
[9] Shelton, Nielsen, and Fletcher, J. Chem. Phys. **21**, 2178 (1953).
[10] S. R. Polo and M. K. Wilson, J. Chem. Phys. **22**, 900 (1954).
[11] J. Cabannes and A. Rousset, Ann. Phys. **19**, 229 (1953).
[12] Gerding, Smit, and Westrik, Rec. trav. chim. **60**, 513 (1941).
[13] C. A. McDowell, Trans. Faraday Soc. **49**, 371 (1953).
[14] R. Vogel-Högler, Acta Phys. Austriaca **1**, 323 (1948).

TABLE I. Vibrational spectra and assignments of SOF_2.

Infrared (gas) cm^{-1}	Raman (liquid)[a] cm^{-1}	Assignment
	326	
390	395	$\nu_6(a'')$
(410)[b]		$\nu_4(a')$
530	529	$\nu_3(a')$
748	720	$\nu_5(a'')$
806	795	$\nu_2(a')$
920		$\nu_3+\nu_6(A'')$
940		$\nu_3+\nu_4(A')$
1136		$\nu_5+\nu_6(A')$ (and $\nu_5+\nu_4(A'')$?)
1333	1312	$\nu_1(a')$ and $\nu_2+\nu_3(A')$
1480		$2\nu_5(A')$
1546		$\nu_2+\nu_5(A'')$
1612		$2\nu_2(A')$
1718		$\nu_1+\nu_6(A'')$ (and $\nu_1+\nu_4(A')$?)
2144		$\nu_1+\nu_2(A')$
2652		$2\nu_1(A')$

[a] See reference 3.
[b] Estimated from combination band at 940 cm^{-1}.

The stretching frequencies in SF_6[15] and SO_2F_2[1] indicate that the S−F stretching motions in SOF_2 should be assigned to the bands at 808 cm^{-1} and 748 cm^{-1}. By analogy with $SOCl_2$[11–13] where the S−Cl antisymmetric stretch occurs at a lower frequency than the symmetric motion, in SOF_2 the 748 cm^{-1} band is assigned as $\nu_5(a'')$ and the band at 808 cm^{-1} as $\nu_2(a')$.

The assignment of the bending modes may be made by comparison with PF_3.[16] The masses and geometry are similar to those of SOF_2, and the force constants can be expected to be closely similar. Accordingly, the band at 530 cm^{-1} is assigned to $\nu_3(a')$, in correspondence with the band $\nu_2(a')$ at 487 cm^{-1} in PF_3.

The modes $\nu_4(a')$ and $\nu_6(a'')$ will then correspond to the two modes of the $\nu_4(e)$ degenerate vibration of PF_3 at 344 cm^{-1}. In SOF_2 this degeneracy would be removed, but because of the similarity of the masses and electronegativities of the O and F atoms, the splitting should not be large. If we assign the very strong band at 390 cm^{-1} as $\nu_6(a'')$, there is no obvious absorption available for assignment as $\nu_4(a')$. We have not observed the band at 326 cm^{-1} reported in the Raman spectrum,[3] although the entire CsBr region has been searched with a 10-cm cell filled to a pressure of 1 atmos. However, the band observed at 940 cm^{-1} may be explained as $(\nu_3+\nu_4)(A')$, if $\nu_4(a')$ is assumed to lie at about 410 cm^{-1}. Furthermore, all the observed combination bands involving ν_6, which we assign, namely 1718 cm^{-1} $(\nu_1+\nu_6)(A'')$, 1136 cm^{-1} $(\nu_5+\nu_6)(A')$, and 920 cm^{-1}, $(\nu_3+\nu_6)(A'')$, exhibit atypical band contours which suggest the occurrence of combination bands involving a fundamental of slightly higher frequency than ν_6.[17]

The assignment of the remaining observed bands seems straightforward. The complete interpretation of the observed spectrum is given in Table I.

Calculation of force constants is being postponed until the current investigation of related molecules is completed.

[15] R. T. Langemann and E. A. Jones, J. Phys. Chem. **19**, 534 (1951).
[16] M. K. Wilson and S. R. Polo, J. Chem. Phys. **20**, 1716 (1952).

TABLE II. Thermodynamic functions for SOF_2 (cal deg^{-1} $mole^{-1}$).

$T°K$	C_p^0	S^0	$\frac{(H^0-H_0^0)}{T}$	$-\frac{(F^0-H_0^0)}{T}$
273.15	13.04	58.58	9.76	48.82
298.15	13.58	59.75	10.06	49.69
400	15.32	64.00	11.19	52.81
600	17.27	70.63	12.93	57.70
800	18.24	75.74	14.15	61.59
1000	18.77	79.88	15.03	64.85
1200	19.08	83.32	15.68	67.65
1500	19.35	87.62	16.39	71.23

THERMODYNAMIC FUNCTIONS

Thermodynamic functions for SOF_2 over a convenient temperature range are given in Table II. The calculations were made under a rigid-rotor, harmonic oscillator approximation for an ideal gas at one atmosphere pressure. The moments of inertia were determined from the microwave rotational constants[5]: $a=8614.75$ mc, $b=8356.98$ mc, and $c=4952.96$ mc.

ACKNOWLEDGMENTS

The authors wish to thank Dr. Santiago R. Polo for many helpful discussions.

[17] Professor Paul Bender (private communication). The assignment of the band at 390 cm^{-1} as $\nu_6(a'')$ is based upon Professor Bender's observation that this line is depolarized in the Raman effect.

Raman Spectra of Thionyl Fluoride and Sulfuryl Fluoride

PAUL BENDER AND JAMES M. WOOD, JR.
Department of Chemistry, University of Wisconsin, Madison, Wisonsin

(Received November 7, 1954)

The Raman spectra of liquid and gaseous sulfuryl fluoride (SO_2F_2) and of liquid thionyl fluoride (SOF_2) have been investigated and depolization factors measured for the stronger lines scattered by the liquids. For SO_2F_2 the Raman shift due to the infrared inactive torsional mode has been found to be 388 cm^{-1}, and other previous assignments based on the infrared spectrum have been confirmed. For SOF_2, the symmetric SF_2 stretch occurs at a higher frequency than the asymmetric stretch; the reverse is true for SO_2F_2. The symmetric SF_2 bending mode has escaped detection for both compounds.

INTRODUCTION

THE Raman spectrum of sulfuryl fluoride (SO_2F_2) provides a pertinent complement to the infrared absorption spectrum previously reported,[1] in particular because of the Raman activity of the a_2 torsional oscillation. Earlier work[2] on thionyl fluoride (SOF_2) did not include depolarization factor measurements; the present results require a reversal of the frequency assignments previously suggested for the $2SF_2$ stretching modes.

EXPERIMENTAL DETAILS

Spectrograph

A Steinheil type GH 3-prism glass spectrograph with f/3.5 collimator and camera lenses was employed. Eastman type 103a-j or 103a-o plates were used in conjunction with Kodak D-11 developer. All frequency shifts were measured by comparison with selected Fe lines using the Hartman dispersion formula. The line spacings were measured with a 2-coordinate comparator on densitometer tracings (recorded on Process plates) of the spectra. An accuracy of ± 3 cm^{-1} or better is expected for the stronger Raman lines.

Excitation Unit

For liquids, General Electric type H-11 lamps were used to illuminate a vertical Raman tube of 15 mm i.d. supported in an unsilvered cylindrical Dewar flask filled with a solution of paranitrotoluene in acetone. An adequately constant temperature of *ca* $-65°C$ was maintained by circulating cold trichloroethylene, from a reservoir cooled by a trichloroethylene-dry-ice mixture, through a copper coil immersed in the acetone. A large diam Pyrex tube was placed around the Dewar flask, and a stream of dried air was passed through the annular space between the two, to prevent moisture condensation.

An aqueous solution of crystal violet was circulated through filter jackets surrounding the lamps. The light incident upon the Raman tube was collimated for depolarization factor measurements by a system of baffles of $\frac{1}{2}$ in. spacing. The scattered light passed vertically through the liquid meniscus and the plane window of the Raman tube to an unsilvered glass right-angle prism and thence to the spectrograph. The technique otherwise employed in the depolarization factor measurements followed that previously described[3]; with the present less favorable circumstances the accuracy was less satisfactory, but the maximum uncertainty in the depolarization factor values is estimated at approximately ± 0.05.

The apparatus used in obtaining the Raman spectrum of gaseous SO_2F_2 will be described elsewhere. A pressure of *ca* 2 atmos was used and exposure times of *ca* 40 hr were required with a filter solution whose transmission at 4358 A was about 65 percent. It should be noted that the scattering efficiency was quite low for the liquid phase also.

Preparation of Materials

The compounds were prepared by fluorination of the corresponding chlorides, followed by distillation through a low-temperature fractionation column packed with glass helices. A constant boiling center cut was segregated for use in each case. The infrared absorption spectra of the compounds showed no evidence of the characteristic bands of the logical impurities.

EXPERIMENTAL RESULTS AND DISCUSSION

In Table I are summarized the results obtained for SOF_2. The agreement with the values cited by Yost[2] for the Raman shifts is excellent, except for the line at 326 cm^{-1}, of which we have found no indication whatsoever on plates on which the anti-Stokes line at -393 cm^{-1} did appear. The usual assumption of C_s symmetry for SOF_2, supported by the electron diffraction results of Stevenson and Beach[4] and the microwave results of Ferguson,[5] leads to the prediction of 6 Raman-active fundamental frequencies, 4 polarized and 2 depolarized. The results here obtained are in

[1] W. D. Perkins and M. K. Wilson, J. Chem. Phys. **20**, 1791 (1952).
[2] Best and Trampe, quoted by D. M. Yost, Proc. Indian Acad. Sci. **8**, 333 (1938).
[3] P. Bender and P. A. Lyons, J. Chem. Phys. **18**, 438 (1950).
[4] D. P. Stevenson and J. Y. Beach, quoted by D. M. Yost and H. Russell, *Systematic Inorganic Chemistry* (Prentice-Hall, Inc., New York, 1944), p. 306.
[5] R. C. Ferguson, J. Am. Chem. Soc. **76**, 850 (1954).

TABLE I. Raman spectrum of liquid SOF_2 (thionyl fluoride).[a]

This work $\Delta\tilde{\nu}$, cm^{-1}, vac.	ρ	Best and Trampe $\Delta\tilde{\nu}$, cm^{-1}	Assignment
...		326 (1)	
393 (mb, 4)	0.90	395 (6)	$\nu_6(a'')$
526 (s, 4)	0.45	529 (8)	$\nu_3(a')$
721 (b, 4)	0.80	720 (9)	$\nu_5(a'')$
801 (b, 5)	0.17	795 (9)	$\nu_2(a')$
1308 (mb, 10)	0.20	1312 (10)	$\nu_1(a')$

[a] s = sharp, b = broad, mb = medium broad; $\Delta\tilde{\nu}$ = Raman displacement; ν = frequency; and ρ = the depolarization factor.

TABLE II. Raman spectrum of SO_2F_2 (sulfuryl fluoride).[a]

This work $\Delta\tilde{\nu}$, cm^{-1}, vac. gas (25°C, 2 atmos)	liquid (−65°C)	ρ (liquid)	Perkins and Wilson $\tilde{\nu}$, I.R., cm^{-1}	Assignment
388 (vb)	389 (4)	0.80	(385)[b]	ν_5 (a_2)
			539	ν_9 (b_2)
543 (vb)	547 (6)	0.85	544	ν_3 (a_1)
			553	ν_7 (b_1)
847 (vs)	846 (10)	0.08	848	ν_2 (a_1)
883	887 (1)	...	885	ν_8 (b_2)
1270 (vs)	1263 (7)	0.15	1269	ν_1 (a_1)
1502	1497 (1)	0.8	1502	ν_6 (b_1)

[a] vb = very broad, vs = very sharp; $\tilde{\nu}$ = wave number; and other symbols have same meaning as in Table I.
[b] Estimated from infrared active first overtone.

complete accord with this prediction if it is assumed that the symmetrical SF_2 bending fundamental has not yet been observed; the assignments noted in Table I have been made on this basis. A tentative frequency assignment previously given by Wu[6] differs from the above in inverting the assignment of the 2 SF_2 stretching modes, but the observed depolarization factors eliminate this possibility.

The data of Table I also predict a complication of the vibrational spectrum through Fermi resonance. It should be remarked that the lines at 1308 and 801 cm^{-1} are not as sharp as that at 526 cm^{-1}; a possible explanation can be given in terms of the interactions of $\nu_1(a')$ with $(\nu_2+\nu_3)(A')$, and $\nu_2(a')$ with $(2\nu_6)(A')$, respectively. The a'' lines at 393 and 721 cm^{-1} also are somewhat broad. It does not seem entirely satisfactory, since these results are for a condensed phase, for this to be attributed simply to their depolarized character. It has been suggested by O'Loane and Wilson[7] on the basis of their study of the infrared absorption spectrum, that the missing $\nu_4(a')$ fundamental lies close to $\nu_6(a'')$. This possibility would account for the broad appearance of the 393 cm^{-1} line, but cannot be substantiated from our plates.

The results of measurements on SO_2F_2 are given in Table II, wherein the frequency assignment of Perkins and Wilson[1] has been used; these workers have also illustrated the general form of the corresponding normal modes. The depolarized line at 388 cm^{-1} must result from the infrared inactive torsional mode a_2; this value is in good agreement with the prediction of Perkins and Wilson, which was based on their assignment of the infrared band at 767 cm^{-1} as $2\nu_5(a_1)$. The assignment of the symmetric SF_2 stretching mode to a lower frequency than that of the asymmetric stretch is also confirmed. It should be noted, however, that the results given above for SOF_2, where the reverse order is found, nullify the original basis for this classification. The Raman data provide no real information on the suggested piling up of $\nu_3(a_1)$, $\nu_9(b_2)$, and $\nu_7(b_1)$ near 550 cm^{-1}. This should produce a broad Raman line with a resultant depolarization factor somewhat less than 6/7. The line found at 543 cm^{-1} is broad, but experimental error prevents any definitive conclusion to be drawn from the depolarization factor. For other lines the Raman data confirm the assignments of Perkins and Wilson. The agreement between the infrared and Raman results for the gas is very satisfactory. The contrast between the sharp lines associated with the totally symmetric modes and the broad lines given by the asymmetric modes was strikingly apparent in the Raman spectrum of the gas.

Perkins and Wilson have suggested a value equivalent to about 300 cm^{-1} for the symmetric SF_2 bending frequency for SO_2F_2, but no Raman line was found in the corresponding region. Further studies are necessary to clarify this situation for both of the molecules discussed here. To this end it is planned to supplement the spectroscopic work with studies of the heat capacities of the gases.

ACKNOWLEDGMENTS

The assistance of Dr. Mark M. Woyski, who supplied the compounds used in this work, is gratefully acknowledged.

[6] Ta-Yu Wu, *Vibrational Spectra and Structure of Polyatomic Molecules* (J. W. Edwards Brothers, Inc., Ann Arbor, Michigan, 1946), p. 214.

[7] See preceding paper, J. K. O'Loane and M. K. Wilson, J. Chem. Phys. **23**, 1313 (1955).

Concentration of Nitrogen-15 by Chemical Exchange in a Thermal Diffusion Column

W. SPINDEL AND T. I. TAYLOR
Chemistry Department, Columbia University, New York, New York

(Received July 19, 1954)

A concentration of nitrogen-15 has been effected in a thermal diffusion column under conditions where the gaseous exchange action, $N^{14}O_2+N^{15}O \rightleftarrows N^{15}O_2+N^{14}O$, can contribute to the separative process. The top of the column is fed with NO_2 of normal isotopic abundance. Reversible thermal decomposition of NO_2 into NO and O_2 establishes a radial concentration gradient so that the descending cold stream is predominantly NO_2 and the inner hot ascending stream is largely NO and O_2. As a result of the exchange reaction, N^{15} preferentially concentrates in the NO_2 and is carried to the bottom of the column. Here the enriched NO_2 re-enters the hot rising stream and is again decomposed into NO which undergoes further exchange. This reversible thermal decomposition makes it possible to operate the column without a chemical converter as was needed in the $CO-CO_2$ system.

The over-all isotope separation has been studied in a two-meter column as a function of pressure (0.25 to 1.0 atmosphere), temperature (400 to 700°C) and withdrawal rate (5 to 66 cc atmospheres per day). A maximum over-all separation of 2.6 was obtained at a filament temperature of 685°C and a pressure of 0.5 atmosphere. At a withdrawal rate of 27 cc atmospheres the over-all separation is about 70 percent of this maximum value.

The system is a rather complicated one, and it is not yet possible to completely evaluate the contribution of each separative process that can occur in the column.

INTRODUCTION

CHEMICAL exchange reactions have been used successfully in two-phase countercurrent systems to concentrate the rare isotopes of a number of the light elements.[1]

A method has been devised[2–4] by means of which gaseous exchange can be established in a countercurrent system. A thermal diffusion column establishes countercurrent flow between a central hot rising gas stream and an outer cold descending stream. The thermal diffusion effect concentrates the heavier gas molecules in the colder stream while the lighter molecules are more abundant in the hot stream. Where the exchange favors the concentration of the heavy isotope in the heavier molecule, this isotope will concentrate with the heavier gas in the cold stream and will be carried to the bottom of the column by convection.

The exchange reaction: $N^{15}O+N^{14}O_2 \rightleftarrows N^{14}O+N^{15}O_2$ suggested by Urey and Greiff[5] and shown by Leifer[6] to be complete in less than 15 seconds at −35°C seemed to be particularly suitable for study in the gaseous exchange column. Equilibrium constants in Table I were calculated by the method of Bigeleisen and Mayer[7] using a central force field approximation for calculating the frequencies of isotopic NO_2 as described by Spindel.[8] Although the values are low at the higher temperatures, it was hoped the high rate of the reaction would compensate for this in the operation of the column.

TABLE I. Equilibrium constant (K) for exchange.

T(°A)	t(°C)	(K)
298	25	1.0212
473	200	1.0083
673	400	1.0037
873	600	1.0020

The reactions of the nitrogen oxides have been studied extensively.[9] For chemical exchange in a thermal diffusion column, the equilibrium: $NO_2 \rightleftarrows NO+\frac{1}{2}O_2$ is of particular interest. The variation in mole fraction of NO resulting from the decomposition of NO_2 at various temperatures and pressures is shown in Fig. 1. If NO_2 gas is subjected to a temperature gradient such as exists in a thermal diffusion column, a radial concentration gradient is established. In the cool region near the wall, the gas is richer in NO_2 (or rather an equilibrium mixture with the dimer, N_2O_4) while in the hot zone the gas is richer in NO and O_2 which result from the thermal decomposition of NO_2 (Fig. 1). A convective countercurrent flow of hot and cold gas is established in the thermal diffusion column. The descending cold stream is predominantly NO_2 and the inner hot ascending stream is a mixture of NO, O_2, and NO_2. Exchange occurs between NO and NO_2 with N^{15} preferentially entering the NO_2 which is then carried to the bottom of the column by the cold stream. Here, the enriched NO_2 re-enters the hot rising stream and is again decomposed into NO which then undergoes further exchange. This thermal decomposition of NO_2

[1] G. H. Clewett, Ann. Revs. Nuclear Sci. **1**, 293 (1952).
[2] T. I. Taylor and R. B. Bernstein, J. Am. Chem. Soc. **69**, 2076 (1947).
[3] R. B. Bernstein and T. I. Taylor, J. Chem. Phys. **16**, 903 (1948).
[4] T. I. Taylor and W. Spindel, J. Chem. Phys. **16**, 635 (1948).
[5] H. C. Urey and L. J. Greiff, J. Am. Chem. Soc. **57**, 321 (1935).
[6] E. Leifer, J. Chem. Phys. **8**, 301 (1940).
[7] J. Bigeleisen and M. G. Mayer, J. Chem. Phys. **15**, 261 (1947).
[8] W. Spindel, J. Chem. Phys. **22**, 1271 (1954).
[9] W. F. Giauque and J. D. Kemp, J. Chem. Phys. **6**, 40 (1938); D. M. Yost and H. Russell, *Systematic Inorganic Chemistry* (Prentice-Hall, Inc., New York, 1944), p. 29; and F. Ephraim, *Inorganic Chemistry* (Interscience Publishers, Inc., New York, 1947), p. 666.

makes it possible to operate the column without a chemical converter such as is customary at the enriched end of a countercurrent chemical exchange system.[1]

EXPERIMENTAL

The general requirements determining the design of the column and associated apparatus were mainly those associated with the corrosive nature of the oxides of nitrogen. Silicone (Dow-Corning high-vacuum type) grease was found satisfactory as a stopcock lubricant, and platinum, gold, or stainless steel was used where metal was required.

A diagrammatic sketch of the apparatus is shown in Fig. 2. The gaseous exchange column (A) consisted of a water-jacketed glass tube 9 mm internal diameter and 200 cm long. The inner heated member was a platinum wire (*B.* and *S.* No. 22, 0.64 mm diam), to which platinum spacers were spotwelded at 50-cm intervals. These spacers maintained the filament concentric with the walls of the column. A 100 g stainless-steel weight at the bottom of the wire maintained the filament taut. Electrical connection was made to the bottom of the filament by means of stranded gold wires, spotwelded to tungsten wires sealed through the Pyrex assembly at the bottom of the column. These gold wires were long enough to allow the weight to move up and down freely a distance of about 2 cm. A by-pass was included at the bottom of the column to provide for mixing of the gas in the reservoir below the filament. The tube was 6 mm in diameter and was heated to approximately 325°C to circulate the gas by convection.

The temperature of the filament was estimated to ±25°C from measurements of the resistance of the wire. Pressure measurements were made to ±1 mm of Hg using a Booth-Cromer[10] type pressure transmitter. The NO_2 gas was obtained from the Matheson Company, East Rutherford, New Jersey and was used

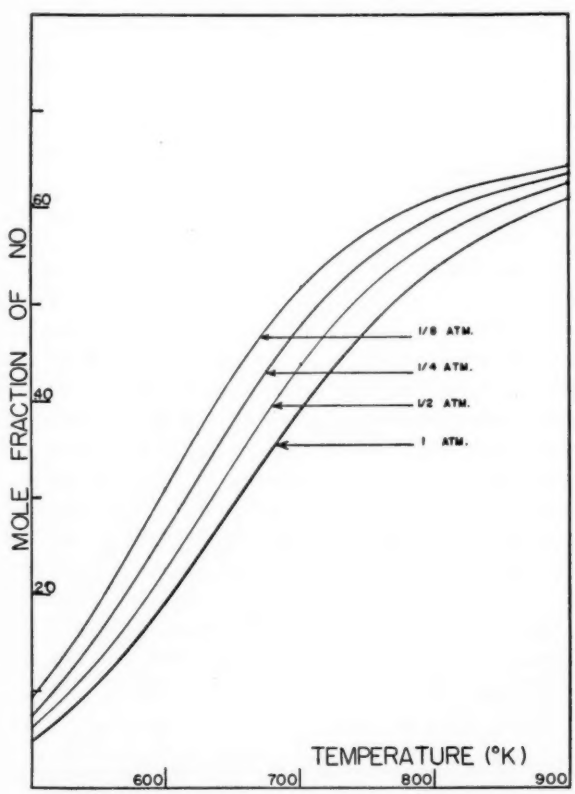

FIG. 1. Mole fraction of nitric oxide in equilibrium with nitrogen dioxide at various temperatures and pressures. Values of the equilibrium constant for the reaction $NO_2 = NO + \frac{1}{2}O_2$ from Giauque and Kemp (reference 9).

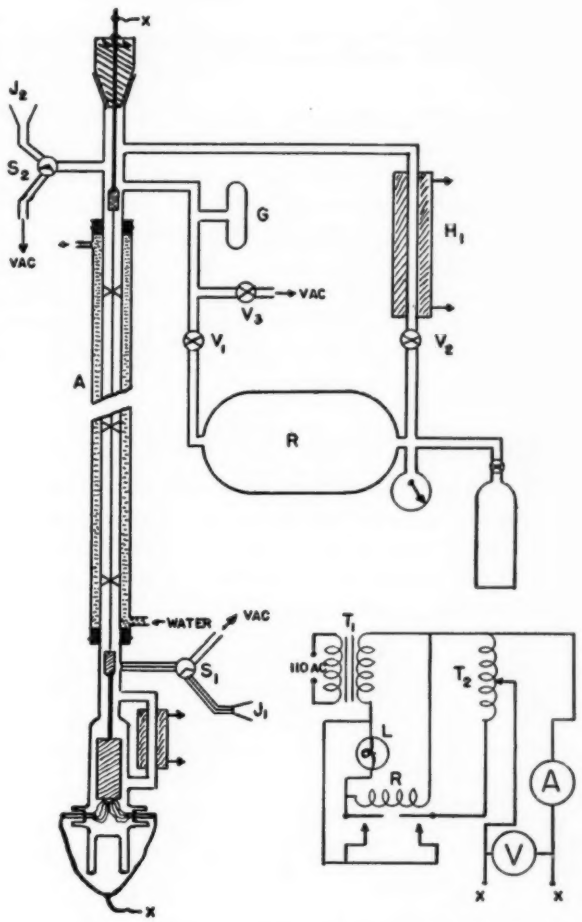

FIG. 2. Experimental system: The column is shown with associated apparatus for measurement of pressure and control of filament temperature. Joints and stopcocks (S_1, S_2, J_1, J_2) permit sampling of the column at the bottom and top. G shows the location of a Booth-Cromer (reference 10) type pressure transmitter, R is a 40-liter stainless steel reservoir for normal NO_2 gas, V_1, V_2, V_3 are Crist (reference 11) corrosion resistant valves to allow evacuation of either the column alone or column and reservoir both, and H_1 is a heater maintained at 325°C to circulate gas from the reservoir to the top of the column by convective action. The circuit at the lower right-hand corner is used for control and measurement of filament temperature. T_1 is a constant voltage transformer, T_2 is a 15-ampere variac, L is a pilot light, R is a holding-type relay, V is a 30-volt ac voltmeter, A is a 10-ampere ac ammeter, and x is the connection to the filament.

[10] S. Cromer, MDDC-803, U. S. Atomic Energy Commission, Technical Information Branch, Oak Ridge, Tennessee.

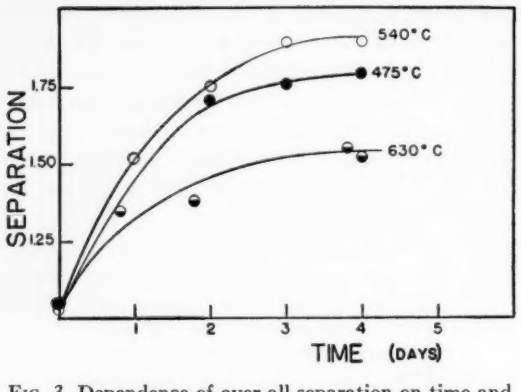

FIG. 3. Dependence of over-all separation on time and filament temperature at 27 cm Hg pressure.

without further treatment. This gas was circulated across the top of the column through corrosion resistant valves[11] by thermal convection as illustrated in Fig. 2.

Preliminary experiments at 0.5 and 1.0 atmosphere showed erratic separations, with some appreciably higher and a few lower than the series of experiments reported in the following sections. After remodeling the apparatus to improve the centering of the filament, and to eliminate corrosion and vibration, more consistent data were obtained.

Preparation of Samples and Isotopic Analysis

To avoid admitting NO_2 into the mass spectrometer, the samples were converted to N_2 in special sample tubes. These tubes were about 10 cc in volume and had a 6-mm tubulation containing iron powder held in place by a loose plug of glass wool. After a sample was withdrawn, the part of the tube containing the iron powder was inserted into a furnace at 450°C. Under these conditions NO_2 was rapidly reduced to nitrogen. Samples were taken from the bottom of the column at 24-hour intervals during the runs. For these samples the peaks at mass 29 and mass 28 were determined. The separation, S, is given by the ratio 29/28 (bottom of column): 29/28 (top of column). Analyses were made with a 60-degree sector mass spectrometer of the type described by Nier.[12] To detect the presence of atmospheric nitrogen in any samples, the peak at mass 40 due to argon was always examined, and samples showing significant atmospheric contamination were rejected. Frequently the mass spectrum from mass 14 to about mass 50 was recorded in order to determine whether impurities were present that might interfere with the analysis.

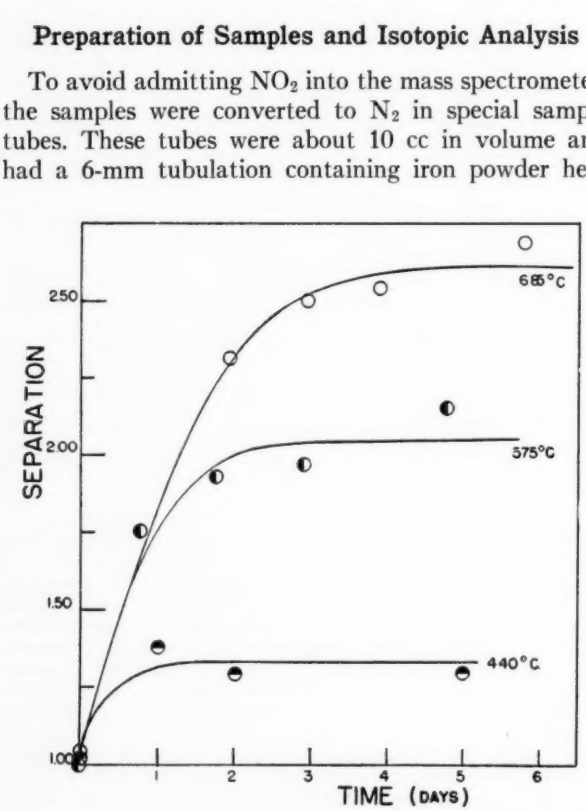

FIG. 4. Dependence of over-all separation on time and filament temperature at 36 cm Hg pressure.

[11] R. H. Crist and F. B. Brown, Ind. Eng. Chem., Anal. Ed. **11**, 396 (1939).

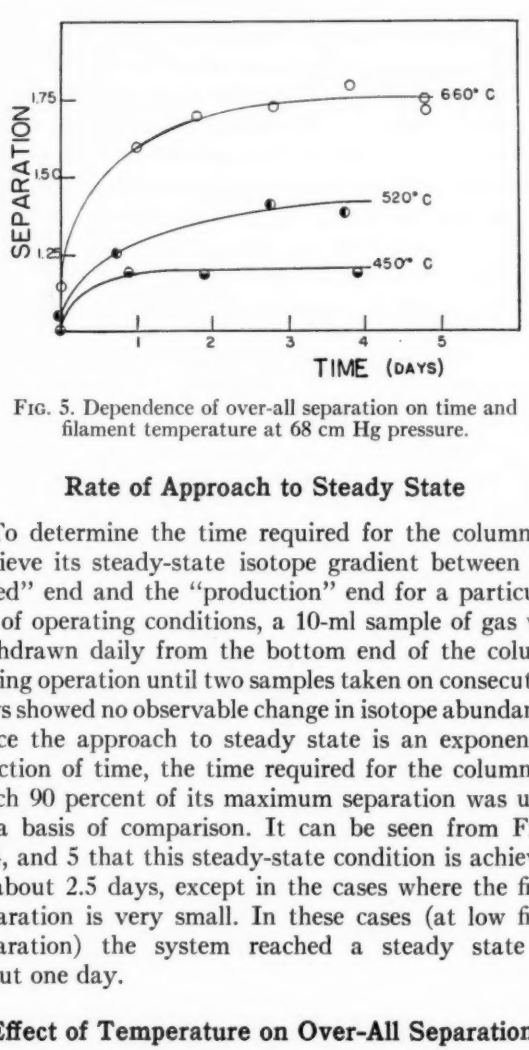

FIG. 5. Dependence of over-all separation on time and filament temperature at 68 cm Hg pressure.

Rate of Approach to Steady State

To determine the time required for the column to achieve its steady-state isotope gradient between the "feed" end and the "production" end for a particular set of operating conditions, a 10-ml sample of gas was withdrawn daily from the bottom end of the column during operation until two samples taken on consecutive days showed no observable change in isotope abundance. Since the approach to steady state is an exponential function of time, the time required for the column to reach 90 percent of its maximum separation was used as a basis of comparison. It can be seen from Figs. 3, 4, and 5 that this steady-state condition is achieved in about 2.5 days, except in the cases where the final separation is very small. In these cases (at low final separation) the system reached a steady state in about one day.

Effect of Temperature on Over-All Separation

The range of filament temperature investigated was 400°C to 700°C. Below 400°C the concentration of

[12] A. O. Nier, Rev. Sci. Instr. **18**, 398 (1947).

NO and O_2 was low and the separations obtained were small. Temperatures above 700°C were not used because of possible decomposition of NO and because the thermal expansion of the platinum wire was greater than could be compensated for by the arrangement at the bottom of the column.

Within the range of temperature studied, the following effects were observed. The over-all separation in the system increased with increasing temperature at pressures greater than 0.5 atmosphere. At lower pressures, an increase in temperature caused an increase in separation with a maximum at about 550°C. Above this temperature, the separation factor fell off rapidly. These results are shown in Figs. 3, 4, and 5, where the separation is plotted against time, for various values of temperature and pressure. The effect of temperature is summarized in Fig. 6, where the final separations at various pressures are plotted against temperature.

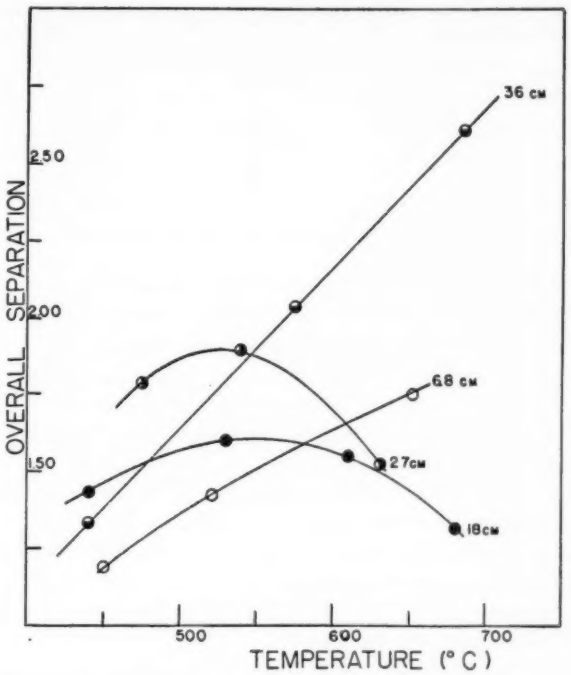

FIG. 6. Dependence of over-all separation on temperature at various pressures. Data from end points of time *vs* separation curves such as Figs. 3, 4, and 5.

Variation of Separation with Rate of Withdrawal

The withdrawal of 10-cc samples per 24-hour interval was found to have very little effect on the over-all separation since the same separation was obtained when samples were withdrawn at 3- and 4-day intervals. To study the effect of withdrawal, the apparatus was operated at optimum conditions of 0.5 atmosphere and at a filament temperature of 600°C. After 12 days of operation at a withdrawal rate of 5 cc atmosphere per day, the rate was increased to 33 cc atmosphere per day, samples being taken at 8-hour intervals. The rate of withdrawal was then increased to 50 cc atmosphere and finally to 66 cc atmosphere per day. The over-all separation returned to its original level when withdrawal was discontinued. The results of these experiments are plotted in Fig. 7. It can be seen that the separation drops to about one-half its maximum value when the amount withdrawn is about 33 cc atmosphere per day.

Samples were also taken at the top of the column during the withdrawal period to determine whether the N^{15} abundance in the feed material was being depleted. A sample taken after withdrawing 66 cc atmosphere per day of concentrated material for 3 days showed the feed material to contain 0.97 times the natural N^{15} abundance. Since this difference is two to three times the experimental error, it indicates that the feed rate should have been increased.

DISCUSSION

Although the complete theory of the gaseous exchange column has not been worked out, it is interesting to compare its operation with that of other types of isotope separating columns.[1,13] The over-all isotope separation, S, is usually expressed by the equation $S=\alpha^n$, where α is the single-process fractionation factor and n is the number of "theoretical plates" in the column. If it is assumed that the enrichment in the $NO-NO_2$ system is primarily due to a chemical exchange process, then, for the purpose of calculating an effective value of n, α may be taken as the equilibrium constant for the exchange reaction. Since the $NO-NO_2$ exchange is rapid even at low temperatures, exchange will occur wherever both NO and NO_2 are present. For the average effective exchange temperature in the column, that temperature is chosen at which an equal molar mixture of NO and NO_2 exists, that is, where the mole fraction of $NO=0.4$, $NO_2=0.4$,

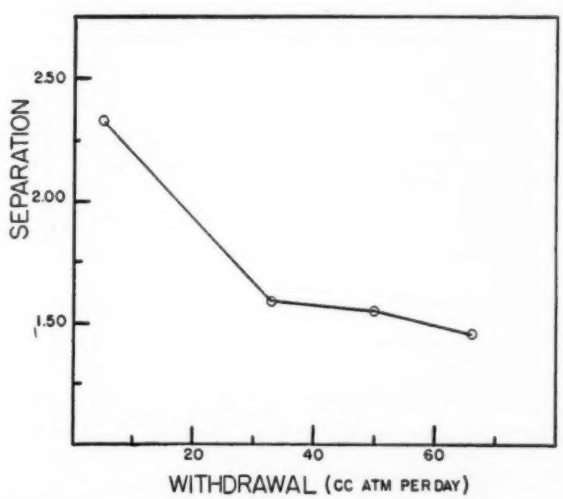

FIG. 7. Dependence of separation on rate of withdrawal.

[13] K. Cohen, J. Chem. Phys. 8, 588 (1940).

TABLE II. Net transport during withdrawal.

NO_2 withdrawn (cc atmos/day)	Over-all separation	Transport of N^{15} (moles/day)
5	2.40	1.1×10^{-6}
33	1.59	3.0×10^{-6}
50	1.55	4.3×10^{-6}
66	1.45	4.6×10^{-6}
(maximum)	···	6.8×10^{-6}

and $O_2=0.2$. From Fig. 1 this temperature at 0.5 atmosphere pressure is 410°C, corresponding to $\alpha=1.0037$. Using this value and an over-all separation S, of 2.6 (Fig. 4) for the run at 0.5 atmosphere and 685°C, the value of n is calculated to be 270, which corresponds to a height equivalent to a theoretical plate (HETP) of 0.76 cm. For a two-phase system such as that used for concentrating N^{15} by chemical exchange between NH_4NO_3 solution and NH_3,[14] α is 1.023 and the HETP is about 7 cm. The transport in such two-phase columns is much greater and they are therefore much more useful for producing quantities of the separated isotopes.

In addition to the chemical exchange mechanism considered above, ordinary thermal diffusion of the isotopic molecules may contribute to the separation process, particularly at the higher temperatures. Dr. W. P. Senett in these laboratories has been studying the relative contributions of ordinary thermal diffusion and chemical exchange effects in this system.* At 650°C and 0.5 atmosphere pressure the over-all separation obtained by thermal diffusion of NO is about 1.4.

Transport of N^{15}

The maximum rate at which N^{15} is transported in the column can be calculated from its initial rate of increase in concentration in the bottom reservoir. Thus, $\tau_{max}=(\nu-\nu_0/t)(pv/RT)$.

In a system where the mole fraction of the rare isotope is always much smaller than that of the abundant isotope this may be approximated by: $\tau_{max}\cong[(S-1)\nu_0/t]\cdot(pv/RT)$. In these equations, ν is the mole fraction of N^{15} at time t, ν_0 is the initial mole fraction of N^{15} at $t=0$, S is the over-all separation, p is the pressure of gas in the bottom reservoir of volume v, and T is the absolute temperature of the gas in the bottom reservoir. In the experiment at 685°C and 0.5 atmosphere (Fig. 4) with a reservoir of 70 cc, the over-all separation was 1.25 after 0.2 day. Thus, τ_{max}, as calculated from this data, is 6.8×10^{-6} mole N^{15}/day.

The transport under normal operating conditions when material is being withdrawn from the bottom of the column can be calculated from the data plotted in Fig. 7. Thus, at the steady-state condition when w moles of NO_2 per unit time are being withdrawn at a mole fraction of ν, the transport τ of N^{15} is given by $\tau=(\nu-\nu_0)w\cong(S-1)\nu_0 w$. The results as summarized in Table II show that as the withdrawal rate is increased, the over-all separation is decreased, but the transport of N^{15} is increased toward the previously calculated maximum.

If operated at about 70 percent of its maximum over-all separation of 2.5, 27 cc of NO_2 per day could be withdrawn at an over-all separation of 1.75. At double normal concentration, about 15 cc could be withdrawn daily. Longer columns or columns in cascade could be used for producing material of higher concentration.

The power required for the $NO-NO_2$ system (0.12 kw/meter) was somewhat less than that required for the $CO-CO_2$ system[3] (0.2 kw/meter) because of the lower operating temperatures. Experiments have not yet been made to determine transport and power requirements when these columns are operated as ordinary thermal diffusion columns. Indirect comparisons indicate that the two methods are about equivalent. The two-phase countercurrent exchange systems used by Urey and his co-workers[14] have much lower power requirements and much greater transport rates. They are, indicated therefore, when chemical exchange is to be used for producing large quantities of separated isotopes.

ACKNOWLEDGMENTS

The authors express their thanks to Dr. R. B. Bernstein for the many helpful discussions and suggestions during the course of the work. One of us (W.S.) wishes to thank the E. I. du Pont de Nemours Company for a fellowship during a part of this work.

[14] H. G. Thode and H. C. Urey, J. Chem. Phys. 7, 34 (1939).

* This work was supported by a grant from the U. S. Atomic Energy Commission, AT(30-1)755.

On the Adsorption of Oxygen on Tungsten as Revealed in the Field Emission Electron Microscope

J. A. Becker and R. G. Brandes
Bell Telephone Laboratories, Inc., Murray Hill, New Jersey

(Received August 23, 1954)

The tungsten surface in a field emission microscope is exposed to oxygen gas at a pressure near 5×10^{-8} mm and the effect of the gas on the field emission is observed. During the first 30 seconds, the emission decreases rapidly, but some regions deactivate more rapidly than others. During the next 12 minutes, the rate of deactivation is much slower, but again the change in activity for some planes is much more pronounced than for others. After the surface is heavily covered, the oxygen is desorbed by glowing the tungsten for one minute at successively higher temperatures.

The chief conclusions are: Oxygen is adsorbed on tungsten in three stages or layers. In the first layer, the bond strength is about 5 electron volts and the oxygen cannot be removed below about 1500°K. In the second layer, the bond strength is about 2.5 ev and the oxygen cannot be removed below about 750°K. These bond strengths depend somewhat on the crystallographic plane. In the third layer, the oxygen forms a variety of molecular complexes with the substrate. These reveal themselves as intensely bright, highly localized groups of spots. Each spot is due to electrons emitted by individual atoms in a molecule. The conditions necessary to observe such adatoms are given.

INTRODUCTION

BECAUSE the field emission electron microscope reveals how easily electrons are emitted from all crystallographic planes, it should constitute a very powerful tool in the study of the adsorption of a system such as oxygen on tungsten. This paper describes some of the results of such a study. The chief results are: When oxygen is adsorbed on clean tungsten, it makes first valence bonds whose strength is about 5 ev (electron volts equivalent). When every tungsten atom has made such a bond, additional adsorbed oxygen can make only second valence bonds and a second "layer" is adsorbed. The bond strength for this layer is only about 2.5 ev. After this second layer is completed, any additional adsorbed oxygen can no longer contact tungsten atoms, but can only contact adsorbed oxygen atoms. The adsorption forces are now much weaker and are not able to completely break the oxygen-oxygen bond in the molecule. Such adsorbed molecular complexes produce intensely bright, highly localized spots on the screen, which reveal the location of individual atoms in these molecules.

Before describing our experiments, we will discuss briefly the results obtained by older techniques. The adsorption of oxygen on tungsten has been studied by measuring the amount adsorbed as a function of pressure, at constant temperature. The heat of adsorption also has been measured as a function of the amount of oxygen adsorbed.[1–5] It has also been shown that adsorbed oxygen increases the thermionic work function.[6] As a result of these studies it is generally held that when oxygen molecules are adsorbed on tungsten in the first layer, the molecules are broken up into adatoms or negative adions which cannot be desorbed by decreasing the gas pressure; they are said to be chemisorbed.[7] At sufficiently low temperatures the oxygen is adsorbed as molecules which are held to the tungsten by much weaker forces; they are said to be physically adsorbed. At high enough gas pressures and ordinary temperatures, the first layer is chemisorbed while higher layers may be physically adsorbed.

Roberts[5] and Van Cleave[8] found that the accommodation coefficient of neon on polycrystalline tungsten wire is greatly increased as the amount of oxygen adsorbed increases. By covering the tungsten with a large amount of oxygen and then measuring the accommodation coefficient after the oxygen is partially desorbed by heating the tungsten to successively higher temperatures, they found evidence that the oxygen is desorbed in three stages in three ranges of temperature.

In all of these experiments the tungsten was in the form of finely divided powders, evaporated films, or polycrystalline wires or ribbons. Consequently, the results measure some kind of an average adsorption on a variety of crystallographic planes. It seemed to us quite likely that the results for individual planes would be simpler and more revealing. Consequently we used the field emission electron microscope[9,10] with

[1] N. K. Adam, *The Physics and Chemistry of Surfaces* (Oxford University Press, London, 1941).
[2] S. Dushman, *Vacuum Technique* (John Wiley and Sons, Inc., New York, 1949).
[3] I. Langmuir and D. S. Villars, J. Am. Chem. Soc. **53**, 486 (1931).
[4] I. Langmuir, J. Am. Chem. Soc. **37**, 1139 (1915).
[5] J. K. Roberts, Proc. Roy. Soc. (London) **A152**, 464–477 (1935).
[6] I. Langmuir and K. H. Kingdon, Phys. Rev. **24**, 510–522 (1924).
[7] O. Beeck, *Advances in Catalysis* (Academic Press, Inc., New York, 1950), Vol. II, p. 155.
[8] A. B. Van Cleave, Trans. Faraday Soc. **34**, 1174 (1938).
[9] E. W. Mueller, Naturwiss. **27**, 290–360 (1953). Professor Mueller, the inventor of the field emission microscope and its chief exponent, has published a great many important articles on its uses. We refer the reader to the above succinct review article for the original papers.
[10] R. Klein, J. Chem. Phys. **21**, 1177 (1953).

which one can observe the effects of adsorbed oxygen on individual planes having any desired crystallographic direction. As a means of following the amount of adsorbed oxygen, we used the work function as deduced from the field emission current density. From our experiments we conclude: The adsorption properties vary with the crystallographic planes; the chemisorbed oxygen on some planes exists in two states or "layers"; the first layer can be removed only at temperatures above about 1400°K; the second layer can be removed at temperatures above about 700°K; the third layer consists of adsorbed molecules or "admols" which are only partially dissociated and form molecular complexes with the underlying adatoms; these can be removed at temperatures near 600°K; the molecular complexes change their configuration at 300°K or higher.

E. W. Mueller,[9] R. Klein,[10] and Gomer and Hulm[11] have reported experiments on oxygen adsorbed on tungsten in a field emission microscope. Our experiments are an extension of theirs and were performed under a greater variety of experimental conditions or with a more systematic variation of these conditions. Where our conditions were similar to theirs, our observations confirm theirs.

Since the field emission microscope reveals such a wealth of detail for the various planes, it is highly desirable to understand the arrangement of the W atoms on these planes. For this purpose we constructed a model of a body-centered cubic crystal whose surface was in the form of a portion of a hemisphere. Glass marbles represent W atoms. All atoms which protrude beyond the radius of the hemisphere are excluded. This radius corresponds to about 25 marble diameters. Figure 1 is a photograph of the model. This model shows the following three features: (1) The 110, 211, 100, and 111 planes cover appreciable areas of the surface. (2) All other planes can be thought of as being composed of small areas or facets of these simple planes; as a first approximation the structure of the surface surrounding a simple plane is dominated by that plane in the sense that the structure consists of terraces of that plane. (3) The number of first nearest neighbors of a surface atom varies for different planes—six for the 110 plane, five for the 211, and four for the 100, 111 planes and 100 region. In Fig. 1 these appear as white, grey, and black marbles. In the interior of the crystal, a W atom touches eight nearest neighbors. This model has been very useful in explaining the migration and evaporation of W on W and Ba on W.[12] As will appear later, the model is also useful in interpreting the main features of the adsorption of O on W.

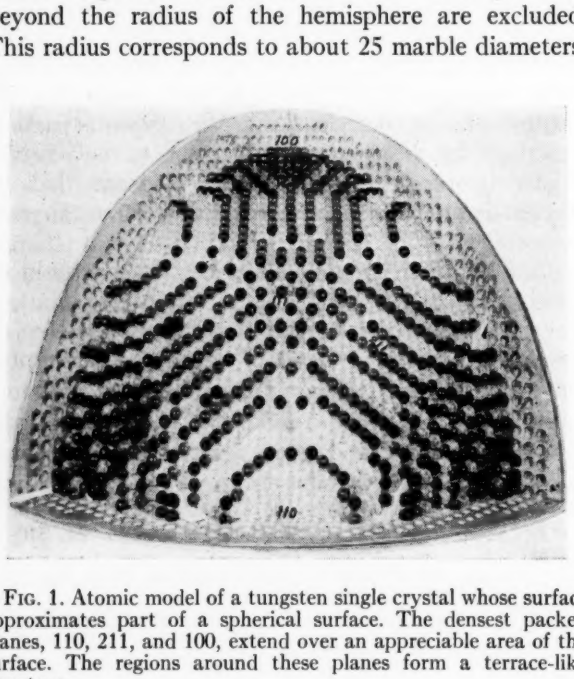

FIG. 1. Atomic model of a tungsten single crystal whose surface approximates part of a spherical surface. The densest packed planes, 110, 211, and 100, extend over an appreciable area of the surface. The regions around these planes form a terrace-like structure.

EXPERIMENTAL PROCEDURES AND RESULTS

The field emission electron microscope has been described in previous articles.[9,13] The particular system used in the present studies is shown schematically in Fig. 2. The valve used to control the rate of flow of oxygen into the system can be baked out and can be adjusted over a wide range of relatively small leak rates so that the O_2 pressure in the system can be maintained at any desired value from about 10^{-8} mm to 10^{-5} mm with a reservoir pressure of about 10 mm. When very low O_2 pressures are desired, the valve is "closed" and the reservoir is pumped out to about 10^{-3} mm. The system is baked, cooled, and all metal parts are outgassed; it is then rebaked. Oxygen is then

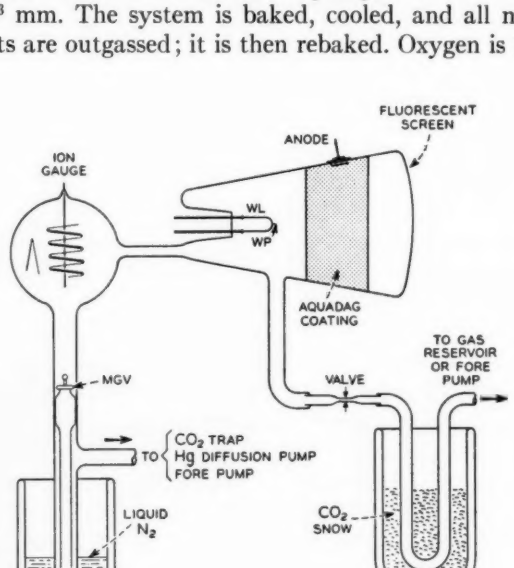

FIG. 2. Schematic diagram of the system.

[11] R. Gomer and J. K. Hulm, J. Am. Chem. Soc. **75**, 4114 (1953).

[12] J. A. Becker, Bell System Tech. J. **30**, 907 (1951).

[13] J. A. Becker and C. D. Hartman, J. Phys. Chem. **57**, 153 (1953).

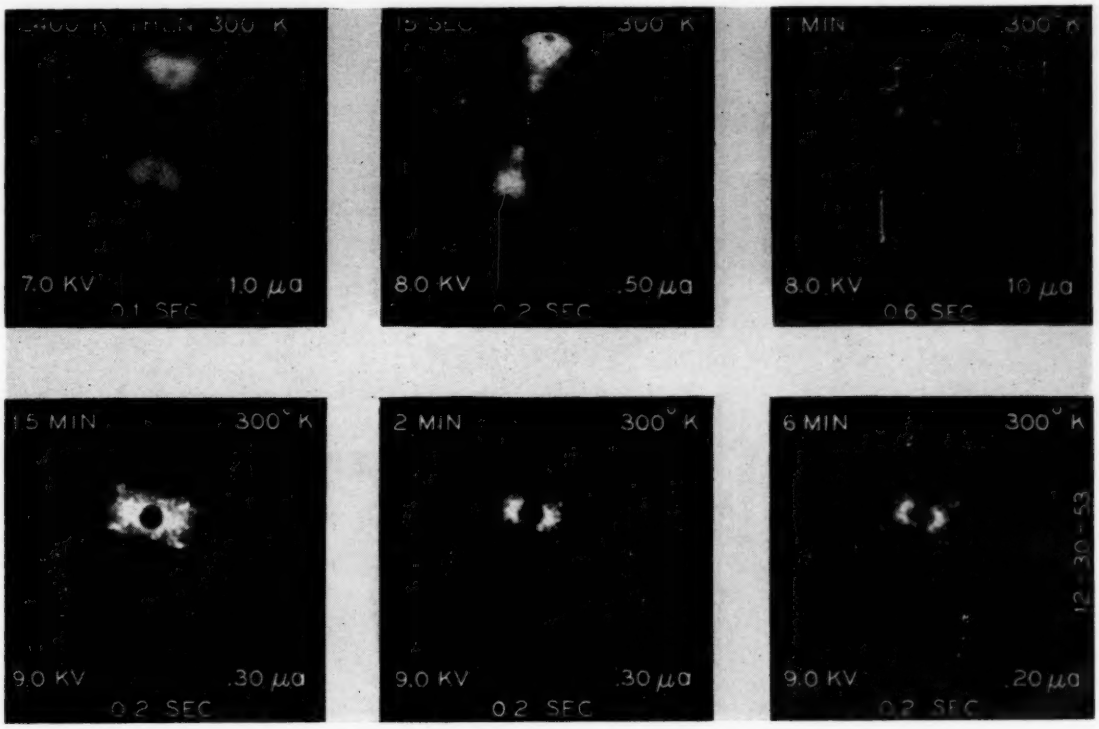

FIG. 3. Series of patterns produced by increasing amounts of adsorbed oxygen. $p=5\times10^{-8}$.

introduced to a pressure of 10^{-2} mm as measured by a thermistor gauge. The O_2 is pumped out to 10^{-7} mm. This O_2 treatment is repeated. The tungsten loop and point is flashed to 2400°K; on cooling it rapidly adsorbs some of the residual oxygen. If the system is pumped for hours, the pressure gradually reduces to about 5×10^{-9} mm. This slow reduction of pressure is due to the fact that the glass walls desorb the oxygen slowly.

When the pressure is in the neighborhood of 10^{-8} mm, the loop and point is flashed at 2400°K and suddenly cooled to near room temperature. The anode voltage is rapidly raised until the field emission current is 1 microampere. At first the pattern on the screen is that characteristic of clean W. Soon, however, the emission density decreases, from some planes more than from others, and the total emission current decreases. If desired, this current can be increased to one microampere by periodically increasing the applied voltage. The rate at which the emission from the W surface decreases is directly proportional to the pressure. At appropriate pressures, this rate is so slow that photographs of the screen can be taken at suitable intervals to show the progress of the deactivation due to increasing amounts of adsorbed oxygen.

Figure 3 shows a series of such photographs for a pressure of 5×10^{-8} mm. Above each picture is given the time during which oxygen has been adsorbed. The numbers below each picture give the anode voltage in kv, the total field current in μa, and the exposure time in sec. During the first 30 sec to 1 min, the decrease in emission current is rapid, but some regions deactivate more rapidly than others. Between about 1 and 12 min, the rate of deactivation is much slower, but again the change in activity for some planes is much more pronounced than for others. After 12 min, the relative activity of the different regions is almost completely reversed from that for clean tungsten. Such a series would tell us how the emission density from various planes decreased as the amount of adsorbed oxygen, θ, increased, provided that we knew the sticking probability, s, or condensation coefficient for each plane and knew how s varied with θ for each plane. Unfortunately this is not known.

In some cases we used the W loop as a "flash filament" to determine how much oxygen had been adsorbed at any time during which the filament was cold. The procedure has been previously described.[13] From these data one can determine that in Fig. 3 the surface of tungsten is covered with an average of one layer of oxygen in about one minute. During this time the rate of adsorption is constant and about one oxygen molecule is chemisorbed for every five which strike the surface. The second layer is adsorbed much more slowly. At a pressure of 5×10^{-8} mm, a maximum of two layers are adsorbed.

A second procedure, which we have found more revealing, is to cover the tungsten surface with a large amount of oxygen and to study the emission as the oxygen is desorbed by raising the temperature, for a fixed time, to successively higher values. The tungsten

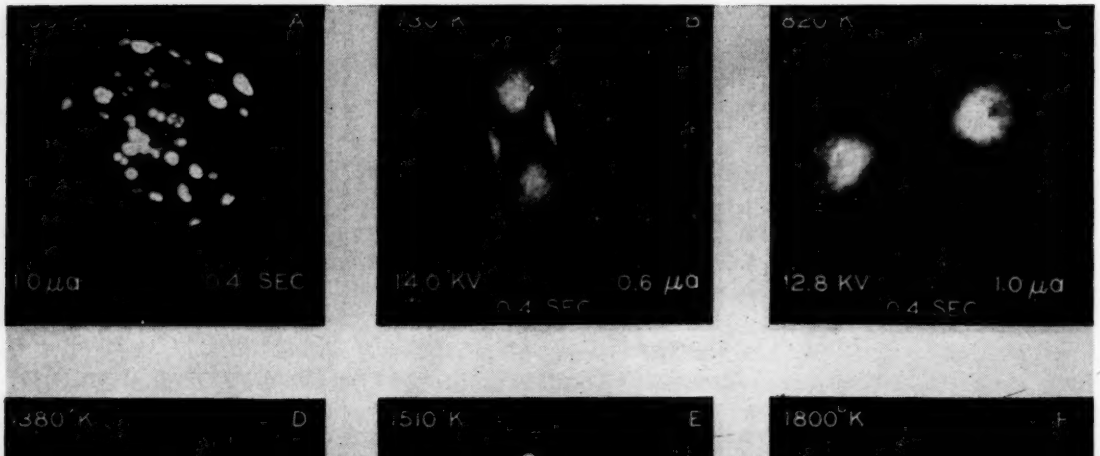

FIG. 4. Some patterns produced as oxygen was desorbed, for one minute.

is first cleaned by flashing at 2400°K in a low pressure of O_2. It is cooled to room temperature and adsorbs some oxygen. To adsorb larger amounts, the pressure is raised to about 10^{-2} mm for about a minute. The O_2 is then pumped out. The system is baked for one hour at about 600°K and is then cooled. The pressure is then about 4×10^{-9} mm.

With the point at room temperature, the anode voltage is increased until the field emission current is about one microampere. The pattern on the screen is observed to consist of a variety of about 100 bright units or groups of spots any one of which may change suddenly into another variety. (See Fig. 4A.) The behavior of these units is extremely interesting and will be described later.

When the tungsten point is heated to about 600°K, the units disappear and the field emission current decreases. This situation does not change as the point is cooled to 300°K. To increase the current and produce a pattern on the screen, it is then necessary to raise the anode voltage.

This pattern is now of an entirely different nature. (See Fig. 4, B to F.) It shows large bright and dark regions revealing the locations of the various crystallographic planes. The intensity of the emission depends upon the plane and on the amount of oxygen adsorbed on this plane. The intensity distribution does not change with time at 300°K. For a systematic study the following procedure was adopted: The point was heat treated at 600°K for 1 min; the temperature was reduced to 300°K; the anode voltage was raised until the field current was one microampere; and a picture of the screen was taken at a standard exposure time. This whole procedure was repeated in approximately 100°K steps up to 2200°K. The tungsten is then clean and the characteristic pattern for normal clean tungsten was obtained.

Figure 4 shows a few of the patterns. In each case the photograph was taken with the tungsten at 300°K. The heat treating temperature is given above the picture. The time of heat treatment was always one minute. The anode voltage, emission current, and exposure time are given below each picture. Note that as the heat treating temperature is increased, the voltage required for 1.0 μa decreases and that the distribution of emission from different regions changes drastically.

Values of work functions, φ, can be computed from the density distributions observed in the photographs, the anode voltage required for one microampere, and the Fowler-Nordheim equation.[12] To determine the constants in this equation, the known value of 4.4 volts is put in for φ for the 111 plane for normal clean tungsten.[14] In this way values of φ are determined for the 111 plane (or 111P) as a function of the heat treating temperature, T_h. The results are plotted in Fig. 5 for the curve marked 111P.

From these data we conclude that oxygen on the 111 plane of tungsten is adsorbed in two layers. The second layer is stable for $T<600$°K; it evaporates rapidly at

[14] M. H. Nichols and G. F. Smith, ONR Report N6 ONR 24433, June 1952.

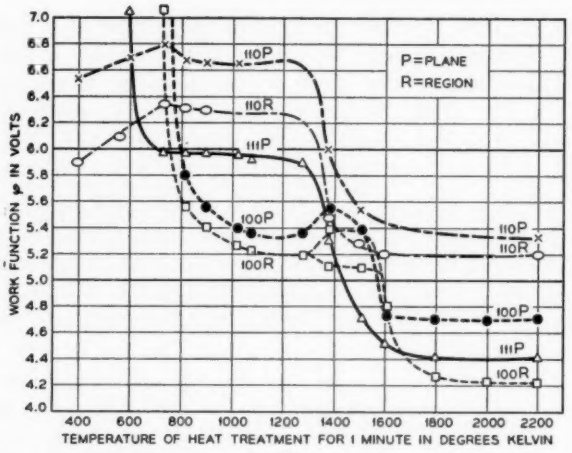

FIG. 5. Work function, φ, *versus* temperature of heat treatment, T_h, for 111P, 100P, 100R, 110P, and 110R. P stands for plane; R stands for region surrounding the plane.

600°K and more rapidly at 700°K, so that it is completely removed in one minute at 700°K. The first layer is stable for all temperatures less than 1300°K; the rate of evaporation of O_2 is appreciable but small at 1300°K and increases rapidly at higher temperatures. At 1800°K the first layer is nearly completely removed in one minute.

Figure 5 also shows the φ *vs* T_h curve for the 100P and the region surrounding the 100 plane (or 100R); they are similar to that for the 111P. However, the temperatures at which the second and the first layers begin to evaporate rapidly are 150 to 200°K higher than for the 111P. Apparently the bond strength of the O atoms to the W atoms is about 15 percent greater on the 100P and 100R than on the 111P. From the φ *vs* T_h curve for the 110P and 110R, it would appear that only a single layer is formed and that this layer begins to evaporate rapidly at about 1300°K.

Dr. R. Gomer and others prefer to deduce a "work function" from the slope of a plot of $\log i/F^2$ *vs* $1/F$. This procedure is correct only if φ is independent of F. For clean metal surfaces, the two methods yield nearly the same value of φ. For adsorbed films, the two methods yield appreciably different values of φ. For these films, the large applied fields modify the electron distributions near the adatoms, and hence φ will vary with F. Consequently, we prefer our procedure for calculating φ.

In Fig. 5 we give values of φ which range from 4.2 to 5.3 volts after heat treatment at 2200°K, and from 5.3 to 6.6 volts after heat treatment at 1000°K. One might question the reliability of such a large range of values in view of the uncertainties involved in obtaining ratios of light emission intensities from the various planes and regions. Mueller (reference 9, page 327) and others have pointed out these difficulties, especially for the regions of low emission. We have been able to measure and estimate much greater ratios of light intensities than have other workers for two reasons: (1) We use a flat screen and larger distances from point to screen. This greatly reduces light scattering in the dark regions and false light due to secondary electron and x-ray scattering. (2) We obtain φ values for the bright and dark regions in a series of steps. For a given pattern, we first take a picture at a normal exposure and deduce φ values for the relatively bright regions. We then take a picture with 3X normal exposure and deduce φ values for less bright regions, some of which overlap those deduced in the normal exposure. We repeat this process for 10X, 30X, and 100X normal exposure.

By this procedure we have been able to determine, for example, that the emission from the 110 plane is in the form of an ellipse (as it should be on the basis of Fig. 1) and that the emission from this plane is less than that from the surrounding 110 region. This was shown in reference 13, Fig. 2. That this procedure yields values of φ which are approximately correct is shown by the approximate agreement of our values for clean tungsten with those obtained from thermionic emission and those obtained by Mueller from field emission in more elaborate tubes. It is quite apparent that our method does not yield exact values of φ and that the errors become greater as φ increases. For the lower φ values deduced from any one picture, we estimate that our error may be 0.1 volt while for the higher φ values our error may be 0.4 volt. These uncertainties do not invalidate the conclusions which we deduce from Fig. 5.

These experiments together with the available information on heats of adsorption[1–5] and sticking probability[13] lead us to the following interpretation: When O_2 molecules strike a clean W surface they are physically adsorbed for a very short time during which they may either evaporate as molecules or become chemisorbed as O atoms for which the O—O bond is broken and replaced by stronger O—W bonds. The strength of the O—W bonds will depend on the plane or region; the strength of the bond will also depend on whether or not the bond is made to a W atom which has already made one bond to an O atom. Thus, when the first layer is complete, each W atom contacts one and only one O atom. Each O atom may contact 3, 4, or 5 W atoms, depending on the plane or region. In the second layer, an O atom can contact only W atoms which have already made one O bond, and consequently its heat of adsorption is now less than for the first layer. Since these bonds are probably shared electron bonds, they are of very short range so that the bond strength does not decrease much with amount adsorbed in any layer.

For the third layer, the situation is drastically changed. Now an incoming O_2 molecule cannot touch any W atom; it can contact only O adatoms. The adsorption forces are reduced to the point where the O—O bond can no longer be broken; the bond can be weakened and the distance between oxygen atoms can be increased; also electrons can be shared between

the two atoms and the underlying O layers. There results a molecular complex in which the O—O bond and the O—OW bonds are comparable in intensity. If two such complexes approach each other and are properly oriented, they may form a larger complex of four O atoms. Such complexes will protrude above the underlying surface. The field above an atom will be 2 to 4 times that of the normal field. From the Fowler-Nordheim equation, it follows that the emission density above a protruding atom should be many times that for the substrate of adatoms.* Hence, the emission density should have appreciable values only from these complexes and should be highly localized near the upper parts of an atom. The path of such localized electron bundles results in increased local magnification and resolution. As a result of this, we believe that the bright spots observed experimentally portray the location and changes in location of individual atoms in molecular complexes.

Figure 6 is a schematic diagram of equipotential lines and lines of flow for electrons for a doublet which is clearly resolved.† If, as we have postulated, the atoms share or interchange electrons with the substrate, it should be permissible to treat them as conductors and to draw equipotential lines as shown. From these it follows: (1) that the highest fields should occur near the outer surface of the atoms in about the positions indicated by the highest concentrations of flow lines, and (2) that the flow lines strike the screen such that the electrons appear to come from a region in the neighborhood of the atom whose diameter is several times the atom diameter. The enhanced resolving power, the enhanced magnification, and the extra high field strength should depend upon how far the atoms are separated from each other and how far they protrude above the substrate of chemisorbed oxygen. At 300 to 500°K, this substrate is likely to be sufficiently agitated so that occasionally a hole or vacancy is momentarily produced. A molecular complex near this hole can sink into it and become adsorbed in the substrate. The extra high field disappears and with it the bright doublet. If the hole is only large enough to permit the "molecules" to sink part way into it, there may result a closer approach of the two atoms, a smaller resolution or unresolved doublet, or a single spot; it might also result in less protrusion, less field, and hence a dimmer doublet. Conversely there should occasionally occur an unusually high concentration of atoms in the substrate which pushes two atoms from the substrate into the third layer. This would result in the sudden appearance of a doublet. Higher temperatures should make such changes occur more frequently.

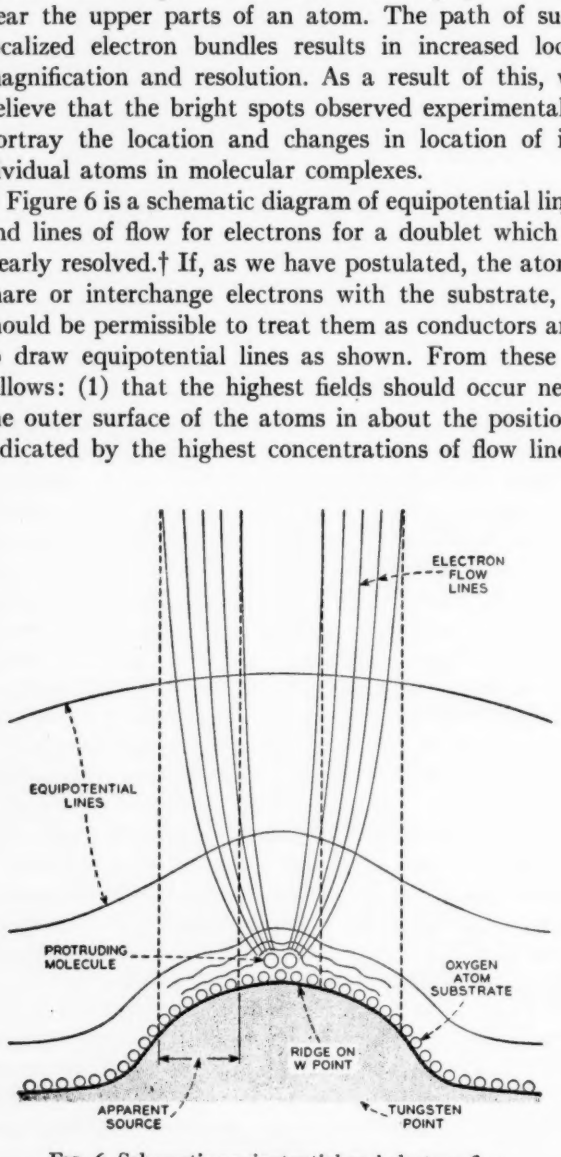

FIG. 6. Schematic equipotential and electron flow lines near a molecular complex.

All of these expectations and many others are confirmed by experiment. During the course of observations extending over hours, we have seen a great variety of groups of bright spots or units. A few varieties are: A single round spot, a doublet with a clear dark axis, a quadruplet with four bright spots at the corners of a square or at the corners of a rhomb, a bright ring with a dark center, a unit of six bright spots. The size of these units increases with the point to screen distance and increases as the radius of curvature of the point decreases. For one condition, the size of the units varied from 2 to 4 mm on the screen. A unit may suddenly disappear or change its size and intensity. A new unit may suddenly appear. The rate at which units change to other forms increases with field strength and with temperature between 300° to 500°K. Whenever a unit changes all the spots in the unit change together.

Figure 7 shows sketches of the transformations which we have observed for a doublet and for a quadruplet; the last line shows some of the units which have been observed on rare occasions while watching the screens in about 10 tubes for many hours.

Experiment shows that the rate of transformation of units increases with an increase in applied voltage. This probably means that the increased field strength exerts greater forces on chemisorbed atoms tending to weaken the O—W bond. This should increase the surface agitation and the probability of the formation of "holes" or condensed regions in the chemisorbed layer.

That the electron paths shown in Fig. 6 are essentially correct is corroborated by the following observations:

* In reference 16, Muller computes a factor of about 80 for a single W atom.

† Mueller (reference 16) proposed a similar diagram to account for the bright units which he observed when he introduced large organic molecules into his system (reference 9).

Out of perhaps 100 bright units, two may be seen to overlap on the screen. The lower right sketch in Fig. 7 shows a case in which a singlet and doublet overlap. In time, one of these units will suddenly disappear. When this happens the other unit remains unchanged in size, intensity, and orientation. This proves that even though the screen images of two units overlap, the source of the electron beams must be far enough apart so that the disappearance of one has no effect on the other.

The interpretation that the observed quadruplet unit is due to an O_4 molecular complex is supported by the first and last sketch in the second row of Fig. 6. On a few occasions we have observed a square quadruplet suddenly change into an extended quadruplet like that in the last sketch. However, it would persist in this form for only a fraction of a second and would then return to a square unit. During about three to five seconds the unit was observed to oscillate back and forth between these two forms about ten or twenty times. It then disappeared completely or became steady as another form of unit.

One might ask, "Why should not the first few molecules or atoms which are adsorbed on clean tungsten produce singlets or doublets." Our answer is that in this case the adsorption forces are so great that the shared electron spends almost its entire time between the oxygen nucleus and the tungsten atoms. The probability of finding the electron beyond the oxygen nucleus is so small that even the extra high field in this region produces negligibly small field currents. The observed field currents come most likely from the W atoms which are not covered by O.

Quantitative calculations on the magnification and resolving power for a molecule on top of a substrate as discussed above have been made by D. Rose‡ of the Bell Telephone Laboratories. He finds that the observed sizes and resolutions of the bright spots are too large if the tungsten point is smooth and has a radius of curvature of about 1×10^{-5} cm. However, if on such a point there are protrusions or ridges having a radius of curvature of about 2×10^{-7} cm, then any molecules on such protrusions or ridges could be magnified and resolved to give bright spots like those observed. Such sharp ridges or protrusions conceivably can be produced by the interaction of chemical etching, resulting from adsorbed atoms and temperature agitation, or by the interaction of temperature agitation and high fields.[11]

CONDITIONS NECESSARY TO OBSERVE ADATOMS AND ADMOLS

We might summarize by restating our views on the conditions necessary to obtain bright spots or units from adatoms or admols: (1) The adatoms or admols must share electrons with the substrate so that the unit acts like a metal and so that emitted electrons

‡ We thank our colleague for this advance information.

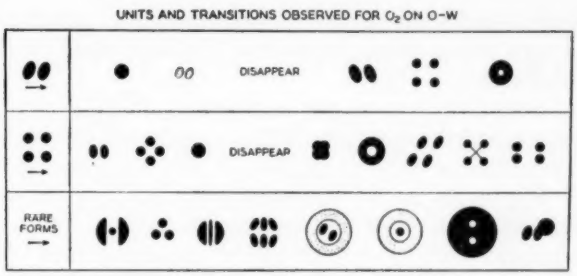

FIG. 7. Abrupt transformations observed for a doublet (top row); for a quadruplet (middle row); and rarer forms of units (bottom row). The last sketch in the bottom row shows the overlapping on the screen of a doublet and a singlet. The last sketch in the middle row shows an O_4 complex splitting into two O_2 complexes.

can be replenished very quickly from the substrate; (2) the unit must protrude above the surrounding surface in order that the field above the unit be abnormally high and that the emission come predominantly from the unit; (3) the bond strength of the atoms in the unit with the substrate must not be too great; (4) the bond strength between atoms in the unit must not be too great; (5) the atom-atom bond must be weakened and must be comparable with the atom-substrate bond; (6) the number of units per cm^2 of surface must be small enough so that the images from neighboring units overlap only occasionally—this means that the protruding layer should be only a few percent covered; (7) the substrate must be reasonably compact or complete; (8) the radius of curvature of the tungsten near the protruding unit should be about 30×10^{-8} cm or smaller; (9) the protruding molecule should be in a region in which the field diverges rapidly, i.e., the molecule should be subjected to forces which are parallel to the surface.

None of these conditions state that the units must consist of oxygen only. In preliminary experiments with nitrogen we have found bright units similar to those described above. We expect that other molecules will show intensely bright spot emission. We also expect that metal atoms which are not adsorbed too strongly will yield bright spots. Cu atoms on W have been reported to do this.[15] However, we would not expect strongly electropositive metal atoms to yield bright spots. Here the valence electron has been transferred to the underlying metal and is not available to be pulled out by the extra high field above the adatom. In such cases, the field emission electrons come from many underlying W atoms and are not concentrated in one bright spot on the screen. Mueller[16] has reported bright spots or units resulting from the adsorption of organic vapors.

If, in the pretreatment of the point, the oxygen pressure never exceeds 10^{-5} mm, no intensely bright doublets, quadruplets, etc., are observed; even the

[15] F. Ashworth, *Advances in Electronics* (Academic Press, Inc., New York, 1951), Vol. 3, pp. 1–41.
[16] E. W. Mueller, Z. Naturforsch. **5A**, 473 (1950).

single spots are faint. We interpret this to mean that at such low pressures no oxygen is chemisorbed on the third layer.

Several readers of the manuscript for this article have raised the question, "What part do tungsten oxide crystallites or WO_3 films play in the desorption series of Fig. 4 or in the production of the bright units depicted in Fig. 7?" To answer these questions it is necessary to know the conditions under which WO_3 films form on W and the conditions under which WO_3 evaporates. According to Langmuir,[4] iridescent films of WO_3 form on W at 700 to 800°K at pressures of about one mm or higher. Such films can be removed in a vacuum at 1200°K. In O_2, at pressures from 2×10^{-4} to 5×10^{-2} mm and at a temperature of 1200°K or higher, WO_3 evaporates as fast as it is formed and no layers of WO_3 accumulate on the surface. Most of the O_2 which strikes the W surface comes off as O_2 gas. Since in our experiments leading to Figs. 4 and 5 we did not expose our W to conditions which are conducive to WO_3 film formation, we believe that WO_3 films or crystallites played no important role.

This conclusion is supported by the following observations: In the experiments described in connection with Fig. 5, we sometimes flashed the filament at about 1300°K; the pressure suddenly rose by an amount corresponding to about one layer of O_2. When the filament was then flashed to about 2000°K, the pressure again rose by a similar amount. This convinced us that the oxygen which was adsorbed came off as O_2 and not as WO_3. Oxygen has a low sticking probability on glass and can reach the ion gauge; WO_3 has a high sticking probability and cannot reach the ion gauge.

In order to determine what kind of field emission patterns are obtained from multilayers of WO_3 on W, we deliberately treated the W under conditions which should form such layers, namely $p\sim10^{-2}$, $T\sim1100$°K, and for several minutes. The patterns which we observed at low pressures and at temperatures from 300 to 500°K consisted of one or more rather large, irregular shaped patches of bright emission. At high currents or at the higher temperatures, these patches were in a continuous state of agitation. These patches might well be due to WO_3 crystallites. They are entirely different in appearance and behavior from any of the patterns shown in Figs. 3 and 4 or those sketched in Fig. 7.

During the bake-out process, it is conceivable that conditions might favor WO_3 crystallite formation. If such crystallites were formed, we would expect them to reveal themselves like the patches described above. However, in the experiments on which Figs. 5 and 7 are based, they did not so reveal themselves.

Dr. Gomer, in private discussions, has interpreted the patterns like those shown in D and E of Fig. 4 as due to WO_3 crystallites.§ In contrast to this, we interpret the bright line emissions and the bright localized regions as due to enhanced fields caused by ridges or protrusions of W covered with chemisorbed oxygen. We believe that the presence of chemisorbed oxygen weakens the W−W bonds and thus permits the tungsten surface to distort itself in such a way as to enlarge certain planes to a much greater extent than is the case for clean W. The 211 plane especially is greatly enlarged when W is heated at 1300 to 1400°K in the presence of one layer of chemisorbed oxygen (see Fig. 5). Where two such enlarged planes meet, they form a sharp ridge. Where three such planes meet, i.e., the 111 region, they produce a protruding peak. Above 1500°K most of the oxygen is desorbed, and the ridges and peaks disappear. This interpretation is discussed more fully in the paper on Adsorption and Catalysis which will appear in Vol. VII of *Advances in Catalysis*. In it, the theory that strongly chemisorbed atoms enlarge some planes of an adsorbent metal will be shown to hold for other systems.

If, in the pretreatment of the point, the oxygen pressure is raised to 10^{-2} mm but the tube is not rebaked, the number of bright units, their size, and their persistance are diminished. This raises the question, "What goes on during the rebake?" We have no conclusive answer, but suggest the following possibilities: At the baking temperature of 600°K, water vapor reacts with the tungsten to produce ridges or hills which have a very small radius of curvature. This results in a second stage of magnification and extra resolving power. A second effect of the baking may be that the second layer forms a more perfect film with fewer oxygen vacancies and hence the molecular complexes in the third layer have fewer possibilities of dropping back into the first two layers. Another possibility is that a small amount of hydrocarbon vapor deposits on the tungsten point during the baking or while the liquid air is removed from the trap. This might result in the adsorption of a very few carbon atoms with the oxygen in the first two layers. These carbon atoms might act as centers at which molecular complexes in the third layer are held more tightly. It is known that carbon is strongly adsorbed on tungsten[9] and one might expect that adsorbed carbon forms molecular complexes with adsorbed oxygen. Perhaps this is the reason for the great variety of units shown in Fig. 7. If this suggestion should be confirmed by further experiments, it would illustrate once again the great versatility of this microscope in the study of adsorption, catalysis, and the arrangement of atoms in adsorbed molecules.

§ This interpretation is to be published in Vol. VII of *Advances in Catalysis*.

Theory of Dielectric Relaxation for a Single-Axis Rotator in a Crystalline Field. II

JOHN D. HOFFMAN
National Bureau of Standards, Washington, D. C.
(Received November 18, 1954)

Previous work on the relaxation times associated with a polar single-axis rotator where the dipole may occupy three or four orientational sites by turning in a lattice point has been extended to include the more general case where the energies of the sites (as well as the intervening barriers) are all different. The results for these more general models tend to confirm the view that the presence of barriers of different magnitudes between the equilibrium orientations of a dipole can be the source of a set of discrete dielectric relaxation times.

The dielectric properties of some specialized three- and four-position models are then considered in detail. A very narrow or an extremely wide set of relaxation times can be obtained depending on the nature of the barrier system, and accordingly, a wide range of dielectric behavior can be accommodated. Despite the wide range of behavior, certain qualitative features (noted in Sec. VII in italics) appear to persist in many of the models. These features may be useful in applying the theory in a general way.

The equations given will facilitate the calculation of the properties of three- and four-position models not already considered.

I. INTRODUCTION

In a recent paper[1] it was shown that a set of discrete dielectric relaxation times can arise in a lattice consisting of polar single-axis rotators provided that each dipole might occupy three or more orientational sites. Each model was simplified to the extent that only two different activation barriers, and hence only two transition probabilities, were required to specify the relaxation times. It seems desirable to extend the treatment to include local free energy barriers of a more general nature. For this work we have chosen the three- and four-position models where the energies of the sites, as well as the intervening barriers, are all different.

A survey of the dielectric properties exhibited by the general three- and four-position models is most readily obtained by reducing each of them to a set of more special models. Apart from leading to useful quantitative results for the special cases, the survey is of utility in illuminating (*a*) the range of dielectric properties which are possible and (*b*) the existence of any characteristics which the models may have in common. Certain polar long-chain molecules behave like single-axis rotators, so the special models may be of assistance in interpreting their dielectric properties.

II. METHODS AND ASSUMPTIONS

As a dipole situated on a lattice point turns about a single axis, we suppose that it traverses local free-energy barriers which result from the crystalline field. The minima between these barriers correspond to the orientational sites. In our simplified problem, we assume that the barrier structure is the same for all the dipoles in the lattice, i.e., local fluctuations of structure are ignored. It is further assumed that there is no correlation in the motion of the dipoles. The methods used to obtain the relaxation times, polarizabilities, and characteristics of the relaxation spectrum are outlined below.

[1] J. D. Hoffman and H. G. Pfeiffer, J. Chem. Phys. **22**, 132 (1954).

The molecular relaxation times are calculated from the differential equations describing the net rate, dN_i/dt, at which dipoles enter and leave each orientational site. The dN_i/dt are expressed in terms of the elementary process transition probabilities k_{12}, k_{21}, $k_{23}\cdots$, and the population of each site, N_i. Each of the k represents the probability that a dipole will leave a certain site in a specified direction and turn over an activation barrier to another position; e.g., k_{12} is the probability that a dipole will turn from site 1 to site 2. In writing the dN_i/dt we assume that the only important *elementary* process is the turning of a dipole to an adjacent site (*single-jump hypothesis S-J*).[1]

An example will indicate how each of the required equations is obtained. We consider a model with Ω sites, numbered 1 to Ω, and fix our attention on site 2. We then have

$$dN_2/dt=k_{12}N_1-(k_{21}+k_{23})N_2+k_{32}N_3. \tag{1}$$

To avoid cumbersome notation, a single subscript will be used henceforth to denote each of the k: $k_{12}=k_1$, $k_{21}=k_2$, $k_{23}=k_3$, $k_{32}=k_4$, $\cdots$.

For a model with Ω sites, the solutions of the differential equations of the type illustrated in Eq. (1) are of the form[1]

$$N_i=\sum_{\beta=1}^{\Omega} C_{i\beta}\Psi_\beta; \quad i=1,2,\cdots\Omega, \tag{2}$$

where i refers to a particular site, β is the mode of decay, and Ψ_β is a decay function of the form

$$\Psi_\beta=\exp[-f_\beta(k_1,k_2\cdots)t]. \tag{3}$$

The decay functions describe the rate at which equilibrium is approached by each mode after the abrupt removal of a disturbance at $t=0$. The molecular relaxation times are given by

$$\tau_\beta=-1/f_\beta(k_1,k_2\cdots). \tag{4}$$

The $f_\beta(k_1,k_2,\cdots)$ are obtained by forming the characteristic determinant of the differential equations and solving for eigenvalues of the operator d/dt.[1] One of the $f_\beta(k_1,k_2,\cdots)$ is always zero; this mode is designated by $\beta=1$, and the corresponding C_{i1} are the equilibrium values of the N_i. The sum of the C_{i1} is N, the total number of dipoles in the system, while the sum of the $C_{i\beta}$ for any mode where $\beta\geqq 2$ is zero.

One can elucidate the nature of the over-all process by which a given mode of decay promotes the attainment of equilibrium after the abrupt removal of a perturbation (such as a static electric field) by an examination of the sign and magnitude of the $C_{i\beta}$ belonging to that mode. For instance, if $C_{22}=-C_{42}$, and all other C_{i2} are zero, it follows that the decay of the polarization for mode 2 involves a net turning of dipoles from site 2 to 4 (or 4 to 2). As seen from the example just cited, the over-all process associated with a mode of decay may involve the turning of dipoles through a number of positions. This is the result of a succession of elementary processes, and does not violate the *S-J* hypothesis.

Assuming that the molecular and macroscopic relaxation times are equal, the polarization decays with time according to $P(t)=\sum_\beta P_\beta\Psi_\beta=\sum_\beta P_\beta \exp(-t/\tau_\beta)$ after the removal of a static field. It is thus necessary to evaluate the P_β, or the corresponding orientational polarizability α_β, in order to characterize the dielectric relaxation process. Three steps are involved in calculating these quantities for a given mode of decay: (1) the new equilibrium number of dipoles in each site, $C_{i1}{}^F$, in the presence of a local field $\mathbf{F}$ is calculated using the Boltzmann distribution law (2) the $C_{i\beta}$ for $\beta\geqq 2$ are then evaluated by applying the boundary conditions $N_i=C_{i1}{}^F$ at $t=0$, and $N_i=C_{i1}$ at $t=\infty$, and (3) P_β is calculated from the evaluated $C_{i\beta}$ by suitable resolving and averaging procedures; α_β is given by P_β/NF. In carrying out the averaging procedure, it is assumed that the sample is polycrystalline. Details of the above procedure have been published in connection with calculations for models where the dipoles may occupy orientational sites arranged in three dimensions.[2]

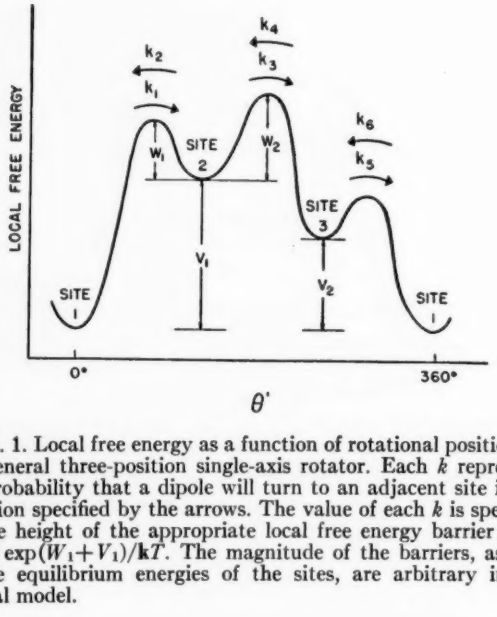

FIG. 1. Local free energy as a function of rotational position for the general three-position single-axis rotator. Each k represents the probability that a dipole will turn to an adjacent site in the direction specified by the arrows. The value of each k is specified by the height of the appropriate local free energy barrier; e.g., $k_1=B\exp(W_1+V_1)/\mathbf{k}T$. The magnitude of the barriers, as well as the equilibrium energies of the sites, are arbitrary in the general model.

It remains to be mentioned how the relaxation times and polarizabilities are utilized with sinusoidal fields. For the purposes of an approximate analysis the relation[1]

$$\epsilon''(\omega)\cong K\sum_\beta \alpha_\beta\omega\tau_\beta/(1+\omega^2\tau_\beta^2) \qquad (5)$$

is used to predict the characteristics of the dielectric relaxation spectrum. $\epsilon''(\omega)$ is the dielectric loss factor as a function of angular frequency ω, and K is a constant. In writing Eq. (5) we have assumed: (*a*) linear superposition (*b*) that the molecular and macroscopic relaxation times are nearly identical and (*c*) that the increment of dielectric constant connected with each mode is proportional to the corresponding orientational polarizability, i.e., $\Delta\epsilon_\beta\cong K\alpha_\beta$. These approximations are at least partially justified by the work of Powles[3] with a modified version of the Onsager internal field. It should be noted that Eq. (5) reduces to the form of the Debye[4] equation for $\epsilon''(\omega)$ in the case where only a single relaxation time appears.

III. GENERAL THREE-POSITION MODEL

The details of the general three-position model are shown in Fig. 1. Each of the six k represents the probability that a dipole will surmount the designated barrier and turn to an adjacent site.

Although it is not necessary to know the relationships between the k and the corresponding local free energy barriers in formulating the rate equations, it is convenient to indicate the relationships here to show how the k will behave with temperature. The assumed connection between the elementary process transition probability and the local free energy of activation barrier is analogous to that proposed by Kauzmann[5] for the over-all relaxation process. Thus we write expressions of the form

$$\begin{aligned} k_1&=B\exp[-(W_1+V_1)/\mathbf{k}T],\\ k_2&=B\exp[-W_1/\mathbf{k}T],\\ k_3&=B\exp[-W_2/\mathbf{k}T],\\ &\cdot\\ &\cdot\\ &\cdot \end{aligned} \qquad (6)$$

where B is a frequency factor, T the absolute temperature, and $\mathbf{k}$ Boltzmann's constant. The W and V are shown in Fig. 1. It should be noted that the k will

[2] J. D. Hoffman and B. M. Axilrod, J. Research Natl. Bur. Standards **54**, 357 (1955).

[3] J. G. Powles, J. Chem. Phys. **21**, 633 (1953); see also J. J. O'Dwyer and R. A. Sack, Australian J. Sci. Research **5**, 647 (1952).

[4] P. Debye, *Polar Molecules* (Dover Publications, New York, 1945), p. 90.

[5] W. Kauzmann, Revs. Modern Phys. **14**, 12 (1942).

tend to converge as the temperature increases. This holds even if W and V are constant. An even more rapid convergence of the k will obtain if the barriers tend to become smaller and more nearly equivalent with rising temperature owing to a cooperative effect.

It is convenient to mention here that the k are restricted by the relation

$$k_1k_3k_5=k_2k_4k_6. \tag{7}$$

This may be seen from the expressions $C_{21}/C_{11}=k_1/k_2$, $C_{31}/C_{21}=k_3/k_4$, and $C_{11}/C_{31}=k_5/k_6$, where C_{11}, C_{21}, and C_{31} are the equilibrium number of dipoles in sites 1, 2, and 3, respectively. We also note that $C_{21}=C_{11}\exp[-V_1/\mathbf{k}T]$ and $C_{31}=C_{11}\exp[-V_2/\mathbf{k}T]$.

Returning to the main problem, we let N_1, N_2, and N_3 be the number of dipoles in sites 1, 2, and 3 at any time t. Then, according to the S-J hypothesis, the rate at which dipoles enter and leave each site is

$$\begin{aligned} dN_1/dt&=-(k_1+k_6)N_1+k_2N_2+k_5N_3\\ dN_2/dt&=k_1N_1-(k_2+k_3)N_2+k_4N_3\\ dN_3/dt&=k_6N_1+k_3N_2-(k_4+k_5)N_3. \end{aligned} \tag{8}$$

The characteristic determinant of these equations is

$$\begin{vmatrix} (\mathbf{D}+k_1+k_6) & -k_2 & -k_5 \\ -k_1 & (\mathbf{D}+k_2+k_3) & -k_4 \\ -k_6 & -k_3 & (\mathbf{D}+k_4+k_5) \end{vmatrix}=0 \tag{9}$$

where $\mathbf{D}=d/dt$. The eigenvalues of the operator $\mathbf{D}$ are $\mathbf{D}=0$, $-(J+Q)/2$, and $-(J-Q)/2$. Thus the solutions are of the form

$$\begin{aligned} N_i&=C_{i1}+C_{i2}\Psi_2+C_{i3}\Psi_3;\\ \Psi_2&=\exp[-(J+Q)t/2],\\ \Psi_3&=\exp[-(J-Q)t/2], \end{aligned} \tag{10}$$

where $J=k_1+k_2+k_3+k_4+k_5+k_6$,

$$Q=[J^2-4(ab+ac+bc-k_1k_2-k_3k_4-k_5k_6)]^{\frac{1}{2}},$$

and $a=k_1+k_6$, $b=k_2+k_3$, $c=k_4+k_5$. The relaxation times are given by

$$\begin{aligned} \tau_2&=2/(J+Q),\\ \tau_3&=2/(J-Q). \end{aligned} \tag{11}$$

These results yield some information regarding the general model where the k are arbitrary. For instance, it can be shown that τ_2 always differs from τ_3 when the k are all different. Thus the general model leads to a set of discrete relaxation times. Furthermore, it can be demonstrated from the properties of Eq. (9) and the condition expressed in Eq. (7) that the eigenvalues, and hence the relaxation times, are always real.[6] If the k are identical, Q is zero, and $\tau_2=\tau_3=1/3k$. Information regarding the range of properties which are possible can best be obtained by considering specialized three-position models.

[6] The theorems required for the proof that the relaxation times are always real and positive have been developed by K. Goldberg (to be published in J. Research Natl. Bur. Standards).

In the ensuing discussion of the specialized models it is convenient to know the relationships between the $C_{i\beta}$ in Eq. (10) for $\beta=2$ and $\beta=3$. These are

$$\begin{aligned} C_{12}&=C_{22}\frac{[-Q-a+b-c]k_5+2k_2k_4}{[-Q+a-b-c]k_4+2k_1k_5},\\ C_{22}&=C_{32}\frac{[-Q-a-b+c]k_1+2k_4k_6}{[-Q-a+b-c]k_6+2k_1k_3}, \end{aligned} \tag{12a}$$

for $\beta=2$ and

$$\begin{aligned} C_{13}&=C_{23}\frac{[Q-a+b-c]k_5+2k_2k_4}{[Q+a-b-c]k_4+2k_1k_5},\\ C_{23}&=C_{33}\frac{[Q-a-b+c]k_1+2k_4k_6}{[Q-a+b-c]k_6+2k_1k_3} \end{aligned} \tag{12b}$$

for $\beta=3$.

IV. SPECIALIZED THREE-POSITION MODELS

The three-position model is simplified in two respects. First, a certain degree of symmetry is introduced into the barrier system which establishes a relationship between some of the k. Second, it is assumed for the purposes of simplifying the polarizability calculations that the sites are 120° apart. The selection of other angles between the sites would affect the α_β, but the form of the expressions for the τ_β would remain unchanged.

The orientational polarizabilities are expressed in units of $\mu^2/3\mathbf{k}T$ where μ is the component of the permanent dipole moment which subtends a right angle to the axis of rotation. If μ_0 is the value of the dipole moment, and ξ is the angle this moment subtends to the axis of rotation, $\mu=\mu_0\sin\xi$.

1. Three-Position Model with Two Equivalent Sites

The range of situations covered by this model is shown in Fig. 2. Site 2 is unique, and sites 1 and 3 are always equivalent so that $C_{11}=C_{31}$. Only modification (a) will be discussed here since a model of type (b) has been studied previously.[1]

In modification (a) sites 1 and 3 are more stable than site 2. Thus we have

$$k_2=k_3,\quad k_1=k_4=k_5=k_6;\quad k_2>k_1. \tag{13}$$

When the above is inserted in Eq. (11) the relaxation times are found to be

$$\begin{aligned} \tau_2&=1/(k_1+2k_2)\\ \tau_3&=1/3k_1. \end{aligned} \tag{14}$$

In contrast to the narrow set of relaxation times encountered in case (b),[7] it is seen that $\tau_3/\tau_2\rightarrow\infty$ when $k_2\gg k_1$.

[7] For case (b) the maximum value of the ratio of the τ_β was three.

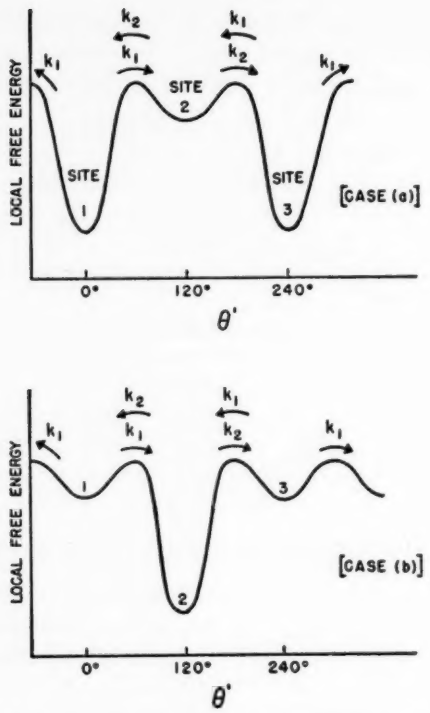

FIG. 2. Three-position model with two equivalent sites.

Upon introducing Eqs. (13) into Eqs. (12) we find that $C_{12}=C_{32}$, $2C_{12}=-C_{22}$ for mode 2, and $C_{13}=-C_{33}$, $C_{23}=0$ for mode 3. Hence the solutions may be written

$$\begin{aligned} N_1&=C_{11}-C_{12}\Psi_2+C_{13}\Psi_3 \\ N_2&=C_{21}+2C_{12}\Psi_2+0 \\ N_3&=C_{11}-C_{12}\Psi_2-C_{13}\Psi_3 \end{aligned} \tag{15}$$

where $\Psi_2=\exp[-(k_1+2k_2)t]$ and $\Psi_3=\exp[-3k_1t]$. Mode 2 promotes the attainment of equilibrium by a net turning of dipoles from site 2 to both 1 and 3 (or *vice versa*). Similarly mode 3 involves a net turning from site 1 to 3, or 3 to 1.

The polarizabilities of modes 2 and 3 are found to be

$$\begin{aligned} \alpha_2&=[9C_{11}C_{21}/2N^2](\mu^2/3\mathbf{k}T) \\ &=[9C_{11}^2/2N^2](k_1/k_2)(\mu^2/3\mathbf{k}T), \\ \alpha_3&=[3C_{11}/2N](\mu^2/3\mathbf{k}T), \end{aligned} \tag{16}$$

where C_{11} and C_{21} are the equilibrium number of dipoles in sites 1 and 2, respectively.

The characteristics of the relaxation spectrum can be obtained by inserting the relaxation times and polarizabilities given in Eqs. (14) and (16) into Eq. (5). It is convenient to discuss the properties of the model in terms of the changes which occur as the k converge.

When sites 1 and 3 are extremely deep (or the temperature very low) so that $k_2\gg k_1$, and $C_{11}/N\cong 1/2$, we have

$$\alpha_2\cong 0; \quad \alpha_3\cong(3/4)(\mu^2/3\mathbf{k}T); \quad \tau_3/\tau_2\to\infty. \tag{17a}$$

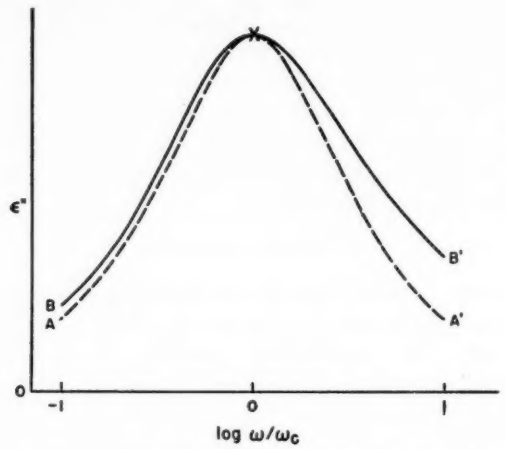

FIG. 3. Shape of the dielectric loss region (schematic). Curve $A-A'$ is the symmetrical loss maximum calculated for a single relaxation time using the Debye equations. Curve $B-B'$ is the broadened and asymmetrical loss curve calculated using two relaxation times where the larger polarizability is associated with the longer relaxation time. ω_c is the frequency where ϵ'' is a maximum for each curve.

Only τ_3 is active, and the corresponding loss peak conforms with the Debye equations (Fig. 3, curve $A-A'$). As the k converge, as for $k_2>k_1$, it is seen that

$$\begin{aligned} &\alpha_3/\alpha_2>1; \quad (3/4)(\mu^2/3\mathbf{k}T)<\alpha_2+\alpha_3<\mu^2/3\mathbf{k}T; \\ &\tau_3/\tau_2>1. \end{aligned} \tag{17b}$$

Both relaxation times are now active, and the polarizabilities differ, so that the loss peak is slightly asymmetrical and somewhat broader than that predicted by the Debye equations (Fig. 3, curve $B-B'$). Owing to the fact that the larger polarizability is associated with the longer relaxation time, the loss region is steeper on the low-frequency side. Finally, as the sites become equivalent so that $k_1=k_2$, we find

$$\alpha_3/\alpha_2=1; \quad \alpha_2+\alpha_3=\mu^2/3\mathbf{k}T; \quad \tau_3/\tau_2=1. \tag{17c}$$

It follows that the loss peak again becomes symmetrical, and may be accounted for by the Debye equations.

Despite the fact that the relaxation times can differ greatly, two separate[8] regions of loss do not appear since α_2 is very small when the relaxation times are widely separated.

2. "Cascade" Model

The details of the model are shown in Fig. 4. It is assumed that barriers for jumps from sites 1 to 2, 2 to 3, and 3 to 1 are equal, as are those for jumps from 3 to 2 and 2 to 1. The largest barrier, that for reorientations

[8] When the ratio of two relaxation times with equal polarizabilities is greater than about seven, a minimum can be discerned between the loss peaks. Our criterion for the appearance of two "separate" regions of loss is the existence of such a minimum. If the polarizabilities associated with the relaxation times differ greatly, the ratio of the relaxation times must be much greater than seven before two separate loss peaks are found. The above is easily verified by graphical means.

from sites 1 to 3, is unique. Hence we have

$$k_1=k_3=k_5, \quad k_2=k_4. \tag{18}$$

It is clear from the diagram that $k_2>k_1>k_6$. It is readily verified that

$$\begin{aligned}\tau_2&=2/(3k_1+2k_2+k_6+Q),\\ \tau_3&=2/(3k_1+2k_2+k_6-Q),\end{aligned} \tag{19}$$

where $Q=(k_6^2-3k_1^2+4k_1k_2-4k_2k_6+2k_1k_6)^{\frac{1}{2}}$. From Eqs. (7) and (18) it is seen that the k must conform with the relation $k_1^3=k_2^2k_6$.

The behavior of this model for the various allowable values of the k is most easily determined if we define a parameter $g=k_1/k_2$, so that $k_1=k_2g$, and $k_6=k_2g^3$. It follows that

$$\frac{\tau_3}{\tau_2}=\frac{2+3g+g^3+(g^6+2g^4-4g^3-3g^2+4g)^{\frac{1}{2}}}{2+3g+g^3-(g^6+2g^4-4g^3-3g^2+4g)^{\frac{1}{2}}}. \tag{20}$$

The results of substituting some values of g in Eq. (20) are shown in Table I. The relationships between the $C_{i\beta}$, and hence the expressions for the α_β, are excessively complicated. Therefore, only numerical values of the ratio of the polarizabilities, α_3/α_2, are given in Table I.

The total polarizability is

$$\alpha_{\text{total}}=[3g/(1+g+g^2)](\mu^2/3kT). \tag{21}$$

The table shows that as the k converge, the relaxation times *diverge* in the range $g<0.1$. However, the relaxation times follow the more usual pattern above $g\cong 0.1$ and tend toward a common value. The Debye equations hold for the cases $g=0$ and $g=1$, but the loss peaks are somewhat broadened and asymmetrical for intermediate values. When asymmetrical, the loss peaks are steeper on the low-frequency side.

V. GENERAL FOUR-POSITION MODEL

The four-position model with eight transition probabilities is shown in Fig. 5. According to the postulates in Sec. II, the rate equations may be written

$$\begin{aligned}dN_1/dt&=-(k_1+k_8)N_1+k_2N_2+k_7N_4,\\ dN_2/dt&=k_1N_1-(k_2+k_3)N_2+k_4N_3,\\ dN_3/dt&=k_3N_2-(k_4+k_5)N_3+k_6N_4,\\ dN_4/dt&=k_8N_1+k_5N_3-(k_6+k_7)N_4.\end{aligned} \tag{22}$$

The characteristic determinant of these equations is

$$\begin{vmatrix}(\mathbf{D}+k_1+k_8) & -k_2 & 0 & -k_7\\ -k_1 & (\mathbf{D}+k_2+k_3) & -k_4 & 0\\ 0 & -k_3 & (\mathbf{D}+k_4+k_5) & -k_6\\ -k_8 & 0 & -k_5 & (\mathbf{D}+k_6+k_7)\end{vmatrix}=0. \tag{23}$$

The eigenvalues of the operator $\mathbf{D}=d/dt$ are solutions of the cubic equation

$$\mathbf{D}^3+p\mathbf{D}^2+q\mathbf{D}+r=0; \tag{24}$$

$$\begin{aligned}p&=k_1+k_2+k_3+k_4+k_5+k_6+k_7+k_8,\\ q&=k_1(k_3+k_4+k_5+k_6+k_7)+k_2(k_4+k_5+k_6+k_7+k_8)\\ &\quad+k_3(k_5+k_6+k_7+k_8)+k_4(k_6+k_7+k_8)\\ &\quad+k_5(k_7+k_8)+k_6k_8,\\ r&=k_1k_3(k_5+k_6+k_7)+k_1k_4(k_6+k_7)+k_2k_4(k_6+k_7+k_8)+\\ &\quad k_2k_5(k_7+k_8)+k_3k_5(k_7+k_8)+k_6k_8(k_2+k_3+k_4)\\ &\quad+k_1k_5k_7.\end{aligned}$$

One root, $\mathbf{D}=0$, which corresponds to the equilibrium values of the N_i, has already been extracted from Eq. (24). The three relaxation times are the negative reciprocals of the $\mathbf{D}$.

TABLE I. Relaxation times and polarizabilities for the three-position "cascade" model.

g	τ_3/τ_2	α_3/α_2	α_{total} $(\mu^2/3kT=1)$
1	1	1	1
0.5	1.70	1.29	0.857
0.1	1.71	1.30	0.270
0.01	1.22	1.13	0.030
0.001	1.07	1.03	0.003

Solution of Eq. (24) is not practical when the k are arbitrary. Despite this, it is still possible to obtain some information from the general model without introducing simplifications. From considerations based on the properties of the characteristic determinant, and the fact that

$$k_1k_3k_5k_7=k_2k_4k_6k_8, \tag{25}$$

it is possible to show that the relaxation times are always real and positive.[6] At present we lack a rigorous proof that the relaxation times are all different when

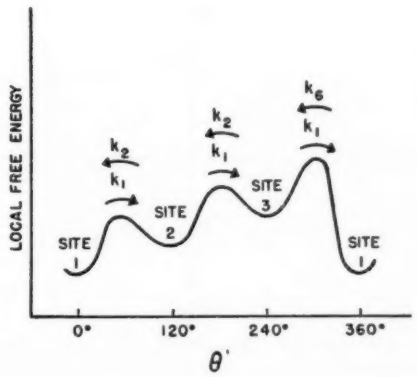

FIG. 4. Three-position cascade model.

the k are arbitrary, but a survey using numerical examples suggests that this is true.

When all the k are identical, the relaxation times are $\tau_2=1/4k$, and $\tau_3=\tau_4=1/2k$. The relaxation time $\tau_2=1/4k$ is inactive in the dielectric relaxation spectrum owing to a compensatory motion of the dipoles $[C_{12}=-C_{22}=C_{32}=-C_{42}]$ so only one relaxation time, $\tau=1/4k$, appears when the barriers between the sites are the same.

The range of dielectric properties which may be achieved with the four-position model can readily be ascertained by simplifying it so that some of the transition probabilities are the same.

VI. SPECIAL FOUR-POSITION MODELS

The simplifications employed are of the same type as those mentioned in Sec. III. In the present case it will be assumed that the sites are 90° apart. Some of the models correspond approximately to the situations which might arise when a long polar molecule is packed into a square network lattice in such a way that the dipole may occupy four orientational sites as the molecule turns about its long axis.

1. "Notch" Model

The local free energy barrier system is depicted in Fig. 6. Comparison of this figure with that for the general four-position model shows that

$$k_1=k_3=k_6=k_8;\quad k_2=k_4=k_5=k_7;\quad k_1>k_2. \tag{26}$$

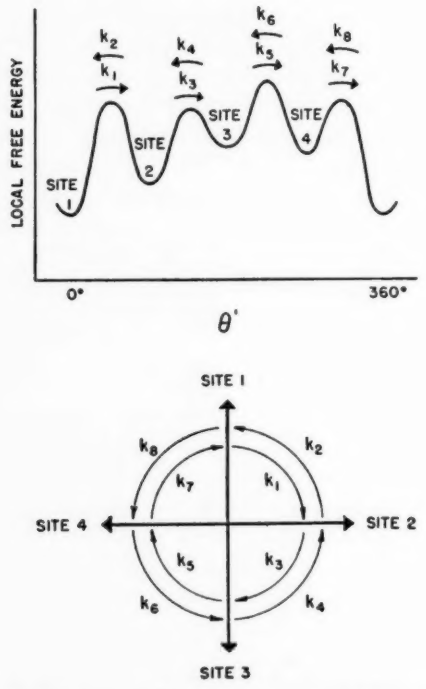

FIG. 5. Upper diagram: Local free energy as a function of rotational position for the general four-position single-axis rotator. Lower diagram: Rate processes for the general four-position model. The heavy arrows represent the equilibrium dipole orientations.

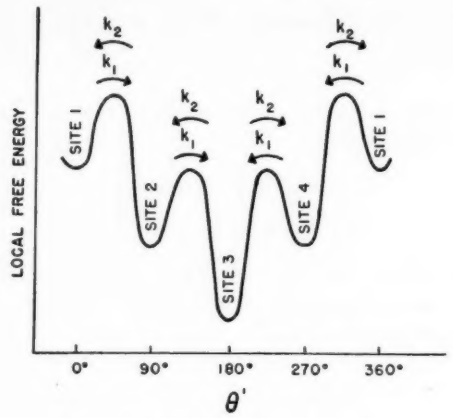

FIG. 6. Four position "notch" model.

When these simplifications are introduced into Eq. (24), it is found that $\mathbf{D}=-2(k_1+k_2)$, $-(k_1+k_2)$, $-(k_1+k_2)$, so that the relaxation times are

$$\begin{aligned}\tau_2&=1/2(k_1+k_2)\\ \tau_3&=\tau_4=1/(k_1+k_2).\end{aligned} \tag{27}$$

When the solution $C_{12}\Psi_2$, where $\Psi_2=\exp[-2(k_1+k_2)t]$, is substituted into Eqs. (22) where the simplifications indicated by Eq. (26) have been introduced, it is found that $C_{12}=-C_{22}=C_{32}=-C_{42}$. Thus, τ_2 is inactive in the dielectric relaxation spectrum. The degenerate modes 3 and 4 are indistinguishable, and the relaxation time $\tau_3=\tau_4$ is active. It follows that this model, like the two-position model proposed by Debye,[9] has the unusual property of always having a single[1,9,10] dielectric relaxation time. The total polarizability is

$$\alpha_{\text{total}}=\alpha_3+\alpha_4=\frac{[2(2C_{11}C_{31}+C_{11}C_{21}+C_{21}C_{31}+NC_{21})]}{N^2}\cdot(\mu^2/3\mathbf{k}T). \tag{28}$$

When site 3 is comparatively stable, as for the case $k_1\gg k_2$, α_{total} may be approximated by $[4C_{21}/N](\mu^2/3\mathbf{k}T)$ where $C_{21}/N\cong k_2/k_1$ is the fraction of dipoles in site 2 or 4; the total polarizability is thus quite small when site 3 is deep (or the temperature low). The polarizability gradually rises as the k converge and assumes the value $\mu^2/3\mathbf{k}T$ when $k_1=k_2$, since all the C_{i1} are then $1/4$. The Debye equations hold for all values of the k, so the loss peak will always be of the shape indicated in Fig. 4, curve $A-A'$.

2. Two Pairs of Equivalent Sites

The details of the model are given in Fig. 7. Site 1 is equivalent to site 3, and site 2 is equivalent to site 4. This model resembles that suggested by Meakins and

[9] See reference 4, p. 104.

[10] H. Fröhlich, *Theory of Dielectrics* (Oxford University Press, London, England, 1949), pp. 68–70 and 82–83.

TABLE II. Relaxation times and polarizabilities for the four-position model with two pairs of equivalent sites.

	k_1/k_2	α_3 ($\mu^2/3\mathbf{k}T=1$)	α_4 ($\mu^2/3\mathbf{k}T=1$)	τ_4/τ_3
$k_1/k_3=1/5$ Case (a)	0.1	0.11	0.89	11.5
	0.01	0.01	0.99	46
	0.001	0.002	0.998	5.1×10^4
$k_1=k_3$ Case (b)	0.5	0.38	0.62	2.68
	0.33	0.31	0.69	2.83
	0.1	0.15	0.85	33.5
$k_1/k_3=10$ Case (c)	0.9	0.49	0.51	10
	0.33	0.37	0.63	40
	0.10	0.16	0.84	350

Mulley[11] in their discussion of the dielectric loss in long-chain esters, except that these authors arranged the sites at 0°, 60°, 180°, and 240°. Assuming the *S-J* hypothesis, the relaxation times given below apply to their model, but the polarizabilities will be somewhat different than those presented here.

The model possesses four different transition probabilities since by comparison of Figs. 5 and 7 we see that

$$k_1=k_5, \quad k_2=k_6, \quad k_3=k_7, \quad k_4=k_8. \tag{29}$$

On introducing the above into Eq. (24) it is found that

$$\begin{aligned}\tau_2&=1/K\\ \tau_3&=2/(K+R)\\ \tau_4&=2/(K-R)\end{aligned} \tag{30}$$

where $K=k_1+k_2+k_3+k_4$, and $R=[K^2-8(k_1k_3+k_2k_4)]^{\frac{1}{2}}$. The solutions may be written

$$\begin{aligned}N_1&=C_{11}+C_{12}\Psi_2+xC_{13}\Psi_3+\ C_{14}\Psi_4\\ N_2&=C_{21}-C_{12}\Psi_2+\ C_{13}\Psi_3+yC_{14}\Psi_4\\ N_3&=C_{11}+C_{12}\Psi_2-xC_{13}\Psi_3-\ C_{14}\Psi_4\\ N_4&=C_{21}-C_{12}\Psi_2-\ C_{13}\Psi_3-yC_{14}\Psi_4\end{aligned} \tag{31}$$

where the decay functions are

$$\begin{aligned}\Psi_2&=\exp[-Kt],\\ \Psi_3&=\exp[-(K+R)t/2],\\ \Psi_4&=\exp[-(K-R)t/2],\end{aligned}$$

and

$$\begin{aligned}x&=2(k_3-k_2)/(k_2+k_3-k_1-k_4+R),\\ y&=(k_2+k_3-k_1-k_4-R)/2(k_3-k_2).\end{aligned}$$

The polarizability resides entirely in modes 3 and 4 since mode 2 is inactive. The polarizabilities are

$$\begin{aligned}\alpha_3&=\frac{2}{N}\left[\frac{C_{21}-xyC_{11}}{1-xy}\right](\mu^2/3\mathbf{k}T),\\ \alpha_4&=\frac{2}{N}\left[\frac{C_{11}-xyC_{21}}{1-xy}\right](\mu^2/3\mathbf{k}T).\end{aligned} \tag{32}$$

[11] R. J. Meakins and J. Mulley, J. Chem. Phys. **21**, 1934 (1954).

It is interesting to note that

$$\alpha_{\text{total}}=\alpha_3+\alpha_4=\frac{2[C_{11}+C_{21}]}{N}\cdot(\mu^2/3\mathbf{k}T)=\mu^2/3\mathbf{k}T \tag{33}$$

for all allowable values of the k.

The characteristics of the model are most easily perceived with the help of examples. It is convenient to distinguish three cases: (*a*) that where $k_1<k_3$, so that sites 2 and 4 are relatively unstable, (*b*) that where $k_1=k_3$, and (*c*) that where $k_1>k_3$, so that sites 2 and 4 are nearly equivalent to 1 and 3, but with a large barrier remaining between every other position (see Fig. 7). The values of the k must conform with the relation

$$k_1k_3=k_2k_4, \tag{34}$$

as may be seen from Eqs. (25) and (29). Thus, if values of k_1/k_3 [corresponding to cases (*a*), (*b*), or (*c*) above] and k_1/k_2 are selected, x and y may be computed numerically, and K and R expressed in terms of one of the k. Observing finally that $C_{11}/N=1/2[1+k_1/k_2]$ and $C_{21}/N=1/2[1+k_2/k_1]$, it is possible to obtain α_3 and α_4, as well as τ_4/τ_3 for various values of k_1/k_3 and k_1/k_2. The results are given in Table II.

An examination of the table shows that the relaxation times tend to converge as the k converge toward a common value. Only a single active relaxation time is found if the k are identical.

A striking feature of the model is that both α_3 and α_4 can maintain relatively high values even when the separation of the τ_β is extremely large; this effect is most marked for case (*c*). The result is that two separate regions of loss can appear in the dielectric relaxation spectrum (Fig. 8). The curves in Fig. 8 were calculated using Eq. (5) together with suitable data from Table II. Insofar as the prediction of two distinct loss regions is concerned, the present results might well have been anticipated from the remarks of Meakins and Mulley concerning their model.

The longer relaxation time is associated with the larger polarizability, so that the loss region which

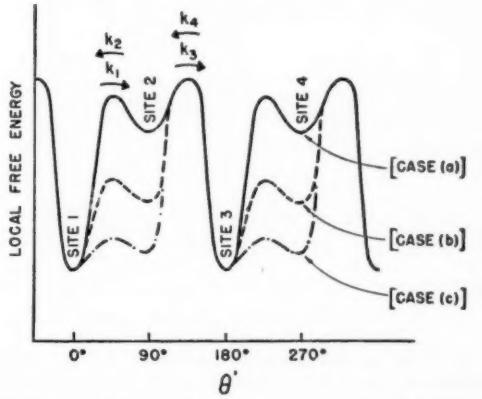

FIG. 7. Four-position model with two pairs of equivalent sites.

appears at the higher frequency is the smaller. As the k begin to converge, the two distinct loss regions tend to merge, and graphs resembling curve $B-B'$ in Fig. 3 are obtained when the k are of comparable magnitude. The Debye equations hold when the k are the same.

3. "Peak" Model

This model, which is depicted in Fig. 9, is included in order to illustrate the effect of a "forbidden" rotation process in an otherwise regular crystalline field. It is seen from the diagram that

$$k_1=k_2;\quad k_3=k_4=k_5=k_6=k_7=k_8;\quad k_3>k_1. \tag{35}$$

The relaxation times are

$$\begin{aligned}\tau_2&=1/2k_3,\\ \tau_3&=1/(k_1+2k_3-R),\\ \tau_4&=1/(k_1+2k_3+R),\end{aligned} \tag{36}$$

where $R=(k_1^2-2k_1k_3+2k_3^2)^{\frac{1}{2}}$. The greatest differences exhibited by the τ_β and the α_β appear when $k_3\gg k_1$, i.e., when reorientations between sites 1 and 2 are highly improbable. Under these conditions we find

$$\begin{aligned}&\tau_2=1/2k_3 \qquad \alpha_2=0.50(\mu^2/3\mathbf{k}T);\\ &\tau_3=1/0.586k_3 \quad \alpha_3=0.43(\mu^2/3\mathbf{k}T);\\ &\tau_4=1/3.414k_3 \quad \alpha_4=0.07(\mu^2/3\mathbf{k}T).\end{aligned} \tag{37}$$

An unusual feature of the model is that the longest relaxation time τ_3, is not identified with the largest polarizability. The corresponding loss region, in addition to being considerably broadened, is slightly steeper on the *high*-frequency side. The loss peak will thus resemble the mirror image of curve $B-B'$ in Fig. 3. The relaxation times converge as $k_3\rightarrow k_1$, and reduce to $\tau_2=\tau_3=1/2k$, $\tau_4=1/4k$ (inactive) when $k_1=k_3$. The asymmetry of the loss peak, which is small to begin with, will further diminish as the k converge, and the Debye equations will hold when $k_1=k_3$. The total polarizability associated with the model is always $\mu^2/3\mathbf{k}T$.

Both the "peak" model and that with two pairs of equivalent sites have the interesting property of sustaining a distribution of relaxation times for the case where α_{total} is $\mu^2/3\mathbf{k}T$.

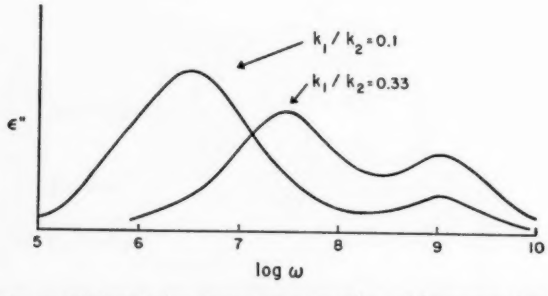

FIG. 8. Dielectric loss factor as a function of frequency for the four-position model with two pairs of equivalent sites. Both curves correspond to Case (*c*) where $k_1/k_3=10$. τ_3 has been set at 10^{-9} sec. for each curve.

VII. DISCUSSION

The range of dielectric properties inherent in the general three- and four-position models is brought out by the studies on the specialized versions. A summary of these properties is given in Table III in terms of the changes which occur as the transition probabilities converge. In what follows, our primary concern will be with qualitative predictions which may be subjected to experimental verification. Detailed application to specific substances must be deferred until more information is available concerning the exact nature of the crystalline field.

1. Width of the Loss Regions

As indicated in Secs. III and V, there is reason to believe that the general models with arbitrary k lead to a set of discrete relaxation times. Also, the calculations for the special models often yield a set of active relaxation times even when a number of the k are the same. On the other hand, a single relaxation time appears for (*a*) the two-position model,[12] (*b*) the "notch" model, and (*c*) any model where the activation barriers between the sites are of exactly equal magnitude. Considering the complicated nature of the crystalline field which dipoles must encounter in the orientation process in real crystals, and the restrictive character of the conditions mentioned above for the existence of a single relaxation time, *the appearance of loss peaks which are broader than those predicted by the Debye equations is commonly to be expected.* It is well known, e.g., from the work of Sillars,[13] Meakins,[14] and Crowe

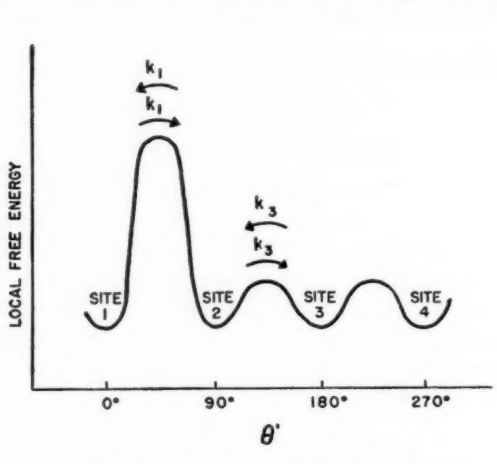

FIG. 9. Four-position "peak" model.

[12] Considerations based on entropy and crystal structure suggest that more than two sites are involved in many materials studied thus far. See reference 11 and 16.

[13] R. W. Sillars, Proc. Roy. Soc. (London) **A169**, 66 (1938).

[14] R. J. Meakins, Australian J. Sci. Research **2**, 405 (1949).

TABLE III. Behavior of the dielectric properties of single-axis rotator models as the transition probabilities converge.

Model	for converging k			α_{total} in units of $\mu^2/3kT$
	Active relaxation times	Shape of loss region	Width of loss region	
Three positions				
1. Two stable and equivalent sites [Sec. IV (1)]	converge	sym.→asym.→sym.	narrow→broad→narrow	$\frac{3}{4}$→1
2. "Cascade" [Sec. IV (2)]	diverge→converge	sym.→asym.→sym.	narrow→broad→narrow	0→1
3. One stable site, others equivalent [ref. 1]	converge	asym.→sym.	broad→narrow	0→1
Four positions				
1. "Notch" [Sec. VI (1)]	Has a single relaxation time; Debye equations hold for all values of the k.			0→1
2. Two pairs of equivalent sites [Sec. VI (2)]	converge	two separate and unequal peaks→asym.→sym.	bimodal→broad→narrow	1
3. "Peak" [Sec. VI (3)]	converge	asym.→sym.	broad→narrow	1
4. One stable site, others equivalent [ref. 1]	converge	asym.→sym.	broad→narrow	0→1

and Smyth,[15] that for many substances which may be regarded as single-axis rotators such an effect does indeed appear.

As mentioned in Sec. III, the k must converge as the temperature increases. Hence, the changes of properties listed in Table III for the case of converging k apply as well to the case of rising temperature. It follows that *a change of width of a dielectric loss region is to be expected as the temperature changes*. Either a gradual widening or narrowing may appear, depending on the model and the temperature range involved; the data in Table III suggests that a narrowing loss peak with rising temperature ought to be particularly common. While we are not aware of an example where an increasing width is observed, several examples where a definite narrowing of the loss peak appears with rising temperature have been observed in long-chain esters.[15]

Two separate regions of loss which tend to merge as the temperature is increased have been observed in long-chain bromides[16] and esters.[17,18] This would appear so support the theory; however, it seems best to defer a discussion of this effect, since it remains to be demonstrated that the coexistence of two distinct phases (or the longitudinally ordered and longitudinally disordered lattices suggested by Crowe, Hoffman, and Smyth[19]) is not the source of the two relaxation regions.

[15] R. W. Crowe and C. P. Smyth, J. Am. Chem. Soc. **73**, 5401 (1951).
[16] J. D. Hoffman, J. Chem. Phys. **20**, 541 (1952).
[17] T. J. Buchanan, J. Chem. Phys. **22**, 578 (1954).
[18] J. S. Dryden and H. K. Welsh, Australian J. Sci. Research **4**, 616 (1951).
[19] Crowe, Hoffman, and Smyth, J. Chem. Phys. **20**, 550 (1952).

2. Shape of the Loss Regions

A significant feature of the present theory is that it indicates that *when a loss region is broader than that predicted by the Debye equations, it will be slightly asymmetrical.* In most of the models studied, the asymmetry is such that the loss peak is steeper on the low-frequency side, but the calculations for the "peak" model show this result is not general. It is worth mentioning in this connection that the prediction of an asymmetric loss function arises rather frequently when a molecular approach is used to study relaxation phenomena. Thus, Kirkwood and Fuoss[20] find a slightly asymmetric distribution of dielectric relaxation times for an isolated chain molecule with free rotation about the internal bonds.

Data confirming the asymmetry of the loss regions for single-axis rotators which are free of the objection that two phases, longitudinal disorder, or mixed chain lengths might be present are for the most part lacking. However, the loss data of Crowe and Smyth[15] on a highly purified sample of *n*-hexadecyl palmitate, a substance which shows but slight evidence[19] of longitudinal disorder, exhibit a noticeable asymmetry (see their Fig. 4).

VIII. ACKNOWLEDGMENT

The author is indebted to K. Goldberg for helpful discussions on the mathematical aspects of the problem, and to Dr. S. G. Weissberg for his valuable criticism. Thanks are also due H. N. Elsheimer for his assistance with the calculations.

[20] J. G. Kirkwood and R. M. Fuoss, J. Chem. Phys. **9**, 329 (1941).

Phase Diagram of Liquid Ozone-Oxygen System

CALLAWAY BROWN, ABRAHAM W. BERGER, AND CHARLES K. HERSH
Armour Research Foundation of Illinois Institute of Technology, Chicago 16, Illinois

(Received August 16, 1954)

Vapor pressure composition data for liquid ozone-oxygen mixtures were obtained at −195.5°, −183°, and −180°C. The vapor pressure isotherms were used to construct the boiling point-composition line at one-atmos pressure. The vapor pressure of pure liquid ozone defines an upper limit for the partial pressure of ozone in the vapor in equilibrium with boiling liquid.

The vapor pressure of ozone-oxygen solutions deviates markedly from Raoult's law in a positive direction. It is suggested that the apparent boiling point maximum reported by Schumacher, which implies negative deviations, may be due to difficulties in analysis of ozone at high concentrations where it is subject to decomposition at ordinary temperatures.

Liquid-liquid equilibrium data are reported which indicate −180°C as an upper bound for the consolute temperature. The region of two liquid phases extends from 9 to 91 percent ozone by weight at −195.5°C, 29.8 to 72.4 percent at −183°.

INTRODUCTION

THE incomplete miscibility of liquid ozone and oxygen in the temperature range of boiling liquid air has been recognized for many years. A number of physical properties of the system were investigated by Riesenfeld and Schwab.[1–4] Thus the composition of the two liquid phases in equilibrium at −183°C was indicated to be 30 and 70 percent ozone, respectively. Mutual solubility increases with temperature and a value of −158°C was obtained for the consolute temperature. The boiling point of liquid ozone at −112°C and its vapor pressure temperature relation were established. Recent work of Jenkins and Birdsall[5] establishes the vapor pressure of liquid ozone more completely over the temperature range from −183°C to the critical temperature at −12.1°C. A recent note of Schumacher[6,7] reports, without experimental details, the phase diagram of the liquid ozone-oxygen system at one-atmos pressure and indicates a critical solution temperature of −180°C. Results reported herein confirm the lower value of the critical solution temperature but indicate a phase diagram for the system differing radically in other respects.

EXPERIMENTAL APPROACH

The experimental approach of the present work is reported in detail in a separate paper.[8] Liquid ozone-oxygen mixtures were prepared volumetrically by vacuum distillation of liquid ozone into a *U*-tube of calibrated volume and addition of oxygen metered from a gas buret. Liquid-vapor equilibrium was assured by circulation of the vapor phase through the liquid mixture in the *U*-tube. This was accomplished by use of the confining liquid in the gas buret (sulfuric acid) as a liquid piston to bubble gas through the liquid in the *U*-tube until pressure equilibrium was reached. Solutions of measured composition in equilibrium with vapor were prepared in this way. The analytical section of the apparatus was immersed in a bath of boiling liquid oxygen (or nitrogen) contained in a strip-silvered Dewar flask which permitted illumination and observation of the test solutions.

Separation of two liquid phases was observed directly and the composition was determined approximately by observation of the concentration at which a second liquid phase appeared. Precise determination of the composition at phase boundaries at −195°C and −183°C was made by measurement of the point of discontinuity in the curve of magnetic susceptibility *versus* composition as described in a previous paper.[8] The constancy of vapor pressure in the two-phase region and discontinuities in density, viscosity, and surface tension[9] served as further criteria to establish the phase boundaries.

The vapor pressure of the solutions was measured on a mercury manometer isolated from the system by concentrated sulfuric acid[8] in a differential manometer. Isotherms of vapor pressure *versus* composition were determined at three temperatures: −195.5°C, boiling liquid nitrogen; −183°C, boiling liquid oxygen; and −180°C, liquid oxygen boiling at 1054-mm pressure. Temperature baths were agitated by a stream of gas of

TABLE I. Composition at the phase boundaries.

Temperature °C	Ozone in Ozone-rich phase Wt percent	Ozone-rich phase Mole percent	Oxygen-rich phase Wt percent	Oxygen-rich phase Mole percent
−195.5	90.8	86.8	9.0	6.2
−183	72.4	63.6	29.8	22.1
−180	No phase separation detected			

[1] E. H. Riesenfeld and G. M. Schwab, Z. Physik **11**, 12 (1922).
[2] G. Schwab, Z. Physik Chem. **110**, 599 (1924).
[3] E. H. Risenfeld and G. M. Schwab, Ber. deut. chem. Ges. **55**, 2088 (1922).
[4] E. H. Riesenfeld and G. M. Schwab, Naturwiss. **10**, 470 (1922).
[5] A. C. Jenkins and C. M. Birdsall, J. Chem. Phys. **20**, 1158 (1952).
[6] H. J. Schumacher, J. Chem. Phys. **21**, 1610 (1953).
[7] Since preparation of this paper the details of Schumacher's work have appeared in Anales Assoc. Quim. Argentina 41, 198–264 (1953).
[8] Brown, Hersh, and Berger. J. Chem. Phys. **23**, 103 (1955).
[9] Paper in preparation by the authors.

TABLE II. Vapor pressure ratio of liquid ozone-oxygen mixtures at −195.5°C and −183°C.

$t=-195.5\pm0.25$°C, $P_0=160\pm5$ mm Hg		$t=-183.0\pm0.2$°C, $P_0=760\pm5$ mm Hg	
Mole percent O_2	Ratio P/P_0	Mole percent O_2	Ratio P/P_0
	Ozone-rich phase		
2.28	0.305	2.13	0.331
2.93	0.389	6.10	0.401
5.72	0.657	7.32	0.486
6.00	0.681	8.91	0.579
8.00	0.773	9.58	0.602
9.54	0.868	9.63	0.592
10.68	0.884	13.88	0.734
12.16	0.932	15.02	0.741
12.68	0.959	15.23	0.792
		21.32	0.858
		21.58	0.867
		29.97	0.919
		30.10	0.918
		30.00	0.926
	Two-phase region		
13.84	0.957	35.57	0.926
14.15	0.99	36.38	0.92
17.25	0.95	36.84	0.943
		39.36	0.921
20.80	0.92	49.58	0.92
26.28	0.97	72.47	0.944
91.59	0.97	72.73	0.947
93.10	0.97	76.37	0.919
93.17	0.96	77.37	0.929
		77.94	0.954
		78.76	0.937
	Oxygen-rich phase		
94.03	0.95	81.18	0.943
94.45	0.99	83.78	0.928
94.52	0.99	87.08	0.964
94.80	0.99	89.33	0.978
95.64	0.99	91.38	0.975
100	1.00	93.74	0.974
		100	1.00

the same composition, and bath temperatures were read on an oxygen vapor pressure thermometer. Variations in barometric pressure and in composition of the liquid baths led to variations in temperature from run to run, so variations in bath temperature are rationalized by use of the vapor pressure of liquid oxygen at bath temperature as a reference standard.

The three isotherms of vapor pressure *versus* composition provide the data needed to define the boiling point at one-atmos pressure as a function of composition. Since the vapor pressure isotherms were determined under truly equilibrium conditions, this method of construction of the boiling point line possesses decided advantages over direct measurements of the boiling point of the solutions. It is limited in principle by the necessity to extrapolate the vapor pressure data over part of the composition range. In practice the region covered by extrapolated data can be made as small as desired. This approach to the boiling point line and a method of bounding the curve of vapor composition *versus* temperature is clarified in the section on treatment of results.

EXPERIMENTAL RESULTS

The composition of the saturated solutions in equilibrium at −195.5°C and −183°C is given in Table I. These values represent a number of observations and are based primarily on the discontinuities in the curves of magnetic susceptibility *versus* composition[8] but include supplementary runs on density, viscosity, and surface tension. On a weight percent basis the compositions of the saturated solutions in equilibrium are remarkably close to symmetrical. This is probably fortuitous, so the usual practice of presenting the data in terms of mole percent is followed in the phase diagram. The rapid increase in mutual solubility with temperature indicates that the critical solution temperature cannot be far above −183°C. The run at −180°C failed to reveal any evidence of liquid phase separation although the composition range was scanned carefully in the region of 50 percent ozone by weight. Visual detection of phase separation is difficult with intensely colored solutions of nearly equal composition, so the capillary rise in the smaller arm of the *U*-tube was observed carefully for a discontinuity as the oxygen concentration was increased. No evidence of discontinuity was observed, so it may be concluded that the critical solution temperature is not above −180°C. Since the two-phase region at −183°C extends from 29.8 percent to 72.4 percent ozone by weight and apparently disappears at −180°C, the critical solution temperature probably deviates from −180°C by less than 1°C.

The data of the vapor pressure-composition isotherms are presented in Table II and III and Fig. 1. Vapor pressure in Table II and III is expressed in terms of the ratio of vapor pressure of the solution to the vapor pressure of pure oxygen in order to rationalize minor variations in bath temperature. It should be noted that

TABLE III. Vapor pressure ratio of liquid ozone-oxygen mixtures at −180°C.

$t=-180$°C, $P_0=1054\pm2$ mm Hg	
Mole percent O_2	Ratio P/P_0
4.52	0.325
9.15 [a]	0.570 [a]
9.44 [a]	0.550 [a]
14.56	0.706
24.64	0.849
25.15	0.852
37.88	0.890
41.60 [a]	0.907 [a]
41.94 [a]	0.889 [a]
48.95	0.911
53.29	0.915
62.56	0.912
63.13 [a]	0.927 [a]
63.13 [a]	0.917 [a]
71.69	0.922

[a] Pairs of values to determine departure from equilibrium. No two-phase region was observed.

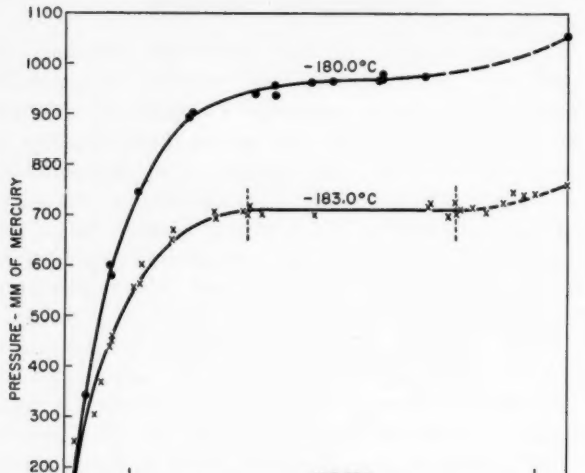

FIG. 1. Vapor pressure composition isotherms at −195.5°C, −183°C, and −180°C.

the vapor pressure of the solution equals the partial pressure of oxygen over the solution within experimental error since the vapor pressure of pure ozone is only 0.2 mm of mercury at the highest temperature studied.

PHASE DIAGRAM

Figure 2 shows the phase diagram at atmospheric pressure. Three boundary lines are of interest: the boundaries enclosing the region of the two liquid phases, the boiling point line which indicates the composition of boiling liquid, and the vapor composition line which indicates the composition of vapor in equilibrium with boiling liquid. Since liquid-liquid equilibria are affected very little by changes in pressure, the data of Table I define the region of two liquid phases down to −195.5°C. The boiling point curve may be obtained directly from the data of Tables II and III and Fig. 1 by plots of the vapor pressure *versus* temperature at constant composition given in Fig. 3.

At −180°C, the vapor pressure of the ozone-oxygen solutions reaches one atmosphere at 15 mole percent oxygen. Therefore, up to 85 mole percent ozone, the boiling point of the solutions is determined by interpolation of the experimental data of the vapor pressure isotherms. In the composition range 0 to 85 mole percent ozone the boiling point rises only 3° from −183° to −180°C. At higher ozone concentrations, extrapolation of the data to higher temperatures is needed to determine the boiling point. Thus at 94 mole percent ozone, extrapolation of the vapor pressure data indicates that the boiling point of the solution at one atmosphere is −172°C. Clearly the further the extrapolation is carried, the less certain the calculated boiling point becomes, but the present results determine the boiling point accurately under conditions of liquid-vapor equilibrium for ozone-oxygen mixtures up to 85 mole percent ozone and estimate the boiling point at higher concentrations within the limitations of the extrapolation of the vapor pressure data.

The qualitative aspects of the vapor composition curve are much simplified by the fact that the major composition range of liquid boils within a few degrees of the boiling point of liquid oxygen. Since the vapor pressure of pure liquid ozone is only 0.1 mm at −183°C, the ozone concentration in the vapor phase is essentially zero for liquid compositions below 90 mole percent ozone. At temperatures at which the ozone concentration in the vapor phase can be an appreciable part of the total pressure, the ozone concentration in the liquid phase is so high that negative deviations from Raoult's law would be required for the vapor concentration of ozone to be significantly below the vapor pressure of pure liquid ozone. The vapor pressure-composition data of Fig. 1 indicate strong positive deviations from Raoult's law so that a radical change in the nature of the solutions at higher temperatures would be necessary for the vapor composition to differ significantly from that determined by the vapor pressure of pure liquid ozone.

Therefore the upper bound of the vapor composition curve was calculated on the assumption that the partial pressure of ozone equals the vapor pressure of liquid ozone. The vapor pressure of liquid ozone as a function of temperature is known accurately[5] so calculation of its maximum concentration in vapor at a total pressure of one atmosphere is a simple matter. The vapor composition curve labeled "ideal solution" is inserted for comparison. It was obtained from the product of the ozone vapor pressure and its mole fraction in

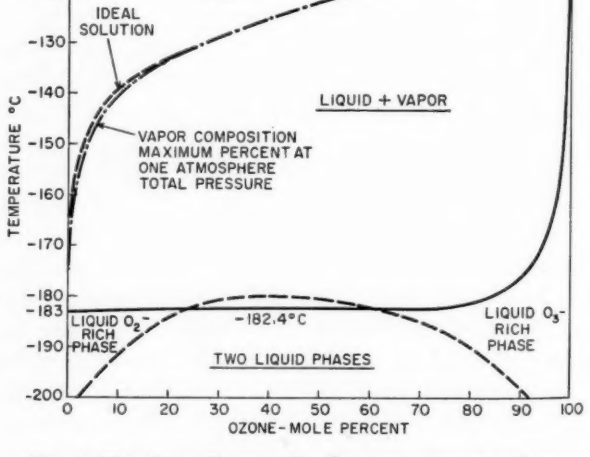

FIG. 2. The phase diagram, for the oxone-oxygen system at one-atmos total pressure.

the liquid in equilibrium with it. At the higher temperatures the two curves are indistinguishable due to the high ozone concentration of the liquid.

SIGNIFICANCE OF RESULTS

The usual method of construction of the liquid-vapor equilibrium diagram of a two component system is to determine the boiling point of solutions as a function of composition and the equilibrium composition of liquid and vapor phases. Attainment of liquid-vapor equilibria is essential for accurate results, and this presents extraordinary difficulties with the present system. The boiling range is at low temperatures, use of a small quantity of liquid is desirable for safety, and analysis of ozone-oxygen mixtures is complicated by decomposition of ozone at ordinary temperatures.

The work of Schumacher[6,7] presents an ingenious approach to overcome these difficulties, but the phase diagram he reports contains inconsistencies which require resolution. Experimental data for the boiling point curve are confined to the composition range of 73–88 percent ozone and show an abrupt rise in boiling point in this range to a boiling point maximum at −106°C, about 6°C above the boiling point of liquid ozone.

There is no evidence of such a boiling point line in the present work. For example, the vapor pressure isotherm at −180°C (Fig. 1) reaches one atmos at 11 percent oxygen by weight (84 mole percent ozone). This composition is close to that for which Schumacher shows a boiling point maximum at −106°C. Furthermore, the vapor pressure curves of Fig. 1 show that the vapor pressure increases very rapidly with increase in oxygen content in ozone-rich solutions, deviating from Raoult's law in a positive direction. A boiling point maximum implies negative deviations from Raoult's law. Analysis of gaseous mixtures containing ozone in high concentration is complicated by decomposition of ozone. A shift of Schumacher's boiling point curve toward higher ozone concentrations would lead to the rapid rise in boiling point asymptotic to the 100 percent ozone axis suggested by the present results. A recent note by Jenkins and Birdsall[10] presents data on boiling liquid ozone-oxygen mixtures which also indicates no boiling point maximum and suggests a similar explanation for the results.

The ozone analysis problem was bypassed in the present work by mixing measured quantities of ozone and oxygen at low temperature where decomposition of ozone was found to be negligible. Liquid-vapor equilibrium was assured by circulation of the vapor phase through the liquid phase. The boiling point curve was thus established accurately by the vapor pressure isotherms up to a composition of about 90 percent ozone. At higher ozone content, the remainder of the curve was estimated by extrapolation of the vapor pressure data. At 95 percent ozone, the extrapolated temperature range is 12°C, at 98 percent ozone, 23°C. In principle, the range extrapolated could be made as small as desired by determination of vapor pressure isotherms at higher temperatures.

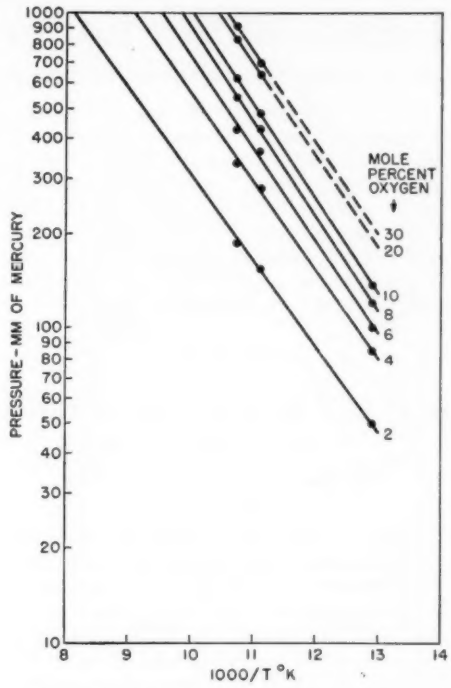

FIG. 3. The relationship of $\log P$ to $1000/T$ at constant composition (mole percent O_2).

The phase diagram presented, therefore, is believed to represent correctly the qualitative aspects of the ozone-oxygen system. Quantitatively the diagram is subject to approximations in extrapolation of vapor pressure data at ozone compositions above 90 percent, and use of vapor pressure data for 100 percent liquid ozone to bound the vapor composition.

ACKNOWLEDGMENTS

The present work received invaluable advice and assistance from members of the Ozone Technology Group of the Armour Research Foundation, especially C. E. Thorp, L. C. Kinney, R. F. Remaly, and G. M. Platz. This is part of a research program carried out under contract with the Air Reduction Company, New York, N. Y.

[10] A. C. Jenkins and C. M. Birdsall, J. Chem. Phys. **22**, 1779 (1954).

Letters to the Editor

THIS section will accept reports of new work, provided these are terse and contain few figures, and especially few half-tone cuts. The Editorial Board will not hold itself responsible for opinions expressed by the correspondents. Contributions to this section should not exceed 600 words in length and must reach the office of the Editor not later than the 15th of the second month preceding that of the issue in which the Letter is to appear. No proof will be sent to the authors. A publication charge of $10.00 per Letter is made which, when honored, will entitle the Institution to 100 free reprints.

Knudsen Flow through a Circular Capillary*

W. C. DEMARCUS AND E. H. HOPPER
Carbide and Carbon Chemicals Company, K-25 Plant, Post Office Box P, Oak Ridge, Tennessee
(Received May 4, 1955)

THE problem of Knudsen flow through a circular capillary has been often discussed, usually by the momentum transfer method.[1,2] However, P. Clausing[3] gave a rigorous formulation for the problem and obtained an integral equation for which he gave an approximate solution. From time to time the accuracy of Clausing's solution has been questioned and since Clausing did not give a rigorous estimate of his error we have reinvestigated the problem.

The integral equation to be solved for the wall collision density $n(x)$ in a capillary of radius r and length L is

$$n(x)=n_1(x)+\int_0^{L/r} K(x,y)n(y)dy,$$

with

$$n_1(x)=\frac{\pi}{2}\left[\frac{x^2}{(x^2+4)^{\frac{1}{2}}}+(x^2+4)^{\frac{1}{2}}-2x\right],$$

$$K(x,y)=\phi\{|x-y|\},$$

$$\phi(t)=\frac{1}{4}\left\{2+\left[\frac{t}{(t^2+4)^{\frac{1}{2}}}\right]^3-\frac{3t}{(t^2+4)^{\frac{1}{2}}}\right\}.$$

We define the iterate of any function $f(x)$ by

$$I\{f(x)\}=n_1(x)+\int_0^L K(x,y)f(y)dy.$$

W. S. Snyder[4] has shown quite generally for kernels of this type that $f(x)\geqq n(x)$ everywhere in $0\leqq x\leqq L/r$ if

$$I\{f(x)\}\leqq f(x)$$

in the same region. Our procedure is to assume a polynomial of the third or fifth degree in $x-L/2$ for $f(x)$ and adjust the constants so that $I\{f(x)\}$ differs from $f(x)$ by as little as possible over the range, but at the same time satisfies the above inequality so that the resultant polynomial is an upper bound for $n(x)$. A similar procedure is followed for a lower bound. The transmission probability W for the capillary is then calculated from the upper and lower bounds and gives two extreme values within which the true transmission probability lies. The results for four nonzero values of L/r are given in Table I below with the error estimates found.

TABLE I. Transmission probability of circular capillaries.

L/r	W (this letter)	W (Clausing)
0	1.0000000	1.0000000
0.5	0.8012716 ±0.0000001	0.8013
1.0	0.671984 ±0.000005	0.6720
1.5	0.581482 ±0.000004	0.5810
2.0	0.514230 ±0.000013	0.5136

It is to be emphasized that a stated limit of error is in an absolute rather than a probabilistic sense. Clausing's values are also given in the last column for comparison. It thus appears that in this range of L/r, which seems of major interest in vapor pressure work, Clausing's values are within 0.1 percent of the correct values. The fact that the limit of error for $L/r=1.0$ is larger than for $L/r=1.5$ reflects the use of the polynomial of higher degree in the latter case.

* This document is based on work performed for the U. S. Atomic Energy Commission by Union Carbide and Carbon Corporation at Oak Ridge, Tennessee.
[1] M. Knudsen, Ann. Physik **28**, 75 (1909).
[2] W. G. Pollard and R. D. Present, Phys. Rev. **73**, 762 (1948).
[3] P. Clausing, Physica **IX**, 65 (1929).
[4] W. S. Snyder, Nucleonics **6**, 2, 46 (1950).

Vibrational Spectra of SiH_3Br and SiH_2Br_2

DANA W. MAYO, HERMAN E. OPITZ, AND JOHN S. PEAKE
Department of Chemistry, Indiana University, Bloomington, Indiana
(Received April 20, 1955)

IN connection with an investigation of organosilyl derivatives we have had occasion to prepare mono- and dibromosilane as starting materials for the synthesis of these compounds. Since the vibrational spectrum of SiH_3Br has not been previously investigated and SiH_2Br_2 only by the Raman effect,[1] we have taken this opportunity to make a preliminary study of the infrared spectra of these compounds. The bromo-silanes were prepared either by reaction of silane and hydrogen bromide over an aluminum bromide catalyst or by cleavage of phenylsilane with hydrogen bromide.[2]

Measurements of the infrared spectra of SiH_3Br and SiH_2Br_2 vapor were recorded with a Perkin-Elmer model 21 spectrophotometer in the region 5000–400 cm^{-1} employing NaCl and KBr prism interchange units. The spectra were obtained at pressures varying from 480 to 2 mm Hg, with a cell path length of 10 cm. The observed frequencies and assignments are listed in Tables I[3] and II.

Monobromosilane contains a threefold axis of symmetry as evidenced by the intensification of every third Q branch of the perpendicular modes ν_5 and ν_6 (see Fig. 1). The infrared data thus support C_{3v} symmetry for the molecule in agreement with the structure proposed for SiH_3Cl.[4] The perpendicular band ν_4 near

TABLE I. The infrared spectrum and band assignments of SiH_3Br.

Assignment	ν cm^{-1}
$\nu_3(a_1)$	428 (m)∥
$\nu_6(e)$	629 (s)⊥
$\nu_2(a_1)$	927 (vs)∥
$\nu_5(e)$	946 (s)⊥
impurity (Si-O-Si)	1107 (w)
$2\nu_6(A_1+E)$	1262 (w)∥ ~1265 (w)⊥
$\nu_2+\nu_6(E)$ $\nu_5+\nu_6(A_1+[A_2]+E)$	1564[a] (vw)
$2\nu_2(A_1)$ $\nu_2+\nu_5(E)$ $2\nu_5(A_1+E)$	1878[a] (vw)
$\nu_1(a_1)$ $\nu_4(e)$	2200[a] (vs)
$\nu_1+\nu_3(A_1)$ $\nu_4+\nu_3(E)$	2625[a] (vw)
$\nu_1+\nu_6(E)$ $\nu_4+\nu_6(A_1+[A_2]+E)$	2830[a] (vw)
$\nu_1+\nu_2(A_1)$ $\nu_1+\nu_5(E)$ $\nu_4+\nu_5(A_1+[A_2]+E)$ $\nu_4+\nu_2(E)$	3130[a] (w)
$2\nu_1(A_1)$ $\nu_1+\nu_4(E)$ $2\nu_4(A_1+E)$	~4300[a] (vw)

[a] Band not resolved.

TABLE II. Fundamental frequencies of SiH_2Br_2.

Assignment	Infrared ν cm^{-1}	Raman[1] ν cm^{-1}
$\nu_4(a_1)$	not investigated	122
$\nu_3(a_1)$	407 (m)	393
$\nu_9(b_1)$	471 (s)	456
$\nu_7(b_1)$	556 (s)	not observed
$\nu_5(a_2)$	inactive	688
$\nu_8(b_2)$	843 (vs)	828
$\nu_2(a_1)$	942 (vs)	925
$\nu_1(a_1)$	2200[a] (s)	2206
$\nu_6(b_1)$		2232

[a] Band not resolved.

2200 cm^{-1} has not been resolved, but the spacings of the Q-sub-bands of ν_5 and ν_6 have been determined as 6.3 and 4.2 cm^{-1}, respectively. Since one would expect the moment about the symmetry axis to exhibit little change among different monohalosilanes similar to the carbon analogs,[5] the value of $I_A = 9.9 \times 10^{-40}$ g-cm^2 determined for SiH_3Cl[6] may be taken as a good approximation for the moment I_A of monobromosilane. Employing $I_B = 196 \times 10^{-40}$ g-cm^2 as determined from microwave data,[7] and the known ν_5 and ν_6 spacings we may deduce the sub-band separation for ν_4 to be 5.5 cm^{-1}.

The pairings of the fundamentals ν_1, ν_4 and ν_2, ν_5 which occur in SiH_3Br result in several clusters of unresolved overtone and combination bands. As all overtones and combination tones are infrared active in monobromosilane, assignments for the unresolved bands include the transitions which would be expected to occur in the region of the observed band. The perpendicular and parallel sub-bands of the overtones $2\nu_6(A_1+E)$ were resolved. However, the origin of the perpendicular sub-band was masked and could not be accurately located.

The observed frequencies of dibromosilane (Fig. 2) are in agreement with the Raman data[1] for the liquid, and the reassignment of these frequencies by Hawkins, Polo, and Wilson[8] has been confirmed. The torsional mode $\nu_5(a_2)$ assigned to the Raman line at 688 cm^{-1} is inactive in the infrared and was not observed. The assignment of the rocking fundamental $\nu_7(b_1)$ to the 688 cm^{-1} Raman band by François and Buisset[1] is therefore not correct. The strong band at 556 cm^{-1} has been assigned to ν_7 in agreement with the calculated[8] value of 535 cm^{-1}.

Thermodynamic functions for SiH_3Br and SiH_2Br_2 are listed in Tables III and IV. Calculations were made using a rigid-rotor, harmonic oscillator approximation for the ideal-gas state at one

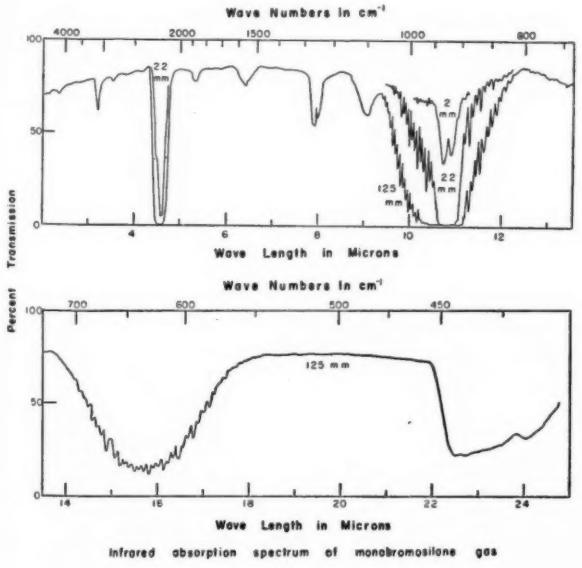

FIG. 1.

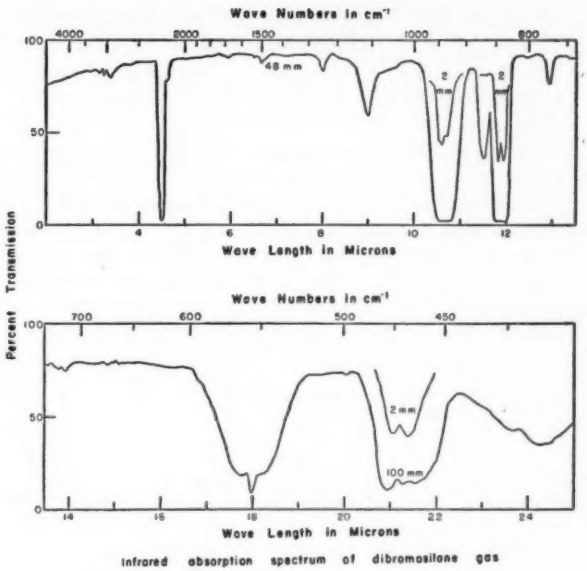

FIG. 2.

atmosphere pressure. The observed infrared frequencies were employed except in the case of SiH_2Br_2, where the Raman values for $\nu_4(a_1)$, $\nu_5(a_2)$, $\nu_1(a_1)$, and $\nu_6(b_1)$ were used. The bond distances taken for SiH_2Br_2 were Si—H = 1.57 A and Si—Br = 2.21 A.[7] The dibromide was assumed to have tetrahedral bond angles. Although the frequencies $\nu_1(a_1)$ and $\nu_4(e)$ of SiH_3Br were not accurately

TABLE III. Thermodynamic functions for SiH_3Br (cal deg^{-1} mole^{-1}).

T(°K)	C_p^0	S^0	$\frac{(H^0-E_0^0)}{T}$	$\frac{-(F^0-E_0^0)}{T}$
275	12.11	61.75	9.21	52.54
298.1	12.69	62.76	9.46	53.30
400	14.87	66.81	10.57	56.24
800	20.02	78.89	14.16	65.43
1200	22.52	87.59	16.59	70.99

TABLE IV. Thermodynamic functions for SiH_2Br_2 (cal deg^{-1} mole^{-1}).

T(°K)	C_p^0	S^0	$\frac{(H^0-E_0^0)}{T}$	$\frac{-(F^0-E_0^0)}{T}$
298.1	15.68	73.92	11.45	62.48
338	16.58	75.98	12.02	63.96
400	17.71	78.82	12.80	66.02
800	21.73	92.59	16.42	76.17
1200	23.51	101.83	18.53	83.30

determined, the contribution of these fundamentals to the vibrational partition function is negligible at low temperatures.

A detailed investigation of these compounds and other halosilanes is now in progress by Professor M. K. Wilson. We are indebted to Professor R. C. Lord and Dr. E. J. Bair for several helpful discussions. The authors wish to acknowledge financial support by the Office of Naval Research [Nonr-908(02)-Task NR356321].

[1] F. Francois and M. Buisset, Compt. rend. **230**, 1946 (1950).
[2] Manuscript in preparation.
[3] A similar assignment of the fundamentals has been proposed independently by M. Kent Wilson (private communication).
[4] A. Monfils, J. Chem. Phys. **19**, 138–9 (1951).
[5] W. H. Bennett and C. F. Meyer, Phys. Rev. **32**, 888 (1928).
[6] A. Monfils, Compt. rend. **236**, 795–6 (1953).
[7] Sharbaugh, Bragg, Madison, and Thomas, Phys. Rev. **76**, 1419 (1949).
[8] Hawkins, Polo, and Wilson, J. Chem. Phys. **21**, 1122 (1953).

Origin of the Line Width of Pure Quadrupole Resonance

Y. KÔI, A. TSUJIMURA, AND T. FUKE
Faculty of Technology, Tokushima University, Tokushima, Japan
(Received May 11, 1955)

AS in the case of nuclear magnetic resonance, the origin of the line width of pure quadrupole resonance is an interesting problem. With the idea that the line shapes and the ratio of the line widths for the bromine isotopes in one and the same chemical compound could give much information about this problem, measurements were made on the bromine isotopes in $NaBrO_3$ at room temperature. The line for the isotope Br^{81} in this substance has a half-width at half-maximum of about 1.5 kc.[1]

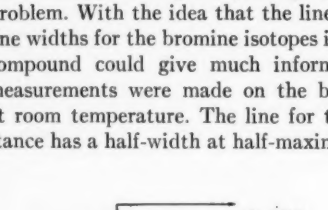

FIG. 1. Regenerative-type detector. The frequency is modulated with a vibrating metal foil placed near the plate Lecher's lines.

In order to get reliable results, it was necessary to use a regenerative-type detector.[2] The circuit in Fig. 1 has proved usable for this purpose.

Since the terrestrial-magnetic field gives rise to a considerable broadening of line width,[3] it was canceled with small permanent magnets. In order to avoid the broadening due to the temperature inhomogeneity in the sample, special care was taken to keep the sample at a constant temperature. The level of oscillation of the detector was held sufficiently weak, though there seemed no tendency for the line to saturate. The sample used was an assemblage of small crystal grains of about 1 mm^3 in volume, which were prepared by means of very slow recrystallization from a saturated aqueous solution of extra-pure $NaBrO_3$.

Figure 2 shows the results obtained. Both the derivative curves have an intermediate character between a Gaussian and a Lorentzian curve, the ratio of the maximum negative to the maximum positive slope being 3:1 for the Br^{79} curve and 3.1:1 for the Br^{81} curve. The interval between the extreme deflections is 3.5 kc for the former and 3.1 kc for the latter.

Now the possible mechanisms of the line broadening are the following: electric quadrupolar relaxation, magnetic-dipole interaction, and field fluctuation due to the crystal strain.[4] If the first mechanism predominates, the ratio of the line widths for two isotopes Br^{79} and Br^{81} will be equal to the ratio of the squares of their quadrupole-coupling constants, i.e., 1.44. If the second predominates, it will be equal to the ratio of their magnetic moments, i.e., 0.928, and if the third predominates, the ratio of their quadrupole-coupling constants, i.e., 1.2. As to the line shape, from the first mechanism a Lorentzian shape would result, and from the second a Gaussian.[5] The line shape due to the third would depend on the nature of the strain.

TABLE I. Contributions from various mechanisms to the line width.

Isotope	Width due to relaxation kc	Width due to dipole interaction kc	Width due to strain kc
Br^{79}	1.7	1.8	0 (Assumed)
Br^{81}	1.1	2.0	0 (Assumed)

Since the observed ratio is 1.13, all the three mechanisms may be responsible for the observed line widths, but their fractional importance cannot be determined from the single observed ratio. If, accordingly, the broadening due to the strain is tentatively assumed to be negligible, the result shown in Table I is obtained.

Since rather large errors are inevitable in the line-width measurements, these assignments are somewhat arbitrary. The widths due to the dipole interaction are, however, in agreement in the order of magnitude with our rough estimations of the dipolar broadening. Moreover, from the above assignments the total width for Cl^{35} in $NaClO_3$ is estimated to be 0.7 kc, if the foregoing argument is extended to Cl^{35}. This value is in substantial agreement with the observed value 0.9 ± 0.1 kc.[6] About the width due to the relaxation further information could be given, if the temperature dependence of the width is measured.

Measurements on other bromine compounds are now in progress.

The authors express their sincere thanks to Mr. T. Kushida of the Hiroshima University for many valuable discussions.

[1] A. L. Schawlow, J. Chem. Phys. **22**, 1211 (1954).
[2] R. V. Pound and W. D. Knight, Rev. Sci. Instr. **21**, 219 (1950).
[3] H. Kruger and U. Meyer-Berkhout, Z. Physik **132**, 221 (1952).
[4] R. V. Pound, Phys. Rev. **79**, 123 (1950).
[5] G. E. Pake and E. M. Purcell, Phys. Rev. **74**, 1184 (1948).
[6] Ting, Manring, and Williams, Phys. Rev. **96**, 408 (1954).

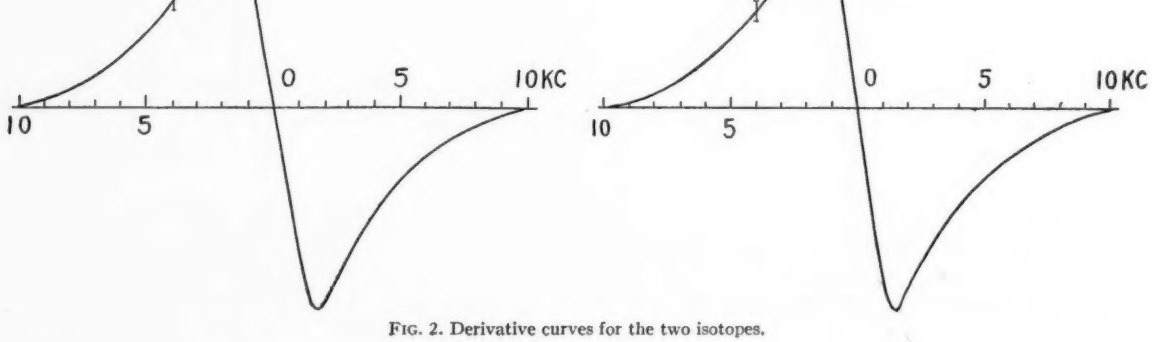

FIG. 2. Derivative curves for the two isotopes.

On the Heat of Dissociation of N_2†

JOHN F. BURNS
K-25 Technical Division, Carbide and Carbon Chemicals Company, Oak Ridge, Tennessee
(Received May 9, 1955)

THE most serious obstacle encountered in the application of electron impact methods to the measurement of dissociation energies has been the inability of the experimenter to determine directly the state of electronic excitation of the resulting fragments. Hagstrum[1] made a notable attempt to overcome this lack of completeness in the experimental data by assigning spectroscopically possible excitation energies to the fragments on the basis of internal consistency of the results. In this way he was led to the assignment of 2.4 electron volts excitation energy to the fragments resulting from the dissociation of nitrogen. At the same time he showed that the fragments were formed with zero relative kinetic energy.

It was suggested by Dr. George Glockler of the University of Iowa that the retarding potential method of Fox, Hickam, Kjeldaas, and Grove[2] might be used to determine the validity of this excitation energy assignment and an investigation of the ionization efficiency curve for the N^+ ion from N_2 was undertaken by the writer. Two of the resulting curves are shown in the accompanying figures.

Since these curves were obtained for the sole purpose of investigating their structure, no attempt was made to evaluate the shift in the electron energy scale introduced by contact potentials and space-charge conditions in the ion source. The point of initial onset of the ion current in both Figs. 1 and 2 has been arbitrarily displaced approximately 0.2 volt to correspond to the appearance potential obtained by previous investigators.[1] In all, some thirty such curves were obtained under a wide variation of instrumental conditions. The detailed structure of these curves differed slightly one from the other, but in all cases the first upward break occurred between 1.7 and 2.1 volts above onset, and the second between 0.4 and 0.7 above the first. The results obtained from successive measurements of the appearance potential curves for nitrogen and neon are compared in Fig. 2. Since the curve for neon has been shown to be linear over the region investigated,[3] the lack of structure in the curve for neon in the region where the upward breaks occur in the nitrogen curve forces the conclusion that these arise from the dissociation process in nitrogen itself and are not instrumental in character.

As a result of the form of the curves obtained in this work it is concluded that both the atom and ion resulting from the dissociation of nitrogen under electron impact are formed in their ground states at onset. The first upward break observed at approximately 1.9 electron volts above onset is then attributed to the process which results in $N(^4S^0)+N^+(^1D)$ and the second at 2.4 volts above onset to the process yielding $N(^2D^0)+N^+(^3P)$.

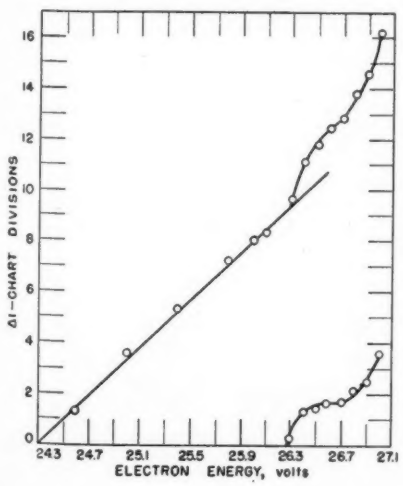

FIG. 1. Appearance potential curve for N^+ from N_2.

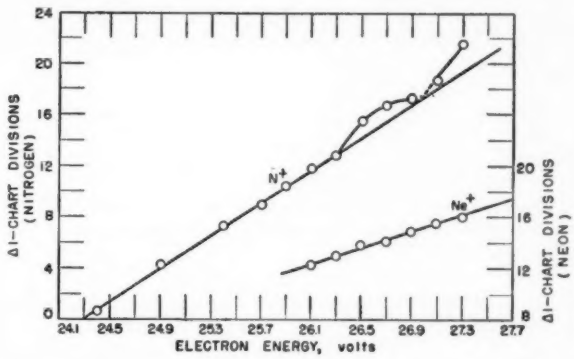

FIG. 2. Comparison of the ionization efficiency curves of N^+ and Ne^+.

Since this work was first reported[4] it has been partially confirmed by Clarke[5] who obtained a single upward break in the ionization efficiency curve at about 2.4 volts above onset. It seems probable that Clarke's inability to resolve the two breaks at 1.9 and 2.4 volts above onset was due to excessive energy spread in his electron beam caused by the presence of the drawing out field in the source during ion formation, and the fact that the 127° electrostatic analyzer used by him did not produce a truly homogeneous beam as is apparent from the curves given in his paper.

The writer wishes to express his indebtedness to Dr. A. E. Cameron of the Technical Division, K-25 Plant, Carbide and Carbon Chemicals Company, and to Dr. A. H. Nielsen of the University of Tennessee for their council and encouragement during the course of this work. He is greatly indebted to the Westinghouse group, in particular Mr. W. M. Hickam, for many helpful discussions of the retarding potential method.

† This work was done at the Oak Ridge Gaseous Diffusion Plant operated for the Government by Union Carbide and Carbon Corporation, and submitted to the Physics Department of the University of Tennessee in partial fulfillment of the requirements for the Ph.D. degree.

[1] H. D. Hagstrum, Revs. Modern Phys. **23**, 185 (1951).
[2] Fox, Hickam, Kjeldaas, and Grove, Phys. Rev. **84**, 859 (1951).
[3] W. M. Hickam (private communication).
[4] J. F. Burns, "The heat of dissociation of nitrogen and the appearance potential of some ions formed in fluorine and hydrogen fluoride by electron impact," Carbide and Carbon Chemicals Company, K-25 Plant (Ph.D. thesis: University of Tennessee, August, 1954), Report K-1147, October 8, 1954.
[5] E. M. Clarke, Can. J. Phys. **32**, 764 (1954).

On the Dissociation Energies of SrO and MgO Molecules*

RICHARD F. PORTER, WILLIAM A. CHUPKA, AND MARK G. INGHRAM
Department of Physics, University of Chicago, Chicago, Illinois, and Argonne National Laboratory, Lemont, Illinois
(Received May 13, 1955)

THERMOCHEMICAL calculations yield about 4.8 ev for the dissociation energy of the SrO molecule.[1,2] The calculations were based on total vapor pressure[3,4] data and require the assumption that $SrO(s)$ vaporizes predominantly as $SrO(g)$. Consideration of recent mass spectrometric data[5–8] favors a value considerably below 4.8 ev, provided the accommodation coefficient of $SrO(g)$ on $SrO(s)$ is not small.

Brewer and Porter[9] measured the volatility of $MgO(s)$ in beryllia effusion cells. From their total vapor pressure data, a value of 4.7 ev for the dissociation energy of $MgO(g)$ was calculated. Using a spectroscopic technique these workers obtained independent evidence that the dissociation energy of MgO may be as high as 4.7 ev. The uncertainty in their spectroscopic value, however, could not exclude a dissociation energy as much as a volt lower.

In the present experiment the partial pressures of gaseous species in thermodynamic equilibrium with the solid, contained in an alumina Knudsen cell, were determined mass spectrometrically. The technique and advantages of this method have been described

TABLE I. Vapor pressure data for SrO(g) and MgO(g).

Gaseous species, X	Temp. °K	Sensitivity of mass spectrometer[a]	X^+ ion current[b]	X pressure over solid oxide (atmos)	$-(\Delta F_T^0 - \Delta H_{298}^0)/T$ of sublimation (cal/deg)	ΔH_{298}^0 of sublimation (kcal/mole)
SrO	2100	7.5×10^{11}	1.8×10^4	3.6×10^{-8}	39.8	155.1
(MgO)	1950	6.3×10^{11}	$<5.5\times10^4$	$<7.5\times10^{-8}$	44.0	>149.4

[a] In arbitrary units of Ag^{107+} ion current for 80-volt electrons per atmosphere of Ag vapor.
[b] Same units as for Ag^{107+}.

earlier.[10,11] In this particular case the ratio of effusion hole area to total geometrical surface area of the oxide was $<10^{-2}$.

In the SrO system, ion currents of Sr^+, SrO^+, and O_2^+ were observed. At cell temperatures of 2100°K, and ionizing electron energies of 50 ev, the relative ion currents were $I_{Sr^+}:I_{O_2^+}:I_{SrO^+}=300:36:1$. The appearance potential of Sr^+ showed that essentially all of the Sr^+ was formed by simple ionization of Sr gas effusing from the cell.

In the MgO system Mg^+ was the major ion observed. Only an upper limit could be set on the relative amount of MgO^+ because of the presence of a calcium impurity of the same mass. At a cell temperature of 1950°K, and ionizing electron energy of 15 ev, the ratio of Mg^+ to MgO^+ was greater than 1000. Appearance potential curve of Mg^+ showed that Mg vapor was the principle species effusing from the cell.

Table I gives results of the calculations of ΔH^0_{298} of sublimation of SrO(g) and MgO(g). Equal ionization cross sections were assumed for Ag, SrO, and MgO. Although the ground states of SrO and MgO are believed to be triplet states, reliable spectroscopic constants are not available for these states. Therefore, as an approximation, the vibrational and rotation contribution to the free energy functions of SrO(g) and MgO(g) were calculated from spectroscopic constants[12] for the lowest $^1\Sigma$ state of these molecules. However, a quantum weight of three was used for the ground state in calculating the free energy functions. Free energy functions for SrO(g) were calculated with the aid of the heat capacity equation used by Drummond and Barrow.[1] Data tabulated by Kelley[13] were used to obtain $-(F_T-H_{298})/T$ for MgO(s). Heats of sublimation of SrO(g) and MgO(g) were combined with heats of sublimation of the alkali and earth metals,[14] heats of formation of the solid oxides,[2] and the dissociation energy of O_2.[15] The results of these calculations give for the reaction

$$SrO(g)=Sr(g)+O(g),\ \Delta H_0=83.6\pm5 \text{ kcal/mole} \quad \text{or} \quad D_0(SrO)=3.6\pm2 \text{ ev.}$$

For the reaction

$$MgO(g)=Mg(g)+O(g),\ \Delta H_0<90 \text{ kcal/mole} \quad \text{or} \quad D_0(MgO)<3.9 \text{ ev.}$$

The present results yield a lower D_0 for MgO(g) than that obtained by Brewer and Porter[9] from total vapor pressure data. The total pressure over MgO(s) may be high because of production of Mg gas by reduction of MgO(s). This was shown by the fact that $Mg^+ \gg O_2^+$. These results, however, are not inconsistent with the spectroscopic work of Brewer and Porter.[9]

In Table II total SrO(s) vapor pressure data of other workers are compared with results obtained in this work. Within estimated probable errors the results obtained in this study agree with those of earlier workers. The present mass spectrometric results, however, are interpreted as showing that SrO(s) vaporizes mainly by decomposition to gaseous Sr and oxygen, not as SrO(g).

TABLE II. Comparison of total vapor pressure data for SrO(s).

Investigator	Total vapor pressure over SrO(s) at T=2100°K (atmos)	Remarks
Classen and Veenemans	4.2×10^{-5} [a]	Calculated as SrO(g)
Moore, Allison, and Struthers	2.5×10^{-5} [a]	Calculated as SrO(g)
This work	1.0×10^{-5} [b]	Calculated as Sr(g)

[a] Obtained by extrapolation of investigator's vapor pressure equation to T=2100°K.
[b] Equal ionization cross sections for Ag and Sr were assumed.

* This work was supported, in large part, by a grant from the National Science Foundation.

[1] G. Drummond and R. F. Barrow, Faraday Soc. **47**, 1275 (1951).
[2] L. Brewer, Chem. Revs. **52**, 1 (1953).
[3] A. Claasen and C. F. Veenemans, Z. Physik **80**, 342 (1933).
[4] Moore, Allison, and Struthers, J. Chem. Phys. **18**, 1572 (1950).
[5] R. H. Plumlee and L. P. Smith, J. Appl. Phys. **21**, 811 (1950).
[6] L. T. Aldrich, J. Appl. Phys. **22**, 1168 (1951).
[7] I. Pelchowitch, Philips Research Repts. **9**, 42 (1954).
[8] P. W. Bickel and L. V. Holroyd, J. Chem. Phys. **22**, 1793 (1954).
[9] L. Brewer and R. F. Porter, J. Chem. Phys. **22**, 1867 (1954).
[10] W. A. Chupka and M. G. Inghram, J. Phys. Chem. **59**, 100 (1955).
[11] Porter, Schissel, and Inghram, J. Chem. Phys. **23**, 339 (1955).
[12] G. Herzberg, *Molecular Spectra and Molecular Structure* (D. Van Nostrand Company, Inc., New York, 1950).
[13] K. K. Kelley, U. S. Bur. Mines Bull. 476 (1949) and U. S. Bur. Mines Bull. 477 (1950).
[14] L. Brewer, University of California Radiation Laboratory Report UCRL-2854, February, 1955.
[15] P. Brix and G. Herzberg, Can. J. Phys. **32**, 110 (1954).

Evaluation of Certain Three-Center Integrals*

J. R. STREETMAN
Department of Chemistry, The University of Texas, Austin, Texas
(Received May 9, 1955)

ONE-ELECTRON three-center integrals are usually evaluated by means of some kind of infinite expansion.[1-4] But if one center, B, is midway between the other two, the integral can be expressed (after integration over the angle ϕ) in terms of two coordinates.[3] For instance, an integral made up of hydrogen-like $1s$ orbitals, the two end orbitals being equivalent, can be written as

$$\frac{(z^3/z'^3)^{\frac{1}{2}}}{\pi}\int\frac{e^{-za}e^{-z'b}}{c}dV=\frac{R^2zz'}{2}\int_1^\infty\int_{-1}^1\exp\left(-\frac{z'R}{2}(f^2+g^2-1)^{\frac{1}{2}}\right)\times\exp\left(-\frac{zR}{2}(f-g)\right)(f-g)\,df\,dg,$$

where a, b, and c are the distances to centers A, B, and C and f and g are elliptical coordinates centered on A and C. R is the distance between A and C.

The fact that this integral can be expressed in terms of two coordinates implies that numerical integration might be practical. To investigate the difficulty and accuracy of such a numerical integration, this integral was evaluated for the special case $z=z'=1$, for which the value has been obtained in closed form.[1]

The numerical integration procedure used was a two-dimensional analog of one-dimensional trapezoid rule integration.[5] The area of integration was broken up into regions so as not to use

TABLE I.

Range of f	Increment (first program)	Increment (second program)	Contribution to integral (first program)	Contribution to integral (second program)	Improvement
1.0 to 2.1	0.1	0.05	0.203895	0.204147	0.000252
2.1 to 3.1	0.2	0.1	0.037295	0.037376	0.000081
3.1 to 4.1	0.25	0.125	0.007058	0.007100	0.000042
4.1 to 6.3	0.4	0.2	(estimated)	0.001451	0.00006

unnecessarily small increments anywhere. The regions used and the increments used in them are given in Table I. Each region included the full range of g and the increment was in each case the same for f and g. This numerical integration scheme was coded for and performed on an I.B.M. Card Programmed Electronic Calculator, requiring about a half-hour of machine time. To investigate the question of whether these increments were small enough, a second program was made using the same regions and increments half as large. The values of the integral obtained from each region are compared in Table I. This would seem to indicate that the first program used too large an increment in the first region, but that the increments used in the other regions were small enough. The value of the integral in the region beyond $f=6.3$ may be estimated[6] to be 0.0000229.

The value of the integral obtained was 0.50017 which may be compared with the value 0.50057 obtained in closed form.

Numerical integrations of this kind should be applicable not only to one-electron three-center integrals that arise in molecular calculations, but to the special one-electron three-center integrals into which certain two-electron three-center integrals can be broken down.[3]

The author wishes to express his thanks to Richard E. Tannich of the Humble Oil and Refining Company at Baytown, Texas, for his help in these computations.

* This work was supported by contract of the U. S. Office of Ordnance Research.

[1] J. R. Streetman and F. A. Matsen, J. Chem. Phys. **22**, 1366 (1954).
[2] C. A. Coulson, Proc. Cambridge Phil. Soc. **33**, 104 (1937).
[3] Roland S. Barker and Henry Eyring, J. Chem. Phys. **22**, 1177 (1954).
[4] Some special cases of these integrals can be evaluated in closed form. See, for example, Hirschfelder, Eyring, and Rosen, J. Chem. Phys. **4**, 121 (1936).
[5] Trazezoid rule integration is equivalent to the Euler-McLauren expansion up to the terms containing derivative.
[6] By taking advantage of the fact that the g cross section of the integrand surface is now so flat that it may be taken as a straight line. This means that the increment for g can now be taken from -1 to 1, thus covering the whole range of g. The integral can then be integrated directly in this region.

Simplified Calculation of Isotopic Exchange Half-Time

LEONARD R. DARBEE
Department of Chemistry, University of Buffalo, Buffalo 14, New York
(Received May 4, 1955)

THE kinetics of isotopic exchange reactions have been explained in detail.[1,2] Because there is no change in concentration of the reactants, many exchange reactions can be represented by one equation. The actual calculation of the exchange half-time, however, is time consuming. Simplification of these calculations can be accomplished by construction of an alignment chart.

If both (1) the isotope effect is negligible and (2), when there is more than one exchangeable atom in a molecular species, these atoms are kinetically equivalent; the kinetic equation reduces to the form

$$-\ln(1-\gamma)=R\cdot G(c)\cdot\Delta t, \quad \text{where} \quad \gamma=(F-I)/(E-I).$$

Here I, F, and E refer to initial, final, and equilibrium fractions of total activity in reactant B. The equilibrium fraction under conditions (1) and (2) assumes the statistical value $B/(AB)$. A and B are concentrations of reactants multiplied by the number of exchangeable atoms per molecule. R is the rate of the reaction, $G(c)$ is a function of concentrations, and Δt is the time between readings I and F.

Combining the rate equation for γ and $\gamma=0.5$ eliminates R and $G(c)$ yielding $t_{\frac{1}{2}}=[0.693/-\ln(1-\gamma)]\cdot\Delta t=T_f\cdot\Delta t$. A chart (Fig. 1) expressing T_f in terms of measured values enables ready calculation of $t_{\frac{1}{2}}$. Such a chart can be prepared easily, using standard principles of nomography.[3,4]

Example: Consider the equation $CX^*+DX_2\rightleftharpoons CX+DX_2^*$, with 0.01 m/l CX and 0.05 m/l DX_2. With initial fraction of activity in $DX_2=0.20$ and final fraction in $DX_2=0.40$ for a time

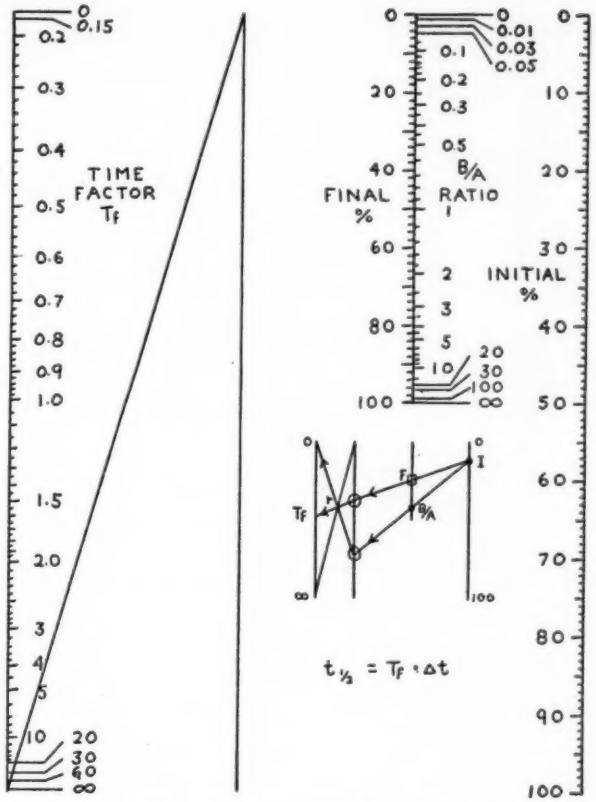

FIG. 1. Diagrammatic calculation of exchange half-time.

interval of five hours, use of the chart would be as follows. With a straight edge connect the initial value 20 percent through the B/A ratio 10 [i.e., $2(DX_2)/(CX)$] to give the first pivot point on the vertical unlabeled line. Connect this pivot point to 0 on the T_f scale and mark r on the slant line. Now, connect the initial value 20 percent through the final value 40 percent to get the second pivot point on the vertical line. This pivot point extended through r yields the multiplying factor 2.1 on the T_f scale. The half-time is therefore 10.5 hours. Exact calculation yields 10.41 hours.

This treatment is of particular value when the initial activity is not all in one component. It also provides a quick method to survey a large number of data.

[1] A. C. Wahl and N. A. Bonner, *Radioactivity Applied to Chemistry* (John Wiley and Sons, Inc., New York, 1951).
[2] G. M. Harris, Trans. Faraday Soc. **47**, 716 (1951).
[3] R. D. Douglass and D. P. Adams, *Elements of Nomography* (McGraw-Hill Book Company, Inc., New York, 1947).
[4] L. H. Johnson, *Nomography and Empirical Equations* (John Wiley and Sons, Inc., New York, 1952).

Values of Thermodynamic Functions to 12 000°K for Several Substances*

W. FICKETT AND R. D. COWAN
Los Alamos Scientific Laboratory, University of California, Los Alamos, New Mexico
(Received April 22, 1955)

IN calculating properties of the detonation products of condensed explosives, temperatures considerably above 5000°K are sometimes encountered. In order to carry out such calculations, values of thermodynamic functions are needed for the molecular species involved, but most presently available tables, such as those published by the National Bureau of Standards (NBS),[1] extend only to 5000°K.[2] We therefore have extended the

TABLE I.

T(°K)	H_2	CO	N_2	NO	O_2	C_2	CO_2	H_2O	C (graphite)
				$(H^0-H_0^0)/RT$					
3000						4.200			
3500						4.251			
4000						4.295			2.717
4500						4.334			2.806
5000	4.172	4.272	4.249	4.346	4.561	4.370	7.010	5.923	2.878
6000	4.274	4.327	4.306	4.398	4.654	4.439	7.160	6.085	3.011
7000	4.361	4.374	4.353	4.446	4.726	4.507	7.283	6.208	3.119
8000	4.437	4.422	4.397	4.492	4.784	4.574	7.388	6.306	3.217
9000	4.506	4.480	4.445	4.539	4.837	4.642	7.483	6.387	3.308
10 000	4.568	4.558	4.503	4.589	4.888	4.710	7.571	6.456	3.395
12 000	4.686	4.796	4.666	4.701	4.989	4.843	7.743	6.577	3.558
				S^0/R					
3000						34.219			
3500						34.922			
4000						35.536			7.136
4500						36.083			7.536
5000	26.721	35.254	34.397	36.989	36.746	36.578	44.183	37.782	7.901
6000	27.595	36.092	35.233	37.834	37.680	37.450	45.635	39.064	8.558
7000	28.351	36.809	35.947	38.556	38.475	38.207	46.879	40.159	9.117
8000	29.017	37.445	36.573	39.190	39.170	38.880	47.962	41.117	9.617
9000	29.616	38.027	37.141	39.757	39.789	39.491	48.946	41.969	10.070
10 000	30.160	38.580	37.668	40.274	40.351	40.051	49.833	42.740	10.487
12 000	31.128	39.667	38.662	41.200	41.349	41.054	51.410	44.099	11.236

NBS values to higher temperatures for a number of substances in the following approximate way.

Approximate values of the thermodynamic functions were computed over the range 3000–12 000°K. In general, the values calculated below 5000°K disagreed slightly with those of the NBS; the differences were plotted and extrapolated graphically to 12 000°K. Final values of the thermodynamic functions above 5000°K were then obtained by correcting our calculated results by the amounts of the extrapolated differences, thus producing a set of values which join smoothly on to those of the NBS. (The corrections were less than 2% in all cases except for the enthalpy of CO_2 and graphite, where they were 7 and 9%, respectively, at 12 000°K.)

Different approximations were used in calculating for the different types of molecular species. For the diatomic molecules, corrections for anharmonicity and stretching were included by means of the formulas given by Mayer and Mayer.[3] For the triatomic molecules a harmonic-oscillator, rigid-rotator model was used. For molecules of both types of gaseous species, several electronic levels were included.[4] For graphite, a two-dimensional Debye theory was employed,[5] and the results were found to be in fairly good agreement with the NBS values. The results are given in Table I.

Coefficients for least-square polynomial approximations of the form

$$(H^0-H_0^0)/RT=a+bT+cT^2+dT^3, \quad (1)$$

$$S^0/R=a\ln T+2bT+\tfrac{3}{2}cT^2+(4/3)dT^3+e, \quad (2)$$

are given in Table II for two ranges of temperature. The approximating expression for S^0/R was obtained from that for $(H^0-H_0^0)/RT$ by making use of the relation $TdS^0=dE^0+p^0dV=dH^0$; values of the integration constant e were determined so as to make the rms error as small as possible. The fits were made to overlapping ranges to ensure approximate continuity of slope, and the constant terms were then adjusted to produce continuity of the polynomials themselves at the dividing point of 3000°K.

This work is reported in greater detail in Los Alamos Report LA-1727, copies of which can be obtained from the Office of Technical Services, Department of Commerce, Washington 25, D. C.

* Work performed under the auspices of the U. S. Atomic Energy Commission.

[1] *Selected Values of Chemical Thermodynamic Properties*, Series III (loose-leaf), U. S. National Bureau of Standards.

[2] Thermodynamic functions have been calculated to 6000°K for a number of substances by a group at Ohio State University; see for example Belzer, Savedoff, and Johnston, Ohio State Univ. Research Foundation Tech. Rept. No. 316-6.

[3] J. E. Mayer and M. G. Mayer, *Statistical Mechanics* (John Wiley and Sons, Inc., New York, 1940), Chap. 7 and Appendix IX.

[4] Dr. Leo Brewer has recently pointed out to us the probable existence of several low-lying electronic levels in the C_2 molecule which were not included in our calculations. The lowest excited electronic level which we included was the $^3\pi_g$ at 19 306 cm^{-1}. The remarks in the preceding paragraph concerning the extrapolation do not apply to C_2; since the NBS, as far as we are aware, has not published values for C_2, the values in Tables I and II are the direct results of our calculations.

[5] J. Krumhansl and H. Brooks, J. Chem. Phys. **21**, 1663 (1953).

TABLE II. Coefficients of analytic fits.

Substance	a	$b\times10^4$	$c\times10^8$	$d\times10^{12}$	e	rms error Eq. 1, %	rms error Eq. 2, %
			Temperature range, 500 to 3000°K				
H_2	3.43328	−0.08171	9.6699	−14.4392	−3.84470	0.06	0.03
CO	3.31700	3.7697	−3.2208	−2.1945	4.63284	0.22	0.04
N_2	3.34435	2.9426	0.1953	−6.5745	3.75863	0.24	0.03
NO	3.50174	2.9938	−0.9588	−4.9036	5.11346	0.26	0.05
O_2	3.25304	6.5235	−14.9524	15.3897	5.71243	0.07	0.01
C_2	...	...	...	...	...	...	...
CO_2	3.09590	27.3114	−78.8542	86.6002	6.58393	0.30	0.06
H_2O	3.74292	5.6559	4.9524	−18.1802	0.96514	0.20	0.06
C (graphite)	−0.10076	22.4467	−70.2263	81.5223	0.06441	1.38	0.85
			Temperature range, 3000 to 12 000°K				
H_2	3.21299	2.87156	−2.28839	0.76656	−2.78598	0.08	0.03
CO	3.53114	2.73436	−3.27672	1.56492	3.41176	0.09	0.01
N_2	3.51443	2.58314	−2.84107	1.24154	2.74113	0.09	0.01
NO	3.74493	1.94975	−1.88284	0.77028	3.71329	0.10	0.07
O_2	3.55064	3.20312	−2.87575	1.00528	4.20945	0.04	0.01
C_2	3.85829	1.37009	−0.86238	0.33821	2.61129	0.08	0.01
CO_2	5.20816	5.90837	−5.61431	2.04685	−4.32923	0.20	0.06
H_2O	3.92119	6.58323	−6.21913	2.15227	−0.24234	0.20	0.19
C (graphite)	1.61766	3.84976	−3.21167	1.12812	−8.68850	0.22	0.66

Observation of the Semiquinone of Benzoquinone*

SCOTT BLOIS
W. W. Hansen Laboratories of Physics, and Department of Physics, Stanford University, Stanford, California
(Received April 12, 1955)

ALTHOUGH the hydroquinone-quinone reversible oxidation-reduction system forms the usual starting point for a discussion of the theory of semiquinone formation,[1] this particular free radical appears to have escaped observation[2] although duroquinone,[3] and phenanthrenequinone-3-sulfonate,[4] were demonstrated some years ago to form semiquinone free radicals. An observation on a paramagnetism in solid quinhydrone adsorbed on barium hydroxide has been recently reported by Bijl, Kainer, and Rose-Innes.[5]

The semiquinones of both *o*- and *p*-benzoquinone have recently been observed in this laboratory using an *X*-band paramagnetic resonance spectrometer and the resulting free radical concentrations have been found to be sufficiently small as to readily explain the failure to observe them through a measurement of paramagnetic susceptibility using magnetostatic methods.

The complete scheme proposed here for *p*-benzoquinone is indicated by Fig. 1. A similar scheme will account for the behavior of the *o*-benzoquinone, in which case the polymeric products are probably similar, if not identical with catechol melanin. It further suggests the role of an *o*-semiquinone in the formation of tyrosine melanin.

It is found that while a strongly alkaline solution (*p*H 10–11) increases the stability of the *p*-benzoquinone free radical, dimerization of this molecule is apparently quite favorable and the resulting concentration is small. An 0.075 M solution of hydroquinone was observed to produce an initial free radical concentration of the order of 10^{-5} M. This may be contrasted with phenanthrenequinone-3-sulfonate which Michaelis observed to form a semiquinone which constituted 44 percent of the original material. That the reaction proceeded steadily toward the fully oxidized form was shown by the behavior of the resonance signal which decreased as the dissolved oxygen in the sealed sample tube became exhausted as shown in Fig. 2 in which the derivative of the resonance is displayed repetitively in time. The envelope of these peaks is therefore the graph of free radical concentration as a function of time.

The same resonance and over-all process was observed by starting with solid quinhydrone which was dissolved in water and brought to *p*H 10. Free radical formation proceeded and a fine blackish insoluble material was formed, the latter appearing to be associated with the alkaline oxidation of all the quinoid materials we have studied. Since this pigment is formed under the conditions which optimize the semiquinone stability it appears probable

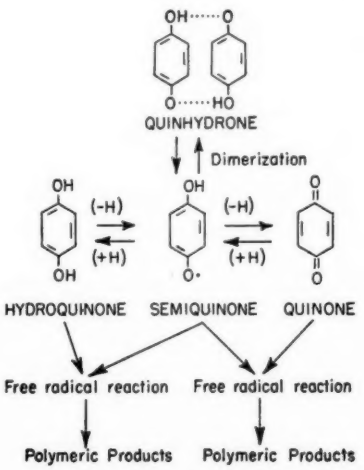

FIG. 1. Reaction scheme for alkaline oxidation-reduction of *p*-benzoquinone.

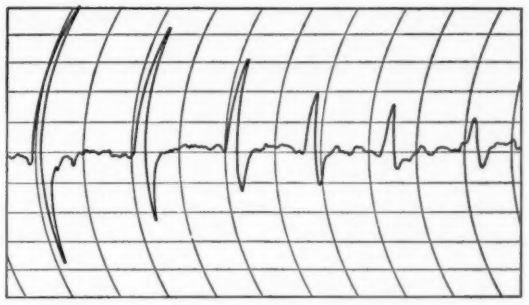

FIG. 2. Repetitive display in time (time scale: 2 divs. per min) of the differentiated absorption curve of *p*-benzoquinone with time increasing to the right. Maximum amplitude corresponds to a free radical concentration of the order of 10^{-5} M. The asymmetry of the resonances is due to a slight mistuning of the transmission cavity and is not a feature of the resonance of this molecule.

that it is a polymeric product of a free radical reaction. It may be noted that the free radical activity appears highest when the solution is a yellowish-brown and that as the pigmentation proceeds the free radical concentration diminishes.

An attempt was made to detect the *o*-semiquinone free radical by oxidizing an alkaline, aqueous solution of catechol and while this solution showed the same color changes and an almost instantaneous formation of the black pigment, no resonance could be detected by the time the sample could be examined in the spectrometer. However, by reducing *o*-quinone in alcohol with sodium hydrosulfite in the *p*H range 10–11, the free radical could be easily demonstrated. The free radical could not be found in the quinone solution prior to reduction, whence the concentration was at that time less than 10^{-7} M (the maximum sensitivity of the spectrometer).

The line widths observed (measured between the inflection points of the absorption curve were less than 10 gauss for both the *p*- and *o*-semiquinones, there being slight evidence for the latter being somewhat narrower. The spectroscopic splitting factors for both were essentially equal to 2.

I wish to thank Professor G. Pake and Dr. R. H. Sands for their courtesy in making the paramagnetic resonance spectrometer available to me.†

* This work was supported in part by the U. S. Atomic Energy Commission.

[1] See for example, P. W. Selwood, *Magneto chemistry* (Interscience Publishers, Inc., New York, 1943), p. 129.
[2] P. H. Hermans, *Theoretical Organic Chemistry* (Elsevier, Amsterdam, 1954), p. 470.
[3] Michaelis, Schubert, Reber, Kuck, and Granick, J. Am. Chem. Soc. **60**, 1678 (1938).
[4] Michaelis, Boeker, and Reber, J. Am. Chem. Soc. **60**, 202 (1938).
[5] Bijl, Kainer, and Rose-Innes, Nature **174**, 830 (1954).

† *Note added in proof.*—After submission of this letter, the report appeared by Venkataraman and Frenkel, J. Chem. Phys. **23**, 588 (1955), on their observation of the semiquinone of *p*-benzoquinone. The reported hyperfine structure has not been observed to date with the aqueous solutions we have used.

Infrared Absorption Spectrum of Deuterated Polyvinyl Alcohol Film

HIROYUKI TADOKORO, SYŪZŌ SEKI, AND ISAMU NITTA
Department of Chemistry, Faculty of Science, Osaka University, Osaka, Japan
(Received May 6, 1955)

IN a previous paper[1] we studied the density, the sorption of water vapor, and the infrared absorption spectrum of polyvinyl alcohol (PVA) films subjected to heat treatments at different temperatures from the point of view of the crystallinity, and concluded that[1] the results of these three methods as well as of the x-ray method are approximately in linear relationship unless the thermal decomposition is not considerable, and they may be used as measures of the crystallinity, and[2] the 1146 cm^{-1} (8.74μ) band is a crystallization-sensitive band. On the other hand, on the

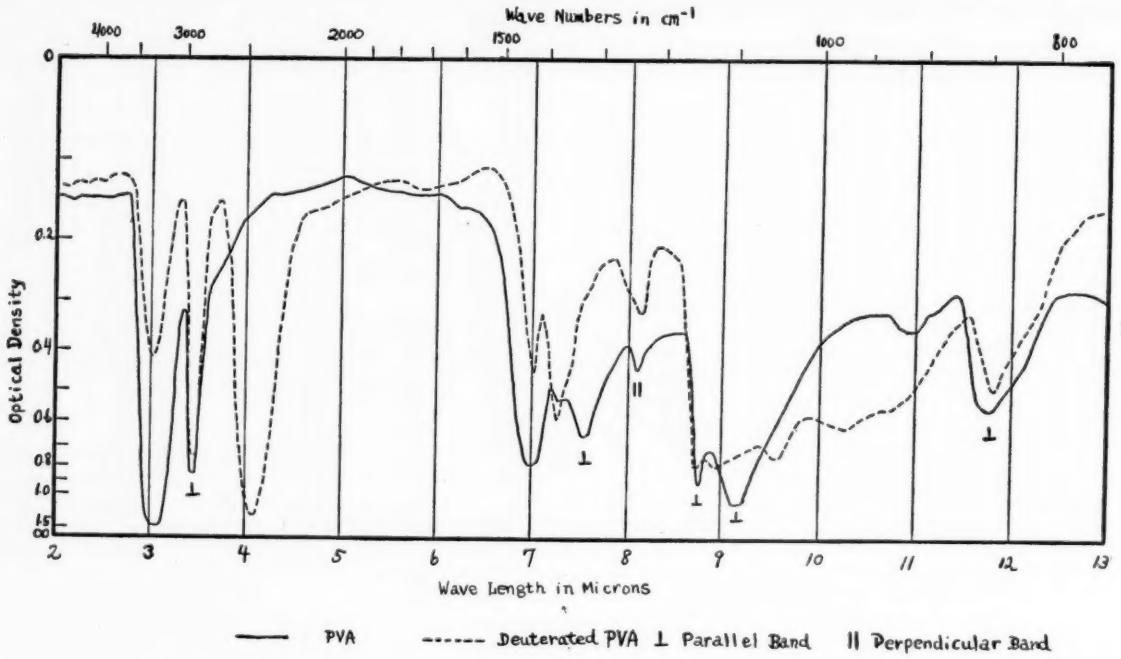

FIG. 1.

absorption bands of this material in the region of 1500∼800 cm^{-1}, various ways of assignment have been proposed.[2] For the purpose of elucidating the nature of crystallinity or accessibility as well as making contribution on the unsettled problem of the assignment of these bands, we have preliminarily investigated the infrared absorption spectrum of the deuterated PVA film.[3]

The obtained spectra of a PVA film both before and after deuteration in vapor phase of D_2O are reproduced in Fig. 1. The degree of deuteration was estimated to be 77 percent from the diminution of the optical density of the ν(O−H) band (3300 cm^{-1}).[4] On deuteration the strength of the absorption of this band decreases, but the band does not show any fine structures, as in the case of cellulose where new four distinct bands appear.[5]

Although the 1430 cm^{-1} band was assigned as δ (C−H) by Thompson *et al.*, and Blout *et al.*,[2] this band should be a superposition of δ(C−H) and some other band connected with OH group, since this band decreases sensitively on deuteration and there remains a sharp band which is to be properly attributed to the δ(C−H). In this respect the suggestion by Elliott *et al.*,[2] may be regarded to be ascertained. The perpendicular 1330 cm^{-1} band should be also related to the OH group from the decrease on deuteration, whereas Elliott *et al.*,[2] assigned to this band merely a hydrogen deformation mode. Just in the middle (1380 cm^{-1}) of the aforementioned two bands, a very strong and sharp band appears on deuteration. This fact suggests that the former bands are connected with the coupling of some modes such as δ(C−H) and δ(O−H).

The parallel 1230 cm^{-1} band may be the result of the CH_2 wagging in contrast to the assignments by Thompson *et al.*, and Elliott *et al.*[2]

Although the crystallization-sensitive band (1146 cm^{-1}) does not change appreciably on deuteration, the perpendicular 1093 cm^{-1} band decreases considerably. The latter is undoubtedly connected with OH groups, and is supposed to be ν(C−OH) as has been previously pointed out by Blout *et al.*, as well as by Elliott *et al.*[2] These two bands somewhat remind us of their resemblance to the 730 cm^{-1} and 720 cm^{-1} bands of polyethylene which have been utilized to estimate the crystallinity.[6] The 1050 cm^{-1} band in deuterated PVA may be assigned to be ν(C−OD). The perpendicular 851 cm^{-1} band remains almost unchanged on deuteration, so this is evidently independent of OH group, and is connected with CH_2 group or skeletal vibration.

The authors express their sincere thanks to Professor S. Mizushima and the members of his laboratory of the University of Tokyo for helpful advice and criticism, to M. T. Kanzawa and Mr. H. Kamio of Takeda Pharmaceutical Industries, Ltd., as well as Dr. M. Momotani of Momotani Juntenkan Company, Ltd. for preparing the infrared absorption spectra, and to Kurashiki Rayon Company, Ltd. for kindly giving them the PVA samples.

[1] Tadokoro, Seki, and Nitta, Bull. Chem. Soc. Japan (1955) (to be published).

[2] H. W. Thompson and P. Torkington, Trans. Faraday Soc. **41**, 246 (1945). E. R. Blout and R. Karplus, J. Am. Chem. Soc. **70**, 862 (1948). Elliott, Ambrose, and Temple, J. Chem. Phys. **16**, 877 (1948). Nishino, Ukita, and Kominami, J. Chem. Soc. Japan, Ind. Chem. Sect. **58**, 159 (1955). Nagai, Mima, Kuribayashi, and Sagane, Discussion Meeting of the High Polymers, Kyoto, Japan, Nov. 9, 1954.

[3] As to the infrared absorption spectrum of deuterated PVA, Ukita *et al.*, have recently pointed out merely the new appearance of broad band of 4.01μ [Ukita, Nishino, and Kominami, J. Chem. Soc. Japan, Ind. Chem. Sect. **58**, 158 (1955)].

[4] All the wave numbers given below refer to the ordinary PVA bands.

[5] H. J. Marrinan and J. Mann, J. Appl. Chem. (London) **4**, 204 (1954).

[6] S. Krimm, J. Chem. Phys. **22**, 567 (1954); R. S. Stein and G. B. B. M. Sutherland, *ibid.* **22**, 1993 (1954); A. Keller and I. Sandeman, J. Polymer Sci. **15**, 133 (1955).

Ionization Potentials and Charge-Transfer Spectra of Substituted Benzenes

L. E. ORGEL

Laboratory of Molecular Structure and Spectra, Department of Physics, The University of Chicago, Chicago, Illinois

(Received May 6, 1955)

THE degeneracy of the $^2E_{1g}$ ground state of the benzene positive ion is removed by suitably arranged substituents, so that two ionization potentials I_1 and I_2 exist in place of the one, I_B, of benzene. They have, to a first approximation, the values

$$I_{1,2}=I_B-n\gamma_S-p_{1,2}\epsilon_S, \tag{1}$$

where γ_S and ϵ_S are a pair of parameters characteristic of a substituent S, n is the number of times the substituent S occurs, and p_1 and p_2 are two numbers derived from perturbation theory. They have the values given in Table I.

Table I. p_1 and p_2 for substituted benzenes.

Positions of substitution	—	1	1,2	1,3	1,4	1,2,3	1,2,4	1,2,5	1,2,3,4	1,2,3,5	1,2,4,5	1,2,3,4,5	1,2,3,4,5,6
p_1	0	1	3/2	3/2	2	3/2	2.37	3/2	5/2	5/2	3	3	3
p_2	0	0	1/2	1/2	0	3/2	0.63	3/2	3/2	3/2	1	2	3

The charge-transfer spectra of the complexes of chloranil with polymethylbenzenes show slight evidence of double bands in the case of the 1,4; 1,2,4 and 1,2,4,5 derivatives,[1] just those for which the biggest splitting is predicted. In Fig. 1(a) we show ν_R the lower frequency at which the intensity of absorption has half its maximum value, together with the values of I_1 predicted from formula (1). The parameters have been adjusted to give the best fit by using $\gamma_{Me}=610$ cm^{-1} and $\epsilon_{Me}=1760$ cm^{-1}. If the absorption maxima of halogen complexes are plotted in the same way the results are very different.[2,3] There is now a good correlation with I_2 but none with I_1 [Fig. 1(b)]. The general agreement is not very important since ϵ_{Me} has been chosen to fit the data, but the correlation between the variations within the triads with the same n is very good. The less complete information on the complexes of ethyl benzenes with iodine monochloride[3] confirms that this correlation is not accidental.

A number of authors have emphasized the relationship between the ionization potential of a donor and the wavelengths of the absorption maxima of the complexes which it forms.[4–6] We believe that our results show that the visible bands of chloranil

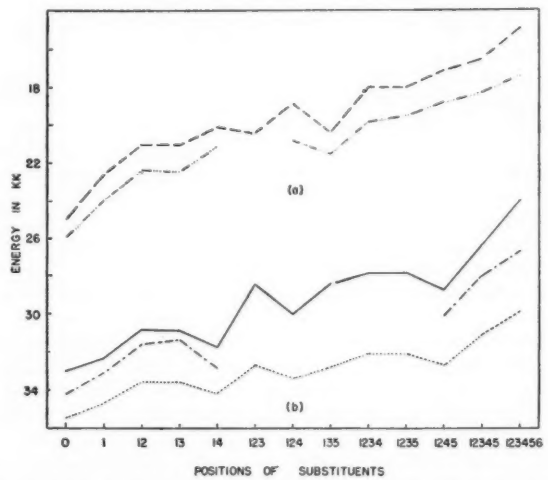

FIG. 1. (a) Ionization potentials I_1 — — — —; energies of charge-transfer transitions for chloranil complexes as defined in text —·—·—·—. (b) Ionization potentials I_2 ————; energies of absorption maxima for iodine complexes — — — —; energies of absorption maxima for iodine monochloride complexes – – – – – –.

complexes with alkyl benzenes are generally composite, consisting of two overlapping charge-transfer bands. The bands of the halogen complexes may also be composite, but if so the component at the shorter wavelength is invariably the more intense.

Much larger splittings of the E_{1g} degeneracy in aromatic amines, phenols, etc., are to be expected. The positions of the two widely separated new bands observed in the complexes of dimethylaniline with chloranil, of *o*-diamino benzene with trinitrobenzene[7] and of anisole with iodine[8] all agree well with the theoretical predictions. Equation (1) can easily be extended to systems with two or more different substituents, and then accounts quite well for the spectra of the complexes of chloranil with substituted anilines.

It should be noted that the electron removed from the substituted benzene in the course of the lowest energy transition is not localized on the carbon atoms of the ring but, particularly in amines, is partly on the substituents. This is not true of the electron removed in the other transition.

The details of this theory and the discussion of its significance in determining the orientation of molecular complexes in solution and the nature of the intermolecular forces involved as well as in estimating ionization potentials of substituted benzenes will be submitted for publication in due course.

The author is indebted to Dr. L. J. Andrews and his collaborators for making available a manuscript prior to its publication.

[1] N. Smith, thesis, The University of Chicago, 1954.
[2] R. M. Keefer and L. J. Andrews, J. Am. Chem. Soc. **74**, 4500 (1952).
[3] Ogimachi, Andrews, and Keefer, J. Am. Chem. Soc. (to be published).
[4] R. S. Mulliken, J. Am. Chem. Soc. **74**, 811 (1952).
[5] McConnell, Ham, and Platt, J. Chem. Phys. **21**, 66 (1953).
[6] Hastings, Franklin, Schiller, and Matsen, J. Am. Chem. Soc. **76**, 2900 (1953).
[7] A. Bier, thesis, Amsterdam, 1954.
[8] P. de Maine (unpublished work).

Rate of the Gaseous Reactions, $X^+ + YH = XH^+ + Y$

D. P. STEVENSON AND D. O. SCHISSLER
Shell Development Company, Emeryville, California
(Received April 18, 1955)

THE occurrence of secondary reactions between ions and neutral molecules in the ionization chambers of mass spectrometers has been long recognized as a potential source of errors in analytical mass spectrometry.[1,2] However, no study of these reactions with respect to their collision cross sections has been reported. This note presents a preliminary report on studies of the cross sections of the "onium ion" forming reactions,

$$D_2^+ + D_2 = D_3^+ + D \quad (1)^3$$

$$A^+ + H_2 = AH^+ + H \quad (2)^4$$

$$CD_4^+ + CD_4 = CD_5^+ + CD_3. \quad (3)^5$$

Ions are formed in a mass spectrometer ion source in a well-defined region at a distance, s, from the first slit of the ion beam accelerating-collimating system. The ions are impelled toward this slit by a uniform electric field and reach the slit with a kinetic energy, $esE_d/300$, where e is the electronic charge and E_d is the impelling field gradient in volts/cm. During this preliminary acceleration the ions travel through the gas (concentration, c_x and/or c_{yh}, molecules/cm^3) from which they were formed. For low conversions the yield of ion-molecule reaction products is,

$$i_{xh}^+ = Qi_x^+ sc_{yh}, \quad (4)$$

where the i^+ are currents of the indicated ions, and Q is the reaction cross section. The mass spectrometrically measured quantity is i_{xh}^+/i_x^+.

We found for reactions, (1), (2), and (3) the cross section, Q, is of the form $B(E_d)^{-\frac{1}{2}}$, ($sE_d \geqslant 0.3$ volt), and that B is temperature independent. In reaction (2) B is inversely proportional to the square root of the mass of the hydrogen molecule (through measurements in HD and D_2).

Since the average speed ($\bar{v}$) with which the ions traverse the distance, s, is proportional to $(E_d)^{\frac{1}{2}}$, Eq. (4) can be rewritten,

$$i_{xh}^+ = d(XH^+)/dt = ki_x^+(s/\bar{v})c_{yh} = kc_x^+ c_{yh}, \quad (5)$$

where k equals $B(600 \cdot m_x/es)^{\frac{1}{2}}$, and may be considered to be the specific rate of the bimolecular-ion-molecule reaction. The relation

TABLE I. Specific rates of the reactions $X^+ + YH = XH^+ + Y$.

Reaction	$k \times 10^9$ cm³/molecule second
$D_2^+ + D_2 = D_3^+ + D$	1.4₄
$A^+ + H_2 = AH^+ + H$	1.8₉
$A^+ + HD = AH^+ + D$	0.6₉
$A^+ + DH = AD^+ + H$	0.7₉
$A^+ + D_2 = AD^+ + D$	1.4₀
$CD_4^+ + CD_4 = CD_5^+ + CD_3$	1.3₈

between concentration of gas in the ion source and the controllable quantity of gas flowing through it was established by measuring the total (+) ion current generated in the ionization chamber by a known current of ionizing electrons in gases of known total ionization cross section.[6]

The specific rates, k, calculated for the reactions from the B's, and the concentrations are given in Table I. The repeatability of the k's is ±2 percent; while systematic errors in absolute calibrations are believed to be less than 10 percent.

The magnitudes of the k's and their temperature independence indicates the reactions take place at every collision and the collision areas for the reactions are about three times greater than ordinary kinetic theory collision areas. It is of particular interest to note that Eyring, Hirchfelder, and Taylor[7] derived from the absolute theory of reaction rates not only the correct form of the rate constants of such reactions as far as dependence on temperature and mass are concerned, but also the correct magnitude for the rate (for $H_2^+ + H_2 = H_3^+ + H$).

By means of measurements of the appearance potentials of the rare gas onium-ions, AH^+ and KrH^+, it has been proved that both are formed exclusively by the reaction of the rare gas ion with a neutral hydrogen molecule. From the absence of activation energy of these reactions, the ionization potentials of krypton (14.0 ev) and hydrogen atoms (13.6), and the dissociation energy of hydrogen (4.5), it follows that the proton affinity of the krypton atom is greater than 4.0 ev. Similarily, the proton affinity of methane is found to exceed 5.0 ev.

[1] Bleakney and Gould, Phys. Rev. **44**, 265 (1933).
[2] Washburn, Berry, and Hall, Mass Spectrometry in Physics Research, Natl. Bur. Standards Circ. 522, p. 141.
[3] H. D. Smyth, Revs. Modern Phys. **3**, 347 (1931).
[4] Norton, Mass Spectrometry in Physics Research, Natl. Bur. Standards, Circ. 522, p. 201.
[5] This reaction, first discovered by G. C. Eltenton (these laboratories, unpublished research, 1940) is more convenient than the one involving CH_4 because there is no interference between the product ion CD_5^+ and the $C^{13}D_4^+$ as is the case for CH_5^+ and $C^{13}H_4^+$.
[6] Massey and Burhop, *Electronic and Ionic Impact Phenomena* (Oxford University Press, New York, 1952), p. 38. The gases were helium, neon, and argon.
[7] Eyring, Hirschfelder, and Taylor, J. Chem. Phys. **4**, 479 (1936).

Infrared Absorption Spectra of Hexammine Metal Complexes

MASAHISA KOBAYASHI AND JUNNOSUKE FUJITA
Department of Chemistry, Faculty of Science, Osaka University, Nakanoshima, Osaka, Japan
(Received April 29, 1955)

RECENTLY the near infrared absorption spectra of Co(III-ammine complexes were reported, but the effects of coordi)nation on the vibrations in a ligand group, or the interpretations about the new bands which appear by complex formation, have not been sufficiently studied. In this letter, we report the measurements of the absorption spectra of hexammine Co(III), Cr(III), and Ni(II) complexes, and discuss the results obtained.

TABLE I. Positions of absorption maxima (cm^{-1}).

$[Ni(NH_3)_6]Cl_2$	682	1172	1606	3320
$[Cr(NH_3)_6]Cl_3$	762	1307	1623	3120
$[Co(NH_3)_6]Cl_3$	830	1325	1610	3080

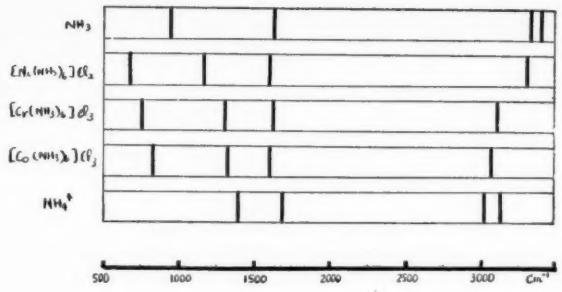

FIG. 1.

The infrared absorption spectra of $[Co(NH_3)_6]Cl_3$, $[Cr(NH_3)_6]Cl_3$, and $[Ni(NH_3)_6]Cl_2$ powders were measured by mulling in Nujol over the range 2 to 15 microns with a Perkin-Elmer Model 21 spectrophotometer, and four prominent bands are found in the spectrum of each complex (Table I). Observed strong bands at about 3000 cm^{-1} for each complex may arise from N−H stretching vibration. On the formation of the H_3N-metal bond, there is considerable shift of the N−H stretching vibration frequency in NH_3. In this case, it is to be expected that the more covalent character of the N-metal bond results in the lower frequency of the N−H stretching vibration.

In fact, comparing these N−H frequencies of the complexes with that of ammonia vapor and NH_4^+ ion which forms the strongest covalent bond H_3N-H^+, it is seen that N−H frequencies of these complexes lie in the region between that of free NH_3 and NH_4^+. The shifts of N−H frequencies to longer wavelength increase in the order of Ni, Cr, Co, as shown in Fig. 1, whereas the stability of the complexes increases in reverse order of them.

Figure 1 shows also that the other bands of the complexes have the different kinds of shift: peaks at about 1300–1200 cm^{-1} shift to higher frequency, in going from NH_3 to NH_4^+, while peaks at 1600 cm^{-1} hardly show any marked shift. These two bands of each complex correspond to the frequencies of free NH_3 and NH_4^+, so we assigned them to the NH_3 group deformation or N−H bending vibrations. This assignment is in disagreement with Hill's[1] estimation. Besides the above bands, there is still a band for each complex: 682 cm^{-1}, 786 cm^{-1}, and 830 cm^{-1} for Ni, Cr, and Co complexes, respectivelv, which does not appear in NH_3 or NH_4^+.

These bands of the lowest frequencies seem to be interpreted as NH_3 deformation vibration,[2] for the symmetry of NH_3 is lowered by coordination to the metal ion. However, this new band has high intensity, and its frequency for each complex decreases systematically. As is shown in Fig. 1, the most stable complex $[CO(NH_3)_6]Cl_3$ shows a peak at the highest frequency side, the most unstable complex $[Ni(NH_3)_6]Cl_2$ a peak at the lowest, and $[Cr(NH_3)_6]Cl_3$ a peak between them. From these experimental facts, it is possible to assign the bands to N-metal stretching vibration, that is, a complex radical vibration. Then the N-metal stretching force constants, assuming NH_3 as one group, are calculated approximately and the results are as follows:

Ni−N	3.62×10^5 dyne/cm
Cr−N	4.38
Co−N	5.36.

These values are reasonable as compared with those of the other compounds.

As is well known, XY_6 molecule with octahedral symmetry [Oh] has the two infrared active vibrations. Therefore, we may estimate that the bands at 830 cm^{-1}, 786 cm^{-1}, and 680 cm^{-1} for $[Co(NH_3)_6Cl_3$, $[Cr(NH_3)_6]Cl_3$, and $[Ni(NH_3)_6]Cl_2$, respectively, correspond to one of these two vibrations. The other infrared active band of each complex radical was not observed, but we expect them in longer wavelength regions.

[1] D. G. Hill and A. F. Rosenberg, J. Chem. Phys. **22**, 148 (1954).
[2] J. P. Faust and J. V. Quagliano, J. Am. Chem. Soc. **76**, 5346 (1954).

Proof of the Staggered Configuration of Ethyl Chloride*

R. S. WAGNER AND B. P. DAILEY
Department of Chemistry, Columbia University, New York 27, New York
(Received May 2, 1955)

IT has been generally accepted that the stable configuration of molecules similar to ethane is the staggered one. This is indicated, at least indirectly by the zig-zag configuration of paraffin molecules in the crystalline state, the greater stability of the rigid isomer of cyclohexane, the nonplanar structure of cyclopentane, and by the molecular vibrational spectrum of ethane.[1] It still may be of interest, however, to note that the microwave spectrum of CH_2DCH_2Cl may be used to demonstrate quite directly that ethyl chloride has the staggered configuration.

The addition of DCl to ethylene results in the formation of two molecular species, both having the structural formula CH_2DCH_2Cl. One deuterated species contains the deuterium in the plane of symmetry of the molecule and is termed *trans* in this letter, since it is diagonally opposite the chlorine atom in the symmetry plane. The other species is called *cis* and has the deuterium atom occupying either of two equivalent positions not in the symmetry plane.

TABLE I. Structural parameters for CH_2DCH_2Cl.

C−C	1.5508 A	
C−H	1.101 A	(−CH_2Cl end)
C−H	1.110 A	(−CH_2D end)
C−D	1.09 A	
C−Cl	1.7770 A	
C−C−Cl	110° 30′	
H−C−H	110° 13′	(−CH_2Cl end)
H−C−H	110°	(−CH_3 end)

Although this is not true for ordinary ethyl chloride, the moments of inertia of these two forms of CH_2DCH_2Cl depend to a significant extent on whether they are in the staggered or eclipsed configuration. Since microwave data allow a very accurate determination of the moments of inertia they may be used to establish the equilibrium configuration of the molecule directly.

For the purpose of distinguishing between the eclipsed and staggered configurations the structural parameters of CH_2DCH_2Cl are sufficiently well determined by the moments of inertia obtained for normal ethyl chloride[2] and by a consideration of the structures obtained from microwave data on similar molecules. The molecular parameters given in Table I were used to calculate the moments of inertia of *trans* CH_2DCH_2Cl in the eclipsed and staggered configurations. In Table II the observed rotational constants for the *trans*-isomer are compared to the values calculated for the *trans*-isomer in the staggered configuration. Good agreement is obtained. When the rotational constants for the *trans*-isomer in the eclipsed configuration are calculated they are found to be approximately 160 Mc larger than those given in Table I. This is a rather sizeable difference and no reasonable change in molecular parameters would produce agreement between observed and calculated rotational constants for the eclipsed configuration.

TABLE II. Rotational constants for CH_2DCH_2Cl.

		Calculated rotational constants	Observed rotational constants
$CH_2DCH_2Cl^{35}$ (*trans*)	*B*	5102.87 Mc	5098.76 Mc
	C	4638.30	4637.54
$CH_2DCH_2Cl^{37}$ (*cis*)	*B*	5296.72	5297.61
	C	4784.11	4784.83

* This research was supported by the United States Air Force through the Office of Scientific Research of the Air Research and Development Command.

[1] L. I. Osterhoof, Disc. Faraday Soc. **10**, 79 (1951).
[2] R. S. Wagner and B. P. Dailey, J. Chem. Phys. **22**, 1459 (1954).

Absorption Spectrum of Polyethylene in the Near Infrared

KURT ROSSMANN
Department of Physics and Astronomy, The Ohio State University, Columbus, Ohio
(Received April 19, 1955)

BECAUSE of the ever increasing use which industry makes of polyethylene, it is of importance to understand better the details of its molecular structure. To this end a study of the infrared absorption spectrum is valuable. In the course of an investigation regarding the adherence of printing ink to polyethylene surfaces,[1] an absorption spectrum was observed which reveals considerably more detail than the spectra reported earlier by other investigators.[2,3] This new information has been obtained by the use of a larger thickness (0.6 mm) of polyethylene film (Du Pont, Ala 10) in conjunction with a Beckman IR-3 spectrophotometer. A useful feature of this instrument is the presence of an auxiliary gain control which makes it possible to double or quadruple the gain in the chart recorder; this allows runs, which would otherwise be referred to 50 or 25 percent of the chart scale, to be expanded to occupy full chart width.

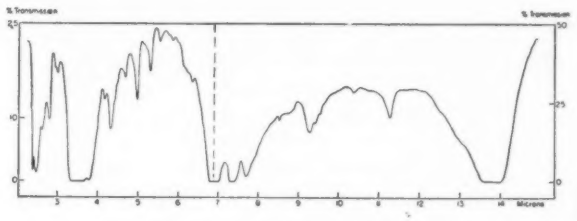

FIG. 1.

The absorption spectrum is shown in Fig. 1. The indicated transmission has not been corrected to take account of the strong scattering occurring in the sample. Measured wavelength positions of the absorptions are given in Table I together with the assignments[4,5] of the eight bands reported earlier by other investigators. The five strongest bands were remeasured during this investigation by using a thinner sample (0.03 mm). Of the newly observed absorptions only a few can be assigned tentatively. The line at 2.96μ might be attributed to the presence of hydroxyl (O−H) groups[6] in the molecule; those at 5.85 and 8.50μ have been observed previously[2] in oxidized polyethylenes and have been associated with carbonyl (C=O) groups and carboxyl (C−O) groups, respectively. Their occurrence in the ordinary polyethylene mole-

TABLE I. Near infrared absorption bands of polyethylene.

Wavelength (microns)	Assignment
2.20	
2.24	
2.33	
2.53	
2.78	
2.97	
3.48	CH_2 stretching
4.13	
4.26	
4.60	
4.91	
5.24	
5.49	
5.85	
6.10	
6.25	
6.82	CH_2 bending
7.26	CH_2 bending
7.66	CH_2 wagging
8.50	
9.24	CH_2 bending
10.32	
11.26	CH_2 bending
13.70	CH_2 rocking
13.88	CH_2 rocking

cule may be explained by the introduction of oxygen during the polymerization process. The absorptions at 6.10 and 6.25μ can be associated with the presence of C=C groups[5] due to incomplete elimination from the original ethylene molecule. This absorption has been observed in the spectrum of cracked polyethylenes.[2]

It is hoped that the assignment of the remaining absorption bands will aid in the further investigation of the molecular structure and of the properties of polyethylene.

I wish to thank the Shellmar Corporation in Mt. Vernon, Ohio, for having supplied the polyethylene samples.

[1] Thesis presented in partial fulfillment of the requirements for the degree Master of Science (1954).
[2] H. W. Thompson and P. Torkington, Proc. Roy. Soc. (London) **A184**, 3 (1945).
[3] J. J. Fox and A. E. Martin, Proc. Roy. Soc. (London) **A157**, 961 (1940).
[4] H. W. Thompson and P. Torkington, Trans. Faraday Soc. **41**, 246 (1945).
[5] H. A. Stuart, *Die Physik der Hochpolymeren I* (Springer Verlag, Berlin, 1952), p. 558.
[6] W. R. Brode, *Chemical Spectroscopy* (John Wiley and Sons, Inc., New York, 1943).

Linear Association in Solution. II. Analytical Solution

ROBERT GINELL AND JOEL SHURGAN
Department of Chemistry, Brooklyn College, Brooklyn, New York
(Received April 29, 1955)

IN a recent paper[1] (hereafter called I) we developed graphical methods for determining the values of the two constants in the case of linear association and gave an example showing its application. In this note we shall develop an analytical way of solving for the two constants which avoids any of the graphical computations and shows its application to the same example.

The basic equations for linear association (Eqs. (5a), (5b), and (11b) of I) are

$$\sum_{x=1}^{\infty} n_x = \frac{n_1(2+D_n n_1)}{2(1-K_{1j}' n_1)}, \tag{1}$$

$$\sum_{x=1}^{\infty} x n_x = \frac{2\sum_{x=1}^{\infty} n_x + D_n n_1^2}{2(1-K_{1j}' n_1)} \tag{2}$$

$$B_n = \sum_x x n_x - \sum_x n_x = \frac{K_{11}' n_1^2}{2(1-K_{1j}' n_1)^2}. \tag{3}$$

Further, Eq. (12h) of I can be written as

$$n_1 = \frac{\sum_x n_x - B_n}{1-K_{1j}' B_n}. \tag{4}$$

By substituting Eq. (4) in Eq. (3) and simplifying we get

$$B_n = \frac{K_{11}'}{2} \frac{(\sum_x n_x - B_n)^2}{(1-K_{1j}' \sum_x n_x)^2}, \tag{5}$$

which upon further simplification yields

$$K_{1j}' + (K_{11}')^{\frac{1}{2}} \left(\frac{\sum_x n_x - B_n}{\sum_x n_x (2B_n)^{\frac{1}{2}}} \right) = \frac{1}{\sum_x n_x}. \tag{6}$$

If now the experimental data can be adequately represented by the two constant linear theory then K_{1j}' and K_{11}' will be truly constant as the concentration is varied. Hence Eq. (6) will be the equation of a straight line in the variables $1/\Sigma n_x$ and $\{[\Sigma n_x - B_n]/\Sigma n_x (2B_n)^{\frac{1}{2}}\}$ with $(K_{11}')^{\frac{1}{2}}$ being the slope and K_{1j}' the intercept. The applicability of the theory can hence be readily checked and further, and more important, the method of least squares can be applied to the data so as to determine the constants K_{1j}' and K_{11}' unambiguously without putting any reliance on graphical methods as in I. In any graphical solution of this sort where we first determine one constant graphically and from its value determine the second constant analytically, the experimental error is not equally minimized but is placed in the larger part on the second constant. Nontheless if sufficient accurate data is available and the graphical work is carried out carefully the results are meaningful.

TABLE I.

	Graphical computation, "paper I"	Least squares, "this paper"
K_{e1j}'	0.7420	0.7434 ± 0.0418
K_{e11}'	0.2865 ± 0.0617	0.2812 ± 0.0200

We have recomputed the case of phenanthrene in ethanol given in I by this analytical method and a comparison of the values with those of I are presented in Table I.

As can be seen the values of the constants are very close, but the error in the second constant has diminished. The change of the value of the constants has no perceptible effect on the illustrative graph in I. This method is, however, of great help in cases where the data is not so exact and hence does not lend itself to an unambiguous graphical solution.

[1] R. Ginell and J. Shurgan, J. Chem. Phys. **23**, 964 (1955).

Vibrational Energy of Deuterium Cyanide*

HARRY C. ALLEN, JR., EUGENE D. TIDWELL, AND EARLE K. PLYLER
National Bureau of Standards, Washington, D. C.
(Received May 2, 1955)

THE infrared spectrum of deuterium cyanide has been observed under high resolution from 1900 cm^{-1} to 8000 cm^{-1}. Rotational structure has been observed for fifteen bands, and Q branches of very weak bands have been observed in five other cases. These bands prove sufficient to evaluate all the constants in the quadratic expression for the vibrational energy in terms of the vibrational quantum numbers. The resulting energy expression predicts all observed energy levels to better than 0.3 cm^{-1}. These constants are

$\omega_1^0 = 1932.99$ cm^{-1} $\quad X_{11} = -\ 7.40 \quad X_{12} = +\ 2.80$
$\omega_2^0 = \ 569.11 \quad\quad X_{22} = -\ 1.98 \quad X_{13} = -32.37$
$\omega_3^0 = 2650.48 \quad\quad X_{33} = -20.18 \quad X_{23} = -15.66 \quad g_{22} = 1.97.$

These constants are somewhat different from those predicted from the HCN spectrum by Douglas and Sharma[1] although the over-all agreement is quite good.

Recently, Checkland and Thompson[2] have measured some of the bands below 2700 cm^{-1}. Their analysis of the bands between 1900 cm^{-1} and 2700 cm^{-1} agrees very well with those made in this laboratory. In addition, the constants given above predict $\nu_2^1 = 569.10$ cm^{-1} and $2\nu_2^0 = 1130.30$ cm^{-1}. These values should be compared to Checkland and Thompson's measured values of $\nu_2^1 = 569.13$ cm^{-1} and $2\nu_2 = 1130.08$ cm^{-1}.

The zero-order frequencies, ω_e's, calculated from these constants together with those for HCN also deduced in this laboratory fit the isotope relations very well.

Additional bands are being measured in the spectrum of DCN, but there is no indication that the constants given above will need to be modified.

* Supported by the U. S. Atomic Energy Commission.
[1] A. E. Douglas and D. Sharma, J. Chem. Phys. **21**, 448 (1953).
[2] P. B. Checkland and H. W. Thompson, Trans. Faraday Soc. **51**, 1 (1955).

Reaction of Methyl Radicals with Methane and Ethane

M. H. J. WIJNEN
Division of Pure Chemistry, National Research Council, Ottawa, Canada
(Received April 21, 1955)

THE reaction of CD_3 radicals, obtained by photolysis of acetone-d_6, with ethane has been investigated over the temperature range 160 to 320°C. Some data on the reaction of CD_3 radicals with CH_4 were obtained at 320°C. If acetone-d_6 is photolyzed in presence of C_2H_6 or CH_4, the following reactions have been shown[1] to occur:

$$CD_3COCD_3+h\nu\rightarrow 2CD_3+CO$$
$$2CD_3\rightarrow C_2D_6 \quad (1)$$
$$CD_3+CD_3COCD_3\rightarrow CD_4+CD_2COCD_3 \quad (2)$$
$$CD_3+C_2H_6\rightarrow CD_3H+C_2H_5 \quad (3)$$

or

$$CD_3+CH_4\rightarrow CD_3H+CH_3. \quad (4)$$

From this mechanism it is clear that

$$k_3/k_2=\frac{R_{CD_3H}}{R_{CD_4}}\cdot\frac{(Ac-d_6)}{(C_2H_6)} \quad (I)$$

and

$$k_4/k_2=\frac{R_{CD_3H}}{R_{CD_4}}\cdot\frac{(Ac-d_6)}{(CH_4)}. \quad (II)$$

The acetone-d_6 contained 97 percent C_2D_6CO. Because of the presence of small fractions of not completely deuterated acetone, some CD_3H was produced when acetone was photolyzed alone. The amount of CD_3H thus produced was 4±1 percent of the amount of CD_4 produced.

Correcting for this in equation (I) and (II) we obtain

$$k_3/k_2=\left(\frac{R_{CD_3H}}{R_{CD_4}}-0.04\right)\frac{(Ac-d_6)}{(C_2H_6)}, \quad (Ia)$$

and

$$k_4/k_2=\left(\frac{R_{CD_3H}}{R_{CD_4}}-0.04\right)\frac{(Ac-d_6)}{(CH_4)}. \quad (IIa)$$

In Table I we give the results obtained for the reaction of CD_3 radicals with ethane and methane. In Fig. 1 we plotted $\log k_3/k_2$, obtained from Eq. (Ia), against $1/T$. From this we obtain $E_3-E_2=-0.1$ kcal, or accepting $E_2=11.3\pm0.3$ kcal[2] we obtain an activation energy of 11.2±0.3 kcal for the reaction of CD_3 radicals with ethane.

This activation energy is somewhat higher than the one previously reported by Trotman-Dickenson, Birchard, and Steacie who found $E_3=10.4$ kcal.[2] A possible source of error in their results, however, is the fact that the acetone-d_6, used in their experiments, contained only 68 percent C_2D_6CO.

TABLE I.

No.	$\frac{Ac-d_6}{C_2H_6}$	Temp °C	$\frac{R_{CD_3H}}{R_{CD_4}}$	k_3/k_2
		$CD_3+C_2H_6$		
1	0.925	224	1.071	0.954
2	1.125	224	0.856	0.918
3	1.117	274	0.867	0.925
4	1.029	162	0.992	0.980
5	1.553	162	0.668	0.976
6	1.730	328	0.568	0.913
7	1.135	341	0.892	0.967
8	1.249	310	0.797	0.945
No.	$\frac{Ac-d_6}{CH_4}$	Temp °C	$\frac{R_{CD_3H}}{R_{CD_4}}$	k_4/k_2
		CD_3+CH_4		
1	0.734	320	0.206	0.122
2	1.043	320	0.142	0.106
3	0.973	320	0.157	0.115

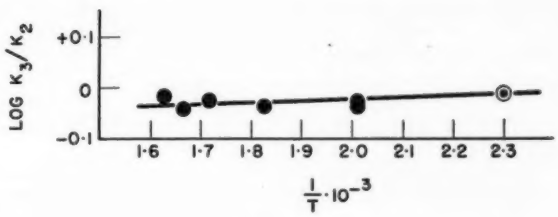

FIG. 1.

No accurate results could be obtained for the reaction of CD_3 radicals with CH_4 below 300°C. The results of three experiments carried out at 320°C are given in Table I. These results indicate that methyl radicals react about 8 times as fast with C_2H_6 as with CH_4 at 320°C. Assuming that the steric factors for both reactions would be of the same order of magnitude we obtain a value of about 13 kcal for the reaction of CD_3 radicals with methane.

[1] Trotman-Dickenson, Birchard, and Steacie, J. Chem. Phys. **19**, 163 (1951).
[2] M. H. J. Wijnen, J. Chem. Phys. **22**, 1075 (1954).

Gas Phase Oxidation of Formaldehyde

MILTON D. SCHEER
Aircraft Gas Turbine Division, The General Electric Company, Evendale, Ohio
(Received April 22, 1955)

HORNER, Style, and Summers[1-3] have recently reported the results of a study of the gas phase photo-oxidation of formaldehyde. Except for the details of an initiating step, they conclude that both the photo and thermal oxidations proceed by the same radical chain mechanism. The mechanism they postulate involves the species H, HCO, HO_2, and an unspecified radical R as the primary chain carriers. Chain termination is assumed to occur by destruction of R at the vessel walls. While the kinetic consequences of their scheme are in good agreement with their measured quantum yields of CO, H_2, and CO_2, it does not seem possible to reconcile their reaction scheme with the facts obtained by this author[4] in a recent study of the thermal oxidation in the region of 300 to 400°C.

These facts are as follows:

(A.) In the presence of mercury vapor and/or freshly cleaned silica surfaces:

(1) Simple pressure-time curves are observed, where

$$(dp/dt)_{initial}=(dp/dt)_{max}.$$

(2) The products are mostly CO and H_2O with small amounts of CO_2 and H_2 formed.

(3) The available analytical data shows that

$$\left(\frac{dp}{dt}\right)_{initial}=\frac{1}{2}\left(\frac{-d(CH_2O)}{dt}\right)_{initial},$$

and the governing rate law is given by

$$-\left(\frac{d(CH_2O)}{dt}\right)_{initial}=K_1(CH_2O)^2_{initial}.$$

(4) The addition of inert diluents are found to decrease the reaction rate.[5]

(B.) In the absence of mercury vapor, and in vessels which had been used without cleaning in many successive experiments:

(1) Pressure-time curves are observed which exhibit a decided convexity towards the time axis;

$$(dp/dt)_{max}>(dp/dt)_{initial}.$$

(2) In addition to the previously mentioned products, significant amounts of HCOOH, performic acid, and $(CH_2OH)_2O_2$ are formed.[4,6]

(3) The observed rate law is

$$-\left(\frac{d(CH_2O)}{dt}\right)_{initial} = K_2(CH_2O)^2_{initial},$$

where $K_2 > K_1$; and for the vessel conditions reported in reference 4, $K_2 = 1.4K_1$.

These experimental results are readily interpreted if one assumes that performic acid is formed by a simple, homogeneous, free radical chain involving HCO and HCO_3 as the chain carriers. The performic acid thus formed is then either rapidly destroyed (by a clean vessel wall, by mercury vapor, or by both) to form the products CO, H_2O, CO_2, and H_2; or it can eventually build up to relatively large concentrations. If the vessel conditions allow the second alternative, then the performic acid can react with CH_2O to form the hydroxyperoxide $(CH_2OH)_2O_2$, which in turn decomposes to form HCOOH, CO_2, and H_2. The details and quantitative consequences of such a scheme are given elsewhere.[4]

The reaction scheme proposed by Horner, Style, and Summers,[2] on the other hand, does not readily account for these rather complicated aspects of the thermal oxidation process. This is perhaps not too surprising since their mechanism was arrived at primarily from photochemical considerations.

[1] E. C. A. Horner and D. W. G. Style, Trans. Faraday Soc. **50**, 1197 (1954).
[2] Horner, Style, and Summers, Trans. Faraday Soc. **50**, 1201 (1954).
[3] D. W. G. Style and D. Summers, Trans. Faraday Soc. **42**, 388 (1946).
[4] M. D. Scheer, Kinetics of the Gas Phase Oxidation of Formaldehyde, "Fifth Symposium (International) on Combustion," University of Pittsburgh, August 30 through September 3, 1954, (to be published).
[5] D. W. E. Axford and R. G. W. Norrish, Proc. Roy. Soc. (London) **A192**, 518 (1948).
[6] W. A. Bone and J. B. Gardner, Proc. Roy. Soc. (London) **A154**, 297 (1936).

Overvoltages at the Electrode: Melted $Pb/PbCl_2$*

R. Piontelli and G. Sternheim
Laboratory of Electrochemistry, Chemical Physics and Metallurgy, Politecnico of Milan, Milan, Italy
(Received April 22, 1955)

PRECEDING papers from this Laboratory[1] explain the experimental methods realized here for measuring electrode overvoltages of melted metals against melted electrolytes.

By carrying into effect some general principles,[2] a cell was built up suitable for accurate measurements. The cathode overvoltages at the electrode, $Pb/PbCl_2$, at 530°C were proved to be practically negligible up to 200 A/dm².

The same problem has now been studied, utilizing a kind of the new class of devices (electrode-probes), recently introduced by ourselves,[3] the experiments being extended to the anodic behavior of the same electrode.

The cell differs from the described one[1] only insofar as the reference electrode is now formed by a silver disk (thickness 1 mm) included in an alundum tube [*G'* of Fig. 1 in reference 1(a)] in a way to expose to the bath only its contour, whose mean elevation over the surface of the polarized electrode is of the order of few mm. We thus obtain a satisfactory reference electrode, when coupled with the $Pb/PbCl_2$ electrode to form a "tensiometric cell." The assembly insures:

(a) The uniformity of the current density distribution at the electrode surface.

(b) The absence of perturbation of this distribution as a consequence of the presence of the probe and of the reference electrode.

The apparent overvoltages (changes in voltage of this cell, when the polarized electrode carries current, referred to the voltage in absence of current) are due:

(1) To the "overvoltage" in the electrochemical process at the surface of the polarized electrodes.

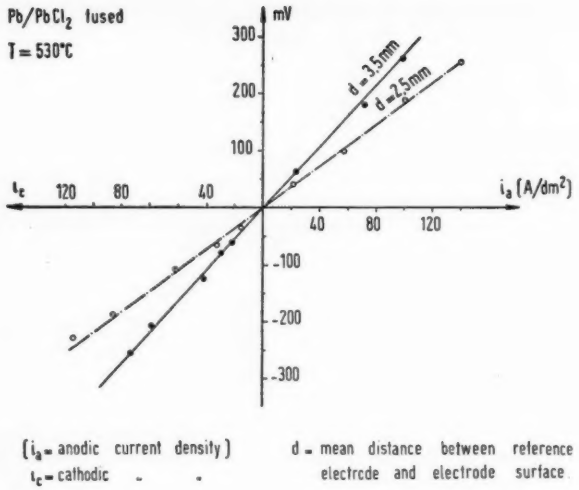

Fig. 1.

(2) To the ohmic drop in the layer between the reference electrode and the polarized electrode.

In the system referred to, the bath being formed by a single constituent, there are no changes in the chemical composition of the bath hence not either the consequent polarization effects of the "concentration" type. These are, on the contrary, contributing too to the measured voltages, for systems, in which the bath composition is changing.

Values (mV) of the apparent overvoltages,[4] obtained as a function of the current density (in abscissa), carried by a $Pb/PbCl_2$ electrode, when functioning both as a cathode and as an anode, at 530°C, are given in Fig. 1, for two different positions of the reference electrode, whose mean distance *d* from the electrode surface was about 2.5 mm in one case and 3.5 in the other.[5] Correcting these results by subtracting the ohmic drop in the layer between the reference electrode and the polarized one, the remaining true overvoltages are zero, on both sides, in the order of approximation allowed by the experiment.

The pure ohmic character of the apparent overvoltages is in agreement with the form and relative position of the mV/A diagrams and is confirmed by oscillographic recording.

This not only confirms and extends to the anodic side the results of our preceding experiments, but also gives a good support to the theoretical prevision on the suitability of the new class of probes,[6] which are now applied by us in a quite large range of conditions (also at ordinary temperature, with aqueous solutions and reference electrodes of the same nature of the polarized electrode).

Opportune coupling of at least two probes gives useful information also on the "concentration polarization" effects, arising in systems, whose bath composition is changing, as for instance the systems $PbCl_2/PbCl_2+KCl$ and similar, recently investigated by us.[7]

Dr. Montanelli and Mr. V. Consonni are giving very valuable help in the experiments.

* The researches reported in this paper have been sponsored in part by the Air Research and Development Command, USAF, under contract, through the European Office, ARDC.
[1] (a) R. Piontelli and G. Montanelli, J. Chem. Phys. **22**, 1981 (1954). (b) Piontelli, Rivolta, and Montanelli, Z. Elektrochem. **59**, 64 (1954).
[2] R. Piontelli, Gazz. chim. ital. **83**, 357, 370 (1953).
[3] R. Piontelli, Rend. ist. lombardo sci. (to be published).
[4] Taken positive when the polarized electrode is the positive pole in the tensiometric cell.
[5] The uncertainty in the measure of *d* is, at present, still of the order of 0.5 mm.
[6] Serious practical hindrance against the use of these devices can arise only because of the materials problem, or of the danger of short circuits, through excessive metallic fog formation. When this danger arises, the previously described arrangement (1) is of course preferable.
[7] Paper in preparation.

Application to Perturbation Theory to the Helium Atom*

J. M. GERHAUSER AND F. A. MATSEN
Departments of Chemistry and Physics, The University of Texas, Austin, Texas
(Received April 21, 1955)

PERTURBATION theory to the fourth order is

$$E_1=H_{11}+\sum_n{}'\frac{H_{1n}'H_{n1}'}{E_1^0-E_n^0}+\sum_{n,m}{}'\frac{H_{1n}'H_{nm}'H_{m1}'}{(E_1^0-E_n^0)(E_1^0-E_m^0)}$$
$$+\sum_{n,m,k}{}'\frac{H_{1n}'H_{nm}'H_{mk}'H_{k1}'}{(E_1^0-E_n^0)(E_1^0-E_m^0)(E_1^0-E_k^0)}+\cdots,$$

with hydrogen functions $H_{ii}^0=-A_iZ^2$ and $H_{ij}'=B_{ij}Z$. Thus, perturbation gives the Hylleras form[1] for any atom

$$E_1=-AZ^2+bZ-C+(d/Z)+\cdots.$$

To the second order, using matrix summation, one may write[2]

$$E_1=H_{11}+[(H'^2)_{11}-(H')_{11}{}^2]/E_1^0+\sum_n{}'E_n^0H_{1n}'H_{n1}'/E_1^0(E_1^0-E_n^0).$$

The quantity $(H'^2)_{11}$ is, for helium, equal to $Z^2/2$ a.u. and the first five terms of the summation give 0.0163 a.u. so that

$$E_1=-Z^2+5Z/8-0.1257 \text{ a.u.},$$

which yields for He, -2.8757. This is a slightly better result than the Hartree calculation. Similar results are obtained for lithium.

* Supported by contract with the Office of Ordnance Research.
[1] E. Hylleras, Z. Physik **65**, 209 (1930).
[2] J. E. Lennard-Jones, Proc. Roy. Soc. (London) **129A**, 598 (1930).

Luminous Zone in the Detonation of Equimolar Acetylene-Oxygen

ARTHUR L. BENNETT AND HENRY W. WEDAA
U. S. Naval Ordnance Test Station, China Lake, California
(Received April 28, 1955)

THE luminescence of the reaction zone of the detonation wave in equimolar acetylene-oxygen at low pressure has been recorded.

The detonation tube consists of a driver section 12 cm in diameter and 97 cm long. Combustion is initiated by a spark at the closed end. A zip-tape diaphragm separates this section from the experimental section. The experimental section consists of 215 cm of 12-cm diameter tubing, a 46-cm transition section, and 183 cm of 10-cm square tubing. Ionization probes at intervals of 36 and 51 cm record the passage of the detonation wave with an accuracy of 0.1 percent.

Premixed equimolar acetylene-oxygen was admitted to the two sections of the tube after evacuation. The driver pressure was equal to that in the experimental section down to 10 mm; at lower pressures the driver pressure was 7 to 20 mm.

The light profile of the detonation was measured at a window 398 cm from the diaphragm (137 cm in square section) by a photomultiplier (type 6199) supplied from batteries connected to a dc oscilloscope (RC=0.1 μsec). The light was collimated by slits 17 cm apart, usually 55μ and 150μ. Neutral filters limited the output to 4 ma (4 volts). The effective response is λ3400 to λ6000.

The sequence of traces in Fig. 1 shows the light profiles. The increase in duration with decrease in pressure is evident. At 1-mm initial pressure the detonation wave is unstable.

TABLE I. Detonation velocity and light output of equimolar acetylene-oxygen.

p mm Hg (a)	No. runs (b)	D m/sec (c)	Peak light (d)	Integrated light (e)	Duration Obs μs (f)	Duration Comp μs (g)	Extent mm (h)
50	2	2772	29	16	1.5	0.2	0.7
20	1	2721	15	12	2.2	0.6	1.7
10	3	2702	12	12	3.2	1.5	4.1
5	3	2661	9	14	3.3	2.4	6.5
2	3	2612	6	20	7.6	6.1	16

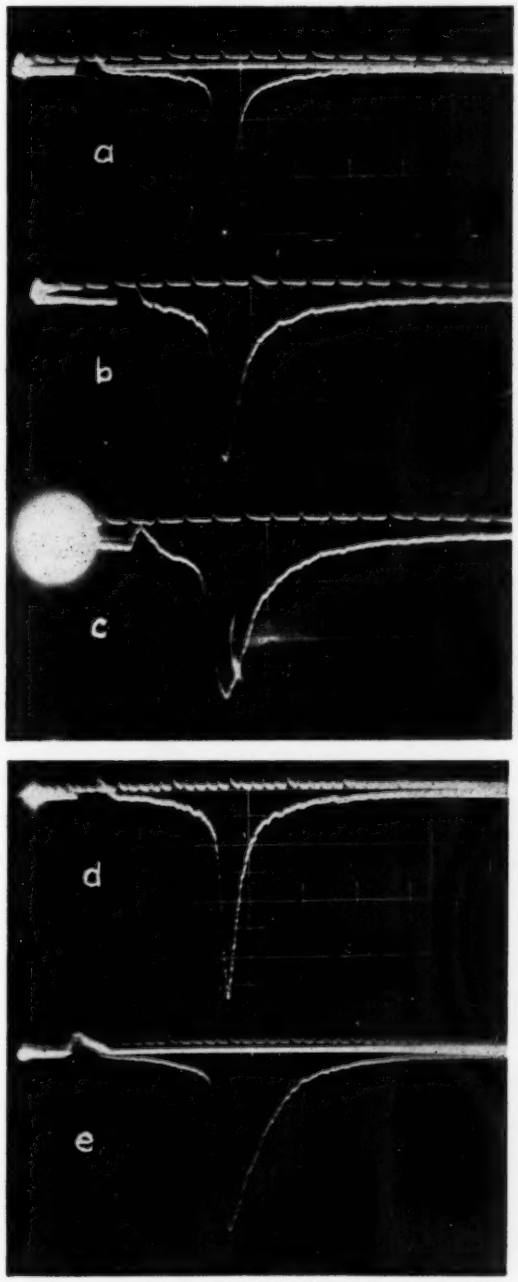

FIG. 1. Light profiles of $C_2H_2+O_2$ in 10-cm tube. Initial pressures: (a) 50 mm, (b) 10 mm, (c) 5 mm, at 2μsec/cm sweep speed; (d) 5 mm, and (e) 2 mm, at 5 μsec/cm. Light increase downward. Time marks 1 μsec. Sensitivity (a) to (e).

It will be noted in Fig. 1 that each profile first shows a gradual rise in light and then the rapid rise which is interpreted as the beginning of the reaction zone. (The pulse at 1 to 2 cm is for timing.) The slow rise is interpreted as stray light reflected from the far wall and scattered by the window, since the sharp rise coincides closely with the abrupt appearance of conductivity at a probe in the far wall of the tube.

The data on detonation velocity and light output are compiled in Table I. The initial pressure is a column (a), the number of runs in column (b), and the average velocity over 1.1 meters starting at 3.25 meters from the diaphragm, in column (c). The peak height, column (d), is measured from the start of the rapid rise.

The integrated light, column (e), is the area of the profile from the same base. The integrated light would be expected to decrease with the pressure. Quenching of the radiating atoms may be important and could account for the rise in total light as the pressure drops from 10 mm to 2 mm.

The observed duration, column (f), is the time interval from the beginning of the sharp rise to the same ordinate on the falling curve. The observed duration, d, can be represented by

$$d-1.4=6.2(2/p)=d',$$

with p in mm Hg, where 1.4 represents the correction required for zero duration at $p=\infty$, and d' is the computed duration. Although the computed broadening of the profile due to diffraction is twice 0.3 μsec, examination of the profiles indicates that 0.7 μsec is closely representative of the steep rise. The duration measured is increased by any tilt of the wave front from normal to the tube axis and by curvature of the wave front. The measured values are, therefore, an indication of the upper limit of the true reaction zone. Column (h), the product of the computed duration and the velocity D, indicates the linear extent of the luminous zone.

Note on the Validity of One-Dimensional Flame Front Models*

ROBERT M. FRISTROM
Applied Physics Laboratory, The Johns Hopkins University, Silver Spring, Maryland
(Received May 16, 1955)

IT is usually assumed that the major aspects of flame fronts can be described by a suitable one-dimensional model.[1] Aside from mathematical expediency this assumption is based upon measurements which indicate that the rate of propagation or burning velocity is independent of position within a given flame.[2,3]

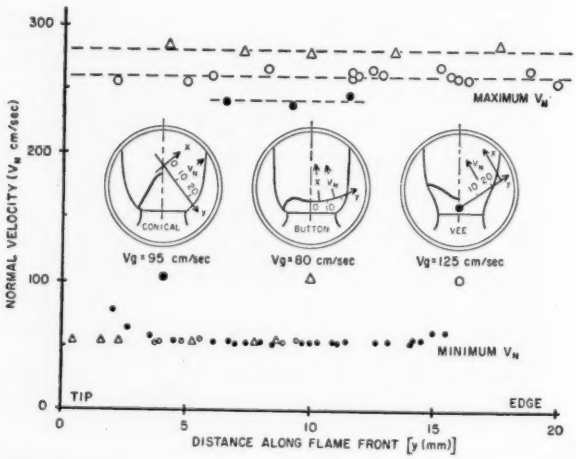

FIG. 1. Maximum and minimum normal gas velocity in a propane-air flame front. The component of gas velocity normal to the flame front is plotted as a function of distance from the axis of symmetry along the flame front. Velocities at the X-positions of maximum and minimum velocity are given for three different flame geometries, and gas velocities for the lean propane-air flame $\phi=0.96$, $P=0.25$. These data indicate that the velocity and time-distance profiles for this flame do not depend upon the coordinate along the flame front and are therefore unidimensional, and that the minimum normal velocity or burning velocity is invariant with total velocity, and flame geometry. For the distribution of velocity as a function of the X-coordinate through the flame front see Fig. 2. The three types of flame geometry studied are indicated in the accompanying sketch. The conical and button flame have circular symmetry, but the Vee flame is a flat inverted flame with a plane of symmetry.

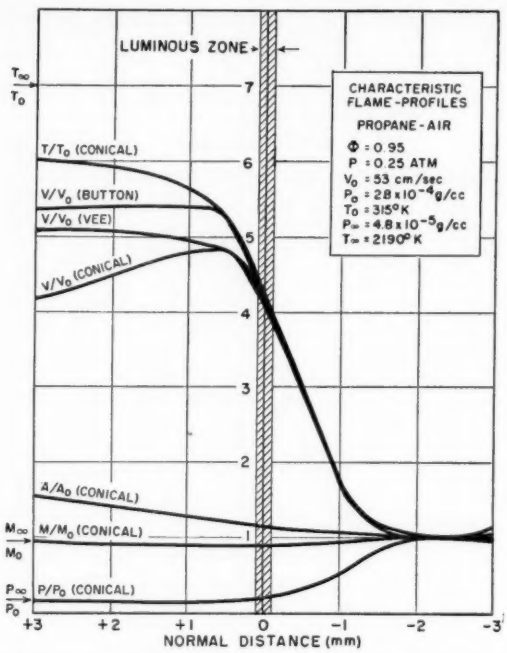

FIG. 2. Characteristic profiles of a propane-air flame. The characteristic profiles which describe the state of the burning gas as it passes through a lean propane-air flame front ($\phi=0.96$, $P=0.25$ atmos, $T_0=315$°C) are plotted as a function of time in milliseconds and normal distance in millimeters. Data from flames of three different geometries (see Fig. 1) and gas velocities are plotted to show the points of similarity and differences. The variables plotted are: (1) normal gas velocity, V/V_0 (see Fig. 1); (2) stream tube area ratio, A/A_0 (area is measured normal to the velocity measurement and compared with the values of the point of first temperature rise); (3) average molecular weight ratio, M/M_0 [average molecular weight is obtained from the mass spectrometric measurements of Prescott, Hudson, Foner, Avery (see reference 7)]; (4) relative gas density, ρ/ρ_0 (the value of relative density is obtained from the continuity equation $\rho VA=\rho_0V_0A_0$); (5) relative temperature, T/T_0, is obtained from the experimental measurement of velocity, area, and average molecular weight using the perfect gas law as the equation of state $T/T_0=(V/V_0)(A/A_0)(M/M_0)$. It represents a transitional temperature. All three flame geometries (and velocities) have identical normal velocity, area, density, and temperature profiles in the reaction region, preceding the luminous zone. Beyond the luminous zone, however, the gas velocities differ and there is not a unique relation between time and distance. In the case of the conical flame in this region ($X\geq 1.5$ mm) the parameters also depend upon the y position.

This view has recently been criticized by Uberoe.[4] Flame aerodynamics has previously only been studied in the two-dimensional case[5] treating the flame as a discontinuity and this represents the first detailed study of flow through three-dimensional flame fronts of finite thickness; a more comprehensive report has been submitted to this Journal.

The range of applicability of one-dimensional flame theories has been tested experimentally by studies of the flow patterns through the flame front of a lean propane-air flame ($\phi=0.96$, $P=0.25$ atmos). Gas density and velocity were determined as a function of position in the flame front by using continuity considerations and time-position information obtained from particle track studies.[6] In the reaction region, normal velocity, its orthogonal relative stream tube area, and the gas density are only functions of the coordinate normal to the flame front (see Figs. 1 and 2). If density is a measure of the state of the gas, then one-dimensional models provide a good approximation for such flames. Propane flames were studied under several conditions of composition ($\phi=0.96$, 1.25), pressure ($P=0.25$, 0.3 atmos), gas velocity (80–125 cm/sec), burner diameter (1.25 cm, 2.54 cm) and flame geometry. Within the limits studied, all of the flames are unidimensional in the reaction region (see Fig. 1) and moreover could be described by a unique set of profiles (see Fig. 2) which are functions only of the initial state of the gas. Outside of this region, however, the profiles are dependent upon flow conditions (as determined by gas velocity, flame geometry, etc.) and time, rather than distance, is probably the important parameter.

From these considerations, it can be seen that, if burning velocity is defined as the normal gas velocity at the position of initial temperature rise, it is a function only of the initial state of the gas (composition temperature and pressure). Burning velocity is independent of: position along a flame front, flame geometry, burner diameter, and gas velocity (see Fig. 1). Confusion has arisen because previous measurements of burning velocity have been made indirectly without the knowledge of the cold flow pattern which is necessary for correct interpretation.

The measurements indicate (see Fig. 2) that one-dimensional flame theories should be modified to include the effects of stream tube area expansion during the course of the reaction by substituting $\rho v a = \text{constant}$ for $\rho v = \text{constant}$. Diffusion and heat conduction equations should also be generalized to include the effect of expansion. The hydrocarbon flame reaction consists of two regions: a fast propagating reaction associated with the luminous regions and the major portion of the heat release, and a slow secondary reaction associated with the post luminous mantel of the flame in which reaction is time but not distance dependent. Flow in this region varies over wide limits with no measurable effect on the propagation of the flame (see Fig. 2). This observation is in agreement with temperature studies of Friedman and Burke[7] and composition studies of Prescott, Hudson, Foner, and Avery[8] shed some light on the mechanism of hydrocarbon flame propagation.

* This work was done under contract with the Bureau of Ordnance of the U. S. Navy.

[1] M. W. Evans, Chem. Revs. **51**, 363–429 (1952).
[2] B. Lewis and G. von Elbe, J. Chem. Phys. **11**, 75 (1953).
[3] J. M. Singer, Fourth Symposium on Combustion, p. 353, Williams Wilkins and Company (1953).
[4] M. S. Uberoi, J. Chem. Phys. **22**, 1784 (1954).
[5] G. Ball, Combustion Project Report, Harvard University, July 1951.
[6] Fristrom, Avery, Prescott, and Mattuck, J. Chem. Phys. **22**, 106 (1954).
[7] R. Friedman and E. Burke, J. Chem. Phys. **22**, 824 (1954).
[8] Prescott, Hudson, Foner, and Avery, J. Chem. Phys. **22**, 145 (1954).

Vector Distributions and Crystalline Proteins*

DOROTHY WRINCH
Department of Physics, Smith College, Northampton, Massachusetts
(Received April 28, 1955)

IN interpreting vector maps[1,2] corresponding to electron density distributions which may or may not be resolved into atoms, guidance is provided by a study of the relation between *general nonperiodic distributions* g and h in space S and their *mutual images* gh and hg and *self-images or vector maps* g_v and h_v in space S_v. If G and H are the Fourier transforms (F.t.) of g and h, gh is defined as the F.t. of $\bar{G}H$, hg as the F.t. of $\bar{H}G$, g_v of $\bar{G}G$ and h_v of $\bar{H}H$. It follows that $[g+h]_v = g_v + gh + hg + h_v$. This note gives examples of these relations and indicates their impact on protein vector map interpretations.[3]

If $g(x)$ is unity for $|x| = o$ to a, and $h(x)$ is unity for $|x| = o$ to b, it follows that

$$G(X) = \sin 2\pi a X/\pi X, \quad H(X) = \sin 2\pi b X/\pi X,$$

and that

$$gh(x) = hg(x) = 2b, \quad a+b-|x|,$$

for $|x|$ in the ranges 0 to $a-b$, and $a-b$ to $a+b$, and zero outside. It results that, for the distribution $D(x) = pg(x) - qh(x)$, the vector transform is

$$D_v(x) = p^2(2a-|x|) + q^2(2b-|x|) - 2pq(2b, a+b-|x|).$$

We extend this result to two and three dimensions. Thus (see Fig. 1) for a square of edge $2a$ with density p from which a square of edge $2b$ with density q has been deleted, the vector function is

$$D_v(x,y) = p^2\ \Pi_2(2a-|x|) + q^2\ \Pi_2(2b-|x|) - 2pq\ \Pi_2(2b, a+b-|x|). \quad (1)$$

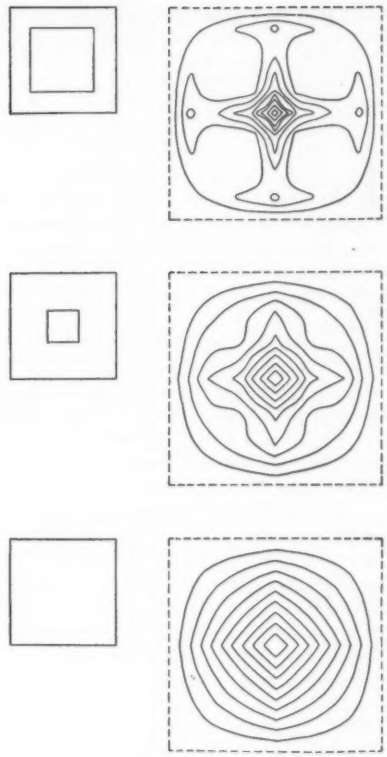

FIG. 1. The vector maps, contoured at 9/10, 8/10, ··· of the height at the origin, of a uniform square and square frames. For the narrower frame, the vector map is not wholly core.

Correspondingly, if we write Π_3 for Π_2 we obtain the vector function for a cube and cube frames.

Let us designate as *the core* of a vector map that region in which g_v is monotonic decreasing from the origin in all directions. From (1) we see that the vector map of a uniform square or cube is all core and that this situation obtains also for a square frame which is not too narrow ($b/a \leq \frac{1}{3}$) and for a cube shell which is not too thin ($b/a \leq \frac{1}{2}\sqrt{2}$). For a narrower frame and thinner shell this is no longer the case and maxima develop in x and y (and z) directions. As we see in Fig. 1, it is the topography of g_v as a whole which is the vector expression of a g distribution and the presence, or absence, of maxima is only part of the expression of the frames in S_v. However, the existence of the maxima for sufficiently narrow frames and sufficiently thin shells is a striking feature of the vector map and has a certain diagnostic value. [From the foregoing formulas we can obtain vector maps of frames and shells with positive or negative interiors and can find the heights of the maxima (if present) as a function of q/p and b/a, etc.] The basic point in the present context is that *a g_v distribution can have a maximum which is merely part of the vector expression of g as a whole and is not* (see Fig. 1) *an indication of the existence in S of a pair (or pairs) of distributions related by the vector which defines its position.*

The discovery that vector maps not wholly core emerge from a variety of cage-like or frame-like structures with low-density interiors[1–4] clarifies the vector maps obtained from various crystalline proteins.[5] The conclusion reached by this approach to the x-ray diffraction data is that some protein entities are composed of surface polycondensations of α-L-amino acids, with skeletons globulite in shape and up to 15 A in diameter having low-density interiors.[6]

* This work is supported by the Office of Naval Research.

[1] D. Wrinch, Phil. Mag. **27**, 98 (1939).
[2] D. Wrinch, Nature **157**, 226 (1946).
[3] D. Wrinch, Acta Cryst. **7**, 627 (1954).
[4] D. Wrinch, Phys. Rev. **79**, 203 (1950).
[5] D. Wrinch (unpublished work).
[6] D. Wrinch, J. Chem. Phys. **20**, 1332 (1952); **21**, 2099 (1953).

Role of the Continuum in Superposition of Configurations

HARRISON SHULL* AND PER-OLOV LÖWDIN
Institute of Mechanics and Mathematical Physics, Uppsala University, Uppsala, Sweden
(Received May 9, 1955)

IN a relatively recent paper, Taylor and Parr[1] have considered the ground state of helium by the method of superposition of configurations. In using configurations built up from the hydrogen-like orbitals $L_n^1(2Zr/n)\exp(-Zr/n)$, they obtained the discouraging result that the series of radial configurations led to an extremely poor convergence for the energy towards the limit to be expected.

In connection with other work in progress, we have had occasion to re-examine an early paper by Hylleraas,[2] which has apparently been overlooked in this connection. Hylleraas has carried through practically the same superposition of configurations as did Taylor and Parr, but, instead of using hydrogen-like s-functions, he used the complete set $L_n^1(2Zr)\exp(-Zr)$, omitting the principal quantum number n in Z/n. In marked contrast to Taylor and Parr's result, the series used by Hylleraas leads to an energy which converges directly and rapidly to the limit that can be expected for purely radial functions, as derived indirectly by Taylor and Parr, too. There is no question that the distinguishing feature between the two expansions is that the one used by Hylleraas is based on a complete set in itself, whereas that of Taylor and Parr is complete only when the continuum wave functions are explicitly taken into account.

In order to verify this hypothesis, we have expanded the $2s$-function $L_2^1(2Zr)\exp(-Zr)$ in terms of the hydrogen-like set with the same Z and summed the squares of the resulting coefficients from $n=1$ to $n=\infty$. This sum, which would be 1 were the series complete, was found to be only 0.56501. Thus 43.5 percent of the contribution of this second term in the Hylleraas expansion comes from the hydrogen continuum.

The importance of the continuum in the helium expansion has also recently been pointed out by Green *et al.*,[3] who have shown that it is possible to minimize the contribution from the continuum by varying Z.

We have repeated and extended Hylleraas' calculation by using the more convenient set $L_{n+1}^2(2Zr)\exp(-Zr)$, which is orthogonal in ordinary space, and confirmed Hylleraas' results for $Z=2$. We have also varied Z, and the results for $Z=1.6875$ in Table I

TABLE I. Energies of superpositions of radial configurations for the ground state of the helium atom expressed in modified atomic units (1 a.u. $=e^2/a_{0,\mathrm{He}}=2hcRy_{\mathrm{He}}$).

Configurations:
$A=(1s)^2$; $B=(1s)^2$, $(1s,2s)$, $(2s)^2$;
$C=(1s)^2$, $(1s,2s)$, $(1s,3s)$, $(2s)^2$, $(2s,3s)$, $(3s)^2$.

	A	B	C
Taylor and Parr[a]	−2.847 656	−2.854 75	−2.857 4
Discrete set $Z=2$	−2.75	−2.850 225	−2.878 116
Discrete set $Z=1.6875$	−2.847 656	−2.860 408	−2.877 266

[a] Taylor and Parr used hydrogen-like functions, but varied Z to an optimum value for each function added.

show that this value leads to a superior starting function but to a slower rate of convergence when subsequent terms are added. In order to be effective, the process of varying Z must therefore be carefully carried through at each step of the series, and it is fortunate that, for a complete basic set, this cumbersome procedure can be entirely avoided.

The result obtained may also be of importance for the theory of molecules, since the MO–LCAO method and the VB method are both based on the use of atomic orbitals. The conclusion seems inescapable that configuration expansions using hydrogen-like functions, atomic self-consistent-field functions, or the analytic atomic functions of Duncanson and Coulson[4] cannot be markedly successful in evaluating atomic and molecular energies unless sufficient account is taken of the rather annoying continuum wave functions. In this connection, we would like to draw attention to the complete orthogonal set

$$L_{n+l+1}^{2l+2}(2Zr)e^{-Zr}Y_{lm}(\vartheta,\varphi)$$

where Y_{lm} are the ordinary spherical harmonics. This set is entirely discrete, which is apparently of essential importance for the convergence of the conventional methods, and, in addition, it renders a great simplification in the computational work, since only a single exponent common to all terms occurs in the atomic and molecular integrals.

We are indebted to *Fil. kand.* Klaus Appel for his valuable assistance in the numerical work.

* Guggenheim Fellow 1954–1955, on leave from Department of Chemistry and Institute for Atomic Research, Iowa State College, Ames, Iowa. Address after Sept. 1955: Chemistry Department, Indiana University, Bloomington, Indiana.

[1] G. R. Taylor and R. G. Parr, Proc. Natl. Acad. Sci. U. S. **38**, 154 (1952). This paper was also presented at the Shelter Island Conference in 1951.

[2] E. A. Hylleraas, Z. Physik **48**, 469 (1928).

[3] Green, Mulder, Milner, Lewis, Woll, Kolchin, and Mace, Phys. Rev. **96**, 319 (1954).

[4] W. E. Duncanson and C. A. Coulson, Proc. Roy. Soc. (Edinburg) **62**, 37 (1944). These functions have been used e.g., in some recent work by S. F. Boys, Proc. Roy. Soc. (London) **A201**, 125 (1950).

Further Observations on Color Center Precursors

M. HACSKAYLO* AND P. SCHWED
Lewis Flight Propulsion Laboratory, National Advisory Committee for Aeronautics, Cleveland, Ohio
(Received May 9, 1955)

IT was found previously[1] that NaCl crystals which had undergone an electrolysis which left them uncolored (to be called type A uncolored crystals) were much more sensitive to irradiation with x-rays than normal ones. Such type A uncolored crystals were consequently said to contain color center precursors. In the present study it was found that NaCl crystals with similar properties can be prepared by first (additively) coloring normal NaCl crystals with Na and then bleaching them by electrolysis (to be

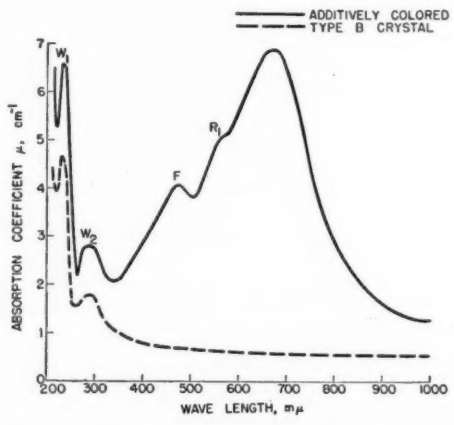

FIG. 1. Optical absorption spectra for NaCl crystal additively colored with Na and for the type B crystal produced from it by electrolysis.

called type B uncolored crystals). The electrolysis for making both types was done much as before.[1] However, the maximum temperatures used in electrolytically producing the type A and B crystals were 650° and 600°C, respectively. Figure 1 shows the optical absorption spectrum of an additively colored NaCl crystal and of the type B crystal produced from it. The coloration is missing in the latter case, but both curves show the bands at

226 mμ (to be called W_1) and at 285 mμ (to be called W_2) previously observed[1,2] in electrolytically colored and type A crystals.

To compare their sensitivities to x-rays, normal NaCl and type A and B crystals were each exposed to 4500 r of x-rays from a Machlett A.E.G. 50 beryllium window tube operated at 50 kv and 30 ma. At the F band maximum, the optical densities of the A and B crystals were, respectively, 3.1 (as also found earlier[1]) and 6.7 times that of the normal crystal, showing the type B crystals are also sensitized. A quantitative comparison of A and B crystals is difficult because of the nonuniform coloration (see, e.g., Fig. 3 of reference 1). A type A, a type B, and an additively

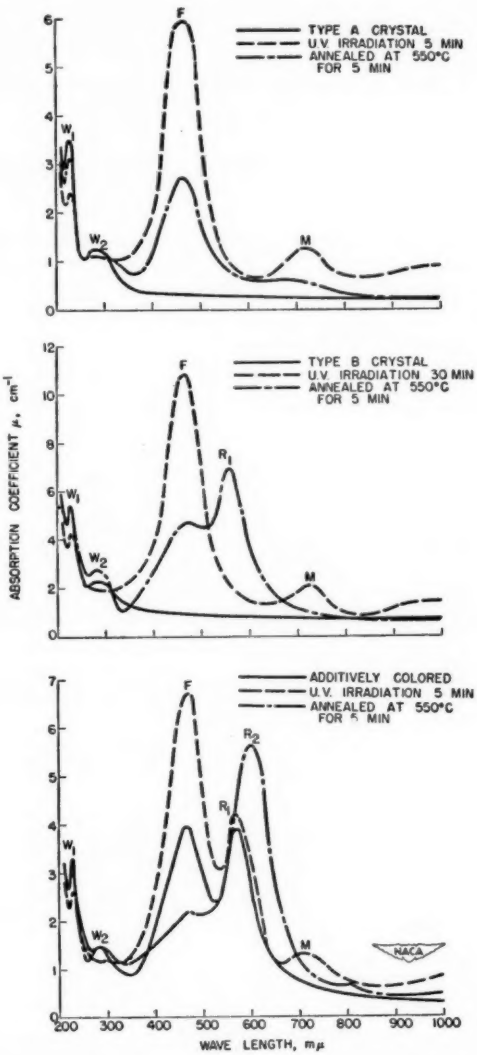

FIG. 2. Effect of ultraviolet irradiation and subsequent annealing upon the optical absorption spectra of NaCl crystals. (a) Type A crystal. (b) Type B crystal. (c) Crystal additively colored with Na.

colored crystal were each irradiated with ultraviolet light from a Hanovia low pressure Hg arc lamp placed 10 cm from the crystal. The crystals were subsequently annealed at 550°C for 5 minutes, a treatment sufficient to bleach an x-ray colored normal crystal; and the resulting set of absorption curves is given in Fig. 2. Although a normal NaCl crystal of the type used (Harshaw optical grade) is not colored by ultraviolet light, a considerable coloration was produced in the three above crystals and a fairly sizeable combined F- and R-band survived the annealing, showing that the color centers were relatively stable. The W_1 band was greatly decreased, and the W_2 band nearly destroyed by the irradiation, but both recovered considerably after the annealing. Uchida *et al.*[2] observed previously that ultraviolet light near the W_2 band maximum diminishes W_2 and at the same time produces an F-band roughly as large as the original W_2 band; and they suggested that the irradiation converts the W_2 centers into F-centers. In Fig. 2, however, the F-band produced is much greater than the W_2 band destroyed so that the process can be only secondary.

Ivey[3] has pointed out that the W_1 band is quite near the V_2 band found by Casler *et al.*[4] in x-ray colored NaCl, and he suggested the two are identical. However, the V_2 band is quite broad[4] while W_1 (see Fig. 1), is very narrow so that the identification seems doubtful.

* Now at Harshaw Chemical Company, Cleveland, Ohio.

[1] M. Hacskaylo and G. Groetzinger, Phys. Rev. **87**, 789 (1952); M. Hacskaylo and D. Otterson, J. Chem. Phys. **21**, 552 (1953); Hacskaylo, Otterson, and Schwed, *ibid.* **21**, 1434 (1953).

[2] Uchida, Ueta, and Nakai, J. Phys. Soc. Japan **6**, 107 (1951).

[3] H. F. Ivey, Phys. Rev. **88**, 1434 (1952).

[4] Casler, Pringsheim, and Yuster, J. Chem. Phys. **18**, 1564 (1950).

Restricted Rotation in Amides as Evidenced by Nuclear Magnetic Resonance

W. D. PHILLIPS

Chemical Department, Experimental Station, E. I. du Pont de Nemours and Company, Wilmington, Delaware

(Received May 11, 1955)

RESTRICTED rotation about the C—N bond of amides has been postulated[1] and is an important consideration in theories pertaining to the structures of protein molecules.[2] The infrared and Raman spectra of N-methylacetamide have been interpreted in terms of the existence mainly of the transconfiguration in the liquid at room temperature.[3] Analysis of the proton magnetic resonance spectra of N,N-dimethylamides has demonstrated unequivocally the existence of restricted rotation in amides.

The proton magnetic resonance spectrum of N,N-dimethylformamide obtained at 30 Mc is shown in Fig. 1. The peak oc-

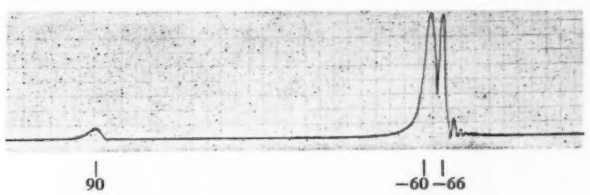

FIG. 1. Proton magnetic resonance spectrum of dimethylformamide—30 Mc.

curring at +90 cps is that of hydrogen bonded to the carbon atom of the carbonyl group, and the two peaks at −60 and −66 cps are the proton resonances of the two methyl groups. The proton magnetic resonance spectrum of N,N-dimethylformamide was also obtained at 40 Mc. The separation between the two methyl resonance peaks is greater by a factor of 4/3 at 40 Mc than at 30 Mc, proving the separation between the two peaks to be due to a chemical shift rather than the unlikely possibility of spin-spin splitting by the hydrogen atom bonded to the carbonyl group. A similar chemical shift of 6 cps at 30 Mc is observed between the proton resonances of the two methyl groups bonded to the nitrogen atom of N,N-dimethylacetamide.

If there were free rotation about the C—N bond of N,N-dimethylamides, the average electrical environments of the two CH_3 groups would be identical and their proton resonances would be coincident. If, on the other hand, rotation about the C—N bond is restricted and the molecule is planar or nearly planar, the two CH_3 groups reside in different electrical environments and consequently exhibit resonances at different frequencies. Even though both methyl groups of N,N-dimethylamides are bonded

to the nitrogen atom, a chemical shift is expected between the two methyl groups in the event of restricted rotation about the C—N bond. The different fields experienced by the hydrogen atoms of the two CH_3 groups in the planar configuration as the result of different intramolecular distances and asymmetric polarization of the C—N bond would be expected to produce different magnetic shieldings of the hydrogen atoms of the two CH_3 groups and give rise to the observed chemical shift.

Restricted rotation about the C—N bond of amides is reasonable from the point of view of molecular orbital theory in that overlap is possible between the *p*-orbital of carbon and the *p*-orbital of nitrogen containing an unshared pair of electrons. The two predominant resonance structures are those given below with resonance structure II making an appreciable contribution to the electronic structure of amides.[1]

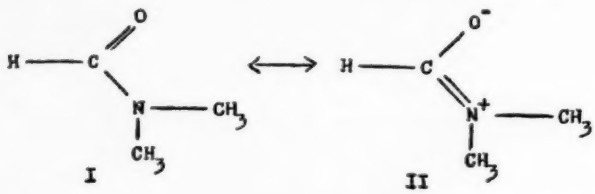

I II

It is possible to place an upper limit on the rotational velocity about the C—N bond of N,N-dimethylamides from the observed chemical shift between the two methyl groups. The chemical shift of 6 cps between the two methyl groups indicates that these groups are exchanging positions by rotation about the C—N bond at a rate of less than $6(2\pi)=38$ sec^{-1}. If the rate of positional exchange of the methyl groups of N,N-dimethylformamide by rotation about the C—N bond were equal to or greater than about 38 sec^{-1}, only a single, average methyl proton resonance located between −60 and −66 cps would be observed.[4] This low value of 38 sec^{-1} at room temperature for the upper limit of the rate of rotation about C—N bonds indicates that the energy barriers for restricted rotation in amides is high.

Observation of single methyl proton resonances for N-methylformamide and N-methylacetamide indicates that only one of the two possible rotational isomers of these compounds is present. Mizushima[3] deduced the same result from analysis of the infrared and Raman spectra of N-methylacetamide.

[1] L. Pauling, *The Nature of the Chemical Bond* (Cornell University Press, Ithaca, 1948), p. 207.
[2] S. Mizushima, *Structure of Molecules and Internal Rotation* (Academic Press, Inc., New York, 1954), pp. 139–152.
[3] Mizushima, Shimanouchi, Nagakura, Kuratani, Tsuboi, Baba, and Fujioka, J. Am. Chem. Soc. **72**, 3490 (1950).
[4] H. S. Gutowsky and A. Saika, J. Chem. Phys. **21**, 1688 (1953).

Ionization Potential of the Free HO_2 Radical and the $H-O_2$ Bond Dissociation Energy*

S. N. Foner and R. L. Hudson
Applied Physics Laboratory, The Johns Hopkins University, Silver Spring, Maryland
(Received May 12, 1955)

THEORETICAL estimates[1–5] of the heat evolved in the reaction $H+O_2\rightarrow HO_2$ have ranged from 36 to 70 kcal/mole. With the mass spectrometric detection by Foner and Hudson[6] and also by Robertson[7] of the HO_2 radical in the reaction of hydrogen atoms with oxygen molecules, the actual existence of this radical was established and the possibility of directly measuring the heat of formation of HO_2 was opened. The essential data are the ionization potential of the HO_2 radical and the appearance potential of the HO_2^+ ion from H_2O_2.

The yield of HO_2 in our experiments on the reaction of atomic hydrogen with oxygen was too small to permit the determination of the HO_2 ionization potential. Recently we have obtained substantial quantities of HO_2 radicals by reacting H_2O_2 at low pressures (~0.5 mm) with the products of electrical discharges in various gases. Discharges in water vapor and hydrogen peroxide are particularly effective, probably because the OH radicals produced can react with H_2O_2 by the exothermic process:

$$OH+H_2O_2\rightarrow HO_2+H_2O+30 \text{ kcal.} \quad (1)$$

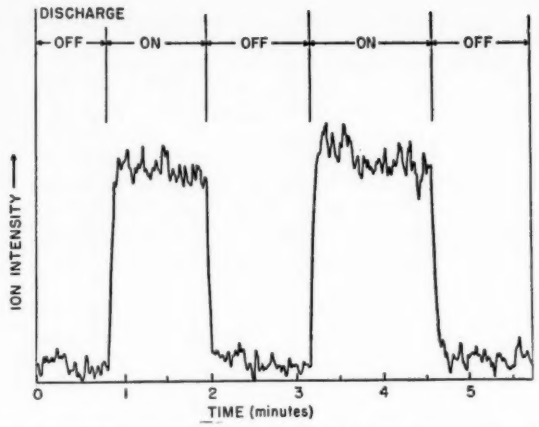

FIG. 1. HO_2 production in the reaction of H_2O_2 with discharge products of water vapor. Ion intensity of HO_2^+ recorded with 2 sec time constant at 15 volts electron energy.

The reactor used in this work was similar to that described in reference 6, the major differences being that the central tube which supplied the H_2O_2 was movable and the sampling orifice was a Pyrex cone instead of a punched gold foil. The mass spectometer and the chopped molecular beam sampling system have been described.[8]

The yield of HO_2 radicals by reaction of peroxide with discharge products from water vapor is shown in Fig. 1, a recording of the mass 33 ion intensity as the discharge was alternately switched on and off. The $O^{16}O^{17}$ contribution from oxygen generated in the reaction is only 3 percent of the mass 33 ion intensity shown here. The small contribution made by HO_2^+ from H_2O_2 is evident from the ion intensity when the discharge is off (i.e., no peroxide decomposed). At 50 volts electron energy the excess HO_2^+ intensity is about 1 percent of the $H_2O_2^+$ intensity which makes the HO_2 concentration in this experiment about 0.3 percent of the gas mixture.

The initial portions of the ionization efficiency curves for the HO_2^+ ion from the radical, the HO_2^+ ion from H_2O_2, the O_2^+ ion from O_2, and the A^+ ion from argon are shown in Fig. 2. The oxy-

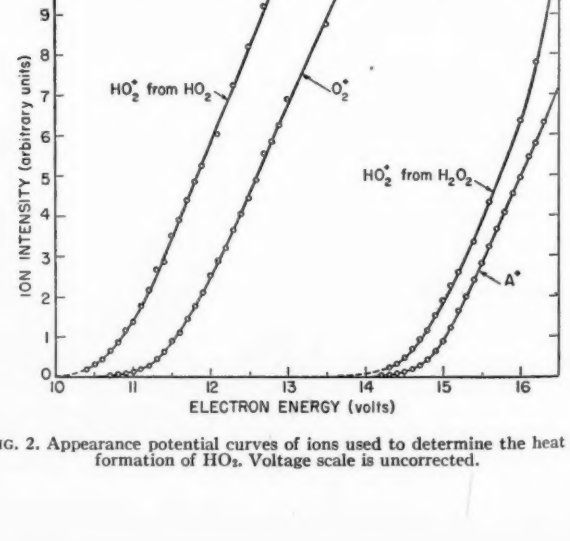

FIG. 2. Appearance potential curves of ions used to determine the heat of formation of HO_2. Voltage scale is uncorrected.

gen appearance potential curve was made, using the oxygen produced in the reaction, while the HO_2^+ curve from H_2O_2 was made with the discharge turned off. Argon was used as the standard gas (IP=15.77 ev) to calibrate the voltage scale. The appearance potentials of the ions were determined by two objective methods: (1) Plotting log ion intensity *vs* voltage curves and determining the voltage shift required to match the curves. Various forms of this method have been used successfully by Honig,[9] Dibeler and Reese,[10] and others. (2) Removing the tail of the ionization curve due to the thermal energy spread in the electron beam by the deboltzmannization procedure of Foner, Kossiakoff, and McClure,[11] a method not too well known and inadequately described in the literature. A preliminary analysis of the data leads to the following ionization energies:

$$I(HO_2)=11.53\pm0.1 \text{ ev},$$
$$I(O_2)=12.15\pm0.1 \text{ ev},$$
$$A(HO_2) \text{ from } H_2O_2=15.41\pm0.1 \text{ ev}.$$

The difference between the energy required to produce HO_2^+ by dissociative ionization of H_2O_2 and the ionization potential of the HO_2 radical, 3.88 ev=89.5 kcal/mole, is the energy for removal of the first hydrogen atom from H_2O_2 on the assumption of zero kinetic energy of the fragments in the process:

$$H_2O_2+e\rightarrow H+HO_2^++2e. \quad (2)$$

The empirical rule proposed by Stevenson[12] for zero kinetic energy in dissociative ionization is satisfied since $I(HO_2)<I(H)$. Using the known heat of the reaction

$$2H+O_2\rightarrow H_2O_2+136.6 \text{ kcal/mole or } 5.92 \text{ ev}$$

with our value of $D(H-HO_2)$ we obtain for the bond dissociation energy of $H-O_2$, $D(H-O_2)=2.04\pm0.1$ ev or 47 ± 2 kcal/mole.

Our value for $D(H-O_2)$ is consistent with the value reported by Robertson,[13] $D(H-O_2)=46\pm9$ kcal/mole. This agreement, however, must be considered as fortuitous since Robertson's value is derived on the assumption that $I(HO_2)\equiv I(O_2)\equiv 12.2$ ev, an estimate which is in error by 0.7 ev, and a measured value for the appearance potential of HO_2^+ from H_2O_2 of 16.1 ± 0.4 ev which is in marked disagreement with our value of 15.41 ± 0.1 ev.

* This research was supported by the Bureau of Ordnance, Department of the Navy.

[1] Urey, Dawsey, and Rice, J. Am. Chem. Soc. **51**, 1371 (1929).
[2] M. Bodenstein and P. W. Schenk, Z. physik. Chem. **20B**, 420 (1933).
[3] F. Haber and J. Weiss, Proc. Roy. Soc. (London) **147A**, 350 (1933).
[4] A. D. Walsh, J. Chem. Soc. **1948**, 331.
[5] Evans, Hush, and Uri, Quart. Revs. (London) **6**, 186 (1952).
[6] S. N. Foner and R. L. Hudson, J. Chem. Phys. **21**, 1608 (1953).
[7] A. J. B. Robertson, Conference on Mass Spectrometry, Institute of Petroleum, London (1953).
[8] S. N. Foner and R. L. Hudson, J. Chem. Phys. **21**, 1374 (1953).
[9] R. E. Honig, J. Chem. Phys. **16**, 105 (1948).
[10] V. H. Dibeler and R. M. Reese, J. Research Natl. Bur. Standards **54**, 127 (1955).
[11] Foner, Kossiakoff, and McClure, Phys. Rev. **74**, 1222 (1948).
[12] D. P. Stevenson, Discussions Faraday Soc. **10**, 35 (1951).
[13] A. J. B. Robertson, Trans. Faraday Soc. **48**, 228 (1952).

Vibrational Analysis of the Emission Spectrum of Coronene as a Forbidden Transition

JEROME W. SIDMAN
Department of Chemistry and Chemical Engineering, University of California, Berkeley, California

(Received March 31, 1955)

THE absorption spectrum of coronene in benzene shows a weak transition from 23 000–27 000 cm^{-1} with $\log\epsilon=2.5$, and this has been interpreted as a weakly allowed electronic transition.[1] The emission spectrum of coronene in heptane at −180°C exhibits much sharp structure,[2] and it is possible to attempt a vibrational analysis of the emission spectrum. The first emission band at 4261 A is very weak, and its intensity varies considerably in different solvents.[3] The analog of this band appears weakly at 4200 A in both the absorption and emission spectra of coronene in benzene at room temperature.[1] The vibrational analysis indicates that most of the bands in the coronene emission spectrum in frozen heptane arise from vibrational additions to the doublet at 4315–4328 A, and not from vibrational additions to the first band at 4261 A. The first band at 4261 A is therefore assigned to the 0−0 band of an electronic transition which is forbidden by symmetry. The intensity in the emission transition is due to a vibrational-electronic perturbation,[4] in which the vibrational interval from the 4261 A band to the 4315–4328 A doublet corresponds to one quantum of the vibration which allows the transition to occur.

According to the LCAO–MO calculations,[5] the highest filled MO of coronene in the electronic ground state is E_{2u}, whereas the lowest unfilled MO is E_{1g}. The lowest one-electron transition is therefore orbitally fourfold degenerate. This is exactly the situation in benzene, which also possesses D_{6h} symmetry. In benzene, electron emulsion removes the occidental fourfold degeneracy to give one degenerate E_{1u} state and two nondegenerate states, B_{1u} and B_{2u},[6] with the B_{2u} state lowest in energy. The absorption and fluorescence spectra of benzene vapor have been vibrationally analyzed,[7] and the emission spectrum arises from a one-quantum addition of an e_g^+ vibration of 606 cm^{-1} to the forbidden 0−0 band. If the lowest excited electronic singlet state of coronene is $^1B_{2u}$, and if the vibration which perturbs the ground state in the emission is also an e_g^+ vibration, then it is possible to account for the doublet nature of the bands at 4315 and 4328 A in the coronene emission spectrum. The doublet is due to removal of the degeneracy of the e_g^+ vibration by interaction of the solvent with the coronene in such a way that the sixfold axis of symmetry is destroyed. The same perturbation by the solvent also allows the 0−0 band at 4261 A to appear weakly, and this is consistent with the fact that the relative intensity of this band depends on the solvent.

TABLE I. Vibrational analysis of the emission spectrum of coronene in heptane at −180°C.

Intensity	λ, A,[a] ±3	N, cm^{-1}, ±15	23 460-N, ±20	Assignment
vw	4261	23 460	0	$^1B_{2u}\rightarrow{}^1A_{1g}$
m	4315	23 170	290	320, e_g^+
m	4328	23 100	360	
vw	4374	22 860	600	640, a_{1g}
vs	4437	22 530	930	320, e_g^+, +640, a_{1g}
vs	4449	22 470	990	
w	4490	22 270	1190	1190, a_{1g}(?)
s, broad	4531	22 060	1400	1400, e_g^+(?)
w	4577	21 840	1620	320, e_g^+, +1320, a_{1g}
w	4595	21 760	1700	
vw	4631	21 590	1870	640, a_{1g}, +1190, a_{1g}
m	4716	21 200	2260	320, e_g^+, +640, a_{1g},
m	4731	21 130	2330	+1320, a_{1g}
vw, broad	4833	20 680	2780	1400, e_g^+, +1320, a_{1g}
vw, broad	4898	20 410	3050	
vw	5040	19 840	3620	320, e_g^+, +640, a_{1g},
vw	5060	19 760	3700	+2(1320), a_{1g}

[a] See reference 2.

The vibrational analysis is given in Table I. The intensity distribution in the bands is consistent with a transition which is forbidden by symmetry but which is allowed by vibrational-electronic perturbation by a degenerate vibration. Perturbations due to the solvent remove the degeneracy of the e_g^+ vibration and also allow the forbidden 0−0 band to appear weakly. The degenerate e_g^+ vibration is approximately 320 cm^{-1} in coronene, and prominent additions of 640 cm^{-1} and 1320 cm^{-1} to the e_g^+ vibration are assigned to a_{1g} vibrations. The broad, strong band at 4531 A may be due to an e_g^+ vibration of 1400 cm^{-1} which adds to the 0−0 band, and partial removal of the degeneracy by solvent perturbation would account for its breadth. A very tentative assignment of an a_{1g} 1190 cm^{-1} vibration is also proposed.

In conclusion, the vibrational analysis of the emission spectrum and the solvent effects on the emission spectrum of coronene both

support the interpretation that the emission transition is forbidden by symmetry and is allowed by a degenerate vibration, as in benzene.

The author acknowledges correspondence with Mr. B. Brocklehurst and discussions with Professor D. S. McClure.

[1] B. Brocklehurst, J. Chem. Soc. **1953**, 3318.
[2] Bowen and Brocklehurst, J. Chem. Soc. **1954**, 3875.
[3] B. Brocklehurst (private communication).
[4] H. Sponer and E. Teller, Revs. Modern Phys. **13**, 75 (1941).
[5] Moffitt and Coulson, Proc. Phys. Soc. (London) **60**, 309 (1948).
[6] M. Goeppert-Mayer and A. L. Sklar, J. Chem. Phys. **6**, 645 (1938).
[7] Sponer, Nordheim, Sklar, and Teller, J. Chem. Phys. **7**, 207 (1939).

Dissociation of Nitrogen in Shock Waves*

J. P. Toennies and E. F. Greene
Metcalf Chemical Laboratories, Brown University, Providence, Rhode Island
(Received May 13, 1955)

THE dissociation energy of nitrogen has been a matter of dispute for some time and it is only recently that results from a variety of experiments[1–3] have shown reasonable agreement on a value of $D_{N_2}=225$ kcal per mole. We have been studying the properties of strong shock waves in nitrogen and our results also support this so-called high value for the dissociation energy.

For steady flow the conservation equations and the equation of state for a gas permit calculation of the properties of the heated gas behind a shock front in terms of the pressure, temperature, and flow velocity of the undisturbed gas. Thus a measurement of the shock velocity (i.e., the flow velocity of the undisturbed gas relative to the shock front) permits a complete description of the shock if equilibrium between the various degrees of freedom is ultimately attained behind the shock front. If the equation of state contains an unknown parameter, in our case the degree of dissociation or the dissociation energy, it may be calculated if one more property of the shock can be obtained. We have measured incident and reflected velocities for strong shocks in nitrogen and have compared the results with calculations for $D_{N_2}=170$ and 225 kcal per mole using published data for nitrogen.[4,5]

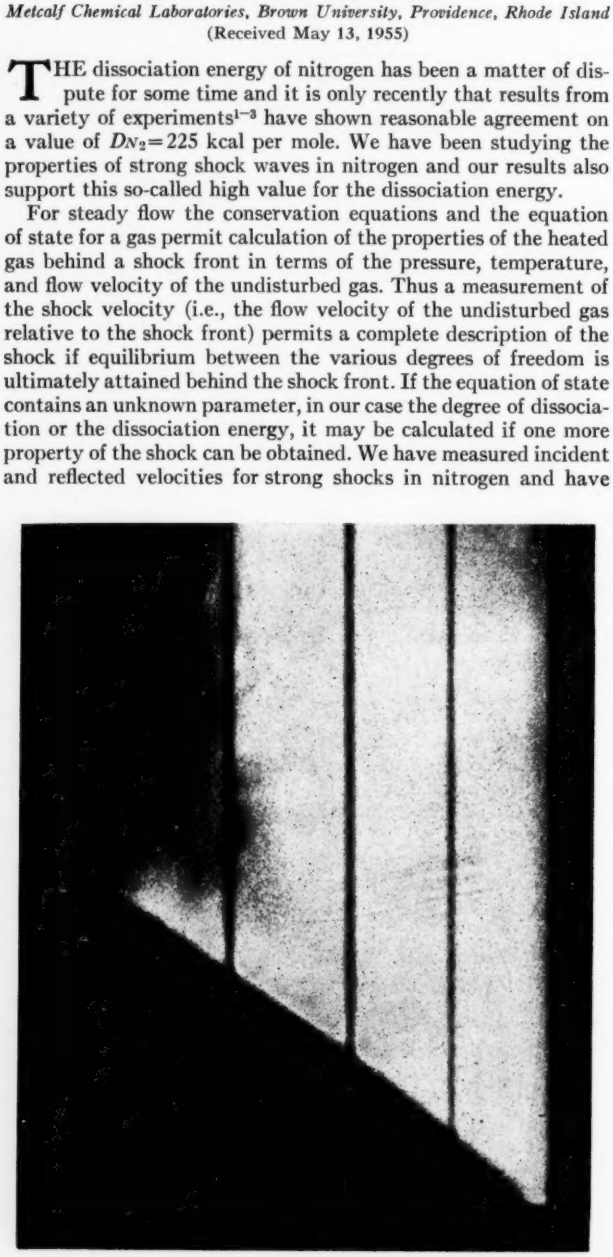

FIG. 1. Moving film camera picture of a reflected shock in nitrogen. Time increases upwards and the end plate is at the right.

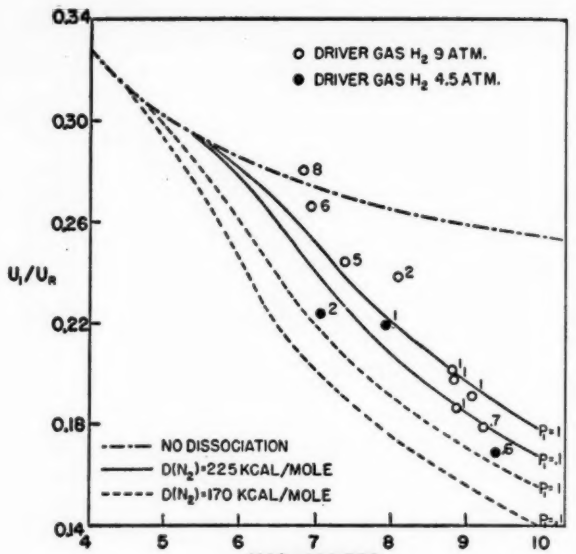

FIG. 2. The ratio of reflected to incident shock velocity in nitrogen as a function of Mach number.

The shocks were produced in the 2 in. i.d. glass shock tube previously described.[6]

The velocity of the incident wave was measured by timing the light pulses emitted as the shock passed successive photomultiplier tubes, while the velocity of the wave reflected from the brass end plate was recorded by a moving film camera. Tank nitrogen was used, and spectra showed that the light came mostly from small concentrations of impurities present in the shock tube. Figure 1 is a moving film picture of a reflected wave (0.64 km/sec). The incident shock is not visible but comes in from the lower left. An interesting feature is the acceleration of the reflected shock. This does not happen with reflected shocks in argon which either have a constant velocity or decelerate slowly. We attribute the acceleration to a relaxation process in the gas heated by the incident shock, or to an initial dissociation in excess of equilibrium behind the reflected wave.

The results for nitrogen are shown in Fig. 2 where the ratio of the reflected to incident shock velocity, $^UR/U_I$, is plotted against the incident shock Mach number. The reflected velocity used is the approximately constant value reached furthest away from the end plate. This allows the maximum time for equilibration to occur. The small numbers by the points indicate the initial pressure in the shock tube, P_1, in mm while the calculated curves are for the cases $P_1=1$ and 0.1 mm for $D_{N_2}=225$ and 170 kcal per mole. It is clear that in spite of considerable scatter the points fit the value $D_{N_2}=225$ fairly well and do not agree with $D_{N_2}=170$. It is difficult to make an exact correction for the attenuation of the flow but a preliminary attempt indicates that the correction will not affect our conclusions.

Experiments with argon, for which the corresponding process is ionization, show similar agreement with published calculations[7] using the known ionization potential.

We feel that measurements of the reflected velocities of shock waves provide a useful method for investigating the properties of gases, especially at temperatures high enough to be not readily accessible by other means.

* Assisted by the Office of Naval Research.
[1] Kistiakowsky, Knight, and Malin, J. Chem. Phys. **20**, 876 (1952).
[2] J. M. Hendrie, J. Chem. Phys. **22**, 1503 (1954).
[3] A. E. Douglas, J. Phys. Chem. **59**, 109 (1955).
[4] W. F. Giauque and J. O. Clayton, J. Am. Chem. Soc. **55**, 4875 (1933).
[5] W. Döring, Z. Elektrochem. **53**, 106 (1949).
[6] E. F. Greene, J. Am. Chem. Soc. **76**, 2127 (1954).
[7] Resler, Lin, and Kantrowitz, J. Appl. Phys. **23**, 1390 (1952).

Wavelength Dependence of Photoisomerization Equilibria in Azocompounds

ERNST FISCHER, *Photochemical Laboratory, The Weizmann Institute of Science, Rehovoth, Israel*
AND
MAX FRANKEL AND REUVEN WOLOVSKY, *Department of Organic Chemistry, The Hebrew University, Jerusalem, Israel*
(Received April 26, 1955)

WHEN solutions of the compounds azobenzene, 1:1′-, 1:2′-, and 2:2′-azonaphthalene are irradiated with light from the sun or a mercury arc, a photoisomeric equilibrium is established in each case, containing a certain fraction of the respective *cis*-isomers, which under suitable conditions can be separated from the *trans*-isomers (azobenzene,[1] azonaphthalenes[2]). Quantum yields of the photoisomerization have been reported for azobenzene and several of its derivatives.[3,4]

The dependence of this photoisomerization equilibrium on the wavelength of the light used for irradiation was now investigated. Toluene solutions of azobenzene and the three azonaphthalenes were irradiated at minus 25°C with each of the principal mercury bands at 365, 405, 436, 546, and 578 mμ, isolated by suitable combinations of Corning Glass filters from the light emitted by a Hanovia Utility mercury high-pressure arc. The position of the equilibrium set up in each case was calculated from the absorption curves of the equilibrium mixtures and those of the pure *cis*- and *trans*-isomers, given in Fig. 1.

Both irradiations and spectrophotometric determinations were carried out at the required temperatures in special Dewar cells placed in an attachment to the Beckman DU spectrophotometer.[5] With a distance of about five cm between light source and solution, photoequilibration took from a few minutes to about two hours, depending on the wavelength and the concentration (5 mg/liter for the azonaphthalenes, 40 mg/liter for azobenzene). At the conclusion of each experiment, the concentration of the solute was checked by measuring the absorption curve after heating the solution *in situ* to 90°C and recooling, thereby completely converting the solute into the *trans*-isomer.

The results obtained are summarized in Table I, as the percentage of *cis*-isomer formed after irradiation at each wavelength. The final photoisomeric equilibrium was always independent of the isomeric composition before irradiation.

Irradiation with the 254 mμ mercury line from a "resonance" lamp in all cases decreased the concentration of the *cis*-isomer obtained at 365 mμ. However, such irradiation also results in slow irreversible changes, probably owing to the occurrence of secondary photochemical reactions. Irradiation with the 620 mμ mercury line, or with light from a 1000 candlepower "Pointolite" lamp, passed through a filter transmitting only beyond 600 mμ, did not cause any detectable photoisomerization during times comparable with those used at shorter wavelengths. With azobenzene this was also the case with light at 578 mμ.

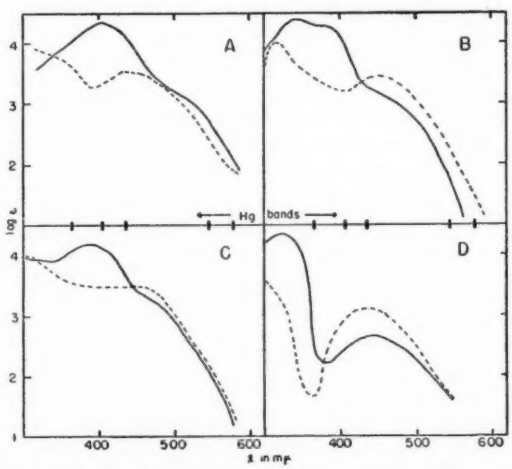

FIG. 1. Spectral absorption curves of azocompounds in toluene at minus 25°C: (A) 1:1′-azonaphthalene, (B) 2:2′-a.n., (C) 1:2′-a.n., (D) azobenzene. Broken lines = *cis*, full lines = *trans*.

TABLE I. Percentage of *cis*-isomer formed after photoequilibration at various wavelengths.

Wavelength, mμ	365	405	436	546	578	Full Hg arc[a]
Azobenzene	91	12	14	25	...	37
1:1′-a.n.	61	95	65	55	52	...
1:2′-a.n.	83	93	60	34	...	66
2:2′-a.n.	92	87	33	10	2	48

[a] Passed through a 2-mm Pyrex plate to exclude light below 280 mμ.

In Table II the relative spectral absorptions of the two isomers of each compound at each wavelength are compared with the equilibria set up in each case. The qualitative parallelism between the ratios (a) and (b) in this Table is apparent and suggests that in the cases studied the position of the photoequilibrium between the *cis-trans*-isomers is determined to a large extent by the ratio between the molar extinction coefficient ϵ at the wavelength of the light used for irradiation, the equilibrium being in favor of the isomer with the smaller ϵ.

TABLE II. Relation between spectral absorption and position of photoequilibrium. (a) $=\epsilon_{cis}/\epsilon_{trans}$ at indicated wavelength, (b) = percent *trans*/percent *cis* in equilibrium resulting from irradiation at indicated wavelength.

Wavelength, mμ		365	405	436	546	578
Azobenzene	(a)	0.03	3	2.7	1.3	...
	(b)	0.1	7	6	3	...
1:1′-a.n.	(a)	0.3	0.1	0.3	0.55	0.8
	(b)	0.6	0.05	0.5	0.8	0.9
1:2′-a.n.	(a)	0.3	0.25	0.7	1.4	...
	(b)	0.2	0.1	0.7	1.9	...
2:2′-a.n.	(a)	0.1	0.2	1.4	3.2	9
	(b)	0.1	0.15	2.0	9	49

[1] Campbell, Henderson, and Taylor, J. Chem. Soc. 531 (1953), where previous references are cited.
[2] Frankel, Wolovsky, and Fischer, J. Chem. Soc. (to be published).
[3] Hausser, Naturwiss. **36**, 315 (1949).
[4] Birnbaum and Style, Trans. Faraday Soc. **50**, 1192 (1954).
[5] Hirshberg and Fischer, J. Chem. Soc. 629 (1953); 297, 3129 (1954).
The authors are indebted to Dr. Y. Hirshberg for permission to use the apparatus mentioned here.

Infrared Absorption Spectra of Inorganic Coordination Complexes. III. Deformation Frequencies of the NH_3 Ligand

SAN-ICHIRO MIZUSHIMA AND ICHIRO NAKAGAWA, *Faculty of Science, Tokyo University, Tokyo, Japan*
AND
J. V. QUAGLIANO,* *Department of Chemistry, University of Notre Dame, Notre Dame, Indiana*
(Received February 25, 1955)

NAKAGAWA and Mizushima[1,2] have calculated the deformation frequencies of the CH_3 group contained in different organic molecules and have assigned the observed frequencies to the degenerate deformation, symmetric deformation, and rocking vibrations. It is expected that when the NH_3 group is coordinated about a central atom in metal complexes, this ligand would show deformation vibrations similar to those of the CH_3 group in organic molecules.

The kinetic energy matrix G and potential energy matrix F are set up according to Wilson's method.[3] Approximate calculations of the deformation frequencies of the NH_3 ligand have been made from the product of the diagonal terms, as in the case of carbon hydrogen deformation frequencies,[1,2] because the diagonal terms of G-matrix containing the reciprocals of hydrogen mass are much

greater than the cross terms containing the reciprocals of masses of heavier atoms. In this calculation a potential function of the Urey-Bradley type has been used. The values of force constants with the same notations as those used in previous papers[4] are shown in Table I. The calculated values are in good agreement

TABLE I. Force constants in 10^5 dynes/cm and intramolecular tension in 10^{-11} dynes/cm.

H_{HNH} =0.540	$F_{H\ldots H}$ =0.060	$k = -0.040$
H_{HNM} =0.182	$F_{H\ldots M}$ =0.100	

with those observed for $[Co(NH_3)_6]^{+++}$ as shown in Table II. The reasonableness of the values of the force constants will be shown elsewhere.[2] The assignment of the observed frequencies can be made with certainty since in this case no other absorption peaks have been observed in this frequency region. Furthermore this assignment has been checked by observing the isotopic shift of these frequencies. As shown in Table II the frequencies observed

TABLE II. The calculated and observed deformation frequencies in cm^{-1} of the NH_3 and ND_3 ligands in $[Co(NH_3)_6]^{+++}$

Type of vibration	NH_3 ligand calc	NH_3 ligand obs	ND_3 ligand calc	ND_3 ligand obs
degenerate deformation	1579	1610	1156	1162
symmetric deformation	1340	1330	1021	1024
rocking	854	835	628	outside the NaCl region

for the deformation vibrations of the ND_3 ligand are in good agreement with those calculated from the isotopic relations.

We have observed the infrared absorption spectra of many other coordination compounds containing NH_3 ligands, especially cobalt(III) ammines. In all these compounds we found three absorption bands similar in frequency and in general behavior to the three bands of the octahedral complex cation $[Co(NH_3)_6]^{+++}$

TABLE III. Observed deformation frequencies in cm^{-1} of NH_3 in some metal ammine complexes.

Complex	Type of vibration degenerate	symmetric	rocking
$[Co(NH_3)_6]I_3$	1615	1330	810
$[Co(NH_3)_5Cl]Cl_2$	1600	1310	845
$[Co(NH_3)_5Br]Br_2$	1570	1310	830
$[Pd(NH_3)_4]PdCl_4$	1632	1283	785
$[Co(NH_3)_5H_2O]Cl_2$	1610	1325	840

referred to above. Table III lists the deformation vibration frequencies of the NH_3 ligand in some different types of metal coordination compounds.

Some authors have explained these bands as arising from the metal-ligand vibrations of the octahedral cation.[5] However, as has been shown by us, such vibrations appear in a much lower frequency region.[6] From the result of the present research we can conclude that the metal-to-ligand bond should be fairly covalent. If this bond were ionic, we could conclude that there is no rocking vibration of the NH_3 group.

* Member, Radiation Project operated by the University of Notre Dame and supported in part under U. S. Atomic Energy Commission Contract AT(11-1)-38.

[1] I. Nakagawa, J. Chem. Soc. Japan **75**, 1259 (1954).
[2] I. Nakagawa and S. Mizushima (to be published).
[3] E. B. Wilson, J. Chem. Phys. **7**, 1047 (1939); **9**, 76 (1941).
[4] T. Shimanouchi, J. Chem. Phys. **17**, 245, 734, 848 (1949); see also S. Mizushima, *Structure of Molecules and Internal Rotation* (Academic Press, Inc., New York, 1954).
[5] D. G. Hill and A. F. Rosenberg, J. Chem. Phys. **22**, 148 (1954).
[6] Sweeny, Mizushima, and Quagliano, paper presented at the 120th National Meeting of the American Chemical Society, New York, New York, September 16, 1954.

Production of a Blue Color in Irradiated Plastic Scintillators*

J. H. PANNELL AND B. MANNING
Technical Operations, Incorporated, Arlington, Massachusetts
(Received April 25, 1955)

UNDER beta irradiation an intense blue color is formed at room temperature in polystyrene or polyvinyltoluene containing certain fluors and protected from light. This color is unstable and is bleached by light but sufficiently slowly that absorption measurements can be made without difficulty. Using sources containing 100 millicuries of strontium-90, and producing a maximum dose rate at the surface of about 100 rep per second, a visible amount of color has been produced in 10 minutes. In a plastic 1-in. thick, a dose of 20 000 r of Co^{60} gamma rays delivered in 10 minutes also produces a visible amount of color.

At dry ice temperature, −70°C, production of this color is apparently accelerated (i.e., decay is slowed down) and becomes obvious in many plastic scintillators, being most evident in those containing the following: terphenyl, terphenyl+diphenylstilbene, diphenylbutadiene, tetraphenylbutadiene, diphenylstilbene, and tetraphenylethylene. When plastics irradiated at −70°C are allowed to warm to room temperature, a considerable amount of

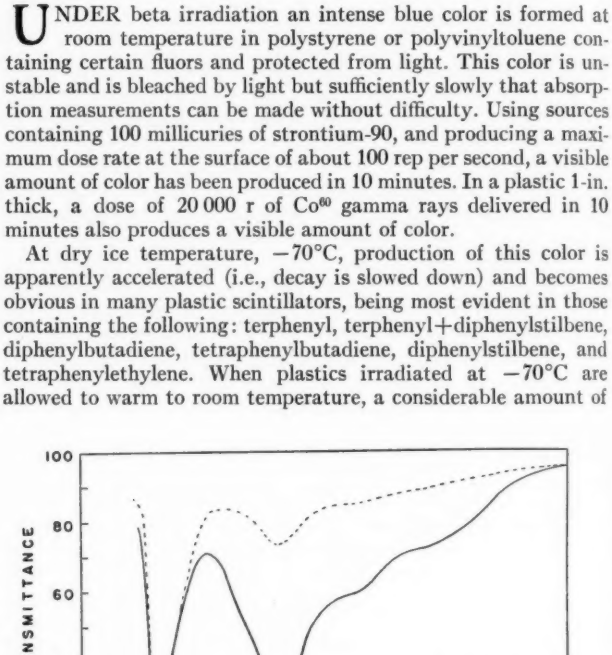

FIG. 1. Absorption spectra of irradiated plastic which show fading of the blue color during a 5-hr period in the dark.

phosphorescence occurs and this too is readily visible. This phosphorescence, associated with thermal bleaching of the color, indicates that the color is associated with trapped electrons and is perhaps the first suggestion of such trapping in an essentially amorphous substance.

Measurements of light absorption were made in a Beckman Model DU spectrophotometer. The absorption curves for a representative terphenyl-tetraphenylbutadiene polystyrene plastic after irradiation for 16 hours are shown in Fig. 1. Unirradiated plastic was used as a reference substance. The blue color results from a broad absorption band having a maximum at 580 mμ where it remains throughout the fading process. A narrow absorption band centered at 410 mμ is responsible for a small amount of yellow color that is not apparent after short-time irradiations and that fades very slowly. Polystyrene alone produces no color under the same irradiation conditions.

The rate of fading, in the dark, of the 580 mμ peak at room temperature is complex and not readily duplicated accurately, but can be approximated by the sum of two exponentials with decay constants of 0.045 hr^{-1} and 2.3 hr^{-1}.

The phosphorescence exhibited by the above phosphor, that is warming up after being irradiated at dry ice temperature, has a peak at about 450 mμ. Further analysis of the characteristics of this light has not been made but spectrally it resembles the fluorescence emitted by the phosphor during irradiation by beta

rays or ultraviolet light. Therefore, the blue color is caused by a metastable state in the sequence of events occurring between absorption of ionizing radiation and emission of fluorescence.

Some of the other substances tested produced, at room temperature, a yellow color of low intensity, e.g., triphenylmethanol, tetraphenylethylene, and triphenylmethane.

Measurements of dielectric constants at one megacycle indicate that in the colored plastic the dielectric constant is increased and that its decay to a normal value occurs at the same rate as does fading of the color.

If it were assumed that a band-structure model were not applicable to plastic scintillators, the production of color would be attributed to new molecular species. Both free radicals and degradation products, produced by ionizing radiation, may cause this effect although the properties which have been described are characteristic of free radicals. Unfortunately for this hypothesis, the same color is formed in plastics containing compounds with widely different structures, and none is formed in those most susceptible to free radical formation. We are, therefore, reporting a phenomenon most easily explained by an "F-center" theory but in a noncrystalline environment.

* This work was supported by the United States Air Force through the Office of Scientific Research of the Air Research and Development Command under contract. This publication comprises Air Force technical note number OSR-TN-55-83.

Rate of Evaporation of Graphite

R. J. Thorn and G. H. Winslow
Chemistry Division, Argonne National Laboratory, Lemont, Illinois
(Received April 22, 1955)

FOR about two decades the determinations of the heat of sublimation of graphite by rate of evaporation measurements have been criticized because of the uncertainty in the degree of saturation of the vapor. Simpson, Thorn, and Winslow[1] obtained results which indicated that the rate of sublimation from a graphite surface at 2500°K may be about 0.7 times the rate of sublimation from a cylindrical hole (ratio of cross section to interior area $=6.5\times10^{-2}$). On the other hand Doerhard, Goldfinger, and Waelbroeck[2] obtained results which tend to show that carbon sublimes from an open surface at 2500°K at a rate 10^{-3} times that at which it effuses out of a Knudsen cell (ratio of orifice to interior area $=10^{-4}$). In an attempt to resolve these divergent observations, the authors have undertaken a more direct and careful determination.

The method consisted in measuring the rate of deposition by observing the change with time of the apparent temperature of the source measured through the deposit.[1,3] The source was a hole in a hollow graphite cylinder with closed ends. The cylinder was surrounded by a closely fitting split cylindrical graphite radiation shield which attained a temperature about 300° below the orifice or surface temperature. The ratio of orifice to interior area was 6×10^{-4} for some exposures, and 9×10^{-4} for others. To obtain the deposition from a surface a closely fitting cylindrical plug was inserted into the cavity, so that a graphite surface was immediately behind the orifice, but the original geometry was preserved. The graphite cylinder was enclosed in a double-walled water-cooled fused silica condenser which received the deposit. The cylinder was heated inductively. Background pressures during an exposure were 2×10^{-6} mm Hg or less.

The source temperature was determined by three different procedures. A thermostatted rf meter of the thermocouple type which gave a measure of the heating current was calibrated, prior to each exposure, at temperatures below the sublimation temperature, and an extrapolation was made to the sublimation temperature. Subsequently the apparent temperature of the source was measured through the deposit as a function of the rf current in the range of the calibration. From these data and the apparent temperature at the end of the exposure the source temperature was calculated. Finally the initial temperature was found by extrapolating the apparent temperature to zero time. In one exposure these three procedures gave values of 2467, 2466, and 2456°K respectively. Of these, the last is the least reliable.

Typical results are shown in Fig. 1. The positive curvature at the upper end of the "surface" curve is contrary to expectations.[4] It is possible that the energy reflected back to the surface source significantly increased its temperature. Other explanations are conceivable. Nevertheless, it seems impossible that any such explanations would uncover a real ratio of 10^3 in the rates of evaporation for these two types of exposure.

These experiments, however, do indicate a somewhat lower rate of sublimation from the surface than from the cell. By comparing slopes at approximately equal deposit thicknesses, rate ratios of 0.31 to 0.93 are found, in qualitative agreement with a previous result.[1]

There might be several factors contributing to such a result, only one of which arises from a barrier at the surface. Another

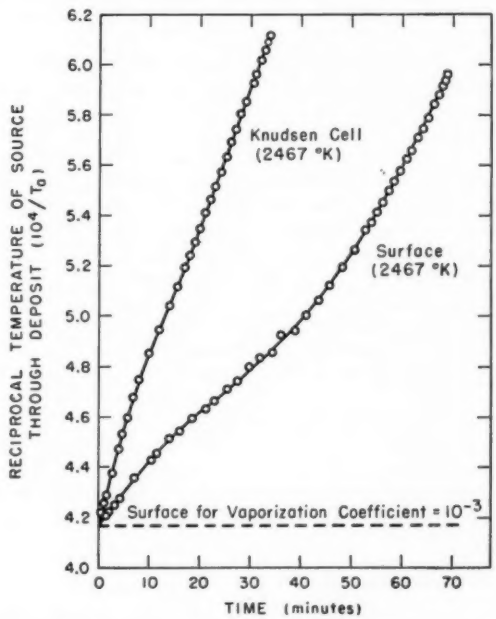

FIG. 1. Plots of reciprocal temperature of source measured through deposit collected from Knudsen cell and surface. The latter was obtained at 2477°K and corrected to 2467°K. Dotted line represents curve if rate from surface were 10^{-3} that from cell.

example[5] is uncertainty in the "temperature" of the surface which, when roughened by sublimation, presents a distinctly mottled appearance in the pyrometer. Real temperature differences may well be involved. The "effective heat of sublimation" for photons [$Rc_2/\lambda \doteq 43$ kcal/mole] is much less than the heat of sublimation for carbon atoms. Thus it is critical, as regards interpretation, that the temperature actually read be that of those portions of the surface for which the rate of evaporation is equal to the net rate.

This investigation is being continued so that a more detailed report will be given later.

* Based on work performed under the auspices of the U. S. Atomic Energy Commission.

[1] Simpson, Thorn, and Winslow, Argonne National Laboratory Report ANL-4264, March, 1949.

[2] Doerhard, Goldfinger, and Waelbroeck, Bull. soc. chim. Belges **62**, 498 (1953).

[3] O. C. Simpson and R. J. Thorn, Rev. Sci. Instr. **20**, 504 (1949).

[4] Consideration of the optical properties of these thin films with the assumption that their optical constants are independent of thickness has led to a "predicted" curve having the shape of the one marked "Knudsen Cell."

[5] See also, L. Brewer and J. S. Kane, J. Phys. Chem. **59**, 105 (1955).

Energy Exchange between Cold Gas Molecules and a Hot Graphite Surface*

ROBERT GOMER AND LOTHAR MEYER
Institute for the Study of Metals, University of Chicago, Chicago, Illinois
(Received April 26, 1955)

GRAPHITE of fiber structure can be produced by decomposing diluted hydrocarbons on carbon wires heated to ~1500°C.[1,2] It was attempted to improve the ordering and increase the crystal size by decomposing pure CH_4 and C_2H_6 at pressures $<10^{-2}$ mm where the mean free path exceeds the dimensions of the vessel precluding reactions in the gas phase. The method was similar to that of reference 1. A liquid hydrogen trap was used to condense reactants and all reaction products except H_2.

Surprisingly no reaction was observed with filament temperatures $T_f = 1000$–2300°C provided the graphite surface was so smooth that an impinging molecule had only a negligible chance of making a second collision with it before reaching the cold wall. Filaments roughened by decomposition at only slightly higher pressures subsequently decomposed CH_4 and C_2H_6 at any pressure in the whole temperature range.

A systematic investigation of the energy exchange between hot smooth graphite and various gases has been undertaken, measuring the heat transport by the Schleiermacher method with a fiber structure graphite filament as hot wire. The initial fast resistance change after gas admission (due to heat conduction) is followed by a slow reversible change probably caused by absorption. This necessitated the use of a Wheatstone bridge with the wire as one arm; the unbalancing voltage was used to actuate an amplifier whose stabilized output provided part of the heating current for the graphite wire. This circuit maintained the filament at constant resistance by varying the amplifier output, the change in current being plotted on a Brown recorder. Figure 1 shows a typical record. The rate of heat transport by the gas was calculated from the break B in the plots. The estimated error is ±5 percent.

It was found that the heat transported per molecule is essentially independent of T_f from 850–1500°C but varies with the gas. Figure 2 shows the rate of heat transport $\dot{Q}$ of Kr as a function of pressure for different temperatures. These results can be interpreted in terms of a temperature T_e at which the molecules "evaporate" from the hot surface. T_e is found from

$$\dot{Q} = \dot{n}\bar{C}(T_e - T_w), \qquad (1)$$

where $\dot{n}$ is the number of impacts/second, T_w the wall temperature, and $\bar{C}$ is $R/2$ + the average specific heat between T_e and T_w. The addition of $R/2$ is necessary because the faster molecules carry more energy. We assume that the rotational degrees of freedom are excited for H_2 and CH_4, and also the vibrational ones for CH_4, thus yielding minimum values for T_e. However, these are consistent with those found for the rare gases. Table I contains a summary of the results. The last column T_e' is derived on the assumption that only translational energy is transported, leading, at least for CH_4, to rather improbable temperatures.

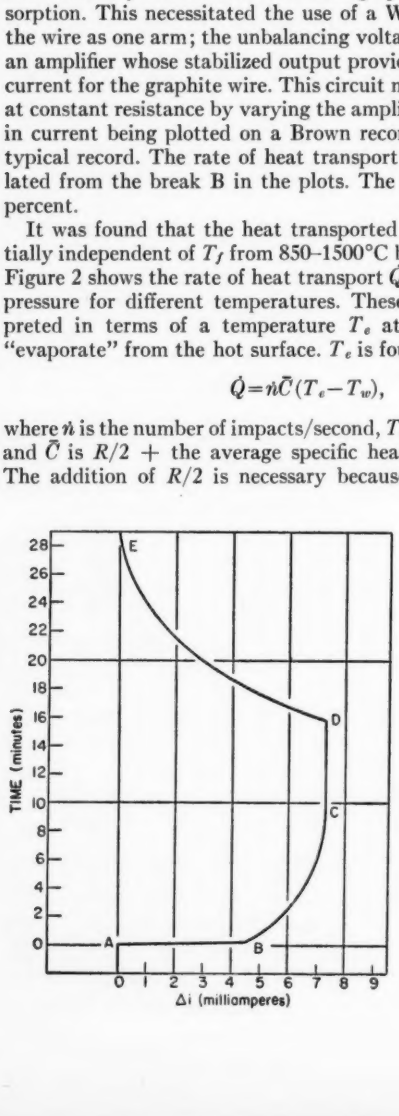

FIG. 1. Drawing of recorder trace during experiment: A. 14.8 microns Kr admitted, $T_f = 1100$°C. B. Cooling resulting from heat transport of gas is compensated. C. Steady state is reached. D. Gas pumped off. E. Return to initial state.

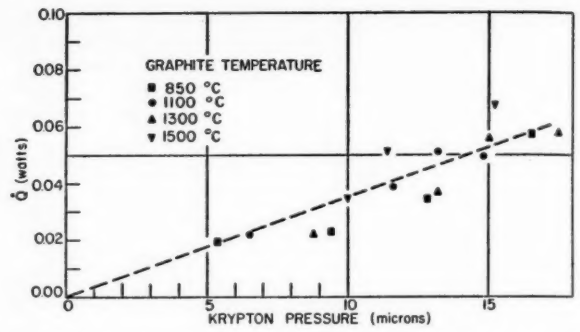

FIG. 2. Rate of heat transport in watts as function of pressure in microns for Kr. Surface area of graphite = 1.0 cm².

TABLE I. Temperature T_e at which different gases "evaporate" from a hot graphite surface derived by Eq. (1) from the rate of heat transport and the specific heat of column 3. T_e' derived on the assumption that only translational energy is transported, i.e., $c = 4$ cal/mole in all cases.

Gas	T_e °C	$c_v + R/2$ cal/mole	T_e' °C
He	165	4	165
Ne	320	4	320
Kr	540	4	540
H_2	195	6	280
CH_4	360	10.5	905

These results suggest that energy exchange between a smooth graphite surface and gas molecules proceeds by quasi-adsorption and evaporation, independent of T_f as long as $T_f > T_e$. T_e should be a measure of the van der Waals potential between surface and molecule. Our results do not seem to agree with present theories of accommodation derived for $T_f - T_w \to 0$.[3–5] Experiments with different wall temperatures including $T_w > T_e$ are in progress.

We wish to thank Mr. A. H. Dewey for his help with the measurements.

* Research supported in part by U. S. Atomic Energy Commission contract.

[1] L. Meyer, Trans. Faraday Soc. **34**, 1056 (1938).
[2] Meyer, Picus, and Johnston, Natl. Bur. Standards Circ. No. 519, October 1952, p. 249.
[3] C. Zener, Phys. Rev. **40**, 472, 1016 (1932).
[4] L. Landau, Physik Z. Sowjetunion **8**, 489 (1935).
[5] A. F. Devonshire, Proc. Roy. Soc. (London) **158**, 269 (1937).

Critical Constants of *n*-Butanol

R. SINGH* AND L. W. SHEMILT†
Department of Chemical Engineering, University of British Columbia, Vancouver, Canada
(Received April 22, 1955)

THE experimental determination of P-V-T relationships on pure compounds is increasingly important both for high pressure process design and for evaluating theoretical and empirical methods of obtaining thermodynamic data. As part of an experimental investigation of the normal alcohols, the P-V-T relationships of *n*-butanol have been determined from normal temperature and pressure to above the critical point. Critical constants, including the critical density, are reported here.

The apparatus, designed after that of Kay,[1] consisted of an adjustable steel block filled with mercury and connected to a

TABLE I.

Temp. °C	Densities: g per cc ρ_L obs	ρ_L calc	ρ_V obs	ρ_V calc
155.8	0.70520	0.7052	0.0079	0.00903
173.3	0.67059	0.6705	0.012494	0.01241
123.6	0.62478	0.6500	0.01587	0.01530
198.9	0.61920	0.6192	0.02106	0.02120
212.0	0.59305	0.5935	0.02775	0.02745
232.4			0.04280	0.04255
237.3	0.5359	0.5350		
244.6	0.51993	0.5202	0.05516	0.05400
260.6	0.48589	0.4835	0.07733	0.07750
268.9	0.45740	0.4570	0.09480	0.09520
272.25	0.43200	0.4460	0.1023	0.1024
276.45	0.42370	0.4205	0.1300	0.1270
283.94	0.3620	0.3580	0.1681	0.1662
285.72	0.3620	0.3220	0.2402	0.2220

calibrated glass capillary containing the samples and enclosed in a constant temperature apparatus. Pressures were measured by a Barrett dead weight test gauge with calibrated piston diameters and weights. Temperatures were maintained by an atmosphere of pure organic vapors distilling at constant temperature, and were measured by copper-constantan thermocouples calibrated against a platinum resistance thermometer with an NBS certificate. For a series of specific temperatures, the pressures and volumes were read, the latter by using a cathetometer calibrated against a standard meter stick. Corrections for menisci, interphase levels, and ambient conditions were made. Corrections for expansion of the glass capillary due to pressure and temperature changes were made using the Bridgman equation[2] $\Delta V = V_0(30.27\times10^{-7}p + 9.9\times10^{-12}p^2)$ where p=pressure in Kgm/cm², and a coefficient of cubical expansion of 9.9×10^{-6}.[3]

The *n*-butanol (C.P. grade) was distilled at high reflux successively from calcium oxide, fresh magnesium, and activated alumina. Middle cuts were collected, and the final product gave a refractive index of 1.3973 at 25°C and a boiling point of 117.5°C at 760 mm.

Densities for the saturated vapor and liquid are given in Table I. Equations for the saturated vapor and for the liquid densities have been determined as

$$\rho_V = 0.1424 + 0.44\times10^{-2}n + 5.93125\times10^{-4}n^2 + 1.8408\times10^{-4}n^3 + 1.6317\times10^{-5}n^4,$$

and

$$\rho_L = 0.39718 - 0.005899n - 2.1212\times10^{-4}n^2 - 1.48145\times10^{-4}n^3 - 2.3350\times10^{-5}n^4,$$

where $n = t°C - 280.5°C$.

In Table I observed values are experimentally determined, and calculated values were those obtained by the above equations and show a mean deviation of 0.15 percent for the liquid densities and 0.6 percent for the vapor densities. The critical density has been determined by the "law of rectilinear diameters,"[4,5] and the equation for rectilinear diameters determined as

$$d = 0.28637 - 0.6165\times10^{-3}m + 5.7986\times10^{-7}m^2 + 5.324\times10^{-8}m^3 + 1.35732\times10^{-9}m^4,$$

where $m = t°C - 250.0°C$. The critical constants were determined both analytically and graphically with excellent agreement, and the results are shown, in comparison to other investigations, in Table II. It is considered that the critical temperature is accurate to ±0.05°C, the pressure to ±0.05 atmos and the density to ±0.0002 g per cc. A more extensive report on the P-V-T relationships for *n*-butanol will be submitted for publication shortly.

Acknowledgments.—The assistance of R. W. Esplen and D. Clegg in making measurements, of W. Pye in glassblowing, and of the National Research Council of Canada in making a grant-in-aid is gratefully acknowledged.

TABLE II.

Date	t_c°C	p_c atmos	ρ_c g/cc	Investigators
1883	287.1			Pawlewski[a]
1884	270.5			de Heen[b]
1923	287.0	48.4		Herz and Neukirch[c]
1943	288.0			Fischer and Reichel[d]
1955	286.95	48.60	0.2700	This investigation

[a] B. Pawlewski, Ber. deut. chem. Ges. **15**, 2143, 2460 (1882).
[b] de Heen, Landolt, and Bornstein (Verlag Julius Springer, Berlin, 1923), Vol. 1, p. 256.
[c] W. Herz and E. Neukirch, Z. Physik **104**, 433 (1923).
[d] R. Fischer and T. Reichel, Mikrochimie **31**, 192 (1943).

* Demonstrator, Department of Chemical Engineering, University of British Columbia.
† Associate Professor, Department of Chemical Engineering, University of British Columbia.

[1] W. B. Kay, Ind. Eng. Chem. **24**, 291 (1932).
[2] P. W. Bridgman, Am. Sci. J. **7**, 81 (1929).
[3] Catalog No. L. P. 34 (1954), Corning Glass Works, Corning, New York.
[4] L. Caillette and E. Mathies, Compt. rend. **102**, 1202 (1886).
[5] S. Young, Sci. Proc. Roy. Dublin Soc. **12**, 374 (1909–10).

Frequency Shift of the CO Stretching Band in Polypeptides and Proteins

SAMUEL KRIMM
Harrison M. Randall Laboratory of Physics, University of Michigan, Ann Arbor, Michigan
(Received April 28, 1955)

IT has been observed[1,2] that the frequency of the CO stretching mode in synthetic polypeptides and natural proteins depends upon the configuration of the polypeptide chain: in the α, or folded, form this frequency is close to 1660 cm^{-1}, whereas in the β, or extended, form this frequency is close to 1630 cm^{-1}. Although used as a means of distinguishing between α and β forms of polypeptides and proteins,[2] it does not appear that any explanation has been offered for the frequency shift. It is the purpose of this note to suggest a possible reason, one which seems to be supported by the presently available experimental evidence.

Although heretofore correlated with the α and β configurations of the polypeptide chain, it is clear that the shift is more a reflection of the local environment of the CO group than it is of the over-all chain configuration. Such a change in environment would most naturally be related to the hydrogen bonding in which the CO group participates. Frequency shifts involving hydrogen bonding have been correlated with the distance between the atoms partaking in the hydrogen bond.[4,5] This cannot, however, be the entire explanation in the present case, because the significant fact is that the NH stretching frequency does not shift by any appreciable amount from α to β polypeptides,[1] which it would be expected to do if the only result of the configurational change was a change in the O···N distance.

It is suggested that the frequency shift results from a configurational change in the CO···NH angle of the type schematically illustrated in I and II below. Assuming that the O···H force

I II

constant is essentially the same in I and II, it is clear that we would expect a relatively larger change in the CO frequency from I to II than in the NH frequency, since the CO force constant is more strongly affected. We would further expect that the CO frequency in I would be lower than in II. If the H atom were not along the O···N line, the result would be essentially the same, although the NH stretching frequency might undergo a small shift.

This explanation for the frequency shift seems to be consistent with the known structural features of present protein models and

TABLE I. Correlation between CO stretching frequency and CO···NH angle.

Substance	CO···HN angle	CO stretching frequency, cm^{-1}	References
Silk	~180°	1640	b; see footnote 3
Nylon	~160°	1650	c; d
Acetanilide	145°	1660	e; f
Urea	180°[a]	1680	g; h
Diketopiperazine	~120°	1705	i; j

[a] But not colinear (see text).
[b] Marsh, Corey, and Pauling, Biochim. et Biophys. Acta **16**, 1 (1955).
[c] Ambrose, Elliott, and Temple, Proc. Roy. Soc. (London) **A199**, 183 (1949).
[d] Elliott, Ambrose, and Temple, J. Chem. Phys. **16**, 877 (1948).
[e] C. J. Brown and D. E. C. Corbridge, Acta Cryst. **7**, 711 (1954).
[f] J. Mann and H. W. Thompson, Proc. Roy. Soc. (London) **A211**, 168 (1952).
[g] P. A. Vaughan and J. Donohue, Acta Cryst. **5**, 530 (1952).
[h] W. E. Keller, J. Chem. Phys. **16**, 1003 (1948).
[i] R. B. Corey, J. Am. Chem. Soc. **60**, 1598 (1938).
[j] Ambrose, Elliott, and Temple, Proc. Roy. Soc. (London) **A206**, 192 (1951).

of simple compounds. In Table I we present some results which correlate the CO···HN angle with the CO stretching frequency. It is seen that the relationship discussed above is well obeyed. The case of urea corresponds to structure II in which the H is not on the O···N line (but CO and HN bonds are parallel), and is seen to fit in well with the present explanation. The frequencies do not correlate as well with the hydrogen bond distances; e.g., 2.76 A in silk, 2.85 A in diketopiperazine, 2.97 A in acetanilide. In all cases the NH stretching frequency is close to 3300 cm^{-1}, the value expected when hydrogen bonding occurs. Data on simple amides in solution and in the solid state[6,7] are also in agreement with the above explanation: the more nearly colinear the CO···HN hydrogen bond, the lower the CO stretching frequency. An accompanying shift in the 1530 cm^{-1} band[1] from α to β polypeptides is perhaps a result of the interaction between the CO frequency and the other modes of the peptide group.[8]

To the extent that the CO frequency is a measure of the CO···HN bonding angle, variations in this frequency would be indicative only of variations in the configuration of this hydrogen bond. It may not always be justifiable, therefore, to extrapolate from the value of this frequency to a particular polypeptide chain configuration.

[1] E. J. Ambrose and A. Elliott, Proc. Roy. Soc. (London) **A205**, 47 (1951).
[2] A. Elliott, Proc. Roy. Soc. (London) **A221**, 104 (1953).
[3] E. J. Ambrose and A. Elliott, Proc. Roy. Soc. (London) **A206**, 206 (1951).
[4] R. E. Rundle and M. Parasol, J. Chem. Phys. **20**, 1487 (1952).
[5] R. C. Lord and R. E. Merrifield, J. Chem. Phys. **21**, 166 (1953).
[6] S. Mizushima *et al.*, J. Am. Chem. Soc. **72**, 3490 (1950).
[7] S. Mizushima *et al.*, J. Am. Chem. Soc. **75**, 1863 (1953).
[8] R. D. B. Fraser and W. C. Price, Nature **170**, 490 (1952).

Absorption Coefficients of Nitric Oxide in the Vacuum Ultraviolet*

H. SUN AND G. L. WEISSLER
Department of Physics, University of Southern California, Los Angeles, California
(Received April 25, 1955)

PRELIMINARY results of the absolute absorption of light in NO have been obtained between 374 A and 1300 A from photometric measurements of 60 light source emission lines (Fig. 1 and Table I). The coefficients μ, in units of cm^{-1} at NTP, are defined by the relation $I=I_0\exp(-\mu x)$, and the techniques used were essentially those described in earlier papers[1] for a grazing incidence vacuum spectrograph. The impurities of NO were stated by the manufacturer (Matheson Company) to be nitrogen and its higher oxides, and it was attempted to freeze out the latter by passing the continuously flowing gas through alcohol cold traps (−110°C). Because of the fact that the absorption

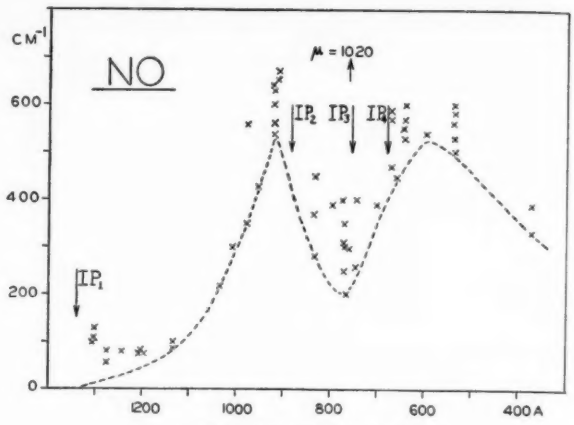

FIG. 1. Absorption coefficients in NO.

coefficients of most gases in their ionization continua are of about the same order of magnitude, it was assumed that the observed absorption in the NO continuum was probably not seriously falsified by any remaining impurities. This received further support from the fact that Zelikoff *et al.*[2] reported a broad absorption region (half-width about 55 A) in N_2O with a peak of 2465 cm^{-1} at 1285 A, whereas the measurements for NO at 1276 A and 1302 A yielded values of $\mu=81$ cm^{-1} and 130 cm^{-1}, respectively.

Previous NO results obtained by Marmo[3] and Watanabe[4] between 1100 A and 2300 A agree reasonably well with those presented here in the region where overlapping occurred. It should be kept in mind, however, that all those coefficients which fall into resonance bands with well-delineated structure can only give an indication of the magnitude of the absorption there, except for those values which lie within a diffuse band or within dissociation and ionization continua and can therefore be expected to be more accurate. The region from 680 A towards longer wavelengths is well populated with bands which have been classified by Tanaka[5] and others into Rydberg and non-Rydberg progressions, and his series limits are indicated by arrows in Fig. 1. This band structure is also apparent in the figure, where adjacent coefficients show widely different values such as $\mu=1020$ cm^{-1} at 764.357 A and $\mu=200$ cm^{-1} at 765.140 A.

The value of the continuum below 1300 A may be estimated by connecting together with a line the lowest coefficients, and the

TABLE I. Absorption coefficients (μ) of NO.

λ(A)	μ (cm^{-1})	λ(A)	μ (cm^{-1})
1306.038 O I	100	796.661 O II	390
1304.864 O I	110	775.957 O II	400
1302.192 O I	130	772.975 N III	310
1276.18 N II	81	772.385 N III	300
1276.06 N II	56	771.901 N III	250
1243.297 N II	82	771.544 N III	350
1200.706 N I	74	765.140 N IV	200
1200.22 N I	82	764.357 N III	1020
1199.527 N I	74	763.340 N III	300
1134.98 N I	84	746.976 N II	260
1134.419 N I	100	745.836 N II	400
1037.332 C II	220	703.805 O III	390
1037.020 C II	220	702.899 O III	390
1006.051 N II	300	702.332 O III	390
979.919 N III	350	673.768 O II	590
977.020 C III	560	672.948 O II	570
955.335 N IV	430	671.397 N II	470
924.274 N IV	640	660.280 N II	450
923.669 N IV	630	645.167 N II	550
923.211 N IV	600	644.825 N II	570
923.045 N IV	560	644.621 N II	600
922.507 N IV	540	644.148 O II	530
916.708 N II	670	599.589 O III	540
916.01 N II	650	539.853 O II	560
915.96 N II	670	539.547 O II	530
835.293 O III	370	539.086 O II	600
834.467 O III	370	538.318 O II	500
833.749 O III	280	537.830 O II	580
833.332 O II	450	374.330 O III	390
832.930 O III	280	374.075 O III	340

resulting contour is clearly a complex one. As in O_2 the first ionization continuum starting at IP_1 is weak. The large absorption near 920 A is probably due to the dissociation of NO caused by transitions from the ground state to the upper $^2\Pi$ state of the so-called β bands.[6] The pronounced peak at 620 A ($h\nu = 20$ ev) corresponds energetically to Hagstrum's[7] dissociative ionization process $NO \rightarrow N + O^{-*}$ which occurred in his electron impact experiments at 19.9 ev. To what extent this mechanism contributes to or dominates over a normal photoionization transition into the continuum of Tanaka's γ series cannot be assessed from the present data.

* The aid of the Office of Naval Research is gratefully acknowledged.

[1] Weissler, Lee, and Mohr, J. Opt. Soc. Am. **42**, 80 (1952); **43**, 512 (1953).
[2] Zelikoff, Watanabe, and Inn, J. Chem. Phys. **21**, 1643 (1953).
[3] F. F. Marmo, J. Opt. Soc. Am. **43**, 1186 (1953).
[4] K. Watanabe, J. Chem. Phys. **22**, 1564 (1954).
[5] Y. Tanaka, Sci. Papers, Inst. Phys. Chem. Research (Tokyo) **39**, 456 (1942).
[6] G. Herzberg, *Molecular Spectra and Molecular Structure, Diatomic Molecules* (D. Van Nostrand Company, Inc., New York, 1950), second edition Vol. 1, p. 420.
[7] H. Hagstrum, Revs. Modern Phys. **23**, 185 (1951).

Influence of Applied Potential on the Characteristics of Photosensitive Non-Self-Maintained Region of a Low-Frequency Electric Discharge

B. D. KHOSLA
Department of Chemistry, University of Delhi, Delhi, India
(Received February 7, 1955)

THE current i in non-self-maintained region of a discharge is given by[1-3]

$$i = i_0 \exp(\alpha d), \qquad (1)$$

where α is the coefficient of ionization; d, the electrode separation; and $i_0 = n_0 \epsilon$; here n_0 is the number of primary electrons of charge ϵ. While in dc discharges with metallic electrodes, external ionizing radiations like ultra-violet, cosmic, alpha rays, etc. give n_0,[1-3] the non-self-maintained region of low-frequency electric discharge with glass electrodes is, however, sensitive[4-6] to even visible radiation

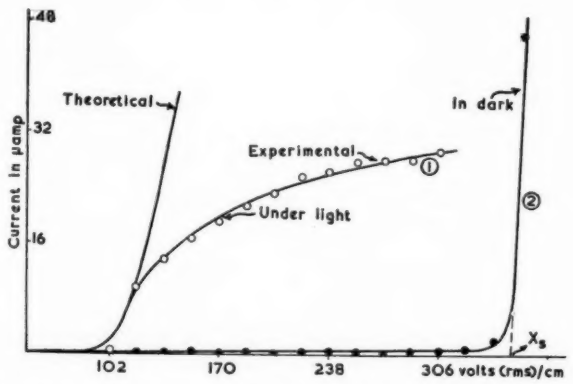

FIG. 1. Characteristic variation of the discharge current in a low-frequency electric discharge in iodine vapor. (Pressure of iodine vapor = 0.45 mm Hg; the curve 2 enables one to determine the breakdown potential (X_s) at which the secondary processes become operative.)

with quantum energy lower than the ionization potential of the medium (V_i) or of adsorbed phase shown[7] to be the source of secondary electrons in discharges with glass electrodes; thus, $\lambda = 4037$ A initiated the discharge in iodine vapor (Fig. 1).[8] When radiation was cut off, the discharge ceased indicating that the applied field X was sufficient only to produce avalanche(s) by electron(s) introduced by $\lambda = 4037$ A, but not to develop the secondary processes. Further, the current under light (i_L) appeared to disobey (1): curiously enough, i_L tended to saturate at large X (Fig. 1). This communication reports determination of α at varied X in non-self-maintained region of ac (50~) discharge in I_2 vapor,[8] which enabled the author to propound a hypothesis for variation of i_L not only with X but also light intensity[9] and frequency.[10]

Figure 2 gives the variation of $\log i_L$ with d at different X/p. Over a limited range of X/p, the curves $\log i_L$ *vs* d were sensibly linear in accord with (1). Unlike in dc discharges, the Y-axis intercept [$\log i_0$, see Eq. (1)], a measure of n_0, was not the same for all

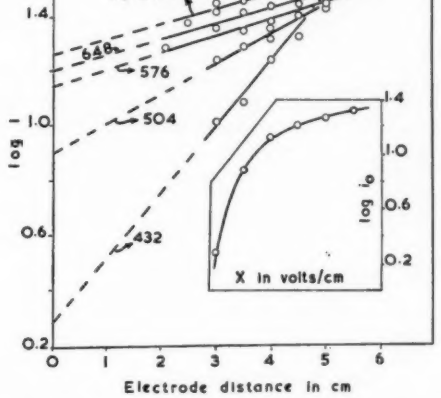

FIG. 2. Variation of the discharge current i with electrode separation d. [These data were obtained from i *vs* X curves, similar to curve 1, Fig. 1, recorded at different d. In these measurements, X was never increased beyond the breakdown value X_s since at $X \geq X_s$, Eq. (1) fails.]

curves: n_0 increased exponentially with X (inset, Fig. 2). Furthermore, the slope of the lines giving α, instead of increasing with X/p as in dc discharges with metallic electrodes,[2] decreased markedly with X/p in systems with glass electrodes and alternating fields, which accounts for the observed deviation from (1) of the variation of i_L with X (Fig. 1).

When once an electron starts ionization, a decrease in its multiplication factor α with X is incomprehensible; some mechanism therefore appears operative before the initiating electron acquires energy to cause ionization by collision. The following hypothesis may be considered: Assuming that i_L is due to introduction of electrons obtained by photoionization of pre-excited particles in the neighborhood of cathode,[11] we get

$$i_L = \epsilon \cdot n = e\psi \textcircled{X} Z \exp(\alpha d), \qquad (2)$$

where Ⓧ is the number of incident photons of energy q; ψ, the coefficient of absorption; and Z, that of photoionization, i.e., a measure of pre-excited particles. The observed increase of n_0 with X is presumably due to enhancement with increase in X of population of pre-excited particles with energy $V_i - q$. In (2), n is the number of electrons or positive ions produced in avalanches created by $\psi \textcircled{X} Z$ initiating electrons at a fixed X/p. Of these, electrons go to the anode, while positive ions move slowly towards cathode. When these last permeate the Crookes dark space, they develop a powerful potential drop F which is governed by n and controls the energy E of the positive ion[12] falling on the cathode, rather on the molecular layers adsorbed by van der Waal's forces on glass electrode. If, with increase of X or n and therefore of F, E approaches the dissociation energy of the adsorbed molecule, this last dissociates to give electronegative atoms or/and radicals; these *evaporate* into gas phase and capture the initiating electrons

to form negative ions, which on account of their low mobility, are ineffective in electron-multiplication.

[1] Harrison and Geballe, Phys. Rev. **93**, 1 (1953).
[2] B. Loeb, *Fundamental Processes of Electric Discharge in Gases* (John Wiley and Sons, Inc., New York, 1939).
[3] S. Korff, *Electron and Nuclear Counters* (D. Van Nostrand Company, Inc., New York, 1947).
[4] Subrahmanyam and Ramaiah, Z. Physik **135**, 274 (1953).
[5] Ramaiah, Gaur, and Khosla, Current Sci. (India) **23**, 399 (1954).
[6] Ramaiah, Khosla, and Gaur, J. Chem. Phys. **23**, 212 (1955).
[7] N. A. Ramaiah, J. Sci. Ind. Research (India) **13B**, 583 (1954).
[8] For experimental technique, see Reference 4.
[9] H. J. Arnikar, J. Opt. Soc. Am. **43**, 804 (1953).
[10] N. A. Ramaiah, J. Sci. Research Benares Hindu Univ. **2**, 1 (1951–52).
[11] This assumption is based upon the heights of the oscillographic pulses observed below and at the breakdown potentials; the details will be presented elsewhere.
[12] Massey and Burshop, *Electronic and Ionic Impact Phenomena* (Oxford University Press, New York, 1952).

Errata: Kinetics of Oxidation of Ammonia by Nitric Oxide

[J. Chem. Phys. **22**, 1463 (1954)]

HENRY WISE AND MAURICE F. FRECH
Jet Propulsion Laboratory, California Institute of Technology, Pasadena 3, California

PAGE 1464, the rate expression should read:

$$k=1.1\times10^{6}e^{-54\,700/RT}\ \mathrm{mm}^{-\frac{1}{2}}\ \mathrm{sec}^{-1}.$$

Page 1463, the ordinate for Fig. 3 should carry the designation

$$5+\log k.$$

Announcement

IN accordance with the By-Laws, By-Law III, Section 6c and 6d, the Nominating Committee has informed me of nominations for the new officers of the Division of Chemical Physics of the American Physical Society and I have accordingly cast a ballot whereby they are elected. These new officers are G. Herzberg as Vice-Chairman, J. R. Platt as Secretary, F. G. Brickwedde as Treasurer, and B. L. Crawford as Executive Committee member.

The complete new list of officers, with the years of retirement, is as follows:

J. G. Kirkwood	Chairman (1956)
G. Herzberg	Vice-Chairman (1956)
J. R. Platt	Secretary (1958)
F. G. Brickwedde	Treasurer (1958)
Bryce Crawford, Jr.	Executive Committee (1958)
C. H. Townes	Executive Committee (1957)
A. A. Frost	Executive Committee (1956)
K. S. Pitzer	Executive Committee (1956)
H. H. Nielsen	Executive Committee (1956)

Bryce Crawford, Jr.
Retiring Secretary

CONTENTS—*Continued*

Letters to the Editor:

Knudsen Flow through a Circular Capillary . . . W. C. DeMarcus and E. H. Hopper 1344

Vibrational Spectra of SiH_3Br and SiH_2Br_2 . . . Dana W. Mayo, Herman E. Opitz, and John S. Peake 1344

Origin of the Line Width of Pure Quadrupole Resonance . . . Y. Kôi, A. Tsujimura, and T. Fukc 1346

On the Heat of Dissociation of N_2 . . . John F. Burns 1347

On the Dissociation Energies of SrO and MgO Molecules . . . Richard F. Porter, William A. Chupka, and Mark G. Ingram 1347

Evaluation of Certain Three-Center Integrals . . . J. R. Streetman 1348

Simplified Calculation of Isotopic Exchange Half-Time . . . Leonard R. Darbee 1349

Values of Thermodynamic Functions to 12 000°K for Several Substances . . . W. Fickett and R. D. Cowan 1349

Observation of the Semiquinone of Benzoquinone . . . Scott Blois 1351

Infrared Adsorption Spectrum of Deuterated Polyvinyl Alcohol Film . . . Hiroyuki Tadokoro, Syûzô Seki, and Isamu Nitta 1351

Ionization Potentials and Charge-Transfer Spectra of Substituted Benzenes . L. E. Orgel 1352

Rate of the Gaseous Reactions, $X^+ + YH = XH^+ + Y$ . . D. P. Stevenson and D. O. Schissler 1353

Infrared Adsorption Spectra of Hexammine Metals Complexes . . . Masahisa Kobayashi, and Junnosuke Fujita 1354

Proof of the Staggered Configuration of Ethyl Chloride . . R. S. Wagner and B. P. Dailey 1355

Absorption Spectrum of Polythylene in the Near Infrared . . . Kurt Rosmann 1355

Linear Association in Solution. II. Analytical Solution . . Robert Ginell and Joel Shurgan 1356

Vibrational Energy of Deuterium Cyanide . . . Harry C. Allen, Jr., Eugene D. Tidwell, and Earle K. Plyler 1356

Reaction of Methyl Radicals with Methane and Ethane . . . M. H. J. Wijnen 1357

Gas Phase Oxidation of Formaldehyde . . . Milton D. Scheer 1357

Overvoltages at the Electrode: Method Pb/$PbCl_2$ . . . . R. Piontelli and G. Sternheim 1358

Application to Perturbation Theory to the Helium Atom . J. M. Gerhauser and F. A. Matsen 1359

Luminous Zone in the Detonation of Equimolar Acetylene-Oxygen . . . Arthur L. Bennett and Henry W. Wedaa 1359

Note on the Validity of One-Dimensional Flame Front Models . . . . Robert M. Fristrom 1360

Vector Distributions and Crystalline Proteins . . . Dorothy Wrinch 1361

Role of the Continuum in Superposition of Configurations . . . Harrison Shull and Per-Olov Löwdin 1362

Further Observations on Color Center Percursors . . . . M. Hacskaylo and P. Schwed 1362

Restricted Rotation in Amides as Evidenced by Nuclear Magnetic Resonance . W. D. Phillips 1363

Ionization Potential of the Free HO_2 Radical and the $H-O_2$ Bond Dissociation Energy . . . S. N. Foner and R. L. Hudson 1364

Vibrational Analysis of the Emission Spectrum of Coronene as a Forbidden Transition . . . Jerome W. Sidman 1365

Dissociation of Nitrogen in Shock Waves . . . . J. P. Toennies and E. F. Greene 1366

Wavelength Dependence of Photoisomerization Equilibria in Azocompounds . . . Ernest Fischer, Max Frankel, and Reuven Wolovsky 1367

Infrared Absorption Spectra of Inorganic Coordination Complexes, III. Deformation Frequencies of the NH_3 Ligand . . . San-ichiro Mizushima, Ichiro Nakagawa, and J. V. Quagliano 1367

Production of a Blue Color in Irradiated Plastic Scintillators . J. H. Pannell and B. Manning 1368

Rate of Evaporation of Graphite . . . R. J. Thorn and G. H. Winslow 1369

Energy Exchange between Cold Gas Molecules and a Hot Graphite Surface . . . Robert Gomer and Lothar Meyer 1370

Critical Constants of *n*-Butane . . . R. Singh and L. E. Shemilt 1370

Frequency Shift of the CO Stretching Band in Polypeptides and Proteins . . Samuel Krimm 1371

Absorption Coefficients of Nitric Oxide in the Vacuum Ultraviolet . H. Sun and G. L. Weissler 1372

Influence of Applied Potential on the Characteristics of Photoconnitive Non-Self-Maintained Region of a Low-Frequency Electric Discharge . . . . B. D. Khosla 1373

Errata: Kinetics of Oxidation of Ammonia by Nitric Oxide . . . 1374

Announcement . . . 1374

Clifford Frondel and C. [illegible], Jr. 1215

John A. Howe and [illegible] Goldstein 1223

[illegible] Taylor, B. H. Johnson, and John [illegible] Kilpatrick 1225

R. Dean Taylor and John [illegible] Kilpatrick 1232

R. De Vogelaere and M. Boudart 1236

Charles [illegible], George C. Pimentel, and James [illegible] Shoolery 1240

E. L. Pace and [illegible] Pierce 1248

B. Widom and O. K. [illegible] 1250

[illegible] and F. Wells 1256

David A. Dows and George C. Pimentel 1258

Howard G. Zobbel, William H. Hamill, and Russell R. Williams, Jr. 1263

Russell E. Dutt and Edwin Houston 1268

Paul G. Sears, Eugene D. Wilhoit, and [illegible] R. Dawson 1274

Richard H. Mayberry, Sheffield Gordon, and Joseph J. Katz 1277

H. C. Penny and Henry Aroeste 1281

Edward Catalano and J. W. Stout 1284

J. C. Decius 1290

Ling Yang and M. Simnad 1295

Mary Foulks Gourley and [illegible] D. Crozier 1298

J. R. Dobey and [illegible] M. Young 1302

Oliver A. Schaeffer and [illegible] R. Owen 1306

Oliver A. Schaeffer 1309

J. Kenneth O'Loane and M. [illegible] Wilson 1313

Paul Bender and James [illegible] Wood, Jr. 1316

W. Spindel and [illegible] Taylor 1318

J. A. Becker and [illegible] G. Brennan 1323

[illegible] D. Mayfield 1331

Callaway Brown, Abraham W. Berger, and [illegible] E. Smith 1340

(continued on cover three)

LANCASTER PRESS, INC., LANCASTER, PA.